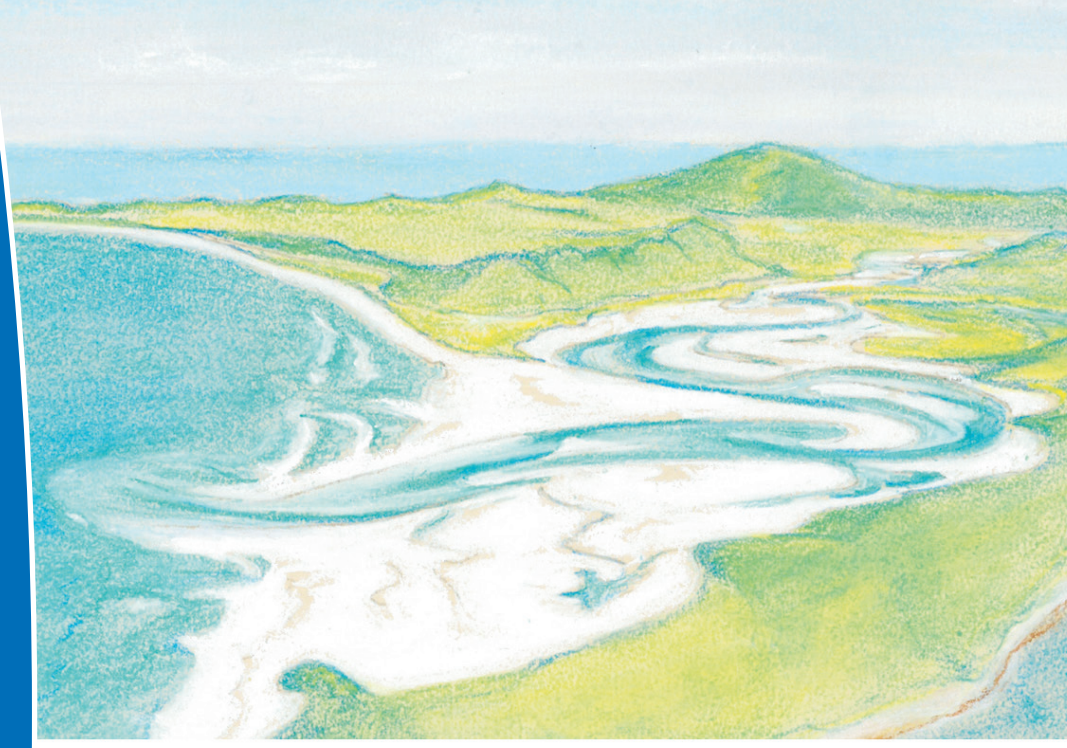

Bar and channel patterns in estuaries

Jasper R.F.W. Leuven

180 UTRECHT STUDIES IN EARTH SCIENCES

Bar and channel patterns in estuaries

Bank- en geulpatronen in estuaria

(met een samenvatting in het Nederlands)

PROEFSCHRIFT

ter verkrijging van de graad van doctor aan de Universiteit Utrecht
op gezag van de rector magnificus, prof. dr. H.R.B.M. Kummeling,
ingevolge het besluit van het college voor promoties in het openbaar te verdedigen
op woensdag 22 mei 2019 des middags te 12.45 uur

door

Jasper Robrecht Frans Willem Leuven
geboren op 8 oktober 1991 te Nijmegen

Promotor:
Prof. dr. M.G. Kleinhans

This work was financially supported by the Dutch Technology Foundation TTW
(Vici grant 016.140.316/13710).

Bar and channel patterns in estuaries

Promotor:
Prof. dr. M.G. Kleinhans

Examination committee:
Prof. T.J. Bouma
Royal Netherlands Institute for Sea Research, The Netherlands

Prof. S. Lanzoni
Università di Padova, Italy

Prof. H.E. de Swart
Universiteit Utrecht, The Netherlands

Prof. I. Townend
University of Southampton, United Kingdom

Dr. M. van der Vegt
Universiteit Utrecht, The Netherlands

Prof. Z.B. Wang
Technische Universiteit Delft, The Netherlands

ISBN 978-90-6266-534-1

Published by Faculty of Geosciences, Universiteit Utrecht, The Netherlands, in:
Utrecht Studies in Earth Sciences (USES 180), ISSN 2211-4335

Typeset using XeLaTeX

Cover: Pastel painting, Annerie Rutenfrans

Photography chapter covers: Edwin Paree [1, 2, 8 & 10] | Maarten Kleinhans [3] | Rob Leuven [5] | Huub Zwart [7] | Jasper Leuven [4, 6 & 9]

Printed by Ipskamp Printing, Enschede, The Netherlands

Correspondence to: Jasper Leuven, mail@jasperleuven.nl

Utrecht Studies in Earth Sciences 180

Bar and channel patterns in estuaries

Jasper Robrecht Frans Willem Leuven

Utrecht 2019

Faculty of Geosciences, Utrecht University

Contents

Samenvatting

Een estuarium is een ander woord voor een riviermonding die een overgang vormt van de rivier naar de zee of oceaan. Estuaria komen voor over de hele wereld in verschillende afmetingen, variërend van tientallen meters tot kilometers lang en breed. Door een open verbinding met de zee stroomt er periodiek een vloedstroom naar binnen en een ebstroom naar buiten. Aangezien een estuarium tussen een rivier en oceaan of zee ligt, is er sprake van een overgangszone tussen riviergedomineerde stroming die uitsluitend in zeewaartse richting gaat en getijdengedomineerde stroming afwisselend in twee richtingen. De overgangszone leidt tot ruimtelijke gradiënten in stroomsnelheid, sedimenttype, zoutgehalte en vegetatie. In estuaria wordt zand uit de rivier en slib vanuit de zee of rivier afgezet. Door de stroming ontstaan patronen in het sediment. Water vormt zand en slib tot zandbanken (ook wel platen genoemd), slikken en schorren, die ook wel tot het (inter)getijdengebied gerekend worden, omdat ze dagelijks overstromen tijdens vloed en droogvallen tijdens eb.

De geulen in estuaria vormen belangrijke vaarroutes naar grote havens, zoals in de Westerschelde naar de havens van Antwerpen, Vlissingen, Terneuzen en Gent. De getijdengebieden vormen leefgebieden voor een grote variëteit aan planten en dieren. Het land rondom estuaria is vaak dichtbevolkt; 21 van de 30 grootste steden ter wereld liggen in de buurt van een estuarium. Ondanks het belang van estuaria voor scheepvaart en biodiversiteit, en het potentiële overstromingsrisico voor de omringende gebieden, is het grotendeels onbekend hoe estuaria in de toekomst zullen reageren op zeespiegelstijging en menselijke invloed, bijvoorbeeld op het uitbaggeren van geulen om de bevaarbaarheid te bevorderen. Er is weinig bekend over de processen die geulen en zandbanken vormen en hoe die zich op de tijdschaal van tientallen jaren ontwikkelen. Dit staat in scherp contrast met wat bekend is over rivieren. Voor rivieren bestaan classificaties zoals *meanderend* en *vlechtend* en daarnaast is het bekend welke processen leiden tot bijbehorende bank- en geulpatronen. Dit proefschrift gaat over de bank- en geulpatronen in estuaria en de resultaten zijn van belang om management van zand en water in estuaria te optimaliseren.

In dit proefschrift onderzoek ik wat de bank- en geulpatronen in estuaria bepaalt (Hoofdstukken 2-8) en hoe deze patronen verschillen met die in rivieren (Hoofdstukken 2-6). Daarna wordt de vergaarde kennis gebruikt om te voorspellen wat het effect van zeespiegelstijging zal zijn op de morfologie van en het overstromingsrisico in estuaria wereldwijd (Hoofdstuk 9). De resultaten in dit proefschrift zijn gebaseerd op een combinatie van schaal-experimenten (Hoofdstukken 4 & 6), data van natuurlijke estuaria (Hoofdstukken 2, 3, 5, 7 & 8) en eendimensionale waterbewegingsmodellen (Hoofdstuk 9). De belangrijkste resultaten en implicaties uit dit proefschrift worden hieronder samengevat. Voor een gedetailleerde context en achtergrond wordt verwezen naar de Introductie (Hoofdstuk 1). Aanbevelingen voor toekomstig onderzoek en management worden gegeven in de Synthese (Hoofdstuk 10).

Wat bepaalt de vorm en dimensies van banken en geulen in estuaria?

Om dit te onderzoeken heb ik een grote dataset verzameld met de vormen en dimensies van 190 zandbanken in 45 estuaria wereldwijd (Hoofdstuk 2) en 823 meanderende geulen in 68 estuaria wereldwijd (Hoofdstuk 3). Op basis van theoretische voorspellingen was verwacht dat bankdimensies zouden schalen met de excursielengte van het getij. De excursielengte is de afstand die een waterdeeltje aflegt in een halve getijdencyclus. Analyse van de dataset liet echter zien dat bankdimensies schalen met de estuariumbreedte. Ook meanderdimensies, i.e. meanderlengte (afstand hemelsbreed tussen opeenvolgende bochten) en meanderamplitude (grootte van de bocht), schalen met estuariumbreedte. Bank- en geuldimensies nemen toe in zeewaartse richting, omdat in

die richting ook de estuariumbreedte toeneemt. Banken komen voor in een grote verscheidenheid aan vormen, variërend van lang en smal tot meer U-vormig tot andere complexe combinaties van simpelere vormen. Al deze bankvormen, behalve de lineaire banken, die lang en smal zijn, hebben als overeenkomst dat ze doorsneden worden door doodlopende geulen. De doodlopende geulen worden ondieper in de richting van de stroming en eindigen op een zandbank. Alle complexe banken zijn een samenstelling van simpele lineaire banken, gescheiden door doodlopende geulen. Het opsplitsen van banken bij de doodlopende geulen resulteerde in een universele relatie die beschrijft dat de banklengte gelijk is aan zeven keer de bankbreedte.

Wat is de relatie tussen de estuariumvorm, het bankpatroon en de stroomsnelheden?

Het concept van het *ideale estuarium* beschrijft estuaria als perfect convergerende geulen, waarin de stromingsenergie per eenheid breedte constant blijft langs de geul. Aan deze ideale toestand kan voldaan worden wanneer de getijslag en stroming constant zijn langs het gehele estuarium, zodanig dat energieverlies als gevolg van wrijving wordt gecompenseerd door de toename in energie door de convergentie van de geul. Toch blijkt uit observaties van natuurlijke estuaria dat de vorm regelmatig afwijkt van de perfect convergerende vorm (Hoofdstuk 5). Hoofdstuk 5 laat tevens zien dat getijdenbanken voorkomen op plekken in het estuarium die veel breder zijn dan verwacht op basis van de ideale vorm. Dit betekent ook dat de morfologie die onderwater voorkomt correleert met de horizontale variaties in vorm van het estuarium (Hoofdstuk 7). Omdat de morfologie hiermee voorspelbaar is, kunnen ook de waterdiepte en stroomsnelheid van het water geschat worden (Hoofdstuk 8). Alle voorspellende relaties voor bankpatronen zijn gecombineerd met al bestaande relaties voor estuaria en geprogrammeerd in een toolbox. Met behulp van deze toolbox is het mogelijk om, op basis van alleen het breedteprofiel van het estuarium en getijslag bij de monding, een voorspelling te maken van de evenwichtsmorfologie en karakteristieke stroomsnelheden (Hoofdstuk 8).

Hoe ontwikkelen getijdenbanken zich door de tijd?

De tijdschalen waarop banken en geulen dynamisch gedrag vertonen in natuurlijke systemen varieert van decennia tot eeuwen. Omdat de periode waarover in het verleden gemeten is vaak korter is, zijn vaak onvoldoende data beschikbaar om bankvorming en ontwikkeling in natuurlijke systemen te bestuderen. Vandaar dat de dynamiek van geulen en banken bestudeerd is met behulp van de *Metronoom*, een kantelende stroomgoot. Deze stroomgoot is een zandbak gevuld met water en zand, die periodisch over zijn breedteas kantelt om eb- en vloedstromen na te bootsen. Met behulp van de stroomgoot zijn een serie experimenten uitgevoerd.

In de initiële fase van de experimenten vormen zich alternerende banken in een rechte geul. Deze alternerende banken zijn onderling verbonden met kaarsrechte drempels (Hoofdstuk 4). Deze drempels zijn minder diep dan de banken, waardoor het water er nog gemakkelijk overheen kan stromen. Al snel ontwikkelt de stroming zich zodanig dat de eb- en vloedstroom beide een ander pad nemen. Deze karakteristieke stroming vervormt de drempel in zogenaamde U-vormige banken, met een doodlopend einde in de tegenoverliggende geul (Hoofdstuk 4). In latere fases ontstaan zandbanken in het midden van het estuarium. Vervolgens wordt de stroming om deze banken heen geleid, waardoor de botsing van de stroming tegen de oevers van het estuarium leidt tot verbreding. Dat betekent dat het estuarium juist daar verbreedt waar zich initieel banken vormden, terwijl het estuarium relatief smal blijft op tussenliggende locaties (Hoofdstuk 6). De experimenten laten zien dat, in afwezigheid van harde begrenzingen, zoals harde geologische lagen of dijken, een estuarium zich ontwikkelt tot een onregelmatige vorm, in tegenstelling tot de perfect convergerende vorm, die te verwachten is op basis van een ideaal estuarium.

In hoeverre lijken banken en geulen in estuaria op deze in rivieren?

In dit proefschrift heb ik herhaaldelijk een vergelijking gemaakt tussen estuaria en rivieren om te onderzoeken in welke mate het mechanisme van bankvorming en de schaling van banken overeenkomt (Hoofdstukken 2-6). Dit resulteerde in een overzicht van de belangrijkste overeenkomsten en verschillen tussen bank en geulpatronen in estuaria en rivieren (Hoofdstuk 10).

In zowel rivieren als estuaria schalen de bank- en geuldimensies met de grootschalige dimensies van de vorm van het estuarium, bijvoorbeeld met estuariumbreedte. Dit betekent dat relaties voor rivieren als benadering toegepast kunnen worden voor estuaria. Vernauwingen van het estuarium leiden bijvoorbeeld zeer waarschijnlijk tot het verdwijnen of verkorten van banken, net als in rivieren. Daarnaast kunnen geologen de schalingsrelaties tussen bank- en geuldimensies gebruiken wanneer zij dagzomend gesteente interpreteren. Uit dagzomend gesteente is bijvoorbeeld een typische geuldiepte of -breedte af te leiden, die gebruikt kan worden om een inschatting te maken van bankdimensies en stroomsnelheden. Andersom geredeneerd zou een enkele meting, of bij voorkeur meerdere, van bank of geuldimensies al voldoende zijn om een inschatting te maken van de geulbreedte en getijdenprisma en daarmee ook stromingscondities. In tegenstelling tot rivieren kan het grootschalige patroon van estuaria niet samengevat worden in een enkele klasse (bijvoorbeeld meanderend of vlechtend). Immers gaat het patroon in estuaria over van meer meanderend aan de landwaartse zijde naar meer vlechtend in de zeewaartse richting. Deze verandering in bankpatroon gaat gepaard met een sterke toename van bank- en geuldimensies. Dit kan gebruikt worden als een indicator voor invloed van eb en vloed. De dynamische processen die geulmigratie en omvorming van banken beschrijven zijn uniek voor estuaria. Daarmee zijn relaties voor rivieren, die afhankelijk zijn van dynamische processen, niet direct toepasbaar op estuaria, zoals relaties die de sedimentaire opbouw of bewaarkans van afzettingen beschrijven.

Wat zijn de gevaren als gevolg van voorspelde zeespiegelstijging?

De morfologische toolbox (Hoofdstuk 8) is gekoppeld aan een eendimensionaal hydrodynamisch model om te kwantificeren wat het effect van zeespiegelstijging is op de zandbehoefte van en waterstand in estuaria (Hoofstuk 9). In de toekomst stijgt niet alleen de zeespiegel, maar verandert ook de getijslag bij de monding doordat amfidromische punten verschuiven als gevolg van zeespiegelstijging. Amfidromische punten zijn knooppunten waaromheen het getij circuleert in ondiepe zeeën, bijvoorbeeld op de Noordzee.

Het was verrassend dat kleine (i.e. ondieper dan 10 m) en grote estuaria (i.e. dieper dan 10 m) andere bedreigingen te wachten staan als de zeespiegel stijgt. In kleine estuaria zal het overstromingsrisico toenemen in de komende 100 jaar. Berekeningen tonen een stijging tot wel 1 meter aan extra waterstand, bovenop de toename in zeespiegel van 1 meter. Dit effect is het sterkst als de estuaria te weinig sediment ontvangen om mee te groeien met de nieuwe zeespiegel. Als ze wel voldoende sediment krijgen, zullen de waterstanden alleen toenemen met de zeespiegelstijging van 1 meter. Grote estuaria lopen het risico op zandhonger, vooral als de getijslag bij de monding afneemt. Een afnemende getijslag leidt namelijk tot een afname in de totale hoeveelheid water die door het estuarium stroomt. Het gevolg is dat de geulen moeten verkleinen om aan het nieuwe evenwicht te voldoen; hiervoor is een grote hoeveelheid extra sediment nodig. Mocht er onvoldoende sediment beschikbaar zijn, dan zal het estuarium verdrinken, wat betekent dat getijdengebied verloren gaat. Het getijdengebied is belangrijk voor de biodiversiteit. De resultaten in Hoofdstuk 9 laten ook zien dat deze bedreigingen sterk gereduceerd kunnen worden wanneer we in de toekomst meer ruimte maken voor estuaria, in analogie met Ruimte voor de Rivier projecten. Meer ruimte voor estuaria leidt tot grotere getijdengebieden, wat helpt bij het dempen van de getijgolf en zo wordt het overstromingsrisico verminderd. Het wordt daarom aangeraden om deze opties verder te

onderzoeken voordat mogelijk dijkdoorbraken leiden tot landverlies en sociaal-economische schade in dichtbevolkte gebieden.

Welk onderzoek naar bank- en geulpatronen in estuaria is nodig in de toekomst?

Het is nog steeds onbekend hoe estuaria zich ontwikkelen onder invloed van menselijk handelen en zeespiegelstijging op lange tijdschalen, dat wil zeggen van eeuwen tot millennia, en hoe de dynamiek van banken en geulen de vorm van estuaria op deze tijdschaal stuurt. Daarom heb ik de volgende onderwerpen aangewezen voor toekomstig onderzoek, die bijdragen aan het begrip en management van de morfologische ontwikkeling van estuaria (Hoofdstuk 10):

1. Het effect van variaties in zeespiegel op de ontwikkeling van estuaria behoeft verder onderzoek met morfologische modellen en experimenten;
2. De effecten van planten, bodemvroeters en -filteraars op de morfologie van estuaria moet worden onderzocht in experimenten, modellen en toolboxen, omdat ze de stroming, erosie en sedimentatie beïnvloeden en daarmee de ontwikkeling van estuaria sturen;
3. Theoretische voorspellers voor bankvorming hebben een revisie nodig, zodat duidelijk wordt welke mechanismen leiden tot bankvorming;
4. De oorzaken voor de vorming en blijvende aanwezigheid van eb- en vloedgeulen, die elkaar ontwijken, moet verder onderzocht worden in numerieke modellen en experimenten.

Summary

Estuaries, also called river mouths, form the transitional zones between rivers and oceans. Estuaries occur all over the world at a wide range of spatial scales from tens of metres to tens of kilometres. The open connection to the ocean allows for tidal currents to periodically flow in and out of estuaries. Since estuaries are also connected to rivers, a transitional zone arises from river dominance with unidirectional flow to tidal dominance with bidirectional flow. The transition creates an along-channel gradient of flow velocity, sediment type, salinity and vegetation. Estuaries accumulate fluvial sand and finer marine mud, which are sediments available for the formation of intertidal sand bars, mudflats and salt marshes.

The channels in estuaries provide access to billion-dollar-harbours (e.g. the Western Scheldt, Elbe, and Yangtze), while the intertidal bars form valuable habitat for biodiversity and the surrounding land is often densely populated. In total, 21 of the world's 30 largest cities are located in the vicinity of estuaries. Despite the importance of estuaries, it remains largely unknown how estuaries will respond to future sea-level rise and human intervention. Moreover, little is known about the equilibrium bar and channel patterns in estuaries and the dynamics of bars and channels over time. In contrast, for rivers, classifications such as *meandering* and *braided* are available, and it is known which processes cause these bar and channel patterns. This thesis contributes to the understanding of bars and channels in estuaries, which can be used to optimise the management of sediment and water in estuaries.

In this thesis I assess what determines the bar and channel pattern in estuaries (Chapters 2-8) and how tidal bars differ from their fluvial counterparts (Chapters 2-6). Subsequently, the effects of sea-level rise on morphology and flood risk of estuaries worldwide are predicted based on the aforementioned assessment (Chapter 9). The results in this thesis are based on a combination of physical scale experiments (Chapters 4 & 6), data from natural systems (Chapters 2, 3, 5, 7 & 8) and one-dimensional hydrodynamic modelling (Chapter 9). The main findings and implications of this dissertation are summarised below. For a detailed context and background information, the reader is referred to the Introduction (Chapter 1). Recommendations for future research and management are given in the Synthesis (Chapter 10).

What determines the shapes and dimensions of bars and channels in estuaries?

I collected a large database with 190 bars in 45 estuaries worldwide (Chapter 2) and 823 meandering channels in 68 estuaries worldwide (Chapter 3). From theory, it was expected that tidal bars scale with the tidal excursion length, which is the distance a particle of water travels in half a tidal cycle. However, analysis of the dataset showed that tidal bars scale with the estuary width. Moreover, also meander dimensions, i.e. meander length and meander amplitude, scale with local channel width. All bar and channel dimensions in estuaries increase in seaward direction. Bars occur in a large variety of shapes: from long and narrow to more U-shaped and other more complex combinations of simpler types. All bar types, except for the linear bars, are characterised by the presence of so called *barb channels*. Barb channels shallow in either the ebb or flood direction, terminating on a bar. All complex bars are amalgamations of multiple simple linear bars that are partly separated by barb channels. Partitioning (i.e. splitting-up) of the bars at the barb channels resulted in a universal relation between bar width and bar length of 1 to 7.

What is the relation between the planform shape, the bar pattern and flow velocities in estuaries?

The concept of an *ideal estuary* describes an estuary as a perfectly converging channel in which the energy per unit width remains constant along-channel. The ideal state can be met when the loss of tidal energy by friction is balanced by the gain in tidal energy per unit width by channel convergence such that the tidal range and tidal currents are constant along-channel. However, in natural systems planform shapes often deviate from the converging shape (Chapter 5). Moreover, Chapter 5 shows that tidal bars typically occur at locations where the estuary is much wider than expected from a perfectly converging shape. This also means that subaqueous morphology correlates with horizontal variations in the estuary planform (Chapter 7). Because flow velocities typically depend on water depth, the predictability of estuarine morphology also enables the prediction of typical flow velocities (Chapter 8). The predictive relations for bar patterns were combined with existing relations and programmed in a toolbox. This tool predicts the equilibrium morphology and typical flow velocities, based only on the tidal range at the mouth and the estuary width profile (Chapter 8).

How do tidal bars and channels evolve over time?

The timescale over which bars and channels are dynamic in natural systems is typically in the order of decades to centuries. Available data are often insufficient to study bar formation and evolution in natural systems. Therefore, the dynamics of bars and channels were studied in the *Metronome*, which is a tilting flume. The flume is a sandbox filled with water and sand, and it periodically tilts over the short central axis to simulate ebb and flood flow.

In the initial phase of the experiments, alternating bars form in a straight channel with a narrow, straight sill between consecutive bars (Chapter 4). Mutually evasive currents modulate the sill into U-shaped bars forming in both opposing channels. In later phases, sand bars build up in the centre of the estuary, after which flow is diverted around the bars. The diversion of flow results in local widening where tidal bars initially formed, while the estuary remains relatively narrow at zones between the bars (Chapter 6). The experiments show that estuaries without any hard boundaries (such as bedrock geology or dikes) evolve into planforms with an irregular shape rather than the perfectly converging shape.

How do the bar and channel patterns in estuaries compare to those in rivers?

In this thesis, I repeatedly compared estuaries with rivers to test the hypothesis that mechanisms of bar formation and scaling in estuaries are similar to those of bars in rivers (Chapters 2-6). After rigorous tests, the key similarities and differences between rivers and estuaries were determined (Chapter 10).

In both rivers and estuaries, bar and channel dimensions scale similarly with the large-scale planform dimensions, e.g. the channel width. Typical relations for rivers can thus be applied as approximate relations for estuaries. For example, narrowing of an estuary will most likely lead to the disappearance or shortening of tidal bars, as is the case in rivers. Similarly, geologists can use the scaling relations between channel dimensions and bar dimensions in outcrop interpretation, where the shape of tidal channel belts or estuaries has been identified, but wherein bar configuration is typically not recognisable and typical flow conditions are unknown. With the empirical assessment tool presented in this thesis, a single measurement, or preferably a few measurements, of bar or channel dimensions would be sufficient to reconstruct typical channel width and local tidal prism and therefore also typical flow conditions. While the overall bar patterns of a single estuary cannot be generalised in a single class (e.g. meandering or braided) as in rivers, the seaward transition from meandering to braided and the strong increase in channel and bar dimensions can be used as an indicator for tidal influence, for example when interpreting the rock record. However, the dynamic processes of channel migration and bar reworking, including the formation of channels, bars, sills and

barb channels in estuaries are unique. This implies that it is not straightforward to apply relations for rivers that depend on the dynamics of channels and bars on estuaries, such as relations for preservation and subsurface architecture.

What are the threats induced by expected future sea-level rise?

The morphological tool (Chapter 8) was coupled with a one-dimensional hydrodynamic model to quantify the sea-level rise induced threats to be expected in estuaries (Chapter 9). Not only will mean sea level increase in the future, but also tidal amplitude at estuary mouths is likely to change because of sea-level rise induced shifting of amphidromic points. Amphidromic points are tidal nodes around which tidal waves rotate on shallow continental shelf seas.

Surprisingly, the results show that small (shallower than 10 m deep) and large (deeper than 10 m) estuaries face opposing threats under future sea-level rise. In the next 100 years, small estuaries face enhanced flood water levels of up to 1 metre on top of the 1 metre increase in mean sea level expected from climate change, provided they receive insufficient sediment to adapt. However, if they receive sufficient sediment, they will adapt to their new boundary conditions and water levels only increase by the increase in mean sea level. In contrast, large estuaries face sediment starvation, especially if the tidal amplitude at the mouth decreases: this reduces the total volume of water flowing through the estuary. The required channel volume scales with the volume of water flowing through; channel dimensions thus have to reduce to adapt to the new equilibrium, requiring excessive amounts of sediment. Insufficient sediment supply means drowning of the estuary with the implication of loss of ecologically valuable intertidal area. However, the results in Chapter 9 also show that managed realignment, i.e. allowing estuaries to increase in width, is an important measure that aids in mitigating the adverse effects of sea-level rise. Managed realignment increases intertidal area and thereby enhances tidal damping, which means that it reduces flood risk. Therefore, realignment measures need to be implemented before potential dike breaches lead to land loss in densely populated areas.

What further research is required on bar and channel patterns in estuaries?

It remains partly unknown how estuaries evolve over longer timescales, i.e. from centuries to millennia, and how the dynamics of bars and channels can modify the estuary planform. Therefore, I identified the following topics for future research that will aid in understanding and managing the morphological evolution of estuaries (Chapter 10):

1. The effects of sea-level variations need further testing in morphological models and experiments;
2. Eco-engineering species, e.g. plants and bioturbators, need to be implemented in experiments, models and toolboxes, because they affect flow and sediment transport and thereby steer further evolution of estuaries;
3. Physics-based theory for bar formation and bar dynamics requires an update, such that it illustrates which underlying mechanisms drive bar formation;
4. The causes for the formation and stable presence of mutually evasive ebb- and flood-dominated tidal channels should be studied further in numerical models and experiments.


1

Chapter 1 | Introduction

1.1 Context

Estuaries form at locations where rivers transition into the sea and occur all over the world at a wide range of spatial scales from tens of metres to tens of kilometres. The open connection to the ocean allows for tidal currents to periodically flow in and out of these systems. The position of estuaries between the river and the ocean results in transitional zones between river-dominance with unidirectional flow and tidal-dominance with bidirectional flow. These transitions create along-channel gradients of flow velocity, sediment type, salinity and vegetation (Pritchard, 1967; Hume and Herdendorf, 1988; Davidson and Council, 1991; Dalrymple et al., 1992; Perillo, 1995; Savenije, 2006). The presence of both river flow and tidal flow results in the accumulation of fluvial sand and finer marine mud (Savenije, 2006), which are available for the formation of intertidal sand bars, mudflats and salt marshes.

From aerial-photography it is apparent that the planform shape of alluvial estuaries is often irregular with periodic variations in width (Fig. 1.1). Within the boundaries of the estuary banks, dynamic patterns of channels and bars, also called shoals, occur. In the landward direction, the bars typically become smaller in length and width and the number of channels reduces (Fig. 1.1). The general trend is that estuaries narrow approximately exponentially in landward direction. However, periodic increases in the estuary width suggest that a complexity is superimposed on the converging shape. The planform shape is an expression of antecedent geology, human interference, and the response time for adaptation to boundary conditions (Townend et al., 2000; Townend, 2005; de Haas et al., 2017), such as sea-level rise and sediment availability. In absence of bedrock geology, the planform shape can be modulated over time by the dynamics of migrating channels and bars.

Most present-day estuaries formed when low-lying glacial and river valleys drowned under rising sea-level in the early to middle Holocene (van der Spek and Beets, 1992; Hijma and Cohen, 2011; de Haas et al., 2017). Such drowning created a considerable volume of accommodation space, making former valleys efficient sediment traps for sediment from both the river and the sea (e.g. Boyd et al., 1992; Dalrymple and Choi, 2007). Sediment input in many of these systems eventually exceeded accommodation space created by sea-level rise, resulting in progressive infilling. Some tidal systems that formed during the Holocene transgression still exist today, whereas others have completely filled in (e.g. Dalrymple et al., 1992; Martinius and van den Berg, 2011), for example the Oer-IJ Estuary in the Netherlands (Vos et al., 2015). Whether estuaries persist or close off is attributed to a wide range of boundary conditions, including river discharge, tidal amplitude at the mouth, sediment supply and wave action (Bruun and Gerritsen, 1960; de Haas et al., 2017). The same boundary conditions are responsible for the processes that drive the morphodynamics of channels and bars within the estuary.

Estuaries such as the Western Scheldt, Elbe, and Yangtze provide access to economically valuable harbours (de Vriend et al., 2011), form valuable ecological habitat (e.g. Bouma et al., 2005) and are often surrounded by densely populated regions, with 21 of the world's 30 largest cities being in vicinity of estuaries (Ashworth et al., 2015). However, estuaries are continuously under pressure by human influence. For example, dikes cut off the ecologically valuable flanking mudflats, salt marshes and freshwater riparian systems. The main shipping channels are dredged for access to harbours

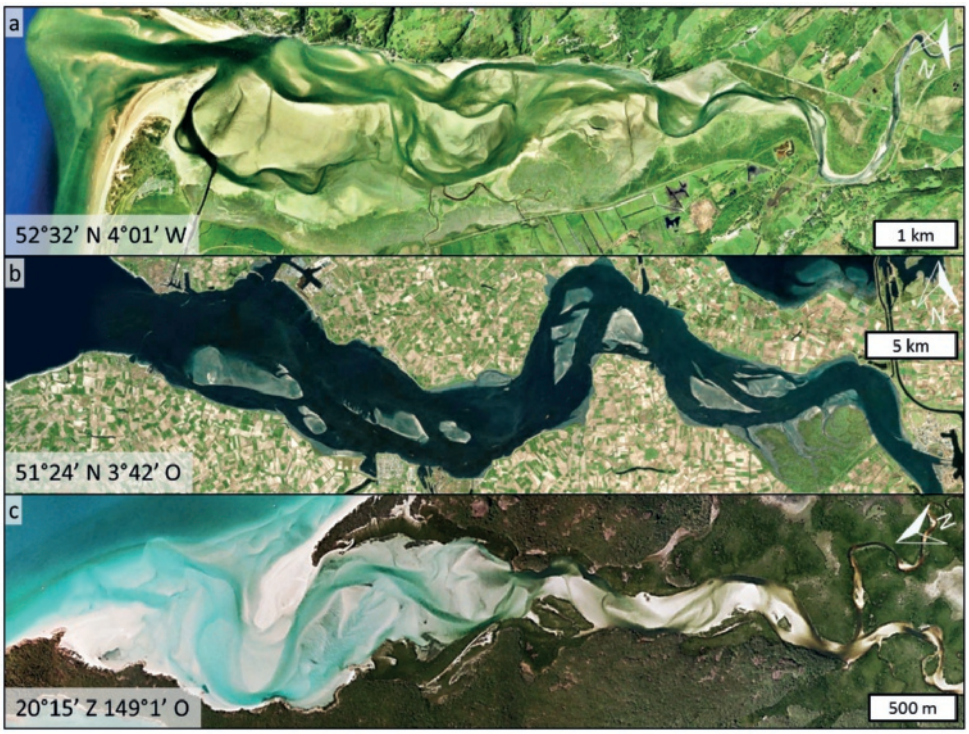

Figure 1.1 Examples of alluvial estuaries filled with tidal bars: (a) a largely natural estuary, the Dovey (UK); (b) a strongly human-influenced estuary, the Western Scheldt (NL); (c) a geologically confined estuary at Whitehaven Beach (AU). Aerial photographs were obtained from Google Earth (a,c) and Bing maps (b) (accessed September 2018).

(de Vriend et al., 2011), enhancing flooding risk and potentially reducing intertidal sandbar area, which forms valuable ecological habitat (e.g. Bouma et al., 2005).

The natural evolution of estuaries and the effects of human interventions and rising sea-level on the equilibrium bar patterns and dynamics of channels are largely unknown. Only a few studies illustrate that estuaries may drown under sea-level rise (van der Wegen, 2013) and that estuary size matters for future water levels and thus flood safety (Ensing et al., 2015; Du et al., 2018). Nevertheless, there is still a pressing need to understand the drivers of estuarine morphodynamics and their likely response to natural and anthropogenic changes (Ashworth et al., 2015). Governments, research institutes and consultancies urgently need to understand whether, for example, the Ems-Dollard and Western Scheldt Estuary will evolve towards a single-channel estuary (Meersschaut et al., 2004; Wang et al., 2011; Monge-Ganuzas et al., 2013), what dredging and disposal strategies are most optimal for both shipping and ecology and if estuaries need protection of secondary channels by management strategies. After all, migrating channels threaten bank stability and impose a risk of land erosion, while migrating bars threaten the minimum navigational channel depth and impose dangerous currents where channel bends become too sharp. Additionally, the perpetual dynamics and reworking of bar tops is important to maintain the low dynamic intertidal area and prevent these areas from accreting above the high water level. Therefore, knowledge on equilibrium shapes and dimensions of bar and channel patterns and their dynamics over time is vital.

This thesis enhances current understanding of bar and channel patterns in estuaries and the temporal dynamics of channels and bars, i.e. over what time period they form and how the patterns evolve over time. To do so, data from present-day estuaries are combined with results from laboratory scale experiments and numerical modelling.

1.2 General objective and approach

In this thesis, I focus on the dimensions, shapes and controls on bar and channel patterns in estuaries. In contrast to their fluvial counterparts, bar and channel patterns in estuaries are poorly understood. Therefore, the objectives of this thesis are:

1. To quantify and understand equilibrium bar and channel patterns in estuaries
2. To assess the temporal dynamics of channels and bars in estuaries

To study this, a combination of stability models, data collection from natural systems, physical scale experiments and numerical modelling was used (Fig. 1.2).

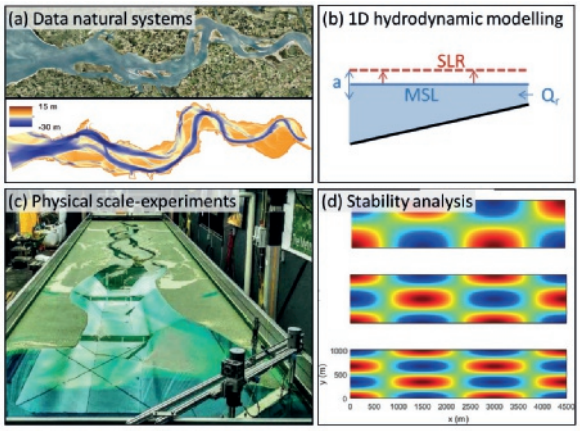

Figure 1.2 Methodologies used in this project.

The research presented in this thesis is part of a larger Vici-project: 'Turning the tide: dynamics of channels and shoals in estuaries with sands and mud'. The aim of this project was to investigate and forecast how channel-shoal dynamics in estuaries result from geomorphological processes and human interference. The effect of cohesive material on the long-term evolution of estuaries is the topic of the PhD thesis of my colleague Lisanne Braat (Braat, 2019) and the bed slope effects are considered in the PhD thesis of my colleague Anne Baar (Baar, 2019). Moreover, I collaborated with Wout van Dijk and Harm Jan Pierik in their Postdoctoral projects, in which we respectively studied the effects of dredging and disposal of sediment and resistant geological layers on the dynamics of channels and bars. Results from these projects will be incorporated in the synthesis of this thesis.

1.3 Bar and channel patterns

Bar and channel patterns in estuaries are poorly understood compared to their fluvial counterparts (Coco et al., 2013). For rivers, the physical mechanisms that explain bar formation have been identified (e.g. Leopold and Wolman, 1957; Ikeda, 1973; Ikeda et al., 1981; Ashmore, 1982; Blondeaux

and Seminara, 1985; Ashworth et al., 2000; Sambrook Smith et al., 2006; van de Lageweg et al., 2014), predictors for bar dimensions (Struiksma et al., 1985; Crosato and Mosselman, 2009) have been tested and detailed classifications for planform patterns have been made (Kleinhans and van den Berg, 2011), such as meandering, braided and anastomosing patterns (Fig. 1.3). In contrast, for tidal systems, only some pioneering stability theories are available (Seminara and Tubino, 2001; Schramkowski et al., 2002; Schramkowski et al., 2004) together with qualitative descriptions of tidal bars (van Veen, 1950; Dalrymple et al., 1992; Dalrymple and Choi, 2007). The limited understanding of bar and channel patterns in tidal systems compared to rivers is mostly caused by theoretical and practical challenges in numerical models and scaled experimental approaches imposed by the bidirectional flow.

Here, I briefly review what is known about bar and channel patterns in rivers, because it provides the source of hypotheses for bar and channel patterns in estuaries, under the tentative assumption that mechanisms of bar formation and scaling of bars in estuaries are similar to those of bars in rivers. Then, the qualitative descriptions that are available for tidal bars are given, along with the available theories, because they provide a frame of reference for subsequent chapters in this thesis.

1.3.1 Bar and channel patterns in rivers

Initiation of channels and bars

Incipient bar formation and meandering has been thoroughly studied for rivers in scale experiments (Leopold and Wolman, 1957; Ikeda, 1973; Ashmore, 1982; Fujita and Muramoto, 1985; Eaton et al., 2006; Visconti et al., 2010; Frascati and Lanzoni, 2013; van de Lageweg et al., 2014), numerical models (Schuurman et al., 2013), theoretical models (Seminara and Tubino, 1989; Struiksma et al., 1985; Repetto et al., 2002) and natural systems (Lewin, 1976; Cant and Walker, 1978; Ashworth et al., 2000; Sambrook Smith et al., 2006). In summary (review by Kleinhans, 2010), the channel width and depth are determined by the balance between bank erosion and floodplain formation. The width and width-to-depth ratio subsequently determine whether the bar pattern becomes meandering or braided. A combination of bank retreat and bar and floodplain formation (Parker et al., 2011; Eke, 2014; van de Lageweg et al., 2014) causes migration of bars in meandering channels, which implies that increased resistance in floodplain material reduces channel migration.

It is important to note here that chute cutoffs are indicative of channel patterns transitioning from more meandering to more braided (Fig. 1.3). The number of downstream confluences and channels splitting around bars increases with the degree of braiding. All these splitting points and confluences can be considered as bifurcations (van Dijk et al., 2014), for which stability theory is available. It has been shown that bifurcations are inherently unstable in the majority of rivers on Earth (Kleinhans et al., 2013; Bolla Pittaluga et al., 2015), but it remains unknown whether this theory holds for the tidal environment.

Bar dimensions and shapes

Sand bars occur in a large variety of shapes: from long and narrow to circular or squared, and in a variety of sizes, from metres to kilometres. Detailed classifications exist for river bars, along with a description of the forming mechanisms (Cant and Walker, 1978; Bridge, 1993; Ashworth et al., 2000; Bridge, 2003; Sambrook Smith et al., 2006; Kelly, 2006; Rice et al., 2009; Kleinhans and van den Berg, 2011; Schuurman et al., 2013). Most classifications discriminate between simple unit bars and compound bars. Unit bars are small (100-300 m) bars with a lobate shape that have their highest point at the downstream end followed by a steep face (e.g. Sambrook Smith et al., 2006) (Fig. 1.4). Compound bars comprise multiple amalgamated unit bars and are formed by several stages of erosion and deposition (e.g. Bridge, 2003; Ashworth et al., 2000; Schuurman et al., 2013) (Fig. 1.4). More detailed classifications discriminate between side bars, chute bars, point bars and midchannel

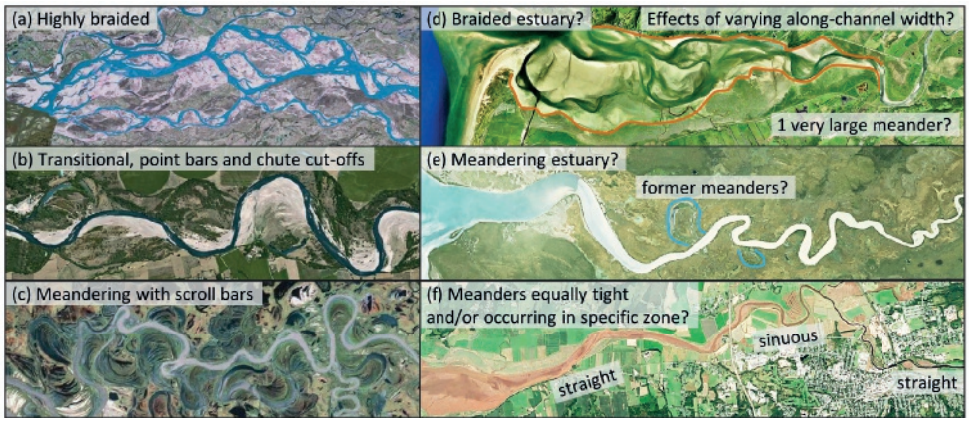

Figure 1.3 [left] River pattern classification. (a) Brahmaputra River, India (10 km wide braid plain), (b) Allier River, France (0.8 km wide meander belt), (c) Koyukuk River, Alaska (10 km wide meander belt). [right] Open questions about estuarine patterns. (d) Dovey Estuary, Wales, (e) South Aligator River, Northern Territory, Australia, (f) Salmon River, Cobequid Bay, Canada. Photographs were obtained from Google Earth (accessed September 2018).

bars, showing that compound bars occur in a wider variety of shapes and are generally larger than unit bars.

In addition to qualitatively describing the bar and channel pattern, it is also possible to quantify the channel pattern. The shapes and dimensions of meanders are a major characteristic of meandering rivers (Leopold and Wolman, 1960). Typical scaling relations exist between meander dimensions, river discharge, and local channel width (e.g. Inglis, 1949; Leopold and Wolman, 1960; Hey and Thorne, 1986). Meander dimensions typically increase for increasing channel width and increasing discharge.

Free and forced bars

The dynamics of river bars are partly determined by the planform pattern of the channel. River bars can be either free or forced. While forced bars are forced to their location by the planform shape of the channel, free bars can migrate freely and occur in straight or weakly curved channels (Ikeda et al., 1981; Blondeaux and Seminara, 1985; Tubino et al., 1999; Seminara, 2010; Schuurman et al., 2013). It was found that the topographic forcing of bars occurs on (1) the scale of individual bars, due to meander bends and embayments, which fix the bars at their location (Struiksma et al., 1985; Repetto and Tubino, 2001; Wu et al., 2011) and (2) the reach scale, an order of magnitude larger than individual bars, due to variations in channel width and discharge (Tubino et al., 1999; Seminara, 2010; Kleinhans and van den Berg, 2011; Schuurman et al., 2013). In addition, the channel width may be non-uniform in space, causing local flow expansion if the channel width is sufficiently wide, which in turn causes the formation of forced bars (e.g. Repetto and Tubino, 2001; Repetto et al., 2002; Seminara, 2010; Zolezzi et al., 2012; Frascati and Lanzoni, 2013).

Controls on bar and channel pattern

Two complementary approaches to predict bar and channel pattern in rivers are based on (1) empirical potential-specific stream power (Kleinhans and van den Berg, 2011) and (2) theory for bar formation and stability (Struiksma et al., 1985; Seminara and Tubino, 1989; Crosato and Mosselman, 2009). The first method is based on pattern-independent channel characteristics, while the latter depends on hydrological measures that caused the channel pattern as well as the width-to-depth ratio.

The potential-specific stream power in combination with sediment particle size results in thresholds for transitions between meandering rivers with scroll bars, meandering rivers with chutes or weakly braided rivers and braided rivers (Kleinhans and van den Berg, 2011). Higher stream power means more power to erode banks, which results in rivers with a high width-to-depth ratio – relatively wide and shallow. From bar theory (Struiksma et al., 1985; Crosato and Mosselman, 2009), it follows that these relatively wide rivers develop more bars across the width and are classified as braided. In contrast, rivers with low stream power (and low width-to-depth ratios) hardly develop bars or meanders and are straight, sinuous or anastomosing. In between these two extremes, weakly braided and meandering rivers are found. Predicted channel pattern from empirical prediction agrees with predicted braiding index from theoretical predictions (Kleinhans and van den Berg, 2011), which suggests that if estuaries are like rivers, empirical as well as theoretical predictors could be of use to describe bar and channel patterns in estuaries.

1.3.2 Bar and channel patterns in estuaries

Qualitative descriptions of channels and bars

For estuaries, van Veen (1950) and Dalrymple and Choi (2007) defined three different types of tidal bars: linear bars, U-shaped bars and sidebars. However, this leaves a large range of bars with more complex shapes unclassified. Because these bars probably amalgamated from other smaller bars, they could be classified as compound bars in analogy with rivers (see also Chapter 2 and Fig. 1.4).

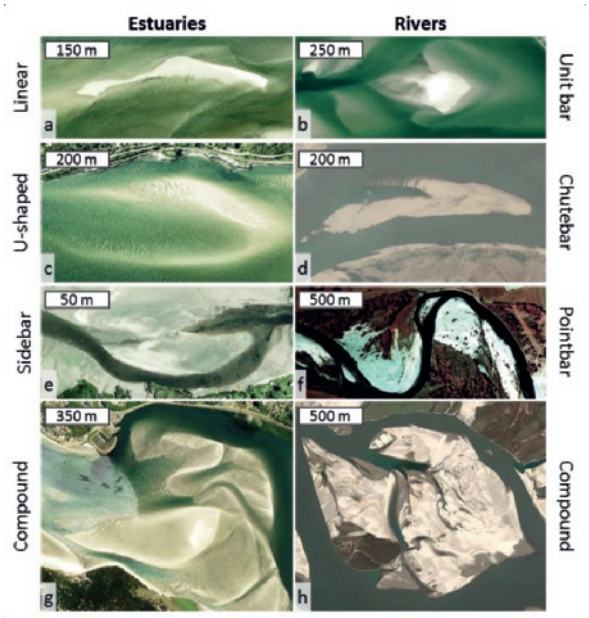

Figure 1.4 Aerial photographs of estuarine bars, with their potential counterparts in rivers. (a) Dovey Estuary (UK, 52°32' N 4°01' W); (b) Saskatchewan River near Outlook (Canada, 51°33' N 107°04' W); (c) Dovey Estuary (UK, 52°32' N 4°01' W); (d) Brahmaputra (Bangladesh, 25°24' N 87°05' E); (e) Nyfer Estuary (UK, 52°01' N 4°49' W); (f) Allier River (France, 46°29' N 3°19' E) (Kleinhans and van den Berg, 2011); (g) Netarts Bay (USA, 45°25' N 123°56' W); (h) Brahmaputra (Bangladesh, 25°24' N 87°05' E) (Schuurman et al., 2013). Photographs without reference were obtained from Google Earth (accessed September 2018).

Perhaps the most typical and unique features of channel patterns in tidal basins and estuaries are the mutually evasive ebb- and flood-dominated tidal channels (Figure 4.1). Mutually evasive channels are predominantly used in either the ebb or the flood phase and evade each other laterally (van Veen, 1950; Fenies and Faugères, 1998; Hibma et al., 2003; Dalrymple and Choi, 2007; Kleinhans et al., 2015b). This process results in linear bars when the channels simply evade each other laterally, but can also form U-shaped bars when one of the channels bifurcates around an opposing channel that is met head-on (Fig. 1.4 and Chapter 2). The tails of a U-shaped bar embrace a barb channel, which is a one-ended channel that partly crosscuts the bar and becomes shallower in the direction of flow (Dalrymple and Choi, 2007). Compound bars and side bars are often dissected by barb channels. Possible interpretations for barb channels are that they either form by the convergence of bedload around an initial bar core, as was previously described for rivers (Sambrook Smith et al., 2006), or that they are failed chute cut-off channels that are remnants of cross-bar channels, where successful chute cut-offs would increase the braiding index. Dalrymple and Choi (2007) hypothesised that estuary width and curvature determine both the shape and the number of bars in cross-section, which is also expected by analogy from rivers (Kleinhans and van den Berg, 2011).

Mutually evasive ebb- and flood-dominated tidal channels can be regarded as bifurcations (Kleinhans et al., 2014). Such bifurcations are inherently unstable in the majority of rivers on Earth, which is also associated to the process of active braiding. This leads to asymmetrical bifurcations such that one channel becomes the main path for flow and sediment (Kleinhans et al., 2013; Bolla Pittaluga et al., 2015). However, in the tidal environment, bifurcations of mutually evasive ebb- and flood-dominated tidal channels abundantly show opposed asymmetry in the sense that the channels are of similar size but the bifurcations in the flood and ebb phases asymmetrically partition the flow into the opposite channels. This raises the question what causes this, and whether, in contrast to bifurcations in rivers, their configuration might be stable over time.

On a larger spatial scale, it is possible to identify a main meandering channel in estuaries with braided bars, which connects to the landward river. Many of the world's major river systems seemingly have one or a few disproportionally large meanders with tight bends in the fluvial-tidal transition. However, the empirical relations that were previously found for rivers (e.g. Inglis, 1949; Leopold and Wolman, 1960; Hey and Thorne, 1986) have never been tested on a large dataset with data from fluvial-tidal transition zones and estuaries. Observations of small tidal meanders (i.e. tidal creeks) show that their planform dimensions scale similarly as in rivers (Barwis, 1977; Marani et al., 2002; D'Alpaos et al., 2017; Finotello et al., 2018). However, these observations mainly cover meanders on tidal flats and salt marshes, which are much smaller (typically 2–200 m wide) than fluvial and estuarine meanders. Moreover, they predominantly form under ebb dominant flow and may thus be comparable with small river meanders (Kleinhans et al., 2009). This hypothesis has not yet been tested for lack of a comprehensive dataset of fluvial meanders, tidal meanders and meanders in fluvial-tidal transitions.

Theory development for tidal bars

Only two analytical physics-based models are currently available for tidal systems. These theories predict bar length to predominantly increase with flow velocity or tidal excursion length (Seminara and Tubino, 2001; Schramkowski et al., 2002), which is the distance that a water particle travels in half a tidal cycle. The theories both also predict a weaker dependency of bar length on channel width and in Schramkowski et al. (2002) an increasing channel width increases the number of bars per cross-section. Similar instability mechanisms in meandering channels lead to point bar-pool patterns (Solari et al., 2002). Only when overtides are introduced, causing ebb or flood asymmetry, bars become net migratory (Garotta et al., 2006).

The results from the analytical physics-based models have been reproduced with numerical models (Hibma et al., 2004), but also revealed a stronger dependency on channel width than expected from

theories. Toffolon and Crosato (2007) first tested the prediction of braiding index of Seminara and Tubino (2001) for the Western Scheldt, which supported earlier hypotheses that the braiding index increases with the width-to-depth ratio. Numerical modelling also showed that the braiding index and bar length scale with the estuary width-to-depth ratio (Hibma et al., 2003) and observations in tidal channels suggested that meander radius and channel width control point bar dimensions (Barwis, 1977). However, the theoretical predictions have not yet been tested against a larger set of field data. Therefore, the explanation for the shapes and dimensions of bar and channel patterns in natural estuaries remains uncertain. This is further discussed in Chapter 2.

Tidal bars in numerical models and experiments

Numerical model studies showed that bar and channel patterns evolve over two timescales: initially alternate bars forms over decades, while later the main channel deepens over centuries (van der Wegen and Roelvink, 2008; van der Wegen and Roelvink, 2012). Bar length was found to scale with a combination of the tidal excursion length, basin width and width-averaged depth (van der Wegen and Roelvink, 2008). Moreover, model runs and scale experiments suggested that estuarine geometry controls the evolving bar and channel pattern (Hibma et al., 2003; Tambroni et al., 2005; van der Wegen and Roelvink, 2012; Tambroni et al., 2017) with increasing braiding index and bar length for increasing width-to-depth ratio (Hibma et al., 2003). For example, scale experiments with non-erodible boundaries and a relatively low width-to-depth ratio (<40) resulted in systems with a braiding index of 1 and alternate bars (Tambroni et al., 2005; Tambroni et al., 2017).

Recent modelling showed that stratification, i.e. salinity gradients, and Coriolis acceleration, induced by Earth's rotation, affect bar and channel patterns in estuaries (Olabarrieta et al., 2018). In case flow is purely driven by water level variations (barotropic pressure), estuaries with a width-to-depth ration of 40-60 evolve into alternate bar systems, which is in agreement with previous models (Hibma et al., 2003; van der Wegen and Roelvink, 2008) and experiments (Tambroni et al., 2005; Tambroni et al., 2017). As a result of tidal flow asymmetry, sediment accumulates in the landward zone, while the more seaward zone becomes net erosional (Olabarrieta et al., 2018). Moreover, stratification (baroclinic pressure) can promote flood dominance and thereby import of sediment, available for the build-up of bars. In the case with Coriolis acceleration this can even lead to the disappearance of the alternate bar pattern. Instead, a deep channel stabilises on the right side of the estuary with a large flat on the left (looking landward in estuaries on the Northern hemisphere) (Olabarrieta et al., 2018).

Estuary planforms

In ideal estuaries, the energy per unit width is constant along-channel. This ideal situation is met when tidal range and tidal current are constant along-channel such that the loss of tidal energy by friction is balanced by the gain in tidal energy per unit width by channel convergence (Pillsbury, 1956; Dronkers, 2017). In the case that the depth is constant along-channel, the ideal estuary conditions are approximately met when the width is exponentially decreasing in the landward direction, forming a planform shape that resembles a trumpet shape (Pillsbury, 1956; Langbein, 1963; Savenije, 2006; Toffolon and Lanzoni, 2010; Savenije, 2015).

Planforms of alluvial estuaries filled with bars are rather irregular than converging, which deviates from the concept of the "ideal estuary" (e.g. Pillsbury, 1956; Langbein, 1963; Savenije, 2006; Dronkers, 2017). Many natural estuaries are neither in morphological equilibrium nor in a condition of constant tidal energy per unit width and deviate from the ideal as a result of the antecedent geology, human interference and the response time for adaptation to boundary conditions (Townend et al., 2000; Townend, 2005; de Haas et al., 2017). This means that planforms of varying shapes and estuaries with varying degree of adaptation are expected in nature. The relation between planform shape, deviations from the ideal shape and bar patterns is further investigated in this thesis.

1.4 Advancements and available data

Advancements in physical scale modelling

Former physical experiments of tidal systems relied on periodic sea-level variations (Reynolds, 1887; Reynolds, 1889; Mayor-Mora, 1977; Tambroni et al., 2005; Garotta et al., 2008; Stefanon et al., 2010; Vlaswinkel and Cantelli, 2011). Indeed, water level variations generate tides in natural systems and numerical models. However, the down-scaled magnitude of the water level variations in experiments with periodic sea-level variations is too low to induce landward sediment transport when grain size is unscaled. Experiments relying on periodic water level variations thus resulted in systems with mainly ebb-related transport (Kleinhans et al., 2014). Scaled estuary experiments require a much steeper bed gradient than natural systems to obtain similar mobility, because of their smaller water depth and bed shear stress (Kleinhans et al., 2014; Kleinhans et al., 2015a). A similar mobility as in nature is obtained by tilting the entire flume, which is possible in the facility called 'The Metronome'. The tilting produces hydrodynamic conditions capable of transporting sediment during both the ebb and flood phases (Kleinhans et al., 2015a; Kleinhans et al., 2017a), which generates dynamic tidal morphology. Therefore, the periodically tilting flume was used in this thesis (Chapters 4 & 6) to study dynamics of bars and channels.

Available datasets

Available datasets have largely expanded over the last century. Space borne imagery is now easily and freely available online through programs such as Google Earth and USGS LandLook. In some cases, imagery can even show temporal dynamics of channels and bars. However, the main difficulties with these datasets are that (1) the timing with respect to the tidal period is often unknown and (2) typical channel depth and bar height are not derivable. For the latter, detailed bathymetry is required, which also becomes available with increasing spatial and temporal resolution. For example, in the Netherlands, Rijkswaterstaat obtains almost yearly bathymetries of the Western Scheldt (NL) since 1955. Similarly, digitisation of historic maps allowed to derive bathymetries for the Ems-Dollard Estuary (NL) since 1812 (Pierik et al., 2019). Other governments also increasingly make detailed bathymetries available (e.g. NOAA program (USA), data.gov.uk). Nevertheless, most detailed bathymetries are for systems that are under pressure by human influence, such as dredging and disposal of sediment to maintain shipping fairways, which means that we generally lack bathymetry to study the natural dynamics of channels and bars. In addition to field data, the set of results from numerical modelling has also largely expanded over time, such as for Western Scheldt (Verbeek et al., 2000; Vroom et al., 2015) and Columbia River Estuary (Elias et al., 2012; Stevens et al., 2017). A combination of these datasets is used in this thesis (Chapters 7 & 8) to induce empirical relations for bar and channel patterns in modern-day estuaries.

Advancements in numerical modelling

Increased computational power has decreased computational times of models such as Delft3D and Telemac, which increased their application to morphological modelling of estuaries. Previous studies used numerical models to study the long-term morphodynamic evolution (e.g. Canestrelli et al., 2014, with a one-dimensional model) and the dynamics of bars and channels in estuaries (e.g. Hibma et al., 2003; Hibma et al., 2004; van der Wegen and Roelvink, 2008; Dam et al., 2016; Olabarrieta et al., 2018, with two- and three-dimensional models), but often estuary boundaries were non-erodible and the interactions between sand, cohesive material, vegetation and morphology remained under-investigated. Only more recently also effects of and on estuary shape were considered (van der Wegen and Roelvink, 2012; Braat et al., 2017; van de Lageweg and Feldman, 2018). Earlier hydrodynamic models already showed how morphological elements such as tidal bars affect flow asymmetry in tidal systems (Friedrichs and Aubrey, 1988; Fortunato et al., 1999; Fortunato and

Oliveira, 2005). For example, these studies showed that tidal flats enhance ebb dominance, whereas friction and increased tidal amplitude enhance flood dominance. While numerical modelling is not the main methodology used in this thesis, I compared the occurring bar and channel patterns in numerical models (Braat et al., 2017) with natural bars. Additionally, a one-dimensional hydrodynamic model (Friedrichs and Aubrey, 1988; Kleinhans et al., 2017a) has been modified to allow for irregular estuary planforms and varying boundary conditions. This model is applied in Chapter 9 to predict the effect of future sea-level rise on the hydrodynamics of estuaries from all over the world.

1.5 Specific research questions and thesis outline

The following objectives are addressed in this thesis: (1) to quantify and understand the equilibrium bar and channel patterns in estuaries and (2) to assess the temporal dynamics of channels and bars. These objectives encompass all spatial scales, from individual bars (10s of m to 1000s of m long) up to the entire estuary planforms (100s of m to 10s of km wide), and all temporal scales, from initial bar formation (days – years) to estuary planform evolution (decades to centuries) (Fig. 1.5). The main objectives have been divided into three sub-objectives:

- Part A: Quantify the dimensions and development of bar and channel patterns in estuaries.
- Part B: Determine the relation between the planform estuary shape and the occurring bar patterns and dynamics.
- Part C: Explore the possible future response of estuaries to sea-level rise scenarios.

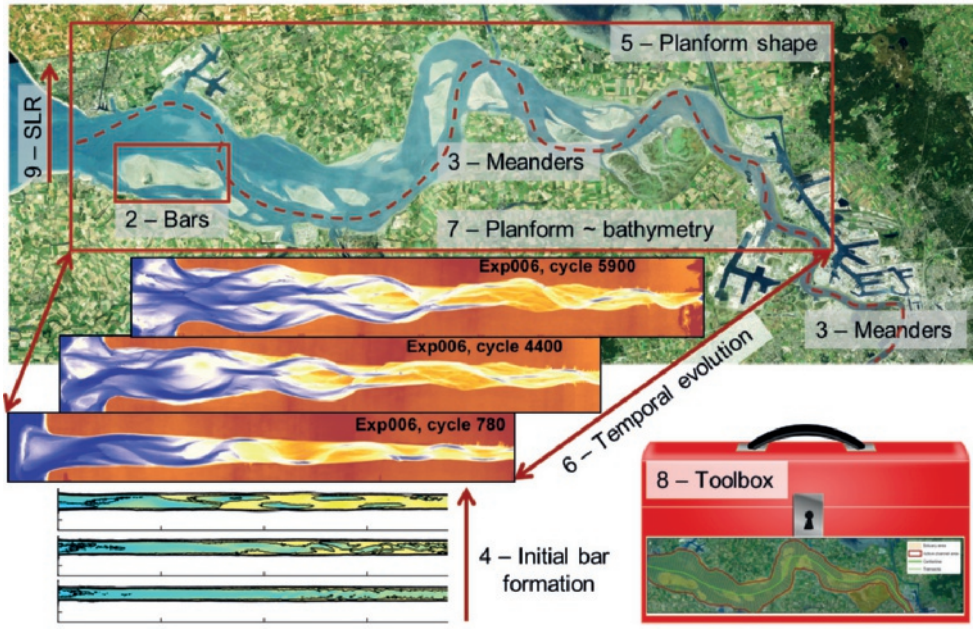

Figure 1.5 An overview of the spatial and temporal scales studied in this thesis. Numbers correspond to the chapters in this thesis.

Chapter 2 reviews the available classifications for tidal bars and theory to predict bar dimensions in tidal systems with stability analyses. The results from theory are compared with a large novel dataset of tidal bars measured in natural systems. Based on the data, bar types are summarised in a classification scheme and empirical relations are induced to predict dimensions of individual bars (Part A). The empirical relations can be used to study bar and channel patterns on the estuary scale (Part B).

Chapter 3 addresses the hypothesis that fluvial-tidal meanders are disproportionally large when compared to their local channel dimensions and upstream and downstream meanders. Typical scaling relations are derived for meander dimensions as a function of local channel dimensions along the entire fluvial-tidal transition zone (Part A).

Chapter 4 describes the process of tidal bar initiation, which is a first step towards understanding the forming mechanism. These results are based on a series of experiments in the tilting flume, in which the initial channel planform and boundary conditions were varied, and the initial evolution was monitored (Part A).

Chapter 5 analyses the degree to which the location of intertidal bars depends on the planform shapes of estuaries. The results can be used to predict bar and channel patterns in estuaries (Parts A & B).

Chapter 6 studies the long-term morphodynamics of channels and bars in physical scale experiments. This chapter explains which mechanisms are responsible for the irregular planforms observed in many estuaries in Chapter 5 (Part B) and how the planform can be forced by self-formed bars and channels (Part A) or forced by inherited geology.

Chapter 7 considers the three-dimensional shape of bars in estuaries. In Chapters 2 and 4, bars are described as discrete elements on what is essentially a continuous field of bed elevations. Results from these chapters showed that there is a strong relation between estuary planform and bar dimensions. Therefore, in this chapter, it is investigated how the surface topography of estuaries, i.e. horizontal dimensions, translates in the sub-water morphology, i.e. the vertically occurring bed levels (Part B).

Chapter 8 combines and extends a set of theoretical and empirical predictors for estuarine morphology, hydrodynamics and salinity. The comprehensive set of relations can be applied in data poor environments, because the only required input is tidal amplitude at the estuary mouth and the estuary outline, which are both generally publicly accessible (Parts B & C).

Chapter 9 shows how the tool presented in Chapter 8 can be used to predict the effect of rising sea level on the morphology and hydrodynamics of estuaries from all over the world. First, the three-dimensional morphology is predicted with the tool for each scenario. The output depends on SLR induced changes in along-channel width profile and boundary conditions, i.e. river discharge and tidal amplitude at the mouth. Second, the morphology is translated in a one-dimensional profile of the channel width and depth and shoal width and depth, which serves as input for a one-dimensional hydrodynamic model. The latter is used to predict effects of sea-level rise on future water levels in the estuary. The results allowed to classify estuaries based on their sensitivity to future changes, which indicates which type of estuaries are most susceptible to drowning under sea-level rise (Part C).

Chapter 10 is the synthesis, wherein I summarise the main results of this thesis and assess to what degree and in what aspects bar and channel patterns in estuaries are similar to bar and channel patterns in rivers (Parts A & B). I will also discuss potential applications in estuary management (Parts B & C) and implications of future sea-level rise for the morphology of estuaries (Part C). Finally, I make recommendations for future research.

2

Chapter 2 | Tidal sand bar dimensions and shapes in estuaries

Abstract

Estuaries show dynamic patterns of channels and bars, which are also valuable habitats, while channels provide access to harbours. In contrast to bars in rivers, we still lack explanations, theory and classifications for bars in estuaries. Theories for river bars show bar properties to be strongly dependent on channel width-to-depth ratio. For estuaries, only two physics-based theories are available. One predicts bar length to increase with flow velocity and tidal excursion length and the other with flow velocity and estuary width. However, these theories have not been tested for lack of data and experiments. Our objective is to determine bar shape and dimensions in funnel shaped alluvial estuaries and to provide predictive relations for bar shapes and dimensions. We present a new dataset measured in imagery and bathymetry with bar lengths spanning from centimetres (in experiments) to tens of kilometres. We visually identified and classified 190 bars and measured their width, length, height and number of cross-cutting barb channels. Estuarine geometry and tidal characteristics were obtained from available databases and literature. We found that many compound bars can be seen as simple linear bars partly cut by barb channels, where partitioning of bar width collapses the data of bar length to width ratio. This is in agreement with the transverse wave form of bars assumed in linear stability theories that are supported by data in fluvial and coastal environments. Our empirical trend shows that sand bars in estuaries have similar length-to-width ratios as bars in rivers but that they are more elongated. This trend was also found to hold for bars in numerical models and scaled laboratory experiments. Bar height is linearly related to local water depth. Natural bar length, bar width and braiding index are strongly correlated to estuary width. This relation is also evident in published data of bars in rivers and numerical models of rivers. The theoretical braiding index of tidal bars indeed depends on local width-to-depth ratio and is reasonably well predicted for our dataset. However, the theoretical models for tidal bar wave length and width surprisingly lack this correlation with estuary width and overpredict by an order of magnitude, pointing at a need to revisit tidal bar theory. The empirical relations provide a means of estimating bar dimensions when limited data are available and in order to evaluate results from numerical models and physical experiments.

Published as: Leuven, J.R.F.W., Kleinhans, M.G., Weisscher, S.A.H. & van der Vegt, M. (2016). Tidal sand bar dimensions and shapes in estuaries. *Earth-Science Reviews, 161, pp. 204–223*, DOI: 10.1016/j.earscirev.2016.08.004.

2.1 Introduction

An estuary is a body of water that has inflow of river water at the landward boundary and an open connection to the sea. Many definitions and classifications have been proposed for estuaries, which mostly depend on their application (Pritchard, 1967; Hume and Herdendorf, 1988; Davidson and Council, 1991; Dalrymple et al., 1992; Perillo, 1995; Townend et al., 2000; Townend, 2005; Savenije, 2006). In most cases, estuaries were defined based on the relative influence of tides, waves, rivers, sediment types, sediment supply, vegetation, geology or time (see Savenije, 2006, for review).

Here we focus on funnel shaped alluvial estuaries that are characterised by complicated patterns of dynamic channels and sand bars, often flanked by tidal mud flats and salt marshes. Savenije (2006) defined alluvial estuaries as estuaries with erodible beds, influenced by both river flow and tidal flow from the sea. Therefore, the sediment bed of alluvial estuaries comprises both sediment types: the coarser fluvial sand and finer marine mud. Depending on the relative importance of the hydrodynamic processes, one can further discriminate between river-dominated and tidal-dominated estuaries. Nevertheless, data to assess this are often lacking and if data is available, the question rises what defines for example the threshold for fluvial dominance. Dynamic sand bar patterns can form when the estuary received sufficient fluvial sediments. Our main question is: what determines the bar pattern in funnel shaped alluvial estuaries?

The understanding of bar patterns is relevant for the management of channels, which are used as shipping fairways, and bars or shoals, which are valuable ecological habitats (Wang et al., 2012; Coco et al., 2013). Furthermore, tidal sand bar deposits form large and complicated hydrocarbon reservoirs of which architecture is difficult to reconstruct from limited data (Wood, 2004).

Sand bars, also called shoals, occur in a wide variety of shapes: from long and narrow to circular or squared, and in a variety of size, from metres to kilometres (Fig. 2.1). In contrast to estuaries, detailed classifications exist for river bars (Fig. 2.2), along with a description of the forming mechanisms (Cant and Walker, 1978; Bridge, 1993; Ashworth et al., 2000; Bridge, 2003; Sambrook Smith et al., 2006; Kelly, 2006; Rice et al., 2009; Kleinhans and van den Berg, 2011; Schuurman et al., 2013). Most classifications discriminate between simple unit bars and compound bars. Unit bars are small (100-300 m) bars with a lobate shape that have their highest point at the downstream end followed by a steep face (e.g. Sambrook Smith et al., 2006). Compound bars comprise multiple amalgamated unit bars and formed by several stages of erosion and deposition (e.g. Bridge, 2003; Ashworth et al., 2000; Schuurman et al., 2013). Therefore, they occur in a wider variety of shapes and are generally larger than unit bars, for example forming sidebars and bars with a U-shape (Fig. 2.2).

It is unknown to what extent tidal bars in estuaries have similar dimensions, shapes and forming mechanisms as bars in estuaries. For estuaries, van Veen (1950) and Dalrymple and Choi (2007) defined three different types: linear bars, U-shaped bars and sidebars (Fig. 2.3). All other bars in estuaries, which are more complex bars that probably amalgamated from other bars, we define here as compound bars (Fig. 2.1g,h) in analogy with rivers.

In all these definitions we describe bars as discrete recognisable elements on what is essentially a continuous field of bed elevation that changes over time. In contrast to the situation of merging bars, of which the history is captured by the term amalgamated or compound bar, one bar can become two bars when a channel cuts through it with sufficient depth, meaning that the history of these bars being one bar is lost. In rivers such deep channels are called chute channels. Moreover, an intermediate stage is recognised as cross-bar channels, which generally have smaller dimensions than the main channel, but may enlarge over time, forming a chute channel (Bridge and Tye, 2000; Bridge, 2003; Sambrook Smith et al., 2006). For estuaries, Swinkels et al. (2009) described similar channels as smaller connecting channels that may increase or diminish over time.

The presence of mutually evasive ebb- and flood-dominated tidal channels is unique in tidal environments. These channels develop around the sand bars (van Veen, 1950; Dalrymple and Choi, 2007; Hibma et al., 2003; Kleinhans et al., 2015b). When they meet head-on, either they evade each other laterally (Fig. 2.3a,c,e,g) or one of the channels bifurcates and a U-shaped bar forms between the channels (Fig. 2.3b,f). The tails of a U-shaped bar embrace a barb channel (Fig. 2.1e,f), which is a one-ended channel that partly crosscuts the bar and becomes shallower in the direction of flow (Dalrymple and Choi, 2007). Compound bars and side bars are often dissected by barb channels (Fig. 2.1h), while linear bars lack barb channels. Possible interpretations for barb channels are that

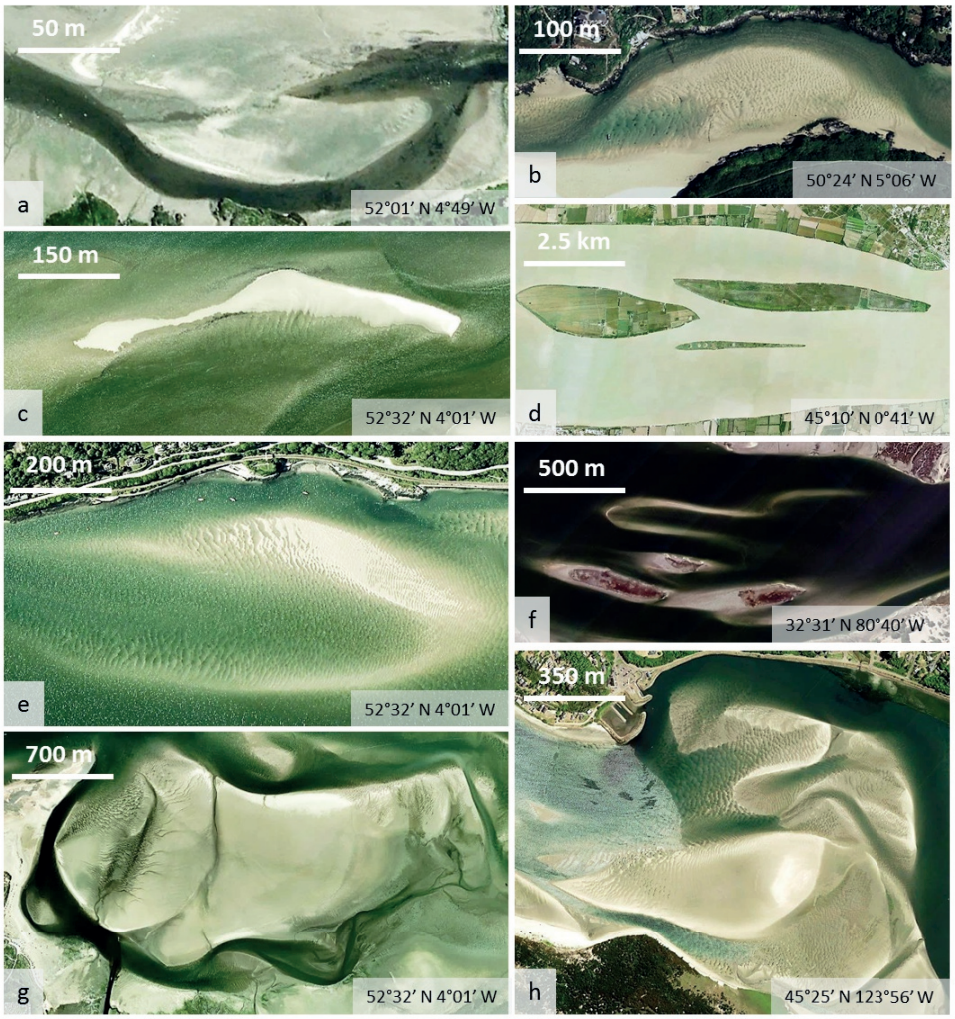

Figure 2.1 Aerial photographs of bars in estuaries. Sidebar with barb channel in the (a) Nyfer Estuary (UK) and (b) Gannel Estuary (UK); linear bar in the (c) Dovey Estuary (UK) and (d) Gironde Estuary (Fr); U-shaped bar in the (e) Dovey Estuary (UK) and (f) St. Helena Estuary (USA); compound bar in the (g) Dovey Estuary (UK) and (h) Netarts Bay (USA). In all cases flood flow is from left to right. Google Earth, accessed May-September 2015.

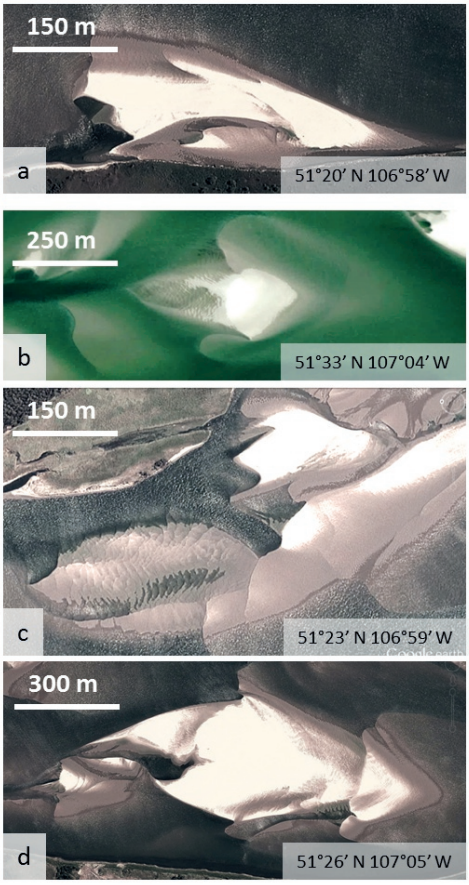

Figure 2.2 Aerial photographs of river bars in the Saskatchewan River near Outlook (Canada): (a) side bar; (b) compound bar amalgamated from a few smaller unit bars; (c) chute bars; (d) compound midchannel bar. Compare respectively to Fig. 2.1a,b, Fig. 2.1c,d, Fig. 2.1e,f, Fig. 2.1g,h. Google Earth, accessed May-September 2015.

they either form by the convergence of bedload around an initial bar core, as was previously described for rivers (Sambrook Smith et al., 2006), or that they are failed chute cutoff channels that are remnants of cross-bar channels, where successful chute cutoffs would increase the braiding index.

Dalrymple and Choi (2007) hypothesised that estuary width and curvature determine both the shape and the number of bars in cross-section, which is also expected by analogy with rivers (Kleinhans and van den Berg, 2011). Here, we define local estuary width as the width between the vegetated marshes or banks at the location of the measured bar, including the sand bars (see Fig. 2.1e). Only two analytical physics-based models are currently available for tidal systems. These theories predict bar length to increase with estuary width (Seminara and Tubino, 2001) or with flow velocity and tidal excursion length (Schramkowski et al., 2002), which is the distance that a water particle travels in half a tidal cycle. In contrast, theory for rivers predicts bar properties to be mainly determined by channel width-to-depth ratio (see Kleinhans and van den Berg, 2011, for review). Toffolon and Crosato (2007) validated the prediction of braiding index of Seminara and Tubino

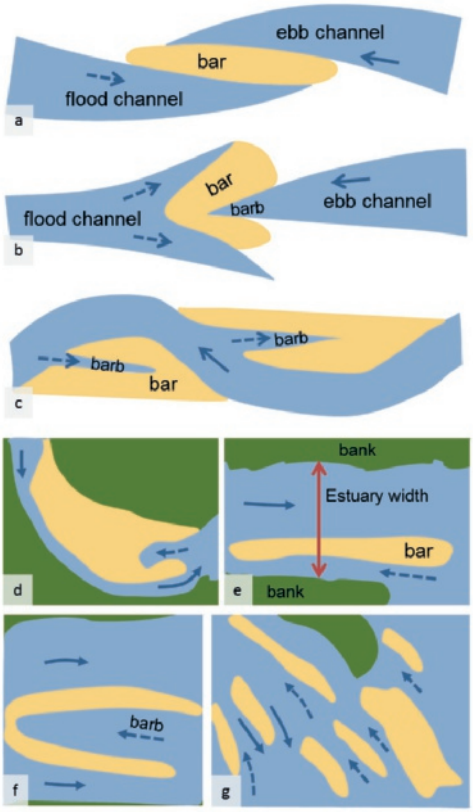

Figure 2.3 Sketches of bar types recognised in literature. (a,b,c) Mutually evasive ebb- and flood-dominated channels separated by bars (after van Veen (1950)); (d,e,f,g) Variation in the morphology of elongated sand bars in estuaries (after Dalrymple and Choi (2007)). Solid arrows: ebb-dominated channels, dashed arrows: flood-dominated channels.

(2001) for the Western Scheldt, which supported the earlier hypotheses that the braiding index increases with width-to-depth ratio. Numerical modelling showed that the braiding index and bar length scale with estuary width-to-depth ratio (Hibma et al., 2003). However, these hypotheses on sand bar properties in estuaries have not been validated against a larger set of field data. Therefore, we still lack a full explanation for the shapes and dimensions of bar patterns in natural estuaries. Moreover, a classification scheme for bar pattern in estuaries is absent, in contrast to bar patterns in river systems.

The objectives of this study are (1) to quantify bar shapes and dimensions in natural estuaries while accounting for water level effects on bar visibility on imagery, (2) to investigate relations between bar dimensions and hydrodynamic and geometrical properties of estuaries, and (3) to test physics-based bar theories.

This chapter is organised as follows: first, we review bar theories for rivers and estuaries. Then we present data of 190 bars in 45 estuaries collected from imagery and explain methods of characterisation and analysis. We test effects of water level variation on emergent bar shape and pattern in bathymetric

data of three cases. This is followed by discussion of our data compared to known river bar properties and possible applications of the novel empirical relations.

2.2 Bar theory

Stability analysis predicts the initial formation of bar patterns through a mathematical method to study wave lengths and migration of periodic patterns. It has proven to be a powerful technique with predictive capability used to gain basic understanding of the mechanisms causing such patterns and their dimensions. The stability models generally consist of a system of equations for momentum, continuity, sediment transport and bed evolution (Dodd et al., 2003). Simplification of the equations, when the nonlinear effects are ignored, allows an analytical solution that does not have the potential problems of numerical models, for instance when bars grow to amplitudes approaching the water depth (Dodd et al., 2003). Initial and boundary conditions are also simplified: bar theories used in this chapter assume a long straight channel with constant width, non-erodible banks and an erodible sediment bed. However, despite such simplifications, stability analysis was successfully applied in many types of systems (Dodd et al., 2003), for example, river bars (Struiksma et al., 1985; Kleinhans and van den Berg, 2011), offshore sand ridges (Hulscher et al., 1993; Komarova and Hulscher, 2000), bedforms (Colombini, 2016) and sand waves (Blondeaux and Vittori, 2016). Part of what we know about river bars comes from these theories and given these past successes and that relatively little is known about tidal bars, it is of interest to test the few available theories for tidal bars. To set a frame of reference and link to the successful application in river bars that occur upstream of estuaries, we also include a theory for bars in rivers (Struiksma et al., 1985).

Our aim is to understand which factors influence bar patterns in the stability analyses and to obtain hypotheses for bar dimensions and braiding index in natural estuaries. Below, we first describe how linear stability analysis generally works in bar theory. Subsequently, we detail the main model components and compare the underlying assumptions. We show how the predicted bar dimensions and braiding index depend on the input parameters. After that, the results of all three theories are compared for a range of velocities (0.5-2.0 m s^{-1}) and channel widths (50-4000 m) found frequently in nature. In a sensitivity analysis, we systematically vary model input for Struiksma et al. (1985) and Schramkowski et al. (2002), because only these theories were originally applied to the full range of channel widths that are considered in this study. For detailed descriptions of the model setup or derivations of the solutions, the reader is referred to the original papers.

The models are applicable to converging estuaries despite the assumption of constant width because of what this assumption means in the context of linear stability theory. The stability analyses of Seminara and Tubino (2001) and Schramkowski et al. (2002) are local models, valid under the assumption that horizontal length scales are much smaller (i.e. an order of magnitude) than the length of the basin, the tidal wavelength, and the length scale of width variations of the basin (de Swart and Zimmerman, 2009). In other words, as long as the length scale of the tidal bars is much smaller than the length of estuaries and the tidal wavelength, and the channel width is not varying too abruptly due to constructions or geological constraints, bar patterns can be predicted for every point along an estuary, given the local geometry and set of flow conditions at that point. Model predictions are thus dependent on the local estuary width for which they predict bar pattern formation. Therefore, this is how we applied the theory to natural systems: we use the measured estuary width at the measured bar location to predict the local bar pattern formation.

In all stability models, first the basic state is determined, which is a channel without any bar patterns (Dodd et al., 2003). Second, a small spatially periodic perturbation (h') is applied to the bed, resulting in local water depth variations that represent the initial bars and channels (Fig. 2.4). The evolution of these patterns over time is determined. In linear stability analysis, it is assumed that the perturbation

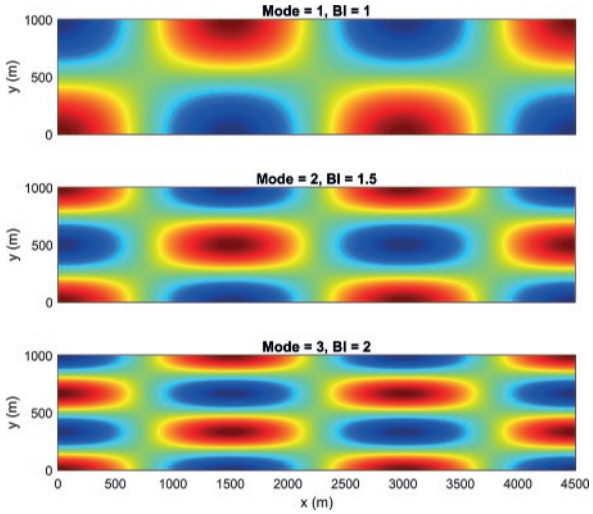

Figure 2.4 Examples of the applied periodic perturbations, which in this case have the same wavelength and different cross-channel modes or braiding indices.

height h' is small with respect to the equilibrium water depth and is given by:

$$h'(x,y) = a_{h'} e^{\omega t} cos(\frac{2\pi x}{L}) cos(\frac{m\pi y}{W}) \tag{2.1}$$

where $a_{h'}$ is the amplitude of the perturbation, L is the wave length of the perturbation and $L/2$ is thus the bar length, W is the width of the channel and m is the cross-channel mode number. The growth rate of a perturbation (ω) is in principle a complex number, but it has only a real part in the studies discussed here. The growth rate ω determines whether the configuration with perturbations persists ($\omega = 0$), grows ($\omega > 0$) or disappears ($\omega < 0$) for fixed model parameters. For each wave length L and mode number m, the growth rate is determined. The configuration with the highest growth rate determines the dominant bar pattern, which is most likely to evolve in the river or estuarine channel. Bar mode relates to the braiding index (BI) as

$$BI \equiv \frac{m-1}{2} + 1 \tag{2.2}$$

Here, we used the resulting analytical relations for Struiksma et al. (1985), the numerical solution for Schramkowski et al. (2002) and the data presented in Seminara and Tubino (2001, their Fig. 10).

2.2.1 Theory for bars in rivers

While many predictive theories for river bar dimensions are available (Schielen et al., 1993; Kleinhans and van den Berg, 2011), we limit our review to bar theory of Struiksma et al. (1985), which proved effective for a large dataset of various river patterns. On the basis of Struiksma et al. (1985), Crosato and Mosselman (2009) derived a predictor for bar length and braiding index. Struiksma et al. (1985) calculated the adaptation length of flow (λ_w) and bed (λ_s), where λ_w is the longitudinal distance needed for the water to adapt to a perturbation of the bed and λ_s is the longitudinal distance needed for the downstream bed to adapt to a forced upstream bed perturbation. The ratio λ_s/λ_w predicts whether bars dampen out or excite (Crosato and Mosselman, 2009; Kleinhans and van den Berg, 2011), which are given as:

$$\lambda_w = \frac{1}{2}\frac{h}{c_f} \tag{2.3}$$

$$\lambda_s = \frac{h}{(m\pi)^2}\left(\frac{W}{h}\right)^2 f(\theta) \tag{2.4}$$

which is the equation by Struiksma et al. (1985), adapted for higher mode bars ($m > 1$) (see also Parker, 1976), in which the transverse bed slope function is given by

$$f(\theta) = \frac{\theta^{m_{bs}}}{r_{bs}} \tag{2.5}$$

with parameters r_{bs} (typically 0.56) and m_{bs} (typically 0.5). θ is defined as

$$\theta = \frac{\tau_{nl}}{(\rho_s - \rho)gD_{50}} \tag{2.6}$$

in which

$$\tau_{nl} = \rho c_f \overline{u}\,|\overline{u}| \tag{2.7}$$

where ρ_s is the sediment density, ρ is the water density, h is the channel depth, g is the gravitational constant, D_{50} is the median grain size, c_f is the friction coefficient, $\overline{u}$ is the depth-averaged river flow velocity, $|\overline{u}|$ the magnitude of the flow velocity and τ_{nl} is the nonlinear bed shear stress. Sediment transport consists of only bed load transport with negligible sorting effects: the equation of Engelund and Hansen (1967) was used and adapted for bed slope effects.

Crosato and Mosselman (2009) reformulated the linear model of Struiksma et al. (1985) to directly define an estimator for the number of bars in cross section – rather than defining stable and unstable bar configurations as was previously done by Struiksma et al. (1985). They derived an expression for bar mode and bar length from Struiksma et al. (1985). The mode is given by the floor to the nearest integer of

$$m = \frac{W}{h\pi}\sqrt{(p-3)f(\theta)c_f} \tag{2.8}$$

where p is the nonlinearity of sediment transport ($p = 4$ for sand).

The growing bed perturbation is harmonic in downstream direction (Crosato and Mosselman, 2009), which results in an equation for bar wavelength:

$$L_p = \frac{4\pi\lambda_w}{\sqrt{(p+1)\frac{\lambda_w}{\lambda_s} - \left(\frac{\lambda_w}{\lambda_s}\right)^2 - \left(\frac{p-3}{2}\right)^2}} \tag{2.9}$$

2.2.2 Theory for bars in estuaries

Seminara and Tubino (2001) used a linear 3-dimensional model, while Schramkowski et al. (2002) used a linearised 2-dimensional (depth-averaged) model for bars. Both studies prescribed M_2 tidal flow velocities and used a rigid lid approximation, which implies that only tide-induced flow velocities are taken into account while water level variations are neglected. In contrast to Seminara and Tubino (2001), Schramkowski et al. (2002) retained local inertia terms in the momentum equations. The bottom was considered time independent for timescales on the order of a tidal period. Seminara and Tubino (2001) used the same expression for bed shear stress as Struiksma et al. (1985) (Eq. 2.7). Bed shear stress was linearised in Schramkowski et al. (2002), such that the amount of dissipated energy by friction during a tidal cycle is equal to the situation with nonlinear bottom friction:

$$\tau_{lin} = \rho\left[\frac{8}{3\pi}c_f U\right]\left|\overline{u(t)}\right| \tag{2.10}$$

where U is a typical magnitude of flow velocity, assumed to be constant (typically 1 m s^{-1}) and $\left|\overline{u(t)}\right|$ is the tidal flow velocity over time.

Sediment transport consists of both bedload and suspended load transport in Seminara and Tubino (2001). In contrast, Schramkowski et al. (2002) only used the bed slope induced part of the bedload transport ($S_{b,SC}$) and calculated suspended load transport. In Seminara and Tubino (2001), bedload transport was calculated with the Meyer-Peter and Müller (1948) equation and adapted for bed slope effects:

$$\overrightarrow{Q_{b,ST}} = \overrightarrow{Q_{b,cur}} + \overrightarrow{Q_{b,bsl}} \tag{2.11}$$

in which $Q_{b,cur}$ is the tidal current induced transport and $Q_{b,bsl}$ is the bed slope induced, defined as

$$\overrightarrow{Q_{b,cur}} = 8(\theta' - \theta_c)^{1.5}\sqrt{RgD_{50}{}^3} \tag{2.12}$$

$$\overrightarrow{Q_{b,bsl}} = -\overrightarrow{Q_{b,cur}}\frac{W}{2h}\frac{r_{bs}}{\theta^{m_{bs}}}\left(0, \frac{\partial h}{\partial y}\right) \tag{2.13}$$

where R is the relative submerged density and $\frac{\partial h}{\partial y}$ is the transverse bed slope. See Seminara and Tubino (2001) for constitutive equations for θ' and θ_c. Shear stress is calculated from flow velocity and skin friction (van Rijn, 1984). For bed load transport, Schramkowski et al. (2002) only used the part that accounts for the bed slope effect:

$$\overrightarrow{Q_{b,SC}} = -\overrightarrow{Q_{b,cur}}\frac{W}{2h}\frac{r_{bs}}{\theta^{m_{bs}}}\left(\frac{\partial h}{\partial x}, \frac{\partial h}{\partial y}\right) \tag{2.14}$$

in which $\frac{\partial h}{\partial x}$ is the along-channel bed slope. Bed slope transport was independent of flow conditions and channel geometry in Schramkowski et al. (2002) and set to a constant value λ. For comparison (section 2.2.3), we tuned λ such that the bed slope effect is equal at peak tidal velocity for both theories.

For suspended load, Schramkowski et al. (2002) used the advection-diffusion equation of van Rijn (1993):

$$C_t + (uC - \mu C_x)_x + (vC - \mu C_y)_y = S \equiv \alpha(u^2 + v^2) - \gamma C \tag{2.15}$$

where C is the volumetric depth-integrated concentration [m^3/m^3], μ is the horizontal coefficient for sediment diffusion, S is erosion minus sedimentation, α is an erosion constant (typically 10^{-5} s m^{-1}). The settling parameter γ is equal to w_s^2/k_v, in which w_s is the settling velocity (typically 10^{-2} m s^{-1}) and k_v is the depth-averaged vertical eddy diffusivity (typically 0.09 m^2s^{-1}). Seminara and Tubino (2001) used a similar time-dependent equation for sediment concentration in 3D in which horizontal dispersion is neglected. The major difference between Seminara and Tubino (2001) and Schramkowski et al. (2002) is the formulation of the sediment entrainment. In Seminara and Tubino (2001), S is proportional to the difference between the local sediment concentration and the near-bed concentration at equilibrium (C_{eq} in [m^3/m^3]) with the local flow. The equilibrium concentration is calculated with van Rijn (1984):

$$C_{eq} = 0.015\frac{D_{50}}{0.01h}\left(\frac{\theta'}{\theta_c - 1}\right)^{1.5} R_p^{-0.3} \tag{2.16}$$

where R_p is the Reynolds particle number, which is given as:

$$R_p = \frac{\sqrt{RgD_{50}{}^3}}{\nu} \tag{2.17}$$

where ν is the kinematic viscosity.

2.2.3 Comparison

For a fair comparison between Seminara and Tubino (2001) and Schramkowski et al. (2002), it is necessary to determine the value of the settling parameter (γ) and the erosion constant (α) for which the sediment concentration is equal in both models. For γ, we used the depth-averaged eddy diffusivity (k_v) of Seminara and Tubino (2001) and a constant settling velocity. Subsequently, α was chosen such that the model is in morphological equilibrium for a steady flow ($S = 0$ in Eq. 2.15):

$$\alpha = \frac{\gamma C}{u^2} \tag{2.18}$$

where C is the depth-integrated sediment concentration over depth h of Schramkowski et al. (2002) for a certain flow velocity, given by

$$C = \int_0^h C_z dz = \int_0^h C_{eq} exp\left(\frac{-w_s}{k_v} z\right) dz \tag{2.19}$$

where C_{eq} is the near bed sediment concentration of Seminara and Tubino (2001) given by Eq. 2.16.

Bar width was in all cases determined as half the estuary width divided by the braiding index. Furthermore, it should be remarked that flow velocity for river models is constant and unidirectional while the indicated flow velocity for estuaries is a peak velocity and bidirectional.

We calculated the maximum growth rate of perturbations for the theory of Schramkowski et al. (2002) (SC) and compared this with the results of Seminara and Tubino (2001) (ST) and the predictor derived from Struiksma et al. (1985) by Crosato and Mosselman (2009) (CM). We varied the flow velocities in CM and the amplitude of tidal flow velocity in SC from 0.5-2.0 m s^{-1} and applied channel widths varying from 50-2000 m. The default parameters of ST were used for comparison (Table 2.1).

Table 2.1 The values *Default* were used in the comparison of bar theory and sensitivity analysis. Values are based on the defaults of Seminara and Tubino (2001). *Range* indicates the range over which was varied in the sensitivity analysis. Tidal frequency is not applicable in the case of river theory.

name	symbol	Default	Range	unit
Nonlinearity sed. transport	n	4		-
Friction coefficient	c_f	$2.5{\cdot}10^{-3}$	$0.6\text{-}10{\cdot}10^{-3}$	-
Density sediment	ρ_s	2650		kg m^{-3}
Density water	ρ	1000		kg m^{-3}
Median grain size	D_{50}	10^{-4}	$0.25\text{-}4{\cdot}10^{-4}$	m
Kinematic viscosity	ν	10^{-6}		m^2 s^{-1}
Eddy diffusivity	k_v	0.09		m^2 s^{-1}
Settling velocity	w_s	10^{-2}	varied with D_{50}	m s^{-1}
Tidal frequency	σ	$1.4{\cdot}10^{-4}$	$0.35\text{-}5.6{\cdot}10^{-4}$	s^{-1}
Bed slope parameter	r_{bs}	0.56	0.14-2.24	-
Bed slope parameter	m_{bs}	0.5		-
Water depth	h	5	2.5-40	m
Erosion constant	α	10^{-5}		s m^{-1}
Estuary/river width	W	1000	50-4000	m

The most important result is that bar length depends mainly on the amplitude of tidal flow velocity in SC and ST, while in river theory it also depends on river width (Fig. 2.5). All theories predict bar length in the same order of magnitude for systems with the same width and amplitude of tidal flow velocity (Fig. 2.6). CM predicts bar lengths a factor 3 larger than tidal theory for small channels. For wide channels ($> 10^3$ m), bar wavelength becomes independent of increasing braiding index (Fig. 2.5a,c).

Bar width increases with estuary width for all theories. When the estuary width exceeds the threshold for a higher bar mode, bar width reduces (Fig. 2.5). Predicted bar widths are 3-40 times shorter than bar length (Fig. 2.5).

The braiding index increases with estuary width and width-to-depth ratio (Fig. 2.5c,f) for SC and CM. For narrow channels, the braiding index is 1, which is the alternate bar mode. For wide channels, the braiding index increases with higher flow velocities and sediment mobility (Fig. 2.5c,f). When a higher bar mode excites, bar length reduces until the channel width is further increased.

Concluding, SC and ST predict that bar length increases with flow velocity, thus tidal excursion length. Channel geometry determines the braiding index, with higher braiding indices for wider channels. Theory also implies that relatively long and narrow bars form under high flow velocities in narrow channels, while wider and shorter bars form in wide channels with low flow velocities. These results are partly in contrast to the hypothesis of Dalrymple and Choi (2007) and river theory, which

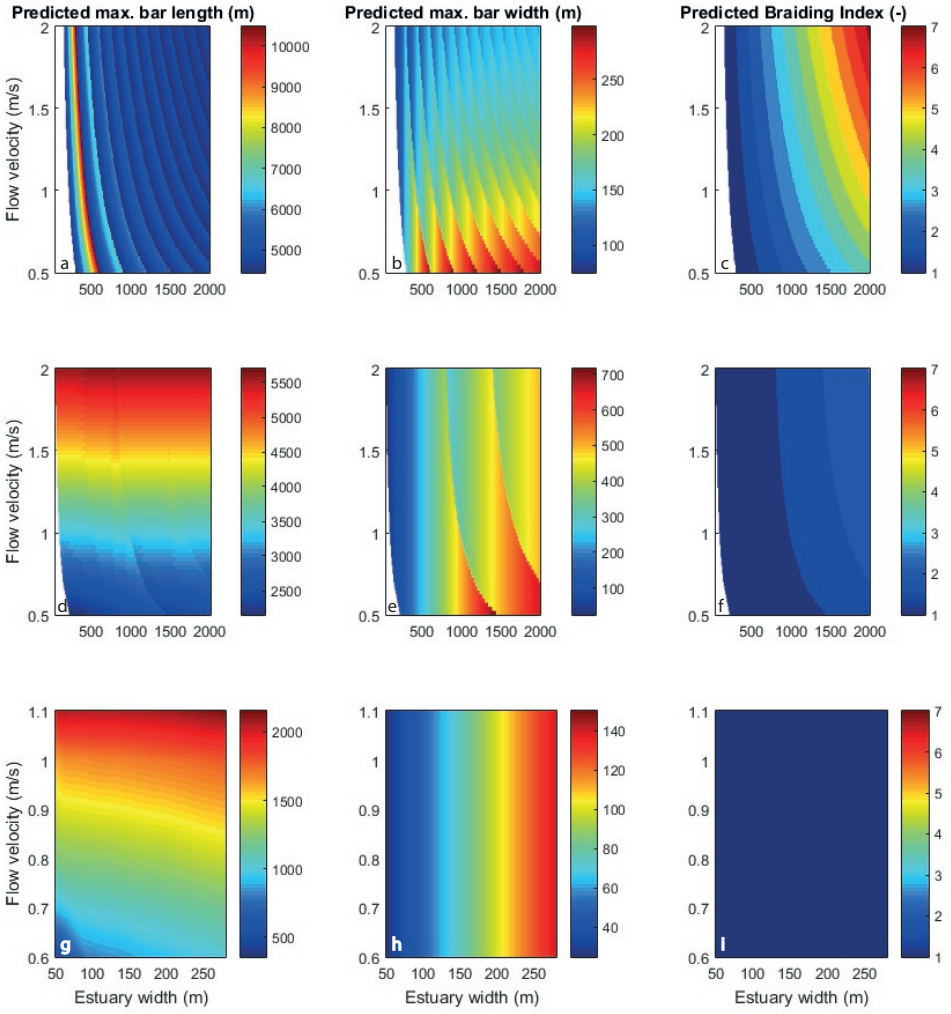

Figure 2.5 Prediction of bar length, bar width and braiding index by the stability analyses of Crosato and Mosselman (2009) (a,b,c), Schramkowski et al. (2002) (d,e,f) and Seminara and Tubino (2001) (g,h,i). Note that the scale of colour bars differs between theories and the range of channel widths shown for Seminara and Tubino (2001) is smaller.

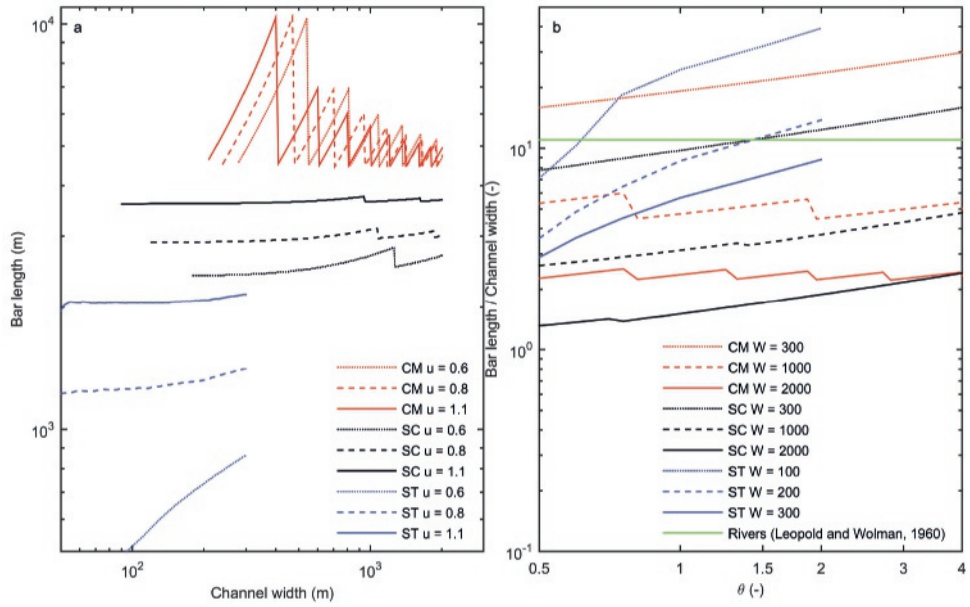

Figure 2.6 Predicted bar length (a,b) plotted as a function of estuary width (a) or Shields sediment mobility parameter (b) for a range of velocities (a) or channel width-to-depth ratios (b).

indicate that bar dimensions and braiding index relate to channel width. The theoretical models described here are compared with data of natural estuaries in section 2.4.4.

2.2.4 Sensitivity analysis

The default values and the range of varied values for the sensitivity analysis are given in Table 2.1. In the comparison, we calculated erosion constant α based on equal sediment concentrations in Seminara and Tubino (2001) and Schramkowski et al. (2002). In the sensitivity analysis, we set α to the default constant of Schramkowski et al. (2002), which is 10^{-5} [s m^{-1}].

The sensitivity analysis shows that predicted bar length and braiding index are most sensitive to friction (c_f) and channel geometry. Larger friction increases braiding index and decreases bar length (Fig. 2.7a,b). Increasing grain size (D_{50}), and coupled increasing settling velocity, results in lower braiding indices and shorter bars (Fig. 2.7e,f). For SC, the braiding index remains constant and the only effect is a decrease in bar length (Fig. 2.7e,f). D_{50} mainly influences bed slope effect in CM, which may explain a similar trend in sensitivity to D_{50} as to bed slope parameter r. Increasing bed slope effect reduces the braiding index, while bar length remains in the same order of magnitude (Fig. 2.7i,j). When the braiding index shifts towards a lower value, bar length increases. For constant braiding index and increasing bed slope effect, bar length decreases.

We varied width-to-depth (aspect) ratio in three manners: (1) by increasing channel depth while keeping width constant (Fig. 2.7c,d), (2) by increasing width with constant depth (Fig. 2.7g,h) and (3) by increasing width and depth according to the width-to-depth ratios found in natural estuaries (Fig. 2.7m,n):

$$h = 2.27W^{0.2} \tag{2.20}$$

Here, we used an estimation of the width-averaged estuary depth and the measured local estuary width of the natural estuaries in our dataset as described in section 2.3.2. The data are given in the

supplementary material. Suppl. Fig. 2.18c shows the data used for this regression. The goodness of fit (R^2=0.17) is sufficient for the purpose of a sensitivity analysis, but explains only part of the variance in estuary geometry as indicated by the confidence limits that plot approximately a factor 3 above and below the regression (Suppl. Fig. 2.18c).

Increasing the aspect ratio results in all cases in higher braiding indices. The braiding index decreases to 1 when width is fixed and depth is increased (Fig. 2.7d). Similarly, the braiding index is very sensitive to increasing width when depth is constant (Fig. 2.7h). When width and depth are coupled (Eq. 2.20), the braiding index increases with larger aspect ratios (Fig. 2.7n). Bar length increases with increasing depth (Fig. 2.7c).

Tidal period and tidal current velocity both influence the tidal excursion length. Therefore, we assessed the sensitivity to tidal period and current velocity in two ways (Fig. 2.7k,l,o,p). The dashed

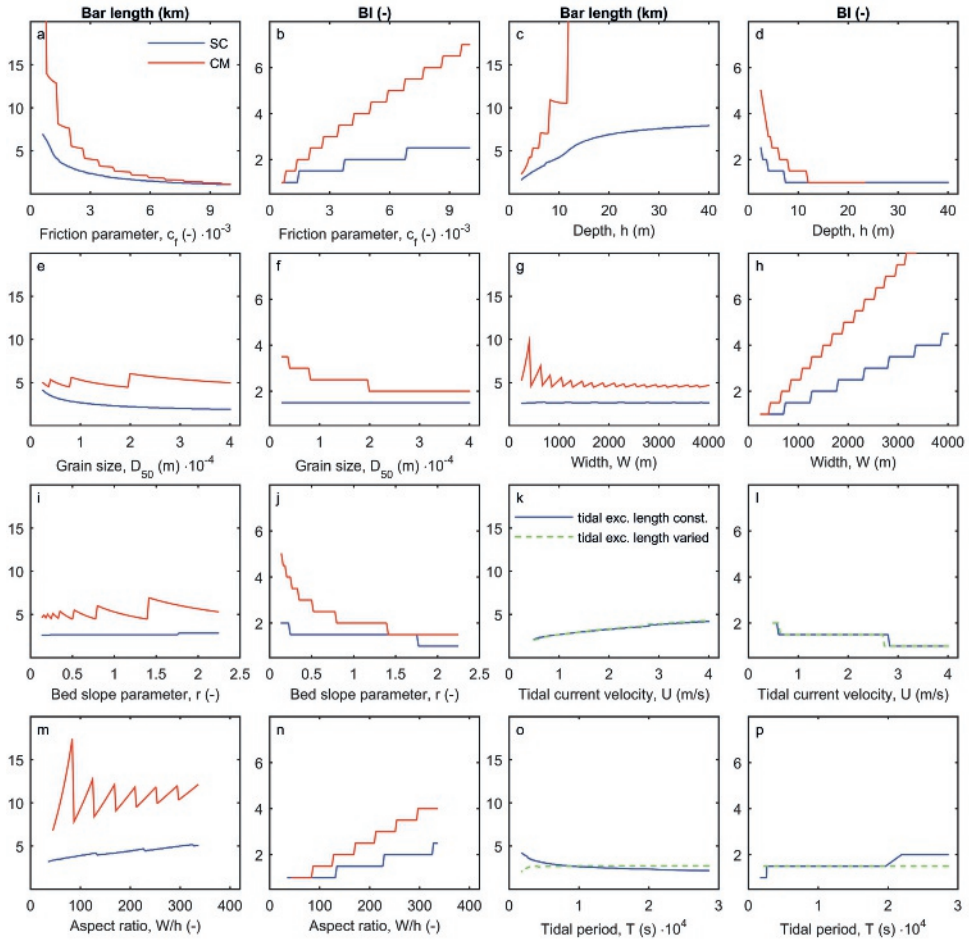

Figure 2.7 Sensitivity analysis of bar length and braiding index as a function of variables and parameters. Blue lines (SC) are calculated with Schramkowski et al. (2002) [fastest growing configuration in Eq. 2.1] and red lines (CM) are calculated with Struiksma et al. (1985) with the braiding index derived by Crosato and Mosselman (2009) [Eqs. 2.8-2.9].

lines in Fig. 2.7k,l,o,p show the cases for which either tidal period or current velocity was varied, thus allowing the tidal excursion length to vary. In the other cases, a change in tidal period was compensated by an opposite change in current velocity in order to exclude the possible effect of varying tidal excursion length (solid lines in Fig. 2.7k,l,o,p). Increasing tidal current velocities resulted in lower braiding indices and longer bars in all the cases mentioned above. This includes the cases where tidal excursion length was kept constant by decreasing tidal period when tidal current increased (Fig. 2.7k,l,o,p). Braiding index was insensitive to tidal period (Fig. 2.7p). Increasing the tidal excursion length by increasing the tidal period only resulted in longer bars when tidal current velocity was kept constant (Fig. 2.7o). Therefore, we concluded that bar dimensions are determined by tidal current velocity rather than tidal excursion length.

2.3 Data collection

2.3.1 Selection of estuaries

Satellite imagery was used to measure the shapes and dimensions of 190 bars in 45 estuaries all over the world (see Suppl. Table 2.2). We selected 45 funnel shaped alluvial estuaries with substantial tidal sand bars in order to be able to visually measure bar dimension from aerial images. Ideally, only laterally unconstrained estuaries *sensu* Townend (2012) would have been selected, analogous to the approach for rivers of Kleinhans and van den Berg (2011), excluding estuaries confined by geology, dams, groynes, artificial cutoffs or other local human interference. However, the sparsity of data on the hydrological and physical properties forced us to select the estuaries for which data were available. The dataset includes some estuaries with local constrains by human interference or by bedrock geology. In these cases, it was recorded in the dataset (see Suppl. Fig. 2.17). In addition, the presence of vegetation and the climate were recorded. All estuaries, except one, were located in temperate climate. Vegetation was present on 29 out of 190 tidal bars.

2.3.2 Data collection

Based on Google Earth images (accessed May-September 2015), we classified 190 bars and measured their dimensions. We used four classes: linear, U-shaped, compound and sidebars. The former three classes were in most cases completely surrounded by water, whereas sidebars were not. Bars were classified as sidebars if the length over which the bar was connected to the side of the estuary was larger than the bar width. Long bars with a relatively small width were classified as linear. The compound class was assigned when the bar was neither linear nor U-shaped (for examples, see Figs. 2.1, 2.3 & 2.8).

For all bars we measured maximum bar length (l), maximum bar width (w), perimeter and surface area (Fig. 2.8). Furthermore, we recorded the along-channel distance from the estuary mouth, the local width (W) of the estuary and the local braiding index (BI). In this study, local estuary width is defined as the width between the vegetated marshes or banks at the location of the measured bar including the sand bars. Moreover, we used this definition, because the timescale over which tidal marshes form is much larger than the timescale for the morphodynamic equilibrium of the bars in cross-section of the estuary (Kleinhans et al., 2015a). Measured local width is thus independent of the tidal elevation. On the other hand, measurements of individual bars were dependent on tidal elevation.

Bars were generally measured from aerial photographs between mean sea level (MSL) and low water level (LWL). The precise water level with respect to mean sea level was unknown for the moment at which an aerial photograph was taken. To investigate the likely measurement error arising from the unknown flow stage, we quantified the possible error for individual bars using high-resolution bathymetries of three estuaries. The following estuaries were used: the Western Scheldt (NL), Dovey Estuary (Wales) and Broad River Estuary (USA). Within each estuary,

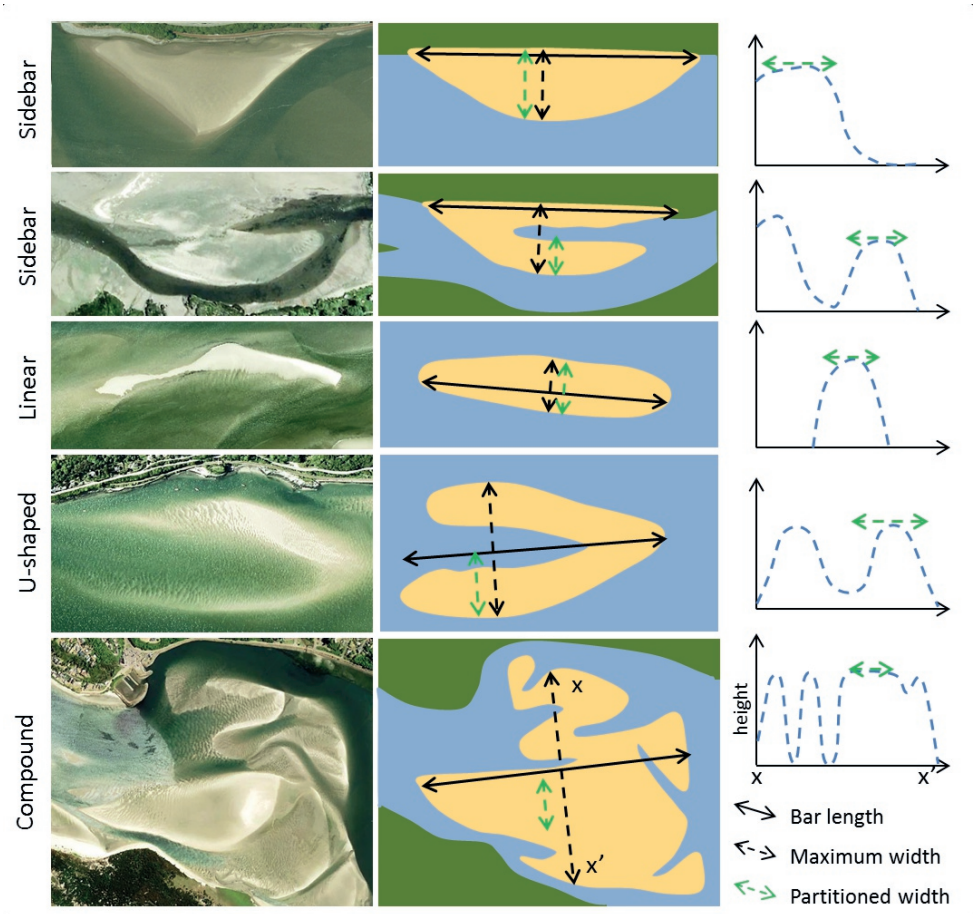

Figure 2.8 Description of four types of bar shapes in estuaries from images [left panels] to bar length and width measurement and recognition of individual bars and barb channels that compose the bar complex in planform [middle panels] and cross-section [right panels]. Partitioned bar width was calculated with Eq. 2.21.

hypsometric curves were calculated for four bars that were surrounded by channels and troughs. The root of the total area above a given elevation was used to obtain a characteristic measurement of length for each bar (Fig. 2.9a). We calculated the typical measurement of length for each bar at the water level exactly between MSL and LWL (Fig. 2.9b). The deviation of measurements taken at MSL or at LWL from the mean measurement of $area^{0.5}$ gave the typical uncertainty in bar measurements (Fig. 2.9c).

Bar height was measured in the three estuaries for which high-resolution bathymetry was available and eight additional estuaries in the UK for which lidar data are available from the UK government. These additional estuaries could not be used to study the sensitivity to water level variations, since accurate lidar data often do not extend to larger water depths. We calculated the total bar height (h_{bar}) as the sum of channel depth and bar height above mean sea level for the estuaries for which bathymetry was available. Channel depth was defined as the average local depth below mean sea level. Furthermore, we recorded the standard deviation of bar height above mean sea level.

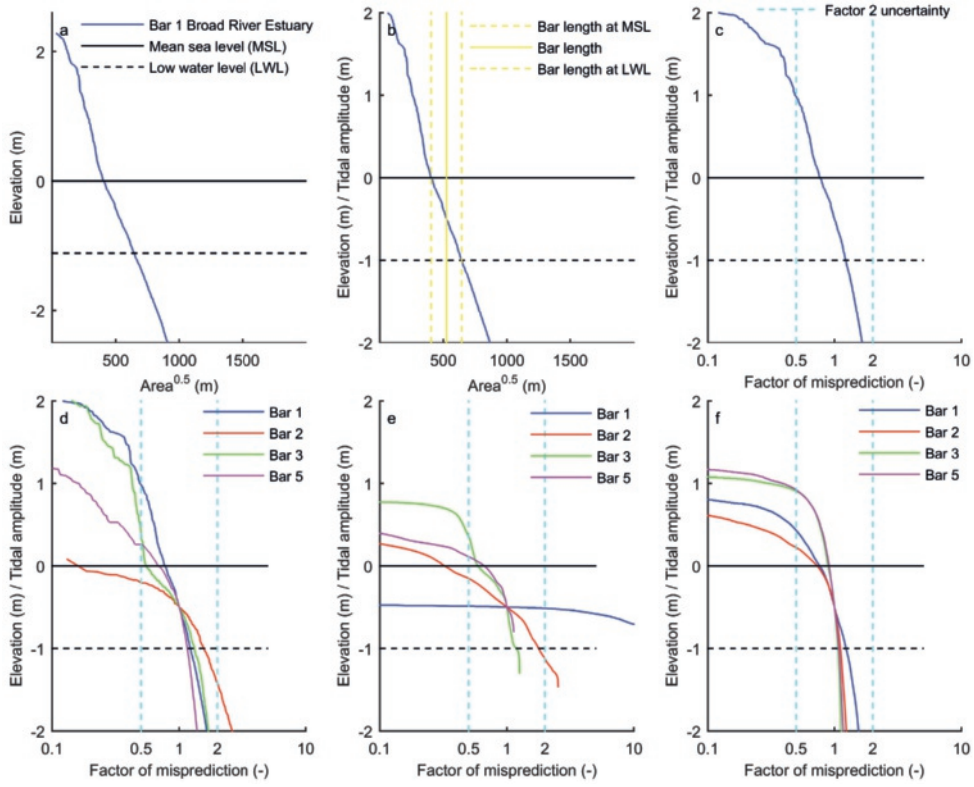

Figure 2.9 (a) Hypsometric curve of bar 1 in the Broad River Estuary. Bar numbers indicated in the legend correspond to bar numbers in the online supplementary material. The root of the total area above a given elevation was used as a characteristic measurement of length on the x-axis. (b) Elevation normalised by the tidal amplitude. A normalised value of 1 indicates the water level during mean high water level. Part of the bar may be elevated higher and only be flooded during spring tides. The dashed yellow lines indicate the range of measurements possible between mean sea level and low water level. The average measurement of $Area^{0.5}$ is indicated by a solid line. (c) Approximate factor of misprediction as a function of normalised water level for the full range of surface elevations. The likely error in measurement arising from the unknown flow stage is approximately a factor 2 for the Broad River Estuary (d), Mersey Estuary (e) and Western Scheldt (f).

Hydrological and physical properties were retrieved from the Enhanced UK Estuaries database (Manning, 2007), the National Estuarine Eutrophication Assessment Estuaries Database (USA, ian.umces.edu/neea), National Ocean Service's Estuarine Bathymetry (USA, estuarinebathymetry.noaa.gov) and in some cases specific data from a case study (Dalrymple et al., 1990; Jeuken et al., 2003; Billy et al., 2012; Wolanski, 2014; Alam et al., 2014). These data include typical flow velocities and estimates of tidal prism. In case of the UK Estuaries database, estimates of tidal prism were based on approximate measurements of high water volume and low water volume (Townend, 2005; Manning, 2007). Townend (2005) assessed the likely error arising from their approach and found that tidal prism is on average overestimated by 30%. Bathymetry and lidar data were obtained from Rijkswaterstaat (NL), Natural Resources Wales and the National Ocean Service's Estuarine Bathymetry (USA).

2.3.3 Data processing

Only the non-amalgamated bars should be compared with the predictions from linear stability analyses. Therefore, measured bar widths were partitioned by the number of barb channels that intersect the bar (Fig. 2.8). The barbs are traces of the amalgamation or incipient splitting of bars. In the framework of the theoretical approach (Fig. 2.4), both sedimentary and erosional mechanisms are indicative of the natural braiding index that develops in a system. Schuurman et al. (2013) showed that theory predicted the length of amalgamated bars well, but overpredicted the braiding index in case of unpartitioned amalgamated bars. Therefore, we divided the maximum width of side bars and compound bars by the sum of intersecting and surrounding channels (Fig. 2.8). Similarly, for U-shaped bars this means dividing the maximum measured width by 2 (Fig. 2.8). We calculated the partitioned bar width (w_p) as:

$$w_p = \frac{w}{(c-1)+b+s} \tag{2.21}$$

where c is the number of surrounding channels, b is the number of barb channels and s is 1 in case the bar type is sidebar and 0 in all other cases.

Based on the bar location, we calculated an estimation of the bar specific or local tidal prism, which is the total volume of water passing the tidal bar over half a tidal cycle. To obtain this, the approximate surface area upstream of the bar location was calculated and divided by the total surface area of the estuary. Consequently, the multiplication of this factor with the total tidal prism gave a bar specific estimate of the tidal prism.

For cases without bathymetry, we estimated width-averaged estuary depth at the bar locations. Savenije (2015) found that the depth along 28 estuaries often show a linear or almost linear profile. This is evidence that a linear interpolation between estuary mouth and upstream river is a reasonable estimate and in this case the only possible estimate for lack of data. Depth at the estuary mouth was available in the Enhanced UK Estuaries database (Manning, 2007) and depth at the mouth was measured from bathymetry when available. Other estuaries were left out this analysis. River depth was calculated based on hydraulic geometry for rivers (Leopold and Maddock Jr, 1953; Hey and Thorne, 1986):

$$h = bQ^q \tag{2.22}$$

where Q is the river discharge and b and q are constants, in which b is 0.33 and q is 0.35. Q was derived from the databases mentioned above. Measured estuary depth at bar locations was compared with the estimated depth, which showed that all predictions are within a range of 10% from the measured value. The Western Scheldt was an exception, with channels being 50% deeper than predicted as a result of the dredging activities. Given the difficulties and uncertainties in the prediction of estuary depth (Gisen and Savenije, 2015; Savenije, 2015) and the lack of detailed data on estuarine geometry, our approach seems a reasonable first step to assess whether a relation between bar dimensions and estuary depth may exist.

In the results section, regressions and confidence limits are given for the presented relations. Linear regressions were calculated minimising the residuals in both the x- and y-directions, which it is the most robust and conservative method. Confidence limits are given for two standard deviations from the regression. The legends show the approximate multiplication factor that the confidence limits plot higher or lower than the trend.

2.4 Results

In this section, we first present empirical relations between bar length, width and height. Then we explore relations between bar dimensions and braiding index with hydrodynamic and geometrical properties of the estuaries. From bathymetric data we check effects of water level variations on bar

shape and braiding index. Subsequently, the theoretical models are compared with the data. Suppl. Fig. 2.18 shows the hydraulic geometry relations in the dataset.

2.4.1 Bar shapes and dimensions

We visually classified four different types of bars based on their shape and connection with the estuary banks or marshes: linear, U-shaped, side- and compound bars. All bar types occur for the full range of measured dimensions: 50-30000 m long and 20-20000 m wide (Fig. 2.10a). Width-to-length ratio relates to bar type: linear bars are generally 3 to 15 times longer than their width, while U-shaped and compound bars are more circular or square with bar lengths of 1 to 5 times their width (Fig. 2.10a). Sidebars occur in width-to-length ratios of 1 to 15.

Fig. 2.10b shows that the range of width-to-length ratios narrows considerably when partitioned bar width is used. As a result of the similarity collapse, the range of all width-to-length ratios is equal to the dimensions found for linear sand bars:

$$l = 6.9 w_p \tag{2.23}$$

which is valid over more than two orders of magnitude (Fig. 2.10b). The similarity collapse supports the hypothesis that the amalgamation or incipient splitting of bars can be used to partition compound bars. A similar relation was found by Kelly (2006) for braided rivers:

$$l = 4.95 w^{0.97} \tag{2.24}$$

This implies that all bar classes in estuaries have approximately the same shape as river bars after partitioning, with sand bars in estuaries being on average slightly longer ($6.9 w_p$) than river bars ($4.95 w$).

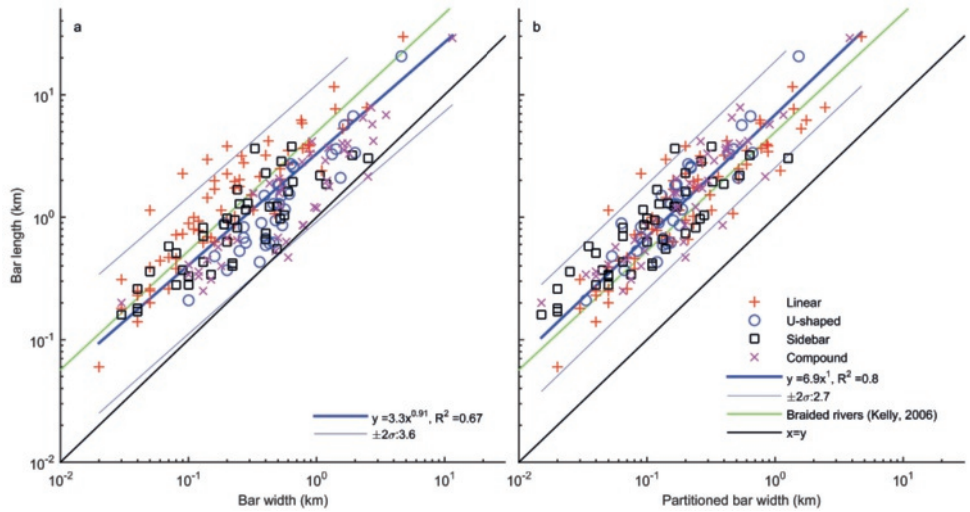

Figure 2.10 (a) Relation between bar length and bar width. (b) Same, with partitioned width after division based on the number of barb channels. The Kelly (2006) relation for braided rivers (Eq. 2.24) and the line of equality are drawn for comparison. Confidence limits are given for two standard deviations from the regression. The legend shows the approximate multiplication factor that the confidence limits plot higher or lower than the trend.

Fig. 2.11a,b shows that bar dimensions appear to be interrelated. We found that bar length could be predicted within a factor 5 when bar height is known (Fig. 2.11b). The goodness of fit for bar width as a function of bar height is much lower and the scatter is larger (Fig. 2.11a).

The three-dimensional shape of bars in estuaries is best characterised with half an ellipsoid (Fig. 2.11c). This results from calculations of bar volume (V), based on measurements of bar length (l), width (w_p) and height (h_{bar}):

$$\frac{1}{2}V_{ellipsoid} = \frac{1}{6}\pi l w_p h_{bar} \tag{2.25}$$

Calculating bar volume as a square box would lead to an overprediction of bar volume, while adapting the shape of half a cylinder would lead to an underprediction. However, when the ellipsoid is used as a characteristic shape, the calculated bar volume predicts bar volume well within a factor 3 (Fig. 2.11d). Either bar length, width or height could be used to predict bar volumes (Fig. 2.11e,f). The prediction is most accurate when bar length is used:

$$V = 0.08l^{2.3} \tag{2.26}$$

We found that U-shaped bars form in both ebb and flood directions and that linear and compound bars have often steep edges on both their seaward and landward side. Ebb- and flood-dominated currents typically produce mutually evasive tidal channels (van Veen, 1950; Kleinhans et al., 2015b) that often end in barb channels. Most of these features seem to be unique for tidal environments, which raises the question: to what extent are the forming mechanisms of bars in estuaries similar to the mechanisms that form bars in rivers?

2.4.2 Relation between bar dimensions and estuarine properties

In general, we found that bar dimensions scale with estuary dimensions, in particular with width and depth. Bars are clearly longer in wider estuaries and in higher tidal current velocities (Fig. 2.12a). Bar length varies from 3 times smaller to 3 times larger than the estuary width (Fig. 2.12c). Part of this spread is the result of two trends. First, bar length normalised with estuary width decreases with estuary width-to-depth (aspect) ratio, where bar length equals estuary width for an aspect ratio of about 200 (Fig. 2.12e). Second, bar length is largest for higher tidal current velocities (Fig. 2.12a,d). Nevertheless, bar length is independent of tidal current in the range of 0.8 to 1.2 $m\,s^{-1}$ (Fig. 2.12d). Moreover, estuary width correlates with bar length within this range (Fig. 2.12a,c). Bar length correlates better with estuary width than with peak tidal current velocity, which is described by:

$$l = 0.97W^{0.87} \tag{2.27}$$

Furthermore, the bar shape correlates with estuary width: sidebars occur in smaller channels and channels with a lower aspect ratio, while U-shaped bars occur on the higher end of the widths and aspect ratios (Fig. 2.12c,e).

Bar length scales with tidal prism (Fig. 2.12f) with a goodness of fit of 0.48. Nevertheless, the approximate multiplication factor that the confidence limits plot higher or lower than the regression indicates scatter of an order of magnitude. The scatter occurs for two reasons: half of the tidal prism data was retrieved from the dataset of Manning (2007), for which Townend (2005) calculated that the error may be approximately 30%. The second reason is that we estimated the local tidal prism based on the location of the tidal bar within the estuary. These results thus provide an initial indication of the relation that is present between tidal prism and bar dimensions. Possibly, the use of measured surface area in combination with tidal amplitude would result in a better prediction of the along-channel variation in bar patterns, but this is beyond the scope of this chapter.

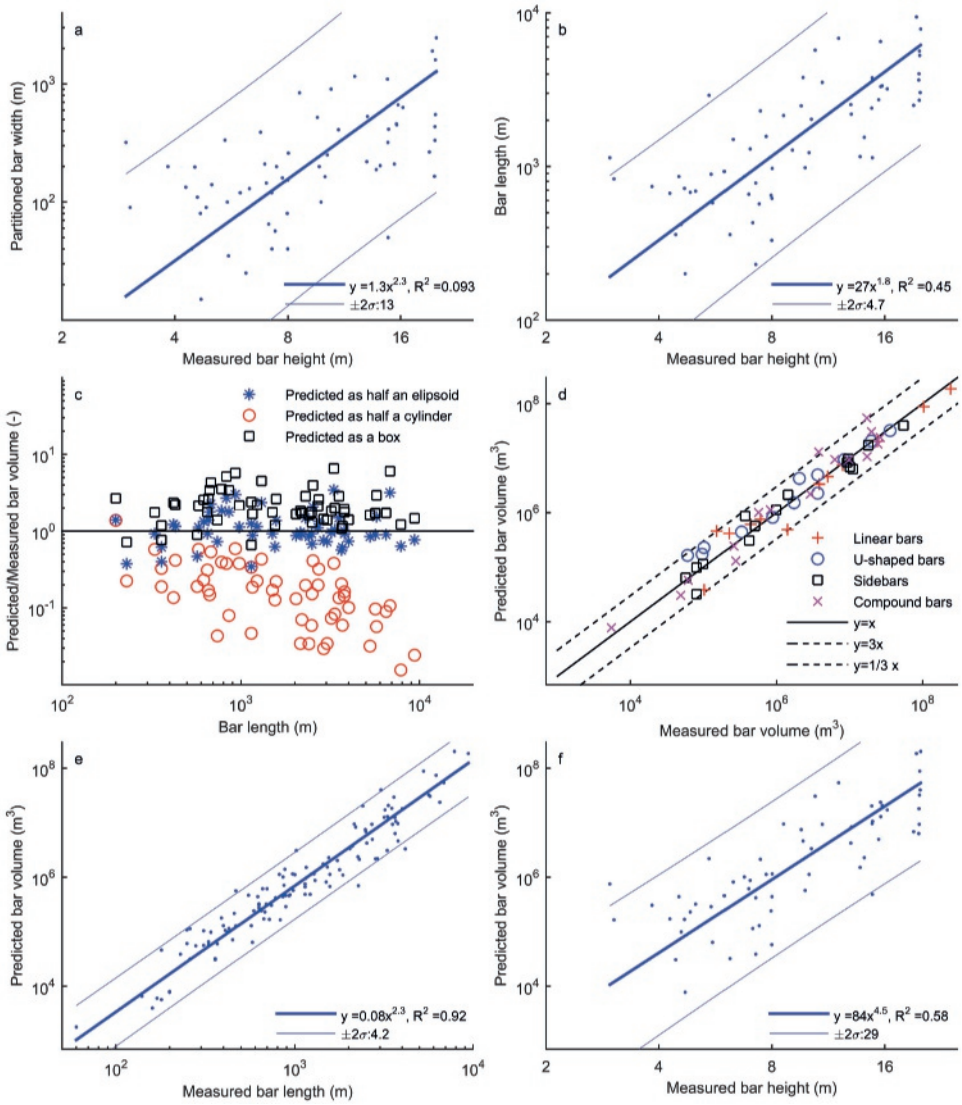

Figure 2.11 (a,b) Relation between (a) partitioned bar width and bar height and (b) bar length and bar height. (c) Comparison of measured bar volume from bathymetric data with predicted bar volume for idealised bar geometries: half an ellipsoid (Eq. 2.25), half a cylinder and a square box. The closest agreement is obtained when bars are represented as half an ellipsoid. (d) Measured bar volume compared with predicted bar volume using half an ellipsoid for different bar types. (e) Predicted bar volume as a function of bar length. (f) Bar volume as a function of bar height. Confidence limits are given for two standard deviations from the regression. The legend shows the approximate multiplication factor that the confidence limits plot higher or lower than the trend.

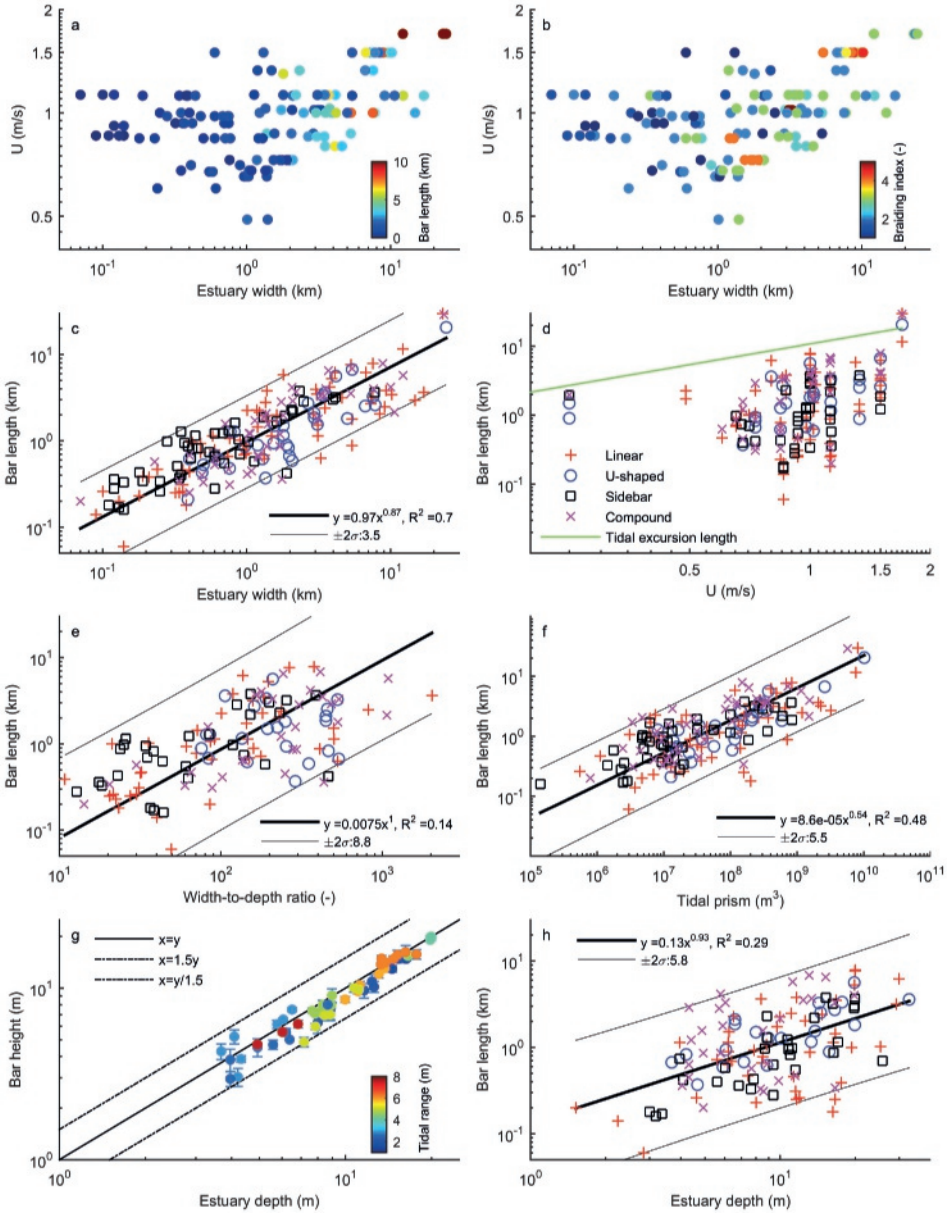

Figure 2.12 Bar dimensions as a function of estuarine dimensions and flow characteristics. (a,b) Lack of relation between tidal velocity amplitude and bar properties. Bar length as a function of local estuary width (c), tidal current velocity (d), estuary width-to-depth ratio (e) and tidal prism (f). (g) Bar height as a function of local water depth. Error bars are one standard deviation and colour indicates tidal amplitude. (h) Bar length against estuary depth. Confidence limits are given for two standard deviations from the regression. The legend shows the approximate multiplication factor that the confidence limits plot higher or lower than the trend.

The braiding index mainly depends on estuary width and aspect ratio (Fig. 2.12b). For equal tidal current magnitude, the braiding index increases with estuary width. However, for the same estuary width, the braiding index may vary between 1 and 5. Local width is thus insufficient to predict braiding index.

For all measured estuaries, bar height equals estuary depth within a factor 1.5 (Fig. 2.12g). In addition, the standard deviation of bar height falls within the tidal range of the estuary. For low estuary depths, the Parrett estuary (UK) seems an outlier with a tidal range of almost 8 m at the mouth. However, in this case the estuary is small (width 100-500 m and depth approximately 4 m), resulting in a much smaller tidal range (2 m) within the estuary.

2.4.3 Dependence of bar shape and braiding index on water level

The braiding index and bar shape depend strongly on water level as illustrated by Figs. 2.13 and 2.14. For example the Western Scheldt shows how bar type may alter from sidebar to linear bar in the transition from low water to higher water (Fig. 2.13c,e,g). Length-to-width ratios of non-partitioned bars support this. It may vary from 2.3 at low water, to 5.5 at higher water and 2.9 at mean sea level. Other estuaries show similar trends. For example the Broad River Estuary shows a U-shaped bar with a length-to-width ratio of 2.6 that alters to a linear bar with a ratio of 15.6 for increasing water levels (Fig. 2.13d,f,h). In addition, the braiding index changes: from 1.5 to 3 and at mean sea level to 2 in Western Scheldt and from 2.5 to 2 in the Broad River Estuary (Fig. 2.13b,d,f). These results imply that U-shaped bars and sidebars may occur as linear bars under higher water levels and that the braiding index is highly sensitive to water level in imagery.

Fig. 2.14 shows the variation of bar shape and braiding index at different bar locations in three estuaries for which bathymetric data was available. Since estuary width is constant for different water levels, the variation of bar shape and braiding index at a specific bar location can be seen in the vertical aligned markers. The variation caused by water level alterations over a tidal cycle spans almost an order of magnitude for both length-to-width ratio and bar length (Fig. 2.14). This is similar to the variation that occurs within our dataset of all 190 bars. Similarly, the variation of braiding indices that occurs for a specific width is almost the same for the full dataset as for one location at different water levels.

Nevertheless, the measurements from aerial photographs were taken between mean sea-level and low water level. Within this range, the uncertainty is limited to about a factor of two (Fig. 2.9d,e,f), which is reasonable given the scatter in the full dataset of estuarine bars. Fig. 2.9d,e,f shows that apparent bar dimensions are particularly sensitive to water level above mean sea level, when they are increasingly flooded. This uncertainty is smaller than the degree to which the bars collapse on a trend with limited scatter, before and after they were partitioned.

2.4.4 Comparison of theory and data

We compared the data with bar length predictions from the theoretical model (Schramkowski et al., 2002) for the same width, depth and tidal current velocity as for the gathered dataset (Fig. 2.15). We assumed here, that all other estuarine properties such as sediment properties and bottom roughness are equal for all estuaries for a lack of more detailed data (see default values in Table 2.1). Theoretical model results of bars are in the same order of magnitude as natural estuaries. For the same range of estuary dimensions as the natural estuaries used in this study, theory predicts bar lengths of 500-30000 m. Both theory and data show bar lengths of 3-40 times bar width (Fig. 2.5 and Fig. 2.10).

Bar theory predicts bar length within the same order of magnitude in case of large bars, which are tens of kilometres long (Fig. 2.15a,b). In contrast, the length of shorter bars is overpredicted by one or two orders of magnitude. In all cases, bar theory predicts bar lengths in the order of the tidal excursion length (Fig. 2.15c), while data shows bar length to be up to an order of magnitude smaller. Surprisingly,

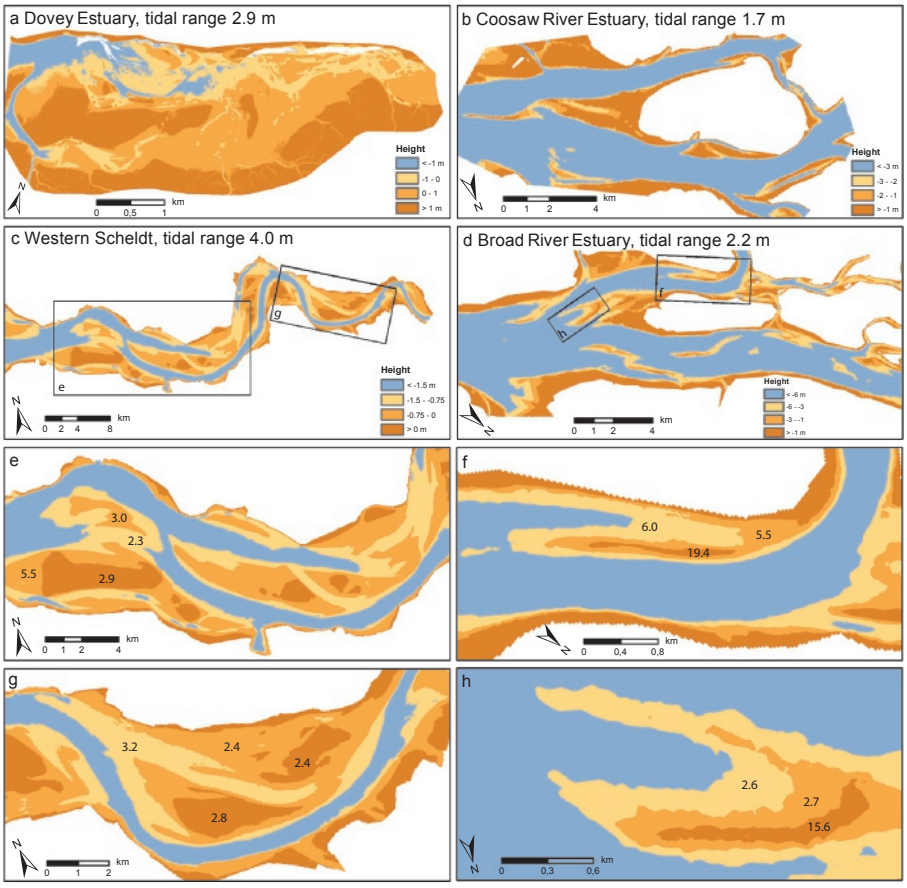

Figure 2.13 Maps showing the effect of water level variation on emergent bar surface in the Dovey Estuary (a), Coosaw River Estuary (b), Western Scheldt (c,e,g) and Broad River Estuary (d,f,h). Values in e-h indicate the length-to-width ratio of the bar at a specific water level.

tidal theory of Schramkowski et al. (2002) predicts bar length reasonably well when the aspect ratio is assumed to be 2000 for all estuaries (not shown here). This shows that the theory is not capturing the observed trends, or that the theory is not valid for fully developed bars, unlike the successful application of river bar theory to fully developed patterns (Kleinhans and van den Berg, 2011).

For aspect ratios below 100, the bar theory predicts a braiding index of 1 (Fig. 2.15d). In natural estuaries a range of braiding indices between 1 and 3 occurs for aspect ratios between 10 and 100. Bar theory predicts fairly similar braiding indices for aspect ratios higher than 100. Bar theory thus underpredicts the braiding index for relatively narrow and deep estuaries. Moreover, the quality of bar length prediction also increases for systems with a high aspect ratio or a large width (Fig. 2.15a,b).

2.5 Discussion

Below, we will first compare the range of bar shapes and dimensions that occur in natural estuaries with results from studies on river bars and laboratory scale experiments. Thereafter, we will compare

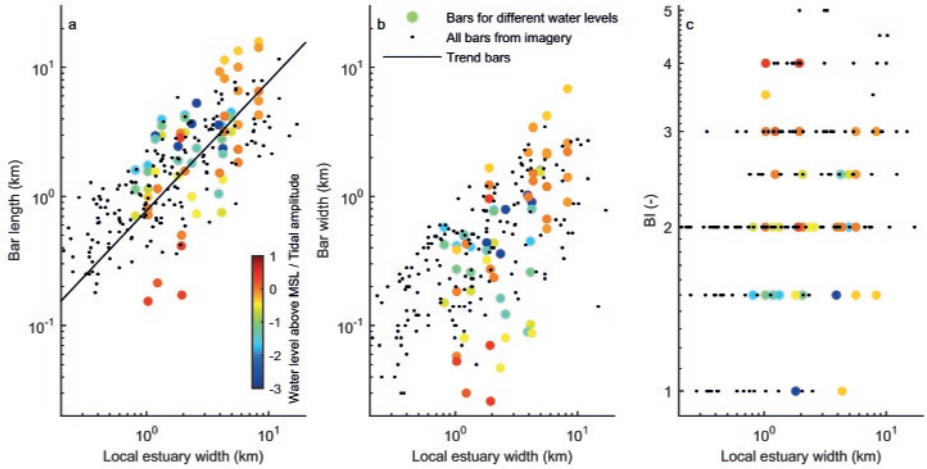

Figure 2.14 The dataset with 190 bars from this study, compared with the variation in bar length (a), bar width (b) and braiding index (c) occurring in three estuaries due to water level variations. Vertically aligned circles represent one bar for different water levels, where colour indicates water level above MSL normalised by tidal range.

the results with hypotheses from physics-based bar theory and previous studies, which enables us to assess the usability of theoretical models for prediction of real world bar patterns. Then, we link the bar dimensions with hydrodynamic and geometrical properties of estuaries. Finally, we describe the major implications for reconstruction of bar architecture by geologists and for future studies on bar patterns.

2.5.1 Bar dimensions in data and theoretical models

We found that bar shapes and dimensions in natural estuaries are similar to bars in braided rivers (Kelly, 2006) and in laboratory scale experiments (Fig. 2.16). Bars in estuaries are on average 6.9 times longer than their width, which is more elongated than bars in rivers, where bars are 4.95 times longer than their width. We obtained this result after partitioning of the bar width based on the number of barb channels (Fig. 2.8). Before partitioning (Fig. 2.10a), bar lengths are on average 3.3 times their width to the power of 0.9, which is very similar to the relation found for model results of braided rivers ($l = 2.98w$) (Schuurman et al., 2013).

Our results are in good agreement with studies on river bars after considering the difference in methodology for measuring bars (Kelly, 2006; Schuurman et al., 2013). Kelly (2006) mainly measured bars as single linear bars without intersecting channels, while Schuurman et al. (2013) recorded bar length and width of full bar complexes including cross-bar channels. They found that river bar length is well predicted by theoretical models, while the braiding index is overpredicted in case of amalgamated braid bars. The methodology of Schuurman et al. (2013) resembles our methodology before partitioning, whereas the methodology of Kelly (2006) is similar to our methodology after partitioning bar width.

Until now, the forming mechanism of mutually evasive channels is unknown. As an example, we describe three theories for the formation of a U-shaped bar. U-shaped bars are better developed in estuaries than on open coast. For that reason, Wood (2004) hypothesised that these bars only form when the ebb- and flood-dominated channels are well-developed. In shallow-water settings, sandbanks spread laterally, merge with each other, and become dissected by ebb- and flood-dominated channels. Potential explanations for the formation of a U-shaped bar are (1) one current depositing sediments in

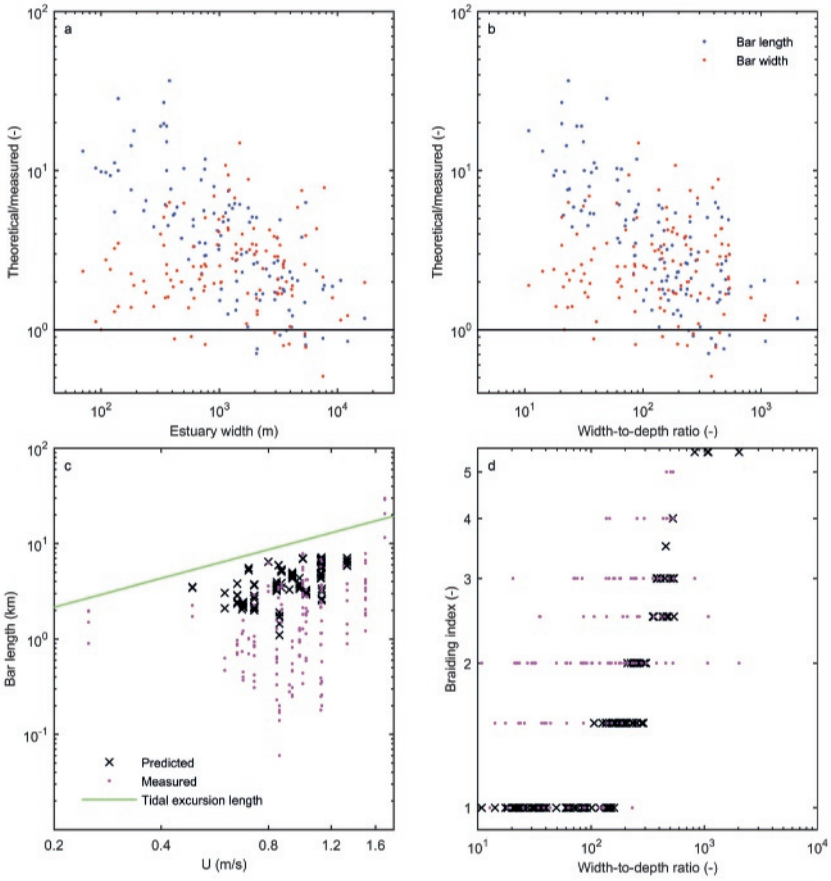

Figure 2.15 Comparison of data with theoretical model results as obtained from the theoretical model of Schramkowski et al. (2002) with the same width, depth and tidal current velocity as for the data.

a fan shape, while the other current evades the fan, (2) a tidal channel forming an unsuccessful chute cutoff and (3) linear bars connecting by lateral migrations (Sambrook Smith et al., 2006; Dalrymple and Choi, 2007).

Furthermore, we found relations between bar dimensions and relations with bar volume (Eqs. 2.23-2.27, Figs. 2.10-2.11). In principle, it should be possible to predict bar length and width with bar height. Nevertheless, predictions may be off by an order of magnitude due to the scatter and as indicated by the lower R^2 values. Bar volume is best represented as half an ellipsoid (Fig. 2.11c), which allows to predict bar volume within a factor 3 if all bar dimensions are measured (Fig. 2.11d). Prediction of bar volume with bar length works better (Eq. 2.26, Fig. 2.11e) than prediction with bar height (Fig. 2.11f). This suggests that bar volume may be mispredicted by an order of magnitude when bar height from a single outcrop or drilling core is used.

Wood (2004) collected bar width and height from geological outcrops and presented data on tidal ridges in open oceans, river mouths, heads of bays and tidal coasts (Off, 1963). For geological outcrops, Wood (2004) found bar heights ranging from 1.4-6.8 m and bar widths from 380-1800 m. For the modern tidal sandbank data (Off, 1963), Wood (2004) found typical median values for bar

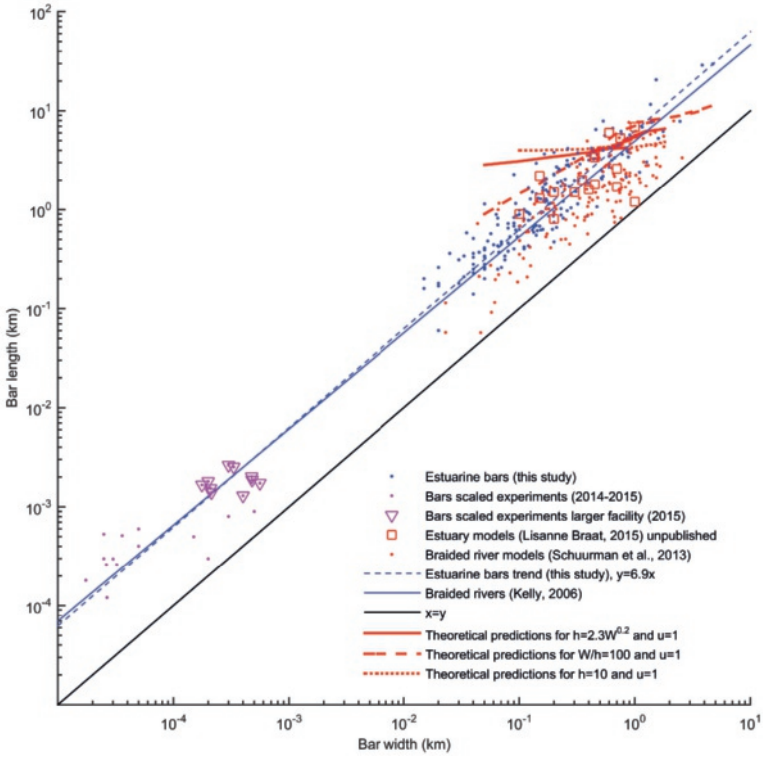

Figure 2.16 Comparison of bars in our dataset with theoretical predictions of Schramkowski et al. (2002), numerical models and scaled laboratory experiments across six orders of magnitude.

length (12 km), width (1.6 km) and height (9.2 m). The data we collected for estuarine systems consist of considerably smaller bars: median length is 1.1 km and width is 0.3 km. The variation in bar height is very similar in our dataset, with a median of 8.6 m. The largest bars in our dataset have similar dimensions as the smallest bars in the dataset of Off (1963). This may be explained by the environment in which the data were collected. Many bars measured by Off (1963) were collected in offshore environments, such as bars in the northern end of the Persian Gulf, which also means that they were formed by a different mechanism (Dyer and Huntley, 1999). In contrast, our data is limited to bars within estuarine systems, where bars are significantly smaller. Nevertheless, the trends on length-to-width ratios of bars are very similar in both datasets. Bars in Off's dataset show slightly more elongated shapes than bars in estuaries with lengths on average 9.9 times longer than their width.

2.5.2 Applicability of the theoretical models

Given similar flow velocities in a large range of estuary scales, bar theory consistently overpredicts bar dimensions by an order of magnitude in the case of small estuaries. Neither imposing aspect ratios of natural estuaries (Fig. 2.16, Eq. 2.23) nor using a constant depth results in well-predicted bar dimensions. Better predictions were found for the braiding index which depends mostly on local channel aspect ratio in the theories. We conclude that the theory underpredicts the strong dependency of bar length and braiding index on estuary width as found in our data and for rivers.

We assumed that properties such as sediment type and bottom roughness are equal for all estuaries, which in principle may cause a misprediction of bar properties. Nevertheless, the sensitivity analysis showed that bar length is rather insensitive to grain size, bed slope effect and estuary width in tidal theory. Bed slope effect only has a minor influence on the braiding index, while estuary width clearly alters the braiding index (Fig. 2.7). Only the friction coefficient may influence bar length such that it alters by an order of magnitude. Longer bars are predicted for lower friction. In conclusion, theoretical model predictions are only slightly sensitive to the default parameters as specified in Table 2.1, meaning a rather general validity of our results.

An important assumption in linear theory is that the perturbations have a small amplitude relative to water depth, to avoid nonlinear effects becoming important. This means that both agreement and mismatch between data and theory can be due to a problem in the theory and due to deviations between incipient bars and fully developed bars. For rivers, bar theory works quite well with accurate bar length and braiding indices despite the full nonlinear development of the bars, which can suggest that something similar should hold for bars in estuaries if there are sufficient similarities in the processes. However, we found very large deviations between trends and magnitudes in the data and the predictions. Future tests with numerical models and experiments may show whether incipient bars are greatly different from fully developed bars. This means that we presently lack understanding of the formative mechanism of sand bars in estuaries.

2.5.3 What determines bar properties?

Bar length is often much shorter than the tidal excursion length and bar length is independent of the amplitude of tidal current in our dataset, in contrast to hypotheses from previous theory (Seminara and Tubino, 2001; Schramkowski et al., 2002). So the hypothesis that bar length depends on system width – which was proposed in river theory (Kleinhans and van den Berg, 2011) and suggested for tidal systems (Dalrymple and Rhodes, 1995; Seminara et al., 2001; Dalrymple and Choi, 2007) – is more appropriate for tidal systems than the hypothesis from tidal theory which states that bar length depends of the amplitude of tidal flow velocity. Previous authors proposed for bar length a ratio of 6-10 times channel width in tidal systems (Seminara et al., 2001) and 6 times channel width for tidal creeks (Dalrymple and Rhodes, 1995). Our data suggests that bar length for estuaries may rather be of the same magnitude as the estuary width (Eq. 2.27).

The dataset with tidal bars includes some constrained and vegetated bars. For rivers with meandering, where floodplain formation is important for the pattern, that would have been a problem (Kleinhans and van den Berg, 2011). However, the dimensions of estuarine sand bars are related to estuary width, regardless how that width came about. For estuaries, the effects of constraints and vegetation on bar shapes and dimensions are thus undiscernible (Suppl. Fig. 2.17).

The Brahmaputra River showed a power relation between bar length and river discharge (Ashmore, 2001). Our data resulted in a broad brush relation for a similar relation for bar length in estuaries: on average larger bars occur in estuaries with larger local tidal prisms (Fig. 2.12f). To capture the along-channel variation in bar patterns within an estuary, we may require a more accurate estimate of the local tidal discharge or a bar specific estimate, which equates to the upstream tidal prism plus any river discharge. A possible estimation could be made with the estuary shape and tidal range, since we often lack data on tidal prisms or the quality of these predictions is low (Townend, 2005).

Field observations and numerical model results for estuaries imply that more braided bars form when the aspect ratio increases (Dalrymple and Rhodes, 1995; Hibma et al., 2003; Toffolon and Crosato, 2007). As a threshold, an aspect ratio of approximately 100 is suggested for the transition from alternate bars to multiple bars (Dalrymple and Rhodes, 1995; Hibma et al., 2003). Both theoretical models and data in this study show that the braiding index increases with increasing estuary width and increasing aspect ratio (Figs. 2.5 and 2.7). This is similar to trends found in river theory, where aspect ratio is

considered the major control on the braiding index (Struiksma et al., 1985; Schielen et al., 1993; Hibma et al., 2003; Kleinhans and van den Berg, 2011). Bar theory for tidal systems predicts that the braiding index depends on tidal current velocities for wide channels and that bar length reduces with higher braiding indices, which does not agree with our data.

2.5.4 Applications

Geological architecture of tidal bar dimensions and thus reservoir size has been estimated with the median, 10th percentile and 90th percentile of modern tidal systems (Wood, 2004), which is rather inaccurate because this assumes independence on estuary dimensions and properties of tidal flow. We found that bar dimensions in estuaries are an order of magnitude smaller than the bars in the dataset of Off (1963), except for bar height.

However, the surface metrics of tidal bars that we collected cannot directly be linked to the subsurface metrics without relying on an empirical preservation ratio between feature height determined from surface morphology and subsurface architecture (Allen, 1984; Paola and Borgman, 1991; Bridge and Best, 1997; Straub et al., 2009; Ganti et al., 2011). Typical preservation ratios for ripples, dunes and river bars are 0.1-0.3 (Storms et al., 1999; Blom and Kleinhans, 2008; van de Lageweg et al., 2015). Although such generalisations are likely to extend to tidal systems, there clearly is a need for further study for application in process-driven reservoir characterisation.

Our analyses showed which factors determine bar dimensions and braiding index. These factors are mainly related to estuary dimensions, for which we have no predictors yet. Previous studies hypothesised that bar height increases with the lateral distance between bars (Allen, 1968), which increases with water depth according to Huthnance (1982). From these relations, one can derive an expression for the braiding index and bar width as a function of water depth. However, these relations would conflict with the hypotheses of Dalrymple and Rhodes (1995), who suggested that narrower bars typically occur in deeper channels. Swift and Field (1981) also documented a systematic decline in the length and width of tidal sandbanks as water depth increases. In short, we require a predictor for estuary width, such as the reference width in river systems (Kleinhans and van den Berg, 2011). Consequently, similar empirical bar pattern predictors may work successfully for estuaries, such as the potential stream power.

Future experiments and numerical modelling will allow us to systematically vary initial and boundary conditions to explore further what determines bar patterns. The empirical relations provided here will form a reference frame for comparison to experiments, analytical and numerical models and provide an estimate of bar dimensions when limited data is available. Additionally, an understanding of what determines the equilibrium bar pattern will enable us to study the evolution of sand bar patterns over time.

2.6 Conclusions

To investigate tidal bar patterns we collected a dataset on sand bar shapes and dimensions in funnel-shaped alluvial estuaries, mainly located in the USA and Europe. Comparison with braided river data shows that bars in estuaries are similar but 30% more elongated, being on average 6.9 times longer than their partitioned width. Bar height in estuaries approximates the local estuary depth. Bar shapes in estuaries show unique features, such as the mutually evasive ebb- and flood-dominated tidal channels, but in other aspects resemble river bars. However, until their formative mechanisms are better understood, it remains unclear to which extent linear, U-shaped, side- and compound bars in estuaries are similar to unit and compound bars in rivers. U-shaped, side- and compound bars are on a average 2-3 times wider than linear bars, which is explained by barb channels, which may either be interpreted as remnants of cross-bar channels or of the amalgamation of smaller bars. After dividing

up the bars at the barb channels, we found a similarity collapse of all bar types for the length-to-width ratio.

We tested a linear stability theory for bar properties in which predicted bar length strongly depends on the amplitude of tidal current or tidal excursion length. Measured bar dimensions, in contrast, show the strongest relation with estuary width. Given that estuaries of a wide range of sizes only exhibit a narrow range of flow velocities, the bar theory of Schramkowski et al. (2002) predicts bars of similar sizes regardless the size of the estuaries. In particular, the theory overpredicts bar dimensions in small estuaries by an order of magnitude. The theory underpredicts the strong dependency of bar length and braiding index on the estuary width as found in the data and for rivers. Better predictions were found for the braiding index which depends mostly on local channel aspect ratio. We present empirical relations for bar dimensions and for bar length as a function of local estuary width. The new relations may aid comparisons between experiments, models and natural systems, and may be applied in outcrop interpretation.

Acknowledgments

We are grateful to George Schramkowski for his help and making his code available and to Maarten Zeylmans van Emmichoven for his GIS support. Discussion with Tjalling de Haas, Wietse van de Lageweg and Lisanne Braat and reviews by Ian Townend and one anonymous reviewer helped to improve the manuscript. The authors contributed in the following proportions to conception and design, data collection, modelling, analysis and conclusions, and manuscript preparation: JRFWL(50, 70, 60, 50, 70%), MGK(50, 0, 10, 30, 25%), SAHW(0, 30, 0, 10, 0%), MvdV(0, 0, 30, 10, 5%). Online supplementary material is available at: http://dx.doi.org/10.1016/j.earscirev.2016.08.004.

Supplementary material

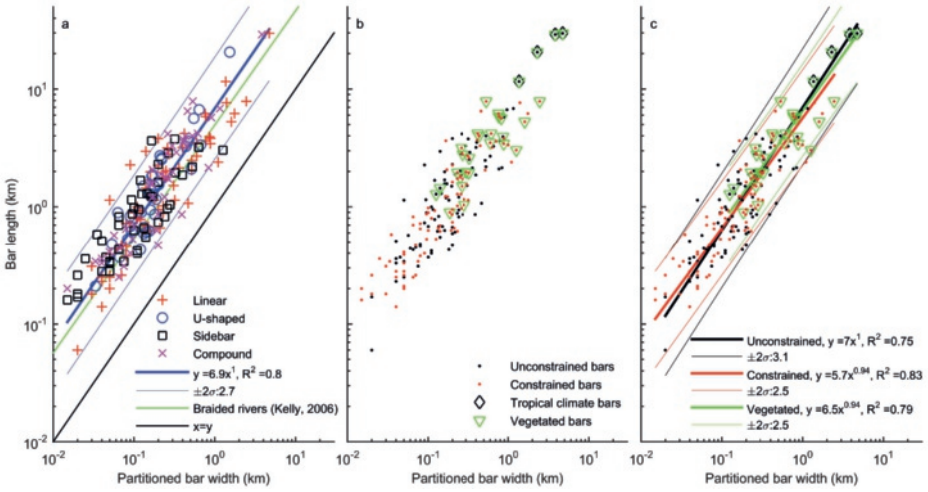

Figure 2.17 (a) Relation between bar length and bar width. The Kelly (2006) relation for braided rivers (Eq. 2.24) and the line of equality are drawn for comparison. (b) The presence of constrains, vegetation or a tropical climate at the location of tidal bars. (c) Constrains, vegetation and climate in our dataset have no discernible effect on bar shape and dimensions. Confidence limits are given for two standard deviations from the regression. The legend shows the approximate multiplication factor that the confidence limits plot higher or lower than the trend.

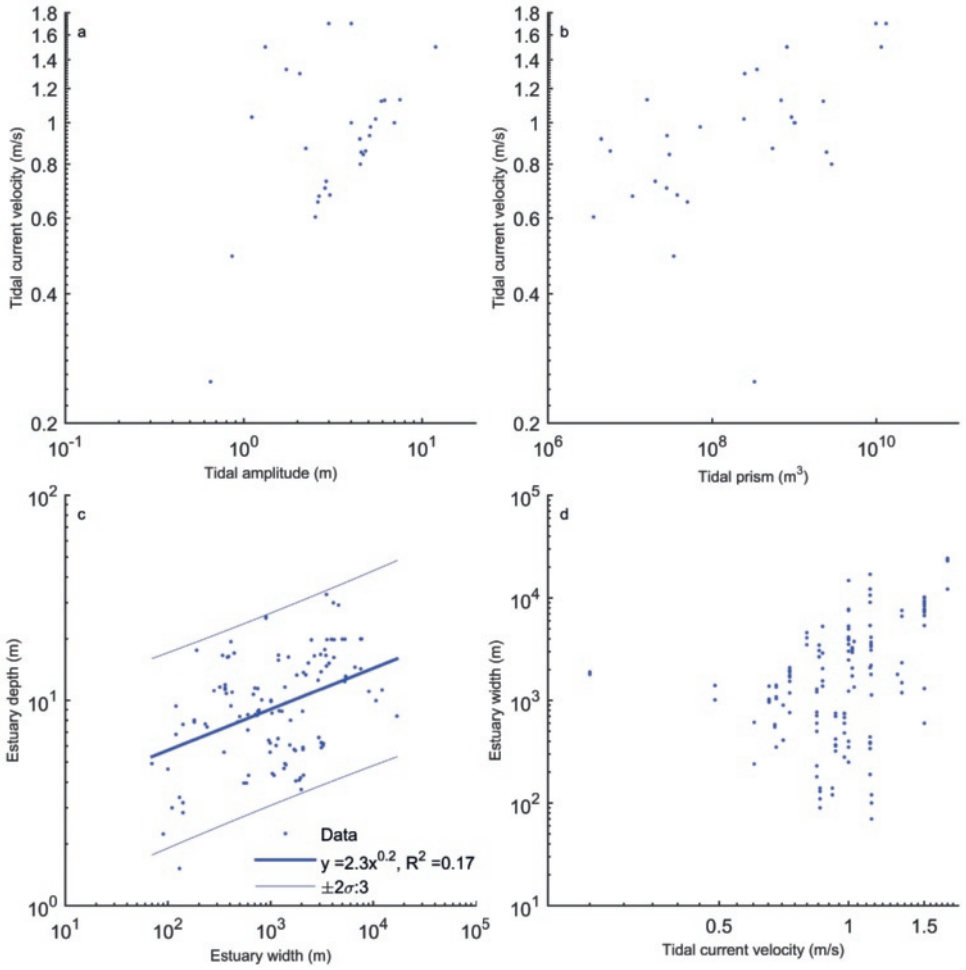

Figure 2.18 Lack of hydraulic geometry correlations in the dataset of estuary dimensions. Tidal current velocity as a function of tidal amplitude (a) and tidal prism (b). Estuary width against estuary depth (c) and tidal current velocity (d). Confidence limits are given for two standard deviations from the regression. The legend shows the approximate multiplication factor that the confidence limits plot higher or lower than the trend.

Table 2.2 Natural estuaries used in this study for bar measurements from Google Earth, accessed May-September 2015. References indicate source of additional data on estuary geometry and tidal characteristics. Sources of available bathymetry: NEEA = National Estuarine Eutrophication Assessment (USA), NOSEB = National Ocean Service's Estuarine Bathymetry.

Name	Location	Reference estuary data	Reference bathymetry
Alsea Bay	USA	NEEA	
Rodds Bay, Queensland	Australia	No data	
Bannow Bay	IRE	No data	
Broad River Estuary	USA	NEEA	NOSEB
Camel Estuary	UK	Manning (2007)	UK Government
Cefni Estuary	UK	Manning (2007)	
Charlotte Harbor Estuary	USA	NEEA	
Clwyd Estuary	UK	Manning (2007)	
Cobequid Bay	Canada	NEEA; Dalrymple et al. (1990)	
Columbia River	USA	NEEA	
Conwy Estuary	UK	Manning (2007)	
Coosaw River Estuary	USA	NEEA	NOSEB
Courtsmacsherry	IRE	No data	
Dart Estuary	UK	Manning (2007)	
Dovey Estuary	UK	Manning (2007)	Aberystwyth University (Wales)
Exe Estuary	UK	Manning (2007)	UK Government
Gannel Estuary	UK	Manning (2007)	
Gironde	France	Billy et al. (2012)	
Glaslyn Estuary	UK	Manning (2007)	
Humber	UK	Manning (2007)	UK Government
La Laïta	France	No data	
Loughor Estuary	UK	Manning (2007)	
Mawddach Estuary	UK	Manning (2007)	
Meghna Delta Estuary	Bangladesh	Alam et al. (2014)	
Merja Zerga	Morocco	No data	
Nestucca Bay	USA	No data	
Netarts Bay	USA	NEEA	
Nyfer Estuary	UK	Manning (2007)	
Ord River Estuary	Australia	Wolanski (2014); Wright et al. (1973)	
Parrett Estuary	UK	Manning (2007)	UK Government
Poole Estuary	UK	Manning (2007)	
San Joachim Bay	USA	NEEA	
San Joachim Suisun Bay	USA	NEEA	
Sandy Neck Colony	USA	No data	
Savannah River	USA	NEEA	
Siuslaw River	USA	NEEA	
Solway Estuary	UK	Manning (2007)	UK Government
Taw-Torridge Estuary	UK	Manning (2007)	UK Government
Teifi Estuary	UK	Manning (2007)	
Teign Estuary	UK	Manning (2007)	UK Government
The Retreat	IRE	No data	
Traeth Melynog Estuary	UK	Manning (2007)	
Western Scheldt	NL	Jeuken et al. (2003); Schramkowski et al. (2002)	Rijkswaterstaat (NL)
Whitehaven Beach	Australia	No data	
Mersey Estuary	UK	Manning (2007)	UK Government


3

Chapter 3 | Dimensions of fluvial-tidal meanders: Are they disproportionally large?

Abstract

Many of the world's major river systems seemingly have one or a few disproportionally large meanders, with tight bends, in the fluvial-tidal transition (e.g. the Thames in the UK, and the Salmon River in Canada). However, quantitative studies on meanders have so far primarily focussed on rivers without tidal influence or on small tidal meanders without river inflow, providing relations between channel geometry and meander characteristics (length, amplitude, and sinuosity). Physics-based predictions of meander size and shape for the fluvial-tidal transition zone remain untested for a lack of data. Therefore, it remains unclear whether the dimensions of meanders in the fluvial-tidal transition zone are indeed disproportionally large, and whether meander characteristics can be used as an indicator for tidal influence. Here, data from 823 meanders in 68 fluvial-tidal transition zones worldwide are presented that reveal broad-brush relations between channel geometry and meander dimensions. Our results show that fluvial-tidal meanders indeed become larger in the seaward direction, but the dimensions are proportional to local channel width, as in rivers. Sinuosity maxima are an exception, rather than the rule, in the fluvial-tidal transition zone. Surprisingly, the width of the upstream river correlates with estuarine channel width and tidal meander size even though river discharge constitutes only a fraction of the tidal prism. The new scaling relations can be used to constrain dimensions of rivers and estuaries and their meanders.

Published as: Leuven, J.R.F.W., van Maanen, B., Lexmond, B., van der Hoek, B., Spruijt, M. & Kleinhans, M.G. (2018). Dimensions of fluvial-tidal meanders: Are they disproportionally large? *Geology, 46 (10), pp. 923–926*, DOI: 10.1130/G45144.1.

3.1 Introduction

The shapes and dimensions of meanders are a major characteristic of meandering rivers (Leopold and Wolman, 1960). Typical scaling relations exist between meander dimensions, river discharge, and local channel width (e.g. Inglis, 1949; Leopold and Wolman, 1960; Hey and Thorne, 1986) (Suppl. Table 3.1). However, these empirical relations have never been tested in the fluvial-tidal transition zone and in estuaries (Fig. 3.1), where one of the signatures of the environment is that local tidal prism (the volume of water leaving an estuary at ebb tide) increases in the seaward direction (Chapter 5) with exponentially increasing channel width. Observations of tidal meanders show that their planform dimensions scale similarly as in rivers (Marani et al., 2002; Solari et al., 2002; D'Alpaos et al., 2017; Finotello et al., 2018). However, these observations mainly cover meanders on tidal flats and salt marshes, which are much smaller (typically 2–200 m wide) than fluvial and estuarine meanders. Moreover, they predominantly form under ebb-dominant flow and may thus rather be comparable with small river meanders (Kleinhans et al., 2009).

The majority of the world's largest cities are located near estuaries and tidal rivers (Ashworth et al., 2015) in which meandering channels are ecologically valuable but also threaten bank stability, affect shipping lanes, and influence flood safety. Therefore, it is of interest whether the meander-forming mechanisms are similar to those of their fluvial counterparts. Physics-based theory can predict dominant meander lengths based on forming mechanisms (e.g. Solari et al. (2002), Schramkowski et al. (2002), and Seminara (2006) and Chapter 2), but the resulting predictions have never been tested due to a lack of data from natural systems. Geological outcrops could provide an alternative source of data. However, preserved meandering channel deposits in Palaeozoic outcrops are orders of magnitude smaller than in modern systems (Davies and Gibling, 2011; Davies and Gibling, 2013) and are possibly biased toward maximum meander dimensions and sinuosity, because meanders at the point of cut-off have the highest preservation potential (e.g. Durkin et al., 2017). A possible exception

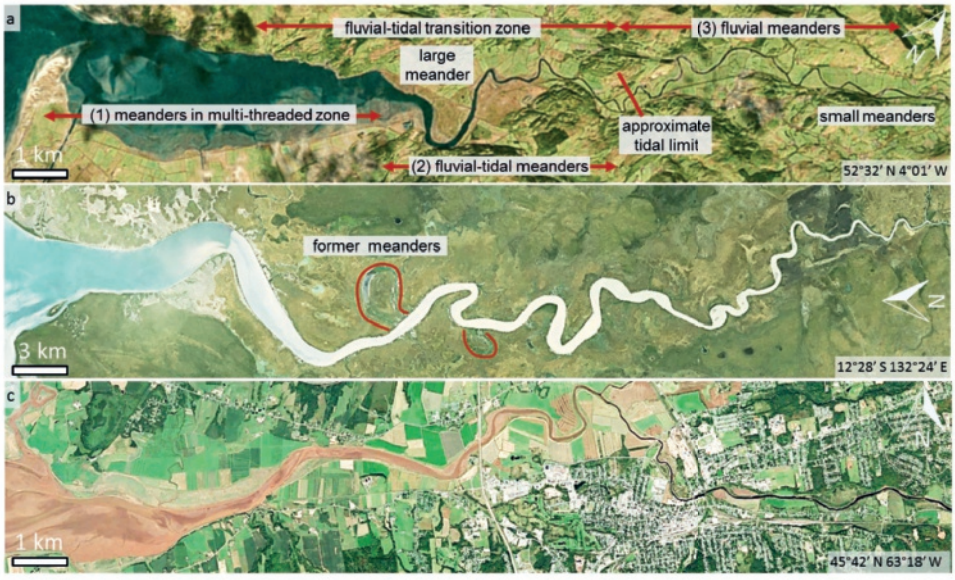

Figure 3.1 Aerial photographs of fluvial-tidal meanders (Google Earth). River flow is from right to left. (a) Dovey River, Wales, UK. (b) South Alligator River, Northern Territory, Australia. (c) Salmon River, Cobequid Bay, Canada.

is found in seismic data of the Cretaceous McMurray Formation (Canada), which has kilometre-scale meander bends (Hubbard et al., 2011; Durkin et al., 2017). Both the morphology and the facies in core data are similar to that of a fluvial environment (Mossop and Flach, 1983; Hubbard et al., 2011), although trace fossils indicate brackish water, which is interpreted as the fluvial-tidal transition zone (La Croix and Dashtgard, 2015; Gingras et al., 2016). Therefore, it would be useful to have a complementary indicator that can discriminate between fluvial, fluvial-tidal, and tidal meanders on the basis of geometry for the full range of scales on which they occur on Earth.

Lack of data and empirical generalisations leave hypotheses untested, such as the hypothesis that fluvial-tidal meanders are very tight, with sinuosities peaking above 2.5 at the bedload convergence zone (Dalrymple et al., 2012). The limited number of analysed cases so far does not demonstrate whether sinuosity peaks significantly beyond the natural temporal and along-channel variability within meandering systems, which occurs due to bend cutoffs, and the scatter in combined observations from multiple systems (Howard and Hemberger, 1991; Camporeale et al., 2007; Hubbard et al., 2011) (Fig. 3.1b). Moreover, a sinuosity peak implies a disproportional scaling relation between meander dimensions and channel dimensions, because it requires a peak in meander amplitude or drop in meander length. Observations from aerial photography and predictions from physics-based theory (Solari et al., 2002) suggest that these meanders are longer than those of their fluvial counterparts.

Therefore, we test whether fluvial-tidal meanders are indeed disproportionally large when compared with their local channel dimensions and upstream and downstream meanders. We derive scaling relations that can be used to obtain broad-brush dimensions of meanders along the fluvial-tidal continuum, for application in geomorphology and geological reconstruction of meander belts. To this end, a new dataset was collected with characteristics of 823 meanders in 68 fluvial-tidal transition zones from around the world. Data were compared with typical relations previously found for rivers and for small tidal meanders.

3.2 Data collection and analysis

We recorded channel planform polygons for 68 rivers that transition into seas (Suppl. Table 3.2). Because hydrodynamic data are generally unavailable, the tidal limit was defined as the landward location where channel width approaches a constant value within a factor two of the most upstream river width. Meanders were digitised beyond that point, such that subsequently, the tidal limit could be derived from the along-channel width profile (Suppl. Figs. 3.5 and 3.6). To allow for comparison between systems, along-channel distance was normalised with the tidal limit. In cases where the single threaded river transitions into an estuary with braided channels and bars, we digitised the main continuous channel. This approach resulted in a classification of (1) main meanders in the multi-threaded zone, (2) single-threaded fluvial-tidal meanders, or (3) fluvial meanders (Fig. 3.1a).

The channel centrelines and along-channel width profiles were automatically determined using GIS software (following the approaches of Davies and Woodroffe (2010) and Chapter 5). All centrelines were smoothed with a Polynomial Approximation with Exponential Kernel (PAEK) algorithm using a tolerance of 0.6 times the local channel width, to prevent the centrelines from being too sensitive to local variations in channel width.

Meander length (λ) and amplitude (a) were calculated from the centrelines as follows (Suppl. Fig. 3.7). Inflection points were determined from channel curvature (Howard and Hemberger, 1991; Marani et al., 2002; Schwenk et al., 2015). Meander length was calculated as the Euclidian distance between two successive inflection points with the same sign of curvature (Leopold and Wolman, 1960). Meander amplitude was estimated as the maximum normal distance of channel position from the meander belt centreline determined by the inflection points. Sinuosity was measured as the

along-channel distance divided by the Euclidian distance per bend and per meander. The channel width for each meander was averaged from digitised channel width. Channel convergence length (L_W), defined as the distance over which the channel width decreases by a factor e (≈2.72), was calculated from a least-squares exponential fit on width as a function of distance. This resulted in a dataset with 823 meanders in 68 fluvial-tidal transition zones.

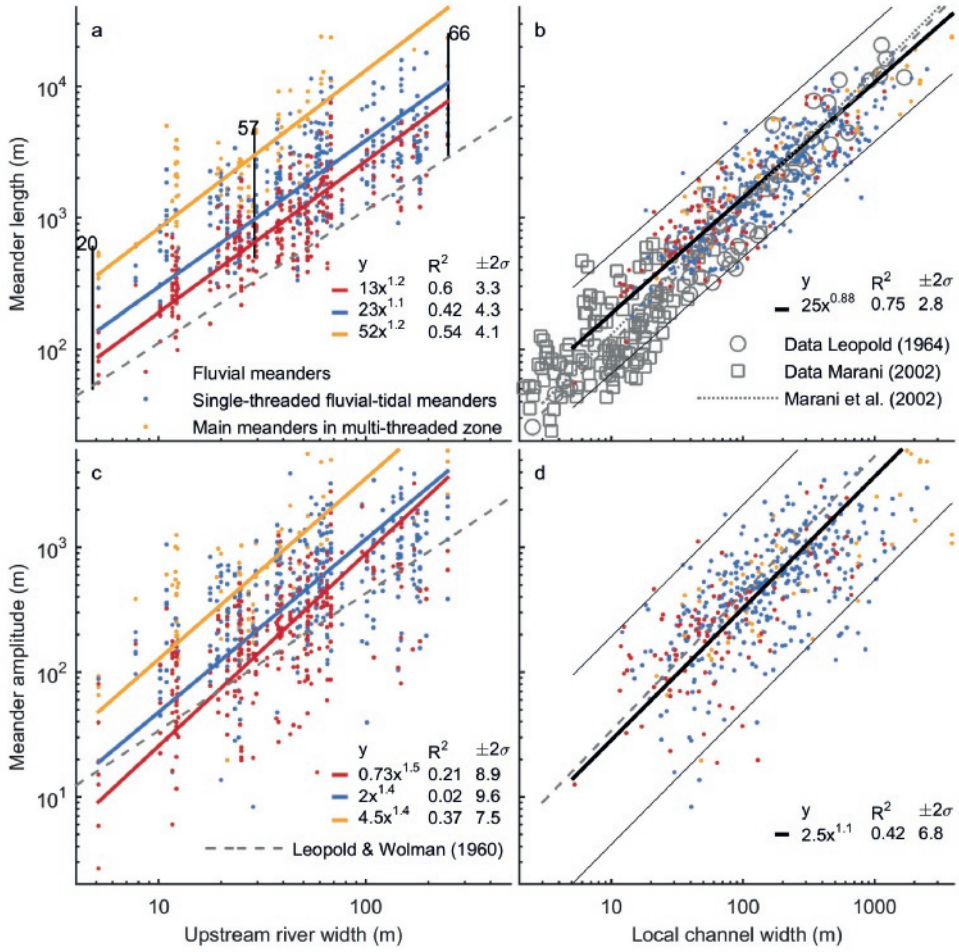

Figure 3.2 Meander length (a) and amplitude (c) as a function of upstream river width. Vertically aligned symbols indicate along-channel variation per system. Numbers correspond to systems in Suppl. Table 3.2. (b,d) Same dimensions as a function of local channel width, and comparison with fluvial and tidal meanders (Leopold and Wolman, 1960; Leopold et al., 1964; Marani et al., 2002). Regression in (b) is based on data from this study only. Confidence limits (95%) are indicated by the 2σ value.

3.3 Results and discussion

3.3.1 Meander dimensions and characteristics

Meander length and amplitude generally increase in the seaward direction (Fig. 3.2a,c; Suppl. Figs. 3.8 & 3.9). The most landward meanders set the minimum meander dimensions, and are consistent with empirical scaling relations on the basis of river width (Leopold and Wolman, 1960). The most downstream meanders are, on average, approximately 4 times larger than their landward counterparts (as indicated by the regression coefficients) but show an order-of-magnitude variation between systems (Fig. 3.2a,c). Surprisingly, downstream meander dimensions also correlate moderately well to the upstream river width, with a similar power relation.

Meander dimensions scale better with local channel width than with upstream width (Fig. 3.2b,d). Given the scatter, the power law is not significantly different from fluvial scaling relations (e.g. Leopold and Wolman, 1960), predictions by stability theory for rivers (Seminara, 2006) (Suppl. Table 3.1), and a relation for small tidal meanders (Marani et al., 2002). The scatter around the trend for meander amplitude is much larger than for meander length, which is at least partly caused by temporal variability due to bend cutoffs, which predominantly reduce meander amplitude but may also affect meander length. These results are consistent with the observed similarity in dimensions and scatter of fluvial and small tidal meanders (Lagasse et al., 2004; Finotello et al., 2018). However, tidal channels show a larger spread of curvature due to the very sharp bends frequently found on tidal flats.

Case studies suggest that channel sinuosity systematically peaks above 2.5 in the fluvial-tidal transition zone (Dalrymple et al., 2012), but in our dataset, only 17 of 823 meanders peak above 2.5 (Fig. 3.3a), which occur in 11 of the 68 systems studied. This shows that sinuosity peaks are an exception rather than the rule for fluvial-tidal meanders, which is also consistent with observations of tidal (Finotello et al., 2018) and fluvial meanders (Lagasse et al., 2004). When sinuosity is calculated per bend instead of for the entire meander, 10 additional systems show a peak. However, these sinuosity values above 2.5 are not unique to the fluvial-tidal transition zone, but also occur in the fluvial zone. Meanders with high sinuosities (asterisks in Fig. 3.3b) are usually caused by large amplitudes, small lengths, or, in some cases, by highly asymmetrical bends (examples are given in Suppl. Fig. 3.10). Meander amplitude correlates well with meander length (Fig. 3.3b), and the lack of correlation between sinuosity and position (Fig. 3.3a) shows that meander bends are not disproportionally large in the fluvial-tidal transition.

3.3.2 Scaling relations for fluvial-tidal meanders

While the forcing factors of river discharge and tidal amplitude are entirely independent, a surprising correlation was found between seaward meander dimensions and landward dimensions. As such, a scaling relation is expected between the typical channel convergence length and the proportional change in the amplitude and length of the meanders (Fig. 3.4a). Previous authors proposed that convergence length scales with tidal range (Savenije, 2006; Davies and Woodroffe, 2010), but our data show the best correlation ($R^2 \approx 0.7$) between convergence length and upstream river-channel width (Fig. 3.4b). In contrast, the correlation between convergence length and most seaward channel width is lower, and convergence length is uncorrelated to tidal range (Fig. 3.4c,d). Not surprisingly, given the convergence length relations, the most seaward and upstream channel widths also correlate (Fig. 3.4e). However, the unexpected implication is that river channel dimensions possibly control estuary dimensions, and the same applies to fluvial-tidal meander dimensions. Channel dimensions (Fig. 3.4e) and meander dimensions (Fig. 3.2a,c) are both, on average, a factor 4 larger at the river mouth.

These results generally indicate a more important fluvial influence than tidal influence on all meander dimensions along the entire fluvial-tidal transition. This is surprising because tidal discharge may exceed fluvial discharge by an order of magnitude (Manning, 2007). Nevertheless, our relations

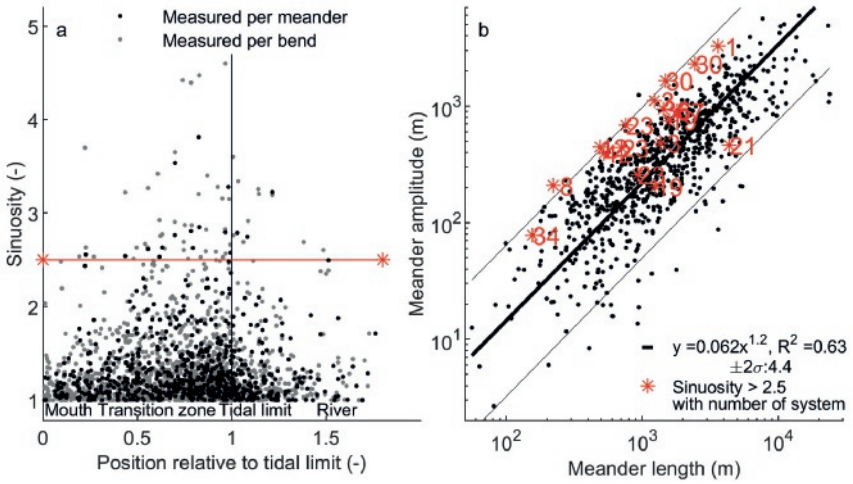

Figure 3.3 (a) Meander sinuosity as a function of position relative to the tidal limit. 11 out of 68 systems have a meander with a sinuosity that peaks above 2.5. (b) Meander amplitude versus length. Numbers correspond to systems in Suppl. Fig. 3.10 and Suppl. Table 3.2.

can be used in reconstructions to get a first-order estimation of the channel length of the system, number of point bars occurring in that length, and their approximate dimensions. The upstream river dimensions correlate with the channel convergence length (Fig. 3.4b). This, in turn, gives an along-channel width profile of the fluvial-tidal transition zone, which can be used to estimate the meander dimensions that scale with local channel width. In the absence of indications for the location of the mouth, the seaward boundary can be estimated through a combination of the convergence length and the relation between upstream and most-seaward channel width (Fig. 3.4e).

3.4 Conclusions

A novel dataset demonstrates that meander dimensions in the fluvial-tidal transition zone generally increase in the seaward direction and scale with local channel width, as in river systems, which shows that the meanders are not disproportionally large. The seaward meanders scale with upstream river dimensions, even in multi-channel estuaries where meanders are, on average, 4 times larger. Sinuosity peaks above 2.5 are an exception rather than a rule for fluvial-tidal meanders. Meander characteristics are mainly correlated with the downstream increase of channel width as tidal influence increases. Surprisingly, the characteristic convergence length of channel width is better correlated with the upstream river channel width than with the downstream estuary width and tidal range. In summary, meanders in the transition zone are not excessively large beyond the usual variation and seaward trends.

Acknowledgments

Paul Durkin and two anonymous reviewers helped to improve the manuscript. Author contributions to conception and design, data collection and processing, analysis and conclusions, and manuscript preparation: JL (50,50,50,65%), BM (30,10,25,20%), BL (0,15,5,0%), BH (0,15,5,0%), MS (0,10,0,0%), MK (20,0,15,15%). The online supplementary data includes a kml-file with the channel planform polygons used in this study.

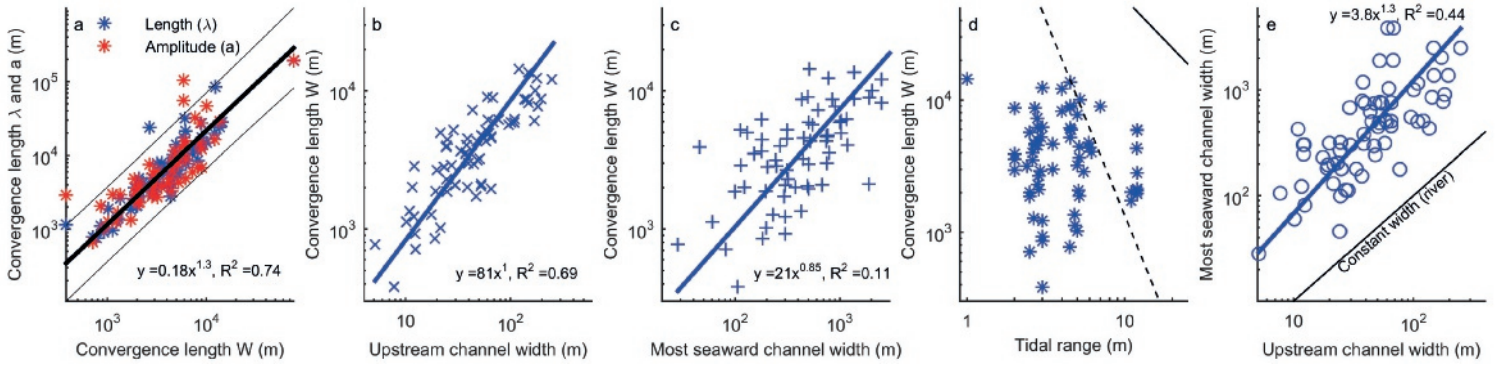

Figure 3.4 (a) Convergence length of meander dimensions (meander length λ, and amplitude a), defined as the distance over which the dimensions decrease by a factor e (≈2.72), as a function of the channel width convergence length. (b,c,d) Channel width convergence length versus upstream channel width (b), seaward channel width (c), and tidal range (d). Two empirical relations between tidal range and convergence (e.g. Savenije, 2006; Davies and Woodroffe, 2010) are indicated. (e) Most seaward channel width versus upstream channel width.

Supplementary material

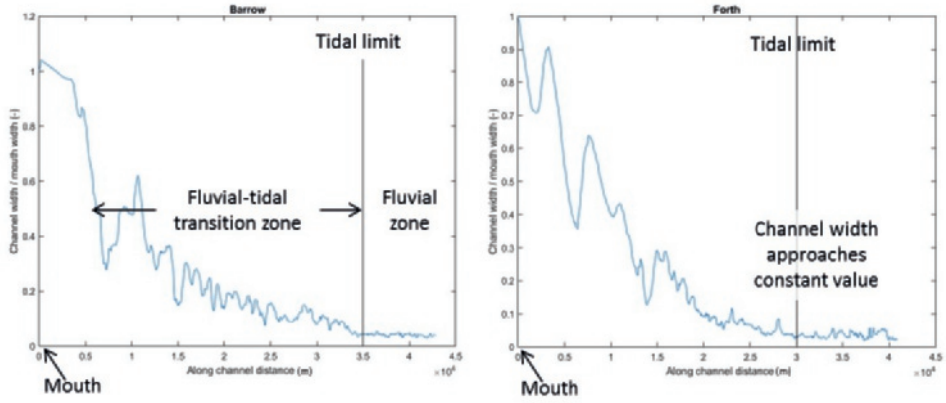

Figure 3.5 Along-channel width profiles. The tidal limit was manually selected as the point where the channel width approaches a constant value. The zone seaward of this point is defined as the fluvial-tidal transition zone and the landward zone as the fluvial zone. The distance to the tidal limit is used to normalise along-channel distance.

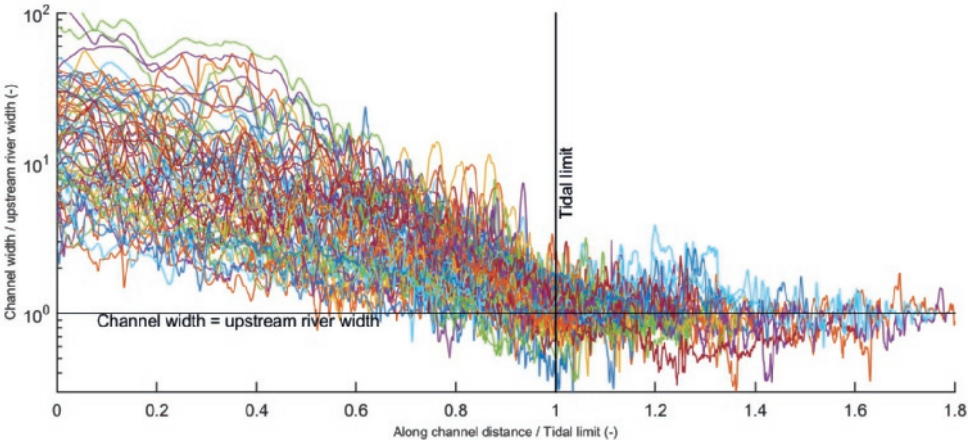

Figure 3.6 Normalised along-channel width profiles of all systems used. Channel width normalised by the width of the upstream river (y-axis) as a function of along-channel distance normalised by along-channel distance to the tidal limit as defined in Suppl. Fig. 3.5.

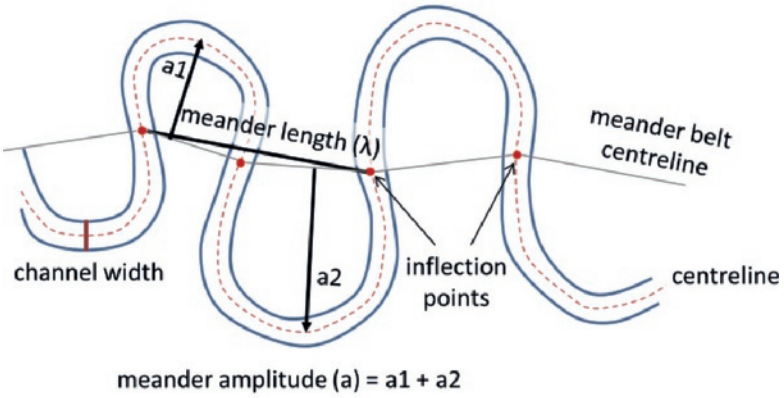

Figure 3.7 Schematic figure of meander definitions in this study.

Table 3.1 Empirical and theoretical relations for meander dimensions. All constants have been recalculated, such that all equations are in metres.

Property	Relation	Author	Environment
Meander length	$\lambda = 11.0b^{1.01}$	Leopold and Wolman (1960)	Rivers
	$\lambda = 6.52b^{0.99}$	Inglis (1949)	Rivers
	$\lambda = 7.50b^{1.12}$	Williams (1986)	Rivers
	$\lambda = 20.0b^{1.04}$	Ferguson (1975)	Rivers
	$\lambda = 6.28b$	Hey (1982)	Rivers
	$\lambda = 6.31b$	Hey and Thorne (1986)	Rivers
	$\lambda = 13.0b$	Marani et al. (2002)	Tidal creeks
	$\lambda = 10.5 - 31.4b$	Seminara (2006)	Theory for forced bars
Meander amplitude	$A = 3.04b^{1.10}$	Leopold and Wolman (1960)	Rivers
	$A = 18.4b^{0.99}$	Inglis (1949)	Rivers
Meander radius	$r = 3.04b^{1.10}$	Leopold and Wolman (1960)	Rivers
	$r = 1.50b^{1.12}$	Williams (1986)	Rivers

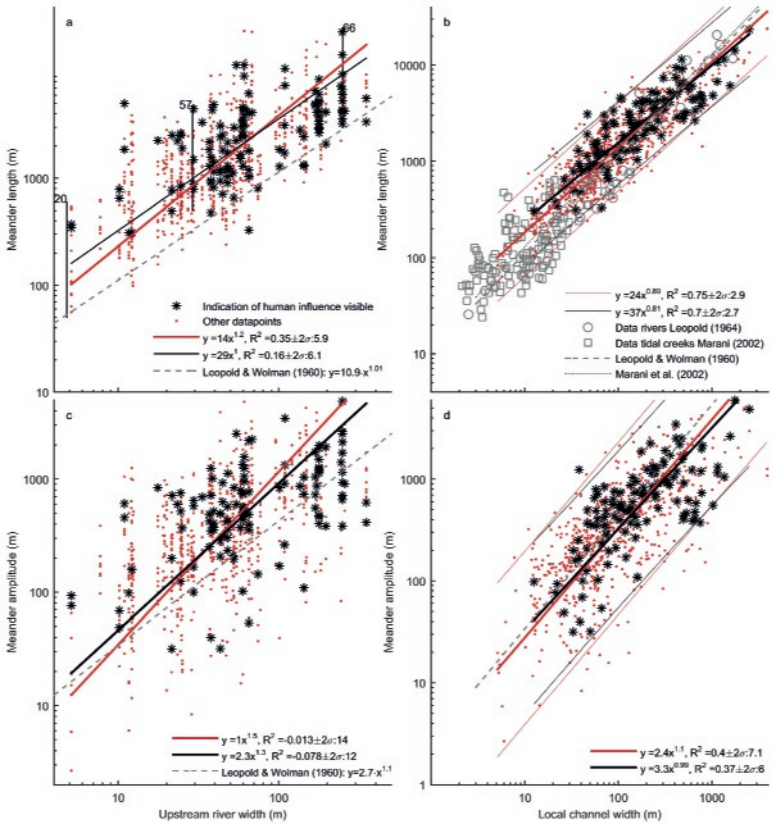

Figure 3.8 In the dataset, it was recorded at which locations human influence may have influenced river pattern (similarly as in Kleinhans and van den Berg (2011) and Chapter 2), such as the presence of harbours or sudden straight sections in a densely populated area. These locations are indicated with asterisks on top of the data in Fig. 3.2. The locations with possible human influence do not significantly deviate from the trends found and neither do they systematically increase scatter or cause outliers, as indicated by the largely overlapping confidence intervals.

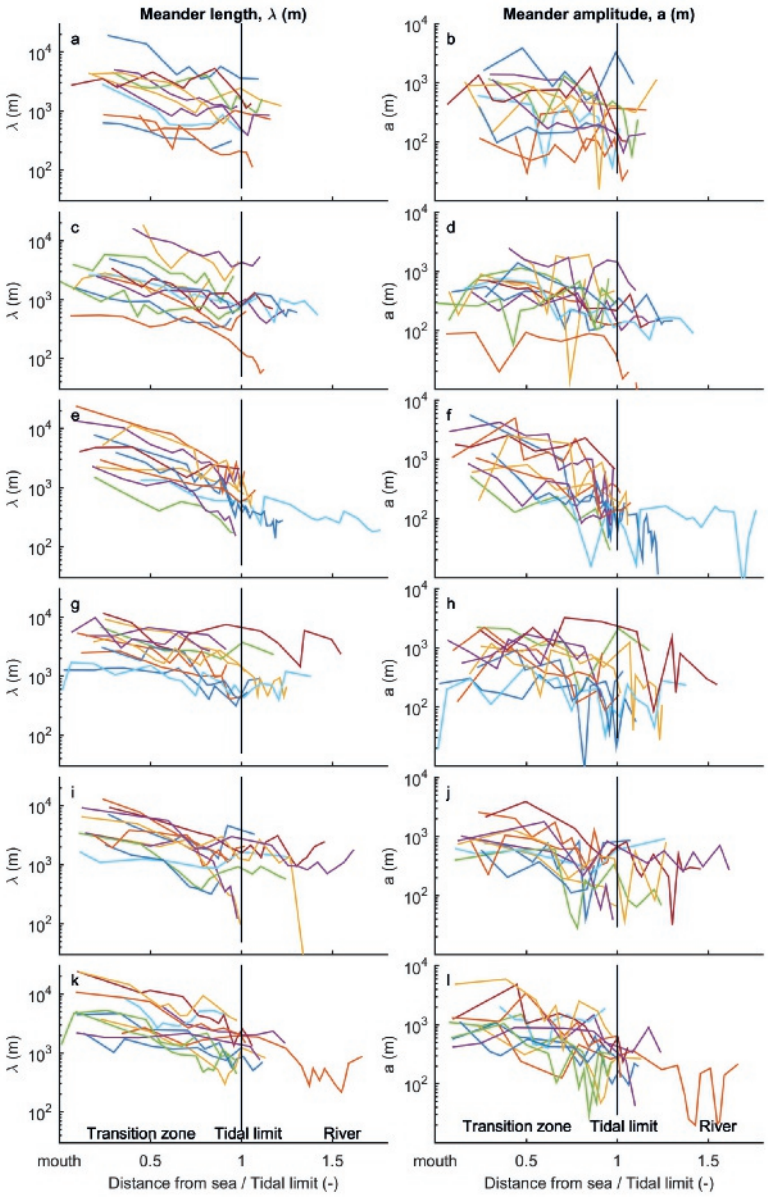

Figure 3.9 [left panels] Meander length and [right panels] meander amplitude as a function of dimensionless intrinsic coordinate, which was calculated as the along-channel distance from the sea measured along the channel centreline divided by the distance to the tidal limit (Suppl. Figs. 3.5 & 3.6). The tidal limit was determined as the location where channel width approaches a constant value. For visibility systems were separated over subplots: (a,b) system number 1-11; (c,d) 12-23; (e,f) 24-34; (g,h) 35-45; (i,j) 46-56; (k,l) 57-68. Numbers correspond to systems in Suppl. Table 3.2.

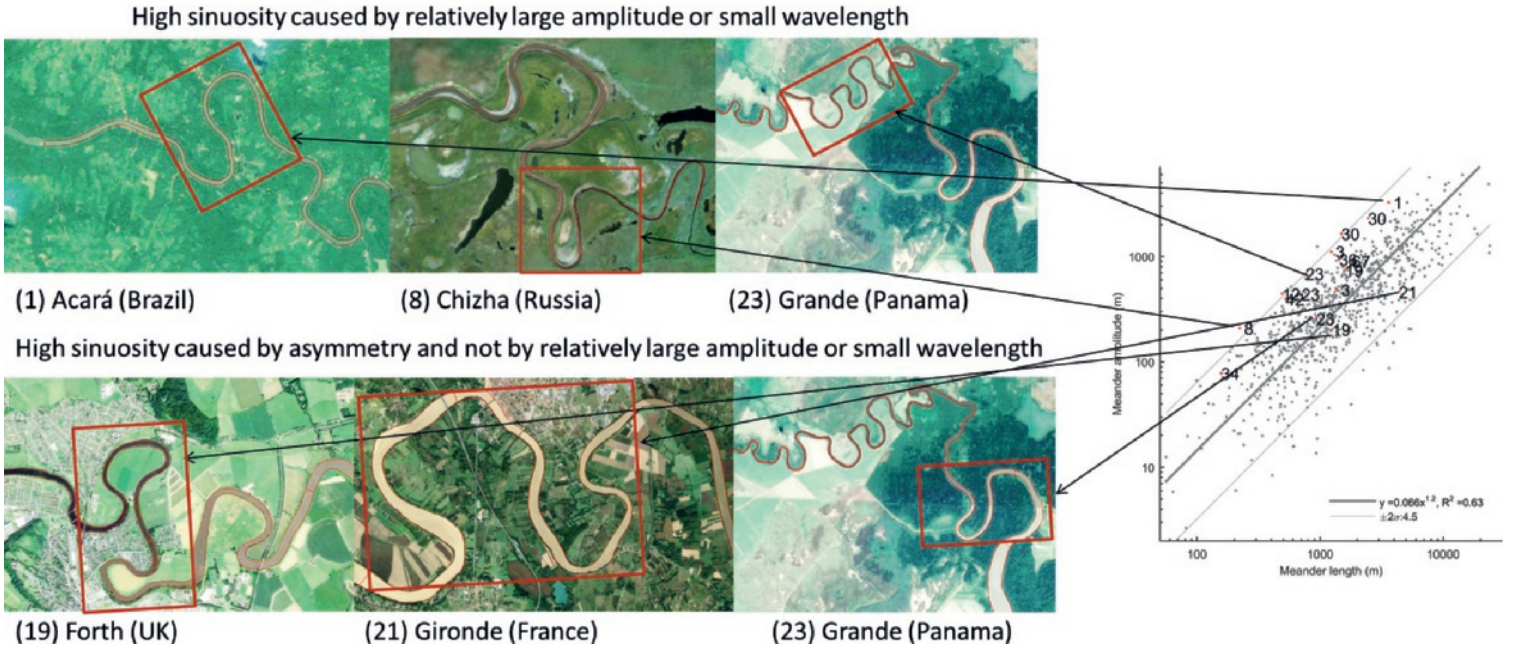

Figure 3.10 Examples of meanders with high sinuosity in Fig. 3.3. The plot on the right corresponds with Fig. 3.3b in the main article and indicates the numbers of the systems that have a meander with a sinuosity above 2.5. High sinuosities occur typically under two conditions: (1, top panels) the amplitude is disproportionally large or meander length is disproportionally short, which cases typically plot close to the upper confidence limit when amplitude is plotted against length; (2, lower panels) along-channel distance is disproportionally large compared to the meander length, usually caused by asymmetry in meander bends, which plot on or below the regression line of amplitude against length.

Table 3.2 Rivers used in this study for meander measurements from Google Earth, accessed January-August 2017. Distance to the tidal limit was measured as along-channel distance from the mouth up to the point where channel width approaches a constant value. Climate zones: Am = Monsoon climate, Af = Equatorial climate, Aw = Tropical savanna climate, Cfa/Cwa = Humid subtropical climate, Cfb = Marine climate, Cwb = Oceanic subtropical highland climate, Csb = Temperate mediterranean climate, Dfc = Subarctic climate, Dfb = Temperate continental climate.

Nr	Name	Location	Distance to tidal limit (km)	Köppen climate zone
1	Acará	Brazil	80	Aw, Am, Af
2	Acarima	New Zealand	8.1	Cfb
3	Alsea	USA	25	Csb
4	Aurá	Brazil	33	Aw
5	Barrow	Ireland	35	Cfb
6	Belmunda	Australia	15.5	Cwa
7	Charente	France	40	Cfb
8	Chizha	Russia	5.8	Dfc
9	Clwyd	UK	6	Cfb
10	Cobequid	Canada	34.5	Dfb
11	Conwy	UK	14	Cfb
12	Cornwallis	Canada	12	Dfb
13	Cree	UK	12	Cfb
14	Dart	UK	22	Cfb
15	Dovey	UK	14	Cfb
16	Estero Real	Nicaragua	42	Af
17	Exe	UK	15	Cfb
18	Ferryside	UK	23	Cfb
19	Forth	UK	30	Cfb
20	Gannel	UK	4	Cfb
21	Gironde	France	90	Cfb
22	Girondesouth	France	90	Cfb
23	Grande	Panama	20	Aw
24	Hebert	Canada	40	Dfb
25	Humber	UK	90	Cfb
26	Kakadu	Australia	80	Aw
27	Kennetcook	Canada	16	Dfb
28	Koumala	Australia	6.5	Cwa
29	L'Authie	France	8	Cfb
30	Limpopo	Mozambique	50	Aw
31	Loughor	UK	27	Cfb
32	Maccan	Canada	16	Dfb
33	Maputo	Mozambique	45	Aw
34	Matola	Mozambique	13.5	Aw
35	Mawddach	UK	14	Cfb
36	Memracook	Canada	16	Dfb
37	Mersey	UK	43	Cfb
38	Merwe	NL, historic map	30	Cfb
39	Mucelo	Mozambique	35	Aw
40	Nestucca	USA	15	Csb
41	Ord	Australia	60	Aw
42	Oreti	New Zealand	25	Cfb
43	Ouse	UK	36	Cfb
44	Pericumã	Brazil	35	Aw
45	Pesca	Mexico	60	Af
46	Petitcodiac	Canada	40	Dfb
47	Púngué	Mozambique	70	Aw
48	Roddsbay north	Australia	12.5	Cfa
49	Roddsbay south	Australia	13.6	Cfa
50	Salmon	Canada	12	Dfb
51	Santa Maria	Panama	15	Aw
52	Severn	UK	45	Cfb
53	Shoyna	Russia	13	Dfc
54	Shubenacadie	Canada	30	Dfb
55	Solway	UK	25	Cfb
56	Solwaysouth	UK	25	Cfb
57	Tamar	UK	25	Cfb
58	Tawtorridge	UK	15	Cfb
59	Tawtorridgesouth	UK	18	Cfb
60	Tembe	Mozambique	35	Aw
61	Tempisque	Costa Rica	34	Aw
62	Thames	UK	90	Cfb
63	Trent	UK	90	Cfb
64	Usk	UK	16	Cfb
65	Wairoa	New Zealand	50	Cfb
66	Western Scheldt	NL	110	Cfb
67	Wye	UK	18	Cfb
68	Wyre	UK	20	Cfb

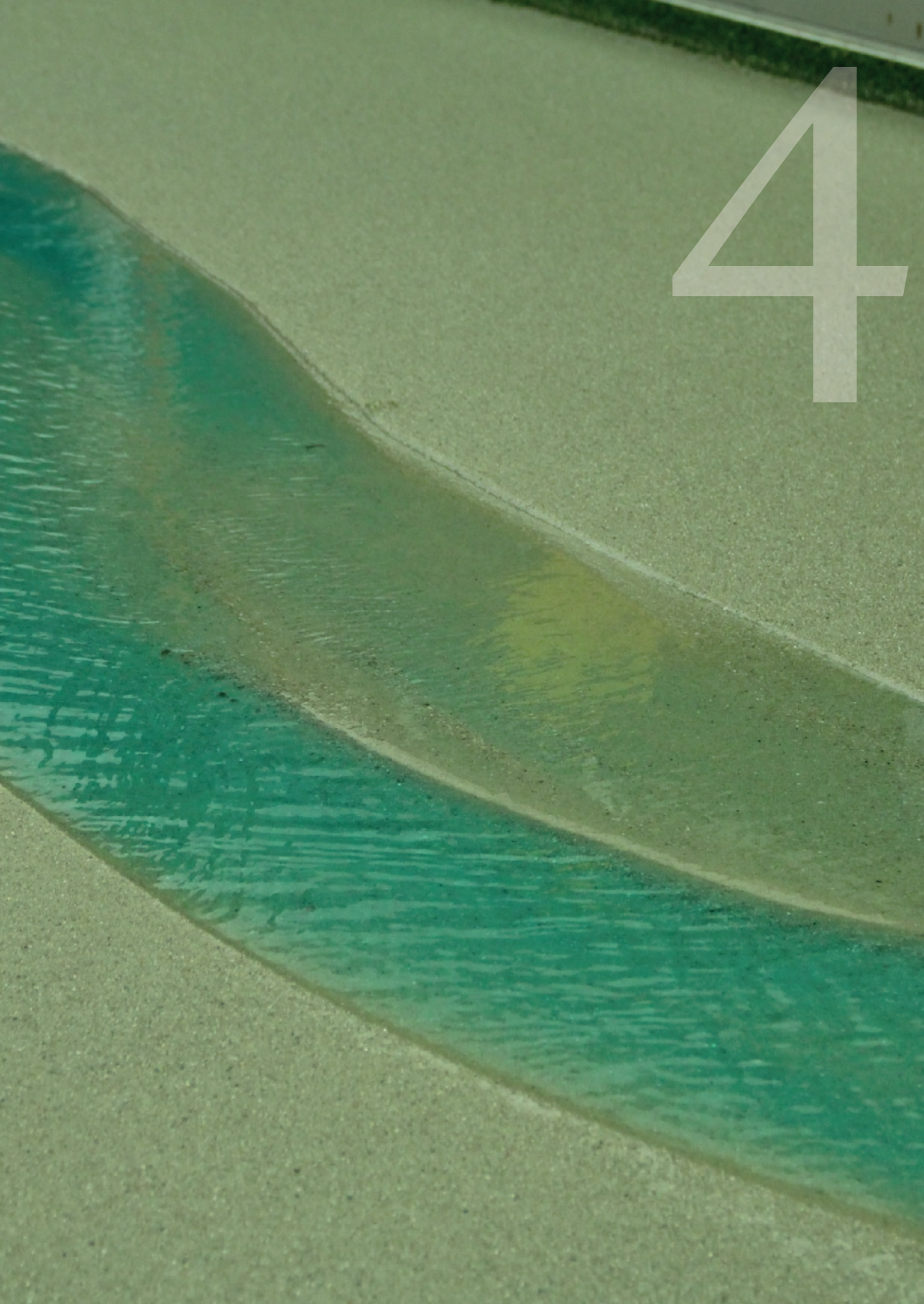
4

Chapter 4 | Incipient tidal bars

Abstract

Estuaries and rivers show dynamic patterns of bars and channels. Mutually evasive ebb- and flood-dominated tidal channels, i.e. parallel tidal channels with net sediment transport in opposing directions, give tidal bars their characteristic shape. Here, we study incipient tidal bars with laboratory scale experiments in a periodically tilting flume. Bar patterns evolved from an initial straight channel in an erodible sand bed. Analysis of time-lapse imagery and bathymetry shows that alternate bars form within 300 tidal cycles. The bars become discrete, recognisable elements after an initial phase characterised by a rhomboid pattern (short and narrow ridges oblique to the channel). Tidal bars show similarities and contrasts with fluvial bars. In general, morphological shapes are similar, including the presence of alternate bars, midchannel bars and point bars. In contrast to rivers, sills are superimposed on incipient tidal bars. Sills are narrow and straight and form by flow divergence and thus sediment convergence between alternate bars. Alternate bars grow further by amalgamation of two opposing U-shaped lobate bars. The dimensions of incipient tidal bars emerge in the first 500 cycles, after which their length and position determine a large-scale quasiperiodic variation in the estuary width. The results imply that sills are initiated with the onset of tidal bar formation in straight channels and trigger formation of mutually evasive ebb- and flood-dominated channels, which explains their ubiquitous occurrence in tidal systems.

Revision submitted as: Leuven, J.R.F.W. & Kleinhans, M.G. (2019). Incipient tidal bars. *Journal of Geophysical Research: Earth Surface*

4.1 Introduction

Estuaries are tidal systems that occur where rivers flow into the sea. Many estuaries were formed in valleys that drowned under fast rising sea-level during the early to middle Holocene (e.g. van der Spek and Beets, 1992; Hijma and Cohen, 2011; de Haas et al., 2017) and were subsequently infilled with sediment from the river and from the sea when sea-level rise decelerated. Dynamic patterns of bars, also called shoals, and channels evolved as a result of the bidirectional tidal currents (Fig. 4.1).

Perhaps the most typical and unique features of channel patterns in tidal basins and estuaries are the mutually evasive ebb- and flood-dominated tidal channels (Fig. 4.1). Mutually evasive channels are predominantly used in either the ebb or the flood phase and evade each other laterally (van Veen, 1950; Fenies and Faugères, 1998; Hibma et al., 2003; Dalrymple and Choi, 2007; Kleinhans et al., 2015b). This process results in linear bars when the channels simply evade each other laterally, but can also form U-shaped bars when one of the channels bifurcates around an opposing channel that is met head-on (Chapter 2). Van Veen already observed and described these striking elements in the 1950s and associated them to meandering of the main channel, which suggests that they are caused by topographic forcing. Our aim here is to describe and explain the process of incipient tidal bar formation and mutually-evasiveness of tidal channels. To this end, we conducted experiments in a tilting flume and monitored the initial evolution bars and channels with high temporal resolution, i.e. measurements every 100 tidal cycles.

It has been debated for quite a long time whether tides can shape forced and free bars as in river systems (Bridges and Leeder, 1976; Whiting and Dietrich, 1993). Only recently, stability theory showed that bars in straight and meandering tidal channels form from a similar instability mechanism as in rivers (Solari et al., 2002). Also data showed that tidal meanders resemble river meanders in dimensions and behaviour (Lagasse et al. (2004), Finotello et al. (2018) and Chapter 3). Free non-migratory bars form due to an instability of the bed above threshold values for width-to-depth ratio and mean Shields sediment mobility (Seminara and Tubino, 2001; Schramkowski et al., 2002), while similar instability mechanisms in meandering channels lead to point bar-pool patterns (Solari et al., 2002). Overtides that cause ebb or flood asymmetry lead to net migration of tidal bars (Garotta et al., 2006). The fact that instability mechanisms for tidal bar formation are similar to rivers leads to the expectation that morphology and development of fluvial and tidal bars are similar.

Incipient bar formation and meandering has been thoroughly studied for rivers in scale experiments (Leopold and Wolman, 1957; Ikeda, 1973; Ashmore, 1982; Fujita and Muramoto, 1985; Eaton et al., 2006; Visconti et al., 2010; Frascati and Lanzoni, 2013; van de Lageweg et al., 2014), numerical models (Schuurman et al., 2013), theoretical models (Seminara and Tubino, 1989; Struiksma et al., 1985; Repetto et al., 2002) and natural systems (Lewin, 1976; Cant and Walker, 1978; Ashworth et al., 2000; Sambrook Smith et al., 2006). In summary (review by Kleinhans, 2010), the channel width and depth are determined by the balance between bank erosion and floodplain formation. The width and width-to-depth ratio subsequently determine whether the bar pattern becomes meandering or braided. A combination of bank retreat and bar and floodplain formation (Parker et al., 2011; Eke, 2014; van de Lageweg et al., 2014) causes migration of bars in meandering channels, which implies that increased resistance in floodplain material reduces channel migration. Wider channels form midchannel bars that bifurcate the flow. Such bifurcations are inherently unstable in the majority of rivers on Earth, which is also associated to the process of active braiding. This leads to asymmetrical bifurcations such that one channel becomes the main path for flow and sediment (Kleinhans et al., 2013; Bolla Pittaluga et al., 2015). However, in the tidal environment, bifurcations of mutually evasive ebb- and flood-dominated tidal channels abundantly show opposed asymmetry in the sense that the channels are of similar size but the bifurcations in the flood and ebb phases asymmetrically partition the flow into the opposite channels. This raises the question what

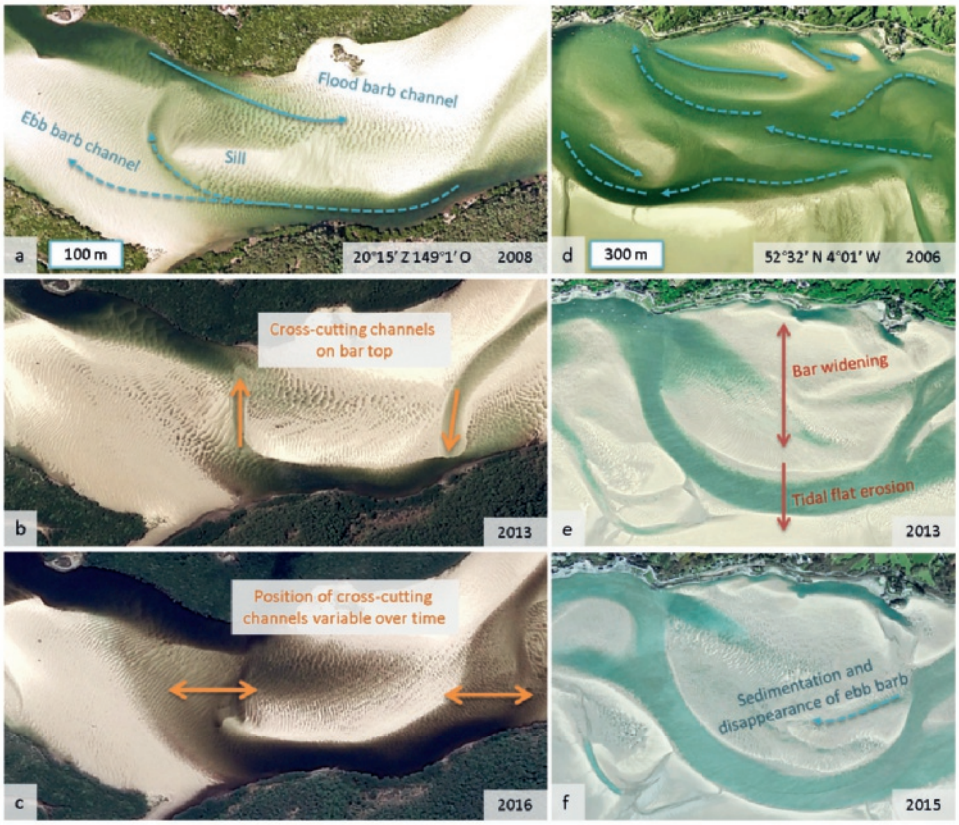

Figure 4.1 Dynamics of bars and mutually evasive ebb- and flood-dominated channels at (a-c) Whitehaven Beach (Australia) and in (d-f) the Dovey Estuary. (a,d) Tidal flow forms ebb and flood barbs, isolating a narrow and elongated sill between the mutually evasive channels. (b,c) Water level gradients cause cross-cutting channels on top of the sill. (e,f) Channels and bars are very dynamic over time, causing tidal flat and salt marsh erosion and formation.

causes this, and whether, in contrast to bifurcations in rivers, their configuration might be stable over time.

Tidal channels appear somewhat discontinuous at the bifurcations because of a persistent shoal, or sill. Sills are smaller-scale morphological elements that are enclosed by ebb- and flood-dominated channels (van Veen, 1950; Robinson, 1960; Tank, 1996), unique to tidal systems. They are observed at transitions between successive bends, which are the channel thalweg inflection points (Fig. 4.1a). Such topographic forcing of flow in two opposing bends causes the main flow momentum to cross the channel centreline in different locations for ebb and flood flow (van Veen, 1950; Ahnert, 1960). This, in turn, leads to shoal formation in the channel inflection zone with opposed net sediment transport directions in the parallel channels around it (van Veen, 1950). While sills resemble tidal bars in their elongated shape and dimensions, with lengths in the order of magnitude of the estuary width, they are smaller and much lower in height and commonly remain submerged over almost the entire tidal cycle. As such, the sills appear superimposed on the dominant pattern of bars and channels. When sills are located within the main navigable channel, regular dredging is typically required in order to

maintain and secure shipping fairways to inland harbours (Verbeek et al., 1999; Sistermans and Nieuwenhuis, 2004).

Sills are not predicted by theory but did emerge in numerical models. In contrast to river systems, only a few numerical models (e.g. Hibma et al., 2003; van der Wegen and Roelvink, 2008) and theories (Seminara and Tubino, 2001; Schramkowski et al., 2002; Solari et al., 2002; Garotta et al., 2006) are available for bar initiation in tidal systems, and the presence of sills is only observed but not explained. Stability theories for both rivers and tidal systems predict that braiding index (BI), i.e. the number of channels and bars in cross-section, increases with channel width (Struiksma et al., 1985; Seminara and Tubino, 2001; Schramkowski et al., 2002; Crosato and Mosselman, 2009). However, in tidal systems the dominant bar length increases with the amplitude of tidal flow velocity, while river bars are less sensitive to flow velocity and mainly determined by channel width-to-depth ratio. Numerical modelling showed that initial tidal bar length depends on both width and tidal flow velocity (Hibma et al., 2004). Moreover, initially straight tidal channels connected to form a weakly meandering channel with flood 'barbs' (BI = 1.5) within 100-200 years (Hibma et al., 2003) as qualitatively described by van Veen (1950). Here, barb channels are dead-ended in either the ebb or the flood direction. Here we aim to link the formation of barb channels with the persistence of sills.

Below, we will first describe the experimental setup and procedure for data collection. Subsequently, the process of incipient channel and bar formation is qualitatively and quantitatively described. In the discussion, incipient bar formation in tidal systems is explained and compared with other studies on tidal bars and the similarities with their fluvial counterparts are assessed.

4.2 Methods and materials

Experiments in a tilting flume (20 m by 3 m), called the Metronome, recently proved useful to study the long-term evolution of bar patterns in estuaries (Braat et al. (2019) and Chapter 6). Tilting the entire flume creates sufficient sediment mobility in both the ebb and the flood direction, which is required to generate dynamic tidal morphology. Moreover, this setup for the first time allows the experimental recreation of a short reach within an estuary, allowing detailed study of bar formation in reversing flow. For a more detailed description of the design and hydrodynamics of the Metronome, see Kleinhans et al. (2017a).

4.2.1 Experimental setup and procedure

In this study, we performed experiments with an initially straight channel with two open boundaries (Fig. 4.2), recreating a reach within an estuary or a double-head tidal channel. After pilot experiments, a total of two experimental conditions were selected for monitoring (Table 4.1). The settings were selected based on a larger set of ca. 23 pilots and 20 well-monitored experiments that also attest to the repeatability of pattern and planform characteristics. Experiments with an initial converging channel have been previously reported (Braat et al. (2019) and Chapter 6). While these studies described the long-term evolution of estuaries with sand and effects of cohesive material in experiments, here we aim to study incipient tidal bars. The previous experiments with a converging channel provided insight on bar pattern formation, based on which the experimental setup was altered in this study. It was found that the bar pattern, i.e. bar width and braiding index, strongly depends on the position along the estuary (Chapter 6), which means that it is not straightforward to describe the formation of incipient tidal bars in general. For this reason, the experimental setup was here modified to an initially straight channel with open boundaries on both ends of the channel, aimed at creating symmetrical reversing flow, which approximates the condition known in linear stability theory as rigid lid.

The Metronome floor was covered with a layer of 0.07 m erodible sand bed, in which an initial channel was carved. The sediment mixture (Suppl. Fig. 4.15) was composed of sand

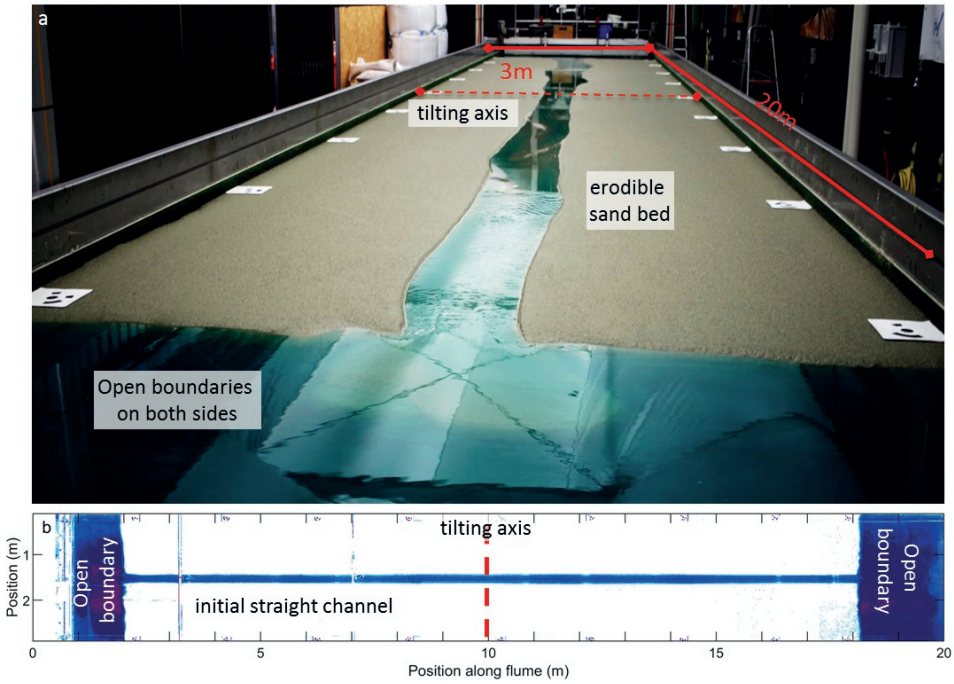

Figure 4.2 (a) The Metronome, a tilting flume of 20 m long by 3 m wide. (b) Overhead image of the experimental setup. An initial straight channel (0.2 m wide) with open boundaries on both sides. Blueness indicates depth except in the first metre where the gantry is located.

(ρ_s = 2650 kg m^{-3}) with a D_{50} of 0.52 mm, which allows for sufficient sediment mobility, and a coarse tail, such that the formation of scour holes is minimised (Kleinhans et al., 2017b). The initial channel width was either 0.2 m or 0.6 m (Table 4.1) and the sediment bed was approximately 16 m long and 3.0 m wide (Fig. 4.2b).

The seaward boundaries of the flume were open and connected by pumps to a large water reservoir. Water could freely flow out of the flume over a weir, which maintained a constant head at the sea. We compensated water depth in the sea for the tilting of the flume by periodically (T = 40 s) moving the weir up and down. This resulted in a constant water level at the boundary between the sediment bed and the sea. The water level was set to 0.065 m above the flume floor. Brilliant Blue FCF colourant was used to dye the water, which could be extracted from overhead imagery to visualise bar and channel morphology.

Tidal currents were produced by flume tilting driven by four accurate actuators moving sinusoidal with a period of 40 s and a maximum tilting gradient of 0.008 m/m. The maximum tilting amplitude at the end-basins of the flume was 75 mm. Tilting was such that sediment mobility was well above the threshold for motion and flow was turbulent and subcritical. We will evaluate these variables in the results section.

Multiple authors have described experimental scaling of bar and channel patterns (e.g. Kleinhans et al., 2015a; Tambroni et al., 2017; Lentsch et al., 2018). These studies showed that the most important scaling requirement is to have the sediment as mobile as in natural systems, which is the case in our experiments (see Kleinhans et al., 2017a, for Metronome scaling). Reducing the length or volume scale, by e.g. a factor of 1000, also results in a reduction of the timescale by the same order of

magnitude. While we found in past experiments that the morphological change was larger than expected from this scale (Kleinhans et al., 2015a), this is not deemed a problem because similar acceleration of morphological change in numerical models, e.g. the Morfac approach (Roelvink, 2006; Ranasinghe et al., 2011), showed that effects on the morphology are limited. Likewise, in our previous tidal system experiments we found that bar proportions in three dimensions compare well with natural systems (Chapter 6).

Table 4.1 Experimental settings: a is maximum tilting amplitude at the end-basins of the flume, T is tilting period, W is initial channel width, bed-level is the height of the plane sediment bed above the flume floor, MSL is the mean sea level above the flume floor and t is the duration of the experiment.

Nr	Type		a [mm]	T [s]	W [cm]	bed level [mm]	MSL [mm]	t [cycles]
017	narrow	tidal	75	40	20	70	65	6000
014	wide	tidal	75	40	60	70	65	3100

4.2.2 Data collection and data processing

During the experiments, the following data were collected: overhead time-lapse imagery for the full duration of the experiment, Digital Elevation Models (DEMs) using structure for motion software, overhead images of a completely submerged sand bed to correlate water blueness to water depth, flow velocities over time using Particle Imaging Velocimetry (PIV), and images of evolving morphology with a digital single-lens reflex camera. An overview of the data collection moments is given in Suppl. Table 4.2.

Seven industrial CMOS MAKO colour cameras were used to collect time-lapse imagery from the experiment. The resolution of each camera was 2048 by 2048 pixels and they had a fixed focal length of 12.5 mm, which resulted in a spatial pixel resolution of 1.5-2 mm. The cameras were installed 3.7 m above the centreline of the flume, equally spaced. Each tidal cycle, images were triggered at the horizontal position of the flume at the onset of flood flow. Because the camera alignment was hampered by the roof supports in the lab, the images were rectified geometrically and corrected for vignetting and lens distortion. Subsequently, images were stitched and converted to LAB (CIELAB) images. Extraction of only the B-band enhanced the visualisation of morphology because it gives contrast between the blue coloured water and yellowish sediment.

Fluorescent light with daylight colour was directed at a white diffusive ceiling from about 4.5 m above the flume floor. This setup resulted in an illumination of about 300 lux. We largely prevented the reflection of light from the water surface by installing white backdrop cloth between the light source and flume, which reduced the intensity of the light and made it more diffuse, but could not prevent reflection of the support beams of the roof. The light intensity allows for low exposure time, which was used for Particle Imaging Velocimetry (PIV).

Digital Elevation Models (DEMs) were obtrained with structure from motion software (Lane et al., 1993; Chandler et al., 2001; Fonstad et al., 2013; Morgan et al., 2017; Agisoft, 2017). To this end, a digital single-lens reflex (DSLR) camera was mounted on a pole, which was stabilised on a bridge that rolled on the flume walls. Photographs were taken slightly inclined to the flume at equal spacings along the flume. 20 ground control points, located on the inner side of the flume walls, were used as references for the DEMs. The referencing allowed for resampling of DEMs on the same grid as used for the stitched time-lapse imagery.

Particle Imaging Velocimetry (PIV) (Mori and Chang, 2003) was used to measure flow velocities over a tidal cycle. First, we seeded white polystyrene particles (diameter ca. 2.5 mm) on the water surface. Second, in 16 phases of the tide, a frequency generator triggered the collection of ten images at 25 Hz, simultaneously by all overhead cameras. Particles were resupplied where and when necessary. Third, images were corrected for illumination with background imagery without particles.

Last, flow velocities were calculated from each pair of consecutive images using the MPIV toolbox in Matlab (Mori and Chang, 2003). The peak cross-correlation algorithm was used to obtain average displacement of particles in a 50x50 pixel window with overlap of 50%. Subsequently, the vector fields with displacement in pixels per second were scaled by the camera footprint. The camera footprint (1.5-2 mm/pixel) was calculated from the flume geometry, average height of cameras, camera resolution and the instantaneous tilting angle. Erroneous vectors resulted from windows that were partially filled with flume wall, spots empty of particles or over seeded with particles, mismatched particles and reflections on the water surface. For further processing and analysis, we calculated the average vector field from each set of ten consecutive images. Flow velocity data was also interpolated on the same grid as used for DEMs and time-lapse imagery. To study flow around sills, flow velocities were also filtered along the thalweg: in the channel, seaward of the sill, on top of the sill and landward of the sill.

Water depth was estimated from overhead imagery. To be able to correlate the blueness from overhead imagery with water depth, the sediment bed was fully submerged and overhead images were taken. Subsequently, a DEM was made for the same state of the sediment bed. A correlation of these two resulted in a predictive relation for water depth [in m] as a function of blueness (b) [on a scale from 0 to 1 for the B-band of LAB images]: $h = 7.0 \times 10^{-6} b^{-11} + 0.01$ (Suppl. Fig. 4.16). The correlation was applied to the background images collected during PIV to obtain time series of water depth with full coverage of the flume. In theory, water depth could subsequently be added to the bed elevation from DEMs to obtain the water surface elevation. However, because the uncertainty in DEMs (ca. 1.0 mm) and correlation between blueness and water depth (ca. 1-5 mm) is within the range of cross-channel differences in water surface elevation, we only use this method to estimate water depth variation over a tidal cycle.

4.2.3 Data reduction

The following characteristics were derived from DEMs: estuary width, cross-sectional area, summed width of bars, bar length, bar width and braiding index. Estuary width was calculated as the width between the non-eroded banks including the sand bars. Cross-sectional area was calculated as the total area below the plane sediment bed.

To calculate the characteristics of bar pattern, first, the bathymetry was converted into a binary image of channels and bars. To do so, median bed level was calculated per cross-section and subsequently a linear fit was used as the threshold between channel and bar. From the classified bar map, the summed width of bars was calculated per cross-section. Braiding index (BI) was calculated as the number of channels plus bars divided by two. The characteristic bar width was calculated as the summed width of bars divided by the BI. Bar length was calculated as the length between two successive inflection points in the along-channel profile of summed width of bars. All characteristics were averaged along the entire flume to obtain characteristic values of bar pattern per time step.

To obtain characteristic hydrodynamic conditions for specific morphological features, we classified channels in the following categories: tip of the ebb channel, ebb channel, straight channel, flood channel, and tip of the flood channel. Ebb and flood channels were recognised as channels with a dead end in one of the flow directions. In contrast to the channels, the tips were chosen on the shallowest part of either the ebb or flood barb, while ebb and flood channels were chosen well within the channel. Straight channel was assigned to the part of the channel that was in the middle between the ebb barb and flood barb in a straight channel, typically at the deepest location.

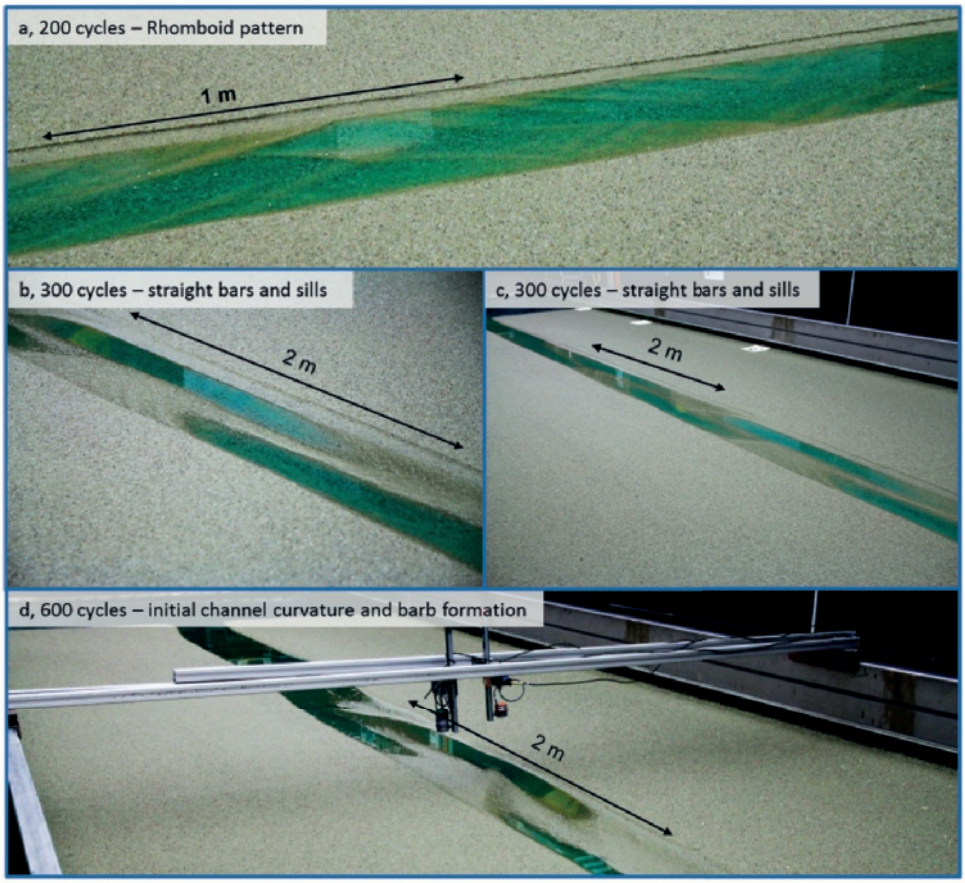

Figure 4.3 Digital single-lens reflex photography of the morphology in experiment 017. Except for panel (a), photographs were taken at a water level lower than Mean Sea Level by draining the flume to enhance the visibility of morphology. (a) Initial rhomboid pattern with a characteristic wavelength in the order of centimetres. (b,c) Alternate bars with a bar length of approximately 0.5-0.7 m separated by straight, narrow and elongated sills. (d) Initial channel curvature and the formation of U-shaped lobate bars in channels with opposing flow.

4.3 Results

First, the phases of incipient bar formation are described along with their dependency on initial channel geometry. Second, we quantify the bar patterns. Last, we study the hydrodynamic conditions that lead to the observed morphology.

4.3.1 Phases of incipient bar formation

The experiments showed three characteristic steps in incipient tidal bar formation. First, a rhomboid pattern evolved, which is a series of parallel short and narrow ridges that are oblique with respect to the channel orientation (Figs. 4.3a & 4.4a).

Second, alternate bars grew with a bar length of ca. 0.6-0.7 m (Figs. 4.3b,c & 4.4c). Initially straight channels formed U-shaped lobate bars in both the ebb and flood direction (Suppl. Fig. 4.17). Two

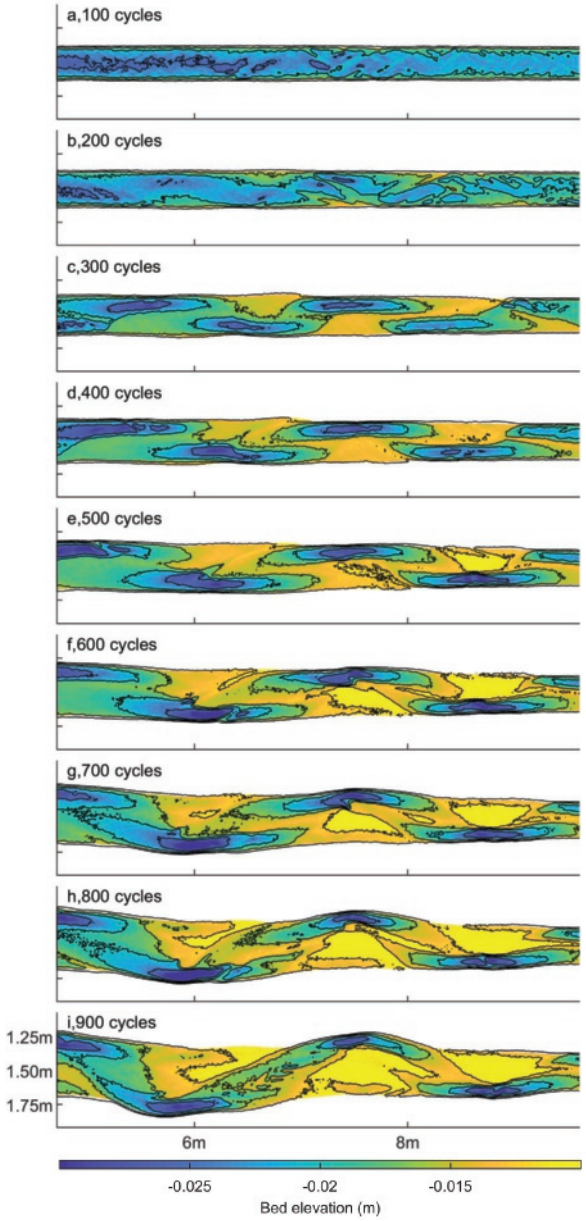

Figure 4.4 Incipient bar pattern formation in an experiment with open boundaries on both sides. Contours are drawn at -4, -12, -20 and -28 mm with respect to the 0 mm reference level of the erodible sand bed. Distinguishable channels and bars formed after 300 cycles (c). Channels remained straight until approximately 500 cycles (e). From that moment onward, channels became more curved and braiding index increased (f-i). Elevation of sand bars increased over time in the zone from 6-9 m. Typical bar length only slightly increased after their initial formation.

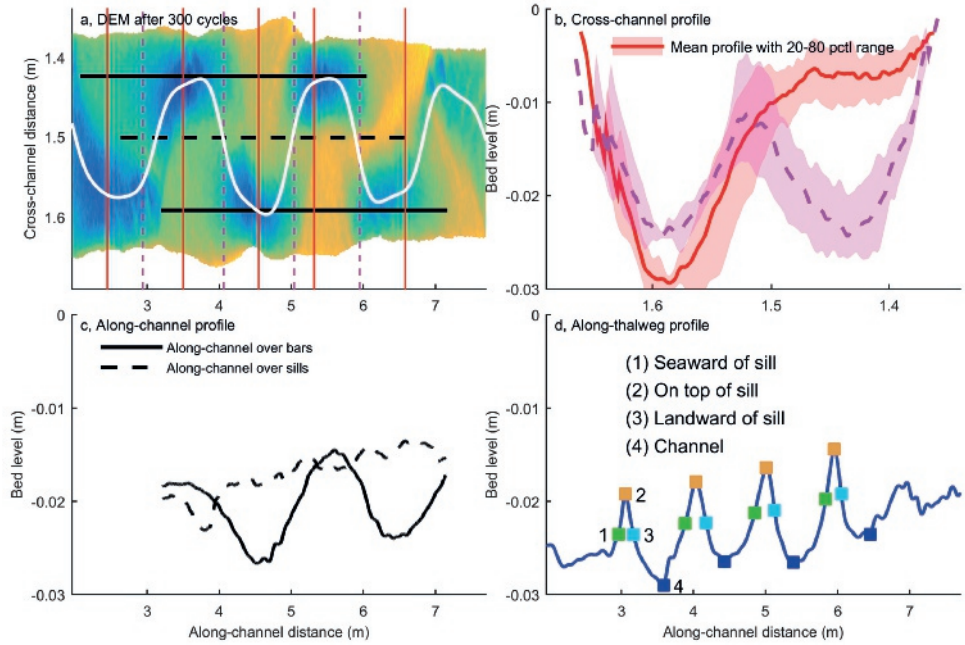

Figure 4.5 (a) Bathymetry after 300 cycles with the location of along-channel [black], cross-channel [red] and along-thalweg [white] profiles. Colourscale is equal to Fig. 4.4. (b) Cross-channel profiles of bed level at bar locations [red solid] and at sill locations [pink dashed]. Bed levels were detrended with the along-channel gradient before calculating the average channel profile. Shaded area indicates 20^{th}-80^{th} percentiles. (c) Along-channel profiles of bed level over the channels and bars [solid] and over the sills and bars [dashed]. (d) Along-thalweg profile of bed level. Coloured squares indicate the locations where flow velocities were extracted from PIV in Fig. 4.10a.

opposing U-shaped bars on the same side of the estuary amalgamated into an alternate bar and the channel on the opposite side of the estuary eroded the side of the alternate bar. Narrow and straight sills were superimposed on and connected successive alternate bars, separating straight tidal channels that were 1-2 m long. This resulted in deepest channels flanking alternate bars rather than occurring between the bars. Typical bed level profiles resulting from alternate bar and sill formation are shown in Fig. 4.5.

Lastly, the ebb dominated ends of channels formed U-shaped lobate bars in the opposing flood tidal channels and vice versa (Figs. 4.3d & 4.4d,e,f), which resulted in continuous outer-bend erosion and migration of the channels towards the sides of the estuary. From that time onward, the opposing channels were pushed sideways, eroding the banks, which allowed for bars to widen (Fig. 4.4e-i). This effect was possibly strengthened because flow from one channel into the other caused flow oblique to the thalweg, i.e. directed towards the outer bend, eroding the bank (Suppl. Movie online). Seaward migration speed of outer bends decreased with distance from nearest mouth (Fig. 4.6).

The initial phase was similar in all experiments, including the experiments with a wider straight channel. Experiments with a wide and straight initial channel (0.6 m) lacked the second phase that was observed in narrower channels. The dominant growing braiding index after the rhomboid phase was 1.5 instead of 1.0 (Fig. 4.7). This became apparent from the deepest channel forming in the middle of the initial channel rather than on the side (Fig. 4.7b,c). Moreover, initially, midchannel bars seemed to grow

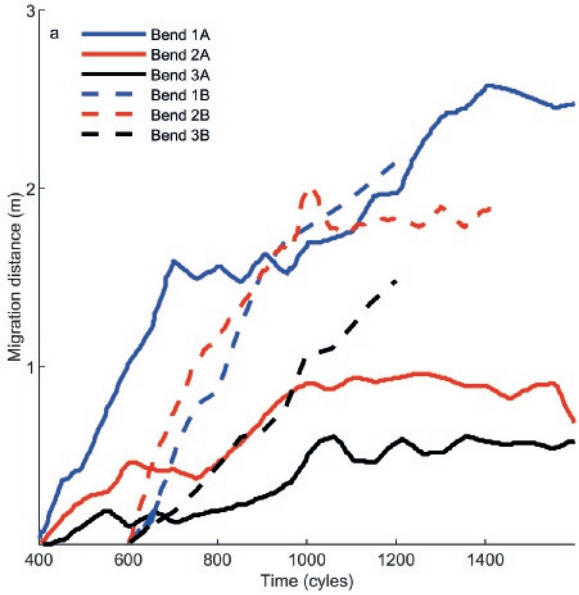

Figure 4.6 Meander bend migration over time. Initial positions of meander bends are indicated in Fig. 4.14d. Solid lines indicate bends on the left side of the flume, dashed lines on the right side. Bends on the right side started migrating 200 cycles later than on the left side.

(Fig. 4.7b,c). However, in later phases, these features were eroded away and the dominant configuration was a single meandering channel with alternate bars and a few barb channels (Fig. 4.7g). These bars were longer and wider compared to the experiment with a narrow channel (Fig. 4.7g,n).

Narrow and straight sills formed between successive alternate bars (Fig. 4.3b). Although their morphology formed discrete, recognisable elements in images taken while draining the flume (Fig. 4.3), their presence is less recognisable on overhead imagery and bathymetry because their elevation was typically low and less pronounced compared to the surrounding bars and channels. Nevertheless, the sills remained present after the phase of incipient tidal bars and channels. For example, contour lines indicate the presence of the sill at 8 m (Fig. 4.4f-i), which grew in height, disconnected from the bar located at 9 m (Fig. 4.4f,g) and migrated seaward to merge with the bar at 7.5 m (Fig. 4.4h,i).

While not accentuated by contour lines, the sills also remained present at the other locations along the flume (e.g. at 5.5 m and 6.5 m, Fig. 4.4i). In all cases, their orientation became oblique to the centreline of the flume and they were enclosed by opposing ebb and flood tidal channels. The elevation of the sills and bars increased with distance from the sea. However, only in the zone around 7-9 m, sill height approached bar height. This implies that the dynamics and morphology of sills can interfere with the bars.

4.3.2 Quantified bar pattern: channel and bar dimensions and braiding index

Average estuary width increased about linearly in the initial phase of the experiment (Fig. 4.8b). Experiments that were run for a longer period of time suggest that channel widening decreased over time, but continues until flume walls are reached. Only with the addition of cohesive material (Braat et al., 2019) estuary widening was inhibited, because cohesive material fills up intertidal area and thereby reduces the tidal prism that otherwise continues to increase. Average estuary depth initially

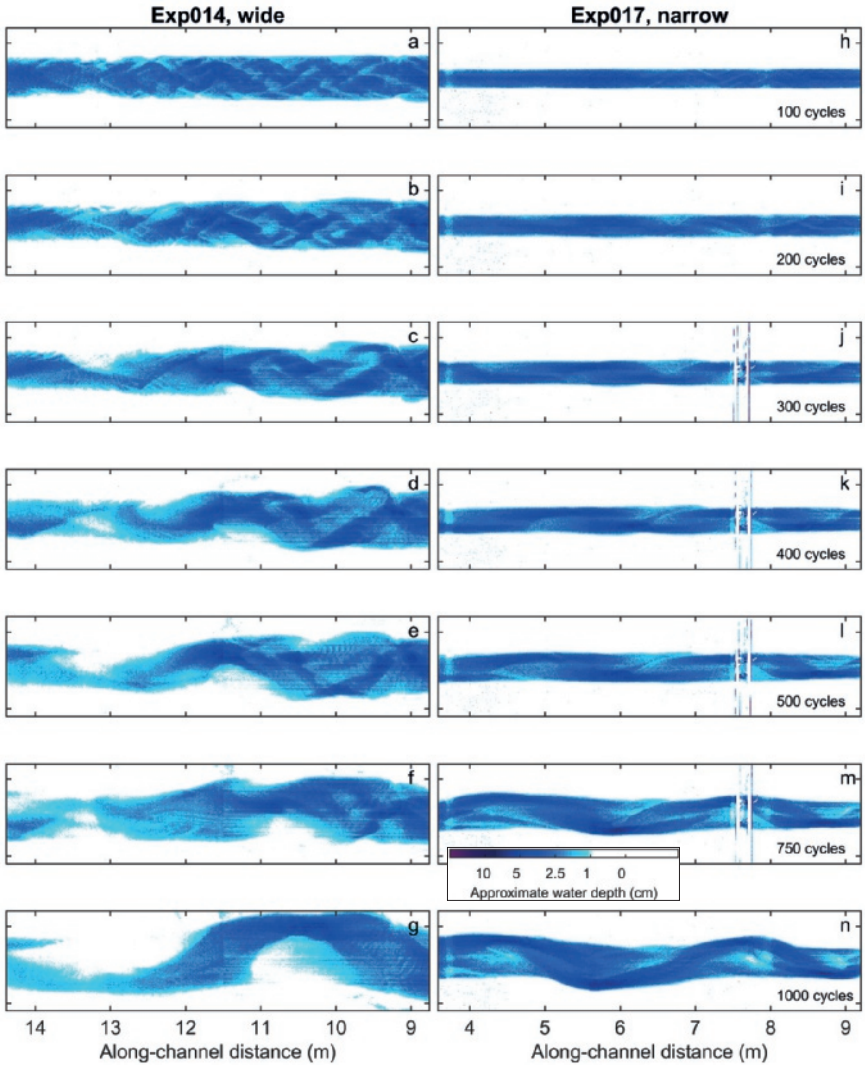

Figure 4.7 Time series of overhead imagery of experiment 014 and 017. Time-steps are indicated in the right panel. The colourbar indicates the approximate conversion between blueness and water depth (see also Suppl. Fig. 4.16). In both cases, the initial phase is characterised by a rhomboid pattern, followed by an alternate bar pattern (see also Fig. 4.3). In later phases, channels become more curved and braiding index increases by the formation of barb channels.

became more shallow, but stabilised on the longer term (Fig. 4.8b). Bar length and braiding index (BI) increased with increasing estuary width (Fig. 4.8a,b). For bar length, scatter and along-channel variation was relatively large, but average values suggest that it kept increasing. The same holds for BI. Bar width stabilises in the first 1000 cycles of the experiment at about 0.2 m (Fig. 4.8a). As the width of the estuary increases, there is more space to fill with bars. Given the almost unlimited sediment supply from the estuary banks, bars rapidly form after estuary widening, resulting in the observation that BI increases with estuary width.

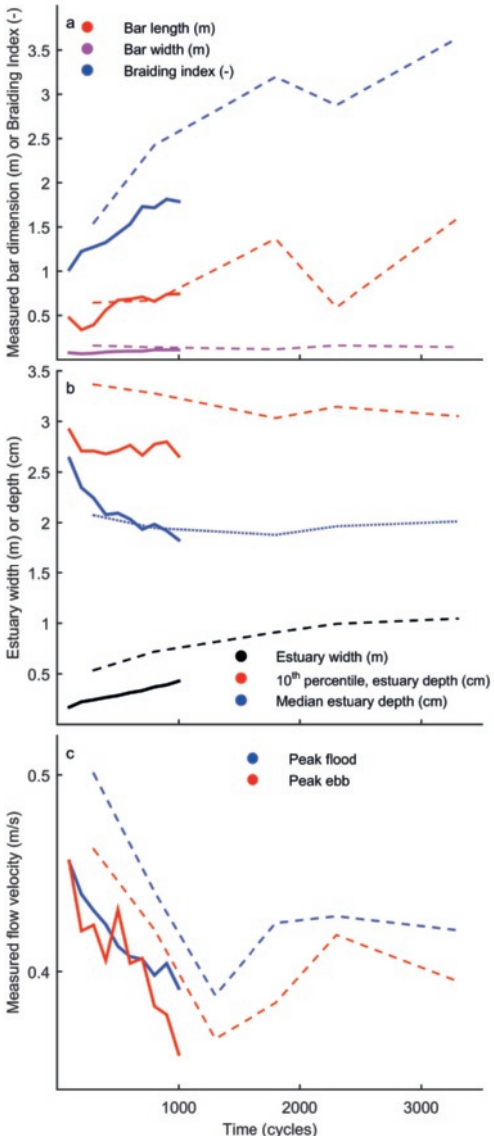

Figure 4.8 (a) Bar dimensions and braiding index, (b) estuary dimensions and (c) peak flow velocity over time for Exp. 006 (dashed lines) and Exp. 017 (solid lines). Bar dimensions and braiding index are along-channel averaged values. Average estuary width is larger for Exp. 006, because the experiment started with an initial converging channel that was much wider at the seaward boundary than the straight channel of Exp. 017. Characteristic estuary depth was calculated as the 10^{th} percentile and median value. Peak flow velocities are the 5^{th} and 95^{th} percentile values. Exp. 006 was a previous experiment (Chapter 6) with one closed boundary and an initial converging channel, shown here for comparison.

Along-channel profiles reveal considerable spatial variation in estuary width, bar width, minimum bed elevation and cross-sectional area (Fig. 4.9). The initial widening was near constant along-channel, but in later phases the width profile became progressively more irregular (Fig. 4.9b,c). The first reason is that the estuary mouth widened very rapidly due to the sharp corners of the estuary banks at the mouth. Secondly, the build-up of bars (Fig. 4.9d) caused diversion of flow, which caused erosion at banks opposite of the alternate bars. Profiles of minimum bed elevation, i.e. maximum depth, illustrate that the bed profile initially becomes linearly, sloping downward in the direction of the sea (Fig. 4.9e). However, with the onset of alternate bar formation, deep channels formed scours sideways of the alternate bars. This resulted in an along-channel elevation profile with quasiperiodic vartiation related to the length scales of the bars (Fig. 4.9b,e). The resulting cross-sectional area profile evolved from initially near-linear to progressively more irregular (Fig. 4.9f), which was associated with the aforementioned changes in width and depth.

4.3.3 Residual flow and sediment recirculation

In general, peak flood velocities were slightly larger than peak ebb velocities over the entire length of the experiments and both decreased over time (Fig. 4.8c). Peak flow velocities rapidly decreased from approximately 0.45-0.50 ms^{-1} to 0.35-0.40 ms^{-1} in the first 1000 cycles, after which they became more constant. Flow conditions obey to the most important scaling rules as indicated by sediment mobility being above the threshold for motion for the largest part of the tidal cycle and flow being below critical and turbulent for the entire tidal cycle (Fig. 4.10).

Flow conditions, and especially flow divergence and convergence, are indicative of sediment transport in the experiment. The gradients observed in flow velocities and sediment mobility explain the formation and perseverance of the straight sills that occur between the alternate bars. Flow divergence is already noticeable after 300 tidal cycles (Suppl. Movie online). Flow velocities at characteristic locations along the thalweg (i.e. main channel, Fig. 4.5a) indicate that after peak flood the flow decelerates over the sill and accelerates again after the sill (Fig. 4.10a), suggesting sediment convergence seaward of the sill. Over almost the entire ebb phase, flow decelerates landward of the sill (Fig. 4.10a), with sediment being hardly mobile on top and landward of the sill (Fig. 4.10b). The divergence on top of the sill and therefore convergence of sediment explains why sills form in the first place and why they remain stable over time. Moreover, flood flows predominantly flow over and around the sill on its landward side, while ebb flows use the seaward side. On longer timescales, this process modulates the sill, creating a preferential channel for flood and a preferential channel for ebb, also called mutually evasive ebb- and flood-dominated tidal channels (Fig. 4.11a,b,c).

In the straight channels, water depth increased over time, while peak flow velocity decreased (Fig. 4.12a). As expected, peak flood flow velocities are typically larger than ebb flow velocities in the flood channels. Here, peak ebb flow velocity decreased over time. While the average water depth remained fairly constant, the difference in water depth between the ebb and flood phase increased over time. Largest water depths coincided with peak flood velocities, while peak ebb occurred just before lowest water levels, resulting in more inclined ellipses in the tidal stage diagrams (Fig. 4.12b). In the ebb channels, peak ebb and flood velocity were initially approximately equal, but the tidal stage diagrams became progressively more ebb dominated (Fig. 4.12c). Water depth in these channels kept decreasing over time. The tips of both ebb and flood channels were characterised by higher peak flood velocities than ebb velocities (dashed lines in Fig. 4.12b,c). The tips of ebb and flood channels were typically the highest elevated parts, which explains why the flow velocity and water depth were typically low under ebb conditions.

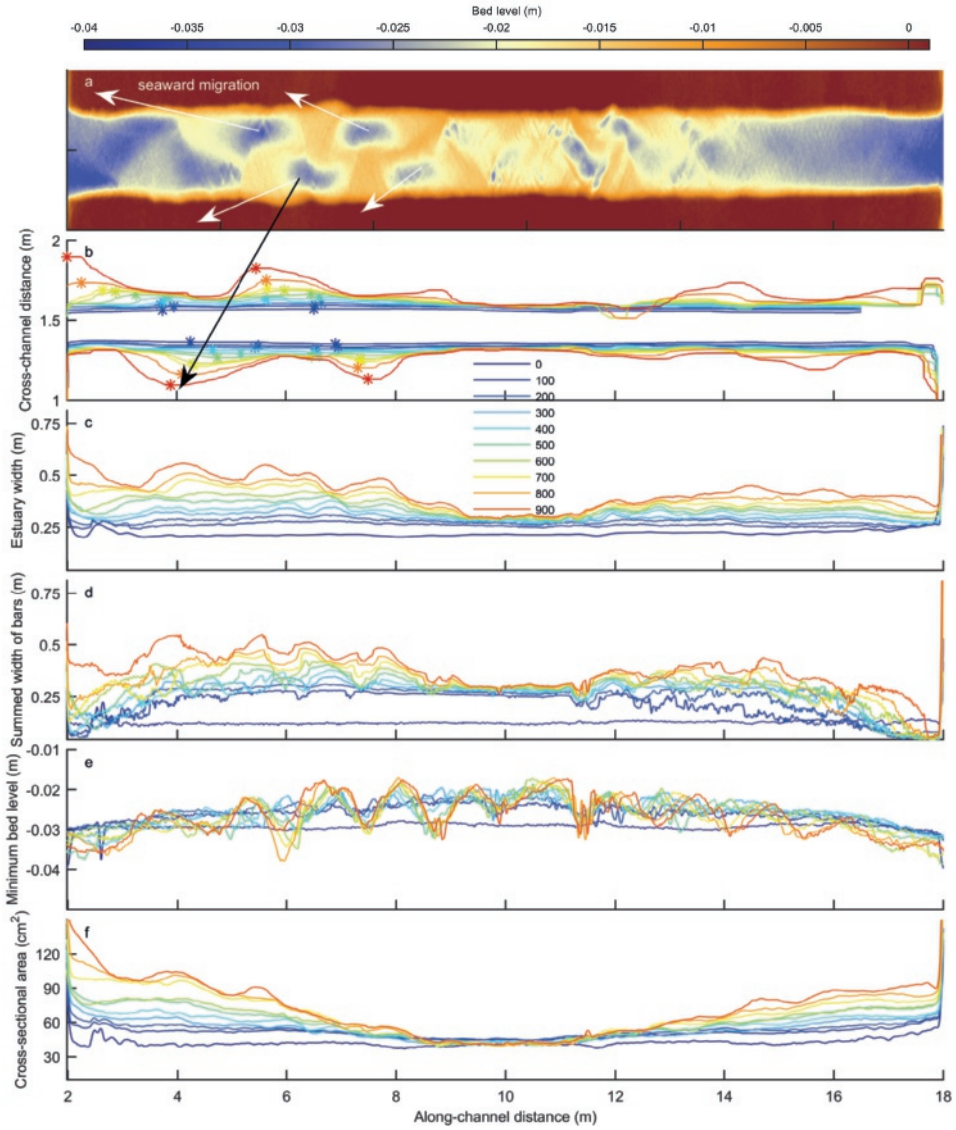

Figure 4.9 (a) Bathymetry after 300 tidal cycles. Along-channel profiles of (b) estuary bank location, (c) estuary width, (d) summed width of bars, (e) minimum bed elevation and (f) cross-sectional area over time in the experiment that started with a narrow channel. The white arrows in panel (a) indicate migration direction of initial channels, resulting in specific zones where the estuary widened in panel b and c. Asterisks indicate maximum lateral bank erosion per time-step.

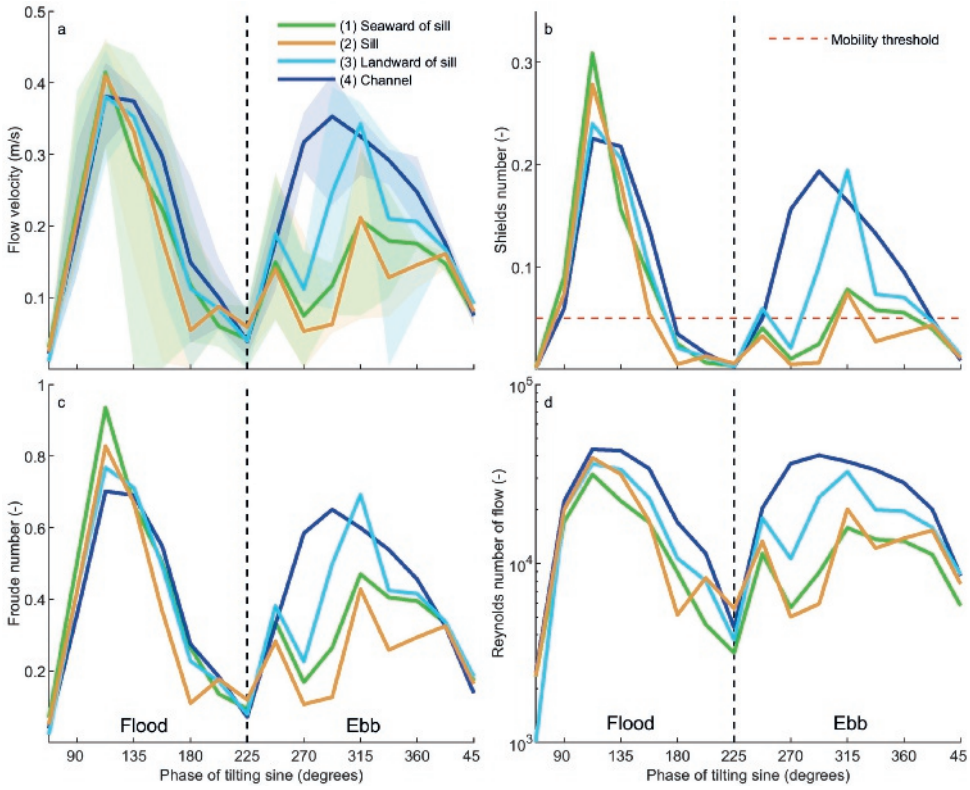

Figure 4.10 (a) Flow velocity over time for the locations indicated in Fig. 4.5d. Velocity profiles were corrected for phase difference induced by the along-channel distance and averaged per class. Areas indicate maximum and minimum per class. During both the ebb and the flood phase flow decelerates at the sills, which indicates flow divergence, especially in the second half of the flood phase and during the middle part of the ebb phase. (b) Shields number, (c) Froude number and (d) Reynolds number over time calculated for the class averaged flow velocity.

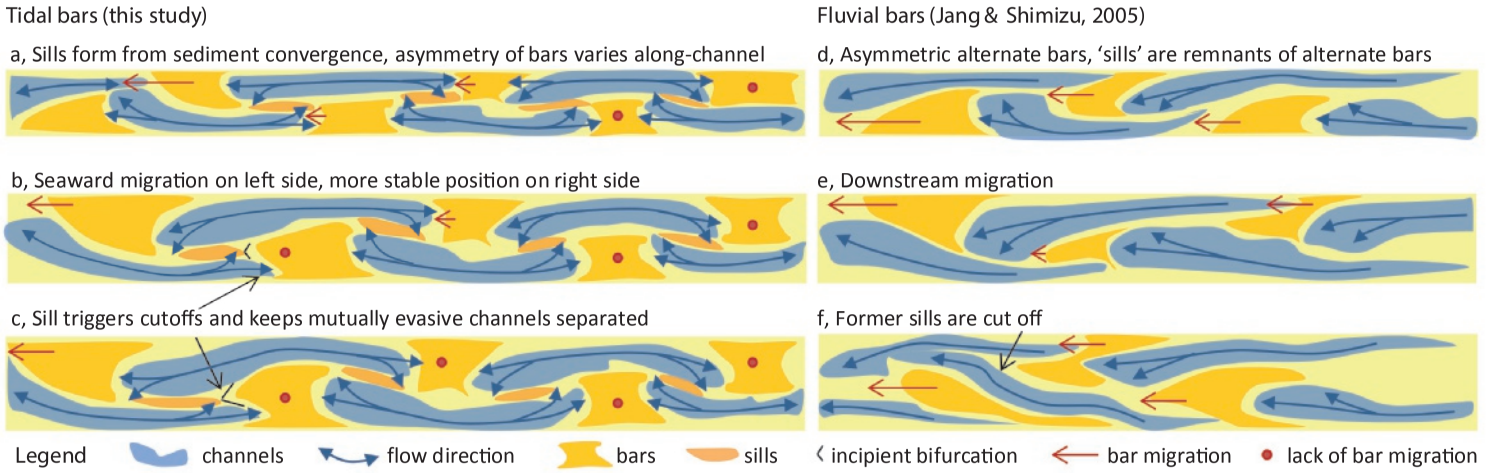

Figure 4.11 (a,b,c) Incipient tidal bar formation based on the experiments presented in this study compared to (d,e,f) incipient bar formation in rivers based on Jang and Shimizu (2005).

Initial flow conditions were similar on the left and right side of the flume (Fig. 4.13a,b,c). Peak flood flow was initially slightly stronger on both sides. The initial flood flow asymmetry and the erodible, sharp corners of the estuary banks at the mouth explain why sediment was imported to converge in the middle of the flume (Fig. 4.9e). Over time, asymmetry in peak ebb and peak flood velocity decreased (Fig. 4.13a,b,e). In the middle of the flume, peak flood velocities reduced, while in the seaward zone peak flood velocities increased (Fig. 4.13a,b), likely due to landward shallowing and seaward deepening (Fig. 4.9e). The flood duration decreased slightly over time, showing a more peaked profile than the ebb flow (Fig. 4.13d). The overall flow asymmetry along the flume explains why alternate bars are more asymmetrical in the seaward zone and more symmetrical in the landward zone (Fig. 4.11a,b,c).

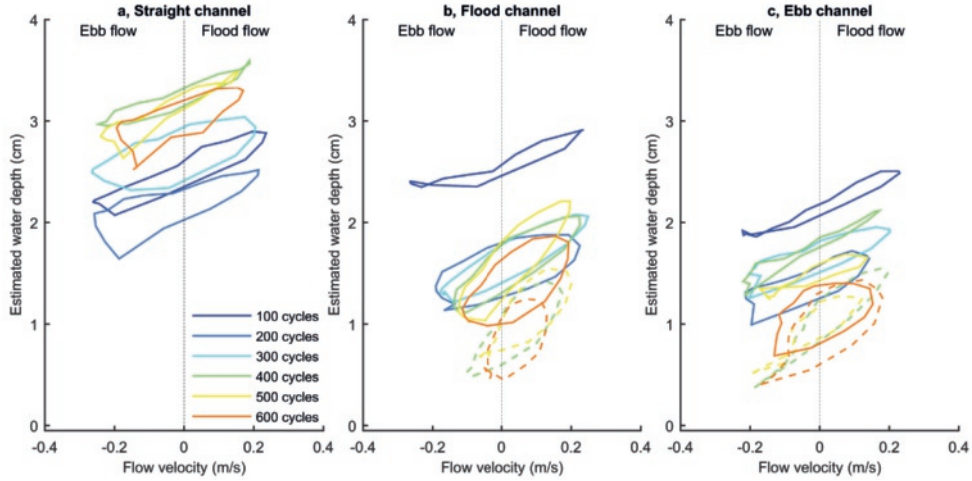

Figure 4.12 Tidal stage diagrams with water depth against flow velocity. Water depth was estimated from a calibration between blueness and bathymetry (Suppl. Fig. 4.16). Flow velocities were measured with Particle Image Velocimetry. Typical stage diagrams were obtained by averaging the measured values at characteristic locations along the flume: (a) centre of straight channels, (b) flood channels (solid) and the bar tips of the flood channels (dashed), (c) ebb channels (solid) and the bar tips of the ebb channels (dashed).

4.4 Discussion

4.4.1 Incipient tidal bar formation

Mutually evasive ebb- and flood-dominated tidal channels are probably unique to the tidal environment (e.g. van Veen, 1950; Fenies and Faugères, 1998; Dalrymple and Choi, 2007). While past observations in natural systems suggested that mutually evasive ebb- and flood-dominated tidal channels are forced topographically by bends (van Veen, 1950; Ahnert, 1960), our experiments showed that stable sills initiate with the onset of tidal bar formation in the absence of topographical forcing. Sills arise spontaneously in a straight channel, between alternate bars, as follows. Initially, the deepest channels form sideways of alternate bars rather than in between the alternate bars. Secondly, this configuration leads to flow divergence on both ends of the channels, causing convergence of sediment between the alternate bars, building up a sill (Fig. 4.11a,b,c). As such, sills are superimposed on the incipient bar and channel pattern. Sills persist over time and force the ebb and flood flow to take opposite paths around the sill over time.

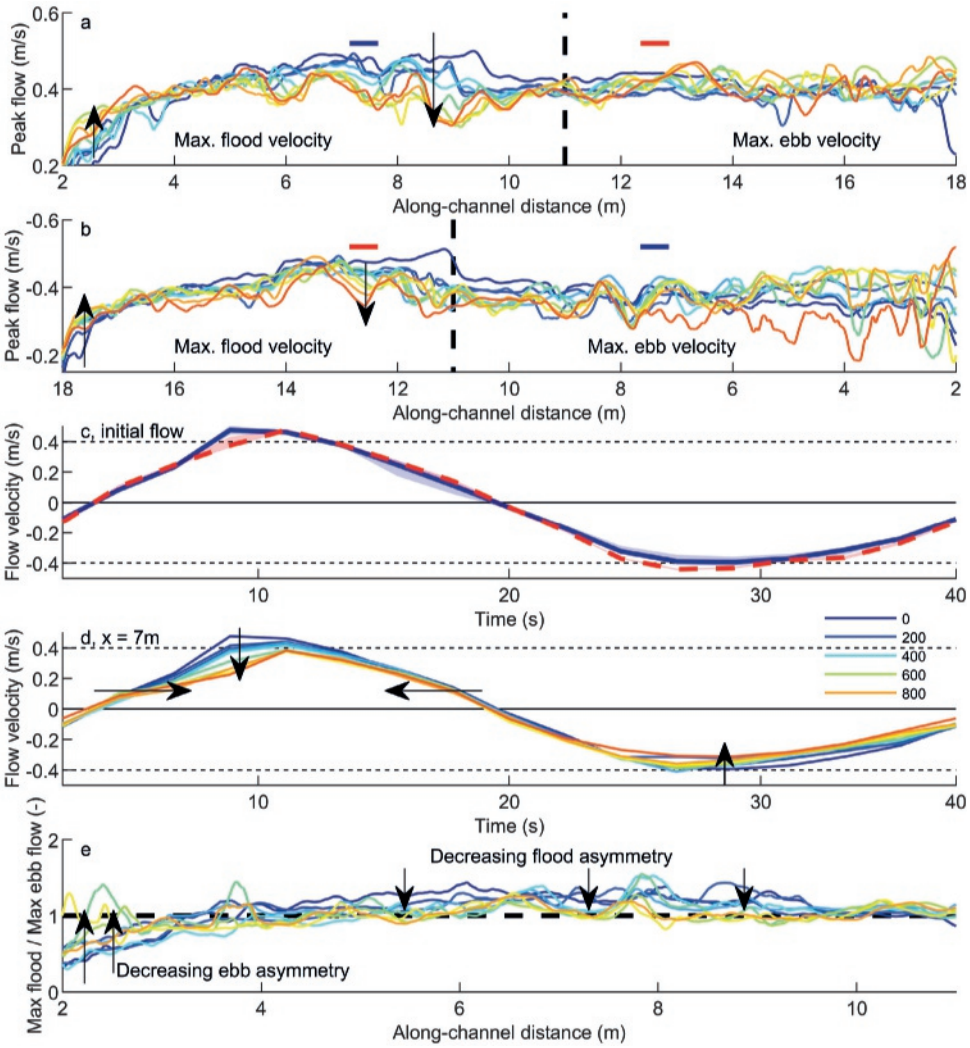

Figure 4.13 Along-channel peak flow velocities for the flume tilted (a) to the right and (b) to the left. Colours indicate time in tidal cycles (legend in panel d). (c) Tidal flow velocity at the start of the experiment at x=7m and x=13m. Measurement locations are indicated in panel a and b. Peak flood flow is initially stronger than peak ebb flow on both sides of the flume. (d) Tidal flow asymmetry over time on the left hand side of the flume. (e) Along-channel ratio of peak flood velocity divided by peak ebb velocity.

The alternative hypothesis for sill formation by topographic forcing requires local width changes and channel curvature effects such as secondary circulation. While secondary circulation can exist in these shallow flows, the bend radius of the intially nearly straight channels was so large that secondary flow was far too small to explain the observed sill slopes (see Fig. 6 in van Dijk et al., 2013a). However, in later phases, two opposing currents created lobate bars and oblique tidal currents that induced channel curvature around the sills (similar to Kleinhans et al., 2014). Only then the increased channel curvature (i.e. reduced bend radius) and estuary widening caused bars to become non-migratory in the inner

bends (also described by Repetto and Tubino, 2001; Repetto et al., 2002; Seminara, 2010; Zolezzi et al., 2012; Frascati and Lanzoni, 2013). At this stage the bars and sills become topographically forced, which is further evidence that the sills formed earlier are not topographically forced.

The sills also determine the location of future tidal bifurcations (Fig. 4.11b,c) and thereby the long-term evolution of estuaries. As channel widening progresses, the flood channels initiate new channels on the alternate bars, forming barb channels (e.g. van Veen (1950), Hibma et al. (2003) and Chapter 2) and isolating midchannel bars. Subsequent diversion of flow around midchannel bars and localised bank erosion cause the quasiperiodic width variation observed along estuaries (Chapters 5 & 6).

The evolution observed in our experiments is qualitatively in agreement with results from numerical models (e.g. Hibma et al., 2003; Hibma et al., 2004; van der Wegen and Roelvink, 2008; Braat et al., 2017), other experiments (Tambroni et al., 2005) and observations in natural systems (van Veen, 1950; Ahnert, 1960; Tank, 1996). Numerical models of straight tidal basins with non-erodible banks also resulted in initially straight channels that later connected into a main meandering channel with flood barbs (Hibma et al., 2003; Hibma et al., 2004; van der Wegen and Roelvink, 2008). In contrast to numerical models and experiments with non-erodible boundaries, numerical models (Braat et al., 2017) and experiments with erodible boundaries result in an initial phase of seaward migrating tidal bars and main meandering channels.

Linear stability theory (Schramkowski et al., 2002) correctly predicts the experimental observations that the braiding index of the initially fastest growing bar pattern increases with channel width. The setup with a wide channel showed initially a braided pattern, which later transitioned into an alternate bar pattern (Fig. 4.7), consistent with earlier work (Dalrymple and Rhodes, 1995; Hibma et al., 2003; Tambroni et al., 2005; Tambroni et al., 2017). The experiments also showed that bar dimensions are initially smaller and that flow velocities are initially larger than in the phase of full-grown bars (Fig. 4.8). This suggests that nonlinear effects are important for the dimensions of full grown bars, which shows the need of further development of nonlinear theory (Schramkowski et al., 2004).

4.4.2 Incipient bar formation in estuaries and rivers

Many of the morphological features and mechanisms observed in fluvial bar systems have a counterpart in tidal systems. A hierarchy of fluvial bars can be indicated by reference to unit bars and compound bars, independent of their shape and location, while the terms point bars, alternate bars and midchannel bars refer to the shape or location where the bars occur (cf. Cant and Walker, 1978; Bridge, 1993; Ashworth et al., 2000; Bridge, 2003; Sambrook Smith et al., 2006; Kelly, 2006; Rice et al., 2009; Kleinhans and van den Berg, 2011; Schuurman et al., 2013). Here we compare these fluvial morphological elements with the tidal bars, as was previously done for fully grown bars in natural systems (Ashley, 1980; Dalrymple and Rhodes, 1995; Tank, 1996).

The alternate bar pattern observed during incipient tidal bar formation and in other tidal experiments (Tambroni et al., 2005; Tambroni et al., 2017) is very similar to alternate bars in rivers and was also observed in former scale experiments of rivers (Jang and Shimizu, 2005; van Dijk et al., 2012). In both environments, alternate bars are self-generating in straight channels, in contrast to nonmigratory forced bars such as point bars (Parker and Johannesson, 1989). Our experiments showed that in contrast to rivers, alternate tidal bars are an amalgamation of two opposing U-shaped lobate bars, which makes them more symmetrical than river bars (Fig. 4.11). However, in the seaward zone, where flow was typically more ebb dominant (Fig. 4.13e), bars were more asymmetrical and thus more similar in shape and formative process to river bars (Fig. 4.11).

Point bars are a shared in-channel element of tidal channels and rivers (Bridges and Leeder, 1976; Barwis, 1977; de Mowbray, 1983; Tank, 1996; Solari et al., 2002; Pearson and Gingras, 2006; Choi et al., 2004; Choi and Jo, 2015; Brivio et al., 2016; Ghinassi et al., 2018), but only in cases where the channel is relatively narrow and deep such that the active braiding index is unity and where channel

curvature strong enough to force the bar to be nonmigratory. However, in the absence of bank strength, the experiments showed behaviour similar to river braiding. Before point bars developed, the inner bends were cut off by a progressively growing flood barb channel resulting in a midchannel bar. Previous experiments with cohesive suspended material that formed mud flats and floodplain (Braat et al., 2019) showed the evolution of a point bar with mud in the landward reach of the estuary.

A characteristic element in gravel bed rivers is the 'riffle-pool' sequence. Similar sequences of shallow sills and deeper channels have been observed in the Western Scheldt (Tank, 1996), a meandering tidal channel (Dury, 1971) and in the experiments presented here, but the forming mechanism is probably different. Water level gradients above riffles in rivers are typically very large, which is not the case above sills in estuaries. An alternative hypothesis is that sills in estuaries resemble unit bars in rivers. While the dimensions of sills in estuaries might be comparable with unit bars in rivers, their dynamic behaviour is different. Unit bars migrate downstream until they amalgamate with compound bars (e.g. Bridge, 1993; Schuurman et al., 2013), while sills in tidal systems are slaved to the larger-scale channel bar pattern because the sediment convergence from the tidal channels forms the sills (Fig. 4.11a,b,c).

4.4.3 Timescales of tidal bar formation

Bar patterns in numerical models evolved over a period of 50-200 yr (Hibma et al., 2003; van der Wegen and Roelvink, 2008), compared to ca. 1000-3000 tidal cycles in our experiments, which would correspond to 1-5 yrs in natural systems, assuming the same spatio-temporal scale factor. This implies that morphological evolution in our experiments is a factor 10-100 faster than in numerical models and in natural systems, as also found for fluvial experiments (Kleinhans et al., 2015a). This is partly explained by complete lack of bank strength in experiments without vegetation and cohesive material (van Dijk et al., 2012), which leads to an almost unlimited sediment supply, which immediately becomes available for bar formation just downstream of the erosion location (van de Lageweg et al., 2014). While bar formation in the experiments is unexpectedly fast, we lack observations of initial bar formation in nature and the timescale in the numerical models is highly sensitive to the chosen sediment transport relation, transverse bed slope effect, and numerical diffusion, which renders the models' unreliable indicators of morphological timescales without calibration.

The experimental setup with a double-head tidal channel led to the formation of two rather separated estuarine systems. The sediment eroded from the estuary banks in the initial phase was partly exported to the sea, but also partly accumulated in the middle part of the flume (at ≈10-11 m, Fig. 4.14a). The higher elevated part formed an obstruction for the flow, reducing the exchange of discharge between the left side (2-11 m) and right side (11-18 m) of the flume. At that location channel width remained narrow, which over time resulted in two separate converging channels in both directions of the flume (Fig. 4.14e). The morphological evolution in the zone between 2-11 m was slightly faster than the evolution in the other part (11-18 m).

The rate of morphological evolution correlates with the tidal prism (e.g. bend migration, Fig. 4.6), which, in turn, depends on the location of the tidal watershed. This correlation is consistent with observations along tidal inlets (Stefanon et al., 2010; Zhou et al., 2014; Kleinhans et al., 2015b) and tidal meanders (Finotello et al., 2018). Incipient bars and channels formed faster (in 300 cycles as opposed to 500 cycles) on the left hand side (2-11 m) of the flume. The left side was also approximately 25% longer than the estuary on the right hand side (11-18 m) of the flume. This either suggests that the initial sand bed was not sufficiently symmetrical or that the location of the tidal watershed is unstable and tends to shift as one watershed grows at the cost of the other in a positive feedback cycle. In reality this is unlikely to happen as the tidal wavelength is limiting the length dimension of tidal basins and estuaries (Schuttelaars and de Swart, 2000; de Swart and Zimmerman,

2009), but here we simulated a reach within a tidal system which allowed reasonable isolation of bar morphology from boundary effects.

Even though we did not anticipate the formation of two separated estuarine systems, the formation of a shore-like morphology acting as a tidal divide is consistent with experimental and numerical observations (Schuttelaars and de Swart, 2000; Lanzoni and Seminara, 2002; Garotta et al., 2008; van der Wegen and Roelvink, 2008; Tambroni et al., 2017). We chose the setup of a double-headed tidal channel (e.g. Dury, 1971; Hughes, 2012) aiming to create symmetrical reversing uniform flow along the entire flume. Uniform flow would allow studying bar formation independent of location along the flume, but unfortunately these conditions were only approximately met before bar initiation. It is therefore recommended to fixate the estuary banks for further research on bar initiation, and to explore the stability of tidal watersheds in upstream connected estuaries.

4.5 Conclusions

Laboratory scale experiments were performed to study incipient bar formation under varying initial and boundary conditions. The resulting evolution of tidal bars was similar among experiments and qualitatively in agreement with previous results from numerical modelling and observations in natural systems. After an initial phase with a rhomboid pattern with very short wavelength and high braiding index, straight initial channels formed with alternate bars. The deepest channels occurred sideways of the alternate bars while shallower zones formed in the cross-overs between the alternate bars. This configuration led to flow divergence on both opposing ends of the channels, causing sediment convergence between alternate bars. Sediment convergence resulted in the build-up of

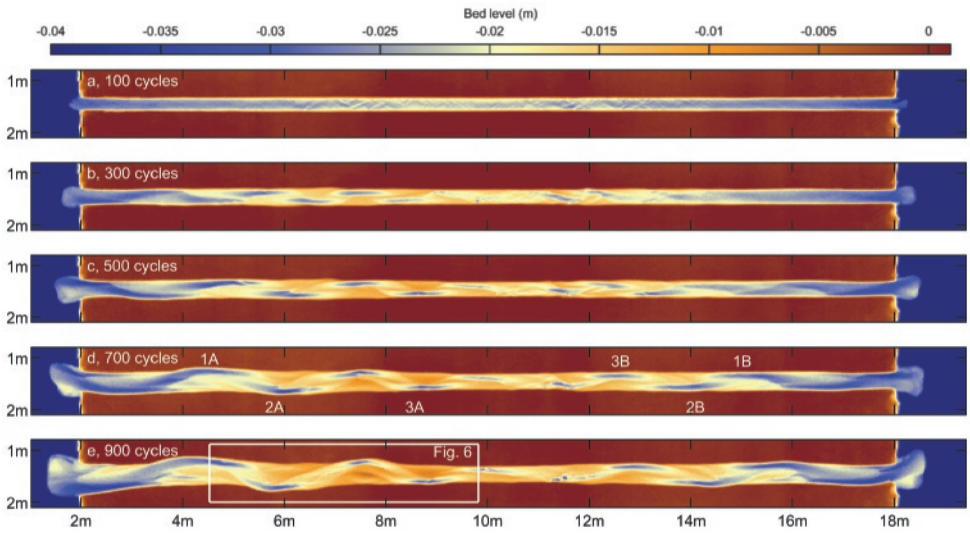

Figure 4.14 Time series of bathymetries obtained with structure from motion. (a) Initially, the channel widened at an equal rate along the entire channel. (b) While incipient bars and channels developed, bed elevations increased in the middle of the flume (≈10-11m). (c,d) In later phases, this elevated zone was the location where channel width remained narrow and widening ceased. (d,e) On both sides, two rather converging systems developed. The rate at which the channel widened, bars formed, channels became curved and braiding index increased, was faster for the left-hand side of the flume compared to the right hand side of the flume.

elongated sills parallel to the main flow direction and located between alternate bars. This pattern is superimposed on the alternate bar and channel pattern and is unique to tidal systems. Even under asymmetric flow conditions the sills persisted. Their stable presence triggered the formation of mutually evasive ebb- and flood-dominated channels that bifurcated around the sill. As channel widening progressed, flood barbs formed onto the alternate bars, which in later phases resulted in midchannel bars and a braided pattern.

Incipient tidal bars are similar to river bars in their morphological shapes and their response to increasing width-to-depth ratio. The key differences are the process of alternate bar formation – by amalgamation of two opposing U-shaped lobate bars – and the formation and stable presence of the sill. Bar dimensions and braiding index were predominantly correlated with estuary width and lacked dependence on channel depth and amplitude of tidal flow velocity. Observations in natural systems may have suggested that mutually evasive ebb- and flood-dominated tidal channels are topographically forced, but here we showed that their stable presence is initiated with the onset of tidal bar formation and thus does not necessarily require topographical forcing.

Acknowledgments

We acknowledge a data processing contribution by Thijs de Lange as part of his MSc research. Discussion with Steven Weisscher helped to improve the manuscript. Constructive reviews by Alvise Finotello, two anonymous reviewers, and steer by the Editor and Associate Editor helped to improve the manuscript. Author contributions: JRFWL performed experiments, collected and analysed data and wrote the manuscript, MGK contributed to conception and design and writing the manuscript.

Supplementary material

Table 4.2 Overview of data collected in the experiments. The numbers correspond with the time of data collection in tidal cycles.

Nr	DEM	Water levels	Mirror reflex	Wet bed images	PIV
014	0; 3100		200; 400; 600; 1860; 3100	3100 (at 65 mm and 77 mm)	
017	every 100 cyles until 1000	once / 100 cyles	once / 100 cyles	300 (at 65 mm, 77 mm and 99 mm)	once / 100 cyles

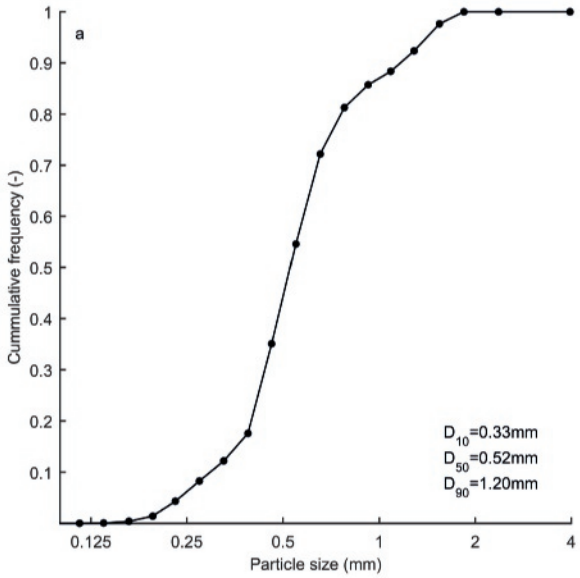

Figure 4.15 Particle size distribution of the sediment that was used in the experiments: a sand mixture ($\rho_s = 2650$ kg m^{-3}) with a median grain size of 0.52 mm and a coarse tail (D_{90} = 1.2 mm, D_{10} = 0.33 mm).

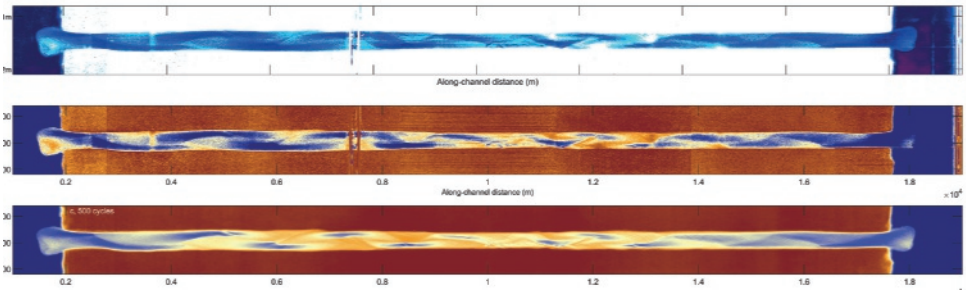

Figure 4.16 (a) Overhead image with blueness extracted. (b) Resulting depth map after applying a correlation between blueness from overhead imagery and bed level from structure from motion bathymetry. (c) Bathymetry obtained with structure from motion.

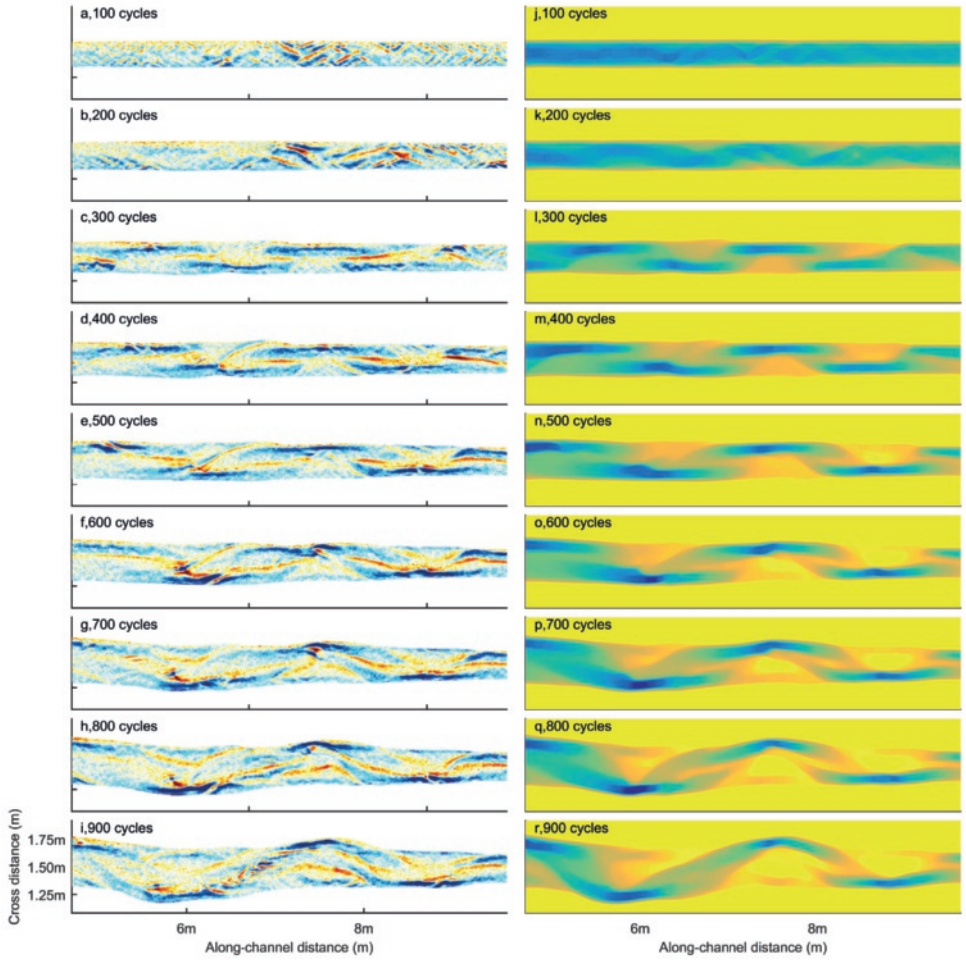

Figure 4.17 To enhance the visualisation of sills and ridges on bar tops, smoothed DEMs were subtracted from the original DEMs. Left panels indicate where bed levels are higher [red] and lower [blue] than in the smoothed DEM. Right panels show the smoothed DEMs. Left panels show that bars are typically built up from two opposing U-shaped lobate bars and that narrow straight sills are present along the centreline of the channel.


5

Chapter 5 | Topographic forcing of tidal sandbar patterns for irregular estuary planforms

Abstract

Estuaries typically show converging planforms from the sea into the land. Nevertheless, their planform is rarely perfectly exponential and often shows curvature and the presence of embayments. Here we test the degree to which the shapes and dimensions of tidal sandbars depend on estuary planform. We assembled a dataset with 35 estuary planforms and properties of 190 tidal bars to induce broad-brush but significant empirical relations between channel planform, hydraulic geometry and bar pattern. We found that the location where bars form is largely controlled by the excess width of a channel, which is calculated as the observed channel width minus the width of an ideal exponentially widening estuary. In general, the summed width of bars approximates the excess width as measured in the along-channel variation of three estuaries for which bathymetry was available as well as for the local measurements in the 35 investigated estuaries. Bar dimensions can be predicted by either the channel width or the tidal prism, because channel width also strongly depends on local tidal prism. Also braiding index was predicted within a factor of 2 from excess width divided by the predicted bar width. Our results imply that estuary planform shape, including mudflats and salt marshes as well as bar pattern, depend on inherited Holocene topography and lithology and that eventually convergent channels will form if sufficient sediment is available.

Modified from: Leuven, J.R.F.W., de Haas, T., Braat, L. & Kleinhans, M.G. (2018). Topographic forcing of tidal sand bar patterns for irregular estuary planforms. *Earth Surface Processes and Landforms, 43 (1), pp. 172–186*, DOI: 10.1002/esp.4166.

5.1 Introduction

Estuaries are converging bodies of water that have inflow of river water at the landward boundary and an open connection to the sea. In ideal estuaries, the tidal range, average depth and current velocity amplitude are uniform in the along-channel direction, whereas the channel width exponentially converges in landward direction (Pillsbury, 1956; Langbein, 1963; Savenije, 2015). Ideal estuary behaviour has been argued to arise when an estuary has adapted its shape to the boundary conditions by sedimentation and erosion (Townend, 2012; Savenije, 2015). However, this requires that (1) the estuary has adapted to Holocene sea-level rise, (2) sufficient sediment and time were available for the adaptation and (3) the antecedent topography could adapt, which excludes substrates that are erosion resistant. Therefore, estuaries in nature are expected to exhibit varying degrees of adaptation towards ideal estuaries, where embayments are partially filled with sand bars, mud flats and salt marshes and where the overall planform is partly determined by antecedent geology (Townend, 2012) (Fig. 5.1).

The planform of estuaries typically converges from the seaward side to the landward side. Within this planform, the dimensions of tidal bars and the number of parallel channels gradually vary, often decreasing in landward direction. However, due to sea-level rise, sediment supply and time for adaptation, the estuary shape deviates from an ideal shape. This has major implications for tidal wave propagation and sediment transport, because it alters the hydrodynamics and net sediment transport over time (Friedrichs and Aubrey, 1994; van den Berg et al., 1996; Lanzoni and Seminara, 1998; Savenije, 2006) and in addition it influences the bar patterns. For example, the mouth of an estuary may be confined by a sand spit, followed by a long and wide compound bar at the landward side (Fig. 5.1a,b). At locations where the estuary is wide, bar dimensions and braiding index generally increase. At the landward end, the number of channels generally reduces towards a single threaded river (Fig. 5.1).

Here we focus on funnel shaped nonideal alluvial estuaries with dynamic patterns of channels and sand bars, often flanked by tidal mud flats and salt marshes. We investigate the effects of natural deviations from the ideal estuary shape, such as embayments, on the bar pattern. Furthermore, we analyse how channel planform of nonideal estuaries topographically forces patterns of tidal bars. It was previously found that tidal bar dimensions depend mostly on the channel width, measured as the width between the vegetated marshes or banks including the sand bars (Chapter 2). In addition, the location of bars in the similar environment of rivers can be forced by embayments, bends and other planimetric non-uniformities (Tubino et al., 1999; Seminara, 2010; Schuurman et al., 2013). At locations along an estuary or river where the width of the cross-section increases, the stream velocity generally decreases and hence, the shear stress, which favours sediment deposition. These observations and theory suggest that sand bar patterns in estuaries partly depend on the present planform shape of the estuary.

For bar pattern in rivers, bars are either classified as free or as forced. While forced bars are forced to their location by the planform shape of the channel, free bars can migrate freely and occur in straight or weakly curved channels (Tubino et al., 1999; Seminara, 2010; Schuurman et al., 2013). It was found that the topographic forcing of bars occurs on (1) the scale of individual bars, due to meander bends and embayments, which fix the bars at their location (Struiksma et al., 1985; Repetto and Tubino, 2001; Wu et al., 2011) and (2) the reach scale, an order of magnitude larger than individual bars, due to variations in channel width and discharge (Tubino et al., 1999; Seminara, 2010; Kleinhans and van den Berg, 2011; Schuurman et al., 2013). For rivers, the latter scale sets independent variables that determine bar pattern. In addition, the channel width may be non-uniform in space, causing local flow expansion or convergence to force the formation of bars. Since estuaries generally have converging channels, we define the non-uniformity of estuary channel width here as the deviation from an ideal exponential profile. Nevertheless, it is unknown if the forcing mechanisms for rivers extend to estuaries. Therefore,

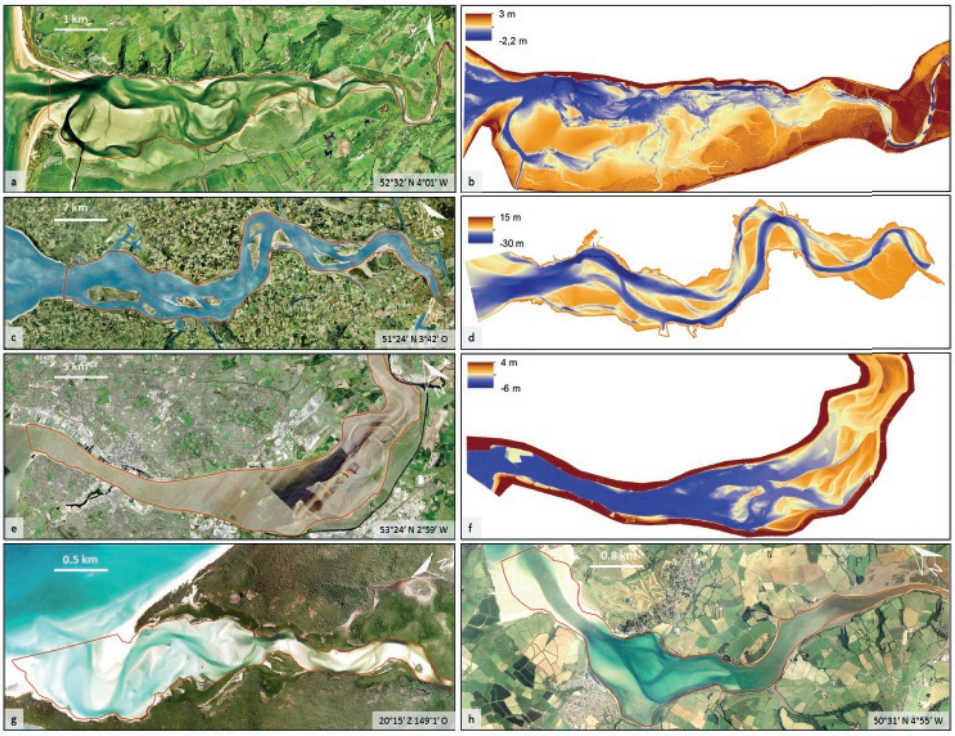

Figure 5.1 Aerial photographs of estuaries and available bathymetries. (a,b) Dovey Estuary (UK); (c,d) Western Scheldt (NL); (e,f) Mersey Estuary (UK); (g) Whitehaven Beach (Australia); (h) Camel Estuary (UK). Red lines: digitised channel planforms. Images: Google Earth, accessed January-September 2016.

we record and analyse forced bars in nonideal alluvial estuaries in this study, to determine how non-uniformity affects the location, shape and dimensions of tidal bars.

Our work partly builds on previous research, that mainly focussed on the dimensions and shapes of individual tidal bars and how they compare to theoretical predictions (Chapter 2). We found that tidal bar dimensions increase with estuary dimensions, in particular with estuary channel width (e.g. bar length $\propto$ channel width$^{0.87}$). Classical tidal bar theory predicts bar length to be stronger dependent on tidal current velocity – or tidal excursion length – than on estuary channel width (Seminara and Tubino, 2001; Schramkowski et al., 2002). The research in Chapter 2 forms a starting point to study the along-channel variation in bar pattern. To obtain a prediction of the bar pattern on the estuary scale, it is required to predict the along-channel variation in the braiding index and the location where bars form. Obtaining these relations will thus be the main focus of this chapter. If relations for individual bar dimensions are required, we rely on the data and relations presented in Chapter 2.

While Chapter 2 showed that theory mispredicts the dimensions of individual bars, it still is the only method to obtain a first idea of the along-channel variation in bar pattern in estuaries up to the present day. Fig. 5.2 shows a prediction of the along-channel summed width of bars and braiding index (BI) for the Western Scheldt (NL) according to theories of Schramkowski et al. (2002) and Crosato and Mosselman (2009). Since theoretical approaches describe tidal bars as wave forms, they predict the summed width of all individual bars to be approximately equal to half the channel width

by definition (Fig. 5.2), which might overestimate the formation of bars at points where the estuary is confined by bedrock geology or human influence. Theoretical predictions form a starting point for this study, but here we aim develop an empirical method. The previous empirical study (Chapter 2) and forcing mechanisms for rivers (Tubino et al., 1999; Seminara, 2010; Kleinhans and van den Berg, 2011; Schuurman et al., 2013) imply that to understand the along-channel variation in bar pattern for estuaries it is necessary to take their converging planform and local variations in width and discharge into account.

The relation between bar dimensions and channel geometry raises the question what the local geometry of an estuary determines. Hydraulic geometry describes relations between discharge, channel width, depth and flow velocity. Previously, relations were derived for specific tidal systems (Sassi et al., 2012; Gisen and Savenije, 2015; Lanzoni and D'Alpaos, 2015) and as a function of independent, external boundary conditions, in particular river discharge, tidal amplitude and estuary mouth dimensions (Davies and Woodroffe, 2010; Townend, 2012). For rivers, it was shown that channel forming or bankfull discharge is a proper indicator to predict channel width (Lacey, 1930; Leopold and Maddock Jr, 1953; Hey and Thorne, 1986; Savenije, 2003; Kleinhans and van den Berg, 2011). In estuaries, discharge varies significantly over a tidal cycle. Therefore, we expect that the channel forming discharge for estuaries may be approximated with the average volume of water flowing through a cross-section over half a tidal period. This was demonstrated to be a good predictor for hydraulic geometry in multiple tidal systems (e.g. O'Brien, 1969; Eysink, 1990; Friedrichs, 1995; Lanzoni and D'Alpaos, 2015) and it may therefore also serve as a predictor for bar patterns.

Our aim is to assess to what degree bar patterns depend on the irregularities in the planform width of estuaries as far as this deviates from the ideal, exponentially converging, shape. We test the hypothesis that the topography, in particular channel width, forces the bar pattern and that local tidal prism predicts the hydraulic geometry of estuaries. Therefore, we assembled a dataset with the planform of 35 estuaries, analysed the effect of planform on bar pattern and compared it with the results from theoretical predictions.

This chapter is organised as follows. First, the methodology is given for collecting bar pattern and estuary planform data. Second, we describe empirical relations between tidal bar properties and planform shape of estuaries. The applicability of the results is discussed for cases where little data is available, such as the reconstruction of bar patterns in former Holocene estuaries.

5.2 Methods

This study partly builds on the previously collected dataset of Chapter 2, which was focussed on the dimensions and shapes of individual bars only. We first summarise this dataset with its underlying assumptions and uncertainties, as far as relevant for this study. Thereafter, it is described how this dataset was extended to enable a study of the bar pattern on the estuary scale. To do so, measurements of the summed width of bars were made and channel planforms were collected. Last, we describe the methodology for data processing and definitions used in the results.

5.2.1 Available dataset

Chapter 2 resulted in a dataset with local measurements of individual tidal bars and collected detailed bathymetries for three estuaries: the Western Scheldt (NL), Dovey (UK) and Mersey (UK) (Fig. 5.1b,d,f). Data for the Western Scheldt was obtained from Rijkswaterstaat, for the Dovey estuary from Natural Resources Wales and for the Mersey from the UK government. In addition, geomorphological maps were available for the Western Scheldt with ecotopes, obtained from Rijkswaterstaat (NL) (Fig. 5.3c). Most of the estuaries for which bar dimensions were measured are located in the USA and western Europe.

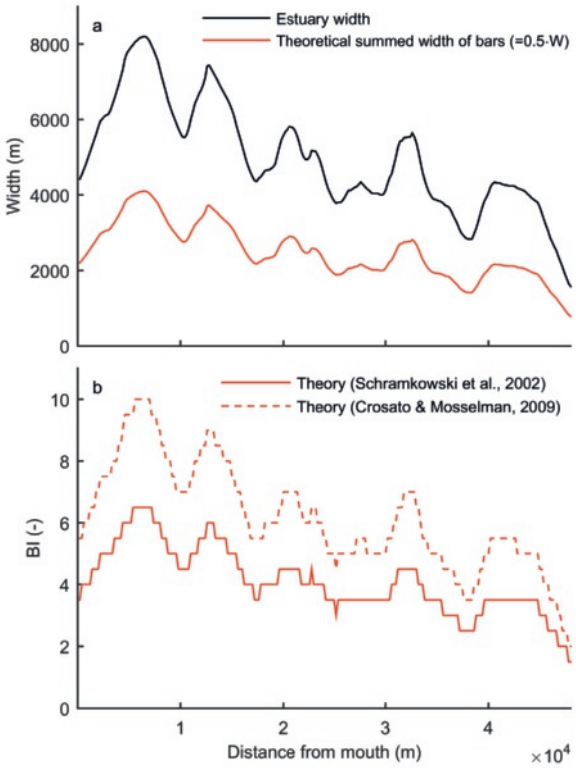

Figure 5.2 Theoretical prediction of summed width of bars (a) and braiding index (b) from channel width, in this case of the Western Scheldt, by the linear stability theories of Schramkowski et al. (2002) and Crosato and Mosselman (2009), following the approach in Chapter 2.

The dataset contains the dimensions (length, width and height) of 190 tidal bars in 45 funnel shaped alluvial estuaries and included data on estuarine properties (Fig. 5.4). Based on their shape, the bars were classified into four classes: sidebars, linear bars, U-shaped bars and compound bars (Fig. 5.4). Analyses of the dataset showed that compound bars and U-shaped bars can be seen as simple linear bars partly cut by barb channels, where a barb channel is defined as one-ended channel that partly crosscuts the bar and becomes shallower in the direction of flow (Dalrymple and Choi (2007) and Chapter 2) (Fig. 5.4). Therefore, we previously introduced two measures of bar width: the maximum bar width and the partitioned bar width. The maximum bar width was recorded at the local maximum of individual bars (Fig. 5.4). The partitioned bar width was calculated as the maximum bar width divided by the number of barb channels (Fig. 5.4). In the present study, we add the measure of the summed width of bars to these definitions. The summed width of bars is defined as the sum of all bar widths in one cross-section (see Fig. 5.4 for an example).

In the dataset, estimations were made for the local channel depth at the tidal bar locations. To do so, a linear depth profile was assumed between the mouth of the estuary and upstream river depth. To validate this, the measurements of the average channel depth excluding bars were compared with the assumption of a linear increasing bed profile for the three cases for which bathymetry was available (the Dovey, Mersey and Western Scheldt estuary). It was found that the predictions with this assumption are within 10% of the measured value. The Western Scheldt formed an exception, because its channels are

dredged. The cross-sectional channel area at the bar locations was estimated in this study. To do so, the estimated average channel depth excluding bars from Chapter 2 was multiplied with the channel width excluding bars. The error of maximum 10% in the prediction of channel depth is linearly propagated in our estimations of cross-sectional area.

As the dataset was collected from aerial photographs, the precise water level with respect to mean sea level was unknown for the moment the aerial photograph was taken. Since the water level influences the apparent bar shape observed from aerial photographs, Chapter 2 showed the likely measurement error that arises from the unknown flow stage. It was found that bar length and width measured at mean sea-level and low water level are at most a factor of 2 larger or smaller than when measured at the exact intermediate water level, which is smaller than the scatter within the full dataset for which the trends that were found span multiple orders of magnitude.

5.2.2 Planform classification and data collection

For 35 of the 45 estuaries in the dataset of Chapter 2, a polygon of the outline of the estuary planform was recorded (Suppl. Table 5.1), which covered 170 of the 190 bars in the original dataset. At these 170 locations the summed width of bars was measured from aerial photography. Due to a lack of bathymetries for estuaries, channel planform was visually recorded using Google Earth, based on the morphology visible on aerial photography. This approach is similar to the classification of ecotopes on the geomorphological map of the Western Scheldt (de Jong, 1999; Bouma et al., 2005). Nevertheless, it excludes any *in situ* measurements such as salinity and mud content and therefore relies more on visual observations.

Ideally, the polygons would extent up to the tidal limit. However, it is impossible to derive the tidal limit from an aerial photograph and detailed depth profiles to estimate this are lacking. Therefore, the polygons were digitised over the extent for which mutually evasive ebb- and flood-dominated tidal channels were present and we included the first single-thread meander. In section 5.2.3, we assess how this influences our approximation of the tidal prism. For each estuary, two types of planform polygons were recorded: the active channel polygon and the estuary polygon (Fig. 5.3a).

Active channel area refers to the area with a dynamic pattern of channels and sand bars, and is approximately the area that is submerged at mean sea level. This means that we here exclude the mud flats and salt marshes from the active bar pattern. The active channel planform covers the part of the estuary in which large (>100s of metres) dynamic channels and bars that lack mud and vegetation are present (Fig. 5.3a). In this area, the orientation of channels and bars is parallel to the centreline. The channel orientation, together with the dimensions of the channel, indicates that substantial sediment transport occurs in the along-channel direction. The presence of bedforms, barb channels and the absence of vegetation were used as indicator of the active channel area, where sediment is regularly transported and vegetation cannot sustain.

Estuary area refers to the area that is approximately submerged during mean sping tide. The estuary area covers the active channel area plus the vegetated marshes, flats and former abandoned estuarine areas. These areas were classified based on the presence of dense vegetation or a muddy layer of surface sediment that is darker than the sediment on the tidal bars. In addition, these areas were often dissected by small (<100s of metres) channels perpendicular to the centreline. The presence of vegetation or pioneering vegetation indicates that the tidal flats are only submerged and active during the highest water levels. The spatial transitions from pioneering vegetation to forest, bedrock geology or human dominated landscape were used as the maximum extent for the estuary area.

The summed width of bars was measured on the same aerial photograph as for which the polygons were digitised. For some cases these differ from the date of the aerial photographs used in Chapter 2. These measurements were added to the dataset of Chapter 2.

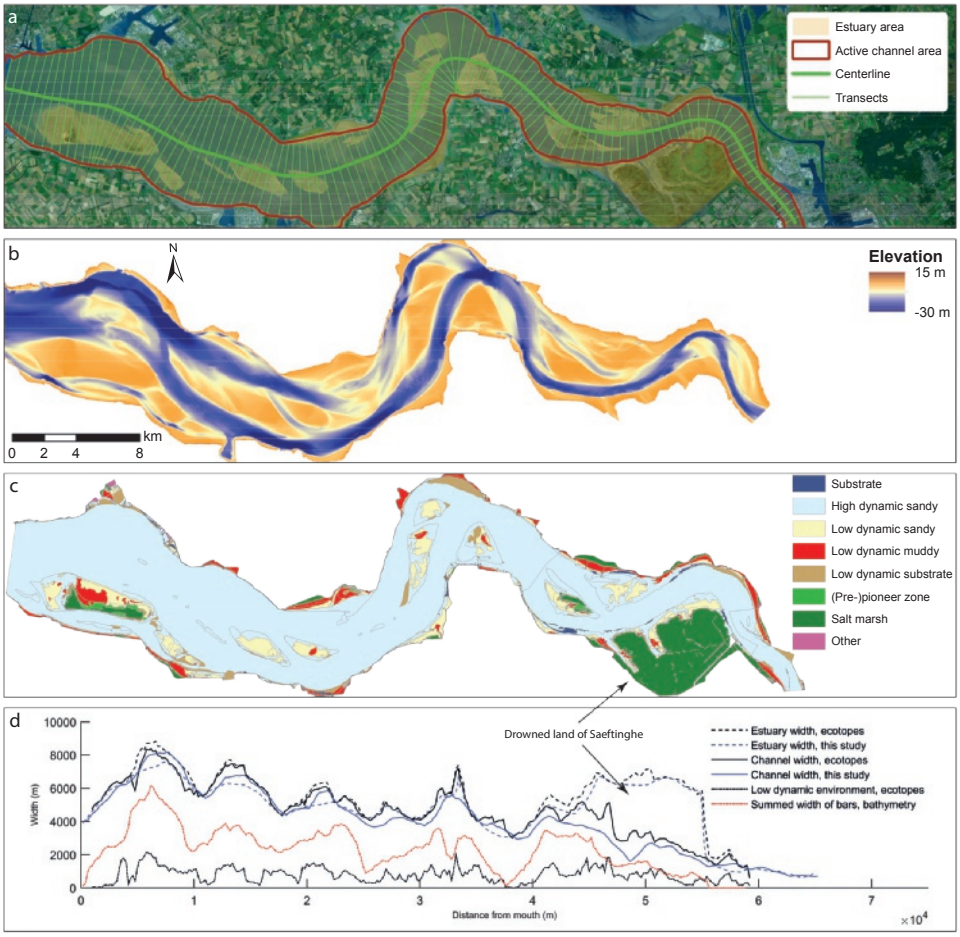

Figure 5.3 Illustration of the methodology to collect channel and estuary planform and channel width along the Western Scheldt. Given the focus on bars, the mud flats and salt marshes are excluded from the channel planform width. (a) Aerial photograph with the definitions used in this study: estuary area, active channel area, centreline of active channel area and transects. Bing Maps, accessed September 2016. (b) Bathymetry and (c) ecotope map of the Western Scheldt (2012), obtained from Rijkswaterstaat. (d) Estuary width, channel width, bar width and low dynamic environments as derived from the polygons drawn on the aerial photograph, the bathymetry and ecotope map.

The supplementary material contains the active channel area polygons (Polygons available in online supplement) and a list of estuaries used in this study (Suppl. Table 5.1) including measurements of the approximate surface areas of the estuary area and bar measurements. Because the active channel planform may change over time, the date of the aerial photograph is given for the recorded planforms (Suppl. Table 5.1). To optimise classification and recording, photographs with relatively low water levels were used.

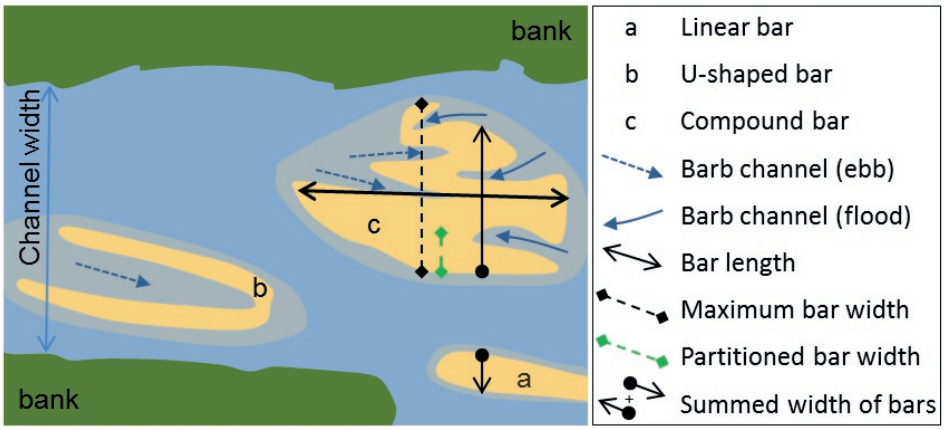

Figure 5.4 Schematic of a linear bar, U-shaped bar and compound bar with the corresponding measurements of channel width, bar length, maximum bar width, partitioned bar width and summed width of bars. Barb channels are channels that become shallower in the direction of flow and taper out onto the bar regardless of water level, while flow during high water diverges out of the barb channel. The summed width of bars is the sum of all bar widths in one cross-section.

5.2.3 Data processing and definitions

After visual classification of the planforms, the estuary centrelines and surface areas were automatically determined using GIS software (Fig. 5.3a). The centreline is defined as the mean location line between the polygon boundaries, similar to approaches of Davies and Woodroffe (2010), Sassi et al. (2012) and Kraaijenbrink et al. (2016). Subsequently, the centrelines were smoothed with a Polynomial Approximation with Exponential Kernel (PAEK) algorithm in GIS using a tolerance of 0.5 times the maximum channel width. The smoothed line was resampled at an interval of 50 m. At all re-sampled points, a cross-section was constructed, perpendicular to the centreline and within the boundaries of the channel area (Fig. 5.3a). Smoothing was performed to prevent that the direction of cross-sections is highly sensitive to local curves and width variations along the estuary. Now, the width along the centreline of the estuary is given by the length of the successive cross-sections (Fig. 5.3d). The total surface area was obtained by integrating the channel width over distance.

To assess the quality of our visual classification, the results were compared with the classification of the ecotopes on the geomorphological map of the Western Scheldt (de Jong, 1999; Bouma et al., 2005). The variation and presence of ecotopes along the Western Scheldt estuary in 2012 (Fig. 5.3c) was derived using the same methodology as described above for channel width: for each successive cross-section the total width of each ecotope was calculated. Comparing both approaches (Fig. 5.3d) shows that both methodologies result in similar measurements of active channel width and estuary width, which allows to extend our visual classification to other estuaries.

It was attempted to digitise up to the tidal limit, but in some cases this was impractical for the PAEK algorithm because of the small size and tight shape of meandering channels at the landward reach of the estuary. For these cases we removed the most landward part of the polygon and defined this area as the offset area (Suppl. Table 5.1). The polygons were then processed without the offset area to obtain the centreline and channel dimensions. We included the offset area only in the calculation of tidal prisms.

The convergence of estuaries is often measured with the width convergence length or estuary shape factor (Davies and Woodroffe, 2010), which is based on the assumption that estuaries ideally have exponentially converging planforms (Pillsbury, 1956; Langbein, 1963; Savenije, 2006; Savenije, 2015).

The convergence length is the distance over which the channel width of the estuary mouth reduces by a factor e ($\approx$ 2.7), which is calculated as:

$$L_W = -s \frac{1}{\ln\left(\frac{W_s}{W_m}\right)} \tag{5.1}$$

where ln is the natural logarithm, W_m is the width at the estuary mouth, W_s is the width of the estuary at the landward side and s is the distance from W_m to W_s along the centreline of the estuary.

Here we calculate the maximum fitting exponential shape for the active channel planform. We use the mouth width to calculate the convergence length and to fit an exponential function (Fig. 5.5a-c), because a least-squares fit would largely overestimate the width of the mouth in all cases and therefore also the maximum fitting exponential shape. The resulting fit we used thus depends on the chosen position for the mouth. Since the positioning of the estuary mouth on aerial photographs can be arbitrary, we used the following approach and rationale.

For estuaries in which the mouth was confined by geology, human activity or a higher elevated spit, we selected the location with the minimum width as the position of the mouth (see for example Fig. 5.1c,e). In these cases, the minimum mouth width limits the amount of water that can enter the estuary over a tidal cycle. In cases where the mouth was confined with a shallow spit that lacked vegetation or the area around the mouth was widening in seaward direction, we either chose the location of the mouth at the point where the first tidal flats occur (Fig. 5.1h) or at the location where the beach ends (see for example Fig. 5.1a,g).

Savenije (2015) used a similar approach to fit exponential functions for ideal estuaries. Because the ideal estuaries presented by Savenije (2015) typically have a confining inflection point after the mouth of the estuary, two exponential functions were fitted to describe the estuary shape. Moreover, a definition for the position of the mouth was not given there. In contrast to ideal estuaries, the irregular estuary planforms in our dataset are mostly confined at the mouth of the estuary by the presence of a spit or bedrock geology. Therefore, using the minimum width as the location of the mouth in this study is appropriate.

The channel width along the estuary is often larger than the ideal exponential fit (Fig. 5.5a-c), since many alluvial estuaries are confined at their mouth by a spit or due to their antecedent landscape. Here, we define the channel width minus the width of the ideal exponential fit as the excess width (Fig. 5.5a-c). The excess width is generally positive, but may be negative in case the channel is constrained by bedrock geology or human interference, for example the construction of bridges in the Clwyd estuary (UK). We tested the sensitivity of excess width calculations to the measurement of the width of the mouth. A 25% increase or decrease in mouth width affects the calculation of the excess width by a maximum of 10%, but in most cases even less than 5%, since the excess width is often much larger than the exponential channel width.

The aim in this study is to assess how the bar patterns are forced by estuary topography. Part of this forcing may be related to variations in tidal prism. Therefore, the local tidal prism P was approximated as

$$P = 2a \cdot A_c \tag{5.2}$$

in which $2a$ is the tidal range, taken as spatially constant (following Savenije (2006) for ideal estuaries), and A_c is the planform channel area landward of the considered location. Here we used an approach that differs from methodologies that approximate the tidal prism from cross-sectional area (e.g. O'Brien, 1969; Jarrett, 1976; Shigemura, 1980; Eysink, 1990; Friedrichs, 1995; Lanzoni and D'Alpaos, 2015; Gisen and Savenije, 2015) for two reasons. First, the previously proposed relations for tidal systems span an order of magnitude, because most of these relations were only validated for one specific tidal system (Suppl. Fig. 5.11a, Suppl. Table 5.2). These relations are given in Suppl. Fig. 5.11a and Suppl. Table 5.2.

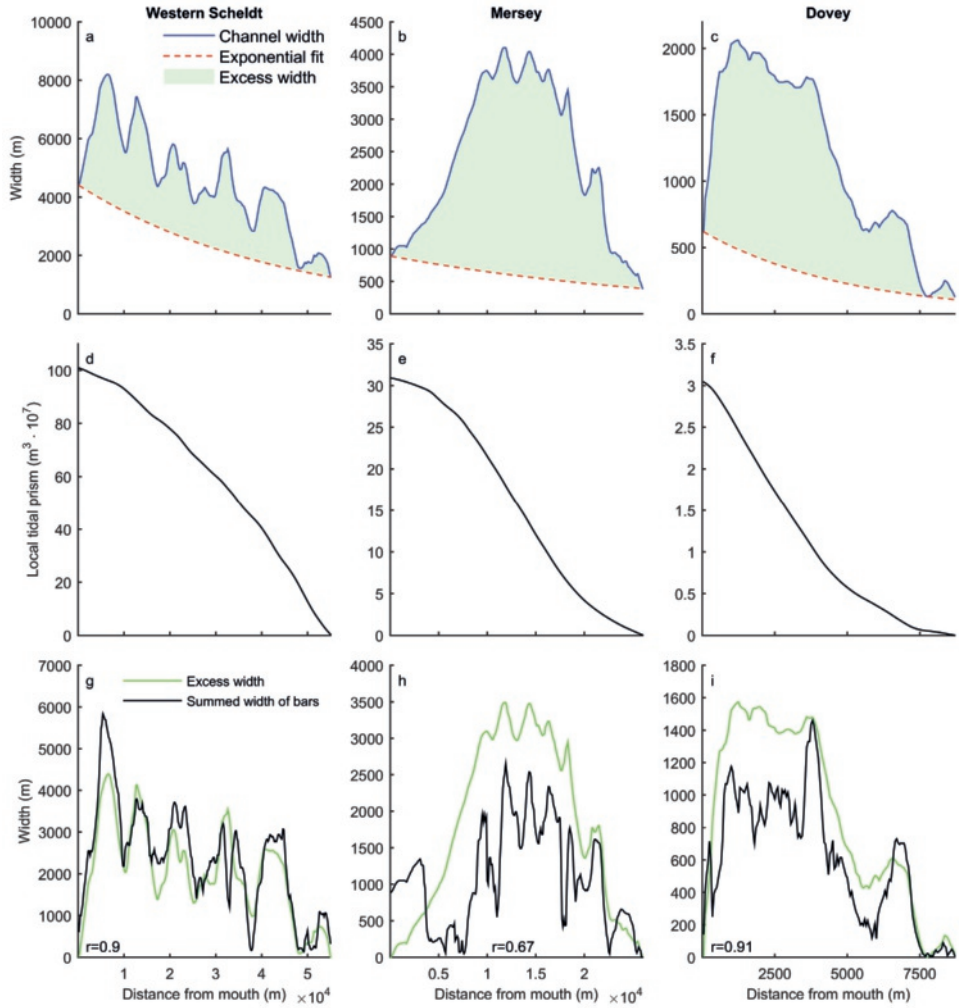

Figure 5.5 (a,b,c) Channel width along the estuary derived from planform polygons for the three estuaries with bathymetric data (see Fig. 5.1). Exponential functions were fitted on the width between the mouth and the upstream minimum river width. Excess width was calculated as the channel width minus the exponential fit. (d,e,f) Local tidal prism as estimated from upstream estuary area at mean sea level (MSL) multiplied by tidal range at the mouth. (g,h,i) Comparison between excess width and measured summed width of bars derived from bathymetries. The r-values indicate the Pearson product-moment correlation coefficients.

Second, the along-channel variation in bar patterns may not be captured by these relations. After all, the measured along-channel variation in cross-sectional area of nonideal estuaries – the Western Scheldt, Dovey and Mersey estuaries are used as an example here – can vary such that the cross-sectional area is equal at two locations along the estuary, while the local tidal prism differs by an order of magnitude (Fig. 5.5a-f, Suppl. Fig. 5.11b).

The endpoint of the digitised polygons affects the calculations of tidal prism with Eq. 5.2. The following three factors likely reduce the sensitivity to the choice for the endpoint. First, estuaries

narrow considerably in landward direction. Therefore, the local tidal prism is thus small compared to the local tidal prism at the mouth. Second, the tidal amplitude decreases upstream in estuaries that are friction dominated, which also limits the contribution of this area to the tidal prism. Last, the displacement of water by tidal wave propagation could cause an overprediction of the tidal prism with Eq. 5.2 in very long estuaries. To assess the quality of our approximation with Eq. 5.2 and the digitised polygons, we compared our approximation with the values reported by Manning (2007).

Manning (2007) approximated the tidal prism with the difference between high water volume and low water volume. The predictions using Eq. 5.2 are on average 40% lower than the values of Manning (2007). However, Townend (2005) assessed that the tidal prisms reported by Manning (2007) are on average overestimated by 30%, suggesting that our approximation is closer to the real value.

This study focuses on the channel shape in relation to bar pattern. We hypothesise that sediment availability affects this relation for alluvial estuaries, most of which likely formed in the Holocene. To estimate the degree to which an estuary has been filled with sediment based on satellite imagery only, we introduce a fill factor:

$$Fill = 1 - \frac{A_c}{A_e} \tag{5.3}$$

in which A_c is the approximate channel area that is active at the present-day and A_e is the approximate area of the estuary including mud flats and salt marshes. The underlying assumptions are that (1) the mud flats and salt marsh are overlying sediment rather than antecedent bedrock and (2) the amount of sediment received in the past is indicative of the amount of sediment available at the present day.

The summed width of bars was calculated along the channel for three estuaries for which detailed bathymetries were available: the Western Scheldt (NL), Dovey (UK) and Mersey (UK). First, the same methodology was used as for the data collection of channel planform (section 5.2.2). Second, bathymetric profiles with bed elevation were extracted at the cross-sections to determine the summed width of bars. To do so, the median bed elevation was determined for each cross-section. Subsequently, a linear and exponential regression were fitted for median bed elevation along the estuary channel (Suppl. Fig. 5.12). Summed width of bars was determined as the total width of the estuary above this regression line. In addition, the summed width of bars was determined as the total width above the mean low water surface plane (Suppl. Fig. 5.12). Suppl. Fig. 5.13 shows the sensitivity of our results to the threshold for bar recognition in bathymetry. Dependent on the type of tidal system (e.g. tidal creeks or estuaries) and along-channel width profile (e.g. constant width or converging), varying approximations were found for the along-channel bed profile, such as concave, linear and horizontal (Savenije, 2006; Toffolon and Lanzoni, 2010; Savenije, 2015). Since the estuary depth profile often shows a linear or almost linear profile (Savenije, 2015), the linear threshold is used here to calculate the summed width of bars in the remainder of this chapter (Suppl. Fig. 5.13).

Since bathymetry is available for three estuaries, we will first describe how tidal bars are forced by topography for these three cases. Then, we assess the uncertainty in the along-channel bar pattern as obtained from our automated approach for bathymetries. Subsequently, we compare the definitions used in the automated approach for bathymetries with the definitions used in a geomorphological map of the Western Scheldt estuary. Last, the results from point observations on aerial photographs of 35 estuaries are compared with the results for the three detailed cases. This will allow testing our hypotheses against a larger database with estuaries.

The larger dataset with point measurements was also used to obtain linear regressions for the hydraulic geometry of estuarine channels and relations for individual bar width as a function of channel width or tidal prism.

In all cases where statistical analyses are presented, the following approach was used. For linear regressions, the residuals were minimised in both the x- and y-directions because this is more robust and conservative than either one of the two. Where regressions are plotted, confidence limits are

given for two standard deviations from the regression. For the confidence limits, the legends show the approximate multiplication factor that the confidence limits plot higher or lower than the trend and the R^2 value, which gives the variance around a regression. The quality of all along-channel predictors for bar pattern was assessed with the r-value (Pearson product-moment correlation coefficient), which is a measure of both the direction and strength of a correlation.

5.3 Results

In this section, we first show how the location of tidal sand bar formation is controlled by the topography. Second, a relation between channel width and tidal prism is presented based on data from 35 estuaries. We assess how this relation is influenced when estuaries deviate from the ideal converging planform and compare the results with previous studies. Lastly, we present empirical rules of thumb to predict bar dimensions, which are subsequently used to predict braiding index.

5.3.1 The locations where bars form

The along-channel variation in summed width of bars correlates well with the excess width for the Western Scheldt and Dovey ($r > 0.9$) (Fig. 5.5g,h,i). This shows that tidal sand bars typically form at locations where the channel is wider than an ideal exponential shape. Moreover, excess width is within a factor 1.25 of the total width of bars at most locations.

The correlation between excess width and summed width of bars is dependent on the threshold that was chosen for bar recognition in bathymetries. This can explain why the correlation for the Mersey is lower ($r = 0.67$) than for the Dovey and Western Scheldt. A linear fit was used on the median bed elevation to recognise bars, because most estuaries have a linearly increasing bed profile (Savenije, 2015; Braat et al., 2017). Moreover, long-term morphological models also showed the evolution of linear bed profiles in estuaries with and without mud (Braat et al., 2017). In our results, the Mercey forms an exception, because it has an exponential bed profile. In this case, fitting a linear threshold on the median bed elevation will result in a threshold that is too low at the mouth of the estuary and too high for the remainder of the estuary. This causes a measurement of the summed width of bars that is too large for the first 4 km from the mouth and too small for the remainder of the estuary. After all, the first 4 km lack tidal bars (Fig. 5.1f). If an exponential fit would have been adopted for the Mersey, the correlation between excess width and summed width of bars would increase to a value of $r = 0.91$ (Suppl. Fig. 5.13b). This implies that the method to determine the threshold for bar recognition should be adapted to the shape of the bed profile, for estuaries that deviate from a linear bed profile. In all other estuaries for which point measurements were made of the summed width of bars, it was measured from aerial photographs. Therefore, the point measurements of summed width of bars presented hereafter are independent of a threshold in bed level as used for the bathymetries.

A comparison of the geomorphological map of the Western Scheldt with our polygons of estuary area and active channel area shows that the definitions of channel width and estuary width are very similar (Fig. 5.3d). Moreover, it shows that the width of low dynamic environments is generally higher at locations where summed width of bars is higher and lower at locations where summed width of bars is smaller (correlation of $r = 0.6$). This shows that ecologically valuable low dynamic environments (Meininger et al., 2003; van Eck and Holzhauer, 2007; Cleveringa, 2007) form at similar locations where bars form, namely the locations with excess width.

The 35 estuaries show similar results as the three detailed cases: summed width of bars increases with excess width (Fig. 5.6a). The scatter significantly increased and the goodness of fit decreased when the excess width was calculated using other definitions, such as fitting an exponential function on the maximum and minimum channel width or using a least-squares fit (e.g. $R^2 = 0.1$ and $2\sigma = 21$).

Fig. 5.6a shows that the along-channel variation for the three detailed cases varies within the same range as the local measurements in 35 estuaries. In Chapter 2, we found that the effect of unknown water level and tidal phase is a factor of 2 uncertainty in measured bar dimensions. The uncertainty in measurement of summed width of bars in bathymetry is also approximately a factor 2 compared to the mean measured value, which arises from the threshold definition for bar recognition (Suppl. Fig. 5.13). The remaining scatter is perhaps due to disequilibrium between the bar pattern and channel geometry.

We estimated the amount of sediment received (Eq. 5.3), because we hypothesised that insufficient sediment supply would reduce the formation of bars and therefore the summed width of bars too. We found that the summed width of bars is on average larger for estuaries that received relatively much sediment ($Fill > 0.3$) compared to systems that received relatively little sediment ($Fill < 0.3$) (Fig. 5.6b). Moreover, only the summed width of bars in filled estuaries exceeds the excess width in some cases, which is illustrated by the points that exceed the line of equality in Fig. 5.6b. This suggests that unfilled estuaries have less bar development. Nevertheless, a regression on the subsets of the data show that the difference between the regressions is insignificant, because their confidence limits would largely overlap. Therefore, we abstain here from a relation between the infilling and the extent to which the summed width of bars approaches the excess width.

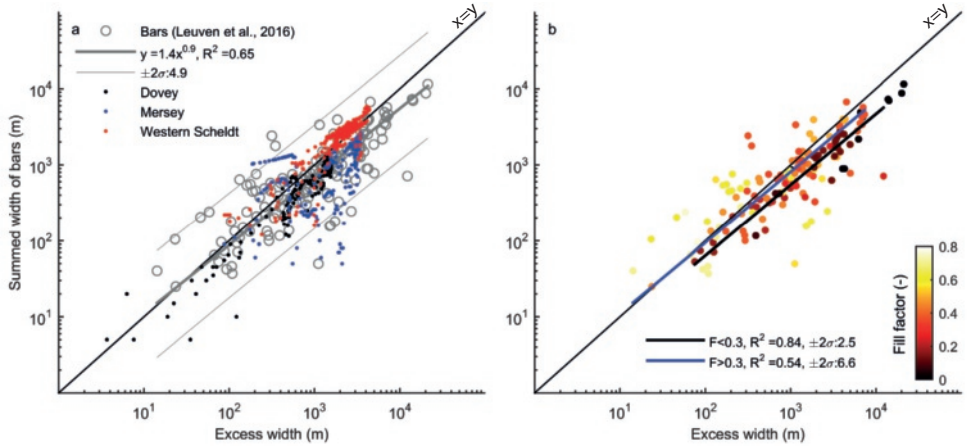

Figure 5.6 (a) Relation between summed width of bars and excess width at bar locations for all estuaries. In addition, the along-channel variation in the Western Scheldt, Mersey and Dovey is shown, which shows similar scatter as the full dataset. Confidence limits are given for two standard deviations from the regression. The approximate multiplication factor that the confidence limits plot higher or lower than the trend is given in the legend. Summed width of bars approaches excess width as can be seen from the scatter around the line of equality. (b) Same, colour-coded with a proxy for the fraction of sediment infill (Eq. 5.3, see text for explanation).

5.3.2 Hydraulic geometry

The dimensions of individual bars relate to channel width (Chapter 2) and the summed width of bars correlates with excess width. This means that to predict bar pattern, channel width and excess width should be predicted first. Using hydraulic geometry, the channel width could be calculated with discharge or tidal prism. Many relations were proposed in the past for hydraulic geometry of rivers and tidal systems (Lacey, 1930; Leopold and Maddock Jr, 1953; Langbein, 1963; Hey and Thorne, 1986; Savenije, 2003; Sassi et al., 2012; Gisen and Savenije, 2015) (Suppl. Table 5.2). However, there are two issues in applying these relations for tidal systems. First, many of the relations consider either ideal systems or describe only the mouth of tidal systems, while to study bar pattern the

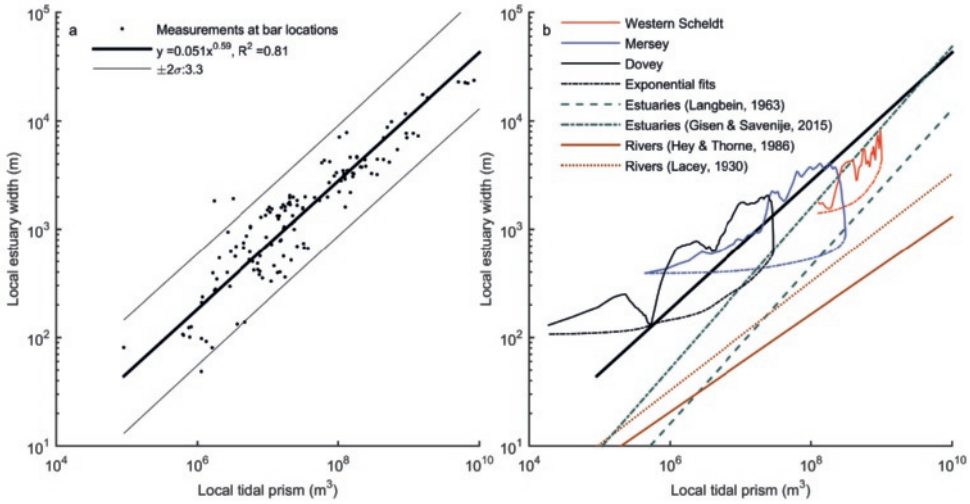

Figure 5.7 Active channel geometry related to tidal flow. (a) Channel width as a function of local tidal prism for 35 estuaries. (b) Along-channel measurements of channel width for the Western Scheldt, Mersey and Dovey. For comparison, representative hydraulic geometry relations for estuaries and rivers are drawn (see Suppl. Fig. 5.11 and Suppl. Table 5.2 for overview of most relations from literature between tidal prism and cross-sectional area).

along-channel width is required. Second, two points on an irregular channel can have an equal channel width but have different local tidal prisms because the geometry upstream differs (e.g. Fig. 5.5a-f). Channel depth can partly compensate for this, but we found that also for two sections with the same cross-sectional area, two different tidal prisms can occur (Suppl. Fig. 5.11).

The dataset with measurement points in 35 estuaries shows that despite the irregularities in channel planform a simple relation exists between the channel width and local tidal prism (Fig. 5.7a):

$$W = 0.05 \cdot P^{0.59} \tag{5.4}$$

In Fig. 5.7b, the along-channel variation of hydraulic geometry in the Western Scheldt, Mersey, Dovey and the regression from the dataset are compared with point measurements and hydraulic geometry relations. The along-channel variation is of the same magnitude as the scatter in the dataset and illustrates that a certain width may be found with different tidal prisms, depending on the amount of excess width at that location. The exponential fits for these three cases are similar to the relations proposed by Langbein (1963) for ideal estuaries and Gisen and Savenije (2015), who predicted channel width based on the upstream bankfull river discharge and a typical estuary convergence length.

The general finding that width increases with tidal prism and with discharge is in agreement with studies in other environments such as rivers, deltas and tidal creeks (Lacey, 1930; Leopold and Maddock Jr, 1953; Langbein, 1963; Hey and Thorne, 1986; Savenije, 2003; Sassi et al., 2012; Gisen and Savenije, 2015; Lanzoni and D'Alpaos, 2015). However, deviations from ideal estuaries (Langbein, 1963; Gisen and Savenije, 2015) or rivers (Lacey, 1930; Leopold and Maddock Jr, 1953; Hey and Thorne, 1986; Savenije, 2003) are present: (1) no significant relations were found between estuary depth and tidal prism, which shows in the wider scatter in Suppl. Fig. 5.11b than in Fig. 5.7a; (2) nonideal estuaries are generally wider and have larger cross-sectional areas than rivers and ideal estuaries under equal discharge (Suppl. Fig. 5.11b), because their width is typically equal to the sum of the ideal width and

the excess width, which is determined by the antecedent topography that was present before Holocene transgression.

5.3.3 Effect of channel planform on bar pattern

The bar pattern, i.e. bar shape, length and width, in estuaries is a result of its channel planform. Section 5.3.1 illustrated that the bar location and the summed bar width was predicted by the excess width. In this section, we present a predictive braiding index that indicates how many channels and bars are likely to be present at a given location. The predicted braiding index (BI) is as follows

$$BI = \frac{W_{excess}}{w} \tag{5.5}$$

where W_{excess} is the excess width and w is a predicted bar width (explained later, Eqs. 5.6-5.9). Because two different measures can be used for w, namely the partitioned bar width (w_p) and the average bar width (w_{avg}), we will first discuss the definition of these measures and of braiding index before the relations for bar width are presented. Partitioned bars are bars that are separated by the number of barb channels. Chapter 2 identified that after partitioning, all bars can be described by an elongated shape for which the bar length is approximately 7 times the bar width.

The braiding index is highly sensitive to water level variations (Chapter 2) and thus also to the threshold between channel and bar recognition from the bathymetries. Applying the partitioned bar width to predict the braiding index would give the sum of channels and barb channels, meaning it will overpredict the braiding index. Therefore, we used the average bar width rather than the partitioned bar width. To record the braiding index from bathymetries, we used a linear fit on the median bed elevation to first distinguish bars (above the fitted median bed elevation) from channels (below the fitted median bed elevation) and subsequently calculated the braiding index from the number of channels. Using this approach, the shallower barb channels are part of the bar and not accounted for in the braiding index. Given this definition of channels and bars we calculated the average bar width to predict the braiding index.

Bar length and bar width depend on local channel width (W) and become longer and wider for increasing W. Analysis of our dataset on channel width for both the partitioned bar width and the average bar width (Fig. 5.8) resulted in a new empirical relation for the partitioned bar width (w), which is

$$w_{p,W} = 0.20 \cdot W^{0.91} \tag{5.6}$$

and, alternatively with local tidal prism (P):

$$w_{p,P} = 0.012 \cdot P^{0.55} \tag{5.7}$$

where $w_{p,W}$ is the partitioned bar width predicted with local channel width (W) and $w_{p,P}$ is the partitioned bar width predicted with tidal prism. All relations are valid over at least two orders of magnitude. These relations allow prediction of the dimensions of individual bars based on solely the channel width, or on the upstream channel planform area and tidal range. The goodness of fit is higher for predictions from channel width than as a function of local tidal prism.

The empirical relations for average bar width (w_{avg}) are

$$w_{avg,W} = 0.39 \cdot W^{0.92} \tag{5.8}$$

and

$$w_{avg,P} = 0.022 \cdot P^{0.55} \tag{5.9}$$

Obviously these relations simplify barbs, channels and bars as discrete elements in a continuous field of bed elevations. Over time, barbs may develop into channels and vice versa, which illustrates the need

for a better understanding of formative mechanisms, dynamics and development of the barb channels, which is beyond the scope of this chapter.

Fig. 5.9d-f shows the predicted braiding index using Eq. 5.5 with either bar width predictions based on the channel width or the local tidal prism. Best predictions are obtained when channel width is used, with correlation coefficients all above 0.62. Predictions for braiding index are all within a factor 2 of the measured value, but generally better. Using the local tidal prism to predict braiding index may result in large overpredictions at the landward part of the estuary (for example for the Dovey, Fig. 5.9f) or underpredictions at the seaward side (for example for the Mersey, Fig. 5.9e).

At the landward boundary, the local tidal prism approaches zero. As the local tidal prism lowers, also the predicted bar width decreases. However, some landward locations may have a relatively large local channel width and excess width. In these cases, dividing the excess width by a very small bar width, the prediction of braiding index will be very high. At the seaward boundary, the same reasoning causes an underprediction of the braiding index. In summary, using the tidal prism one would predict a gradual decrease in bar width that lacks any dependency on channel width and transfers to predictions of braiding index, because it is predicted as the excess width divided by the predicted bar width. In this case, the predictions of braiding index are thus too sensitive to local variations in channel width, where in natural systems the bar width adapts to the varying channel size.

5.4 Discussion

We first summarise how bar pattern is forced by channel planform and discuss why excess width is a measure required to predict bar pattern. Last, we discuss the applications, long-term evolution of bar patterns and estuarine filling.

5.4.1 Forcing of bar pattern by planform

Tidal sand bars form at locations where the estuary is wider than an ideal exponential fit (Fig. 5.5). Here, local flow expansion occurs due to the presence of embayments that were inherited from the antecedent landscape. The local flow expansion results in a reduction of stream velocity and shear stress, which can cause sedimentation when sufficient sediment is available (Cant and Walker, 1978; Ashmore, 1991; Ashworth et al., 2000). In filled estuaries, summed width of bars approximates excess width for most estuaries (Fig. 5.6). In contrast, unfilled estuaries can have a lower summed width of bars, being around 50% of the excess width (Fig. 5.6b).

At the location where bars form, the individual dimensions of bars scale particularly well with channel width (Fig. 5.8a,c). Although local tidal prism could be used, predictions from channel width are better fits and tidal prism is more difficult to measure. In agreement with our hypothesis, bar dimensions are poorly predicted from ideal channel width. The result that bar dimensions are determined by local channel geometry raises the question what sets the size and shape of an estuarine channel and how does it evolve over time. Many estuaries formed during the early to middle Holocene when valleys drowned during rapid sea-level rise (e.g. van der Spek and Beets, 1992; Hijma and Cohen, 2011). Because of a progressively decelerating sea-level rise, sediment input in many of these system eventually exceeded creation of accommodation space by sea-level rise resulting in progressive infilling of these estuaries. The present-day estuary shape is thus the sum of the initial valley size and shape as well as historical creation of accommodation space and infilling, and varies between estuaries.

The measure of excess width is required to explain the variation in bar pattern for two locations with equal channel width along the same estuary. It is a priori known that the seaward location is affected by a larger tidal prism than the landward location. According to hydraulic geometry (Eq. 5.4, Suppl. Fig. 5.11), a larger cross-sectional channel area is expected at the seaward location. Given that

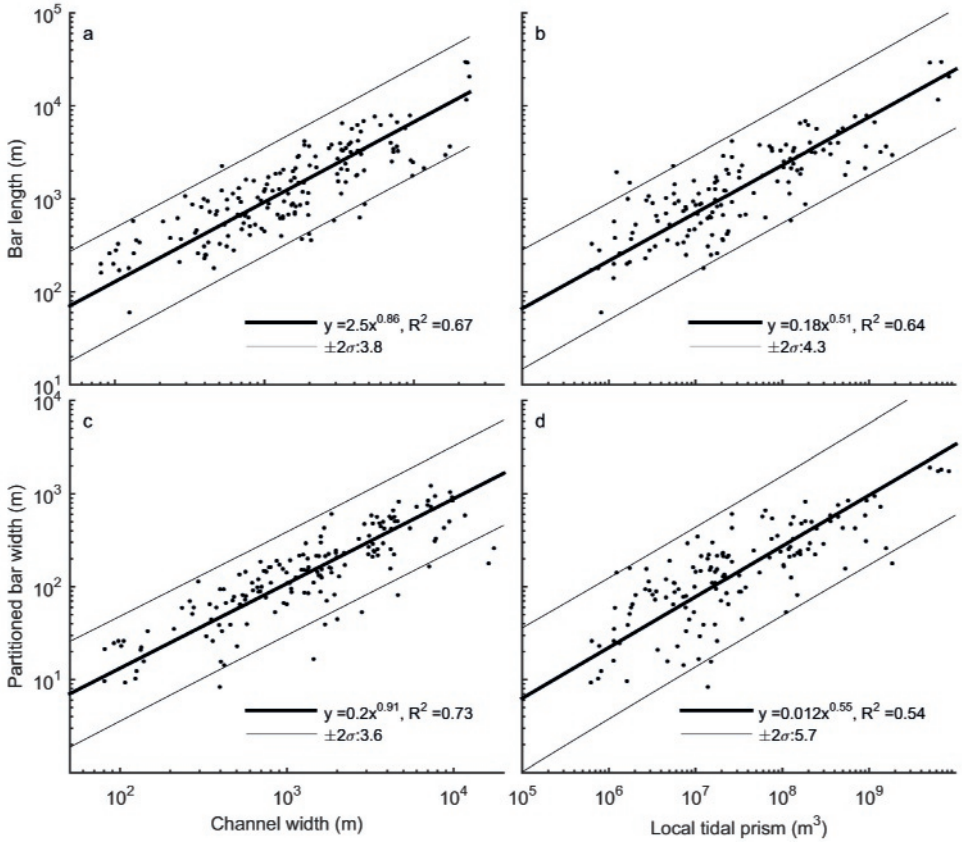

Figure 5.8 Individual bar dimensions related to channel width and local tidal prism. Bar length and width increase with channel width (a,c) and local tidal prism (b,d). Confidence limits are given for two standard deviations from the regression. The approximate multiplication factor that the confidence limits plot higher or lower than the trend is given in the legend.

the prediction of individual bar width is equal at both locations, this also implies that the seaward location has a lower excess width and therefore a smaller summed width of bars and a lower braiding index. Therefore, multiple braiding indices and summed width of bars could occur for the same channel width (Fig. 5.10b,d).

Alternatively, let us consider two locations with equal summed width of bars or equal braiding index. Following the same reasoning, there can be multiple locations along the estuary where either an equal summed width of bars or braiding index occurs. Each of these locations is characterised by a different local tidal prism, which explains that for each braiding index or summed width of bars a wide range of local tidal prisms can occur. This explains the wide horizontal scatter in Fig. 5.10a,c. We thus conclude that a measurement of local tidal prism or local channel width is insufficient to predict bar pattern and that a measurement of the excess width is required to obtain more accurate predictions of braiding index and summed width of bars. In other words, the along-channel context matters for the local expression of bar patterns.

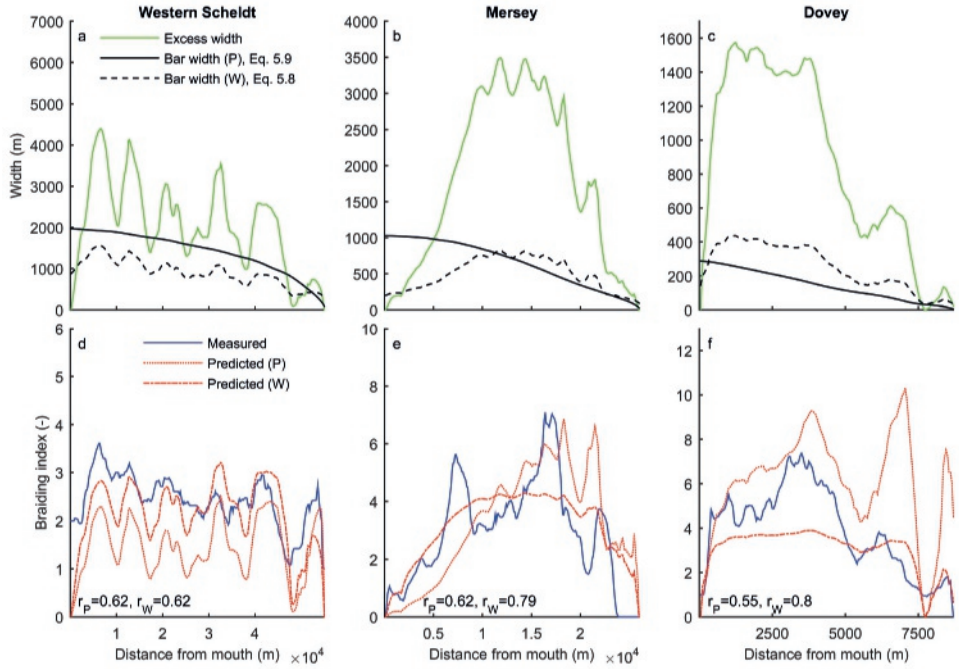

Figure 5.9 (a,b,c) The along-channel excess width and prediction of bar width using the empirical relations with tidal prism (Eq. 5.9) and channel width (Eq. 5.8) for the three estuaries with bathymetric data. (d,e,f) Predicted and measured braiding index. Predicted braiding index was calculated as excess width divided by predicted bar width. The r-values indicate the Pearson product-moment correlation coefficients for measured and predicted braiding index, where subscripts indicate whether bar width was predicted with tidal prism (P) or channel width (W).

5.4.2 Potential applications of empirical bar predictors

Our empirical method predicts the summed width of bars accurate within a factor 1.25 and the braiding index accurate within a factor 2. This insight can be implemented in several types of geological reconstructions where tidal channel belts or estuary shapes may have been identified, but wherein infilling and bar configuration are unknown. On the one hand, the bar pattern within tidal channel belts affects lithological properties of the geological channel body (Wood, 2004), such as the connectivity and permeability that influence storage capacity. On the other hand, our empirical approach may successfully estimate bar pattern for palaeogeographical reconstructions (Vos et al., 2015; Pierik et al., 2016) of former estuaries where the morphology of bars is typically not recognisable in the geological record. This exercise may be especially relevant for bar-built, high-stand, estuaries which are sufficiently filled with sediment, such that the bar pattern has been developed. Estimating bar properties will improve the palaeogeographical maps, because it allows us to estimate the location and number of tidal bars, based on the outline of the palaeo-estuary. It further enables reconstructing past water levels or tidal wave propagation, and therefore may improve the understanding of the evolution of the estuary. The advantage of our empirical predictions is that it only requires channel planform measurements.

Given time, tidal sand bars may stabilise by means of vegetation succession (Gray, 1992; Thomson et al., 2004; van der Wal et al., 2008), finally resulting in supratidal flats that are no longer morphologically active in common tidal conditions (van den Berg et al., 1996; Cleveringa, 2007). This raises the question

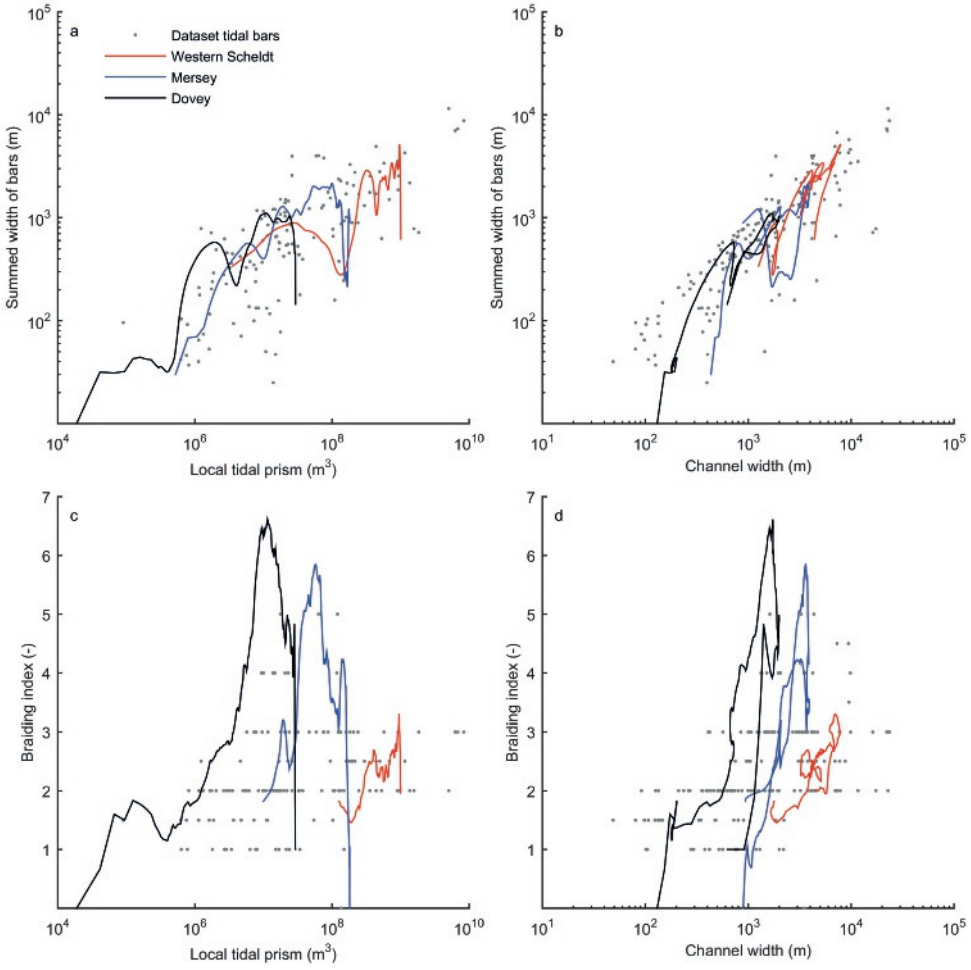

Figure 5.10 Summed width of bars as a function of local tidal prism (a) and channel width (b). Measured braiding index as a function of local tidal prism (c) and channel width (d). The along-channel variation in summed width of bars and braiding index along a single estuary is similar to the scatter within the dataset of 170 tidal bars in 35 estuaries.

to what degree tidal bars are stable in time and space after they have formed. The methods presented herein can now be applied to reconstructed Holocene estuaries (Vos et al., 2015; Pierik et al., 2016), for which boundaries are well-known but bars are usually not preserved, as well as estuaries in numerical models and laboratory experiments (Kleinhans et al., 2015b). This will allow us to systematically study the effects of boundary conditions and vegetation on the dynamics of tidal bars over time and on the evolution of the entire estuary from initiation on inherited landscapes (Chapters 4 & 6).

We found typical relations between tidal bar dimensions, tidal prism and channel width (Fig. 5.8). Using the empirical relations for bar dimensions as a function of estuary dimensions also allows a reverse approach. With single measurements of bar dimensions it would be possible to reconstruct the local tidal prism and width. The architecture of tidal bars in the geological record can possibly be used to obtain predictions of the hydraulic geometry of the corresponding estuary within a factor 3 accuracy.

5.5 Conclusions

Here we empirically studied effects of channel planform on tidal bar patterns in estuaries with a newly collected dataset of sand bar dimensions and channel planforms of nonideal alluvial estuaries. We found that simple empirical relations adequately describe bar dimensions and braiding index. Sand bars mainly form where the estuary is wider than expected from an ideal exponentially converging planform between the mouth and the upstream river. At these locations, local flow expansion causes a reduction of the shear stress, which can result in the deposition of sediment. The summed width of bars approximates the excess width over time, reducing the channel width to the ideal channel width. Bars are narrower when sediment is less abundant. Since channel width and local tidal prism are strongly related, the dimensions of individual bars can be predicted from either of these quantities but the quality of predictions is highest when channel width is used. Dividing the excess width by the bar width resulted in predictions for braiding index, which were accurate within a factor 2. Our results imply that present estuary planform shape, including mud flats and salt marsh, depends on inherited Holocene topography, but that eventually convergent channels will form when sufficient time and sediment are available. The simple relations between bar pattern and local estuarine channel width may aid predictions of geological architecture and palaeogeographical reconstructions of former estuaries.

Acknowledgments

Reviews by two anonymous reviewers and steer by the associate editor helped to improve the manuscript. We are grateful to Maarten Zeylmans van Emmichoven and Philip Kraaijenbrink for their support with GIS. The authors contributed in the following proportions to conception and design, data collection, analysis and conclusions, and manuscript preparation: JRFWL(65,95,85,80%), TdH(15,5,5,5%), LB(5,0,0,5%), MGK(15,0,10,10%). Online supplementary data: (1) a kml-file with the estuary polygons used (see Suppl. Table 5.1); (2) an xls-file with measurements of tidal bars, joined with estuary dimensions and tidal conditions from the literature used in this study.

Supplementary material

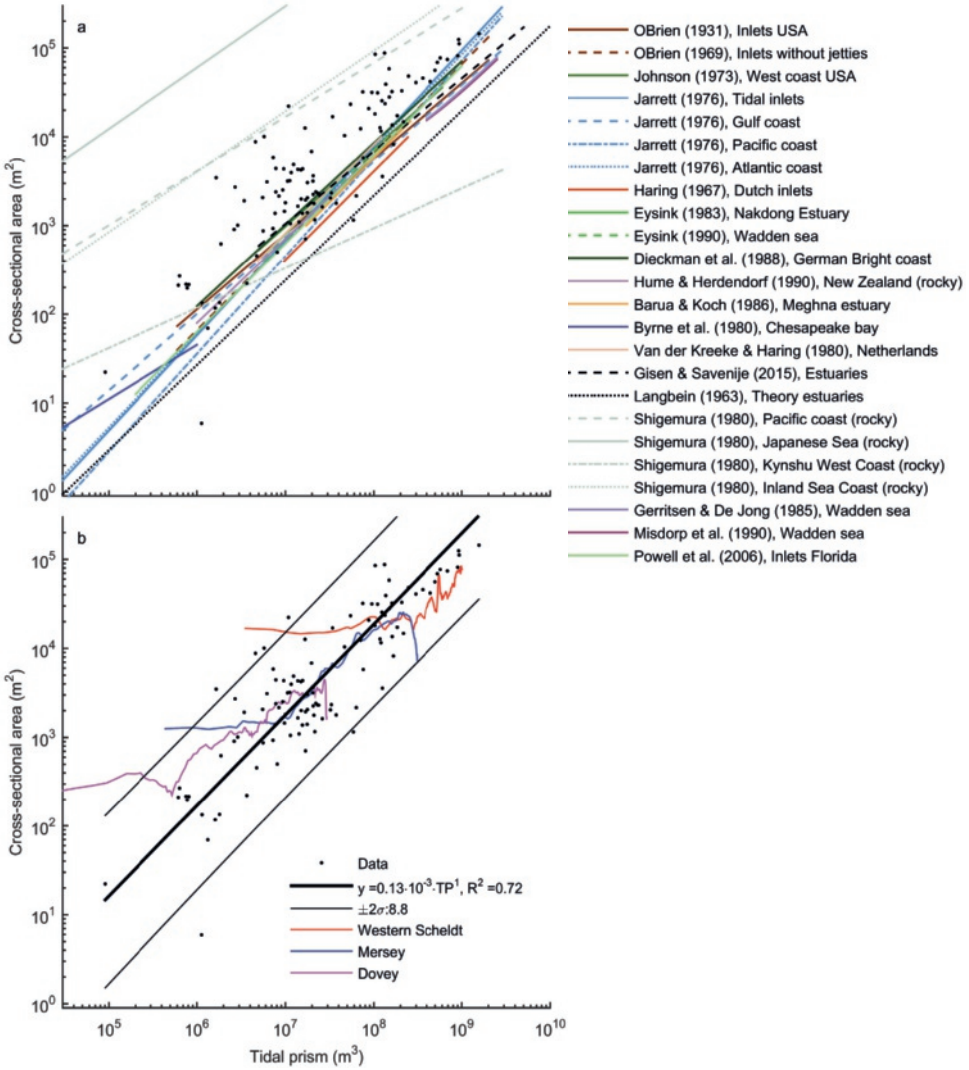

Figure 5.11 (a) Relations from literature between cross-sectional area at mean sea level and tidal prism compared to (b) trends found in the data presented in this study. Recent analysis of Gisen and Savenije (2015) and this study show that the scatter for estuaries is an order of magnitude, which is similar to the spread between the relations for tidal inlets and estuary mouths from literature. Confidence limits are given for two standard deviations from the regression. The approximate multiplication factor that the confidence limits plot higher or lower than the trend is given in the legend.

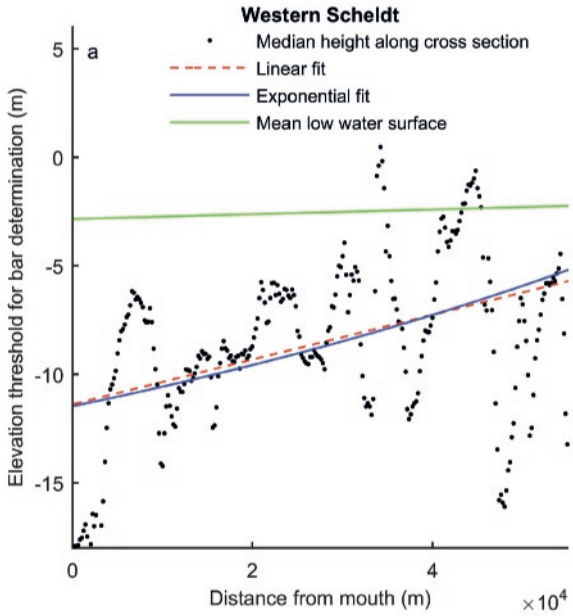

Figure 5.12 Three possible definitions for the threshold of bar perimeter delineation in bathymetries. The Western Scheldt is used as an example here. For each cross section along the estuary the median bed elevation was calculated. Based on these median values, either a linear fit (red) or exponential fit (blue) may serve as a threshold for bar recognition. Alternatively, the water surface at mean low water level may be used. The implications of these thresholds for the calculation of summed width of bars are given in Suppl. Fig. 5.13.

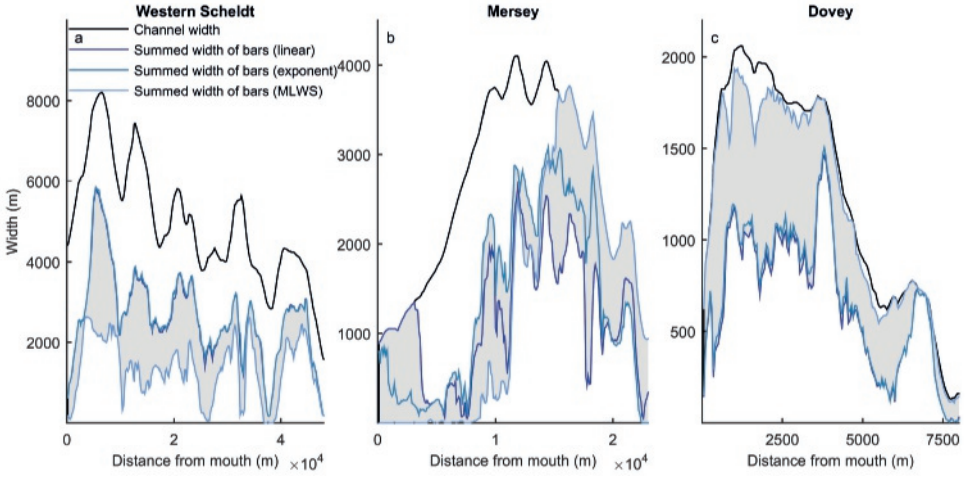

Figure 5.13 The sensitivity of summed width of bars to the selected threshold for bar recognition. The grey zone indicates the range of possible measurements depending on the threshold used. The linear fit was used as the threshold for bar recognition in this chapter.

Table 5.1 Estuaries for which polygons were recorded in Google Earth, accessed January-September 2016. Channel area and estuary area are given. The offset area is the area upstream of the digitised channel polygon that is influenced by tides and was added to the channel area when used for estimates of tidal prism. Offset area is only given for the cases where it exceeds 1% of the channel area and was determined by indicators such as channel convergence, presence of tidal flats and marshes.

Name	Location	Date aerial photography	Channel area (km^2)	Estuary area (km^2)	Offset area (km^2)
Alsea Bay	USA	17-11-2011	4.1	19.3	
Bannow Bay	IRE	5-3-2010	7.2	9.8	
Broad River Estuary	USA	1-1-2011	103.0	283.0	
Camel Estuary	UK	8-10-2009	5.2	6.6	
Cefni Estuary	UK	1-6-2009	1.3	5.4	
Charlotte Harbor Estuary	USA	1-6-2009	291.0	440.0	
Clonakilty (The Retreat)	IRE	3-4-2013	0.5	1.8	
Clwyd Estuary	UK	1-6-2009	0.2	0.8	
Cobequid Bay	Canada	22-4-2016	478.0	485.0	
Columbia River	USA	1-7-2014	351.0	551.0	24
Conwy Estuary	UK	1-6-2009	4.3	8.1	
Coosaw River Estuary	USA	21-11-2014	106.0	238.0	
Dart Estuary	UK	13-12-1999	3.9	4.2	
Dovey Estuary	UK	1-6-2009	9.7	17.6	
Exe Estuary	UK	1-12-2010	8.2	14.2	
Gannel Estuary	UK	8-10-2009	0.3	0.6	
Gironde	France	7-3-2015	435.0		
Glaslyn Estuary	UK	1-6-2009	8.1	12.3	
Humber	UK	31-12-2009	235.0	276.0	
Loughor Estuary	UK	18-4-2015	33.6	67.9	
Mawddach Estuary	UK	1-6-2009	6.0	9.4	
Meghna Delta Estuary	Bangladesh	31-1-2014	2330.0		364
Mersey Estuary	UK	10-10-2010	73.1	83.4	
Nestucca Bay	USA	17-11-2011	1.9	2.9	
Netarts Bay	USA	17-11-2011	3.8	9.1	
Nyfer Estuary	UK	31-12-2009	0.1	0.6	
Ord River Estuary	Australia	28-11-2015	651.0	858.0	
Parrett Estuary	UK	2-6-2009	5.1	6.1	
Rodds Bay, Queensland	Australia	2-6-2009	9.4	17.0	
Solway Estuary	UK	14-3-2011	290.0	470.0	
Taw-Torridge Estuary	UK	14-3-2011	8.2	21.8	
Teign Estuary	UK	31-12-2010	2.9	3.8	
Traeth Melynog Estuary	UK	31-12-2006	13.0	17.8	
Western Scheldt	NL	31-12-2005	266.0	307.0	14
Whitehaven Beach	Australia	21-7-2008	2.2	5.4	

Table 5.2 Hydraulic geometry relations for tidal systems in literature (see Suppl. Fig. 5.11).

Author	Relation	Location	System
O'Brien (1931)	$CSA = 9.0 \cdot 10^{-4} P^{0.85}$	USA	Inlets
O'Brien (1969)	$CSA = 6.6 \cdot 10^{-5} P^{1.00}$	USA	Inlets without jetties
Johnson (1973)	$CSA = 6.8 \cdot 10^{-4} P^{0.88}$	USA	West Coast
Jarrett (1976)	$CSA = 2.2 \cdot 10^{-5} P^{1.07}$	USA	Tidal inlets (un- and single jettied)
Jarrett (1976)	$CSA = 7.0 \cdot 10^{-4} P^{0.86}$	USA	Gulf Coast
Jarrett (1976)	$CSA = 9.0 \cdot 10^{-6} P^{1.10}$	USA	Pacific Coast
Jarrett (1976)	$CSA = 3.8 \cdot 10^{-5} P^{1.03}$	USA	Combination three above
Jarrett (1976)	$CSA = 3.0 \cdot 10^{-5} P^{1.05}$	USA	Atlantic Coast
Haring (1967)	$CSA = 4.1 \cdot 10^{-5} P^{1.00}$	The Netherlands	Tidal inlets
Gerritsen and de Jong (1985)	$CSA = 3.0 \cdot 10^{-5} P^{1.00} + 3844$	The Netherlands	Wadden sea
Misdorp et al. (1990)	$CSA = 2.8 \cdot 10^{-5} P^{1.00} + 4227$	The Netherlands	Wadden sea
Shigemura (1980)	$CSA = 9.0 \cdot 10^{-1} P^{0.61}$	Japan	Pacific coast (rocky coast)
Shigemura (1980)	$CSA = 4.4 \cdot 10^{-0} P^{0.69}$	Japan	Japanese Sea (rocky coast)
Shigemura (1980)	$CSA = 2.4 \cdot 10^{-1} P^{0.45}$	Japan	Kynshu West Coast (rocky coast)
Shigemura (1980)	$CSA = 3.4 \cdot 10^{-1} P^{0.68}$	Japan	Inland Sea Coast (rocky coast)
Eysink (1983)	$CSA = 8.0 \cdot 10^{-5} P^{1.00}$	South Korea	Nakdong Estuary
Eysink (1990)	$CSA = 7.0 \cdot 10^{-5} P^{1.00}$	The Netherlands	Wadden sea
Dieckmann et al. (1988)	$CSA = 3.7 \cdot 10^{-4} P^{0.92}$	Europe	Coast of German Bight
Hume and Herdendorf (1990)	$CSA = 1.6 \cdot 10^{-4} P^{0.95}$	New Zealand	Northeast coast of the North Island (rocky coast)
Barua and Koch (1986)	$CSA = 5.8 \cdot 10^{-5} P^{1.00}$	Bangladesh	Lower Meghna estuary
Byrne et al. (1980)	$CSA = 9.9 \cdot 10^{-3} P^{0.61}$	USA	Small inlets in Chesapeake Bay
van de Kreeke and Haring (1980)	$CSA = 8.2 \cdot 10^{-5} P^{1.00}$	The Netherlands	Estuary mouths, zeeland
Langbein (1963)	$CSA = 5.0 \cdot 10^{-5} P^{0.96}$		Theory for estuaries
Gisen and Savenije (2015)	$CSA = 1.9 \cdot 10^{-3} P^{0.82}$	Worldwide	Estuaries
Powell et al. (2006)	$CSA = 6.3 \cdot 10^{-5} P^{1.00}$	USA	Inlets Florida


Universiteit Utrecht

Chapter 6 | Growing forced bars determine nonideal estuary planform

Abstract

The planform of estuaries is often described with an ideal shape, which exponentially converges in landward direction. We show how growing topographically forced nonmigratory (i.e. anchored) bars determine the large-scale estuary planform, which explains the deviations observed in the planform of natural estuaries filled with bars compared to the ideal planform. Experiments were conducted in a 20-m long, 3-m wide tilting flume, the Metronome. From a narrow, converging channel a self-formed estuary developed characterised by multiple channels, braided bars, a meandering ebb channel, and an ebb delta. Bars hardly migrated due to the alternating current, but the bar width increased with increasing estuary width. At locations where the estuary width was narrow, major channel confluences were present, while the zones between the confluences were characterised by a higher braiding index, periodically migrating channels, and a relatively large estuary width. At the seaward boundary, confluences were forced in place by the presence of the ebb tidal delta. Between confluences, bars were topographically forced to be nonmigratory. Diversion of flow around forced midchannel bars caused bank erosion. This resulted in a planform shape with a quasiperiodic widening and narrowing at the scale of forced bars. Observations in natural systems show that major confluence locations can also be caused by inherited geology and human engineering, but otherwise the estuary outline is similarly affected by tidal bars. These observations provide a framework for understanding the evolution of tidal bar patterns and the planform shape of the estuary, which has wide implications for navigation, dredging, and ecology.

Published as: Leuven, J.R.F.W., Braat, L., van Dijk, W.M., de Haas, T., van Onselen, E., Ruessink, B.G. & Kleinhans, M.G. (2018). Growing forced bars determine nonideal estuary planform. *Journal of Geophysical Research: Earth Surface, 123 (11), pp. 2971–2992*, DOI: 10.1029/2018JF004718.

6.1 Introduction

Estuaries are tidal systems that occur where rivers debouch into the sea. The planform of estuaries is often described by an ideal shape (Pillsbury, 1956; Langbein, 1963; Savenije, 2015), which is defined as an equilibrium state wherein the channel planform converges with a constant along-channel tidal range, average depth and current velocity amplitude. The imposed landward-decrease in tidal prism has a first-order control on the planform shape, resulting in converging (*funnel-shaped*) channels for delta branches and tidal creeks. However, previous research showed that in alluvial estuaries a second-order complexity is superimposed on the converging shape, which results in more irregular planforms with locally widened zones (Chapter 5) (Fig. 6.1). Deviations from the ideal shape may occur because the estuary adapted in varying degrees to its equilibrium shape, depending on the time and sediment available to adapt to changing boundary conditions, such as Holocene sea-level rise and antecedent topography (Townend, 2012; de Haas et al., 2017). In addition, the outline may be shaped by external restrictions that impose local confinements, such as inherited geology or human engineering, as well as self-formed restrictions, such as salt marshes and riparian forest (Townend, 2012) (Fig. 6.1). Current theoretical and empirical descriptions for estuary planforms neglect the effect that bar formation and bar evolution may have on the planform of the estuary. We propose that the irregular planform of many alluvial estuaries is shaped by a forcing mechanism in which growing midchannel bars determine bank erosion, leading to quasiperiodic widening and narrowing of the estuary.

In contrast to tidal systems, the forcing mechanism of bars has been thoroughly studied for river systems. Bars can be described as either free or forced, where forced bars are anchored to their location by the channel planform shape, while free bars can migrate freely and typically occur in straight or weakly curved channels (e.g. Tubino et al., 1999; Seminara, 2010; Schuurman et al., 2013). For rivers, low-amplitude alternate bars may cause channel curvature, after which the alternate bars evolve into point bars, forcing a meandering planform (Schuurman et al., 2016).

A recently identified mechanism of coupling between meander and bar formation and bank erosion in rivers (e.g. Parker et al., 2011; Eke, 2014; van de Lageweg et al., 2014) may also be relevant for their tidal counterparts. In the *bank pull* condition, outer-bend bank erosion causes local flow deceleration resulting in inner bend bar growth, while in *bar push* inner bend sedimentation causes transfer of flow momentum to the outer-bend, which increases bank erosion. Modelling suggests that well-developed bends fluctuate around a balanced state of bar push and bank pull (Eke, 2014), but initially the alternate bars form in a straight channel (van Dijk et al., 2012) suggesting that the process of pattern formation starts with bar push. While this concept has not been applied in estuarine context, the presence of bars and bends suggests that it plays a similar role in estuarine shape and size development. Once variations in width are present, the location and size of forced bars may be induced by channel width variation, for example due to the presence of embayments (Leopold and Wolman, 1960; Yalin, 1971; Struiksma et al., 1985; Tubino et al., 1999; Repetto and Tubino, 2001; Seminara, 2010; Wu et al., 2011; Kleinhans and van den Berg, 2011; Schuurman et al., 2013). This suggests an intimate link between bars and river planforms, and we hypothesise a similar dependency between tidal bars and estuary planforms.

Indeed, observations in modern estuaries support the hypothesis that the location where tidal bars occur correlates with by the deviation of the estuary planform from an ideal shape (Chapters 5 & 7). In addition, bar and meander dimensions scale with estuary width (e.g. Dalrymple and Rhodes (1995) and Chapter 2). From aerial photographs one can observe that the locations where the estuary is relatively narrow, correspond to locations with major confluences, defined as the location where two (or more) major channels connect (Fig. 6.1). For braided rivers, the dimensions and spacing of confluences scale with bar dimensions (Ashmore, 2001; Hundey and Ashmore, 2009). Confluence locations associated to downstream bifurcations steer the morphodynamics of channels and bars (Schuurman and Kleinhans, 2015). For example, the deposition of a midchannel bar downstream of a confluence location can create a bifurcation and subsequently erode the channel banks, creating a more irregular planform (Hundey

Figure 6.1 Aerial photographs of (a) Whitehaven Beach (Australia), (b) Rodds Bay (Australia), and (c) Netarts Estuary (United States). The outline of these estuaries shows an irregular rather than ideal converging shape. Local confinements occur due to externally imposed restrictions, such as bedrock geology and human engineering, as well as by self-formed restrictions. The major confluences occur at locations of confinement. Google Earth, accessed January-April 2017.

and Ashmore, 2009; Schuurman and Kleinhans, 2015). Here, we explore the relation between channel and bar dynamics and estuary planform. In particular, we assess whether channel and bar dynamics can cause the often observed irregular estuary planform and the locations of major channel confluences.

Current knowledge on long-term evolution – timescales larger than decades – of bars and channels in estuaries is limited by a lack of data (de Haas et al., 2017). This is mainly due to the fact that observations in modern systems are hampered by the timescale for morphological evolution, which is much longer compared to fluvial systems. In our previous work, we studied present-day bar patterns in natural systems (Chapters 2, 5 & 7). Here we shift focus to the morphodynamics of channels and bars. Physical scale experiments and numerical models complement observations in natural systems because they can provide higher temporal resolution, enabling detailed observation of the morphodynamic evolution of bars. In this study we use physical experiments, because the produced channel and bar patterns in numerical models (e.g. van der Wegen and Roelvink, 2012; Braat et al., 2017) depend on calibration parameters such as the transverse bed slope effect that strongly affect channel-shoal interaction and bar dynamics (Baar et al., 2018; Schuurman et al., 2018).

6.2 Methods and materials

6.2.1 Experimental setup and procedure

We use a periodically tilting flume of 20 m by 3 m, called the Metronome (Fig. 6.2), that generates dynamic tidal morphology. It produces hydrodynamic conditions capable of transporting sediment during both the ebb and flood phase (Kleinhans et al., 2015a; Kleinhans et al., 2017a), which is uniquely different from earlier physical experiments of tidal systems that relied on periodic sea-level variations (Reynolds, 1887; Reynolds, 1889; Mayor-Mora, 1977; Tambroni et al., 2005; Stefanon et al., 2010; Vlaswinkel and Cantelli, 2011). The downscaled magnitude of the water level variations in experiments with periodic sea-level variations, while large relative to water depth, is too low to induce landward sediment transport due to the unscaled grain size. Therefore, previous experiments with periodic sea-level variation resulted in systems with mainly ebb-related transport (Kleinhans et al., 2014). To obtain similar sediment mobility, scaled estuary experiments with natural sand would require a much steeper bed gradient than natural systems, because of their smaller water depth and bed shear stress, which we obtain by tilting the flume (Kleinhans et al., 2014; Kleinhans et al., 2015a). The tilting flume allows us to characterise the spatiotemporal patterns of channel and bar evolution. For a more detailed description of the design and hydrodynamics of the Metronome see Kleinhans et al. (2017a).

Here we describe one of the experiments with detailed monitoring of the bed elevation and flow velocities and study the long-term evolution of channels and bars. The experiment was run for 15,000 tidal cycles, which corresponds to approximately 20 years of natural tidal cycles assuming a semidiurnal tide. The experimental settings were selected based on a set of approximately 30 pilot experiments in which boundary conditions have been varied systematically, which are reported in the supplementary material of Braat et al. (2019). The settings were selected to ensure that sediment was well above the threshold for motion and that the tidal excursion length, which is the distance a water particle travels in half a tidal cycle, was shorter than the flume length.

A plane bed of 0.07 m thick sediment was installed on top of a mat with artificial grass in the basin. Sediment consisted of a sand mixture ($\rho_s = 2650$ kg·m^{-3}) with a median grain size of 0.52 mm and a coarse tail ($D_{90} = 1.2$ mm, $D_{10} = 0.33$ mm) (Suppl. Fig. 4.15). This sediment mixture was selected to prevent the occurrence of scour holes as much as possible (Kleinhans et al., 2017b). Another set of experiments were conducted with the addition of crushed walnut shell to simulate the effect of cohesive material, which are reported in (Braat et al., 2019). We will summarise the effect of this as far as relevant for bar growth and estuary widening in the discussion. The bed was approximately 18 m long and

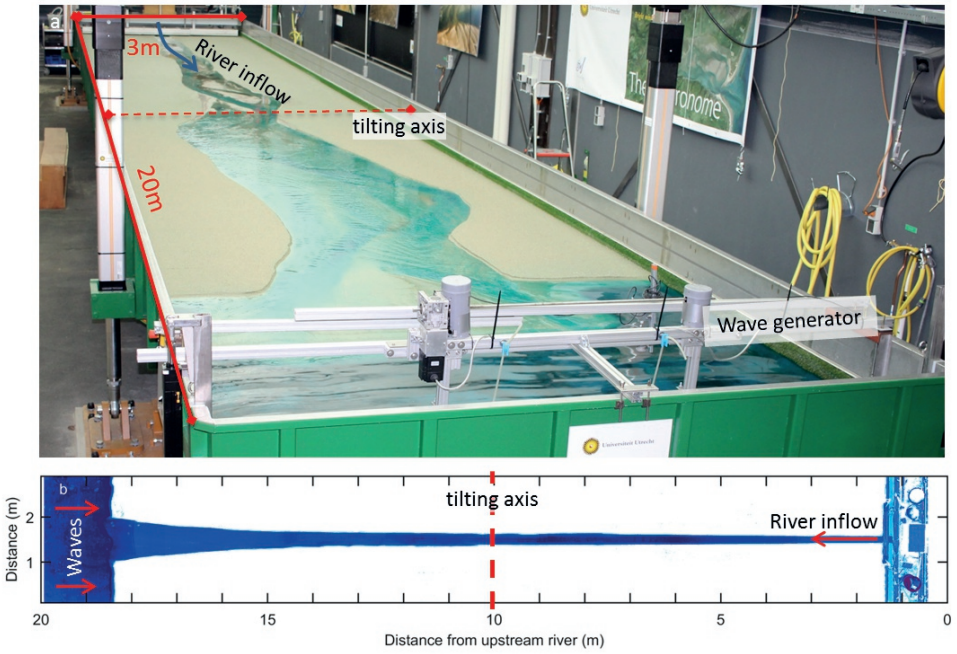

Figure 6.2 (a) The Metronome, a tilting flume of 20 m long by 3 m wide. (b) Overhead image of initial converging channel bathymetry. Blueness indicates depth, except in the first metre where the gantry is located. At the landward side, river discharge (0.1 $L{\cdot}s^{-1}$) was added during the ebb phase. At the seaward end, paddle-generated waves were applied during the flood phase.

3.0 m wide. An initial channel was carved in the sediment bed to facilitate the initial flow from the upstream boundary to the sea and back. This initial channel was 0.03 m deep and the width increased exponentially from 0.2 m at the river to 1.0 m at the seaward boundary (Fig. 6.2b).

Tidal currents were produced by four actuators that ensured a repeatable tilting with a period of 40 s and a maximum tilting gradient of 0.008 $m{\cdot}m^{-1}$. At the upstream boundary water discharge was added to the flume during the ebb phase at a constant rate of 0.1 $L{\cdot}\,s^{-1}$. River discharge was disabled during the flood phase, because otherwise water would pile up at the upstream boundary, resulting in an extreme water pulse when tilted seaward again. The contribution of the river discharge to the tidal prism is 0.002 m^3 (0.1 $L{\cdot}s^{-1} \times 20$ s), while the total tidal prism is about 0.11 m^3 at the start of the experiment and 0.3 m^3 at the end of the experiment (Braat et al., 2019). This means that the relative contribution of river discharge to the tidal prism is 1.8% at the start and 0.7% at the end of the experiment. This is within the range that typically occurs in estuaries, for example between 0.01% and 20% for estuaries in the UK, with an average of 3% and a median of 0.7% (Manning, 2007).

The water level at the boundary between the sea and the land was kept at a fixed elevation by a constant head at the downstream boundary of the flume, allowing free inflow and outflow of water. Water depth in the sea was continuously compensated during the tilting by periodic vertical motion of the weir at the seaward boundary, such that the water depth in the sea was always 0.065 ± 0.005 m (Kleinhans et al., 2017a). The water was dyed blue with Brilliant Blue FCF colourant to enhance the visualisation of morphology.

Paddle-generated waves were introduced at the seaward boundary with a frequency of 2 Hz and an amplitude of approximately 0.01 m during the flood phase. Waves were only introduced during the flood phase, because only in that phase the stirring of sand by the waves would cause slight sediment transport in landward direction. Scale effects of gravity waves in the Metronome tidal facility are described in the Supplementary material, but our general conclusion is that the wave-induced sediment mobility is much lower than in natural systems even though the relative wave height with respect to shoreface and channel depth is much larger. Nevertheless, waves in combination with the tidal currents were found to subdue the delta height and the tendency to form large, irregular deltas dominated by channel avulsion.

Pilot experiments showed that tilting with a simple sine function results in net exporting systems (Supplementary material in Braat et al. (2019)), which means that the system could be classified as a delta sensu Dalrymple et al. (1992). However, we here refer to the system as an estuary, because the relative contribution of river discharge to the tidal volume is too low ($\approx$1%) while ebb and flood currents are much larger and approximately equal (Kleinhans et al., 2017a). Furthermore, the observed channels and bars in experiments resemble bars in natural estuaries (Chapter 2). Such bars are expected to form much more quickly than the timescale over which the entire estuary attains equilibrium with its forcing conditions, because bar building only requires lateral sediment displacement over short distances while estuary deformation requires displacement of sediment volumes through the entire system (Lanzoni and Seminara, 2006; Kleinhans et al., 2015a). We therefore argue that the main conclusions in this chapter are not sensitive to this simplification.

6.2.2 Data collection and data processing

Time-lapse imagery from seven overhead cameras was collected each tidal cycle at the horizontal position of the flume when transitioning from ebb to flood flow. The cameras were mounted at equal distances 3.7 m above the centreline of the flume. The CMOS MAKO colour cameras have a resolution of 2,048 by 2,048 pixels with lenses of a fixed focal length of 12.5 mm. The resulting spatial pixel resolution was 1.5-2 mm. Images were geometrically rectified and a lens correction (vignette and distortion) was applied before they were stitched, and then converted to LAB (CIELAB) colourspace images, in which L represents the colour band with light intensity, A represents red to green and B yellow to blue (also used in van Dijk et al., 2013b). The B-band was extracted from the LAB images, because it enhances the visualisation of morphology by the largest contrast between coloured water and sediment.

The flume was illuminated at about 300 lux with daylight-coloured fluorescent light aimed upward at a white diffusive ceiling at approximately 4.5 m above the flume floor. Light reflection from the water surface on the photographs was minimised by white photography backdrop cloth between the ceiling and flume.

To create digital elevation models (DEMs), photographs were taken with a digital single-lens reflex (DSLR) camera on a dry bed and processed with structure from motion software (Lane et al., 1993; Chandler et al., 2001; Westoby et al., 2012; Fonstad et al., 2013; Morgan et al., 2017; Agisoft, 2017). Drainage of the flume, prior to data collection, was slow enough to prevent modification of the morphology. The first five DEMs were made with an interval of 500 tidal cycles, starting at 300 cycles. Subsequently, seven DEMs were made with an interval of 1,000 cycles and the final three had an interval of 2,000 cycles. The DEMs were referenced with 20 ground control points at equal spacing on the sides of the flume, such that the resulting DEMs could be resampled on the same grid as the stitched images from the overhead cameras.

Flow velocities were measured over a tidal cycle with Particle Imaging Velocimetry (PIV) (Mori and Chang, 2003) at 12 moments during the experiment. These 12 moments correspond with the timing of the first 12 DEMs. White floating particles (diameter $\sim$ 2.5 mm) were seeded on the water surface

and resupplied when necessary. At 16 equally spaced phases of the tide, 10 images were collected with the overhead cameras at 25 Hz, using a pulse train from a frequency generator. Flow velocities were subsequently calculated from pairs of consecutive images with the MPIV toolbox in Matlab (Mori and Chang, 2003). As in Kleinhans et al. (2017a), we used the peak cross-correlation algorithm to determine mean particle displacement in pixels in a 50 × 50 window with 50% overlap. The resulting vector fields were scaled to metrics with the pixel footprint of the cameras (1.5-2 mm per pixel), correcting for the tilt of the flume. Erroneous vectors were obtained and filtered out where particles were sparse or overly-abundant, as well as when the Particle Imaging Velocimetry-window partly covered the flume wall or reflection on the water surface was too large. For processing, the average vector field was calculated for each tidal phase from 10 consecutive images and for plotting purposes it was interpolated on a grid with the same size and resolution as used for the overhead cameras and DEMs. Residual currents were calculated as the average flow vector over a full tidal cycle.

6.2.3 Data reduction

Experimental results are compared with data from natural systems (Chapter 2) to assess how well the tidal bars in our experiment scale to nature. A detailed comparison is made with the Western Scheldt (NL), for which detailed bathymetries over time and flow velocities are available. In this study, the important scaling properties are the planform dimensions of bars and the elevation distribution of the bathymetry. Therefore, maximum bar length and width were measured in the experiments following Chapter 2. Hypsometric curves, which are cumulative depth elevation curves, were calculated for four zones in the experiment as well as for the Western Scheldt. These zones were chosen as the part between two successive width confinements in the estuary (Fig. 6.3k, Suppl. Fig. 6.17a).

Estuary width was measured in our experiment as the local width between the noneroded estuary banks. Channel width was measured as the width of the estuary below an along-channel linear profile that was fitted on the median bed level per cross-section, whereas above the median bed level was classified as bar. Excess width is defined as the estuary width minus the width from an ideal converging estuary shape and summed width of bars was measured as the sum of the width of all bars in a cross-section (Chapter 5).

The locations of major channel confluences and the spacing between them over time were determined for the experiment and the Western Scheldt. In addition, these quantities were measured on aerial imagery for a fixed moment in time in seven other natural systems: Dovey (UK), Bannow (UK), TawTorridge (UK), Teign (UK), Rodds Bay (Australia), Whitehaven Beach (Australia) and Netarts (US). In case of aerial photographs, major confluence locations were visually determined as the deepest point where multiple channels converge, while these points were extracted from bathymetric data for the experiments and Western Scheldt (Fig. 6.4). Deep scours as a result of bank protection, resistant layers that consist of shell fragments (so called crags, Cleveringa (2013)), or scours associated with outer bends of meanders were excluded. Subsequently, the location and spacing between successive channel confluences were measured with respect to local zones of confinement in the estuary outlines.

The dynamics of channels and bars over time were studied from the blueness images, which is a proxy for the water depth. Blue represents the channel and white the bar. Changes in blueness values were used to study where erosion and sedimentation occurred in the experiment and to determine the youngest time step during which sediment was deposited. The same approach was applied using successive DEMs of the experiment, but the temporal resolution for this was lower. Cumulative bed level change was calculated as a measure of the spatial dynamics within the system and to assess whether the experiment was in dynamic equilibrium during the final stages. Cross-sectional profiles were taken from the LAB images and plotted over time, creating time stack diagrams that show the migration of channels and bars in cross section over time.

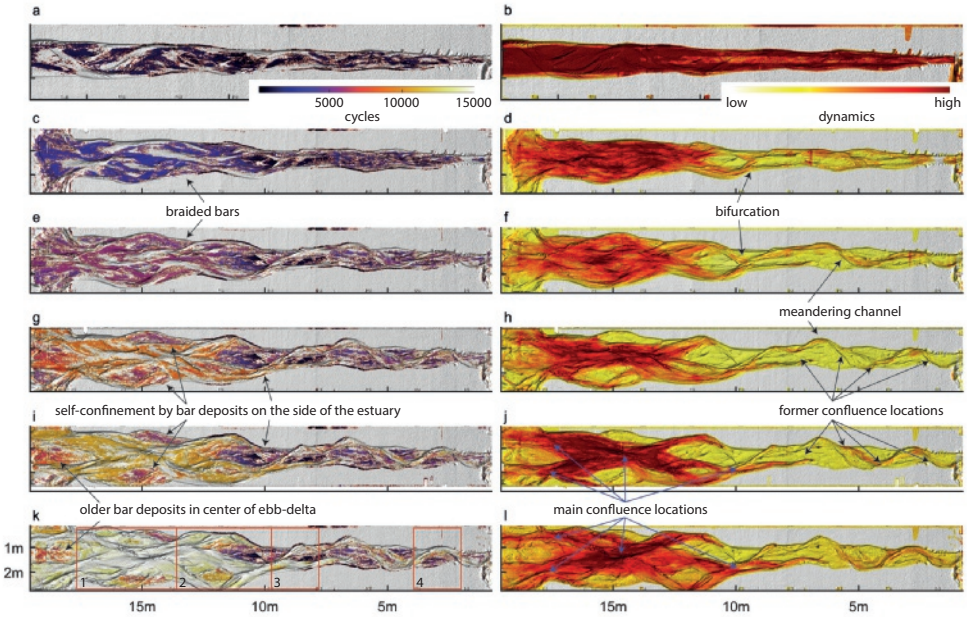

Figure 6.3 Two representations of spatiotemporal patterns of morphodynamics. [left] Hillshade map of morphology at several time steps, showing increasing age variation as the system develops (top to bottom). The colour scale indicates time of deposition of the top surface, where light colours are the youngest. [right] Hillshade map of morphology at several time steps, in which the colour scale indicates cumulative bed level change between two successive digital elevation models, which is an indicator of dynamic activity. Maps are given for the following time steps: (a,b) 1,250, (c,d) 3,300, (e,f) 5,900, (g,h) 8,900, (i,j) 10,900 and (k,l) 15,000 cycles. Red numbered boxes in (k) show the zones for which hypsometric curves are calculated (Fig. 6.11c).

6.3 Results

6.3.1 General morphological evolution

In the initial phase of the experiment, an alternate bar pattern evolved (Fig. 6.5a). As channel widening continued, a main meandering channel formed with riffles between two successive bends. The meandering channel and alternate bars initially migrated seaward (Suppl. Movie online). Later, the increased curvature of the meandering channel forced the bars to become anchored to their inner bends, while lateral erosion and deposition increased the width of the forced bars. In a later stage, channels stabilised in the landward part of the estuary, while the estuary width kept increasing in the seaward part. This allowed the development of multiple bars and channels in cross section, which were first observed when flood *barbs* intersected the forced bars (Fig. 6.5a,b). Barb channels are channels that become shallower in the direction of flow and have a dead end on the bar. Net sediment transport toward the sea formed an ebb tidal delta, which is a term more commonly used in the context of tidal basins and also applies to estuaries (e.g. Davis Jr and Hayes, 1984; Elias et al., 2017). The ebb tidal delta limited the inflow of water to the estuary. As widening progressed, forced midchannel bars diverted the flow and periodically caused bank erosion. These zones were alternated by locations where the estuary width remained narrow or was self-confined by sidebar deposits, resulting in a quasiperiodic planform (Fig. 6.5d,e).

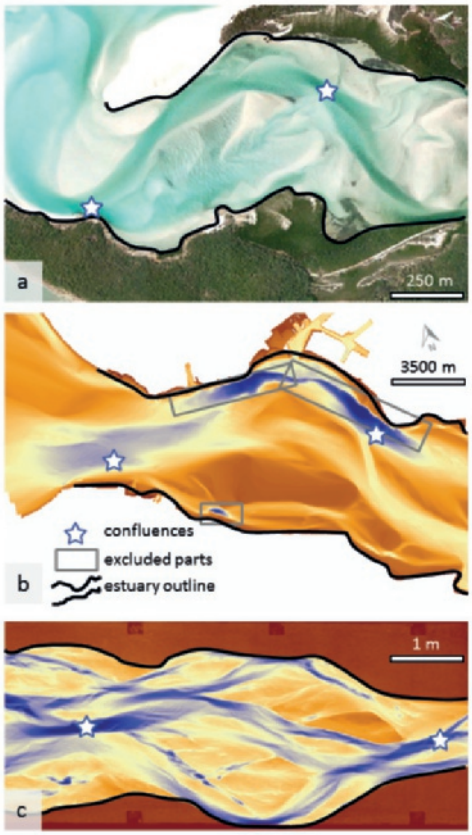

Figure 6.4 Locations of major confluences were determined in (a) aerial photographs of natural systems, (b) bathymetry of the Western Scheldt and (c) and experiments. Warm colours denote high elevation; cool colours denote low elevation. In case of aerial photographs, major confluence locations were chosen where multiple main channels converge. For the bathymetry of the Western Scheldt and experiment, these points were automatically determined as the maximum depth within a confluence zone. Deep scours as a result of bank protection, presence of hard layers, or outer-bend erosion were excluded.

6.3.2 Channel widening and incipient meandering

The initial phase of the experiment was characterised by the development of the initial converging channel into an incipient meandering ebb tidal channel (Fig. 6.5a). In the first 200 cycles, the converging straight channel widened (Fig. 6.6) and initially free (seaward migrating) alternate bars formed. The resulting channel pattern consisted of multiple straight channels parallel to the centreline of the estuary, which were separated by sills that connected the alternate bars in along-channel direction. Over time, the straight channels became more oblique to the estuary centreline and curved until they developed a meandering ebb tidal channel, which forced the bars in place. On top of the alternate bars, circulating flow patterns developed, with residual currents dominantly moving in landward direction onto the bars, then diverting to the channel and flowing back in seaward direction via the meandering channel (Fig. 6.7a). Both the ebb and flood flows caused erosion of the estuary banks by lateral migration of channels in the following tidal cycles (Fig. 6.7b).

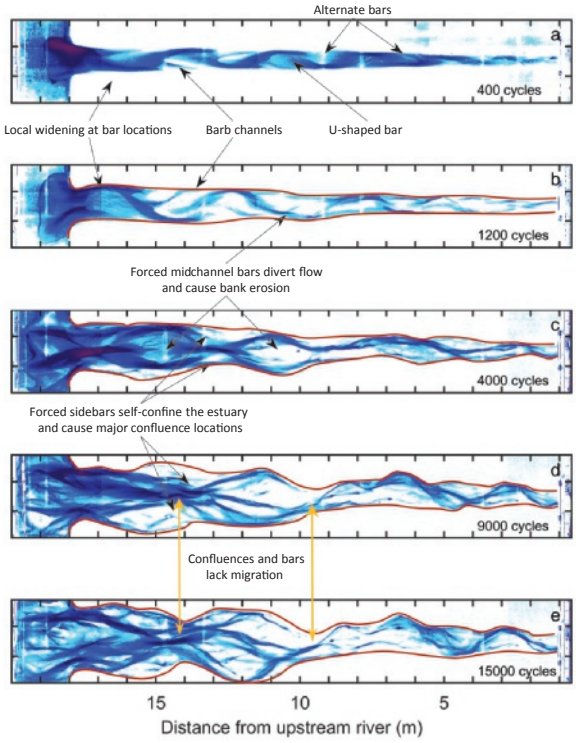

Figure 6.5 Overhead imagery of the experiment for five moments in time. Blueness was extracted as an indicator for channel depth. For all time-steps, see Suppl. Fig. 6.15 or the Suppl. Movie online.

6.3.3 Alternate bars with initial barb formation

This phase was characterised by the formation of barb channels in the inner bends of the alternate bars. The main meandering ebb channel migrated laterally eroding the estuary banks and alternate bars grew in width. At the landward side shallow sills formed between two successive alternate bars. The sill separated the ebb flow from the flood flow in two separate channels. As the ebb channel migrated further seaward and the flood channel landward, U-shaped bars formed (Fig. 6.5a). The U-shaped bars thereby partly blocked the channel with opposing flow (Fig. 6.5a).

From 1,000 tidal cycles onward the braiding index, which is the average number of channels or bars in the cross section, kept increasing as a result of the increasing channel width, which allowed for multiple braided bars (Fig. 6.5a). Bars were particularly abundant in specific zones (at approximately 8 m, 11 m, 14 m and 15 m) where the summed width of bars was large (Fig. 6.8a,b) and the compound bars were dissected by one or multiple barb channels. Compound bars are more complex bars that probably amalgamated from other bars, in analogy with rivers (e.g. Bridge, 2003; Ashworth et al., 2000; Schuurman et al., 2013).

At the seaward side, the export of sediment during the first 2,000 cycles formed an ebb tidal delta. After this period, the delta was large enough to limit the inflow of water into the estuary, while erosion on the delta formed a single major channel at the northern side of the inlet (Suppl. Fig. 6.15h,i).

The location of the main meandering channel shifted from north at 1,000 cycles, to south around 2,000 cycles and back north at about 3,000 cycles at approximately 15 m from the upstream boundary

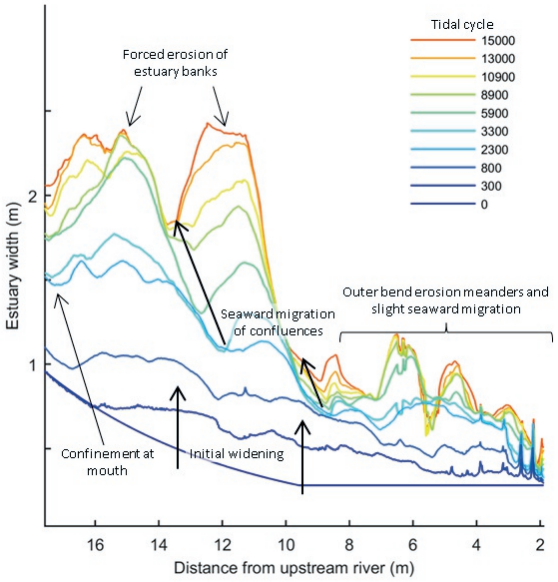

Figure 6.6 Evolution of the estuary width profile. The planform initially widened and, from 2,300 cycles onward, became more irregular. After 3,300 cycles, bars and landward meanders rapidly force local widening, while confinements migrate seaward. In the last phase, after 8,900 cycles, the bars became static (forced) and bank erosion ceased at the confluence locations, while the amplitude of the quasiperiodic width variation increased where midchannel bars were present.

(Suppl. Fig. 6.15e,h,i). Interestingly, the adjacent channel confluence positions (at 13.5 m and at the mouth of the estuary) were relative stable over time, with dynamic bar and channel zones in between. This caused a rather irregular pattern in the outline of the estuary where some parts remained relatively narrow while other parts became relatively wide (Fig. 6.6).

6.3.4 Midchannel bars, confluences and evolution of quasiperiodic planform

In the central part of the estuary (8-18 m), widening resulted in the formation of forced midchannel bars that diverted flow, which caused bank erosion. For example, after 4,000 cycles, a large estuary width at 15 m allowed the existence of two major channels: one on the northern side and one on the southern side of the estuary, separated by a relatively wide bar in the centre of the estuary (Fig. 6.5c). The confluences of these two channels occurred at the mouth of the estuary and at 13.5 m in a channel located in the middle of the estuary. While the two major channels at 15 m continued to migrate toward the outer banks of the estuary (Fig. 6.9d), the bar between these channels obtained an oval shape as a result of an almost symmetrical ebb and flood barb on both its landward and seaward side. The residual current showed two major circulation cells at this compound bar (Fig. 6.7c). The flood barb facilitated flow onto the bar, which diverged over the bar to the channels north and south of the bar. The ebb flow predominantly used the northern and southern channels around the bar and any flow entering the ebb barb also diverged into these channels. This caused bank erosion on both the north and south sides of the estuary and sedimentation that increased the width of the midchannel bar (Fig. 6.7d). A similar process occurred in a more landward part slightly later in the experiment.

In the landward part of the estuary (0-8 m) the individual channels became more curved and connected, so that a main meandering channel formed from 5,000 cycles onward (Fig. 6.5c,d). The

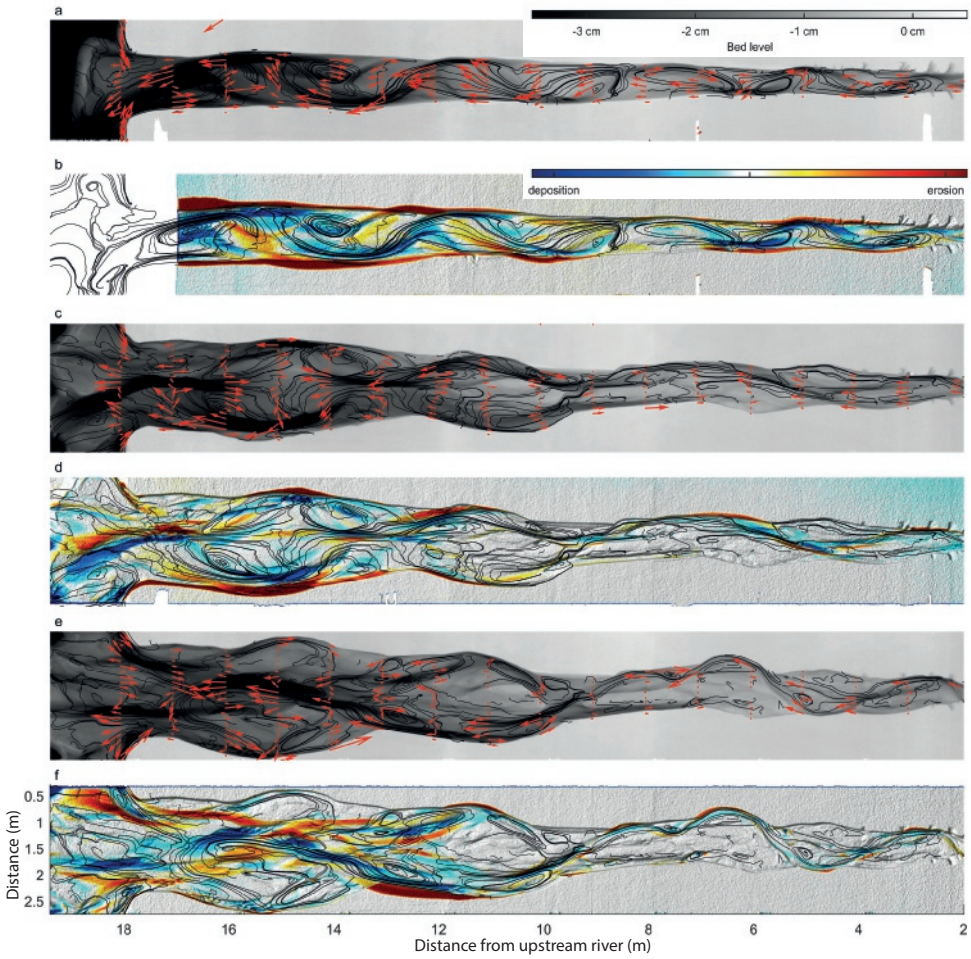

Figure 6.7 (a,c,e) Vectors indicating the residual currents after (a) 800, (c) 4,400 and (e) 6,900 cycles for transects with a spacing of a metre on top of a map with the streamlines based on a vector field with residual currents and the bathymetry. (b,d,f) Streamlines based on a vector field with residual currents, plotted on top of a map that indicates the erosion (in increasing magnitude from yellow to red) and sedimentation (from cyan to blue) in the subsequent phase of the experiment.

channel orientation of the upstream channel affected division of flow and sediment at the former bifurcation at 9 m, so that now the landward river system fed the southern branch instead of the northern branch (Fig. 6.5c,d). This channel subsequently migrated (Fig. 6.9c) by eroding the southern bank of the estuary at 10 m (Fig. 6.7f), whereas the northern channel was only connected during flood flow. Seaward, the southern channel merged with the major channel that formed in the middle of the estuary at approximately 13 m. At this point multiple smaller barb channels formed onto the bar at 11 m that evaded each other and migrated over the bar.

At the mouth, the estuary was slightly narrower than the part of the estuary directly landward of the mouth at 16 m. Specific zones occurred where estuary width was relatively narrow with a major confluence and approached its ideal width. The zones were alternated by zones in which the estuary

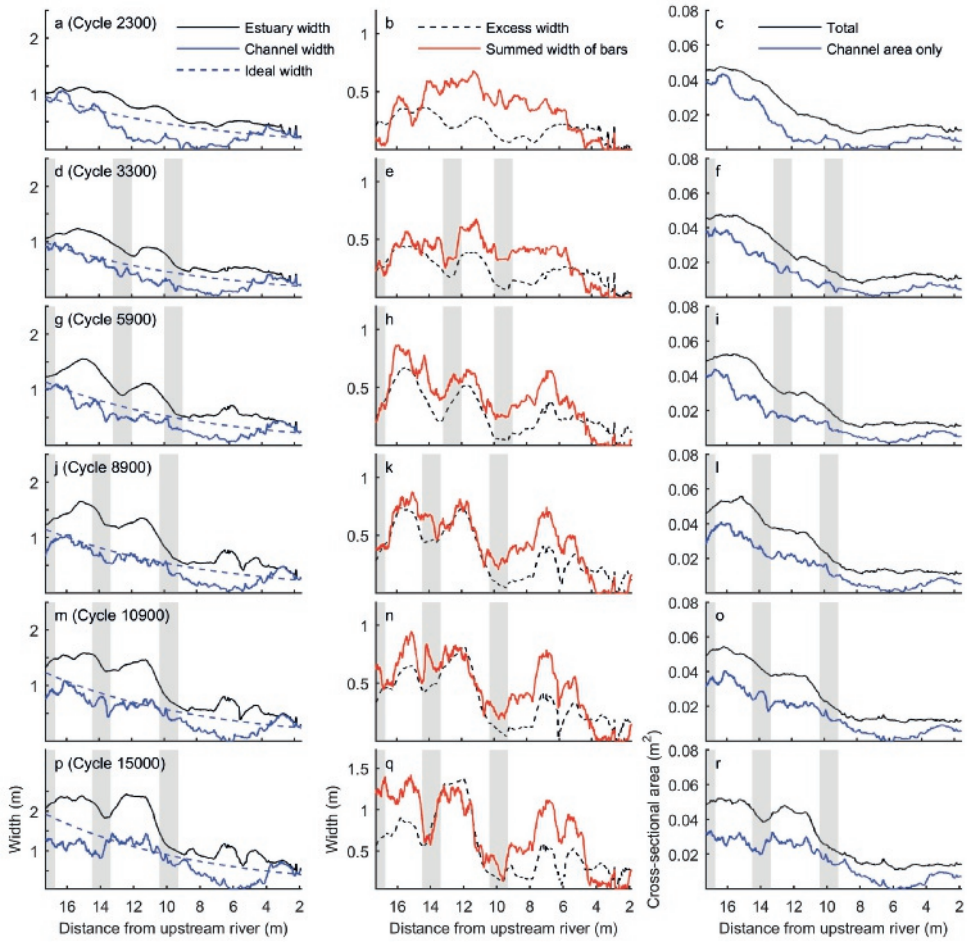

Figure 6.8 [left] Evolution of estuary width, channel width and ideal width. [middle] Evolution of excess width and summed width of bars. [right] Evolution of cross-sectional area. Estuary width is the sum of channel and bar width. Ideal width is the largest fitting exponential shape in the estuary outline. Excess width is the estuary width minus the ideal width. The channel width approaches an ideal converging shape over time. Summed width of bars approaches the excess width. Total cross-sectional area is the area below the estuary banks. Channel cross-sectional area excludes the area above bars. Shading indicates the locations where the estuary remained confined. At these locations, the summed channel width and summed bar width remain relatively low.

was much wider (Fig. 6.8). Over time, the confluences migrated slightly seaward and the planform became progressively less ideal (Fig. 6.6). The landward channel (0-8 m) eroded the estuary banks in the outer bends of the meanders until approximately 8,000 tidal cycles. From that moment on the configuration of channels and bars in the landward part (0-8 m) remained relatively stable over time (Fig. 6.5d,e, Fig. 6.9a,b). The later phases of the experiment (6,000-15,000 cycles) were characterised by specific zones that were active (Fig. 6.3h,j,l). These zones connected the major channel confluences at 10 m, 14 m and 18 m. The active zones were relatively narrow at locations where the confluences occurred (e.g. at 14 m and 18 m in Fig. 6.3j) and relatively wide in the zones in between (e.g. at 16m).

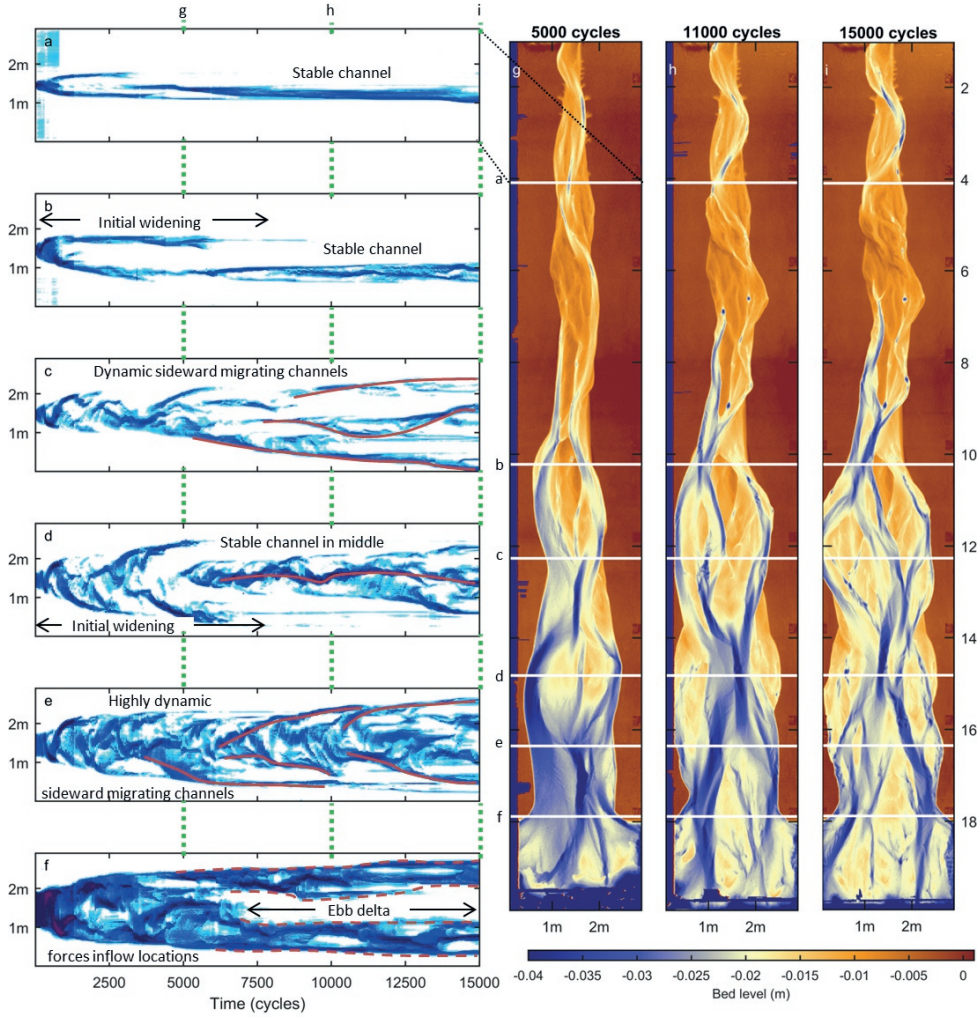

Figure 6.9 (a-f) Time-space diagrams of cross sections at 4, 10, 12, 14.5, 16 and 17.5 m, which are indicated in (g,h,i) bathymetry after 5,000, 11,000 and 15,000 tidal cycles. (a,b) A single landward channel stabilises from 7,500 tidal cycles onwards. (c) In the centre, dynamic, sideward migrating channels occur. (d) Outward migrating channels erode the estuary banks. From about 6,000 cycles the midchannel bar is cross-cut and a single main channel forms in the middle of the estuary. (e) In the seaward part, multiple very dynamic, migrating channels occur. The channels migrate from the estuary centreline toward the estuary banks. (f) An ebb tidal delta forms and stabilises after 7,500 tidal cycles. This diverts the inflow locations to be on the sides of the ebb tidal delta.

6.3.5 Cross-cutting of midchannel bars

In the seaward part, the phase with midchannel bars and bank erosion continued until 5,000 cycles, when a channel was able to progressively cut through the middle of the bar, connecting the barb channels around 5,000-5,500 cycles (Fig. 6.5c,d). This caused a main channel along the centreline of the estuary. During this phase, the major inflow and outflow were focussed in the middle of the ebb

tidal delta. This reduced bank erosion in the most downstream part of the estuary from that moment onward (Fig. 6.6, 14-18 m), preventing the estuary shape from becoming more irregular.

In the central part of the estuary, the cross-cutting event also caused the direction of the residual circulation cells to reverse, with flood flows now predominantly occurring along the sides of the estuary, while the channel in the middle of the estuary was ebb dominant (Fig. 6.7e). This reduced erosion of the estuary banks at this location and triggered the formation of new channels that connected the main ebb channel with the newly formed outflow locations on the ebb tidal delta (Fig. 6.7f). Because the main channels in the middle of the seaward part of the estuary (14-18 m) gradually exported sediment to the central parts of the ebb tidal delta, this process eventually blocked the inflow and outflow of water (6,000-8,000 cycles) (Suppl. Fig. 6.15n-p). The ebb delta thus stabilised in place after 7,500 tidal cycles (Fig. 6.9f,h), after which the inflow and outflow of water became diverted to the northern and southern sides of the ebb tidal delta (Fig. 6.9f).

Similar to the previous bar cross-cutting event around 5,000 cycles, a similar process occurred at the compound bar more landward (9.5-13 m), where after 9,000 cycles the cross-cutting of the middle parts of the bar occurred (Fig. 6.5d). This isolated a southern part of the compound bar at 9.5 m. In short, the estuary evolved from an initially converging channel into an estuary filled with bars that inherited its quasiperiodic planform from phases in which midchannel bars diverted flow laterally, causing bank erosion.

6.3.6 Progressive infill from the sea and dynamic equilibrium with stable confluences

The zones where the estuary was confined reflect the locations where bars were relatively less abundant. For natural systems, a correlation was found between the occurrence of tidal bars and locations where the excess width is large (Chapter 5), which is defined as the local estuary width minus the ideal estuary width. This is in agreement with the experimental results (Fig. 6.8h,k,n), where summed width of bars indeed approaches the excess width in the later stages of the experiment. While the zones between 4-8 m and 14-18 m deviated from this rule in magnitude, the along-channel pattern is the same, that is, low excess width corresponds to low summed width of bars and vice versa.

In the last phase, the estuary reached a dynamic equilibrium with stable confluences, while active channel migration remained in the parts between the confluences. Mean changes in bed level and sediment export illustrate that the experiment was close to dynamic equilibrium (Suppl. Fig. 6.14). Generally, the increase in estuary width that was observed in previous stages decreased and only in the part 10-13 m and at the mouth of the estuary a slight increase in width occurred during the last 2,000 cycles of the experiment (Fig. 6.6).

In the final stages of the experiment, flow from the landward side bifurcated around the newly isolated bar at 11 m (10,000-12,000 cycles, Fig. 6.5d,e), after which the northern branch began to erode the southern side of the former bar between 9.5 m and 12 m. At the same time the southern branch continued to erode the southern bank of the estuary until reaching the flume wall, which was the reason to end the experiment after 15,000 cycles.

6.4 Discussion

This study presents the first physical scale experiment of an estuary with dynamic channels and bars, stable confluences, and a self-formed planform. Below, we first describe a conceptual model on how forced bars determine the estuary outline. Second, we discuss the spatial and temporal scaling of bars. Then, the effect of bar patterns on the flow patterns is compared with the evolution of natural estuaries. Last, the observed experimental cyclicity in channel and bar migration is compared to natural systems.

6.4.1 Conceptual model for estuary planform forcing

We summarise the evolution of a self-formed estuary in a conceptual model containing three phases. In the first phase (Fig. 6.10a) an alternate bar pattern develops, while the estuary widens. The initially straight channels connect to form a meandering channel with alternate bars (comparable to alternate bars in rivers Struiksma et al., 1985; Ikeda and Parker, 1989; van de Lageweg et al., 2014). As soon as the bars exceed a width-to-length ratio of approximately 1/7, the flood flow is capable of forming barb channels onto the alternate bars (Fig. 6.10a). The barb channels progressively cut through the alternate bars. Both the outer bends of the meandering channels and the flood barbs erode the estuary banks, which creates an irregular estuary planform.

In the second phase, the first midchannel bars have formed that are large enough to divert the flow such that the outer bend erosion is accelerated and major confluences are formed seaward and landward of the midchannel bars, forming a quasiperiodic estuary planform (Fig. 6.10b). At the confluence locations, estuary width generally remains narrow and dynamic channels and bars only occur within a small stretch of the estuary width. As outer bend erosion continues, the gradient over the midchannel bar becomes favourable for both the ebb and the flood flows. These flows create new barb channels onto the midchannel bar, which over time are capable of cross-cutting the bar, forming a new main channel in the middle of the estuary (Phase III, Fig. 6.10c). The timing of this event may vary along the estuary and confluences typically migrate seaward over the course of these phases.

After this phase, a dynamic equilibrium at the bar confluence scale is reached, in which sediment from bars and banks is reworked into new bars within the estuary. The confluences remain stable, and bank erosion is reduced. Dynamic zones of channels and bars typically occur in stretches between the major confluences. In both experiments and natural systems we observed the development of irregular estuary planforms and the forcing of channel confluences and zones with dynamic channels and bars. The conceptual model implies that quasiperiodic deviations from the ideal estuary shape can be formed autogenically. This means that the planform shape of natural estuaries is not necessarily externally forced, that is, allogenic, for example, by the presence of bedrock or resistant layers.

Our observations show that the mechanisms of bar push and bank pull identified in rivers (e.g. Parker et al., 2011; Eke, 2014; van de Lageweg et al., 2014) may apply in estuaries as well. Initially, the alternate bars form in a straight channel, which was also the case in river experiments (van Dijk et al., 2012), suggesting that the process of pattern formation starts with bar push. However, in later phases, as soon as the increased curvature and local widening (e.g. Repetto and Tubino, 2001; Seminara, 2010; Zolezzi et al., 2012) forces the bars to be non-migratory, the usual meander bend migration mechanism of curvature-driven momentum displacement toward the outer bank kicks in, causing bank retreat. This is followed by inner bend accretion, meaning that this phase is dominated by bank pull. Upon further widening, the bar regime shifts to midchannel bars that are non-migratory because of curvature and local widening as well as the reversing tidal flow, and the process continues on both sides of the bar. We hypothesise that this stage is dominated by a balance between bank pull and bar push as in Eke (2014).

6.4.2 Spatial and temporal scales of channels and bars

The dimensions of tidal bars in the experiments scale well with bars observed in natural systems, as reported in Chapter 2 (Fig. 6.11a). All experimental bars are within the uncertainty margins given for natural bars. However, most experimental bars plot above the trend line, indicating that their shape is slightly more elongated compared to the bars in natural systems (length-to-width ratio of approximately 8 in experiments, compared to 7 in nature). Moreover, the bar length is well within the range as expected based on local estuary width (Fig. 6.11b). The experimental bars have similar dimensions as the alternate bar pattern reported in Tambroni et al. (2005) where the average bar wavelength is 3-6 times channel width; thus, bar length is 1.5-3 times channel width. However, in

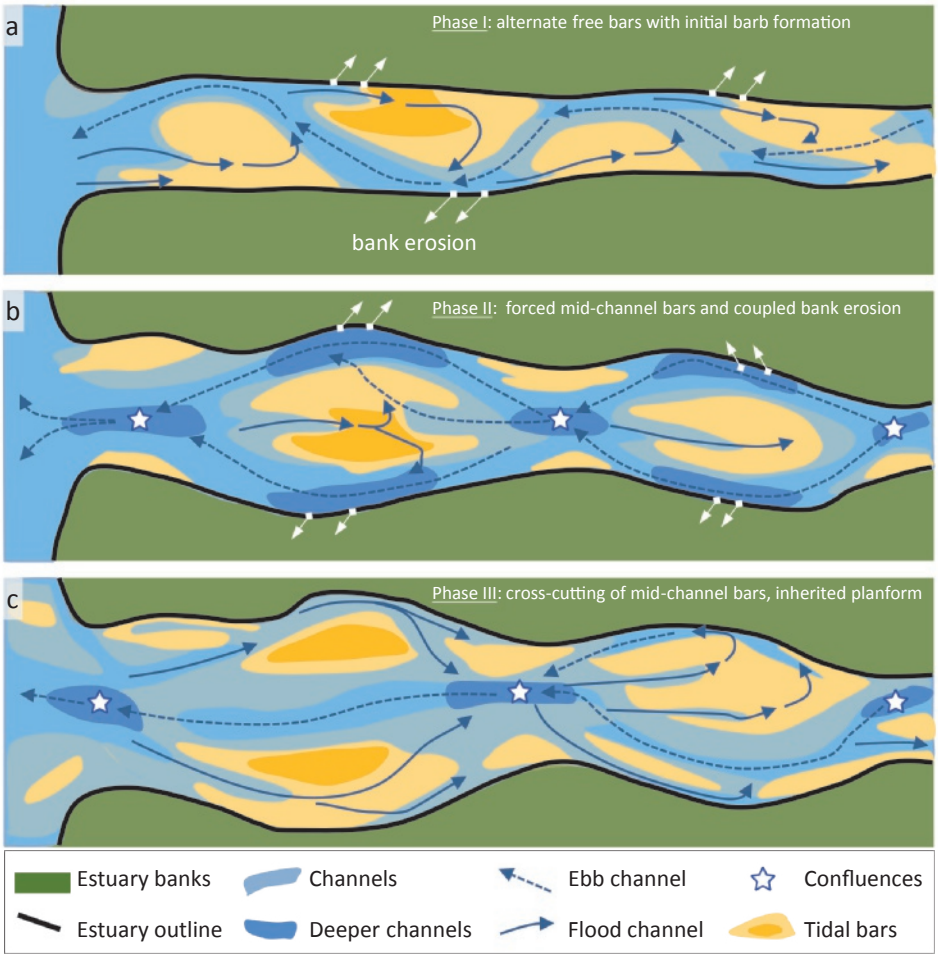

Figure 6.10 Conceptual model for the development of self-formed estuaries. (a) Phase I: the initial converging channel widens and (free) migrating alternate bars form. The meandering channel around the alternate bars is predominantly used as ebb channel, eroding the outer bends. While the alternate bars widen, initial flood barbs form onto the alternate bars. The main meandering channel migrates slightly seaward in Phase I, causing a longitudinal displacement in the next phase. (b) Phase II: the flood barb channels progressively cut through the alternate bars, isolating forced midchannel bars in the middle of the estuary. This creates two major confluences: one at the mouth and one upstream of the mid channel bar. The flow is diverted around the midchannel bar, which causes bank erosion, resulting in an even more irregular planform. (c) Phase III: the barb channels on the midchannel bar enlarge and subsequently connect, cross-cutting the bar. This forms a new channel in the middle of the estuary and limits the erosion of the estuary banks. The resulting quasiperiodic planform is inherited from phase II. Major confluences separate zones in which channels periodically rework tidal bars.

contrast to experiments with fixed channel planimetry (Tambroni et al., 2005; Tambroni et al., 2017) that result in a system with a braiding index of 1, we observed rapid widening of the estuary, which allows braiding index, bar width, and bar length to increase. Most experimental bars fall exactly on the trend expected from natural systems. The largest outliers occur at the lower uncertainty band.

These bars are an order of magnitude smaller than the other bars and formed in later phases of the experiment in one of the larger channel branches in the estuary. In this case, the width of the single branch is responsible for the bar dimensions. Therefore, scaling with the full estuary width may result in large deviations from the expected trend.

Hypsometric curves for four zones within the estuary (indicated in Fig. 6.3k and Suppl. Fig. 6.17a) show a large similarity between the experiment and the Western Scheldt (Fig. 6.11e), where zones were defined as the estuary area between two successive confinements. Only zone 4 in the Western Scheldt deviates significantly from the hypsometry in the experiment (Fig. 6.11e). At this location the estuary width is smaller and thus a larger part of the width is influenced by dredging to maintain shipping fairways. When channels are excluded and thus hypsometric curves are drawn for compound bars only, bars in the Western Scheldt show a more linear elevation profile, while bars in the experiment have a more s-shaped curve (Fig. 6.11f). The s-shaped curves for the experiment are caused by a small portion of the compound bars being highly elevated and a small portion being very low elevated. High elevated parts developed on the oldest parts of bars that accreted over time and lack flooding and morphodynamic activity in later phases. The relative scarcity of high elevated areas is caused by the lack of cohesive material and vegetation, which would otherwise accrete tidal bars and estuary banks (Braat et al., 2017; Braat et al., 2019; Lokhorst et al., 2018). Low elevated parts are previous channels or scours on bars for which time was too short to fill in.

As bars separate the major confluences, it was expected that confluence spacing scales with bar dimensions, which scale with estuary width (bar length $\propto$ channel width$^{0.87}$, Chapter 2). Indeed, this was found to be the case (Fig. 6.11c,d), which means that the spacing of confluences scales well with bar dimensions and estuary width. In general, this also implies a decreasing confluence spacing along-channel from the sea in landward direction, because estuary width and bar dimensions decrease. To quantify the location where confluences occur, we measured the distance from the location of the major confluences to the local minima in the outline of the estuary. The measured distance was normalised by the average spacing with the successive landward and seaward confluence locations. Results show that the major confluences in all cases occur within 16% of local confinements for the experiments and Western Scheldt over time, as well as for the aerial photographs of eight natural systems (Suppl. Fig. 6.16).

The timescale over which the channels and bars in the experiment evolve is 15,000 tidal cycles, which corresponds to approximately 20 years of natural tidal cycles. All the sediment eroded in the experiment is either used for bar formation or exported to the ebb delta, which is a long-term sink for the eroded sediment because of the lack of intense littoral processes. Most modern estuaries typically evolved over centuries to millennia during the middle to late Holocene under rising sea level (van der Spek and Beets, 1992; Hijma and Cohen, 2011; de Haas et al., 2017). As such, their evolution comprised many more tidal cycles than our experimental estuary. Typically, modern estuaries initially enlarged as former river valleys that drowned, because of the rapid sea-level rise around the start of the middle Holocene. Part of the slower evolution may thus be explained by the time required for aggrading after sea-level rise decreased, in contrast to the erosional behaviour in the experiment. The relatively rapid evolution of bar patterns and bank erosion was also observed in river experiments and may partly be explained by a lack of bank strength in experiments without vegetation and cohesive material (van Dijk et al., 2012).

Additional experiments with added cohesive material (Braat et al., 2019) revealed two major effects compared to the experiment reported in this study. First, the mud fills up inactive areas and predominantly accretes on the tidal bars and estuary banks, which reduced the tidal prism. This counteracts the positive feedback mechanism between estuary widening, increased tidal prism, and therefore increased cross-sectional area at the mouth. The second effect is that the cohesiveness of mud has a slight stabilising effect on gentle slopes. However, the cohesion has no effect on the bank erosion rate as bespoke experiments demonstrate. The combined effects result in a narrower, confined

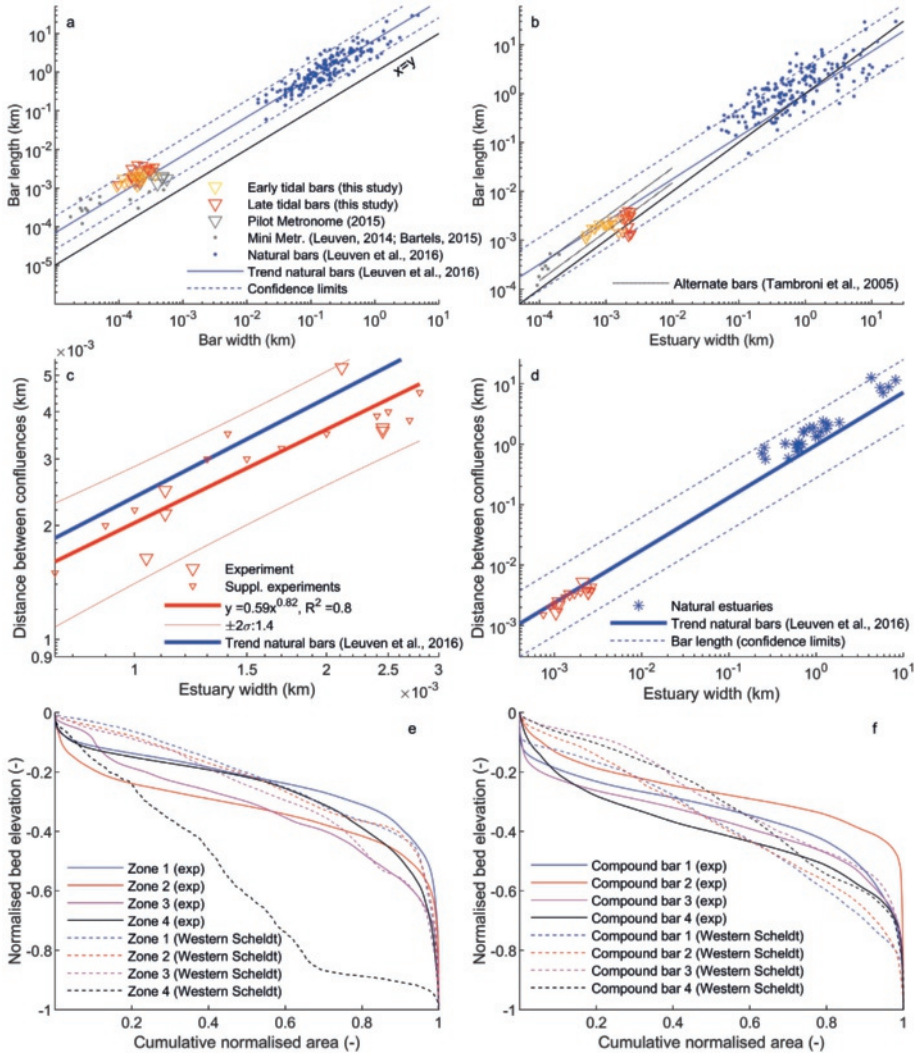

Figure 6.11 (a) Comparison of planform bar dimensions (length versus width) in the experiments and in natural systems. Triangles represent bars in the experiment, with colour indicating the tidal cycle during which the bars were measured: yellow was early in the experiment; red was at the end. (b) The scaling relation between estuary width and bar length that was found for natural systems holds for the experiments (Tambroni et al., 2005; Leuven, 2014; Bartels, 2015). (c) Confluence spacing as a function of local estuary width for experiments. Each triangle is the spacing between two successive confluence locations. (d) Comparison of confluence spacing in experiments with natural systems. A line with predicted bar length ($\times 1.5$) is drawn for comparison and shows that confluence spacing scales with bar dimensions and estuary width. (e) Hypsometric curves of zones between two successive confinements in the estuary outline, with numbering increasing in landward direction. The corresponding zones are given for the experiment in Fig. 6.3k and for the Western Scheldt in Suppl. Fig. 6.17a. Parts above the high water level were excluded. (f) Hypsometric curves of compound bars in the same zones.

estuary planform, but with similar bar patterns and dynamics, although higher in elevation, compared to the experiment without cohesive material reported here (Braat et al., 2019).

The general evolution of the experiment can be compared to the Western Scheldt, which evolved in the past 2,700 years from a narrow creek in a peat bog to an alluvial estuary with a quasiperiodic planform (Fig. 6.12). The timescale over which estuaries widen from a narrow creek after ingressions is typically in the order of hundreds of years, which may still be an estimate on the higher end for organic peat, which decays rapidly after erosion (Pierik et al., 2017; de Haas et al., 2017) and thus does not contribute to sediment available for bar formation. Despite their contrasting early evolution, the later stages of the experiment and natural systems were more similar.

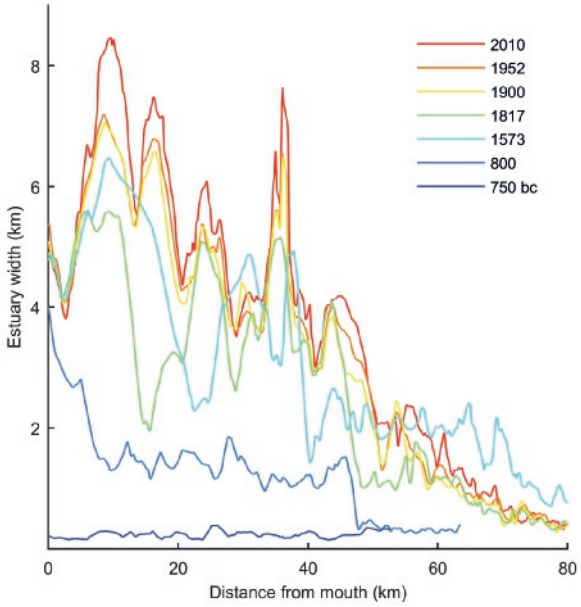

Figure 6.12 The estuary width profile of the Western Scheldt (The Netherlands) over time, which shows a similar evolution as the experiment (Fig. 6.6).

Bar dynamics typically occurs in tidal inlets, embayments and estuaries on timescales from 15 to 40 years (Israel and Dunsbergen, 1999; Levoy et al., 2017). A comparison of the experiment with this timescale may be more appropriate, because these processes are not limited in sediment supply. Nevertheless, scaling relations for bar patterns in experiments (Kleinhans et al., 2015a) and the natural processes that form bars (Chapter 2) and confine estuaries are not well understood. Recent numerical models show that mud deposits may be required to confine estuary planform and that self-formed estuaries with mud can reach an equilibrium within 500-1,000 years (Braat et al., 2017).

6.4.3 Role of circulation cells and confluences on the evolution of estuaries

The historic evolution of channel and bar patterns in the Western Scheldt (1800-1900) was characterised by an initial phase of migration and meandering of the main ebb channels, after which the meander bends reached the embankments on the sides (Jeuken, 2000). In the inner bends, the compound bars extended laterally and flood barbs formed. This evolution is very similar to the initial phases of the experiment (Figs. 6.6 & 6.12). However, after 1900, the morphological evolution was

largely influenced by human interference: dikes were constructed, side branches that slowly filled-in were embanked, and the first dredging activities started in 1922 (Kleinjan, 1938; Jeuken, 2000).

In 1944, van Veen, described the occurrence of circulation patterns in the Western Scheldt, where flow circulates through an ebb and a flood channel enclosing an intertidal bar. These circulation cells are similar to the circulation cells observed in the experiment, where the main meandering channel is ebb dominated and circulation cells covered the flood barb and adjacent ebb channel. These circulation cells divide the Western Scheldt into six main zones, which were later described as macrocells (Winterwerp et al., 2001; Toffolon and Crosato, 2007; Jeuken and Wang, 2010; Monge-Ganuzas et al., 2013) (Suppl. Fig. 6.17). These cells were determined from the observed morphology of the main ebb and flood tidal channels and numerically modelled residual flow, which resulted in cells that covered the enclosed area of an intertidal compound bar with its surrounding meandering channel. The boundaries of these cells in along-channel direction were chosen at the location of major channel confluences and correspond to the locations where the estuary width is relatively narrow. The concept of macrocells (e.g. Winterwerp et al., 2001; Toffolon and Crosato, 2007; Jeuken and Wang, 2010; Monge-Ganuzas et al., 2013) is similar to concept of mutually evasive transport paths (e.g. Ludwick, 1975; Harris, 1988; Dalrymple et al., 1990; Wells, 1995; Harris et al., 2004; Dalrymple and Choi, 2007). The latter, for example, occur around elongated tidal bars, where the opposite sides of the bar crest have opposing directions of residual sand transport and residual water flow, forming a circulation pattern. The difference between the latter and former group of authors is that the macrocells describe only the largest scale of bars, whereas the mutually evasive transport paths occur at a range of scales, including that of the smallest shoals as also observed in experiments (Kleinhans et al., 2014; Kleinhans et al., 2015b).

The experimental results in this study show that already after 800 tidal cycles serial circulation cells have evolved and that these circulation patterns can be used to explain how forced midchannel bars cause bank erosion (Fig. 6.7a,b). After the experimental estuary became wide enough, a pattern with parallel circulation cells or cells with a mixed coupling (Winterwerp et al., 2001) evolved (Fig. 6.7c,e). Later phases of the experiment illustrated that the boundary of two successive circulation cells typically occurred at a major confluence and at locations where the estuary width is relatively narrow. The length of circulation cells scales with bar length, and both bar length and circulation cell length correlate with estuary width (Fig. 6.11b,c,d). These patterns resemble the patterns observed in the Western Scheldt (Fig. 6.13, Suppl. Fig. 6.17).

6.4.4 Cyclicity of channels and bars in tidal systems

Cyclicity is the periodic migration of channels and bars, in which the original configuration reoccurs after a given period. This has previously been reported for natural tidal systems as well as experiments. For example, experiments of short tidal basins show periodic migration of channels and shoals, which is coupled to reorganisation of the channels in the tidal basin (Kleinhans et al., 2015b). Most of the studies so far focussed on cyclicity on the ebb tidal delta (e.g. Oost, 1995; Israel and Dunsbergen, 1999; Elias and van der Spek, 2006), on which channels migrate from one side to the other, after which they disappear and reappear at their initial position. However, besides ebb deltas and the quasi-cyclic morphologic behaviour of the smaller-scale connecting channels that link the large ebb and flood channels in macrocells (van Veen, 1950; van den Berg et al., 1996; Jeuken, 2000; Toffolon and Crosato, 2007; Swinkels et al., 2009; de Vriend et al., 2011), little is known about the cyclicity of bars and channels within tidal basins or estuaries.

Levoy et al. (2017) observed an 18.6-year cycle in the migration of channels and tidal flats in the Bay of Mont-Saint-Michel (France). They state that the periodic increase and decrease in flood dominance correspond with the periodic shift in the location of the channel, which is either located in the north or the south of the embayment. In this case, the bayward migration of tidal sand ridges forced a change in

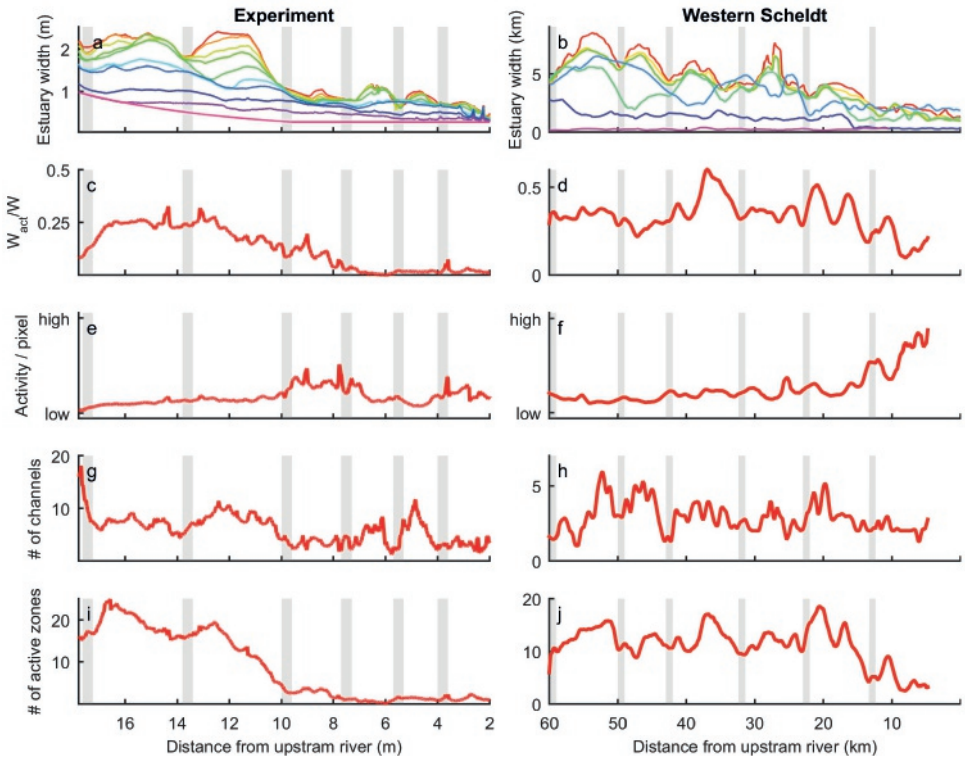

Figure 6.13 Along-channel profiles of (a,b) local estuary width over time, (c,d) time-averaged active channel width normalised with local estuary width, (e,f) sum of absolute bed level change per pixel, (g,h) number of channels in cross section and (i,j) number of active areas in cross section. Shading indicates locations of confinement in the estuary outline. These locations correspond with locations where the active width, activity per pixel and number of channels are generally low. The along-channel profiles (c-j) were averaged over the period 7,500-15,000 cycles for the experiment and the years 2000-2015 for the Western Scheldt.

the inflow and outflow directions of the tidal channels. It is hypothesised that a progressively northward swing of the northern channel configuration is caused by sand choking, that is, a large sediment supply partly blocking the main channel. This latter mechanism could be similar to the observations in the final stage of the scale experiments, in which the ebb tidal delta progressively expands in landward direction, followed by a southward migration of the channel at 11-12 m (Suppl. Fig. 6.15s-u).

While not explicitly stated in the original paper (Levoy et al., 2017), the presence of a monastery and some local bedrock in the middle of the entrance of the embayment may have had a forcing effect on the inflow location and direction of the tidal channels. Similarly, the local confinement present eastward in the embayment could force the main confluence location there. The observation in our experiments, where major confluences and narrow zones in the outline are self-formed thus fits with observations in this natural system. In addition, Levoy et al. (2017) recorded that infill of channels by reworking of bar sediments can cause sudden shifts of channels, which was also observed in the experiments when an ebb channel progressively blocks the evading flood channel by forming a U-shaped bar into that channel.

Our experimental results suggest that without any human interference (e.g. dredging or bank protection), the morphodynamics of macrocells remain active: the roles and locations of ebb and flood tidal channels may reverse within approximately 1,000 tidal cycles and intertidal bars between these channels are continuously reworked. This is in contrast to natural systems under human interferences, in which dredging may cause degeneration of the affected cell and subsequently evolve into a single-channel system (Wang and Winterwerp, 2001; Jeuken and Wang, 2010; Wang et al., 2015) and for which smaller connecting channels are disappearing by marsh formation on top of the shoals (Swinkels et al., 2009). Open questions include what the effect of dredging and dumping will be on the morphodynamics of estuaries and how an engineered estuary compares to a reference case with exactly the same initial and boundary conditions but without any human interference.

6.5 Conclusions

An experiment in a periodic tilting flume revealed the long-term evolution of channel and bar patterns in self-formed estuaries. Typically, in the landward part a stable meandering channel forms, whereas in the seaward part dynamic channels and bars form that periodically shift laterally. The estuary banks are eroded in phases when forced midchannel bars are present, which results in an estuary planform that is locally wider than the ideal converging shape. Zones with abundant and dynamic bars are separated by locations of channel confluences. We conclude that stable confluence locations in self-formed estuaries are controlled by the spacing of tidal bars, which both are a function of estuary width. The channels between the stable confluences are highly dynamic, which results in a quasiperiodic estuary planform.

The self-formed experimental estuary specifically shows that major confluences occur at relatively narrow parts in the outline and that these confinements are self-formed by sidebar formation. This corresponds to observations in natural systems in which major confluences also occur at self-formed confinements, for example, by salt marsh formation, as well as at forced confinements, for example, by inherited geology or human engineering. However, natural channels and bars are limited in their dynamics, because channels are largely fixed or maintained in place. While the ideal estuary shape may be applicable to tidal creeks and branches of deltas in equilibrium, the experimental results and observations in natural systems suggest that in self-formed alluvial estuaries in absence of any external forcing (geology and human influence) an autogenically-formed quasiperiodic estuary planform evolves.

Acknowledgments

Detailed reviews by Bob Dalrymple, one anonymous reviewer and steer by the Editor and Associate Editor helped to improve the manuscript. The authors contributed in the following proportions to conception and design, data collection and processing, analysis and conclusions, and manuscript preparation: JRFWL(55,45,75,75%), LB(5,45,0,0%), WMvD(5,5,10,10%), TdH(5,5,5,5%), MGK(30,0,10,10%). EPvO conducted scaled gravity wave experiments in the Metronome and analysed the resulting data as part of his MSc research and BGR contributed to conception and design of the wave scaling. The online supplement contains a movie with the time-lapse of the experiment.

Supplementary material

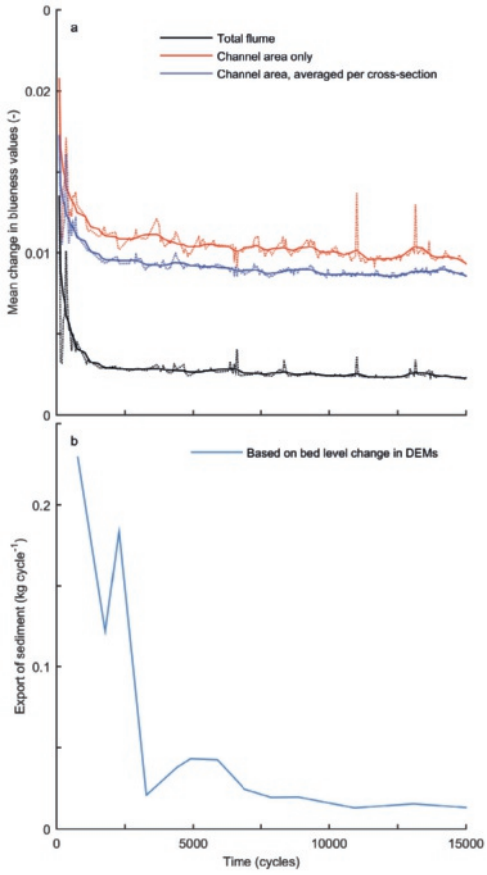

Figure 6.14 (a) Mean change in blueness values per time step is a proxy for the dynamics of channels and bars in the experiment. Three methods were used to calculate the mean change in blueness: by calculating the mean change for the full flume, (1) including the estuary banks, (2) excluding the estuary banks and (3) calculating a mean value per cross-section and using the average of these values. (b) Export of sediment from the estuary (in kg cycle^{-1}) as calculated from successive DEMs. The temporal resolution of DEMs is lower, but the trend is similar as for the blueness values. The evolution of these profiles over time shows that the experiment was close to dynamic equilibrium in the final stages of the experiment.

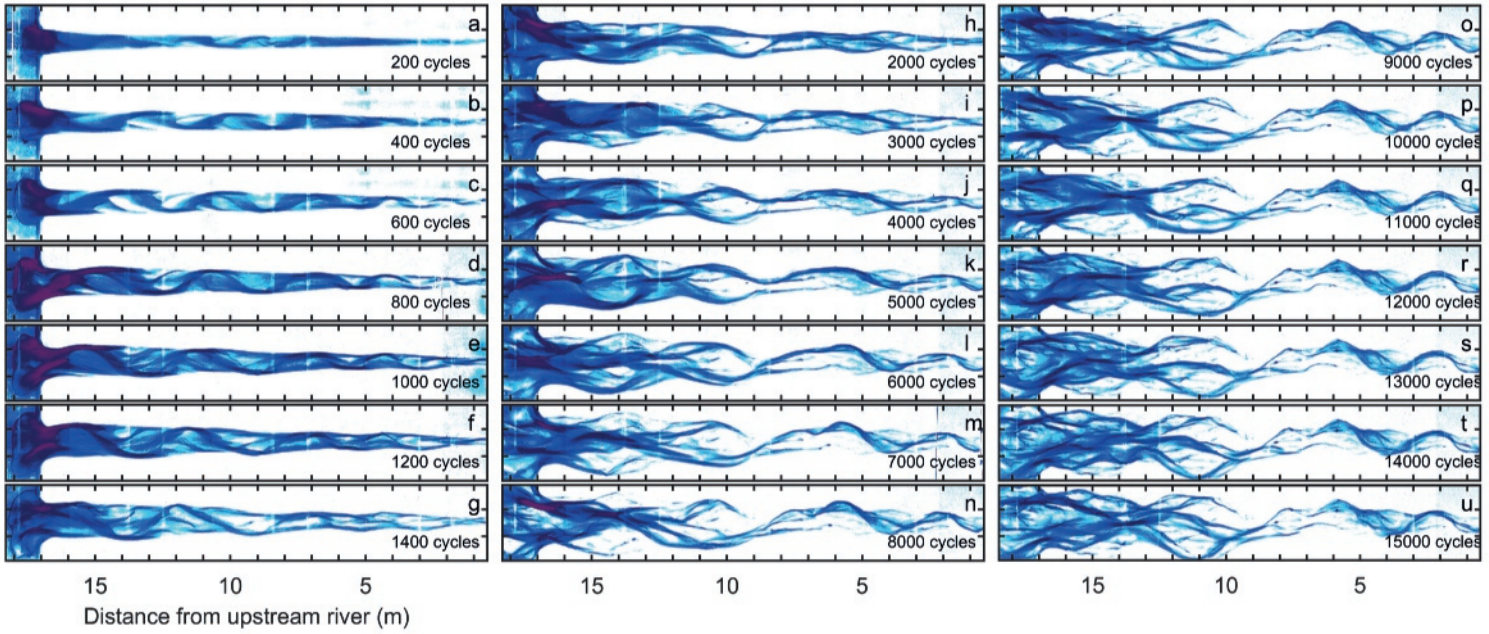

Figure 6.15 Time series of overhead imagery of the main experiment. Blueness is an indicator for channel depth. Estuary evolution started off with an initially straight converging channel. Within the first 500 tidal cycles an alternate bar pattern formed, which later evolved into multiple braided bars. The formation of midchannel bars caused flow diversion and bank erosion, resulting in a progressively more irregular estuary planform.

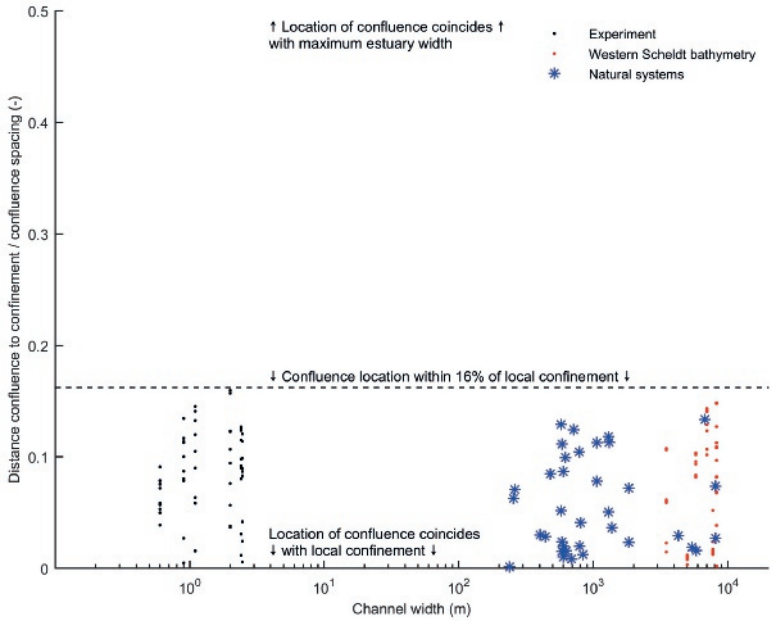

Figure 6.16 To study the location where confluences occur, the distance between the confluence location and the local minimum in estuary width was measured. For natural systems locations were selected based on the occurrence of major confluences and relatively deep scours in the main channel. For the experiments and bathymetry of the Western Scheldt, confluence locations were determined as the locations with the maximum depth within the zone of two successive maximum estuary widths. In all cases, confluence locations occurred within a distance of maximum 16% of confluence spacing from the local confinements.

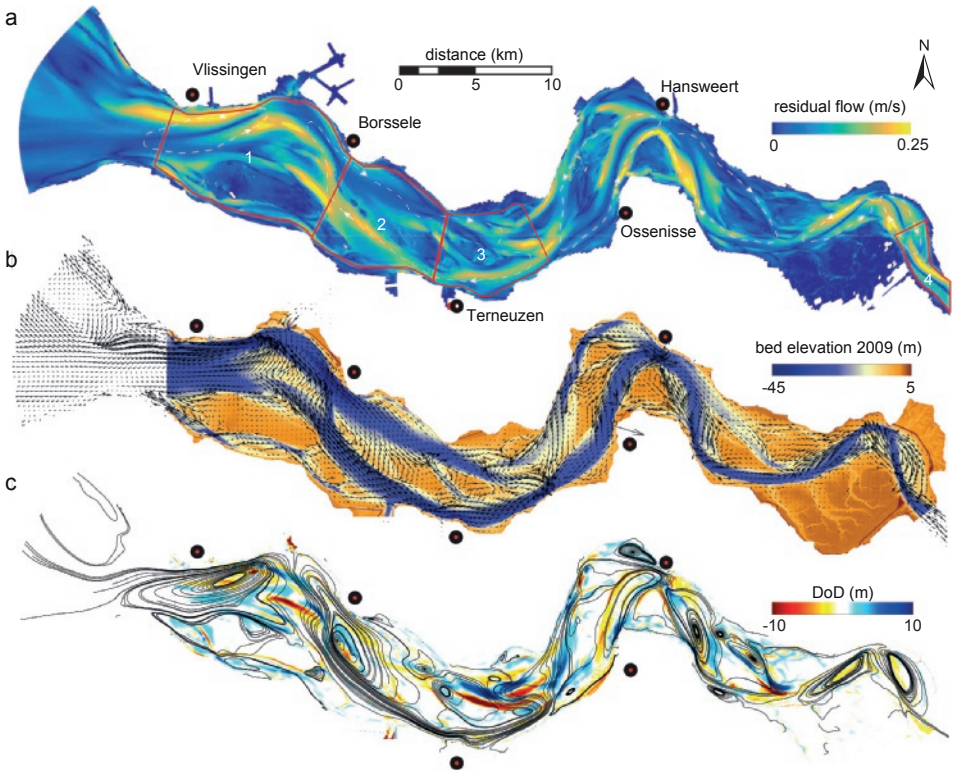

Figure 6.17 (a) Residual currents based on the outcome of a calibrated hydrodynamic model of Rijkswaterstaat (SCALWEST, Verbeek et al., 2000) for the bathymetry of the Western Scheldt in 2009. The white dotted lines indicate the chain of macro-cells that schematize the channel system (modified from Winterwerp et al., 2001). Red boxes show the zones for which hypsometric curves are calculated in this chapter. (b) Vectors indicating the residual currents, drawn on top of the bathymetric map of 2009. (c) Streamlines based on a vector field of the residual currents, plotted on top of a map that indicates the erosion (red) and sedimentation (blue) from the bathymetry data of 2009 and 2015.

6.5.1 Scaling of gravity waves generated in the Metronome tidal facility

Methodology

Two types of experiments were performed to study the effect of gravity waves generated in the Metronome tidal facility: (1) wave transformation experiments without tidal flows and (2) morphological experiments including waves and tidal flows.

Regular waves were generated in the Metronome with a horizontal paddle. The wave generator did not obstruct tidal flow from flowing in and out the constant head tank. The wave paddle was oriented perpendicular to the flume resulting in offshore wave propagation parallel to the Metronome's major axis. The horizontal wave paddle measured 3 m by 0.1 m and generated waves over the full width of the flume by vertical motion. Frequencies between 2 and 2.5 Hz were used; test runs with waves with lower frequencies were found to not mobilise the sediment at all and higher frequencies were technically impractical and would have led to oversteepened waves and breaking off the paddle. A wave generator frequency of 2 Hz yielded waves with a wavelength of about 0.3 m and height of about 0.01 m when the water depth was about 0.065 m.

Wave transformation was measured and sediment mobility was assessed in two wave measurement experiments described in van Onselen (2017): (Exp. 3) a straight coastline with a steep, linear beach profile, and (Exp. 4) a submerged semi-circular flat off a straight coast, with an idealised shape but similar dimensions as the deltas that formed in the sea during our estuary experiments (Suppl. Table 6.1). This flat was exposed to waves for 24 hours to assess the morphological changes by waves in isolation from the tidal flows, but morphological effects were so minor that they were not recorded. Therefore, the effect of the waves on the morphology of the estuary and ebb-tidal delta was measured during a series of control experiments in the tilting flume with and without waves, which included tidal flows generated by tilting (see main text of this chapter for methodology and Braat et al. (2019) for the other control experiments).

During both experiments, water surface was recorded for two minutes by a downward-looking Massa M320/150 single beam echo sounder (SBES) with a sampling frequency of 20 Hz and a footprint diameter of about 0.02 m. Measurements were conducted in the center of the flume at a 0.02-0.05 m interval depending on where the largest gradient of wave height was expected. Skewness and asymmetry, which can result in net onshore sediment transport (Hoefel and Elgar, 2003; Ruessink et al., 2011; Brinkkemper et al., 2018), were calculated according to definitions by Elgar (1987).

Table 6.1 Overview of conducted wave experiments.

Parameter	Exp. 3	Exp. 4
Coastal profile type	Straight	Delta
Cross-shore basin length (m)	2	1.7
Slope of coastal profile (m/m)	1:05	1:01
Offshore water depth, h_{off} (m)	0.069	0.062
Offshore mean wave height, H_{off} (m)	0.012	0.009
Input wave frequency, f (Hz)	2.5	2.25
Offshore wavelength, L_{off} (m)	0.22	0.28
Offshore wave celerity, C_{off} (m/s)	0.55	0.63

Wave transformation and sediment mobility

Cross-shore profiles of the wave parameters are given in Suppl. Fig. 6.18 with typical locations of the breakpoint being indicated in Suppl. Fig. 6.18b. The water depth at the coast was so shallow that waves dissipated over a short distance (e.g. between x=0.34-0.45 m in Suppl. Fig. 6.18b for Exp. 4 with delta).

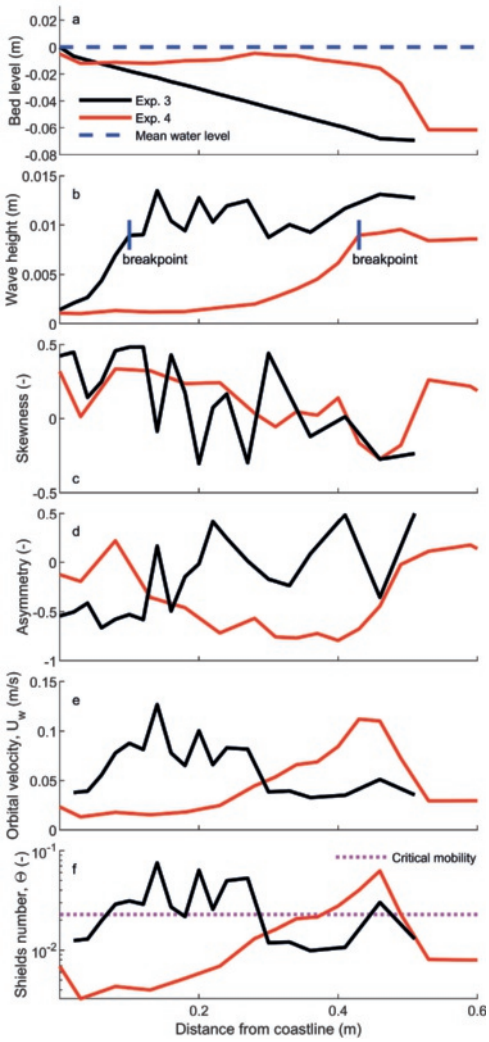

Figure 6.18 (a) Imposed morphology of the coast in Exp. 3 with a 1:5 slope straight sloping coast [black] and in Exp. 4 with a delta [red]. (b) Measured wave height. Parameters derived from sea-surface elevation: (c) skewness, (d) asymmetry. Parameters calculated from measured wave parameters: (e) maximum near-bed orbital velocity and (f) Shields number with mobility threshold.

The wave skewness slightly increased in onshore direction, but cross-shore variation was large (Suppl. Fig. 6.18c). The skewness in the experiment was much lower than under natural shoaling and breaking waves (Ruessink et al., 2012). In the case of a straight linear sloping coast (Exp. 3), asymmetry did not show a clear trend in onshore direction (Suppl. Fig. 6.18d). However, in the case of the delta (Exp. 4), asymmetry decreased to -1 where waves break (x=0.4-0.5 m in Suppl. Fig. 6.18d) and then reduced back to 0 towards the coast. This is in contrast to cross-shore trends observed on natural coasts and values in the experiment are lower as well (Ruessink et al., 2012).

On-shore transport caused by waves is likely to be underdeveloped compared to natural systems because the skewness and asymmetry of waves is underdeveloped (Suppl. Fig. 6.18b,c). Moreover, the

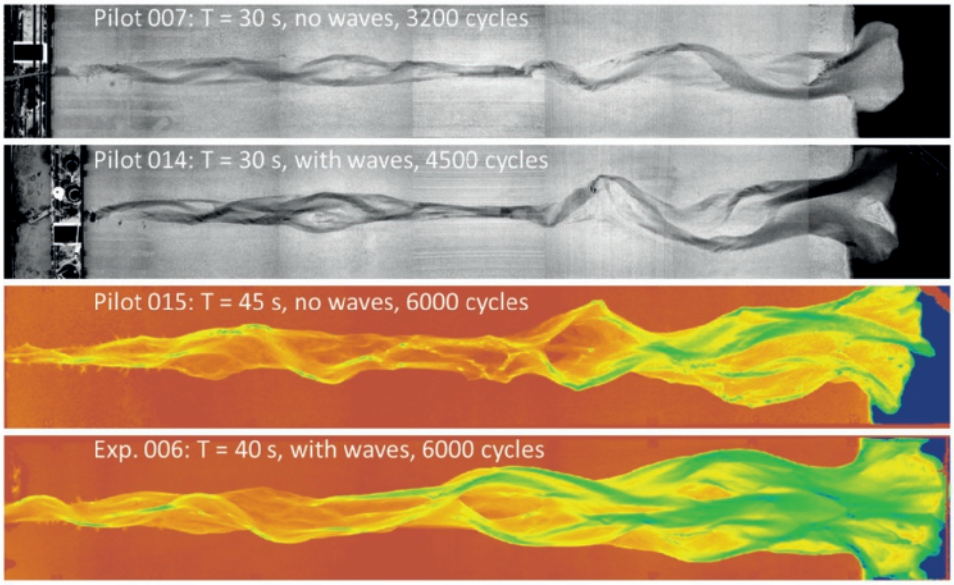

Figure 6.19 [top] Overhead imagery of pilot 007 without waves and pilot 014 with waves. [bottom] Bathymetry of pilot 015 without waves and Exp. 006 with waves. Exp. 006 is the experiment reported in the main text of this chapter. Length of the flume is 20 m. Colours in the bathymetry are stretched between -5 cm (blue) and 0 cm (red), which is the level of the plane sediment bed.

calculated sediment mobility was very close to the threshold of motion (Suppl. Fig. 6.18f). Values were thus much lower than under breaking waves at natural coasts (were Shields numbers are typically 0.5-1.0), which resulted in experimental conditions in which sediment only became mobile in a very narrow zone at the most seaward tip of the delta (Exp. 4) or in case of a straight coast (Exp. 3) approximately 0.2 m in front of the coast (Suppl. Fig. 6.18f).

6.5.2 Morphological effect during estuary experiment with tilting flume

Even though the induced mobility due to only waves was too low (Suppl. Fig. 6.18f) to affect the morphology, a combination with periodically tilting the flume to obtain tidal flows clearly affected the morphology of the seaward part of the estuary and the ebb-tidal delta (Suppl. Fig. 6.19).

The waves stirred the sediment in narrow zones during flood flow only, which subsequently redistributed the sediment in the delta area. The more even distribution of sediment resulted in a smoother delta planform with lower height differences between the channels and delta lobes (Suppl. Fig. 6.19). Moreover, the addition of waves resulted in a larger but shallower delta. Without waves, the delta lobes were more pronounced and the shape was more irregular, because the lobes formed after capturing the main outflow and subsequently avulsed. Locally, shallower wave-formed deposits developed as in the idealised delta experiment without tides.

The elevation of the delta also affected the height of bars in the most seaward part of the estuary. For example, in pilot 015 without waves, the bar height in the seaward part of the estuary was considerably higher than in Exp. 006 with waves (Suppl. Fig. 6.19). Visual observations suggest that the inner estuary remained morphologically more active when waves subdue the delta, perhaps due to stronger tidal penetration and the sediment stirring effect of waves that penetrated the estuary superimposed on the flood-tidal current.

Implications for scaled (estuary) experiments

Even though wave height in our experiments was relatively large compared to the offshore water depth ($\pm$0.15), the resulting sediment mobility was considerably lower than in natural sandy systems (Suppl. Fig. 6.18f). Sediment only became mobile in a very narrow zone at the most seaward tip of the delta (Exp. 4) or in case of a straight coast (Exp. 3) approximately 0.2 m in front of the coast (Suppl. Fig. 6.18f). If higher wave-induced mobility is desired in future scale experiments, it is recommended to lower sediment density or use higher and steeper waves. While the latter might improve the similarity to natural systems, it also implies a larger distortion in the vertical scaling of the experiment. Therefore, we conclude that the present paddle-generated waves can aid in scale experiments to smoothen out the lobate morphology of deltas, but sediment transport is too small to induce significant on-shore transport or transport of sediment back into the estuary other than through wave-stirring.

Chapter 7 | Morphology of bar-built estuaries: Empirical relation between planform shape and depth distribution

Abstract

Fluvial-tidal transitions in estuaries are used as major shipping fairways and are characterised by complex bar and channel patterns with a large biodiversity. Habitat suitability assessment and the study of interactions between morphology and ecology therefore require bathymetric data. While imagery offers data of planform estuary dimensions, only for a few natural estuaries are bathymetries available. Here we study the empirical relation between along-channel planform geometry, obtained as the outline from imagery, and hypsometry, which characterises the distribution of along-channel and cross-channel bed levels. We fitted the original function of Strahler (1952) to bathymetric data along four natural estuaries. Comparison to planform estuary shape shows that hypsometry is concave at narrow sections with large channels, while complex bar morphology results in more convex hypsometry. We found an empirical relation between the hypsometric function shape and the degree to which the estuary width deviates from an ideal convergent estuary, which is calculated from river width and mouth width. This implies that the occurring bed-level distributions depend on inherited Holocene topography and lithology. Our new empirical function predicts hypsometry and along-channel variation in intertidal and subtidal width. A combination with the tidal amplitude allows for an estimate of inundation duration. The validation of the results on available bathymetry shows that predictions of intertidal and subtidal area are accurate within a factor of 2 for estuaries of different size and character. Locations with major human influence deviate from the general trends because dredging, dumping, land reclamation and other engineering measures cause local deviations from the expected bed-level distributions. The bathymetry predictor can be used to characterise and predict estuarine subtidal and intertidal morphology in data-poor environments.

Published as: Leuven, J.R.F.W., Selaković, S. & Kleinhans, M.G. (2018). Morphology of bar-built estuaries: Empirical relation between planform shape and depth distribution. *Earth Surface Dynamics, 6 (3), pp. 763–778*, DOI: 10.5194/esurf-6-763-2018.

7.1 Introduction

Estuaries develop as a result of dynamic interactions between hydrodynamic conditions, sediment supply, underlying geology and ecological environment (Townend, 2012; de Haas et al., 2017). One model for the resulting morphology is that of the "ideal estuary" that is hypothesised to have along-channel uniform tidal range, constant depth and current velocity, and a channel width that exponentially converges in the landward direction such that the loss of tidal energy by friction is balanced by the gain in tidal energy by convergence (Savenije, 2006; Savenije, 2015; Townend, 2012; Dronkers, 2017). One would expect that in this case the along-channel variation in hypsometry is also negligible. However, natural estuaries deviate from ideal ones as a result of a varying degree of sediment supply, lack of time for adaptation and sea-level rise (Townend, 2012; de Haas et al., 2017), and locations wider than ideal are filled with tidal bars (Chapter 5) (Fig. 7.1). Differences in bed-level profiles between ideal and nonideal estuaries are further enhanced by damming, dredging, dumping, land reclamation and other human interference (e.g. O'Connor, 1987; Wang and Winterwerp, 2001; Lesourd et al., 2001; Jeuken and Wang, 2010; Wang et al., 2015). All these natural deviations from the ideal estuary mean that there is no straightforward relation between the planform geometry of the estuary and the hypsometry or distribution of depths.

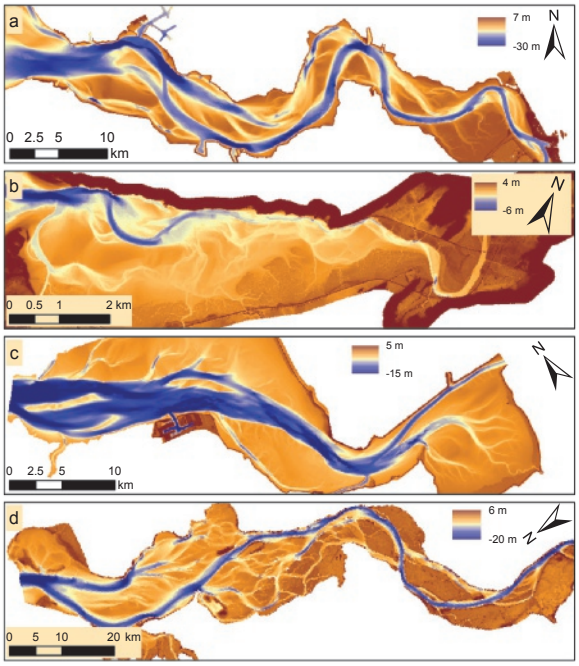

Figure 7.1 Bathymetry from (a) the Western Scheldt (NL), (b) the Dovey (Wales), (c) the Ems-Dollard (NL) and (d) the Columbia River Estuary (USA). Source: (a,c) Rijkswaterstaat (NL), (b) Natural Resources Wales, (d) Lower Columbia Estuary Partnership.

Hypsometry captures key elements of geomorphological features (Strahler, 1952; Boon and Byrne, 1981; Dieckmann et al., 1987; Kirby, 2000; Toffolon and Crosato, 2007; Townend, 2008; Townend, 2010; de Vet et al., 2017) (Fig. 7.2). The hypsometric method was developed by Strahler (1952) and Boon and Byrne (1981) to relate the planform area of a basin to elevation. Later the resulting functions were used to predict the influence of basin morphology on the asymmetry of the horizontal and vertical tides,

to predict flood or ebb dominance and maturity of an estuary (Boon and Byrne, 1981; Wang et al., 2002; Moore et al., 2009; Friedrichs, 2010), and to characterise the trend of salt marsh development (Gardiner et al., 2011; Hu et al., 2015). Furthermore, hypsometry was used as a data reduction method to characterise entire reaches spanning bars and channels in estuaries (Toffolon and Crosato, 2007) and shapes of individual tidal bar tops (de Vet et al., 2017). Hypsometry has also been used to describe the dimensions of channels and tidal flats in an idealised model (Townend, 2010). In the latter, a parabolic shape was prescribed for the low water channel, a linear profile for the intertidal low zone and a convex profile for the intertidal high zone. While these profiles are valid for perfectly converging channels, it is unknown to what extent they are applicable to estuaries with irregular planforms and whether the currently assumed profiles are valid to assess flood or ebb dominance. Hypsometric profiles and derived inundation duration are also relevant indicators for habitat composition and future transitions from mudflat to salt marsh (Townend, 2008). To predict and characterise the morphology and assess habitat area, we need along-channel and cross-channel bed-level predictions for systems without measured bathymetry (Wolanski and Elliott, 2015).

For only a few natural estuaries is bathymetry available, which leaves many alluvial estuaries with irregular planforms from all around the world underinvestigated. However, many estuaries are visible in detail on satellite imagery, which raises the question of whether there is a relation between planform geometry and depth distribution. Such a relation is known to exist in rivers in the form of hydraulic geometry depending on bar pattern and meander pool depths depending on planform channel curvature (e.g. Kleinhans and van den Berg, 2011; van de Lageweg et al., 2016). Therefore, it seems likely that such a relation between the horizontal and vertical dimensions exists for sandy estuaries as well, but this is not reported in the literature. Morphological models can simulate 3-D bed levels with considerable accuracy (van der Wegen and Roelvink, 2008; van der Wegen and Roelvink, 2012; van Maren et al., 2015; Braat et al., 2017), but these models are computationally intensive and need calibration and specification of initial and boundary conditions. To study unmapped systems for which only aerial photography is available, it would be useful to be able to estimate bed-level distributions from planform geometry. Here we investigate this relation.

Previously, we showed in Chapter 5 how locations and widths of tidal bars can be predicted from the excess width, which is the local width of the estuary minus the ideal estuary width. The summed width of bars in each cross section was found to approximate the excess width. This theory describes bars as discrete recognisable elements truncated at low water level on what is essentially a continuous field of bed elevation that changes in the along-channel direction (Chapter 2). However, to predict morphology in more detail, predictions of along-channel and cross-channel bed elevations are required. While hypsometry can summarise bed elevation distribution as a cumulative profile, it is unknown whether the shape of the profile is predictable. Our hypothesis is that the along-channel variation in hypsometry depends on the degree to which an estuary deviates from its ideal shape. Therefore, we expect that locations with large excess width and thus a large summed width of bars have a more convex hypsometry (Fig. 7.3c,d). In the case of an ideal estuary with (almost) no bars (Fig. 7.3a,b), we expect concave hypsometry.

The aim of this chapter is to investigate the relation between estuary planform outline and along-channel variation in hypsometry. To do so, first hypsometric curves are used to summarise the occurring bed elevations in a cumulative profile. Then, we use the original function of Strahler (1952) to fit the data obtained from the bathymetry of four estuaries (Fig. 7.1). In the results, we develop an empirical function to predict hypsometry. The quality and applications of the predictor are assessed in the discussion.

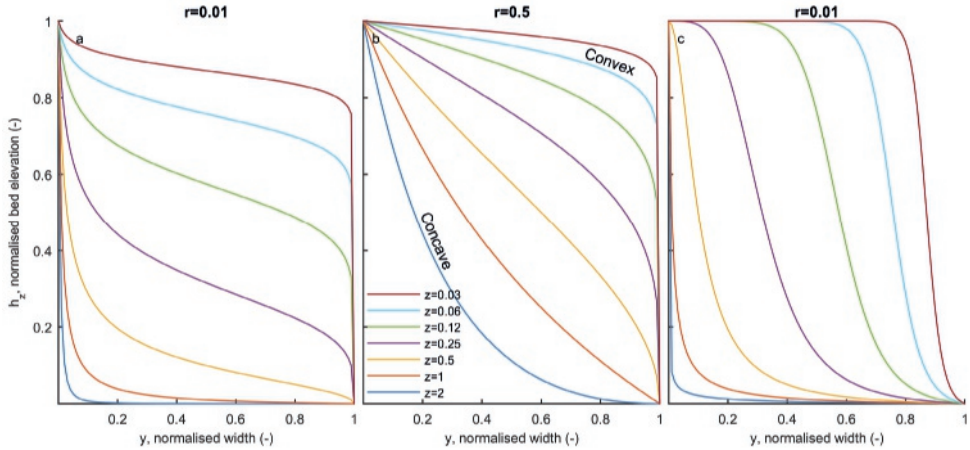

Figure 7.2 Hypsometric functions to describe morphological systems; modified from Strahler (1952). (a,b) Effect of z values with the r value kept constant. (c) Inverted version of the Strahler function (see Eq. 7.4).

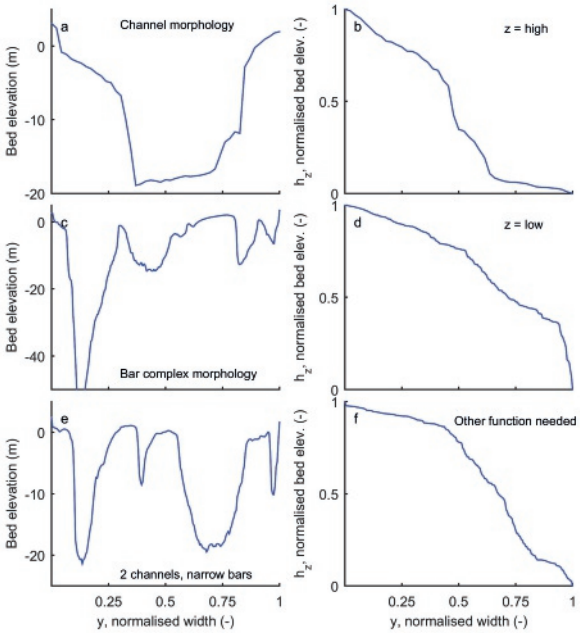

Figure 7.3 Example cross sections and hypsometry, suggesting that channel-dominated morphology (a,b) generally results in concave hypsometric functions (high z value in Fig. 7.2), while bar complexes (c,d) generally result in convex hypsometry (low z value in Fig. 7.2). In the case of narrow bars with a flat top and relatively steep transition from bar top to channel (e,f), the original hypsometry function by Strahler (1952) is less appropriate and the inverted function fits better.

7.2 Methods

In this section, first, the definition of an ideal estuary is given with a description of how we derived a geometric property that characterises deviation from an ideal shape. Second, the general form of a

hypsometric curve is described. Then, the available datasets that were used for curve fitting are given. Last, the methodology to fit a hypsometric function to bathymetry in systems is presented.

7.2.1 Deviation from "ideal"

A useful model to describe the morphology of estuaries is that of the "ideal estuary", in which the energy per unit width remains constant along-channel. The ideal state can be met when tidal range and tidal current are constant along-channel such that the loss of tidal energy by friction is balanced by the gain in tidal energy per unit width by channel convergence (Pillsbury, 1956; Dronkers, 2017). In the case that the depth is constant along-channel, the ideal estuary conditions are approximately met when the width is exponentially decreasing in the landward direction (Pillsbury, 1956; Langbein, 1963; Savenije, 2006; Savenije, 2015; Toffolon and Lanzoni, 2010), which also implies an along-channel converging cross-sectional area. However, when depth and friction are not constant along-channel, for example linearly decreasing in the landward direction, less convergence in width is required to maintain constant energy per unit of width.

Many natural estuaries are neither in equilibrium nor in a condition of constant tidal energy per unit width. They deviate from the ideal ones as a result of a varying degree of sediment supply, lack of time for adaptation to changing upstream conditions and sea-level rise (Townend, 2012; de Haas et al., 2017). Whether continued sedimentation would reform bar-built estuaries with irregular planforms into ideal estuaries remains an open question. While we expect a somewhat different degree of convergence such that the ideal state of constant energy per unit of width is approximately maintained, we do not study the deviation of this convergence length from that in ideal estuaries.

Ideally, we would assess the degree to which an estuary is in equilibrium from an aerial photograph. However, the only indicator derivable is channel width and thus deviation from a converging width profile. Therefore, in Chapter 5, we defined the excess width, which is the local width of the estuary minus our approximation of the potential ideal estuary width. Here, the ideal estuary width is approximated as an exponential fit on the width of the mouth and the width of the landward river. While the empirical measure of "ideal width" should not be confused with the "ideal state" of an estuary, it is the only practical way to estimate deviation from an ideal estuary based on the estuary outline only. Moreover, it proved to be a good indicator of occurring bar patterns (Chapter 5) and will therefore be applied in this chapter to study hypsometries.

7.2.2 General hypsometric curve

In the past, multiple authors have proposed empirical relations for the hypsometric shape of terrestrial landscapes (Strahler, 1952) and (partially) submerged bodies (Boon and Byrne, 1981; Wang et al., 2002; Toffolon and Crosato, 2007) (see Townend, 2008, for a review). All equations, except for Wang et al. (2002), predict a fairly similar hypsometric curve based on the volume and height range of the landform (Townend, 2008). While it is of interest to use these empirical relations to predict the occurring altitude variation of a landform, the framework here is different. Here, we apply the general hypsometric curve to characterise the occurring cross-sectional hypsometry along-channel. This approach is similar to the approach of Toffolon and Crosato (2007), who fitted a power function to 15 zones along the Western Scheldt. However, the zoned approach smooths out all the differences between bar complex and channel-dominated zones, which are of interest for this study. For this purpose, it is less relevant for which environment the hypsometric relation was proposed, as long as it is capable of describing the range of occurring hypsometries. For the case of the estuarine environment (Fig. 7.3), the hypsometric curve should be able to describe variations in concavity and variations in the slope of the curve at the inflection point. Here we use the original Strahler (1952) formulation, which is capable of doing so, but in principle any equation that fits well could be used.

Strahler (1952) formulated the general hypsometric curve as

$$h_z = \left[\frac{r}{r-1}\right]^z \left[\frac{1}{(1-r)y + r} - 1\right]^z, \tag{7.1}$$

in which h_z is the value of the bed elevation, above which fraction y of the width profile occurs. In other words, h_z is the proportion of total section height and y the proportion of section width. r sets the slope of the curve at the inflection point in a range of 0.01–0.50, with sharper curves for lower values of r (Fig. 7.2a,b). z determines the concavity of the function in a range of 0.03–2, with lower values giving a more convex profile and higher values giving a more concave profile (Strahler, 1952) (Fig. 7.2). Our approach changes the original definition of r and z to make them fitting parameters. It is expected that z values depend on excess width because the fraction of the width occupied by bars becomes larger with excess width, resulting in a more convex hypsometric profile (Fig. 7.3c,d), or the presence of bars generates excess width.

Excess width is defined as the local width minus the ideal width, which is given by

$$W_{\text{ideal}}(x) = W_{\text{m}} \cdot e^{-x/L_{\text{W}}}, \tag{7.2}$$

in which x is the distance from the mouth, W_{m} the width of the mouth and L_{W} is the width convergence length (Davies and Woodroffe, 2010), which can be obtained conservatively from a fit on the width of the mouth and the landward river width (Chapter 5):

$$L_{\text{W}} = -s \frac{1}{\ln\left(\frac{W_{\text{s}}}{W_{\text{m}}}\right)}, \tag{7.3}$$

in which W_{m} is the local width measured at the mouth of the estuary, W_{s} is the width measured at the landward side of the estuary and s is the distance between these locations measured along the centreline. This practical method makes the convergence length somewhat sensitive to the selected position of the seaward and landward limit.

The landward limit was selected at the location where the width ceases to converge on an image at the resolution of the full estuary scale and the landward width was measured between the vegetated banks. The seaward limit was selected as the location with the minimum width in the case that bedrock geology, human engineering or a higher elevated spit confined the mouth because in these cases the minimum width limits the inflow of tidal prism. In other cases, the mouth was chosen at the point at which the first tidal flats were observed in the estuary or the sandy beach ends at the mouth of the estuary. However, when the mouth is chosen at a location where sand bars are present, the ideal width will be overestimated and the width of intertidal area underestimated. It is therefore recommended to either choose the mouth at a location where bars are absent or subtract the width of bars from the measured width at the mouth to obtain the ideal width profile.

7.2.3 Data availability and classification

Detailed bathymetries were available for four systems: the Western Scheldt Estuary (NL), the Dovey Estuary (Wales), the Ems-Dollard Estuary (NL) and the Columbia River Estuary (USA) (Fig. 7.1, Table 7.1). Data for the Western Scheldt and Ems-Dollard were obtained from Rijkswaterstaat (NL), for the Dovey Estuary from Natural Resources Wales and for the Columbia River Estuary from the Lower Columbia Estuary Partnership. Bed elevations were extracted from these bathymetries as follows. First, the estuary outline was digitised, excluding fully developed salt marshes, and subsequently a centreline was determined within this polygon (following the approach in Chapter 5). Bed elevations were collected on equally spaced transects perpendicular to the centreline of the estuary. The bed levels extracted at each transect were subsequently sorted by bed-level value and made dimensionless to obtain hypsometric profiles (see Fig. 7.3 for examples).

Table 7.1 Characteristics of the estuaries used in this study. h_m is the maximum depth at the mouth, h_r is the maximum depth at the landward river, W_m is the width at the mouth, W_r is the width at the landward river, a is the tidal amplitude, "Area" is the surface area, "% intertidal" is the percentage of intertidal area and Q_r is the river discharge.

	h_m (m)	h_r (m)	W_m (m)	W_r (m)	$2a$ (m)	Area (km^2)	% intertidal	Q_r (m^3 s^{-1})
Western Scheldt	25	15	4500	350	5	300	20	100
Columbia River Estuary	40	20	4000	800	2.5	900	30	7000
Dovey	10	2	450	50	3	12	75	30
Ems-Dollard	25	8	3500	350	3.5	260	30	80

We classified the transects by morphological characteristics and potential susceptibility to errors. The following morphological classes were used: mouth, bar junction, bar complex, narrow bar, point bar, channel, pioneer marsh. The mouth is the location where the estuary transitions into the sea. A bar junction is the most seaward or most landward tip of tidal bars. A bar complex, also called a compound bar, is a location where a large bar is dissected by barb channels (Chapter 2) or multiple smaller bars are present. Narrow bar is used when the bars present were narrow along their entire length and often also relatively flat on their top. Point bar is a bar in the inner bend of a large meander. Channel was assigned when bars were largely absent. Pioneer marsh was assigned when aerial photographs or bathymetry gave visual indications of initial marsh formation, such as the presence of small tidal creeks and pioneering vegetation. Fully developed marsh is excluded from the outline.

The following classes were used to indicate possible errors: the presence of harbours, major dredging locations, the presence of a sand spit, the presence of drainage channels for agriculture, constraints by hard layers, human engineering works. Either a locally deep channel or scour occurred at one of the sides of these transects or they lacked a natural transition from channel to estuary bank, thus ending in their deepest part on one side of the transect. Major dredging locations have unnaturally deeper channels and shallower bars, resulting in a hypsometric shape that is relatively flat in the highest and lowest part and is steep in between (Fig. 7.3e,f). Furthermore, in a few cases side channels were perpendicular to the orientation of the main channel of the estuary. This resulted in transects being along-channel of these side channels, which biases transect data towards larger depth and creates a flat hypsometric profile at the depth of the side channel.

7.2.4 Data processing

Least-squares fits resulted in optimal values of z and r in Eq. 7.1 (Fig. 7.2) for each transect, using three different approaches. First, a regular least-squares curve fitting was used for r and z, which resulted in along-channel varying values for z, but an almost entirely constant along-channel value for r of 0.5 (Fig. 7.4b,c, solid lines). In the second approach we set r to a constant value of 0.5 and only fitted to obtain z (Fig. 7.4c, dashed line). We found that the quality of the fit was the same, as indicated by the root mean square error (RMSE) (Fig. 7.4d), and therefore apply this second approach in the remainder of this chapter.

Locations where the RMSE was relatively large correspond to locations where major dredging occurred in the past century. This possibly resulted in a hypsometry characterised by a larger fraction of the width occupied by high tidal flats, a larger fraction of the width occupied by deep channels and a smaller fraction of the width occupied by the zone between channels and bars (Fig. 7.3e,f). Because the hypsometric curve at these locations deviated from the original Strahler function (Eq. 7.1), our third approach was to apply a modified function to find optimal values for z and r. To do so, the original formulation of Strahler (1952) was inverted to allow for hypsometries that describe steep

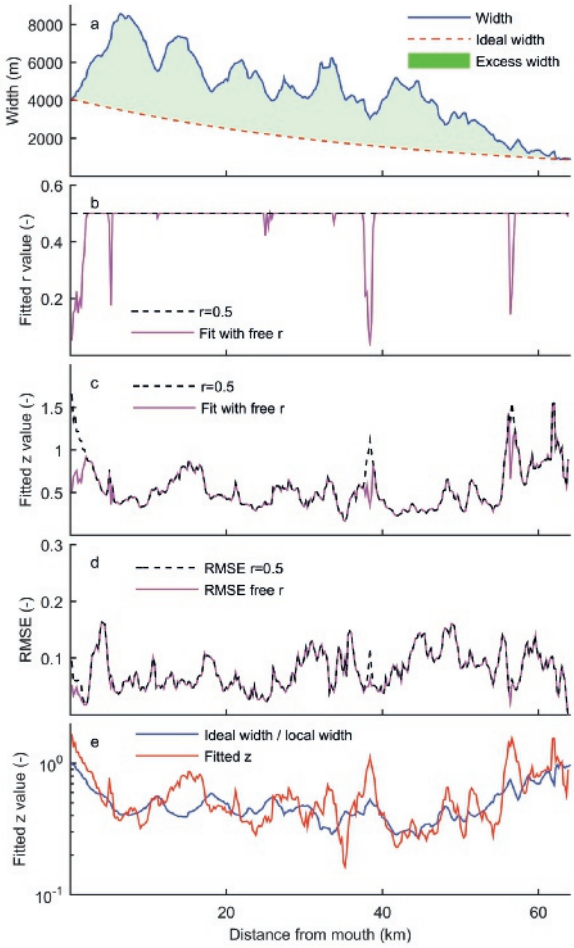

Figure 7.4 (a) Width along the Western Scheldt, with the maximum ideal converging width profile indicated. The green area is defined as the excess width cf. Chapter 5. For each along-channel transect of the estuary, the optimal fit of z and r in the Strahler (1952) function (Fig. 7.2, Eq. 7.1) was determined. (b,c) Results for the Western Scheldt when both z and r are freely fitted (solid line) and the results when r is fixed to a constant value of 0.5 (dashed line). (d) The quality of the fits remains about the same when r is set to a fixed value of 0.5 as indicated by the root mean square error (RMSE). (e) Fitted z values show similar trends as the ideal width divided by local width.

transitions from bar top to channel bottom because the original does not fit nearly as well:

$$h_{z,\mathrm{inv}} = \frac{\left[\frac{y^{1/z(1-r)}}{r} + 1\right]^{-1} - r}{1 - r}. \tag{7.4}$$

Applying this modified function resulted in better fits, but only at locations that were classified to be excluded because of possible errors. Therefore, results from this approach are not shown here and it is suggested to study the effect of dredging and dumping on hypsometry in more detail in future studies.

In principle, both the bed elevation (h_z) and the width fraction y in Eq. 7.1 are dimensionless. To compare the resulting predictions with measured values, the prediction needs to be dimensionalised.

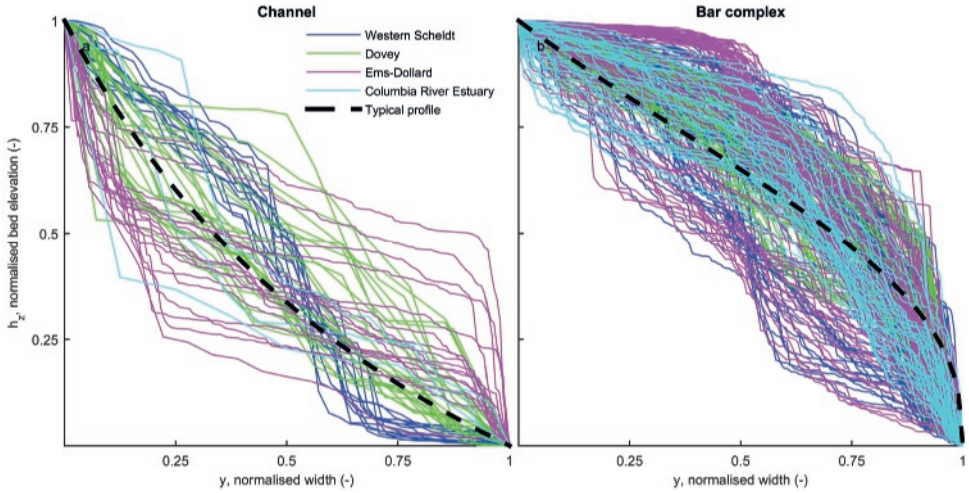

Figure 7.5 Hypsometric curves as extracted from bathymetry in the Western Scheldt, Dovey, Ems-Dollard and Columbia River Estuary. Cross-sectional profiles were extracted along the centreline and were subsequently classified as channel when sand bars were (mostly) absent and as bar complex when one larger bar dissected by barb channels or multiple smaller bars was present. Channel-dominated morphology generally results in concave hypsometric profiles (a) and bar complexes in convex profiles (b).

Values for y are scaled with the local estuary width. We test three options to scale h_z. The first option is to scale h_z between the highest bed elevation and lowest bed elevation in the given cross section, which is sensitive to the precise cut-off of the bathymetry. The second option is to scale h_z between the local high water level (HWL) and the maximum estuary depth in that cross section, which is sensitive to bathymetric information that is usually not available in unmapped estuaries.

The third option requires a prediction of depth at the upstream or downstream boundary. Width-averaged depth profiles along estuaries are often (near) linear (Savenije (2015) and Chapter 5), which includes horizontal profiles with constant depth. Therefore, only the channel depth at the mouth of the estuary and at the upstream river have to be estimated, and subsequently a linear regression can be made. Channel depth at an upstream river (h_r) is estimated with hydraulic geometry relations (e.g. Leopold and Maddock Jr, 1953; Hey and Thorne, 1986): $h_r = 0.12 W_r^{0.78}$. The depth at the mouth is estimated from relations between tidal prism and cross-sectional area (e.g. O'Brien (1969), Eysink (1990), Friedrichs (1995), Lanzoni and D'Alpaos (2015), and Gisen and Savenije (2015) and Chapter 5). Here we used

$$h_m = \frac{0.13 \times 10^{-3} P}{W_m}, \tag{7.5}$$

in which P is the tidal prism, which can be estimated by multiplying the estuary surface area with the tidal range (Chapter 5). This assumes a flat water surface elevation and constant tidal range along the estuary and neglects portions of the estuary that might get dry during the tidal cycle (Boon, 1975). Locally, the maximum depth may be deeper or lower than predicted due to the presence of resistant layers in the subsurface or where banks are fixed or protected. While this may affect the accuracy of the locally predicted maximum channel depth, it has a minor effect on the calculations of subtidal and intertidal area. Moreover, the upper limit for dimensionalisation is chosen as the high water line, which

implies that the supratidal area is not included in the predictions. We will show results with all methods, but only the third can be applied when information about depth is entirely lacking.

Statistical analyses in the remainder of the chapter were approached as follows. In linear regressions, we minimised residuals in both the x and y directions. This results in regressions that are more robust than when residuals in only one direction are minimised. In the case that regressions are plotted, the legend will specify the multiplication factor that the confidence limits plot above or below the trend. R^2 values are given to indicate the variance around the regression. In cases in which the quality of the correlation between two along-channel profiles is assessed, we used the Pearson product-moment correlation coefficient (r).

7.3 Results

We found a strong relation between along-channel variation in hypsometry and the degree to which an estuary deviates from its ideal shape. Below, we will first show how the hypsometry of typical channel morphology deviates from that of bar complexes. Subsequently, the data are presented per system and classified on their morphology and potential for errors due to human interference, method and other causes. Then we combine all data to derive an empirical relation to predict hypsometry. Last, we apply this relation to predict the along-channel variation in intertidal and subtidal width and validate the results with measurements from bathymetry.

7.3.1 Empirical relation between morphology and hypsometry

As hypothesised, it is indeed observed that channel-dominated morphology results in more concave hypsometry profiles (high z value), while bar complex morphology results in more convex hypsometry (low z value) (Fig. 7.5). Values for z in Eq. 7.1 range from 0.83 to 1.14 for channels, with an average value of 1.0. In contrast, z ranges from 0.36 to 0.41 for bar complexes, with an average of 0.39.

Clustering of morphological classes strongly suggests a relation between hypsometry and planform estuary shape (Fig. 7.6). Mouth and channel-dominated morphologies typically plot at the right-hand side of the plots in Fig. 7.6a,c,e,g, thus being locations close to ideal width. In the case of the Western Scheldt this results in the highest values of z. In the case of the Dovey and Columbia River, the mouth region was respectively influenced by a spit and human engineering, which resulted in the formation of tidal flats on the side and thus led to a lower z value.

Bar complexes occur at the other end of the spectrum; these locations are generally much wider than the ideal shape and are characterised by hypsometries with a z value well below 1. Bar junctions, as well as narrow bars, are generally found at the transition from channel-dominated morphology to bar complex morphology and therefore also occur between these types in the plots. The point bar in the Western Scheldt (the Plaat van Ossenisse) shows hypsometry comparable to bar complexes (Fig. 7.6a), which reflects the complex history of formation by multiple bar amalgamations. Also, the locations in the Columbia River Estuary where pioneer marsh is present show the same trend as the locations where unvegetated bar complexes occur (Fig. 7.6g).

In a few cases, the transects used to extract bathymetry were not perpendicular to the main channel of the estuary. For example, landward and seaward of the point bar in the Western Scheldt (Plaat van Ossenisse) transects were inclined, covering a larger part of the channel than perpendicular transects, resulting in higher z values as a consequence of the apparent channel-dominated morphology. Immediately landward of the spit in the Dovey, transects are almost parallel to the shallow side channel. Fitting hypsometry at these locations resulted in relatively low z values because it is a relatively shallow side channel.

For the Western Scheldt and Ems-Dollard it is known at which locations major dredging and dumping takes place (e.g. Swinkels et al., 2009; Jeuken and Wang, 2010; Bolle et al., 2010; Dam et al.,

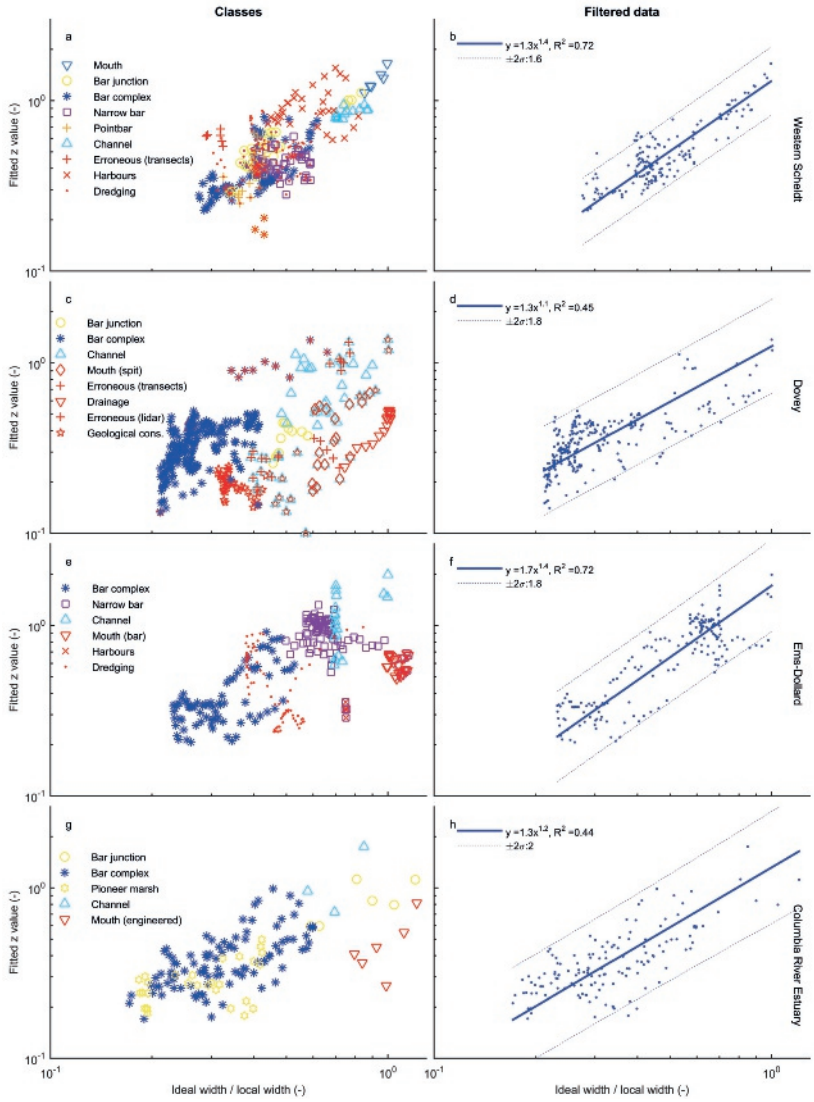

Figure 7.6 Results of hypsometry fitting in which clustering indicates a relation to planform geometry. (a,c,e,g) z values were fitted for cross-channel transects in the bathymetry of four estuaries and plotted by morphological classification. (b,d,f,h) Regressions for z value as a function of ideal width divided by local width. Data points that were influenced by human interference, bedrock geology, or errors in methodology or data, indicated in red (a,c,e,g), were excluded. Confidence limits are plotted at 2 standard deviations above and below the regression and their multiplication factor compared to the trend is given in the legend.

2015; Plancke and Vos, 2016). Even though the resulting z values at these locations do not cause major outliers, the quality of the fits is typically lower and the inverted Strahler function (Eq. 7.4) fitted better. These points were therefore excluded from further analysis.

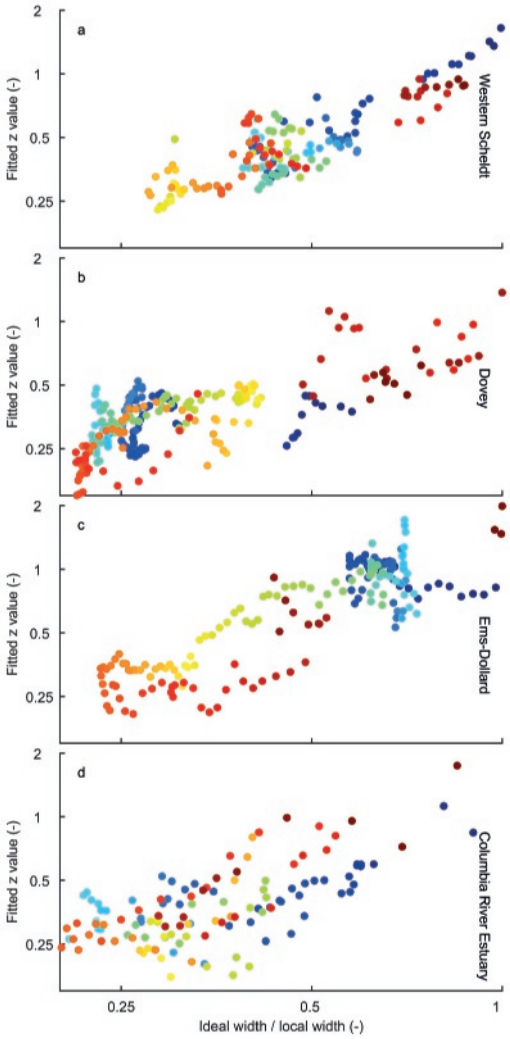

Figure 7.7 Fitted z values as a function of deviation from the ideal width. Colours indicate the location along the estuary, with dark blue colours at the mouth transitioning into dark red colours at the landward end. Some zones show scatter in fitted z values, while some other zones (e.g. green to orange to red in c) show quasiperiodic behaviour.

The filtered data show quasi-cyclicity in along-channel hypsometry (Fig. 7.7). In general, the width at the mouth of the estuary and at the upstream estuary is close to ideal and the hypsometry is concave, except in systems with wide mouths and bars in the inlet. The part in between is characterised by variations in the local width and therefore gradual increases and decreases in the ratio between local width and ideal width. In some cases, quasi-cyclic loops are visible (e.g. Fig. 7.7c) caused by the asymmetry in bar complexes. In other cases, the points show more zigzag or clustered patterns, which indicate minor variation in the bar complexes or scatter in the fit applied to the bathymetry.

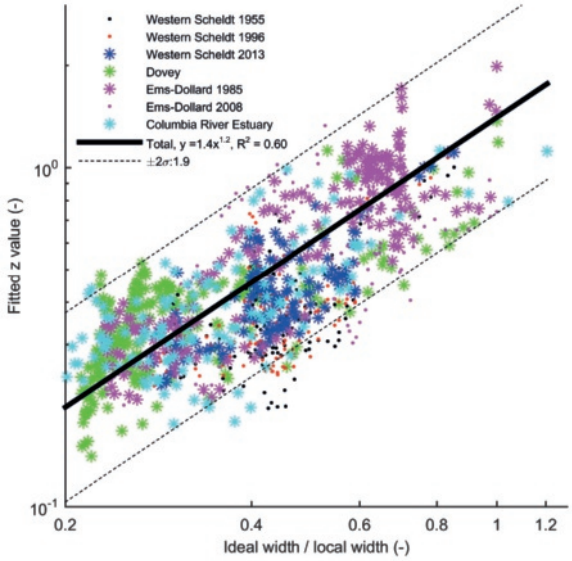

Figure 7.8 Fitted z values of filtered data increase with the fraction of ideal width and local width, which indicates that hypsometric shapes become progressively more concave when the local width approaches the ideal width and become more convex when the local width becomes larger than the ideal width (i.e. the excess width increases). The data shown as asterisks are used for the regression. Confidence limits are plotted at 2 standard deviations above and below the regression and their multiplication factor compared to the trend is given in the legend.

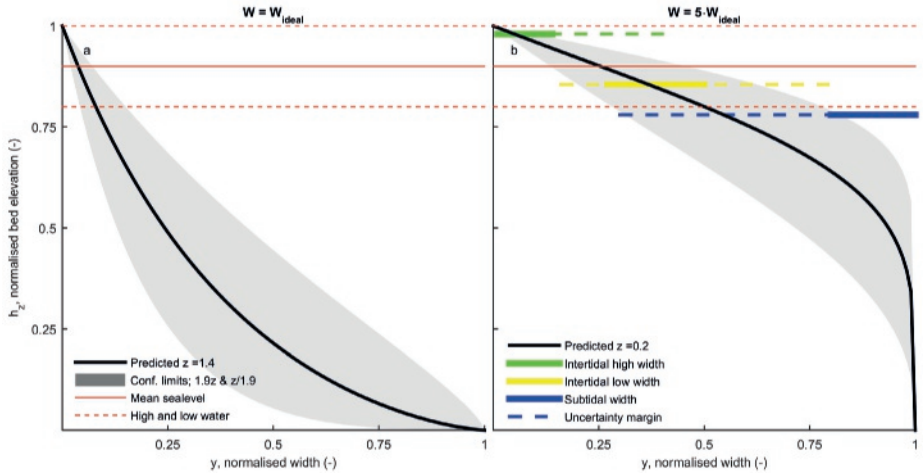

Figure 7.9 Illustration of uncertainty in the predicted hypsometry from Eq. 7.6 with uncertainty margins (Fig. 7.8). Resulting prediction for hypothetical location where (a) local width is equal to the ideal width and (b) local width is 5 times larger than the ideal width. Results are compared against a typical tidal range in order to show the uncertainty of predicted intertidal high width, intertidal low width and subtidal width as a fraction of the total estuary width.

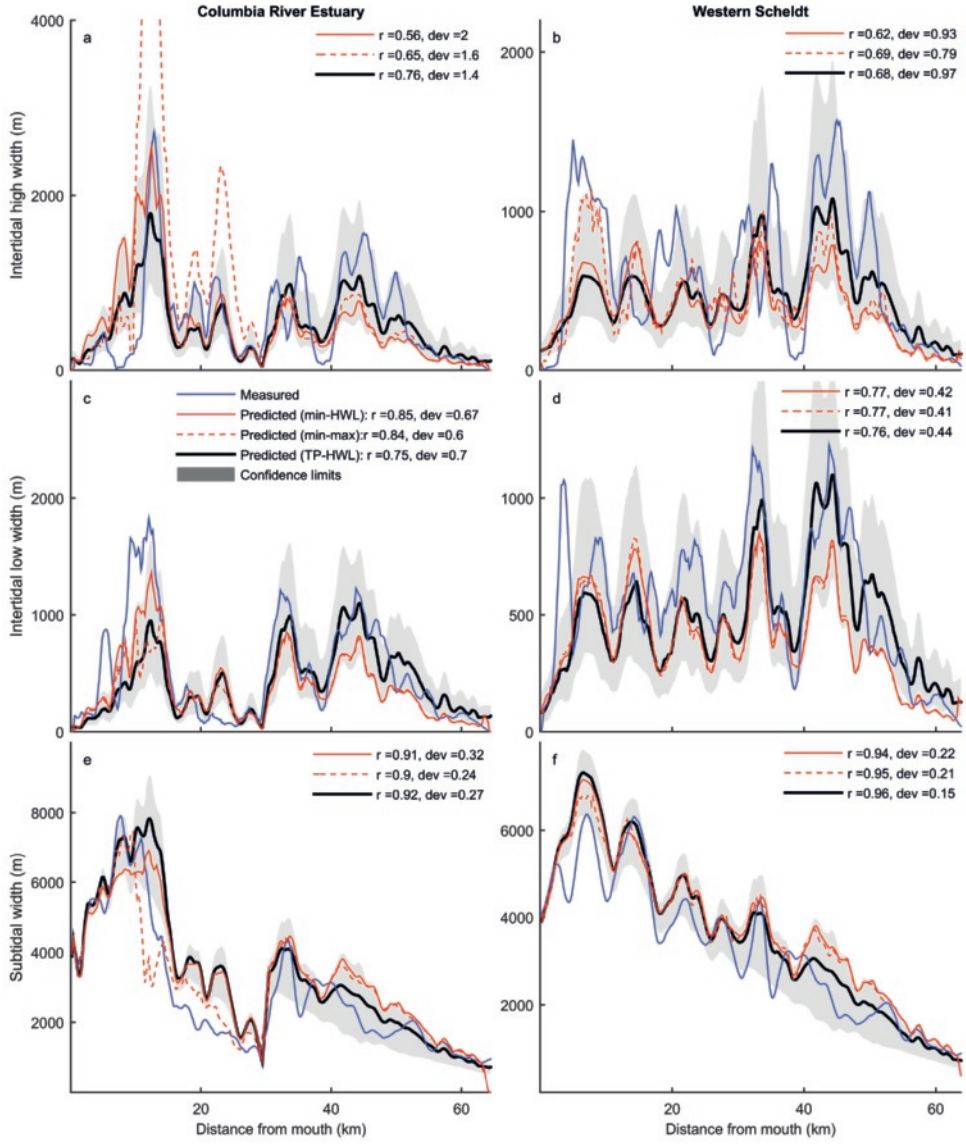

Figure 7.10 Comparison of measured and predicted values of intertidal high, intertidal low and subtidal width for the Columbia River Estuary (a,c,e) and the Western Scheldt (b,d,f). Predicted nondimensional hypsometry was dimensionalised for each cross section using three methods (explained in Methods) and uncertainty margins are given for one of the predictions (solid black line). In the legend, *r* indicates the Pearson product-moment correlation coefficient and "dev" the average factor of deviation between the predicted and measured lines.

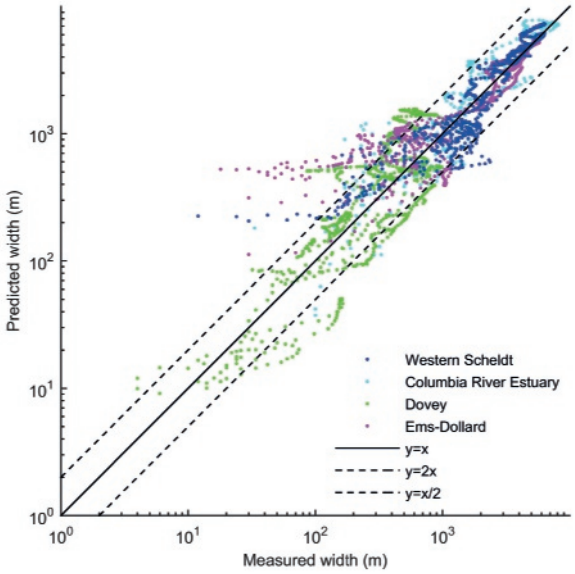

Figure 7.11 Comparison of measured and predicted width of intertidal and subtidal width. The (solid) line of equality indicates a perfect fit and dashed lines indicate a deviation of a factor of 2. The percentage of measurements within these margins is indicated in Table 7.2.

7.3.2 Hypsometry predictor

The relations between excess width and hypsometric function are similar for all estuaries, which suggests that a universal function is of value. Combining all the filtered data resulted in a regression between the extent to which an estuary deviates from the ideal shape and the predicted z value in the hypsometry formulation (Fig. 7.8). Data from the Columbia River Estuary, Ems-Dollard in 1985, the Western Scheldt in 2013 and Dovey were used to obtain this relation. Other data are shown in Fig. 7.8 but not used in the regression.

These results mean that we found a predictive function for hypsometry, where r is set to a constant value of 0.5 and the $z(x)$ is calculated as

$$z(x) = 1.4\left[\frac{W_{\text{ideal}}(x)}{W(x)}\right]^{1.2}, \tag{7.6}$$

in which $W_{\text{ideal}}(x)$ is the ideal estuary width (Eq. 7.2) and $W(x)$ is the measured local width. The confidence limits of the regression plot a factor of 1.9 higher and lower than the regression, which indicates that the z value can be predicted within a factor of 2 (see Fig. 7.9 for an example of prediction with uncertainty). While not used in the regression, hypsometry from bathymetry in other years shows similar trends and scatter as the data used in the regression.

The predictor (Eq. 7.6) was applied to the Columbia River Estuary, Western Scheldt, Dovey and Ems-Dollard to check the quality of the resulting along-channel predictions of intertidal high, intertidal low and subtidal width (Figs. 7.10 & 7.11). These zones can be derived after dimensionalising hypsometry and imposing a tidal range (Fig. 7.9b). For almost the entire along-channel profile, the predictions are within a factor of 2 of the measured value (Fig. 7.11) and the best agreement was obtained when the hypsometry was dimensionalised between the minimum and maximum measured bed level for each transect (Fig. 7.10).

Table 7.2 Percentage of points predicted within a factor of 2 from the measured value.

Estuary	% for subtidal	% for intertidal
Western Scheldt	100	84
Columbia River Estuary	90	79
Dovey	54	71
Ems-Dollard	91	59

7.4 Discussion

Results from this study illustrate that the bed-level distributions of channel and bar patterns in estuaries are topographically forced. The estuary outline that is observable from the surface translates into the three-dimensional patterns below the water surface. Bar-built estuaries typically have a quasiperiodic planform, in which major channel confluences occur at locations where the estuary is close to its ideal shape (Chapter 5 & 6). The parts between the confluences are typically filled with intertidal bar complexes. These findings are consistent with hypsometry zonations previously found for the Western Scheldt with more concave hypsometries for channel-dominated morphology and more convex hypsometries for bar complex morphology (Toffolon and Crosato, 2007). Our cross-sectional approach additionally revealed quasiperiodic behaviour within these zones.

In contrast to an empirical description, ideally, a physics-based determination of the hypsometry would be favourable. However, with the current state of the art of bar theory (Chapter 2) and relations for intertidal area, tidal prism, cross-sectional area and flow velocities (O'Brien, 1969; Friedrichs and Aubrey, 1988) it is not yet possible to derive a theoretical prediction of hypsometry. For example, bar theory (Seminara and Tubino, 2001; Schramkowski et al., 2002) could predict occurring bar patterns on top of an (ideal) estuary shape, but current theories overpredict their dimensions (Chapter 2) and it is still impossible to scale these to bed-level variations because the theories are linear. In addition to that, the resulting predictions would need to meet the requirement that the predicted bed levels and the intertidal area together lead to hydrodynamic conditions that fit the estuary as well.

Previously, hypsometry was used to summarise the geometry of entire tidal basins or estuaries (Boon and Byrne, 1981; Dieckmann et al., 1987; Townend, 2008). The whole system descriptions are consistent with the original Strahler (1952) concept of a basin hypsometry based on plan area, which is a valid description in a landform context. However, these descriptions oversimplify the along-channel variability in estuaries that are relatively long. These estuaries typically have a linear bed profile varying from an along-channel constant depth to strongly linear sloping (e.g. the Mersey in the UK). In the latter case, the elevation at which subtidal and intertidal area occurs varies significantly along-channel (Blott et al., 2006). Additionally, friction and convergence may cause the tidal range to either dampen or amplify, causing variation in tidal elevation, subtidal area and tidal prism (Savenije, 2006). Consequently, the along-channel cross-sectional hypsometry should be assumed to be relative to an along-channel varying high water level or mean sea level rather than an along-channel fixed vertical datum. Interpreting these along-channel variations remains an open question because of the reasons outlined above. Nevertheless, if desired, along-channel varying hypsometry predictions can be converted into one single summarising curve (Fig. 7.12), which shows that the basin hypsometry can also be predicted when limited data are available.

Our results show that hypsometry is not only a tool to predict morphology when limited data are available, but that hypsometry can also be used to reduce a large dataset of bathymetry and to study the evolution of bathymetry over time. In the case of Strahler (1952), hypsometry fits result in along-channel profiles of z and r values, but in practice any function or shape could be fitted. For example, the locations along the Western Scheldt where major dredging and dumping took place showed a weaker correlation with the original Strahler (1952) shape (Fig. 7.13). In these cases, fits with higher quality (lower RMSE) were obtained when we used the inverted hypsometric function (Eq. 7.4) (Fig. 7.13b,e).

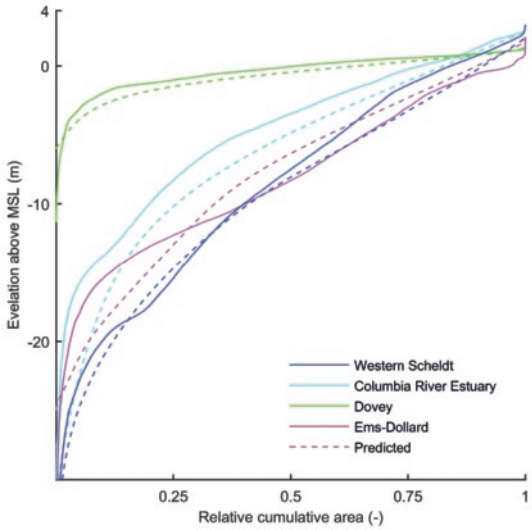

Figure 7.12 Hypsometry as summarised in a single curve for the entire estuaries. Solid lines are measured from bathymetry, and dashed lines are based on the predictions.

So in practice, one could fit a range of different hypsometry shapes and subsequently find out which of these shapes fit best on the dataset used. It can indicate that certain parts along the estuary require a separate hypsometric description. The fitting parameters are a method to describe the along-channel variation (Fig. 7.13b,d). Hypsometry can be fitted to compare data from nature, physical experiments and numerical modelling and subsequently study, for example, the effect of vegetation, cohesive mud and the influence of management on these systems.

7.4.1 Implications for management of estuaries

In many estuaries from around the world, subtidal channels are used as shipping fairways, while the intertidal bars (or shoals) form valuable ecological habitats (e.g. Bouma et al., 2005). For example in the Western Scheldt, the shipping fairway is now maintained at a depth of 14.5 m below the lowest astronomical tide (de Vriend et al., 2011; Depreiter et al., 2012). With empirical hypsometry predictions, we can estimate the width below a certain depth required for shipping, which gives estimates of what volume to dredge and at what locations along the estuary, which is relevant for the construction of future shipping fairways in estuaries for which we may have limited data.

In contrast, low-dynamic intertidal areas are valuable ecological habitats; for example, for the Western Scheldt there is an obligation to maintain a certain amount of intertidal area (Depreiter et al., 2012). Previously, Townend (2008) showed that basin hypsometry can be a tool to design breaches in managed realignment sites and can provide an indication of habitat composition. Hypsometry analysis per cross section shows that estuary outline translates into intertidal area, which implies that locations where the estuary is relatively wide have a relatively wide intertidal area. The ecological value is determined by the area of low-dynamical shallow water and intertidal areas (for settling and feeding) (Depreiter et al., 2012). This means that the edges should neither become steeper nor higher (leading to permanent dry fall) or deeper. Hypsometry fits (in the case of available data) or predictions (in the case of limited data) can indicate which locations along the estuary have a risk to transform away from low-dynamic area or have the potential to become low-dynamic area by the suppletion of dredged sediment.

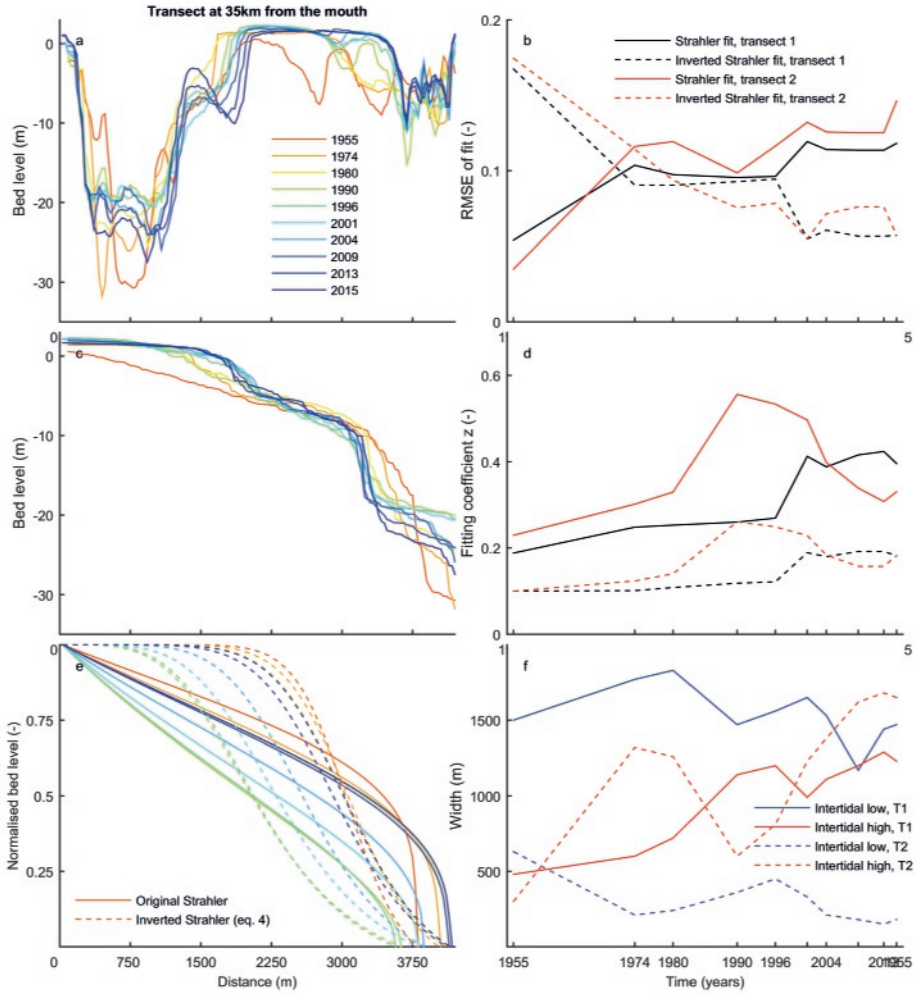

Figure 7.13 (a) Evolution of a cross section in the Western Scheldt where it has been significantly dredged and dumped (the Drempel van Hansweert). (c) Measured hypsometric profiles of the same time steps at the same cross section. (e) Best-fit hypsometries using the original Strahler equation (solid) and inverted Strahler function (Eq. 7.4) (dashed). (b) The quality of the two types of fits shows that the shape of the best-fitting hypsometric curve changes from the original Shrahler to the inverted equation in the 1970s–1980s. An additional transect is added in the panels on the right. (d) Fitting coefficients for z increase over time for both hypsometry types and both transects. (f) Intertidal high area increased over this period, while intertidal low area remained constant (transect 1) or decreased (transect 2).

The occurrence of vegetation species depends on bed elevation, salinity, maximum flow velocity and sediment type (de Jong, 1999; Gurnell et al., 2012). Even though predicted hypsometry only gives bed elevations, a comparison of the height interval in which *Salicornia* and *Spartina* can occur (Mckee and Patrick, 1988; Davy et al., 2001; van Braeckel et al., 2008) showed similar trends and the same order of magnitude as the measured vegetation from ecotope maps of the Western Scheldt in 2012 (Fig. 7.14). Some underpredictions arise in parts along the estuary where bed elevations above the high water level occur, such as at the Drowned Land of Saeftinghe. However, in general, the vegetation width

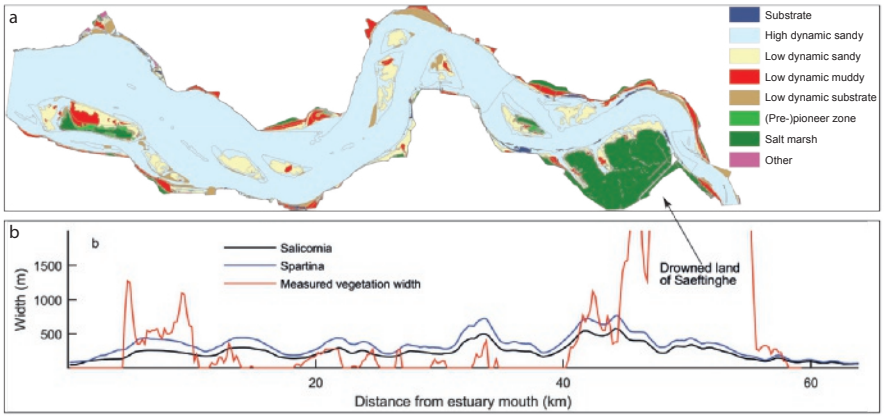

Figure 7.14 (a) Ecotope map of the Western Scheldt (2012) obtained from Rijkswaterstaat. (b) Prediction of the width in which *Salicornia* (black) and *Spartina* (blue) can occur when assuming that *Spartina* occurs between MSL and 1.5 m above and *Salicornia* occurs between 1.0 and 2.5 m, while ignoring velocity, salinity and sediment type constraints. Red line indicates measured width of vegetation based on ecotope map. The Drowned Land of Saeftinghe is excluded in the predictions because the high water line was the boundary of the analysed bathymetry, while it is included in the measured data.

is overpredicted because (1) hypsometry is stretched between the high water line and channel depth and (2) other constraining biotic and abiotic factors were excluded.

7.5 Conclusions

We studied the relation between the along-channel planform geometry of sandy estuaries and their hypsometry, which characterises the distribution of along-channel and cross-channel bed levels. The vertical dimensions were found to relate to the horizontal dimensions. In other words, the degree to which the estuary width deviates from an ideal converging estuary shape is reflected in the occurring hypsometry. At locations where the width is much larger than ideal, convex hypsometric shapes are observed, contrary to the locations where the estuary width is close to ideal, where concave hypsometric shapes are observed. In between these extreme end-members, a gradual transition with quasiperiodic variation was observed. This implies that it is possible to predict the along-channel varying hypsometry of estuaries, which is relevant for estuaries for which limited data are available. To obtain broad-brush estimates of the occurring bed levels, only the estuary outline and a typical tidal amplitude are required. The predictions can be used to study the presence and evolution of intertidal area, which forms valuable ecological habitats, and to get estimates of typical volumes that might need to be dredged when constructing shipping fairways.

Acknowledgments

Author contributions to conception and design, data collection and processing, analysis and conclusions, and paper preparation: JRFWL(70,65,75,70%), SS(10,30,15,15%), MGK(20,5,10,15%). We acknowledge the data processing contribution by Andy Bruijns as part of his MSc guided research. Reviews by Ian Townend and one anonymous reviewer helped to improve the paper. Edited by: Daniel Parsons. Bathymetry was obtained from Rijkswaterstaat for the Western Scheldt and Ems-Dollard Estuary, from Natural Resources Wales via Emmer Litt for the Dovey and from the Lower Columbia Estuary Partnership for the Columbia River Estuary.

Chapter 8 | Empirical assessment tool for bathymetry, flow velocity and salinity in estuaries based on tidal amplitude and remotely-sensed imagery

Abstract

Hydromorphological data for many estuaries worldwide is scarce and usually limited to offshore tidal amplitude and remotely-sensed imagery. In many projects, information about morphology and intertidal area is needed to assess the effects of human interventions and rising sea level on the natural depth distribution and on changing habitats. Habitat area depends on the spatial pattern of intertidal area, inundation time, peak flow velocities and salinity. While numerical models can reproduce these spatial patterns fairly well, their data need and computational costs are high and for each case a new model must be developed. Here, we present a Python tool that includes a comprehensive set of relations that predicts the hydrodynamics, bed elevation and the patterns of channels and bars in mere seconds. Predictions are based on a combination of empirical relations derived from natural estuaries, including a novel predictor for cross-sectional depth distributions, which is dependent on the along-channel width profile. Flow velocity, an important habitat characteristic, is calculated with a new correlation between depth below high water level and peak tidal flow velocity, which was based on spatial numerical modelling. Salinity is calculated from estuarine geometry and flow conditions. The tool only requires an along-channel width profile and tidal amplitude, making it useful for quick assessments, for example of potential habitat in ecology, when only remotely-sensed imagery is available.

Published as: Leuven, J.R.F.W., Verhoeve, S.L., van Dijk, W.M., Selaković, S. & Kleinhans, M.G. (2018). Empirical assessment tool for bathymetry, flow velocity and salinity in estuaries based on tidal amplitude and remotely-sensed imagery. *Remote Sensing, 10 (12), 1915*, DOI: 10.3390/rs10121915.

8.1 Introduction

Estuaries are characterised by fresh water inflow at the landward boundary and an open connection to the sea. Within these boundaries, tidal flows form dynamic patterns of channels and bars (Fig. 8.1a). Many of these systems are managed to balance the needs of flood safety, access to harbours and ecological quality. The main channels in large systems such as the Western Scheldt, Elbe and Yangtze are dredged for access to harbours (de Vriend et al., 2011), while intertidal area on bars and estuarine shorelines forms valuable ecological habitat (Bouma et al., 2005). Depth, inundation time, flow velocity and salinity are the prime abiotic factors that affect living organisms in estuarine environments (de Jong, 1999; Bouma et al., 2005; Gurnell et al., 2012). However, the general lack of information on these abiotic factors limits the prediction and sustainable management of habitat area in most estuaries (Cozzoli et al., 2017). Additionally, the effects of human interventions and rising sea level on the hydrodynamic conditions, equilibrium morphology and, therefore, also on habitat areas are largely unknown. Unfortunately, data to study these effects are generally only available for a few economically exploited estuaries that are already under great pressure by human influence. Data are lacking for most other systems around the world. Here, we explore to what degree it is possible to globally estimate estuarine characteristics, such as bed elevation, inundation duration, flow velocity, and salinity based on limited but widely publicly available data: remotely-sensed imagery and tidal range at the estuary mouth. To aid application and further investigation, we make the toolbox available.

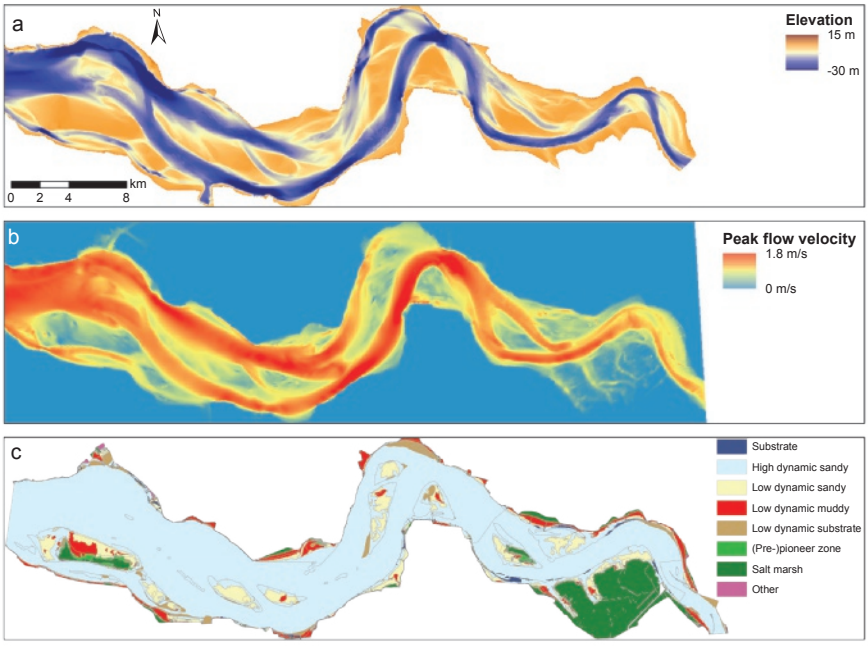

Figure 8.1 (a) Bathymetry of the Western Scheldt in 2012 from the mouth (left) to the Dutch-Belgian border (right). (b) Peak tidal flow velocities from a calibrated hydrodynamic model of Rijkswaterstaat (SCALWEST, Verbeek et al. (2000)) for the bathymetry of the Western Scheldt in 2009. (c) Ecotope map of the Western Scheldt (2012). Bathymetry, hydrodynamic output and ecotope map were obtained from Rijkswaterstaat.

Currently, several alternative methods are available to study the equilibrium morphology and hydrodynamic conditions of estuaries: in situ measurements, numerical modelling (van der Wegen and Roelvink, 2012; Elias et al., 2012; Braat et al., 2017), idealised form models (Townend, 2012), stability analyses (Seminara and Tubino (2001) and Schramkowski et al. (2002) and Chapter 2) and stability relations (O'Brien, 1969; Wang et al., 1999; Lanzoni and D'Alpaos, 2015; Zhou et al., 2018). Only numerical models, for example Delft3D, can predict the spatial patterns of bed elevation, flow velocity and salinity with considerable accuracy at the spatial detail that is required for the purpose of habitat estimation. However, morphological models are computationally expensive and require calibration and detailed measurement of boundary and initial conditions. In situ measurements are an alternative, but they are expensive and equally time-consuming. For example, Rijkswaterstaat typically covers 2 km^2/day in the Western Scheldt. While linear stability analysis may predict typical estuarine bar patterns, it is not straightforwardly applicable to fully developed bars and estuaries with irregular planforms.

For converging ideal estuaries, predictive relations are already available between width-averaged bed elevation and hydrodynamic conditions along the system (Langbein, 1963; Savenije, 2006; Townend, 2012) because of the imposed constraint that the tidal damping by friction is balanced by the gain in energy by convergence. While these concepts are useful when applied to end-members, they leave the more common estuaries with irregular planforms unexplored. We recently found that the concept of an ideal estuary can be used to predict bed elevation and bar patterns in estuaries with irregular planform shapes as a function of the deviation from the ideal shape (Chapter 5 & 6). However, we still lack empirical or theoretical relations that describe flow velocity in these nonideal systems, while this is an essential input variable for salinity predictions (Savenije, 1993; Brockway et al., 2006; Gisen et al., 2015) and habitat suitability (Haasnoot and van de Wolfshaar, 2009; van Oorschot et al., 2018). Based on observations in the Western Scheldt, we hypothesise that a relation exists between the depth and tidal flow velocity amplitude (Fig. 8.1a,b). Here, we derive a predictor for flow velocity as a function of bed elevation to complement the available relations for bed elevations, bar patterns and salinity in estuaries with irregular planforms.

Existing empirical relations and theoretical concepts were selected and combined in a fast-to-apply tool that predicts equilibrium morphology and hydrodynamic conditions. To assess the applicability, we test it against a range of estuaries and other end-member systems, characterised by varying degrees of tidal and river influence (Dalrymple et al., 1992; Townend, 2012) as well as varying degrees of adaptation to boundary conditions (Townend, 2012; de Haas et al., 2017) and varying degrees of bar presence (Fig. 8.2). These systems are a river-dominated delta branch (Dalrymple et al., 1992), a tide-dominated delta branch (an ideal estuary cf. Savenije (2006)), an alluvial estuary filled with tidal bars (Dalrymple et al. (1992) and Chapter 5), a relatively wide estuarine valley partially filled with bars (Dalrymple et al., 1992; Stevens et al., 2017), and a tidal basin lacking fluvial input (Marciano et al., 2005; Wang et al., 2012; van Maanen et al., 2013) (Fig. 8.2). In the discussion, we show applications for management of estuaries, palaeogeographic reconstructions and quantifying habitat area based on species-specific preferences.

8.2 Methods

Below, first, the general approach and minimum data required to run the tool are described. Then, the general structure and functions used in the tool are presented. Finally, it is described how tool output was compared with measured data and numerical modelling for two estuaries filled with bars and three end-member systems (Fig. 8.2), including the Western Scheldt and Columbia River. A general flowchart of the tool is given in Fig. 8.3 and a list of symbols used is given in Suppl. Table 8.2. The full Python code of the tool and instructions on how to use it are available in the supplementary material and accessible

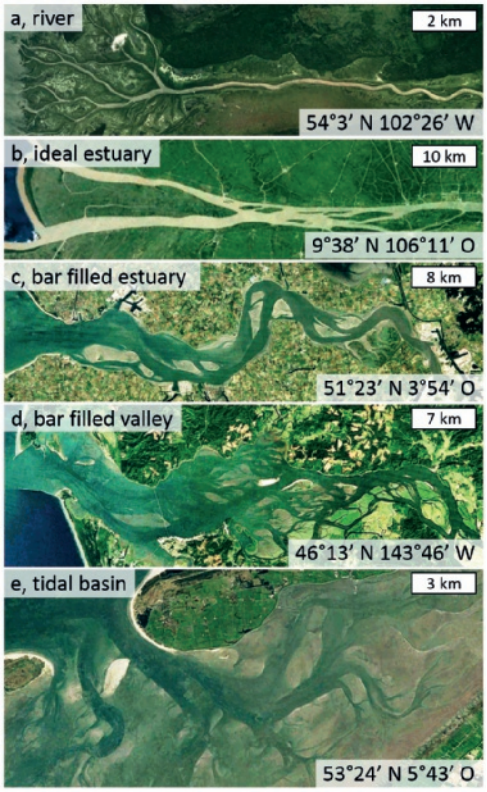

Figure 8.2 Examples of the systems used in this study: (a) a delta branch of a distributary of the Saskatchewan River (Canada); (b) the Tran De branch of the Mekong Delta (Vietnam); (c) the Western Scheldt Estuary (the Netherlands); (d) the Columbia River Estuary (USA); (e) the Ameland Inlet and tidal basin (the Netherlands).

on Github. The tool output comprises data exported in spreadsheet format and maps of bed elevation, inundation duration, peak flow velocity and salinity throughout the estuary.

General assumptions underlying the entire method are as follows. There are no significant geological constraints on the depth along the estuary. At the landward and seaward boundary, we assume hydraulic geometry. Moreover, there is no significant effect of the offshore wave climate on the morphology of the mouth and bed elevations in the estuary. The along-channel tidal range is simplified as an along-channel profile that is constant or linearly increasing or decreasing. For calculations of inundation duration, a sinusoidal M2 tide is assumed.

8.2.1 Tool approach

In general, the level of predictable detail depends on the available data. Data that are generally available for estuaries from all over the world are remotely-sensed imagery and a typical tidal range at the mouth, which means that our predictive relations should be based on and derivable from this information only. From remotely-sensed imagery, the along-channel width profile can be obtained (Section 8.2.2). It was previously found that the along-channel width profile correlates with the cross-sectional hypsometry (Chapter 7). The deviation from a perfectly converging planform translates in the occurrence of intertidal bars and therefore also in the shape of the hypsometric curve

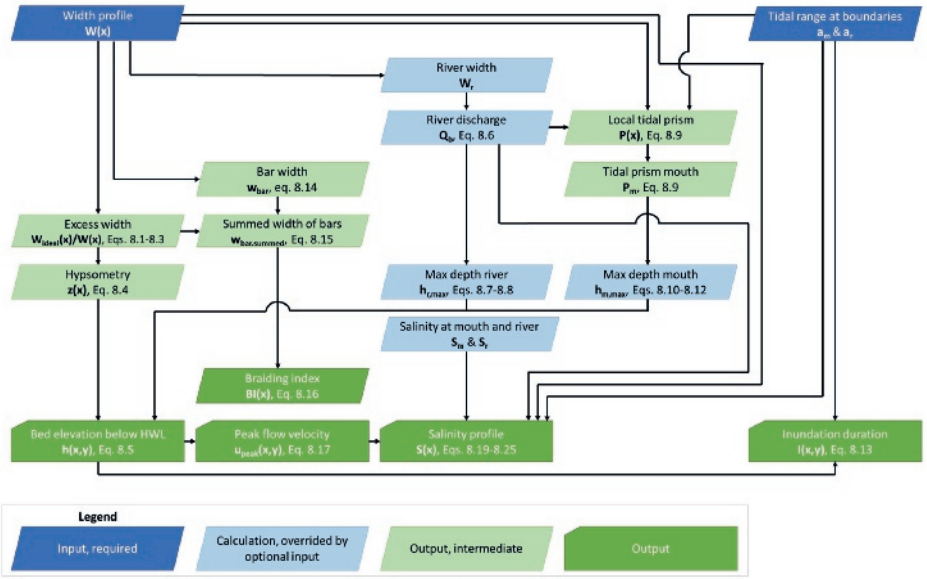

Figure 8.3 Flowchart of the calculation steps in the tool.

(Strahler, 1952; Boon and Byrne, 1981; Townend, 2008). However, to scale dimensionless hypsometry to vertical bed elevation distributions, an along-channel depth profile is required. Estuary depth generally decreases linearly to near-linearly from the estuary mouth to the upstream tidal limit (Savenije, 2015), enabling channel-depth estimation at any location in the estuary when the depth at the mouth of the estuary and upstream river are known. For the landward boundary, hydraulic geometry relations for rivers predict channel depth from width or bankfull discharge (Leopold and Maddock Jr, 1953; Hey and Thorne, 1986), while the geometry of the estuary mouth is related to local tidal prism (Langbein, 1963; O'Brien, 1969; Eysink, 1990; Friedrichs, 1995; Lanzoni and D'Alpaos, 2015). The typical tidal range at the mouth in combination with the along-channel width profile gives an estimate of the local tidal prism. This means that bed elevations and inundation duration are predictable from only the along-channel width profile and tidal amplitude profile, which is the minimum input data required to run the tool.

In order to be able to use additional data when available, we allow some variables to override estimations by the above relations (Fig. 8.3). Specifically, measured maximum mouth depth and maximum depth at the upstream boundary make their estimation based on tidal prism and hydraulic geometry redundant. A specified depth and width at the upstream boundary implicitly impose a user defined hydraulic geometry. Similarly, measured fresh water discharge may override the estimation of discharge based on channel width, which replaces the high uncertainty of the empirical relation with the lower measurement uncertainty. Finally, salinity at the mouth and landward boundary may be specified instead of the default values of 35 ppt at the mouth and 0 ppt at the landward boundary.

8.2.2 Bed elevation prediction

From remotely-sensed imagery, the first step is to obtain the along-channel width profile. Multiple options are available ranging from manually measuring the width at equally spaced transects to software tools that calculate river widths from remotely-sensed imagery (e.g. RivWidth (Pavelsky and Smith, 2008; Donchyts et al., 2016)). Here, the following approach was used (following Chapter 5): first, we

digitised the estuary planform in GIS software. Second, the polygon was imported in GIS software and the channel centreline was automatically extracted (e.g. Polygon To Centerline, ArcGIS function). Last, transects were drawn equally spaced on the centreline (e.g. Generate Transects Along Lines, ArcGIS function) and cropped with the planform polygon. The length of successive transects resulted in the along-channel width profile.

Estuary shape predicts cross-sectional hypsometry

Estuaries typically narrow from the tidal inlet to the upstream river because the tidal wave generally dampens out in landward direction such that the combined discharge, or flow energy, of the river and the tides reduces. The estuary convergence is often characterised by a convergence length of width (Savenije, 2006; Davies and Woodroffe, 2010; Savenije, 2015). In ideal estuaries, the energy loss due to friction is balanced by channel convergence such that the tidal energy per unit of width remains constant up to the estuary head (Pillsbury, 1956; Langbein, 1963; Dronkers, 2017). However, natural estuaries adapted in varying degrees to their initial and boundary conditions (Townend, 2012; de Haas et al., 2017), resulting in planform shapes that deviate from the converging shape expected according to the theory for the ideal estuary state. The deviation in width from a converging shape was found to be a fairly accurate predictor of bar pattern and cross-sectional bed elevation distributions (Chapter 5 & 7).

The convergence length (L_W) is the length over which the channel width reduces by a factor 2.72 (e) and is calculated as:

$$L_W = \frac{-s}{\ln\left(\frac{W_r}{W_m}\right)} \tag{8.1}$$

where W_m is the width of the estuary mouth, W_r is width of the river at the most landward boundary of the estuary and s is the along-channel distance measured between the seaward and landward boundary. We followed the same guidelines on the selection of the landward and seaward boundary as in Chapter 7.

The ideal width ($W_{ideal}(x)$) and excess width ($W_{excess}(x)$) are assumed to be related to this convergence length and the local width ($W(x)$) of the estuary:

$$W_{ideal}(x) = W_m e^{\frac{-x}{L_W}} \tag{8.2}$$

$$W_{excess}(x) = W(x) - W_{ideal}(x) \tag{8.3}$$

Here, x is the streamwise coordinate measured from the mouth along a centreline and y is the coordinate perpendicular to the centreline.

Along-channel variations in excess width translate into bed elevation with cross-sectional hypsometric curves. Hypsometric curves describe bed elevations with a cumulative profile. Multiple empirical relations have been proposed for the hypsometric shape of (partially) submerged bodies (Boon and Byrne, 1981; Wang et al., 2002; Toffolon and Crosato, 2007; Townend, 2008) and terrestrial landscapes (Strahler, 1952). The original formulation of Strahler (1952) (Eq. 8.5) appeared capable to describe hypsometries that occur in estuaries (Chapter 7). Two parameters in the Strahler (1952) equation can be tuned to modify the hypsometric shape: r sets the slope of curvature at the inflection point and z sets the concavity of the function, with lower values representing a more convex cross-sectional bed profile and higher values representing a more concave profile.

Reasonably accurate predictions are obtained in estuaries with r set to a constant value of 0.5, while the along-channel variation of best fitting z strongly depends on the along-channel variation in width (Chapter 7). Moreover, at locations where the estuary is much wider than expected from an ideal shape, bars are typically more abundant, the hypsometry is more convex and z-values are higher. The along-channel variation in concavity (z) is given by:

$$z(x) = 1.4\left(\frac{W_{ideal}(x)}{W(x)}\right)^{1.2} \tag{8.4}$$

The resulting predictions are accurate within a factor 2 of the measured value for intertidal and subtidal area in multiple estuaries of various size and character. This means that it is possible to predict the hypsometric shape per cross-section based on the estuary shape and, in this study, its predictive capacity for end-member cases is assessed as well.

The along-channel variation in concavity of the hypsometric shape ($z(x)$) can subsequently be used in the general hypsometric curve, formulated by Strahler (1952) as:

$$h_z(x,y) = \left(\frac{r}{r-1}\right)^{z(x)} \left[\frac{1}{(1-r)y+r} - 1\right]^{z(x)} \tag{8.5}$$

in which $h_z(x,y)$ is the bed elevation above which proportion y of the width profile occurs. Alternatively said, $h_z(x,y)$ is the proportion of total section height and y the proportion of section width. r is set to a constant value of 0.5 and $z(x)$ is given by Eq. 8.4.

The bed elevation ($h_z(x,y)$) and the width fraction (y) in Eq. 8.5 are dimensionless, where $h_z(x,y)$ is normalised between the local high water level (HWL) and the maximum estuary depth for that cross-section. Values for y are dimensionalised with the local estuary width. Thus, to transform the predicted hypsometry to dimensional depth distributions, an along-channel profile of the maximum depth is required, which is estimated from the channel depth at the mouth and the depth at the landward boundary as explained in the next subsection.

Tidal prism and river discharge predict channel geometry at the mouth and landward river

To calculate dimensional hypsometric profiles, an along-channel depth profile is required. Since the along-channel depth profile often shows a linear or almost linear profile (Savenije (2015) and Chapter 5), we fitted a linear along-channel profile on the maximum depth at the mouth of the estuary and the maximum depth at the landward river. When these values are known, the user can specify them, which overrides the estimation. When unspecified, the maximum and average depth at the mouth and at the upstream river are estimated with hydraulic geometry, using respectively the tidal prism and river discharge.

Hydraulic geometry is an empirical construct and should be used with care. However, it is often the best estimate in the absence of observed data. The resulting predictions are dependent on the specific region or river type for which they were developed. Here, we implemented, and used, the equation Hey and Thorne (1986) as an example. Nevertheless, users of the tool can specify a measured channel depth and river discharge as input when available because it overrides the calculation with Eqs. 8.6 & 8.7 and therefore implicitly impose a hydraulic geometry. Alternatively, the user can calculate these values with a hydraulic geometry equation suitable for the type of river considered or implement their own equation in the source code.

When unknown, river discharge is estimated from the channel width at the landward boundary with hydraulic geometry. Here, we used Hey and Thorne (1986), rewritten as:

$$Q_b = \left(\frac{W_r}{3.67}\right)^{1/0.45} \tag{8.6}$$

in which Q_b is the bankfull discharge and W_r is the width at the upstream river, measured at a location with almost zero tidal influence.

Subsequently, the width-averaged depth at the landward boundary is estimated from bankfull discharge as:

$$\overline{h_r} = 0.33 Q_b^{0.35} \tag{8.7}$$

The maximum depth at the landward boundary is a function of the average depth and the geometric shape of the channel. Therefore, the following equation was adopted:

$$h_{max,r} = s_r \overline{h_r} \tag{8.8}$$

in which s_r is the shape factor of the cross-section at the landward river, where 1 is a perfect rectangular and 2 a V-shaped cross-section. If unknown, a value of 1.65 is assumed for the landward boundary, based on geometry of five rivers upstream of estuaries (Suppl. Fig. 8.14).

The average depth at the mouth ($\overline{h_m}$) is calculated as the cross-sectional area at the mouth ($A_{csa,m}$, Eq. 8.10) divided by the local width (W_m), in which the cross-sectional area is estimated with the tidal prism. The local tidal prism is given as:

$$P(x) = \sum_{x}^{x+E} (2W(x)a(x)) + \frac{Q_b}{4}t \tag{8.9}$$

in which $P(x)$ is the local tidal prism resulting from the tidal amplitude ($a(x)$) and surface area upstream of location x. The contribution of river discharge (Q_r) to the local tidal prism is approximated as the bankfull discharge (Q_b) divided by 4. E is the tidal excursion length, which is the distance a water particle travels over half a tidal cycle. Since E is dependent on flow velocities, which are unknown at this point in the assessment tool, E has to be estimated at this point. The tidal excursion length is estimated by multiplying a typical tidal flow velocity with t, which is the duration of half a tidal period. According to Savenije (2006), the order of magnitude of the tidal excursion length can be estimated even in ungauged estuaries because the peak velocity amplitude in alluvial estuaries from all over the world is remarkably similar, being approximately 1 ms^{-1}. Here, we use this typical flow velocity to obtain an estimate of the tidal excursion length, which will be evaluated in the results. In Chapter 5, the upper limit for summation of the tidal prism was the upstream estuary boundary, but given that the input of the tool may comprise estuaries much longer than the tidal excursion length, the summation is here limited to the tidal excursion length.

Subsequently, the cross-sectional area at the mouth is related to the tidal prism. Earlier approaches derived these relations for tidal inlets or specific tidal systems (O'Brien, 1969; Jarrett, 1976; Shigemura, 1980; Eysink, 1990; Friedrichs, 1995; Lanzoni and D'Alpaos, 2015; Gisen and Savenije, 2015). Recently, we derived an empirical relation for multiple cross-sections within 35 estuaries (Supplementary material of Chapter 5). This equation is used to estimate the cross-sectional area at the mouth:

$$A_{csa}(x) = 0.13 \times 10^{-3} P(x) \tag{8.10}$$

in which $A_{csa}(x)$ is the along-channel cross-sectional area.

Now, the average depth at the mouth is calculated as:

$$\overline{h_m} = \frac{A_{csa,m}}{W_m} \tag{8.11}$$

and converted to a maximum depth at the mouth with

$$h_{max,m} = s_m \overline{h_m} \tag{8.12}$$

in which s_m is the shape factor of the cross-section at mouth. If unknown, a value of 1.65 is suggested based on geometry of five estuary mouths (Suppl. Fig. 8.14).

8.2.3 Inundation duration prediction

Dimensional depth distributions directly translate in inundation durations assuming a simple harmonic tide. Dimensional depth profiles are obtained from scaling the cross-sectional hypsometric profiles with the along-channel profile of maximum depth. Bed elevations below the low water level (below -1 times the amplitude) are always submerged and are therefore assigned a relative inundation duration of 1. For the intertidal zone, the inundation duration was calculated as:

$$I(x,y) = 0.5 - 0.5 \sin\left(\frac{0.5\pi}{a(x)} h_z(x,y)\right) \tag{8.13}$$

8.2.4 Bar pattern prediction: Bar width and braiding index

The along-channel variation in bar pattern correlates with along-channel variations in width. Moreover, the summed width of bars is equal to the excess width and thus braiding index ($BI(x)$) can subsequently be calculated by dividing the excess width ($W_{excess}(x)$) by the predicted bar width ($w_{bar}(x)$) (Chapter 5):

$$w_{bar}(x) = 0.39 W(x)^{0.92} \tag{8.14}$$

$$w_{barssummed}(x) = W_{excess}(x) \tag{8.15}$$

$$BI(x) = \frac{w_{barssummed}(x)}{w_{bar}(x)} \tag{8.16}$$

8.2.5 Flow velocity prediction

A relation for typical flow conditions as a function of estuarine geometry was still lacking. Therefore, we explored this relation in a calibrated hydrodynamic model of Rijkswaterstaat (SCALWEST, Verbeek et al. (2000)) for the bathymetry of the Western Scheldt in 2009. We hypothesised that a relation would exist between bed elevation and typical flow velocity (Fig. 8.1b). Peak tidal flow velocity (u_{peak}) indeed showed a good correlation ($R^2 = 0.73$) with depth below high water level (Fig. 8.4):

$$u_{peak}(x, y) = 0.10 + 0.91_{10} \log(h(x, y)) \tag{8.17}$$

Typical average flow velocity over half a tidal cycle was estimated depending on the deviation from the maximum along-channel tidal amplitude as follows (Suppl. Fig. 8.18):

$$u_{avg}(x, y) = u_{peak}(x, y) \left[1 - \frac{a(x)}{\max(a(x))} \frac{2}{\pi}\right] \tag{8.18}$$

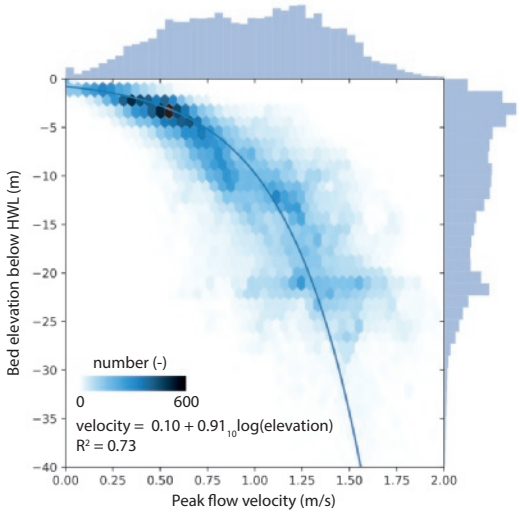

Figure 8.4 Relation between peak tidal flow velocity and depth below high water level from the Western Scheldt model (Fig. 8.1a,b). Histograms indicate occurrence within bins and colours in the plot become more saturated with increasing point density.

8.2.6 Salinity prediction

Salinity along the estuary depends on the freshwater discharge at the upstream boundary and the degree of mixing by the tides. Three along-channel salinity predictors were implemented in the assessment tool (Savenije, 1993; Brockway et al., 2006; Gisen et al., 2015) and the quality of these predictors for the cases studied here will be described in the results.

Savenije (1993) proposed a one-dimensional model that uses predictive equations for mixing and dispersion, such that it can be applied to systems for which limited information is available. The resulting model has been tested on a set of 15 estuaries. Gisen et al. (2015) revised the predictive equation of Savenije (1993), calibrated the model on 20 estuaries and validated it with another 10 estuaries. Brockway et al. (2006) proposed a solution for advection-diffusion equations in converging estuaries and implements an empirical relation for longitudinal mixing based on data from the Incomati Estuary (Mozambique).

The output maps in the tool are based on the averaged prediction of Savenije (1993) and Gisen et al. (2015). Nevertheless, the output for Brockway et al. (2006) is also provided. The along-channel salinity profile of Brockway et al. (2006) is typically exponentially decreasing to a salinity of 0, while the other two are generally more s-shaped with a strong gradient in the middle of the curve. Taking the average of all three predictors would thus not make sense because their characteristic shape would smoothen out. First, the latter is described because it has a simpler solution and less constitutive variables.

The salinity profile of Brockway et al. (2006) ($S_b(x)$) is given as:

$$S_b(x) = S_m \exp\left\{\frac{-Q_r}{{L_{A_{csa}}}^{-1} K A_{csa,m}}\left[e^{({L_{A_{csa}}}^{-1} x)} - 1\right]\right\} \tag{8.19}$$

in which S_m is the salinity at the mouth of the estuary (35 ppt), $A_{csa,m}$ is the cross-sectional area at the mouth, $L_{A_{csa}}$ is the convergence length of the cross-sectional area and K is an empirical equation for the longitudinal mixing coefficient based on average river discharge (Q_r) and tidal range ($a(x)$), being $K = 0.28Q_r + 13\overline{a(x)}$.

The salinity profile of Savenije (1993) ($S_s(x)$) is given as:

$$S_s(x) = (S_m - S_r)\left(\frac{D(x)}{D_m}\right)^{1/K} + S_r \tag{8.20}$$

in which S_r is the salinity at the fresh water river (0 ppt), K is the longitudinal mixing (Van der Burgh) coefficient (typically 0.07), $D(x)$ is the dispersion coefficient and D_m is the dispersion at the mouth of the estuary (typically 7000 $m^2 s^{-1}$). The ratio between the along-channel dispersion and dispersion at the mouth is given in Savenije (1993) as:

$$\frac{D(x)}{D_m} = 1 - \left(\frac{K L_{A_{csa}} Q_r}{D_m A_{csa,m}}\right)\left(e^{\frac{x}{L_{A_{csa}}}} - 1\right) \tag{8.21}$$

with

$$D_m = 220\sqrt{40}\frac{\overline{h_m}}{L_{A_{csa}}}\sqrt{N_r}\max(u_{peak}(mouth, y))E \tag{8.22}$$

in which

$$N_r = \frac{Q_r t / P(m)}{\rho_w \max(u_{peak}(mouth, y))^2 / \Delta\rho g \overline{h_m}} \tag{8.23}$$

where ρ_w is the density of water, $\Delta\rho$ is the density difference between salt and fresh water and g is the gravitational acceleration (9.81 ms^{-2}).

The salinity profile of Gisen et al. (2015) ($S_g(x)$) is equal to the profile of Savenije (1993) for the part landward of the inflection point, which is the part used in this study, except for the equation for K.

The longitudinal mixing coefficient (K) in Savenije (1993) (K_s) is given as:

$$K_s = 0.16 \times 10^{-6} \frac{\overline{h_m}^{0.69} g^{1.12} t^{2.24}}{(2a(m))^{0.59} L_W{}^{1.1} W_m{}^{0.13}} \tag{8.24}$$

while, in Gisen et al. (2015), it (K_g) is given as:

$$K_g = 151.35 \times 10^{-6} \frac{W_r{}^{0.3} (2a(m))^{0.13} t^{0.97}}{W_m{}^{0.30} C_m{}^{0.18} [\max(u_{peak}(mouth, y))]^{0.71} L_W{}^{0.11} \overline{h_m}^{-0.15} r_s{}^{0.84}} \tag{8.25}$$

in which $a(m)$ is the tidal amplitude at the mouth, C_m is the Chezy roughness, estimated in the assessment tool as 42 $m^{0.5}s^{-1}$, which is adjustable in the tool code, $\max(u_{peak}(mouth, y))$ is the peak tidal flow velocity in the cross-section at the mouth, and r_s is the storage ratio, calculated as the width of intertidal area at the mouth divided by the width of the subtidal area at the mouth. The minimum value of K is 0 and the maximum value is 1.

8.2.7 Tool validation

For purposes of illustration and validation, the tool was applied to the Columbia River Estuary (USA), which is an example of a relatively wide valley that is partially filled with bars (Dalrymple et al., 1992), and the Western Scheldt (NL), which is an alluvial estuary with large deviations from a converging along-channel width profile and filled with tidal bars (Dalrymple et al. (1992) and Chapter 5) (Fig. 8.2c,d). For validation, channel depth at the landward boundary was calculated in the tool with measured river discharge. Predicted velocities are validated on the Columbia River only because the regression was based on data for the Western Scheldt. Bed elevation and salinity predictions are validated on both systems. The predicted flow velocities from the tool were compared with results from numerical modelling for the Columbia River Estuary (Elias et al., 2012; Stevens et al., 2017) and from a calibrated hydrodynamic model of Rijkswaterstaat for the Western Scheldt (SCALWEST, Verbeek et al. (2000)). Results from numerical modelling were used because field measurements of flow velocities do not provide full coverage in time and space. Salinity data were obtained from Jay and Smith (1990) for the Columbia River and from de Brauwere et al. (2011) and Vroom et al. (2015) for the Western Scheldt. Habitat preferences for potential habitat maps were obtained from the Marine Life Information Network (MarLIN), which is a database on the biology of species and the ecology of habitats.

8.2.8 Tool application to end-member cases

We tested the tool's performance against end-member systems. The dominant factors controlling the tool output are (i) the along-channel width profile, (ii) river discharge at the landward boundary and (iii) tidal range at the seaward boundary. Given these three factors, we designed the three most extreme end-member cases (Fig. 8.2a,b,e), which were tested in addition to two estuarine cases with variable width profile (the Western Scheldt and Columbia River) (Fig. 8.2c,d). The first end-member is an estuary with a perfectly converging shape from the mouth to the upstream river, i.e. negligible width variation. This case was based on the dimensions of the Tran De branch of the Mekong Delta (Vietnam). The second end-member is a river with a constant channel width, i.e. no tidal range at the seaward boundary and negligible width variation. This case was based on the dimensions of a distributary of the Saskatchewan River, near Cumberland Lake (Saskatchewan, Canada). The third end-member is a tidal basin, i.e. no river discharge and landward increasing width instead of decreasing. This case was based on dimensions of the Ameland inlet and represented by a narrow mouth, an increasing channel width in landward direction and an infinitely small river at the landward boundary. It should be noted that, in the last case, along-channel width is measured perpendicular to the tidal channels, which means that the transects for an idealised tidal basin are

semicircles. The predictions for the Tran De branch were compared with measured data (Nguyen and Savenije, 2006; Nowacki et al., 2015; Xing et al., 2017) and the predictions for the tidal basin were compared with numerical model results (van Maanen et al., 2011; van Maanen et al., 2013).

8.3 Results

8.3.1 Tool output

The tool output comprises maps of predicted bed elevation with respect to the high water level (HWL), relative inundation duration, flow velocity and salinity (Figs. 8.5 & 8.6). In general, the bed deepens in seaward direction. At locations where the estuary is relatively wide, average bed elevations are higher and at locations where the estuary width is close to the ideal width, bed elevations are lower (Eqs. 8.4 & 8.5). Zones where the excess width is large are the locations where stretches of intertidal area are wider and where inundation durations are less than 100%. Peak flow velocities increase in seaward direction with maxima around 1.8 ms^{-1} at the mouth. Peak flow velocities in the intertidal area are generally below 0.8 ms^{-1}. The salinity gradually decreases in landward directions and approaches river salinity at the landward boundary.

Before, we had to estimate a typical peak flow velocity because it was required for the estimation of the tidal excursion length (Eq. 8.9). At that point, a value of 1 ms^{-1} was assumed (Savenije, 2006). This assumption only partly influences the output flow velocity, which depends on bed elevation, which in turn is controlled by the estuary planform shape, the tidal range and the tidal excursion length. Nevertheless, output maps justify the assumption of 1 ms^{-1} for the purpose of calculating the tidal excursion length. The average peak tidal flow velocity is 1 ms^{-1} for the Western Scheldt and 1.2 ms^{-1} for the Columbia River when averaged over the surface area of a typical tidal excursion length (Figs. 8.5 & 8.6). Median values of peak tidal flow velocity per transect are also remarkably close to the typical value proposed by Savenije (2006) along the entire estuary (Fig. 8.7a,c).

Additional output (Suppl. Figs. 8.16 & 8.17) consists of predictions of bar width and braiding index per cross-section, maximum peak flow velocity and maximum average flow velocity per transect. Furthermore, four zones are calculated based on elevation with respect to the tidal range: subtidal ($< -a$), intertidal low (more than 50% of time submerged) and intertidal high (less than 50% of time submerged). For each of these zones, the width of the zone, average depth and average and peak tidal flow velocities are calculated as output.

8.3.2 Tool validation

Bed elevations

To validate the predicted bed elevations, median and minimum values per transect were compared with measurements from bathymetry. Median and minimum bed elevations are generally within a factor 2 of the measured values from bathymetry (Fig. 8.7a,b). Median bed elevations deviate the most in the landward part for the Western Scheldt (Fig. 8.7a). In this section, a larger portion of the width is dredged, which causes the median depth to fall within the deeper dredged channel. The deviation between predicted and measured values lacks a trend with a position along the estuary (as indicated by the colours in Fig. 8.7a,b). The largest outliers for the Columbia River are found at the mouth where the predicted median bed elevation is much lower than measured from bathymetry (Fig. 8.7b). This is caused by the small embayments enclosed by groynes, located on the sides of the mouth area. In this zone, a larger proportion of high bed elevations causes a higher median bed elevation.

Flow velocity

The range of predicted flow velocities is generally in the same range as the modelled values for both the peak and average flow velocities (Fig. 8.7c,d). However, the along-channel variation in minimum and

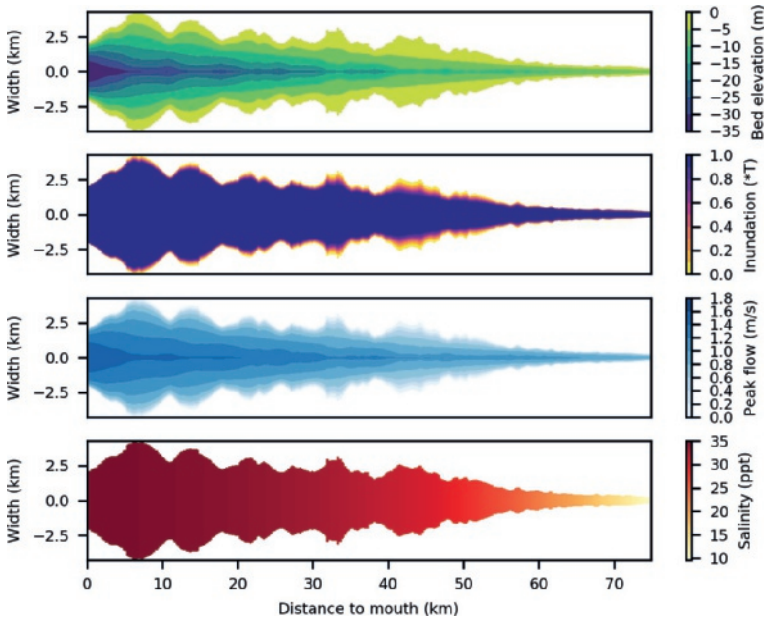

Figure 8.5 Resulting predictions of bed elevation with respect to the high water level, inundation duration, peak flow velocity and salinity for the Western Scheldt.

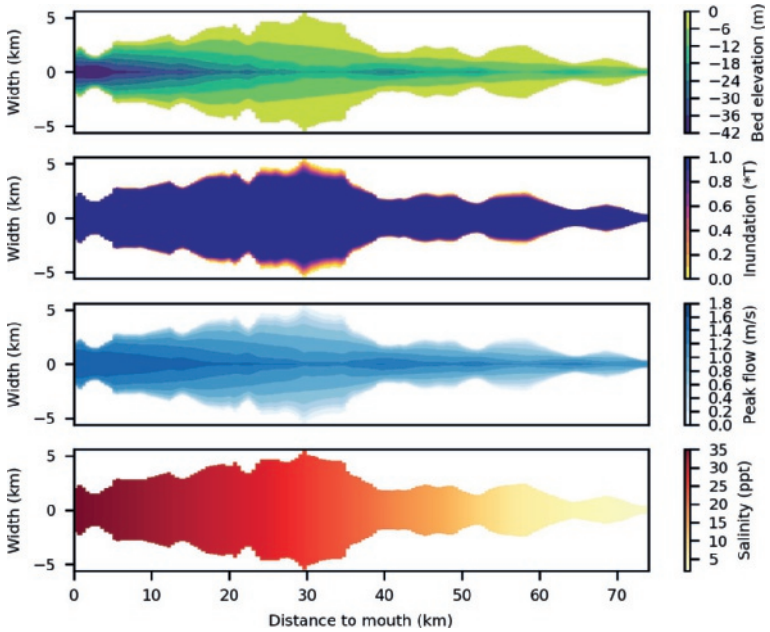

Figure 8.6 Resulting predictions of bed elevation with respect to the high water level, inundation duration, peak flow velocity and salinity for the Columbia River.

maximum flow velocities is larger for the models than for the tool output (Fig. 8.8). We explain this by a simplification of some morphological elements in the tool. For example, the presence and location of scours and sills, which cause variation in the along-channel maximum depth, is not predicted by the tool. However, they do occur in natural systems and therefore also cause variations in along-channel flow velocity pattern. In the tool, the profile of maximum depth is linear along-channel, which results in lower variations in the maximum flow velocity. Nevertheless, the velocity predictions do capture the along-channel variability caused by the large-scale morphological variation in bed elevation, as illustrated with the median values per transect (Fig. 8.8).

The tool does not reproduce the highest observed flow velocities in the Columbia River, which are well above 2 ms^{-1} in the first 15 km from the mouth. To obtain velocities above 2 ms^{-1} in the tool, bed elevation of at least 120 m below high water level are required (Eq. 8.17), which generally do not occur in natural systems. This means that the tool underpredicts flow velocities in cases where the cross-sectional area is relatively small compared to the local tidal prism, which might also suggest disequilibrium. Moreover, the regression between flow velocity and depth, simplifies the increasing scatter for larger depths and flow velocities, which is observed for the Western Scheldt (Fig. 8.4).

Predicted velocity against modelled velocity shows a trend for the Columbia River with modelled velocities below 1 ms^{-1} being overpredicted by the tool and velocities above 1 ms^{-1} being underpredicted (Fig. 8.7d). The degree of misprediction does not correlate with position along the estuary. The only explanation for the deviation is a different depth dependency of peak flow velocity caused by a different ratio between tidal prism and cross-sectional area.

Therefore, an alternative approach for calculating flow velocities was based on the local tidal prism and the cross-sectional channel geometry, i.e. continuity. For each cross-section, a typical velocity is calculated at the average depth of the cross-section (i.e. $P(x)/(T\overline{h(x)})$). Nevertheless, the quality of these predictions appeared to be less (Fig. 8.9) for two reasons: (1) at the upstream boundary, velocities are mainly sensitive to river discharge. Here, local tidal prism approaches river discharge because it is obtained from integrating over the distance of a tidal excursion length upstream (Eq. 8.9) plus river discharge. In the case of the Columbia River, this leads to overprediction of velocities because river discharge is large, while, for the Western Scheldt, it would lead to underpredictions. (2) Flow velocities at the intertidal area and deepest parts still have to be extrapolated from the average prediction creating uncertainty in the most important parts for respectively ecology and shipping.

Following this alternative approach, we anticipated that there would be a relation between the width variation and the misprediction based on depth only (Eq. 8.17). It was expected that a local increase in width would lead to flow expansion and therefore typically lower flow velocities than for a cross-section with similar tidal prism but lower width. However, the lack of trend between velocity deviation and width measures (Suppl. Fig. 8.15) indicates that velocity predictions will not improve from including width in the regression.

The alternative approach shows that a prediction of flow velocities depending on tidal prism and depth does not reproduce modelled flow velocities better (Fig. 8.9a,b,e,f). A predictive relation between flow velocity and depth is thus of value. This urges the need to compile a dataset with flow velocities and water depths of multiple systems. From that data, a relation that is better applicable to more systems could be derived, but this data is not yet available. Nevertheless, the present relation predicted flow velocity within a factor 2 of the modelled values even in the most extreme cases, which means it is of value for an estimate when limited data is available.

Predicted flow velocity and local depth result in a local tidal prism that is in the same range as the modelled values (Fig. 8.10). Local tidal prism obtained from integrating a tidal range over the full length of the estuary is typically 1.5–2 times larger at the mouth than the tidal prism obtained from integrating over a typical tidal excursion length. This explains why using the latter is required to obtain accurate

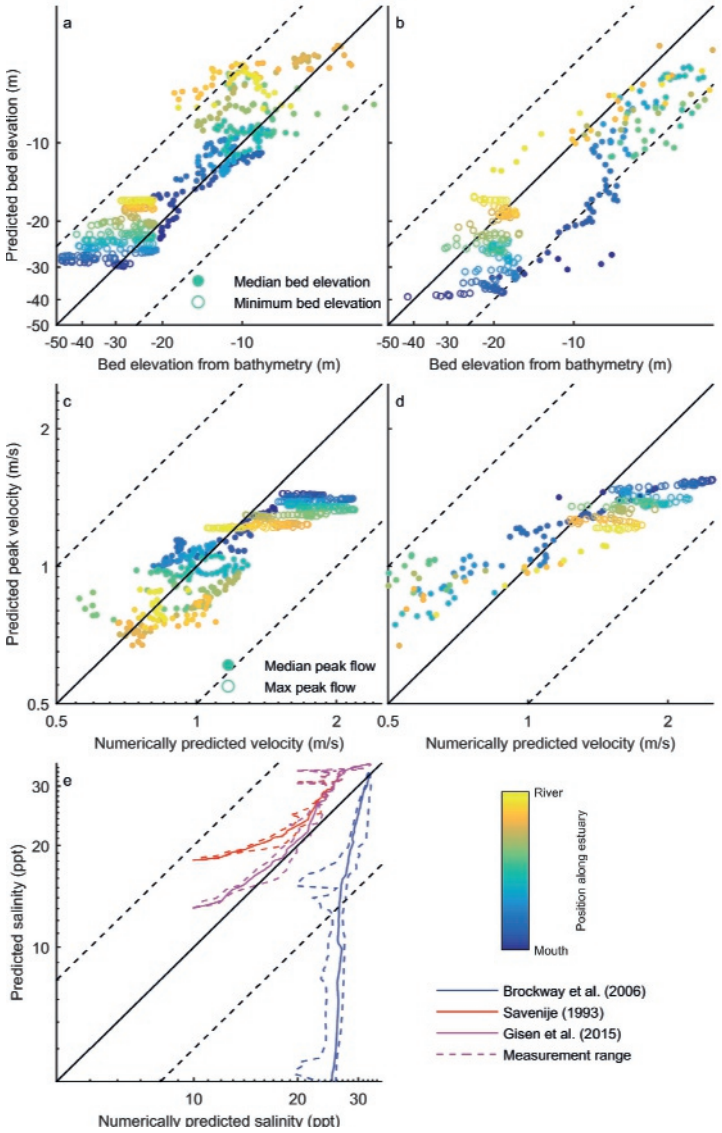

Figure 8.7 (a,b) Predicted bed elevations against measured bed elevations taken from bathymetry for the Western Scheldt (a) and Columbia River (b). (c,d) Predicted flow velocity from the tool against modelled flow velocity for numerical models of the Western Scheldt (c) and Columbia River (d). Filled circles indicate median values per cross section, open circles indicate maximum values per cross section. Dashed lines indicate a spread of a factor 2 around the $x = y$ line. Colours indicate the position along the estuary, with blue being the mouth and yellow being the most landward location. (e) Predicted salinity for the three predictors against measured salinity in the Western Scheldt. Solid lines indicate mean measured salinity per transect against predicted salinity and dashed lines indicate maximum and minimum measured values.

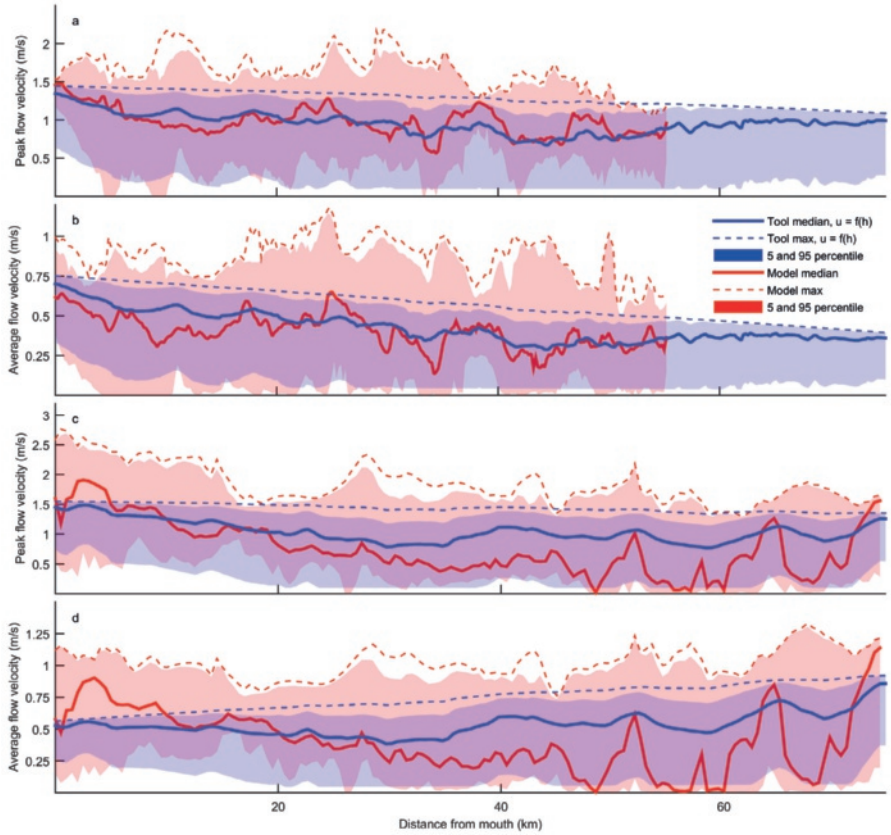

Figure 8.8 Comparison between modelled [red] and predicted [blue] flow velocities along the Western Scheldt (a,b) and the Columbia River (c,d). Shaded area shows the range of peak velocities (a,c) and range of average velocities over half a tidal cycle (b,d) bounded by the 5 and 95 percentile values. The solid line indicates the median and dashed line maximum value per transect.

predictions of the depth at the estuary mouth and additionally is less sensitive to the length of the estuary.

Salinity

Predicted salinities are within the range of measured values (Jay and Smith, 1990) and values obtained with a numerical model with shallow-water and tracer-transport equations (de Brauwere et al., 2011). For the Western Scheldt, local salinity can vary between 4–8 ppt over a tidal cycle, with averages of 28 ppt at 10 km, 22 ppt at 30 km and 16 ppt at 45 km from the mouth (de Brauwere et al., 2011). In the Columbia River Estuary, temporal salinity variation is even larger (Jay and Smith, 1990), with local variations of 20–25 ppt in the most seaward 15 km. Predicted salinities fall within the measured range, but salinities are overpredicted in the most landward reach, where measured values approach 0 ppt from approximately 45 km from the mouth (Jay and Smith, 1990).

The salinity predictor of Gisen and Savenije (2015) is most accurate for the salinities observed in the Western Scheldt (Fig. 8.7e), which was a system used for validation in Gisen and Savenije (2015) and not for calibration. This is the only salinity predictor for which predicted salinity is within a factor 1.5 of the

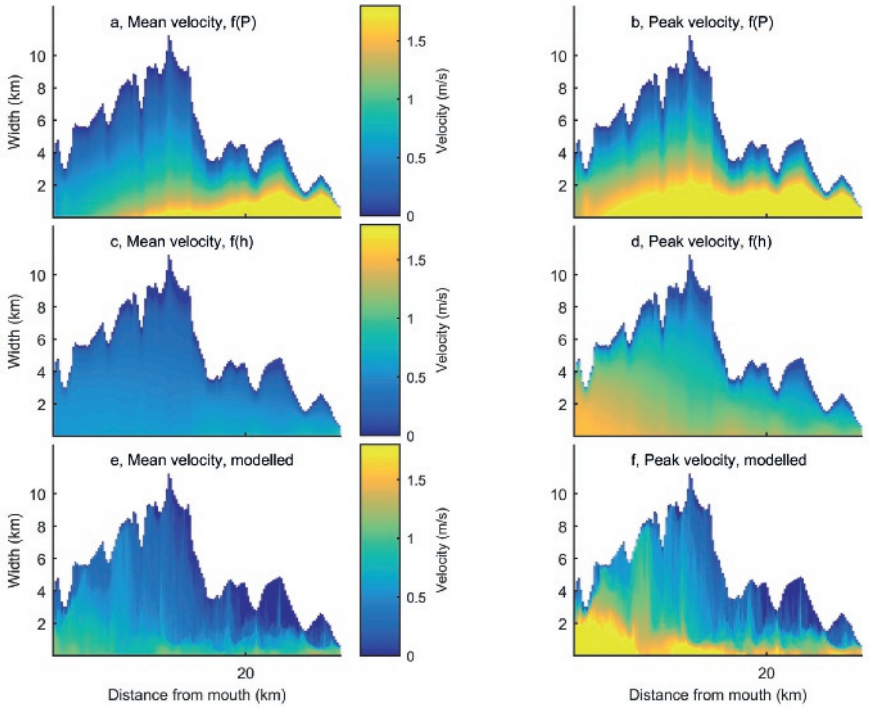

Figure 8.9 Mean velocity over a tidal cycle [left] and peak tidal flow velocity [right] as a function of local tidal prism (a,b), bed elevation (c,d) and numerically modelled values (e,f) for the Columbia River.

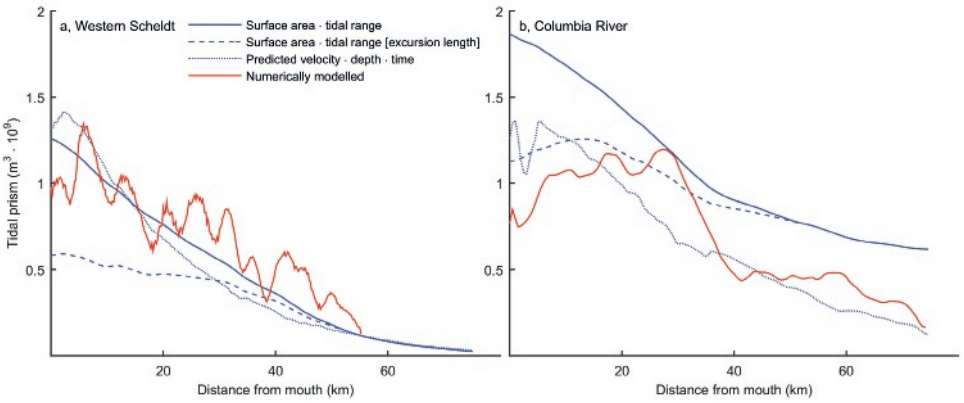

Figure 8.10 Resulting predictions of local tidal prism for the Western Scheldt (a) and Columbia River (b). Red lines are model results, blue lines are tool output.

measured value for the entire along-channel section. Predictors of Savenije (1993) and Brockway et al. (2006) show large deviations at the landward side, where the predicted salinity gradient is respectively too weak and too strong compared to measured values (Fig. 8.7e).

8.3.3 Applicability to end-member systems: A river, an ideal estuary, and a tidal basin

In the case of a river and ideal estuary, the local channel width will always be equal to the ideal channel width as obtained from a maximum fitting converging shape. This means that the shape of the cross-sectional hypsometry is concave and constant along-channel (Eqs. 8.4 & 8.5, Fig. 8.11). The concave hypsometry results in a relatively constant along-channel bed elevation profile (Fig. 8.11). Only the along-channel variation in maximum depth and increase in channel width in seaward direction cause a slight along-channel variation. The implication of an along-channel constant concave hypsometry is that intertidal area is very small and inundation duration is 100% for the largest part of the estuary. Typical flow velocities are also along-channel constant at approximately 1–1.2 ms^{-1}. A strong salinity gradient is predicted at the mouth of the estuary, with salinities dropping to ≈5 ppt at 30 km from the mouth.

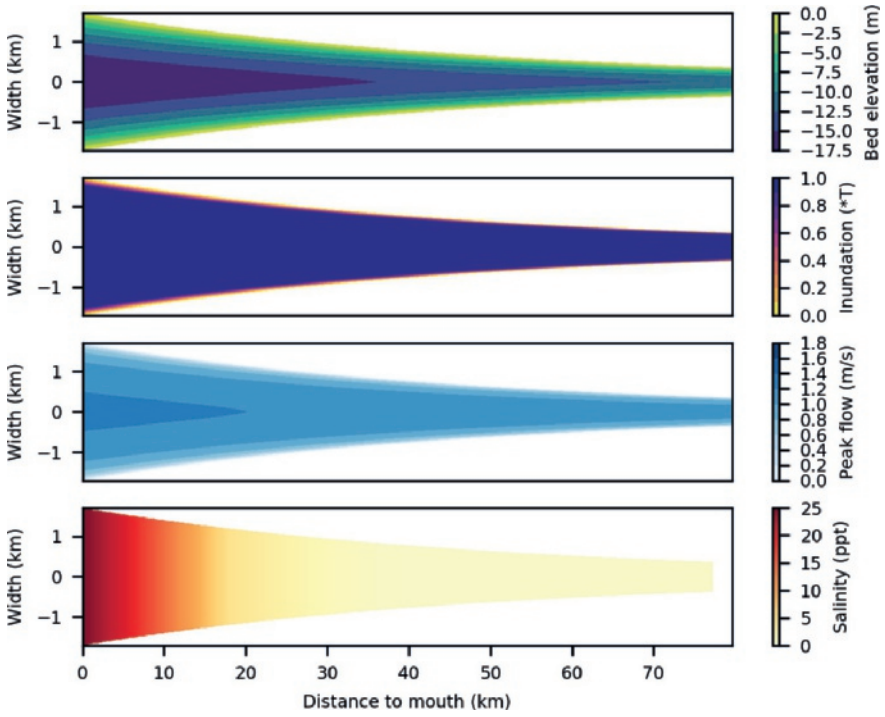

Figure 8.11 Resulting predictions of bed elevation with respect to the high water level, inundation duration, peak flow velocity and salinity for an ideal estuary based on dimensions of the Tran De branch of the Mekong river.

Ideal estuaries are said to be characterised by an along-channel constant velocity amplitude and depth (Savenije, 2006; Nguyen and Savenije, 2006) and these features are reproduced by the tool predictions. Moreover, the predictions correspond to observations in the Tran De branch of the Mekong: observed peak flow velocity is approximately 1 ms^{-1} along the entire branch (Nowacki et al., 2015; Xing et al., 2017) and salinity intrusion reaches up to 45–55 km from the mouth (Nguyen and Savenije, 2006). In addition, the along-channel predicted salinities fall within the range of observed salinities (Nguyen and Savenije, 2006). The only feature not completely reproduced is the along-channel constant depth. When the maximum depth at the mouth is calculated from tidal prism, predicted depth at the mouth is a factor 1.5 larger, 5 m deeper, than observed.

The prediction for depth at the mouth leads to a misprediction at the most downstream boundary for the river (Suppl. Fig. 8.19). In that case, maximum depth at the landward boundary is controlled by river discharge (to the power of ≈0.35), the width of the river without tidal influence (to the power of ≈0.77) or if both of these are unspecified, the channel width at the landward boundary. Depth at the mouth is calculated with the tidal prism, which in the case of a river is equal to the river discharge times the duration of half a tidal cycle. Therefore, depth at the mouth is also a function of river discharge or landward river width, but to the power of ≈1. This means that the predicted channel depth at the mouth will always be deeper than at the upstream boundary, especially in the end-member case of a straight river.

An ideal tidal basin is characterised by a strong landward increase in width, while the ideal width approaches 0 at the landward end. This means that the ratio of $W_{ideal}(x)$ to $W(x)$ strongly decreases in landward direction, resulting in convex hypsometry (Eq. 8.4) and therefore large amounts of intertidal area within the basin (Suppl. Fig. 8.20). In this end-member case, the depth at the mouth is set by the surface area of the tidal basin multiplied with the tidal range. In the case of a tidal basin based on the Ameland inlet, the tool predicts a maximum depth at the mouth of 20 m below the high water level. This seems appropriate when compared with modelled (van Maanen et al., 2011; van Maanen et al., 2013) and measured values (Marciano et al., 2005) (Suppl. Fig. 8.21). Flow velocities at the mouth are in the order of 1 ms^{-1}, which is comparable with measured and modelled values for tidal basins in equilibrium (Dissanayake et al., 2009; van Maanen et al., 2011).

8.4 Discussion

8.4.1 Sensitivity of tool output to tidal range, river discharge, and along-channel width profile

The sensitivity of the input tidal range, river discharge, and along-channel width profile was tested on the following parameters: (1) the ratio between intertidal and subtidal area; (2) the ratio between low and high dynamic environment; and (3) peak flow velocity at the estuary mouth (Fig. 8.12). Low dynamic environment, which forms potential habitat, is defined as intertidal area where flow velocities are below 0.8 ms^{-1}. All other areas are classified as a high dynamic area.

While most sensitive dependent variables are increasing or decreasing monotonously with the independent variable, the ratio of low and high dynamic intertidal area as a function of tidal amplitude shows an optimum. An increase in tidal amplitude increases the ratio between intertidal and subtidal area (Fig. 8.12a) because the increased tidal range increases intertidal area. However, increases in tidal amplitude also generate a proportional increase in tidal prism. A larger tidal prism at the mouth will increase the predicted cross-sectional area and because the width is fixed; this will increase predicted depth at the mouth. Because maximum depth along the estuary is dependent on the maximum depth at the mouth and the maximum depth at the landward river, this increases the maximum depth along the entire estuary. The increased depths subsequently increase the predicted flow velocities (Fig. 8.12g). This means that two opposing mechanisms affect the ratio between low dynamic and high dynamic environment: increased tidal range increases intertidal area which forms a more low-dynamic environment. In contrast, the deepening by increase in tidal prism increases flow velocities and therefore reduces the low dynamic area. Therefore, the combined effect results in an optimum curve for the ratio between low dynamic (velocity < 0.8 ms^{-1}) intertidal area and high dynamic area as a function of tidal range (Fig. 8.12d).

An increase in the river discharge results in less intertidal area, less low dynamic area and larger peak flow velocities (Fig. 8.12b,e,h). After all, increased river discharge increases the tidal prism, which increases channel depths.

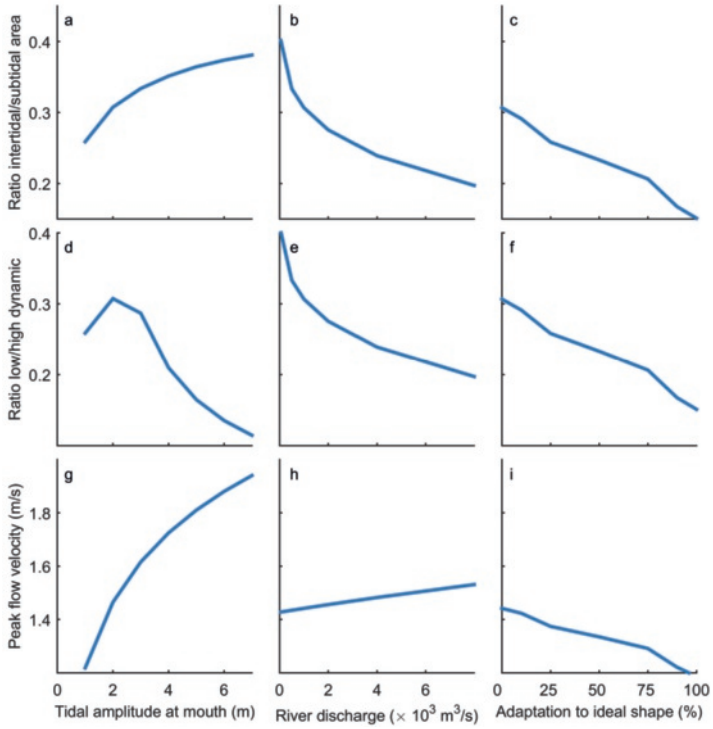

Figure 8.12 Sensitivity of tool output for the Western Scheldt to input tidal amplitude, river discharge and width profile. The ratio between intertidal and subtidal area increases with tidal amplitude (a) and decreases with river discharge and adaptation to ideal shape (b,c). The ratio between low dynamic (velocity < 0.8 ms^{-1}) intertidal area and high dynamic area has an optimum curve for tidal amplitude (d) and decreases with river discharge and adaptation to ideal shape (e,f). Peak flow velocity at the mouth of the estuary increases with tidal amplitude and river discharge (g,h) and decreases with adaptation to ideal shape (i).

The ratio between ideal width and excess width affects the distribution of bed elevations per cross-section and the tidal prism. In estuaries that adapt to the ideal shape, the excess width becomes lower. This results in more concave cross-sectional hypsometry and therefore narrower stretches of intertidal flats (Fig. 8.12c). The tidal prism decreases as a result of reduced estuary area, resulting in lower maximum depths and therefore also lower flow peak velocities (Fig. 8.12i).

A comparison between predicted and measured or modelled values showed that bed elevations, flow velocity and salinity can be predicted within a factor 2 of the measured or modelled values (Fig. 8.7). The largest deviations between predicted and modelled flow velocities occur when they peak above 2 ms^{-1} in natural systems. Largest mispredictions for salinity occur at the transition from brackish to fresh water, where salinity is also the most dynamic over the seasons. Bed elevation predictions are most uncertain when the tidal range is low for the depth at the mouth, which is also sensitive to offshore wave climate that we have not considered here. This implies that the tool is capable to provide a first-order estimation for estuaries with limited data, but that it cannot replace measurements or numerical modelling.

8.4.2 Applications

Illustration of application for ecological assessment

The major abiotic factors that determine habitat area of living organisms in estuaries are depth, flow velocity, salinity and inundation time (de Jong, 1999; Bouma et al., 2005; Dame, 2008; Gurnell et al., 2012). Habitat suitability models (e.g. HABITAT, Haasnoot and van de Wolfshaar (2009)) can translate these abiotic factors into a characteristic habitat suitability index, which for example has been applied to study the effect of climate change and dam construction on potential habitat in rivers (van Oorschot et al., 2018). Multiple case studies of individual systems or individual species are also available for estuaries (Kemp et al., 2004; Vinagre et al., 2006; Barnes et al., 2007; Degraer et al., 2008; Feyrer et al., 2011), but application to more systems worldwide and application to scenarios of future climate change and human engineering are hampered by a lack of data.

The tool presented in this study can provide typical abiotic factors that are input for habitat suitability models within minutes. Therefore, the output can lead to a first-order estimation of the potential habitat (Fig. 8.13) based on species specific preferences (Table 8.1). The potential habitat area based on tool output generally overpredicts the measured habitat. Firstly, the tool always predicts a zone with intertidal area because the predicted hypsometry is stretched between the high water line and maximum channel depth. Secondly, other constraining biotic and abiotic factors were excluded, such as the competition between species and the water quality. Lastly, the settling and growth conditions may deviate from the conditions under which species occur in a later life stage. For example, seedlings of salt marsh species generally only settle when peak flow is below 0.25 ms^{-1} and, in their initial life stage, they may only sustain flows up to 0.5 ms^{-1} (Lokhorst et al., 2018). Nevertheless, the application of the tool for ecological assessment is of value because it is capable of providing abiotic factors of individual systems and scenarios within minutes, rather than days to months for numerical modelling and in situ measurements.

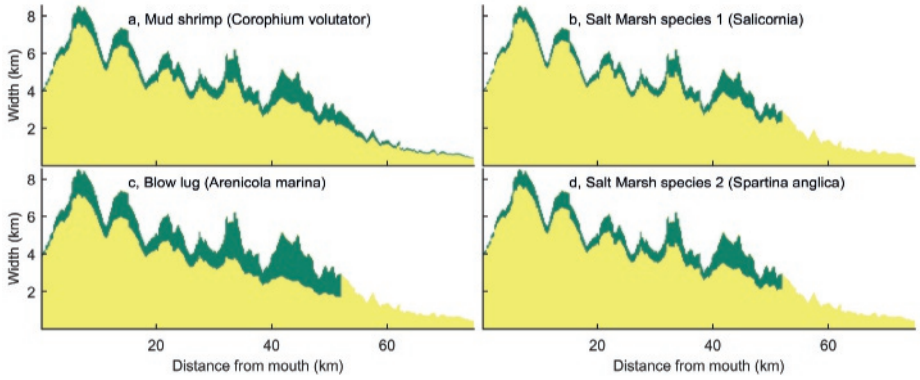

Figure 8.13 Potential habitat area (in green) as part of total width for the species in Table 8.1.

Table 8.1 Habitat preferences of species used in this study based on MarLIN database.

Name	Depth Range (-)	Flow Velocity (ms^{-1})	Salinity (ppt)
Mud shrimp (*Corophium volutator*)	Intertidal	<0.5	2–40
Blow lug (*Arenicola marina*)	Intertidal	<4.0	18–40
Salt marsh species 1 (*Salicornia*)	Intertidal above Mean Sea Level	<0.5	18–40
Salt marsh species 2 (*Spartina anglica*)	Intertidal above $-0.5a$	<1.0	18–40

Application for management of estuaries

The main channels in estuaries are often used as shipping fairways, while the intertidal area forms important ecological habitat (Bouma et al., 2005). Given a certain channel width and depth required for shipping, the empirical predictions of bed elevation can aid in estimating volumes that need to be dredged and typical locations where this is necessary. While for many of the present-day shipping fairways bathymetry is available, this application may be relevant for quick assessments by consultancy in developing countries with growing economies for the construction of fairways, harbours or studies on land loss in these areas (Lotze et al., 2006; Yap and Lam, 2013).

Another implication from this study is that the wider an estuary is relative to the fitted converging shape, the wider the zone of intertidal area will be. Bed elevations and basin hypsometry form an indication of possible habitat composition (Townend, 2008) and low-dynamical intertidal areas are generally labelled as valuable areas (Depreiter et al., 2012) because they are suitable for settling and feeding. The output can indicate which areas satisfy these conditions (e.g. suitable flow conditions) and which areas can be transformed into habitat by disposal of dredged sediment. For example, in the Western Scheldt, dredged sediment has been disposed on the edges of tidal flats to maintain intertidal area (Depreiter et al., 2012), which aids in achieving *European Union Natura 2000* regulations (Vikolainen et al., 2014). This approach requires bathymetry, which may not be available at locations where new fairways or harbours are planned. The predictive tool can provide a first-order estimation in these cases.

Application in palaeogeographic reconstruction

Our empirical method is capable of making quantitative estimates of the bar dimensions, the number of bars and channels (braiding index), channel dimensions, flow conditions and salinities. The tool is applicable for palaeogeographical reconstructions (Vos et al., 2015; Pierik et al., 2016) where the shape of tidal channel belts or estuaries has been identified, but wherein bar configuration is typically not recognisable and typical flow conditions are unknown. If the along-channel width profile is known and the tidal range can be estimated, the tool presented in this study can be applied. This application may be particularly relevant for high-stand estuaries that are filled with sediment. Besides the forward approach of palaeogeographical reconstructions based on estuary outline, the tool and equations also allow a reverse approach. A single measurement or preferably a few measurements of bar or channel dimensions (Wood (2004), Yoshida et al. (2004), Jackson et al. (2005), Steel et al. (2012), Saha et al. (2016) and Chapter 2) would be enough to reconstruct typical channel width and local tidal prism and therefore also typical flow conditions.

Additionally, the combination with ecological habitat analyses may improve the understanding of the evolution of estuaries. It is known that vegetation succession stabilises tidal sand bars (Gray, 1992; Thomson et al., 2004; van der Wal et al., 2008; Lokhorst et al., 2018), but it remains an open question to what extent this succession confines the width of estuaries on the longer term. Additionally, it is unknown what the equilibrium shape of an estuary will be under a given set of stabilising and destabilising eco-engineering species.

8.5 Conclusions

A comprehensive set of empirical relations allows estimating bathymetry, flow velocity, salinity and inundation durations for estuaries for which limited data are available. Morphological characteristics are based on the concept that the degree to which an estuary deviates from a maximum fitting converging shape is reflected in the locations where intertidal bars are found, which also determines the bed elevation distributions. This study provides a new correlation between depth below high water level and peak tidal flow velocity, based on numerical model outcomes, which complements the

bed elevation predictions and allows for salinity predictions. The resulting predictions are within a factor two of the measured or modelled values, but generally better. Largest deviations between predicted and modelled or measured occur for flow velocities when they peak above 2 ms^{-1}, for salinity at the transition from brackish to fresh water and for bed elevations when the tidal range is low for the depth at the mouth. The end-member cases of river-dominated delta branches and tide-dominated delta branches, i.e. rivers and ideal estuaries, are most sensitive to depth at both boundaries. In these cases, when possible, it should be measured in a single cross-section and specified as input to prevent misprediction.

We conclude that the tool is suitable for alluvial estuaries filled with tidal bars, for relatively wide valleys that partially filled with bars and for tidal basins. The results are usable to quantify valuable ecological habitat area, to estimate dredging volumes in management of estuaries or to make palaeographic reconstructions when limited data are available.

Acknowledgments

Author contributions were in following proportions to conception and design, tool programming, data collection and analysis, conclusions and manuscript preparation: J.R.F.W.L. (65%, 50%, 60%, 85%), S.L.V. (5%, 50%, 20%, 5%), W.M.v.D. (5%, 0%, 10%, 5%), S.S. (5%, 0%, 5%, 0%), and M.G.K. (20%, 0%, 5%, 5%). We thank three anonymous reviewers for their comments on the manuscript. We thank Rijkswaterstaat for providing bathymetry of the Western Scheldt and Edwin Elias for providing the model of the Columbia River. Discussion with Sepehr Eslami Arab, Barend van Maanen and Tjeerd Bouma helped to improve the manuscript. The code of the tool is made available open access online with the manuscript and through GitHub (https://github.com/JasperLeuven/EstuarineMorphologyEstimator). Other data sources have been referenced in the text. The following is available online: A zip file with tool code and instructions to use the tool. The ZIP contains: (1) 'Instructions.pdf' with instructions on how to use the tool; (2) 'Input_variables.xls', which is file where input parameters need to be specified; (3) '.csv' files with examples of along-channel width profiles; (4) 'Model_v1_0.py', which is the tool code that needs to be run in Python; (5) 'Examples' folder with examples of the output for the Western Scheldt.

Supplementary material

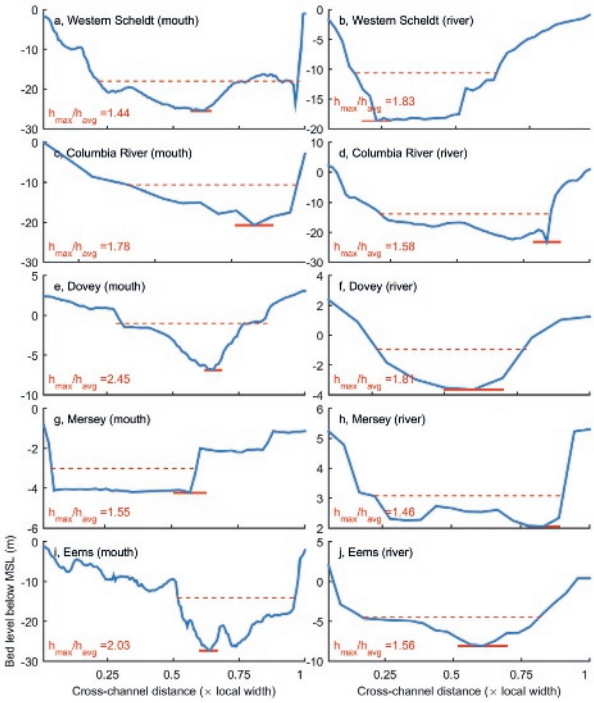

Figure 8.14 Cross-sectional profiles at the mouth [left] and landward river boundary [right] for five estuaries. The maximum depth (solid red line) and an approximation of the average water depth (dashed line) are indicated. The ratio between maximum depth and average depth, which is used in Eqs. 8.8 & 8.12, is given in the figures. Average ratio for the geometry of the estuary mouth is 1.85 and for the landward river boundary 1.65.

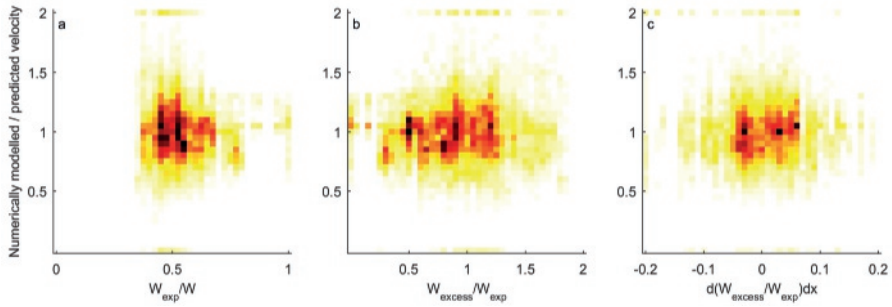

Figure 8.15 Measured velocity from the model divided by predicted velocity from the tool against three expressions of excess width. Lack of trend between velocity deviation and width measures indicates that velocity predictions will not improve from including width in the regression. (a) Ideal width divided by local width, (b) excess width divided by ideal width and (c) along-channel derivative of excess width divided by ideal width. Colours in the plot increase from yellow to red with increasing point density.

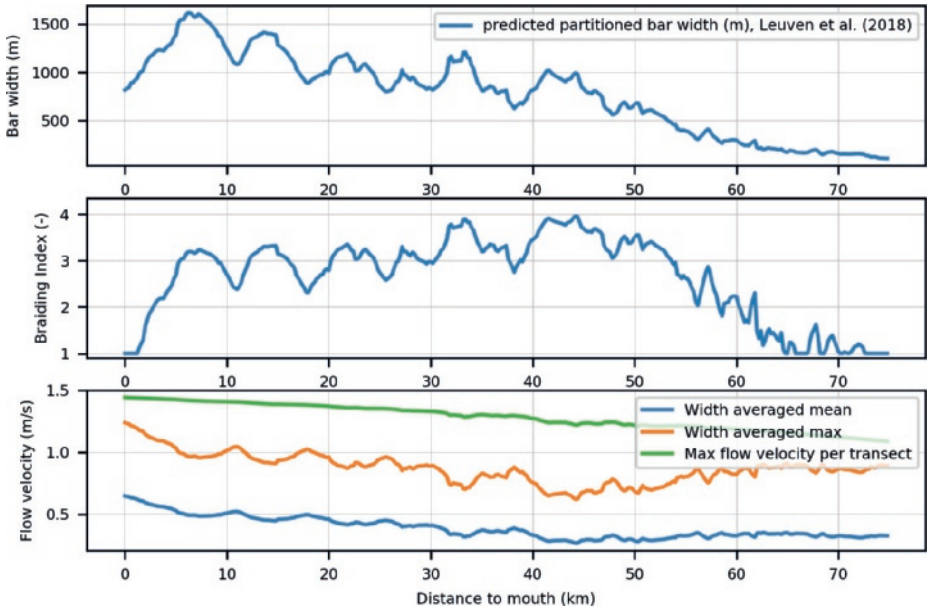

Figure 8.16 Tool output for the Western Scheldt. [top] Predicted along-channel bar width, [middle] predicted along-channel braiding index and [bottom] the cross-sectional maximum and average of the predicted along-channel peak tidal flow velocity and the cross-sectional average of the mean flow velocity over half a tidal cycle.

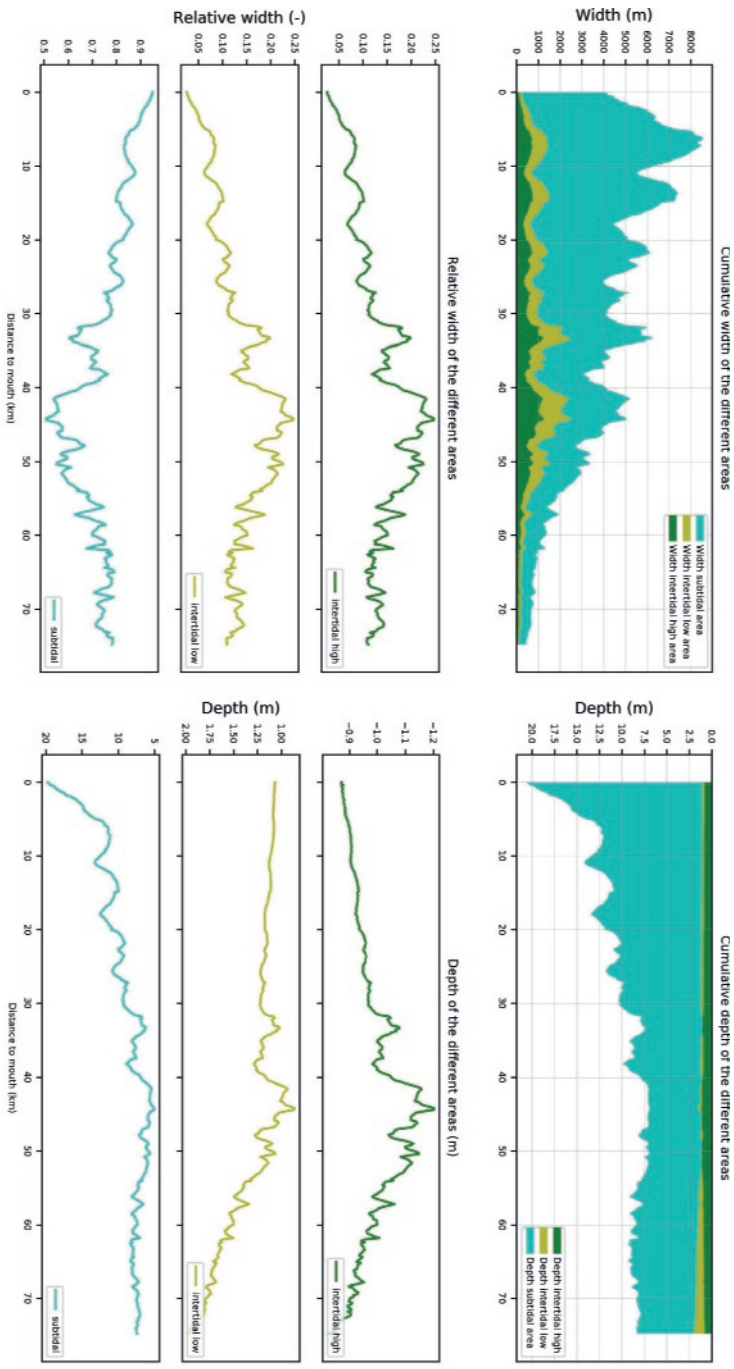

Figure 8.17 *Cont.*

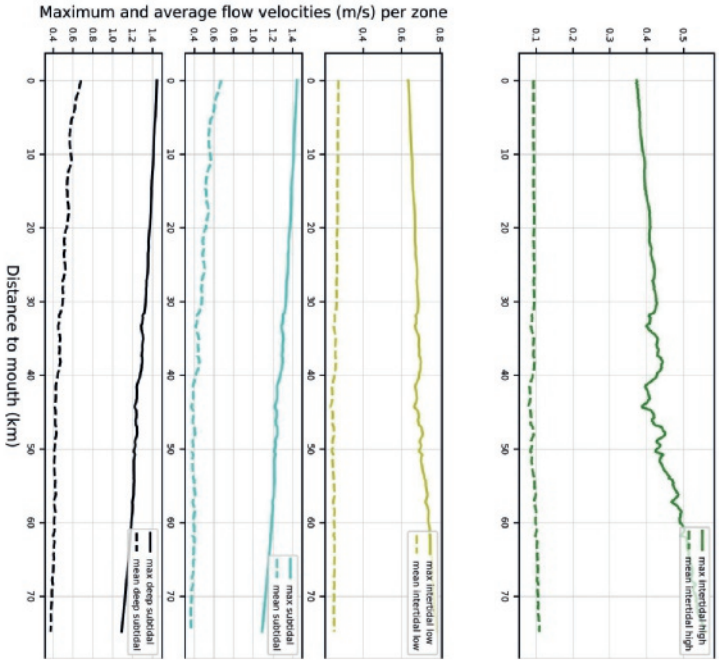

Figure 8.17 Tool output for the Western Scheldt. [top] Along-channel width of subtidal, intertidal low and intertial high zones; [center] average depth of subtidal, intertidal low and intertial high zones; [bottom] average and maximum flow velocity of subtidal, intertidal low and intertial high zones.

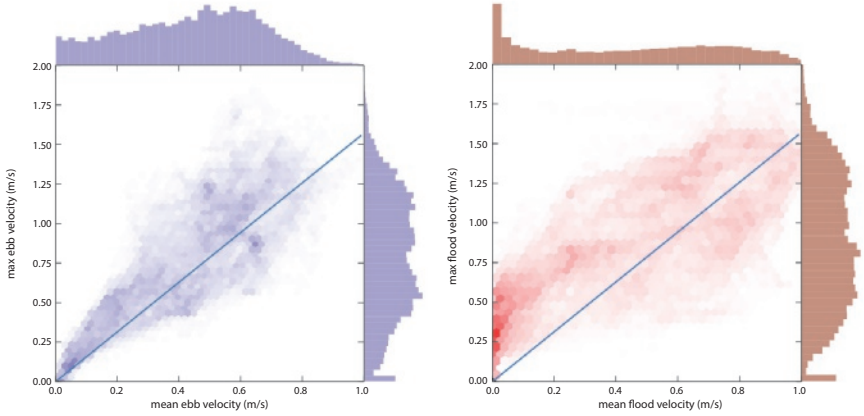

Figure 8.18 [left] Maximum ebb velocity as a function of mean ebb velocity; [right] maximum ebb velocity as a function of mean ebb velocity. Histograms indicate occurrence within bins and colours in the plot become darker with increasing density. Drawn lines indicate the relation $x = 2/\pi y$, which is the expected average velocity when calculated as the average of half a sine function with an amplitude equal to the peak velocity.

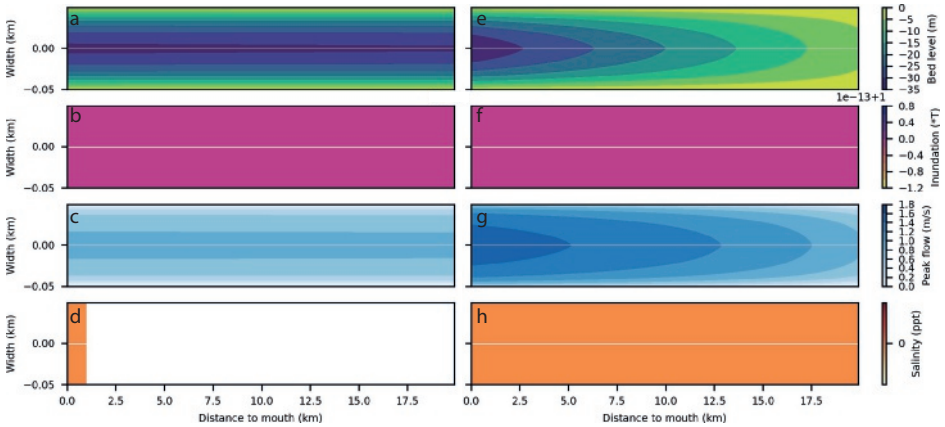

Figure 8.19 Resulting predictions of bed elevation with respect to the high water level, inundation duration, peak flow velocity and salinity for a river based on dimensions of a distributary of the Saskatchewan River, Cumberland Lake (Saskatchewan (Canada), coordinates: 54°04′N 102°22′W) (Fig. 8.2a). In the left panels (a-d) the boundary condition for maximum depth at the mouth and the landward end are both based on hydraulic geometry for rivers (Eqs. 8.6–8.8). In the right panels (e-h), the boundary condition for maximum depth at the mouth is based on the tidal prism relation (Eqs. 8.10 & 8.12) and boundary condition at the landward end is based on hydraulic geometry for rivers (Eqs. 8.6–8.8). See Bolla Pittaluga et al. (2015) for measurements in this river.

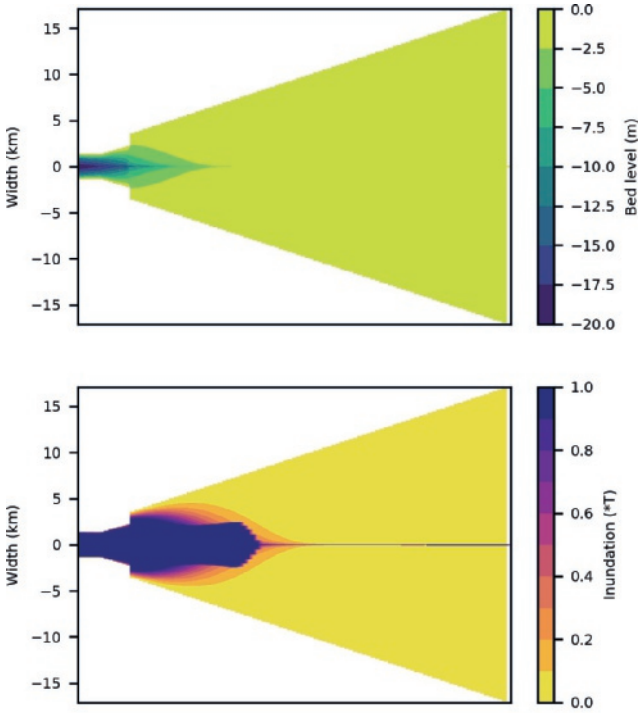

Figure 8.20 *Cont.*

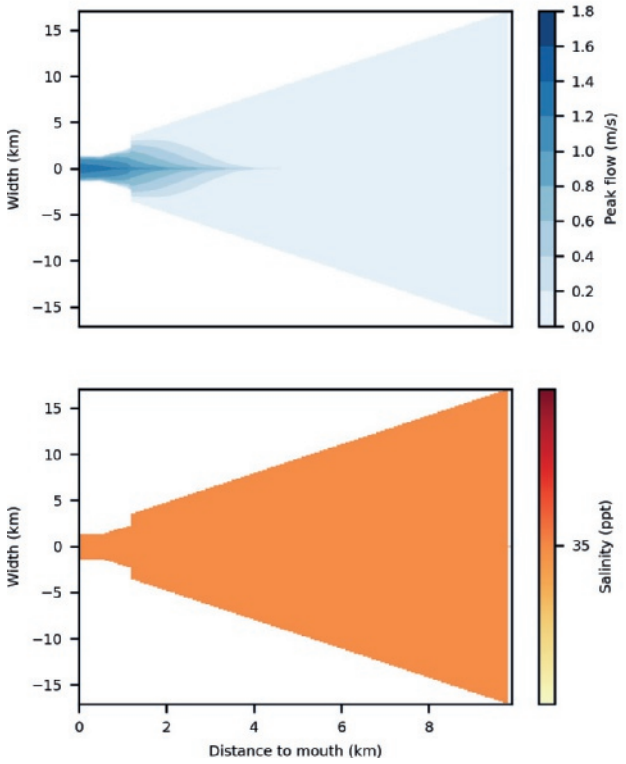

Figure 8.20 Resulting predictions of bed elevation with respect to the high water level, inundation duration, peak flow velocity and salinity for a tidal basin with dimensions based on the Ameland inlet.

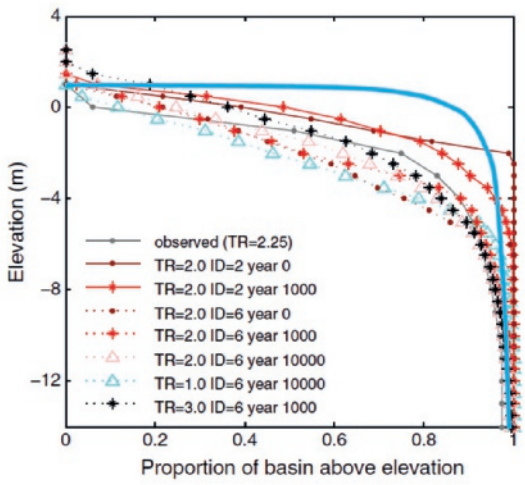

Figure 8.21 The blue solid line indicates the resulting basin hypsometry from the prediction for a tidal basin with dimensions based on the Ameland inlet (Suppl. Fig. 8.20) plotted in Fig. 7 of van Maanen et al. (2013).

Table 8.2 List of symbols used.

Symbol	Units	Variable
$A_{csa,m}$	[m²]	Cross-sectional area at the mouth
$A_{csa}(x)$	[m²]	Cross-sectional area at coordinate x
$a(m)$	[m]	Tidal range at the mouth
$a(x)$	[m]	Tidal range at the mouth
$BI(x)$	[-]	Braiding index at coordinate x
C_m	[$m^{0.5}s^{-1}$]	Chezy roughness at the estuary mouth
D_m	[m^2s^{-1}]	Dispersion coefficient at the mouth of the estuary
$D(x)$	[m^2s^{-1}]	Dispersion coefficient at coordinate x
$\Delta\rho$	[-]	Density difference between salt and fresh water
E	[m]	Tidal excursion length
g	[ms^{-2}]	Gravitational acceleration
$h_{max,r}$	[m]	Maximum channel depth at the landward boundary
$\overline{h_r}$	[m]	Average channel depth at the landward boundary
$h_{max,m}$	[m]	Maximum channel depth at the estuary mouth
$\overline{h_m}$	[m]	Average channel depth at the estuary mouth
$h_z(x,y)$	[-]	Dimensionless bed elevation at coordinate (x,y)
$h(x,y)$	[m]	Dimensional bed elevation at coordinate (x,y)
$I(x,y)$	[× t]	Inundation duration
K	[m^2s^{-1}]	Empirical equation for the longitudinal mixing coefficient
K_s	[-]	Longitudinal Van der Burgh mixing coefficient in Savenije (1993)
K_g	[-]	Longitudinal Van der Burgh mixing coefficient in Gisen et al. (2015)
L_W	[m]	Width convergence length
$L_{A_{csa}}$	[m]	Cross-sectional area convergence length
N_r	[-]	Estuarine Richardson number
$P(x)$	[m³]	Local tidal prism at coordinate x
$P(m)$	[m³]	Local tidal prism at the estuary mouth
Q_b	[m^3s^{-1}]	Bankfull river discharge
Q_r	[m^3s^{-1}]	Average river discharge
r	[-]	Coefficient in the Strahler (1952) equation
r_s	[-]	Storage ratio (intertidal area/subtidal area)
ρ_w	[kgm^{-3}]	Water density
S_m	[ppt]	Salinity at the estuary mouth
S_r	[ppt]	Salinity at the landward boundary
$S_b(x)$	[ppt]	Salinity at coordinate x (Brockway et al., 2006)
$S_g(x)$	[ppt]	Salinity at coordinate x (Gisen et al., 2015)
$S_s(x)$	[ppt]	Salinity at coordinate x (Savenije, 1993)
s	[s]	Distance between the mouth and landward boundary
s_m	[-]	Shape factor of the channel at the estuary mouth
s_r	[-]	Shape factor of the channel at the landward boundary
t	[s]	Duration of half a tidal cycle
$u_{avg}(x,y)$	[ms^{-1}]	Tidal average flow velocity at coordinate (x,y)
$u_{peak}(x,y)$	[ms^{-1}]	Peak tidal flow velocity at coordinate (x,y)
$u_{peak}(mouth,y)$	[ms^{-1}]	Peak tidal flow velocity at the estuary mouth
$W_{excess}(x)$	[m]	Excess width at coordinate x
$W_{ideal}(x)$	[m]	Ideal width at coordinate x
W_m	[m]	Width at the estuary mouth
W_r	[m]	Width at the landward boundary
$W(x)$	[m]	Local width at coordinate x
$w_{bar}(x)$	[m]	Predicted bar width at coordinate x
$w_{barssummed}(x)$	[m]	Summed width of bars at coordinate x
x	[m]	Streamwise coordinate measured from the mouth along the centreline
y	[m]	Coordinate perpendicular to the centreline
z	[-]	Coefficient in the Strahler (1952) equation
$z(x)$	[-]	Value of z-coefficient at coordinate x

Chapter 9 | Sea-level rise induced threats depend on size of tide-influenced estuaries worldwide

Abstract

Effects of sea-level rise (SLR) on the future morphological functioning of estuaries are largely unknown, because tidal amplitudes will change due to combined deepening of the estuary mouth and shifting amphidromic points at sea. Additionally, fluvial sediment supply is globally decreasing. We modelled 36 estuaries worldwide with varying sizes, shapes and hydrodynamic characteristics. Small shallow estuaries and large deep estuaries respond in opposite ways to SLR. Large estuaries are threatened by sediment starvation and therefore loss of intertidal area, especially if tidal amplitude decreases at their mouth. In contrast, small estuaries face enhanced flood risks, being more sensitive to tidal amplification. Widening the estuary can partly mitigate adverse effects of SLR. In large estuaries, expanded intertidal area increases tidal prism and available erodible sediment for adaptation, whereas in small estuaries this practice slightly increases tidal damping.

Revision submitted as: Leuven, J.R.F.W., Pierik, H.J., van der Vegt, M., Bouma, T.J. & Kleinhans, M.G. (2019). Sea-level rise induced threats depend on size of tide-influenced estuaries worldwide. *Nature Climate Change*

9.1 Introduction

Estuaries are highly dynamic wetland zones at the transition from the river to the ocean, susceptible to future climate change and especially to sea-level rise (SLR) (Church et al., 2013; Wong et al., 2014). In estuaries such as the Western Scheldt, Elbe and Yangtze, the channels provide access to inland harbours (de Vriend et al., 2011) and the intertidal bars form valuable ecological habitat (Bouma et al., 2005). The surrounding land is often densely populated, with 21 of the world's 30 largest cities being located next to estuaries (Ashworth et al., 2015). Potential SLR-induced threats are increased flood risk (Nicholls and Cazenave, 2010; Auerbach et al., 2015), reduced navigability (Mao et al., 2004), and drowning of intertidal habitat area (Costanza et al., 1997; Essink, 1999; de Vriend et al., 2011; Yuan and Zhu, 2015; Balke et al., 2016). Estuary size and shape will affect their future response to SLR (Ensing et al., 2015; Du et al., 2018), but so far SLR-induced changes in morphology received little attention. Here we study changes in morphology and the resulting tidal dynamics for estuaries of different sizes worldwide.

Estuarine bars, tidal flats and salt marshes have the potential to grow with SLR if they import sufficient fluvial or marine sediment to adapt the morphology to the new boundary conditions (Lentz et al., 2016). Sediment trapping efficiency can increase when accommodation space increases, flow velocities reduce allowing sediment to settle, or by stronger flood dominance. Three key boundary conditions for estuary morphology and their potential to adapt are (1) planform shape, (2) tidal amplitude at the mouth and (3) sediment supply. Together these parameters control the overall volume of water (tidal prism) and sediment moving in and out of the estuary (Kirwan and Guntenspergen (2010), Du et al. (2018) and Chapter 8), which determine channel volume and the space available to form intertidal bars (Chapter 5). However, under SLR, tidal amplitudes at estuary mouths are likely to change because of shifting amphidromic points (Idier et al., 2017; Pickering et al., 2017) around which tidal waves rotate on shallow continental shelf seas. If the distance between the estuary mouth and amphidromic point increases, the tidal amplitude increases and vice versa. It remains unknown how the combined future SLR and changes in tidal amplitude will affect both the tidal propagation and equilibrium morphology of bar filled estuaries worldwide. Their future equilibrium morphology determines whether present-day fluvial sediment supply will be sufficient for adaptation of the morphology.

Whether the tidal range amplifies (i.e. becomes larger), remains constant or dampens (i.e. becomes smaller) in the landward direction depends on the balance between bed friction, which causes damping, and topographic convergence, which causes amplification (Friedrichs and Aubrey, 1988; Savenije, 2006; Boelens et al., 2018; Du et al., 2018; Silvestri et al., 2018). When convergence and friction are in balance, the tidal range is constant along-channel, which is the condition for an "ideal estuary" (e.g. Savenije, 2006). Under future increase in mean sea level, bed friction effects will become smaller if the morphology does not adapt. In that case, the tidal range can become increasingly amplified. The consequence is flood risk (higher high waters) and reduced navigability (lower low waters).

Human use has largely affected the natural processes occurring in deltas and estuaries in the past centuries (Temmerman and Kirwan, 2015). In particular, dike construction and land reclamation (de Vriend et al., 2011) have cut off the ecologically valuable flanking mudflats and salt marshes from the channels that supply sand and mud during inundations (Kirwan and Megonigal, 2013; Schuerch et al., 2018). However, these intertidal areas form storage space and friction for the tidal wave (Friedrichs and Aubrey, 1988), thereby naturally reducing flood risk. The channels are dredged for harbour accessibility, which reduces friction for the tidal wave, thereby enhancing flood risk (Essink, 1999; de Vriend et al., 2011; Yuan and Zhu, 2015). Additionally, dam construction in rivers has largely reduced fluvial sediment supply to estuaries (Walling and Fang, 2003; Yang et al., 2005). Here we evaluate how flood risk and drowning threats can be mitigated by managed realignment. Managed realignment (Turner

et al., 2007) means removing coastal protection to expose additional – currently terrestrial – area to tidal flooding and erosion. Managed realignment thus leads to widening of the estuary.

9.2 Approach and scenarios

Here we calculated the morphological and hydrodynamic response of 36 estuaries worldwide to SLR and assess the potential for increased space by managed realignment. Estuaries varied from very small to very large (0.1-1000 km^2), which allowed us to test the effect of estuary size on SLR-induced threats. The required sediment for adaptation and flood water levels within the estuary are used as main indicators in coping with SLR.

For each estuary, we estimated the present-day equilibrium morphology and future equilibrium morphology with a novel tool that predicts the estuarine depth distribution (Chapter 8). In short, the predicted depth distribution along the estuary depends on the estuary planform shape, tidal amplitude at the mouth and river discharge (Suppl. Fig. 9.9, Suppl. Table. 9.1). The tool predicts tidal prism at the mouth based on surface area and tidal range. This tidal prism is then used to estimate the maximum and average depth at the mouth (Jarrett, 1976; Eysink, 1990; Gisen and Savenije, 2015). Similarly, a hydraulic geometry relation is applied at the landward boundary to obtain depth from river discharge. Together, these boundary conditions result in an along-channel maximum depth profile. The distribution of bed levels per cross-section, i.e. the hypsometry, depends on the ratio between the local width and the width as expected from a fitted converging shape (i.e. ideal, cf. Langbein (1963), Savenije (2006), Dronkers (2017) and Chapters 5 & 7). We predict convex hypsometry with a wide zone of intertidal area at locations where the estuary is wide compared to the fitted convergent channel. In contrast, a concave hypsometry with narrow stretches of intertidal area is predicted at locations where the estuary width is close to the ideal width profile. Subsequently, the morphological output is translated into 1D-profiles of the channel width (defined as the width below the low water line), average channel depth, shoal width and average shoal depth. The 1D-profiles and tidal amplitude at the mouth and river discharge were used as input to a 1D-hydrodynamic model that solves the shallow water equations, resulting in tidal range along the estuary (Friedrichs and Aubrey, 1988). Along-channel tidal range is used as an indicator for flood safety, navigability and intertidal habitat area.

The effects of SLR were studied in three scenarios of increasing complexity. **Scenario 1** is a worst case increase in mean sea level (MSL) of 1 m in 100 years, i.e. within a century (Church et al., 2013; Idier et al., 2017; Du et al., 2018; Schuerch et al., 2018), to analyse the effect of increased channel depth on tidal amplification (Fig. 9.1). Scenario 1 provides a baseline for the required sediment volume. Because all boundary conditions that affect morphology remain constant, the future morphology is assumed to remain equal to the estimated present-day morphology. This means that the required sediment demand is simply the estuary surface area multiplied by the increase in MSL (Fig. 9.1). In reality, however, the required sediment is modified by changes in tidal amplitude at the mouth due to SLR imposed shifts of amphidromic points (Idier et al., 2017; Pickering et al., 2017), which means the estuary has to adapt to a new equilibrium. Therefore, **Scenario 2** explores the effect of changes in tidal amplitude at the mouth, varying from a decrease of 0.25 m (a^-) up to an increase of 0.50 m (a^{++}) (Fig. 9.1). This scenario illustrates the effect of future changes in tidal amplitude at the mouth on the required sediment for adaptation. In **Scenario 3** the effect of increased estuary width is investigated (Fig. 9.1). Increased estuary width modifies the estimated equilibrium morphology. Furthermore, sediment from former, flooded salt marshes becomes partly available for redistribution.

Scenario 1 is predominantly used to study the effect of increased channel depth on tidal amplification. Scenario 2 reveals a relation between required sediment for adaptation and future changes in tidal range. Scenario 3 elucidates under which conditions managed realignment has the

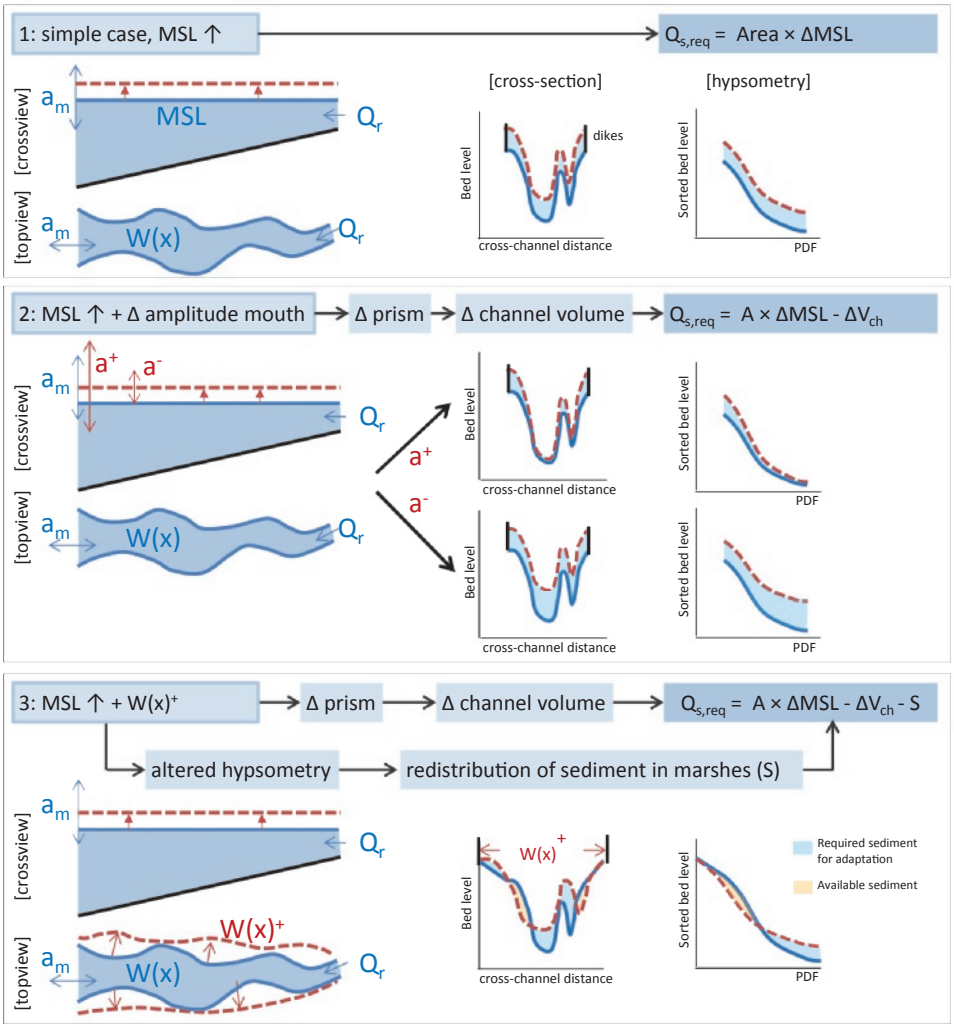

Figure 9.1 SLR effects on boundary conditions of estuaries. Flowcharts indicate main morphological effects. The red dashed line indicates the scenario effects on water level and estuary width in all panels. Red arrows indicate changes in tidal amplitude at the mouth. The PDFs indicate hypsometric curves that summarise cross-sectional bed elevations in cumulative profiles. [**top**] In the most simple case (Scenario 1, an increase in MSL), all boundary conditions remain equal, which means that the required sediment for adaptation is the estuary surface area times the increase in MSL. [**middle**] Tidal range either increases (Scenario 2, a^+ or a^{++}), decreases (Scenario 2, a^-) or remains the same (Scenario 1, a^o) depending on the location of the estuary with respect to its amphidromic point (i.e. tidal node). Changes in tidal amplitude at the mouth modify the tidal prism and thereby alter the equilibrium channel volume. This increases the required sediment for adaptation for decreasing amplitude (a^-) and decreases the required sediment for increasing tidal amplitude (a^+). [**bottom**] The estuary widens (Scenario 3, $W(x)^+$) if surrounding land is drown or by managed realignment. Increased planform width has a similar effect as the previous scenario, but also alters the cross-sectional distribution of bed levels, which means that salt marsh sediments become available for redistribution. All parameters, variables and abbreviations are defined in Suppl. Table. 9.4.

potential to mitigate adverse effects of the previous scenarios. Furthermore, the results of sediment requirement were compared with geological cases, serving as references for the fate of estuaries. For this we used past planform sizes of six systems (Suppl. Table. 9.2) that previously evolved under SLR that was in the same order of the expected future SLR.

9.3 Estuary dimensions control the effects of SLR

For the first time we show that morphological and hydrological responses to SLR are hugely different between small, shallow and damping (i.e. hyposynchronous) estuaries and large, deep and amplifying (i.e. hypersynchronous) estuaries (Fig. 9.2). The size dependency on responses to SLR was found in all three scenarios, for which the results are detailed below. Size related characteristics – i.e. the characteristic channel convergence length, depth of the estuary and present-day tidal prism – proved to be very strong indicators of sensitivity to SLR. Other estuary characteristics, e.g. increase in tidal prism from a widened estuary planform and the ratio between bar area and total area, proved to be less suitable indicators for sensitivity to future SLR (Suppl. Fig. 9.10).

9.3.1 Future flood risk, navigability and intertidal area

We found that large estuaries, which in all cases show tidal amplification, are unlikely to amplify even more under SLR (Scenario 1) even if they receive insufficient sediment to adapt to SLR (Fig. 9.2a). In contrast, small systems, which in all cases currently show tidal damping, respond extremely sensitively by having a large increase in tidal range (Scenario 1, Fig. 9.2a). Small and thus shallow estuaries are typically friction dominated. For these estuaries, a 1 m increase in water depth results in a relatively large reduction in friction (Friedrichs and Aubrey, 1988), which causes tidal amplification. Predictions with a 1D-hydrodynamic model show that small estuaries, when drowning, have maximum water levels in the estuary increased by 0.3-0.8 m on top of the increase in MSL, which is predominantly due to reduction of friction. In contrast, friction in relatively large and thus deep estuaries is much less, which means that the same increase in MSL has a smaller effect on tidal amplification (Fig. 9.2a).

The changes related to estuary size directly translate in opportunities for human use and ecosystem services. If tidal amplitude increases within the estuary, it will reduce navigability during low tide and increase flood risk during high water. The predictions for flood safety are however upper limit estimates, because Scenario 1 excludes morphological adaptation, changes in tidal amplitude at the mouth and the effects of increased mean water levels that occur during storm surges (see Suppl. Text).

Tidal amplification (possible result of Scenario 1) and SLR in combination with changes in tidal amplitude at the mouth (Scenario 2) cause intertidal areas to change in multiple ways, depending on estuary size and sediment supply. First, a change in the tidal amplitude boundary condition (Scenario 2) directly affects intertidal area, which includes pioneering salt marshes (Balke et al., 2016; Kirwan et al., 2016), by increasing or decreasing the range of bed levels that inundate and drain over a tidal cycle. While increased tidal amplitude deepens the estuary and increases channel volume, intertidal area also increases with tidal range (Chapter 8). While channels become deeper and wider, the highest parts of marshes and the subtidal part of bars are transformed into intertidal area due to the increased tidal range. Second, tidal amplification (Scenario 1) increases the tidal range in the landward direction, which could result in increased intertidal area in the landward direction for the same reason. Present results thus illustrate how two opposing threats and values will compete in the future: increased tidal amplitudes will increase flood risk during high waters and reduce navigability during low tides, but increase intertidal habitat, and vice versa for reduced tidal amplitude. The potential morphological adaptation of channels, bars and intertidal area under SLR depends mainly on the required sediment input, which is discussed next.

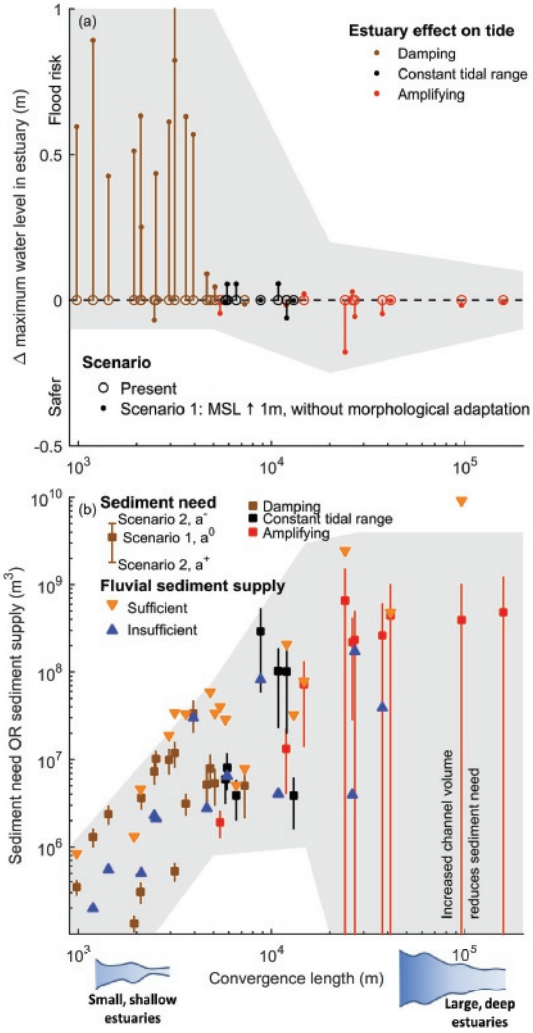

Figure 9.2 Estuary size dependency on sea-level rise induced threats. (a) Trajectories of SLR-induced changes in maximum water level within the estuary against convergence length, which is a measure of estuary size. Lines indicate the effect of 1 m SLR without morphological adaptation (Scenario 1). Shallow damping estuaries are most sensitive to future increases in water level, imposing a flood risk, while deep amplifying estuaries are not sensitive. (b) Sediment need or sediment supply for adaptation with 1 m SLR over a period of 100 years against estuary convergence length. Vertical lines indicate the sensitivity to increased (Scenario 2, a^{+}) or decreased (Scenario 2, a^{-}) tidal amplitude with squares indicating the required sediment when amplitude at the mouth remains constant. Triangles indicate estimated fluvial sediment supply over 100 years. Blue triangles indicate a sediment supply less than the requirement under the a^{o} scenario. Orange triangles indicate a surplus of fluvial sediment input. Large amplifying estuaries are very sensitive to changes in tidal amplitude on required sediment for adaptation, while small damping estuaries are less sensitive. Large estuaries with increasing tidal amplitude have sufficient sediment input from the river for adaptation, while a decrease in tidal amplitude would lead to a larger requirement than supplied by the river.

9.3.2 Future sediment balance

A comparison of present fluvial sediment supply (Milliman and Syvitski, 1992) and required sediment for adaptation to the new equilibrium state (Scenario 2) shows that most large estuaries will have sufficient fluvial input if tidal amplitude at the mouth increases, but that they most likely have a shortage if tidal amplitude decreases (Fig. 9.2b). This surprising result is caused by the increase in channel volume with tidal prism (Scenario 2, a^{+} and a^{++}), which partly compensates for the required sediment due to an increase in MSL (Scenario 1) (Suppl. Fig. 9.11a). A decrease in tidal amplitude (Scenario 2, a^{-}), on the other hand, requires much more sediment (Fig. 9.2b) to follow SLR because it reduces the equilibrium depth and volume of channels (Fig. 9.1).

The morphological response and dependence on sediment supply to Scenarios 2 is different for large and small estuaries. Large estuaries with relatively deep channels and a weak channel convergence show a strong morphological response to changes in tidal amplitude by relatively large changes in channel volume (Fig. 9.2b). Geological examples are the Rhine-Meuse Delta and Tokyo Bay that drowned in the Mid-Holocene (Fig. 9.3). Over the entire Holocene, drowning was eventually compensated, indicating that it took thousands of years of major sediment supply under stabilising sea level to compensate for this drowning. The Ganges is an example of how excessive amounts of sediment supply over the Holocene not only compensate SLR, but even cause delta progradation. In contrast, small estuaries are much less sensitive to changes in tidal amplitude at the mouth (Fig. 9.2b), because the change in tidal prism by amplitude change depends mainly on basin surface area. Whether small estuaries indeed adapt, depends mainly on the current supply of fluvial sediment compared to the estuary size. Our results indicate that estuaries with a larger ratio of catchment area to estuary area are more likely to receive sufficient fluvial input than estuaries with relatively small catchments (Fig. 9.3). Here we showed that estuaries relatively large compared to their catchment are sensitive to drowning, but that this effect can be counteracted by increased tidal amplitude at the mouth.

9.3.3 Management options

Modelling Scenarios 3 show that managed realignment may counteract sediment starvation in large estuaries and increased flood risk slightly in small estuaries, but the latter only to a small extent. In small estuaries, widening in the landward zone (zone C in Fig. 9.4a) or along the entire estuary (zone D) are most effective to reduce water levels in the estuary (Fig. 9.4a). This results in wider tidal flats enhancing tidal damping (Fig. 9.4). The latter (D) also has a strong positive effect on the sediment balance (Fig. 9.4b). If the available sediment thereby becomes sufficient for the estuary to adapt, the effect of increased water depth on tidal amplification is also mitigated. Widening at the mouth (A) or in the tide-dominated zone (B) are not recommended, because widening at the mouth (A) increases the channel width along the estuary, while widening in the tidal zone (B) increases tidal prism and therefore deepens channels in the tide-dominated zone, which outweighs the positive effects of increased shoal area.

For large estuaries, managed realignment (Scenario 3) is most effective when implemented along the entire estuary (Fig. 9.4, Scenario D). Widening in the tide-dominated zone (Scenario B) is also effective for the sediment balance, but at the cost of increased water levels (Fig. 9.4a). Generally, if the estuary is widened close enough to the mouth to be able to affect the tidal prism, channels will enlarge and therefore less sediment is required for adaptation. Thereby, widening also alters the prediction of bed levels per cross section, i.e. the hypsometric curve, which may result in erosion and reworking of sediment from former salt marshes.

If the natural sediment supply is too low for natural adaptation, management options may provide alternative adaptation pathways (Kwadijk et al., 2010; Haasnoot et al., 2013). These options include sediment nourishment on the ebb-tidal delta to increase sediment import from the sea (Wang et al., 2018) or estuary widening by managed realignment (Scenario 3). Our results show that widening,

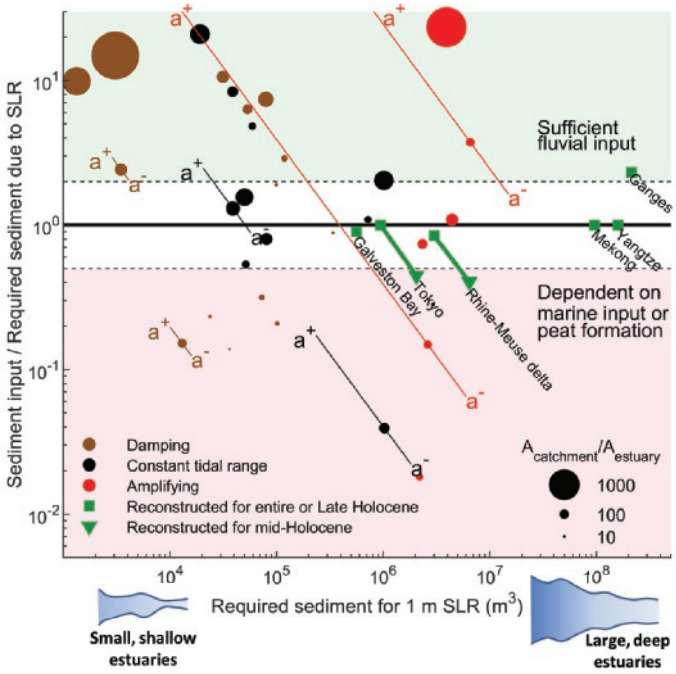

Figure 9.3 Relative upstream sediment input from the catchment versus the range of required sediment for 1 m SLR depending on the change of tidal amplitude. Required sediment is an indicator for estuary size when all boundary conditions remain constant (i.e. Scenario 1). Rivers with a relatively large catchment deliver sufficient sediment to estuaries, which can therefore adapt to rising sea level, while other estuaries will depend on marine sediment input, peat formation or sediment nourishment for morphological adaptation. The sensitivity to changes in tidal amplitude (see Fig. 9.2) are indicated for a small selection of all systems indicated in Fig. 9.2. Holocene sediment budgets from geological cases are added as a reference for minimal sediment supply potential. Mid-Holocene cases experienced SLR comparable to future SLR (see also Suppl. Table. 9.2).

with breakdown and reworking of salt marshes on sandy substrates, would deliver part of the sediment required for adaptation to SLR, but at the cost of intertidal and supratidal habitat. Moreover, local widening would increase accommodation space, which was recently found to stimulate the resilience of global wetlands because it allows them to grow vertically by sediment accretion (Schuerch et al., 2018). Therefore, we conclude that managed realignment is an important measure to implement before potential dike breaching leads to land loss in densely populated areas.

9.4 Conclusions

Sensitivity of estuaries to future SLR depends on changing tidal dynamics, sediment supply and the size of estuaries, but some adverse changes can partly be reduced by managed realignment. Large and deep systems will face the threat of sediment starvation especially when tidal amplitude decreases (Fig. 9.5). In contrast, small and shallow estuaries are most sensitive to tidal amplification causing increased flood risk (Fig. 9.5). Sediment starvation and increased water levels can be counteracted by increasing estuary width. In large estuaries, this will increase tidal prism and available erodible sediment for adaptation, whereas in small estuaries it will enhance tidal damping (Fig. 9.5). The

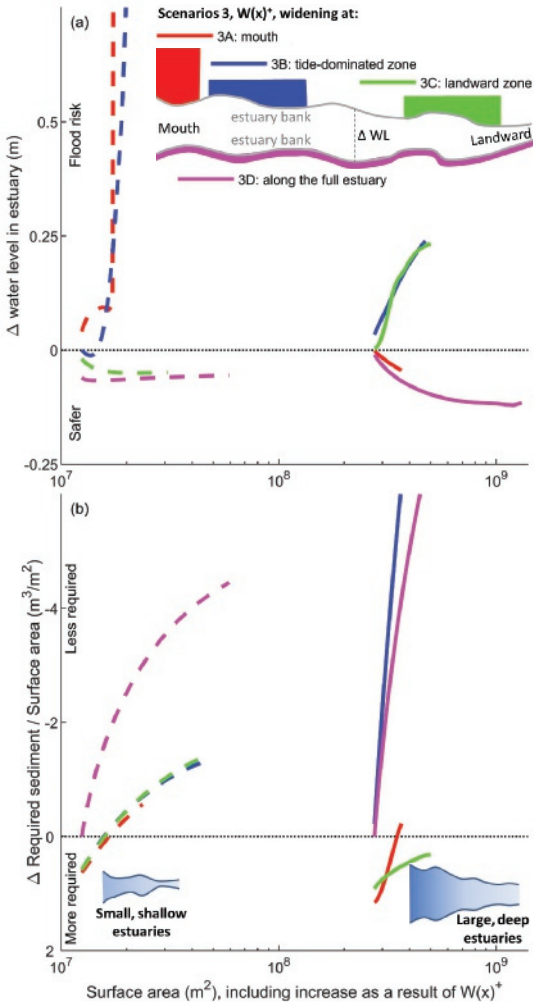

Figure 9.4 Effects of managed realignment. (a) Change in water level within the estuary and (b) change in required sediment for adaptation normalised by surface area plotted against degree of estuary widening. Dashed lines indicate idealised model results for Scenarios 3 A-D for a small estuary (length of 15 km) and solid lines indicate a large estuary (length of 70 km). Widening was implemented on a fixed length and thus with variable local width. The type of widening in Scenario 3 has a large effect on required sediment for large estuaries and on water levels in small estuaries. Increased estuary width increases tidal prism at the mouth, but only when the widening is located seaward of the tidal excursion length, which is the distance a particle of water travels in half a tidal cycle. Increased tidal prism increases channel depth and volume, and therefore reduces required sediment. However, increased depth also reduces friction, which increases water levels in the estuary.

results are promising for further assessment of the vulnerability of specific estuaries to SLR caused by changing estuary shape and changing tidal regimes. Moreover, the tools provided in this study can aid in fast testing of management strategies.

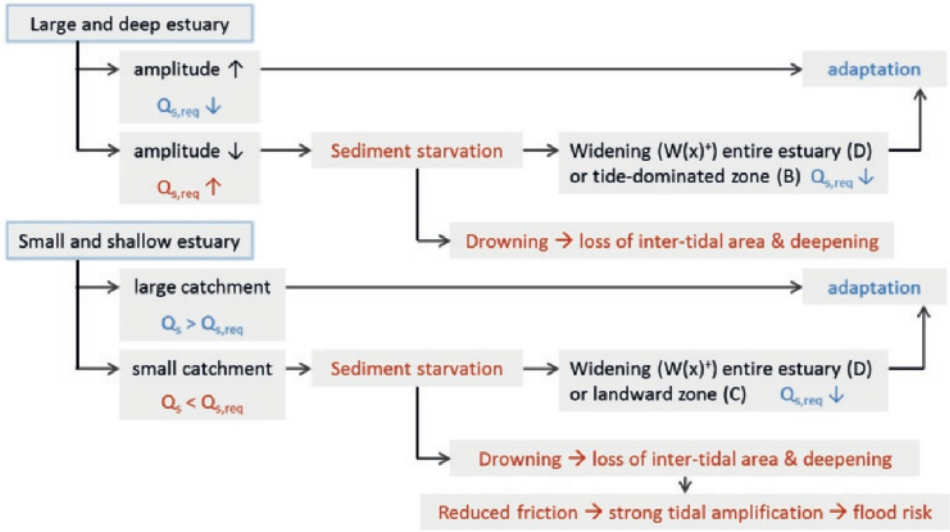

Figure 9.5 Main responses of estuaries to SLR. Large, deep, amplifying estuaries are susceptible to sediment starvation if tidal amplitude at the mouth decreases. The latter can be counteracted by increased space for the estuary along the entire channel, which will increase tidal prism and available erodible sediment for adaptation, or in the tide-dominated zone at the expense of higher water levels in the estuary. Small, shallow, damping estuaries are susceptible to future tidal amplification when sediment supply is insufficient to adapt the morphology to SLR. Managed realignment can potentially reduce amplification, but only when it is implemented in the most landward part of the estuary or along the entire estuary (Fig. 9.4). The benefit of the latter is that it also strongly decreases the required sediment for adaptation.

Acknowledgments

[Author contributions] Conception and design: JRFWL, MGK, TB. Data collection: JRFWL, HJP. Modelling: JRFWL, MvdV. Writing: JRFWL with contributions from HJP, MvdV, TB, MGK. All data are open access available in the figures, tables, and supplement and if used from other sources, it is indicated with references. The code for the one-dimensional hydrodynamic model is appended as online Supplementary material. The code for the morphological tool is available on GitHub (https://github.com/JasperLeuven/EstuarineMorphologyEstimator/). Estuary outlines were collected in Google Earth and are available as online supplementary material with Chapter 5. Along-channel width profiles are appended as .csv files. Input values to run the morphological tool and hydrodynamic model and output values are appended as .xlsx file.

9.5 Detailed methods

The following steps were taken. Firstly, estuary planforms where collected from aerial photography along with the present-day tidal range at the mouth (a_m) and river discharge (Q_r) at the upstream boundary (Suppl. Table. 9.1). Secondly, an empirical assessment tool was used to predict the present-day and future equilibrium morphology of these estuaries (Chapter 8). Thirdly, the output morphology served as input to a 1D-hydrodynamic model (Friedrichs and Aubrey, 1988), which was used to study tidal amplification and damping. Subsequently, we applied three SLR scenarios to study the effect on morphology and tidal amplification. Lastly, the required sediment for morphological adaptation under

SLR was compared with the present-day sediment input to estuaries and reconstructions of former coastal systems under SLR.

To be able to perform a worldwide analysis, we estimated the equilibrium morphology by using empirical relations rather than using coupled hydrodynamic-morphological models. While the latter type of models are very powerful tools, they are unsuitable for performing a worldwide analysis on estuaries due to their time consumption and for a lack of data to calibrate and validate them. In our previous work (Chapters 5, 7 & 8) we validated our methods and estimated uncertainties associated with using them. Here we show in the supplementary material how these uncertainties affect the main results in this study: i.e. predicted flood water levels and required sediment for adaptation. The resulting uncertainty was a maximum of about 0.1 m for flood water levels and a factor 1.5 for required sediment for adaptation (Suppl. Fig. 9.8).

9.5.1 Data collection of estuary planforms

An existing dataset with estuary planforms (Chapter 5) was used in and enhanced for this study. The dataset consists of 36 bar filled estuaries worldwide of varying size, degree of tidal influence, river discharge and human influence (Suppl. Table. 9.1). Channel planform was visually recorded using Google Earth for a lack of sufficient detailed bathymetries. For each estuary, the present-day planform was recorded. The tidal range at the mouth and river discharge were obtained from the datasets reported in Chapters 2 & 5. The present-day planform covers the part of the estuary in which large (>100s of metres) dynamic channels and bars occur and is approximately the area that is submerged at high tide level. This means that we exclude those parts of the high marsh that do not flood daily, similar to other higher elevated areas surrounding the estuary. Presence of dense vegetation is a good indicator of area that is not daily flooded anymore, as an inundation duration above a time fraction of about 50% limits and often inhibits vegetation growth and most vegetation settles permanently above the mean high tide level.

We tested the sensitivity of the 1D-hydrodynamic model results to erroneous estimates of the salt marsh area. To do so, we added salt marshes equal to 20% of the local estuary width along the entire estuary. Our model showed that this affected water levels by less than 5% of the reported values. This implies that addition of salt marshes above the high tide level has a limited effect on the main conclusions of our research.

9.5.2 Tool for equilibrium morphology of estuaries

The along-channel width profile, tidal range at the seaward mouth of the estuary and river discharge are input to the empirical assessment tool that predicts equilibrium morphology (Chapter 8) (Suppl. Fig. 9.6). The tool predicts tidal prism at the mouth based on surface area and tidal range. The tidal prism is used to estimate the maximum and average depth at the mouth from a classic stability relation (Jarrett, 1976; Eysink, 1990; Gisen and Savenije, 2015). Similarly, a hydraulic geometry relation is applied at the landward boundary to obtain depth from river discharge. Together, these boundary conditions result in an along-channel maximum depth profile. The distribution of bed levels per cross-section, i.e. the hypsometry, depends on the ratio between the local width and the width as expected from a fitted converging sha[e (i.e. ideal, cf. Langbein (1963), Savenije (2006), Dronkers (2017) and Chapters 5 & 7). We predict convex hypsometry with a wide zone of intertidal area at locations where the estuary is wide relative to the fitted convergent channel, while concave hypsometry with narrow stretches of intertidal area are predicted at locations where the estuary width is close to the ideal width profile.

This simplified approach to estimate tidal prism neglects the amplification and damping of the tide as well as changes in the character of wave (standing versus propagating character). This means that for small and damping estuaries we might overestimate the tidal prism and for large and amplifying estuaries we might underestimate the tidal prism by 10-40%. However, this simplification has a limited

effect on the results in this study. If we overestimate tidal prism for small estuaries, it also means that we overestimate their depth. If their depth would indeed be smaller, this would lead to larger friction and therefore an even larger sensitivity of future water levels to SLR. For large estuaries, the opposite reasoning holds.

9.5.3 1D-hydrodynamic model

To investigate the degree of tidal amplification (i.e. flood water levels) or damping within each estuary we ran a number of model scenarios. We used a one-dimensional hydrodynamic model that has been demonstrated to reproduce the most important tidal dynamics (Friedrichs, 2010) (Suppl. Figs. 9.7, 9.9 & 9.12, code in online supplementary material). The model solves the shallow water equations (i.e. differential equations that describe fluid flow), excluding the effects of advection, with momentum transported solely through a rectangular channel. The continuity equation incorporates a linearly sloping intertidal area to allow width variation with water level and thereby simulates storage of water on the intertidal flats. For each estuary, the tidal range and depth at the estuary mouth were taken directly from the tool (Chapter 8). Along the estuaries, the cross-sectional hypsometry was divided in a channel part and a shoal part at the low water level, which is how we defined channel width. Subsequently, the average channel depth, channel width, shoal gradient and shoal width were calculated per cross section. The linear cross-channel shoal gradient was calculated such that the storage volume is equal to the storage volume that results from the hypsometry above the low water line. Along-channel profiles of these characteristics were used as input to the model. The spatial step varied between 50 and 500 m depending on the size of the estuary and the time step was adjusted accordingly based on the Courant number.

Roughness was implemented as follows. For the mouth of each estuary a roughness coefficient (k_s) was calculated based on a Chézy value of 50, 60 or 70 for small, middle and large estuaries, respectively. The roughness coefficient at the mouth (k_s) was used in the model to calculate the space- and time-varying Chézy value and drag coefficient (C_d). Friction variations along estuaries are minor and this is a common approach in numerical modelling to estimate friction (Geleynse et al., 2011; van der Wegen, 2013; Nnafie et al., 2018). For example, Nnafie et al. (2018) use a constant Chézy value and Geleynse et al. (2011) and Van der Wegen (2013) use a constant Manning's value for delta branches, which only has a weak dependency on depth. Moreover, our friction assumption does not affect the main trends found. Even with a perfect representation of friction (which would require grain size distributions of all estuaries, among other things), small estuaries will still respond stronger to a 1 m increase in SLR than large estuaries.

9.5.4 SLR scenarios

To study the effect of SLR on the future morphology and tidal range of estuaries we implemented the following scenarios (Fig. 9.1):

[**Scenario 1**, a^0] An increase in MSL of 1 meter in 100 years and all other boundary conditions and estuary shape remain the same. While precise SLR varies among systems, here we used a value of 1 m, loosely based on IPCC scenarios (Church et al., 2013; Idier et al., 2017; Du et al., 2018), to illustrate dominant effects and response mechanisms among estuaries worldwide. For the morphological tool, a change in MSL means that all input variables remain the same and thus the prediction of equilibrium morphology is equal. This also implies that the required sediment [m^3] for morphological adaptation is equal to the estuary surface area [m^2] times the SLR [m]. In the hydrodynamic model, the two extreme cases of full morphological adaptation and no morphological adaptation were calculated. In case of full morphological adaptation, the resulting tidal amplification is equal to the situation before SLR but in the case without morphological adaptation the increased depth of channels and shoals will lead to a different degree of amplification.

[**Scenario 2,** a^{++}, a^{+}, a^{-}] Tidal amplitude at the estuary mouth can either increase, decrease or remain constant as a result of SLR (Idier et al., 2017; Pickering et al., 2017). The two most important reasons are the shift of amphidromic points (i.e. tidal nodes) on the shelf and the reduced friction caused by an increased water depth. If the distance between the estuary mouth and the amphidromic point will increase in the future, the tidal amplitude will increase, while the amplitude will decrease if the distance becomes shorter (Idier et al., 2017; Pickering et al., 2017). Additionally, increased MSL will reduce friction in the coastal seas which means tidal damping will reduce and tidal amplitude will increase. Here we study the sensitivity of all selected estuaries to an amplitude decrease of 0.25 m (a^{-}) and an amplitude increase of 0.25 m (a^{+}) and 0.50 m (a^{++}). Changes in tidal amplitude will lead to modified equilibrium morphology and tidal amplification, because they affect the tidal prism at the mouth and therefore also the channel dimensions.

[**Scenario 3,** $W(x)^{+}$] In analogy with Room for the River projects (Rijke et al., 2012) performed along Dutch rivers, we investigated whether increased space for estuaries (i.e. managed realignment) would counteract possible negative consequences of future SLR. We ran four idealised scenarios to gain understanding of the general effects of the location of widening. In widening scenario A the mouth was widened, in B the estuary was widened in the tide-dominated zone, in C in the landward zone and in D the estuary was widened by an equal distance along the full estuary (Fig. 9.4). In all four idealised scenarios the widening was varied between 1.05-5 times the original estuary area, keeping the length of the widened section constant and thus only varying local width. The idealised scenarios were applied on one large estuary (the Western Scheldt, NL) and one small estuary (Dovey, Wales). The new planform was used to predict a new morphological equilibrium, assuming that sediment from former, flooded salt marshes is entirely redistributed. This assumption is reasonable, given that tidal bars and salt marshes are composed mostly of sand and the contribution of mud is minor (van de Lageweg et al., 2018). The morphological output was subsequently used as input to the hydrodynamic model to calculate tidal amplification. While we conducted model calculations for all possible ranges and combinations of future tidal amplitudes, here we isolate the effect of increased estuary planform by comparing the results to the case without changes in tidal amplitude (a^{o}).

Scenario 1 is predominantly used to study the effect of increased channel depth on tidal amplification. Scenario 2 reveals a relation between required sediment for adaptation and future changes in tidal range. Scenario 3 indicates whether managed realignment has the potential to mitigate adverse effects of the previous scenarios.

9.5.5 Estimation of sediment balance in estuaries and reconstruction of former estuaries and deltas under SLR

To assess whether systems can keep up with future SLR, we compared the incoming fluvial sediment flux (Q_s) to the required sediment flux ($Q_{s,req}$) for 1 m SLR in 100 years. The required sediment for this scenario was calculated as 1 m of additional accommodation space times the area of the system before SLR. We hereby assumed that the planform of the estuary does not change and we excluded changes in tides. Moreover, we ignored that part of the required sediment for adaptation can be compensated by peat formation (Erkens, 2009; Vos, 2015; de Haas et al., 2017), because peat is sensitive to salinity intrusion, which means that the estimates of required sediment are upper limits. Because for many smaller systems systematic sediment load measurements were lacking, we relied on a generic total sediment load predictor (Milliman and Syvitski, 1992):

$$Q_s = cA_c^d$$

in which Q_s is the sediment load [in Mton/yr], A_c is the catchment size [in 10^6 km^2] and c and d parameters depending on the highest topography in the catchment (Suppl. Table. 9.3). Catchment sizes were obtained from a GIS database of the USGS containing spatial data on catchments worldwide

(https://hydrosheds.cr.usgs.gov/datadownload.php?reqdata=30bass) and topography was derived from SRTM-3, v2 sampled at three arc-seconds.

9.5.6 Sediment balance for Holocene deltas and estuaries

To compare modern sediment balances to past situations, Holocene sediment balances were estimated from published geological reconstructions of several deltas and estuaries (Goodbred Jr and Kuehl, 1999; Hori et al., 2001; Saito et al., 2001; Ta et al., 2002; Anderson et al., 2007; Erkens, 2009; Tanabe et al., 2015; Koster et al., 2017). The resulting net sedimentation is a minimum value for past sediment flux, assuming maximal trapping efficiency. The difference in accommodation space between two successive time steps was calculated from relative SLR based on geological reconstructions or detailed geological profiles.

Three types of systems were distinguished: mega-deltas with ample sediment supply, peat filled back-barriers, and bay fills. For the Tokyo Bay and the Rhine Delta, data allowed comparison of a period within the mid-Holocene transgression (1-3 m per 100 yr) to sediment accumulation, which is relevant because SLR in the 22nd century may be equally fast (DeConto and Pollard, 2016). For the Yellow river, Mekong mega-deltas and the filled in Tokyo Bay (Holocene total) we artificially set accommodation space equal to stored sediment to indicate that there was no sediment shortage over the period considered.

9.6 Supplementary material

9.6.1 Model approach: validation, outputs and uncertainty

Here we first show what the model steps and outcome look like for the most crucial steps in our approach. Second, we briefly summarise previous validation of our methods and the corresponding uncertainties (Chapters 5, 7 & 8). Then, we discuss the role of storm surges on flood water predictions. Last, we assess the uncertainties related to main results of this study.

Model steps and outcome

The first step is to specify the along-channel width profile, tidal range and river discharge. The output of the morphological tool (Chapter 8) is a map with predicted bed elevations (Suppl. Fig. 9.6). Subsequently, the output map is translated into 1D-profiles of the channel width, average channel depth, shoal width and average shoal depth. The threshold value between the channel and shoal is the low water line. Supp. Fig. 9.7 shows the resulting along-channel profiles, along with the predictions for water levels in the estuary.

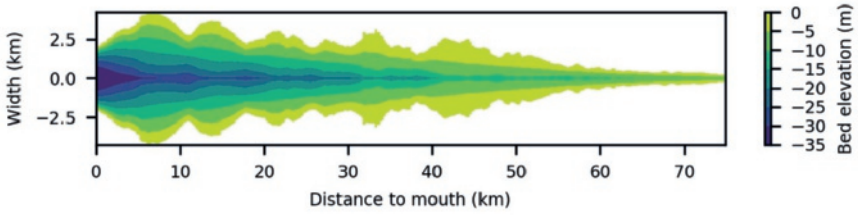

Figure 9.6 Predictions of bed elevation with respect to the high water level for the Western Scheldt.

The required sediment for future adaptation is estimated as follows. The map with predicted bed elevations (Suppl. Fig. 9.6) directly translates in a required sediment volume. First, the sediment presently available in the system is estimated by predicting the present day equilibrium morphology.

Subsequently, the required sediment for 1 m sea-level rise is estimated, when all other boundary conditions remain constant (Scenario 1). Under this condition, the predicted equilibrium morphology (i.e. bed levels) also remains constant. Therefore, the required sediment for adaptation is the surface area of the estuary times the increase in mean sea level (1 m). Next, the effect of changing tidal amplitude at the mouth is assessed (Scenario 2). To do so, the morphological tool is applied to increasing and decreasing tidal amplitude. Subtracting the present day sediment volume from the expected future sediment volume plus the requirement for 1 m SLR gave the required sediment for future adaptation.

Future flood water levels are calculated as follows. The 1D-hydrodynamic model is run on the present day morphology and on the same morphology drowned under 1 m SLR (Scenario 1). Subsequently, the future tidal range is compared with the present tidal range in the longitudinal middle of the estuary to obtain the change in flood water levels. The same calculations are rerun for all managed realignment scenarios (Scenario 3).

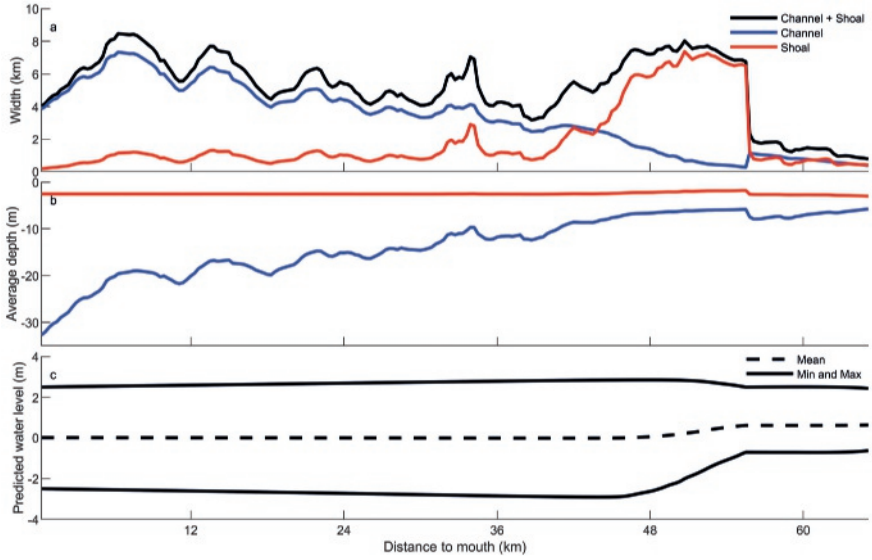

Figure 9.7 (a) Along-channel estuary, channel and shoal width. (b) Along-channel average channel and shoal depth. (c) Predicted along-channel water levels. The difference between minimum and maximum water level gives the tidal range.

Validation

Outlines and tidal prisms: Excess width is used as a measure to predict occurring bars (Chapter 5) and cross-sectional hypsometry (Chapter 7) from estuary planform. Excess width is defined as the local estuary width minus the width from a maximum fitting exponential profile, i.e. the 'ideal' width. We tested how sensitive the excess width calculations are to the position of the mouth, which determines the mouth width (Chapter 5). It was found that a 15% increase or decrease in the mouth width affects the excess width by a maximum of 10% because the excess width is often much larger than the exponential channel width.

Hypsometry: Later, we built on this idea (Chapter 7) and predicted the cross-sectional hypsometry. Hypsometry summarises the occurring bed levels in a cumulative curve (Strahler, 1952; Boon and Byrne, 1981). It was found that the z value in the general hypsometric curve (Strahler, 1952), which

determines the concavity of hypsometry, depends on the excess width. Based on bathymetries for four estuaries (the Western Scheldt, Dovey, Ems-Dollard and Columbia River Estuary), we determined that the z value can be predicted within a factor 2 of the measured value. Subsequently, the novel hypsometry predictor was applied to all four systems. The results showed that also the along-channel shoal width and channel width can be predicted within a factor of 2 (Chapter 7).

Bed level predictions: Last, we combined all empirical relations in a morphological tool that predicts equilibrium bed levels based on the estuary planform, tidal range at the mouth and river discharge at the landward boundary (Chapter 8). Here, predicted bathymetry was compared with measured bathymetry for the Western Scheldt, Columbia River Estuary, a river, ideal estuary and tidal basin. Cross-sectional median and minimum bed elevations were found to be within a factor 2 of the measured values from bathymetry (Chapter 8). Largest deviations occurred at locations that were dredged or that were near human constructs such as groynes. Also, predicted tidal prisms (surface area times tidal range) were compared with tidal prisms from numerical models, which showed that our simplification over- or under-predict tidal prism at the mouth by 10-40% for the Western Scheldt and Columbia River Estuary (Chapter 8).

Effect of storm surges on flood water level predictions

In the main text we stated: 'The predictions for flood safety are however upper limit estimates, because Scenario 1 excludes (...) the effects of increased mean water levels that occur during storm surges'.

Highest flood risks are mostly associated with storm surges. During storm surges, the average water depth is larger than during calm conditions. To assess the flood risk due to SLR, one should actually compare the storm surge conditions before and after SLR. In this study, we compared present-day calm conditions with future calm conditions. Because water depth is larger for storm surges, this means that friction during storm surges is lower than under calm conditions. The effect of 1 m SLR on friction under calm conditions will thus be larger than the effect of 1 m SLR on friction during storm surges. This also implies that the effect of increased MSL on tidal amplification would be less under these circumstances and that the predictions for flood safety in the main text are upper limit estimates.

Uncertainty estimate for this study

To estimate uncertainty, we reran all calculations for an estuary planform 10% larger and 10% smaller than our best estimate from digitising bank lines on aerial photography. This is a very extreme range and errors from digitisation are likely to be much smaller. While it seems as if this only assesses uncertainty in digitisation, it actually implicitly shows the sensitivity to storm surges, mispredictions in tidal prism and various degrees of morphological adaptation. After all, the effect of an increased planform area is an increase in tidal prism, which results in a larger channel depth, and the opposite reasoning holds for a smaller planform.

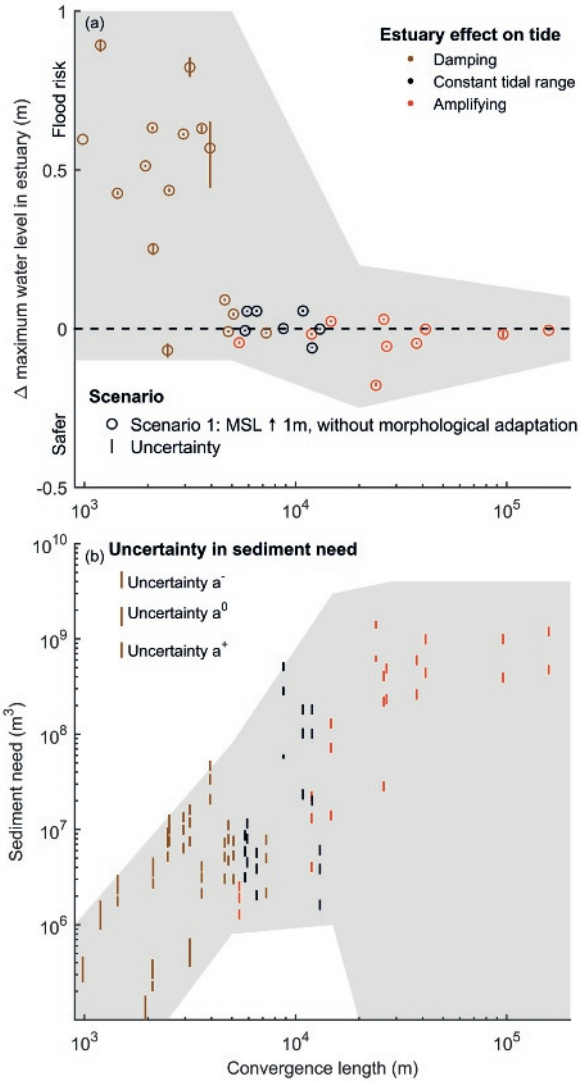

Figure 9.8 Uncertainty in main model results. The figure is the same as figure as Fig. 9.2 in the main text, but now with bars indicating the approximate model uncertainty for (a) flood water levels and (b) sediment need. All scenarios were rerun for an estuary planform 10% wider and smaller. The results indicate that system size effects are much larger than the uncertainty associated with the methodology.

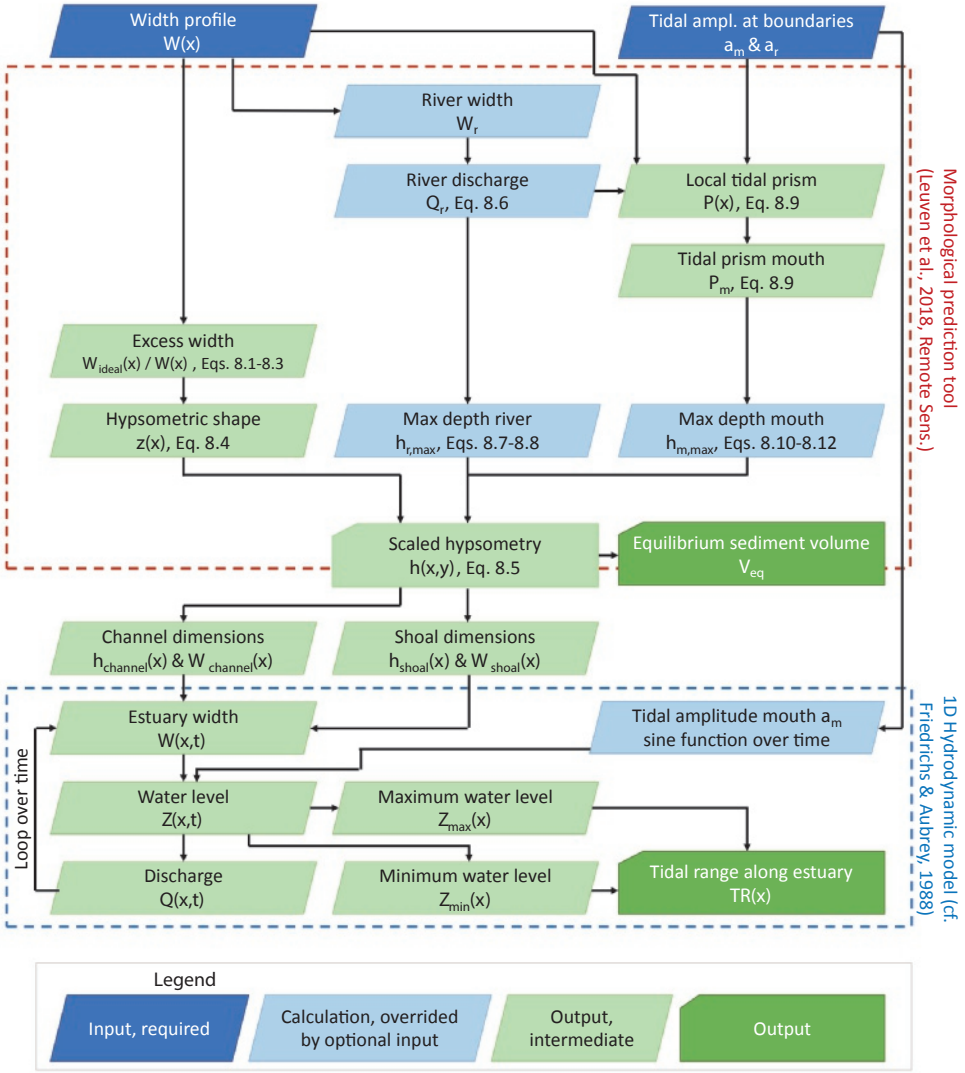

Figure 9.9 Flowchart of morphological assessment tool (Chapter 8), which results in an estimation of the equilibrium sediment volume, and the 1D-hydrodynamic model (Friedrichs and Aubrey, 1988), which results in an estimation of the along-channel tidal range. Equation numbers refer to the equations in Chapter 8. Local tidal prism is the tidal prism landward of a given location. The tool and model were applied in the following scenarios: (1a) SLR without morphological adaptation (a^o), (1b) SLR with full morphological adaptation, (2abc) same as Scenarios 1, but with -0.25 (a^-), +0.25 (a^+) and +0.50 m (a^{++}) tidal amplitude at the mouth, (3abcd) same as Scenario 1, but with estuary widening ($W(x)^+$). All parameters and variables are defined in Suppl. Table. 9.4.

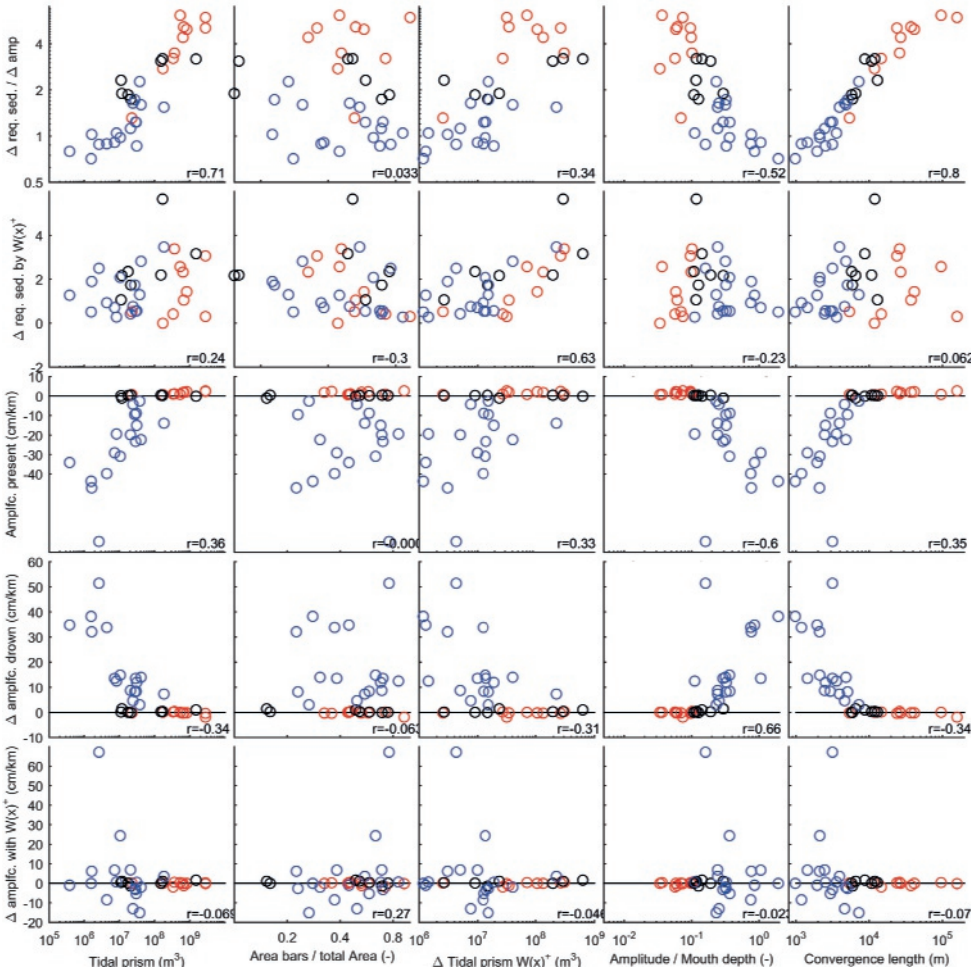

Figure 9.10 Dependent variables from top to bottom: (1) dependency of required sediment on tidal amplitude, (2) change in required sediment with estuary widening, (3) present-day tidal amplification, (4) change in tidal amplification if estuary drowns, (5) change in tidal amplification if estuary adapts and widens. Independent variables from left to right: (1) present-day tidal prism, (2) area of bars divided by total estuary area, (3) change in tidal prism by estuary widening, (4) present-day tidal amplitude divided by depth at the mouth, (5) convergence length. Red colours indicate amplifying estuaries, black indicates ideal (i.e. constant tidal range along-channel) and blue indicates damping. For each panel the Pearson's correlation coefficient (r) is indicated. Please note that the top row has a logarithmic vertical axis, while the rest is linear, and that the second column has a linear horizontal axis while the rest is logarithmic.

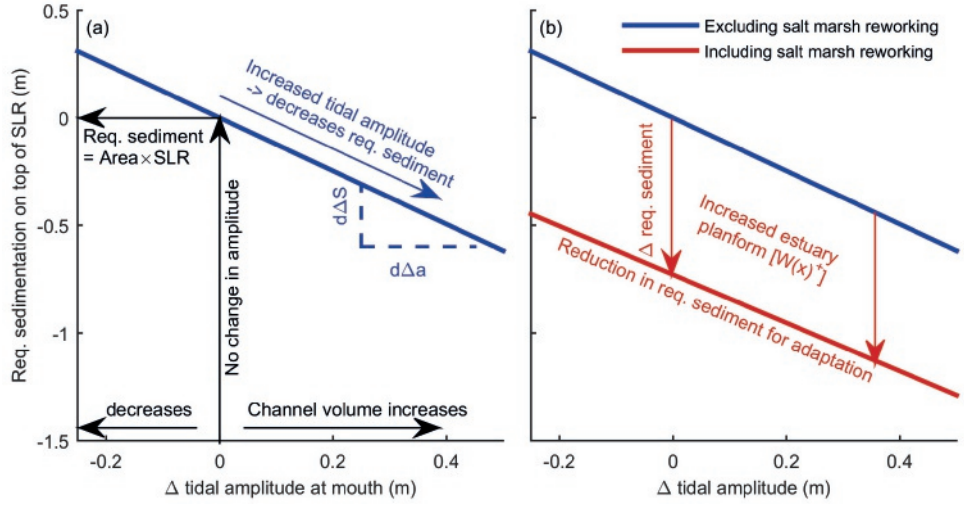

Figure 9.11 (a) The required sediment for adaptation depends on the future change in tidal amplitude at the estuary mouth, which occurs due to the shift of amphidromic points. Increased tidal amplitude increases the tidal prism, which results in deeper and larger channels, which compensates the sediment required for adaptation to an increase in MSL. Decreasing tidal amplitude has the opposite effect. (b) Increased estuary planform reduces the required sediment as well, because it increases tidal prism and part of the sediment in the salt marshes is reworked in the adaptation.

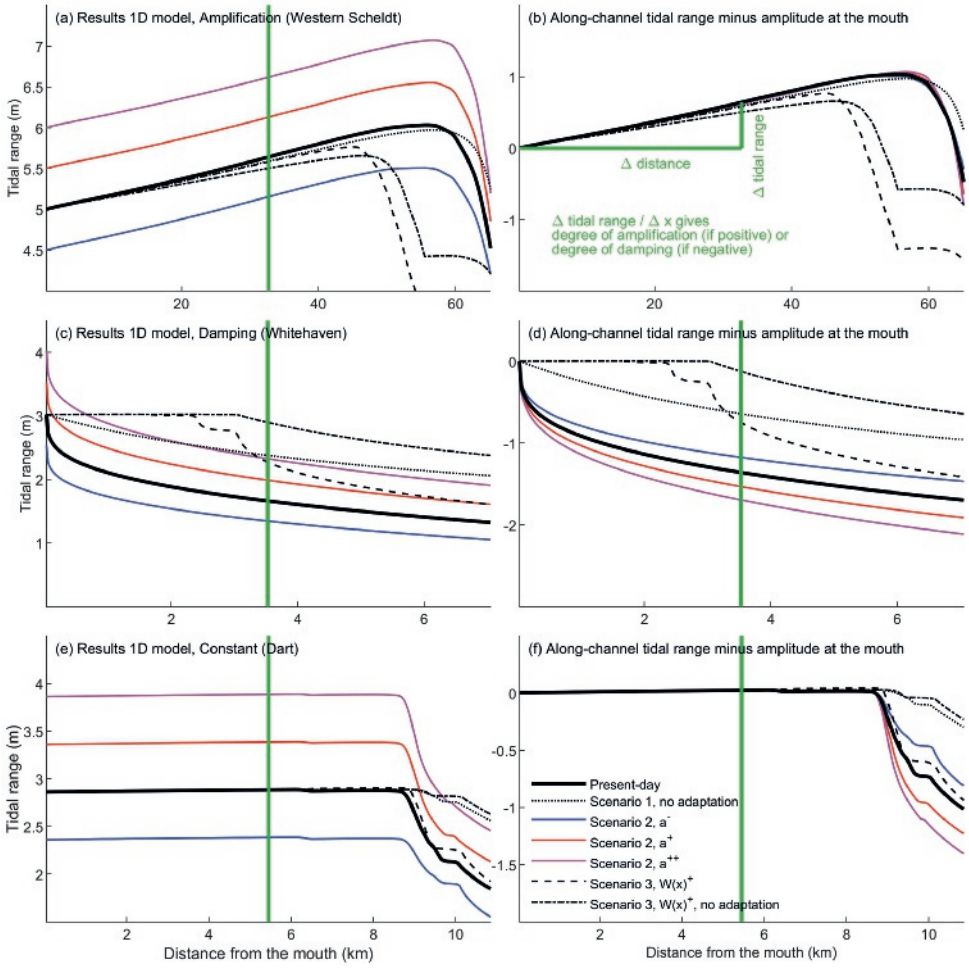

Figure 9.12 Morphological output from the assessment tool was used as input to a 1D-hydrodynamic model (Suppl. Fig. 9.9), in which the effect of SLR scenarios on tidal amplification was calculated. Tidal range either amplifies (a), dampens (c) or remains constant (ideal) (e) in along-channel direction. (b,d,f) Along-channel tidal range minus amplitude at the mouth. Changes in tidal range induced by model scenarios were extracted exactly in the longitudinal middle of the estuary.

Table 9.1 Overview of estuaries used in this study. Along-channel width profiles are appended as a .csv file to the online supplementary material.

Name	Location	Surface area (km^2)	Mean tidal amplitude (m)	Convergence length (km)	Mouth depth (m)	River discharge (m^3/s)
Alsea	USA	3.9	1.40	6.6	4.8	45.4
Bannow	Ireland	7.3	1.25	2.5	5.2	20.0
Broad	USA	101.5	1.12	12.0	9.5	5.2
Camel	UK	5.2	2.34	4.6	9.2	6.1
Cefni	UK	1.3	1.51	1.2	2.0	11.4
CharlotteHB	USA	286.1	0.33	32.8	18.2	58.7
Clonakilty	Ireland	0.5	1.75	3.2	10.9	35.0
Clwyd	UK	0.3	2.41	2.1	3.2	6.6
Cobequid	Canada	483.9	5.95	158.2	80.0	10.0
Columbia	USA	393.1	1.25	96.1	34.4	7000.0
Conwy	UK	5.3	2.54	5.1	7.9	18.7
Coosaw	USA	102.7	0.87	10.8	4.5	85.4
Dart	UK	3.9	1.43	13.0	12.3	1.3
Dovey	UK	11.9	1.45	3.2	5.0	23.2
Eems	NL	219.2	1.75	26.2	17.2	80.0
Exe	UK	8.0	1.30	5.9	10.3	16.2
Gannel	UK	0.3	2.24	1.0	1.2	0.7
Gironde	France	442.9	2.25	41.3	38.6	900.0
Glaslyn	UK	9.9	1.52	2.9	4.1	6.0
Humber	UK	233.7	2.28	27.0	23.1	85.6
Loughor	UK	33.8	2.74	3.9	11.3	1.9
Mawddach	UK	5.9	1.47	5.8	13.6	7.8
Meghna	Bangladesh	2341.4	1.50	104.8	43.5	38129.0
Mersey	UK	72.1	3.08 (2-5)	14.7	54.5	12.6
Nestucca	USA	1.9	1.40	5.4	20.2	100.0
Netarts	USA	3.6	1.40	2.1	3.8	0.4
Nyfer	UK	0.1	1.37	1.9	1.6	0.8
Ord	Australia	657.5	3.50	24.0	36.7	90.0
Parrett	UK	5.0	3.76	7.3	16.2	1.2
RoddsBay	Australia	10.2	1.50	2.5	4.6	2.1
Solway	UK	293.1	2.96	8.8	20.8	92.3
TawTorridge	UK	7.9	2.57	4.8	8.1	34.4
Teign	UK	3.1	1.32	3.6	11.9	1.3
Thraeth Melynog	UK	13.2	1.51	11.9	44.4	3610.0
Western Scheldt	NL	262.3	2.50	37.5	40.8	120.0
Whitehaven	Australia	2.4	1.51	1.4	1.4	2.1

Table 9.2 Sediment balances for Holocene deltas and estuaries. Bold types indicate mid-Holocene transgressive cases, which experienced SLR comparable to expected future SLR.

System	Type	Period (ka BP)	Accommodation ($10^6 m^3/yr$)	Sedimentation ($10^6 m^3/yr$)	References
Ganges	Megadelta, Holocene total	7 - 0	214.3	495.7	Goodbred Jr and Kuehl (1999)
Yangtze	Megadelta, Holocene natural highstand	6 - 2	158.3	158.3	Saito et al. (2001) and Hori et al. (2001)
Mekong	Megadelta, human influenced highstand	3 - 0	120	120	Ta et al. (2002)
Rhine	Delta, Holocene total	9 - 0	3	3	Erkens (2009) and Koster et al. (2017)
	Delta, mid-Holocene transgression	8 - 7.5	3.66	2.5	Erkens (2009) and Koster et al. (2017)
Tokyo	Bay fill, Holocene total	13 - 0	0.95	0.95	Tanabe et al. (2015)
	Bay fill, mid-Holocene transgression	13 - 7	2.05	0.92	Tanabe et al. (2015)
Galveston bay	Bay fill, Holocene total	10 - 0	0.56	0.51	Anderson et al. (2007)

Table 9.3 Values for c and d per maximum elevation class (Milliman and Syvitski, 1992) in the river catchment. Maximum elevation class indicates the highest topography in the catchment.

Class	c	d
1000-3000 US	170	0.52
1000-3000 Europe	50	0.73
500-1000	12	0.42
100-500m	8	0.66
$<$ 100	1	0.64

Table 9.4 List of symbols and abbreviations used.

Symbol	Units	Variable
A	[m^2]	Estuary surface area
A_c	[m^2]	Catchment surface area
a_m	[m]	Tidal range at the mouth
a_r	[m]	Tidal range at the landward boundary
C_d	[-]	Drag coefficient
ΔMSL	[m]	Change in mean sea level, i.e. sea-level rise
ΔV_{ch}	[m^3]	Change in channel volume
$h_{r,max}$	[m]	Maximum channel depth at the landward boundary
$h_{m,max}$	[m]	Maximum channel depth at the estuary mouth
$h_{channel}(x)$	[m]	Along-channel average channel depth
$h_{shoal}(x)$	[m]	Along-channel average shoal depth
$h(x,y)$	[m]	Dimensional bed level at coordinate (x,y)
k_s	[m]	Roughness coefficient
MSL		Mean sea level
$P(x)$	[m^3]	Local tidal prism at coordinate x
P_m	[m^3]	Local tidal prism at the estuary mouth
PDF		Probability distribution function
Q_r	[m^{3}s^{-1}]	Average river discharge
Q_s	[m^3]	Fluvial sediment supply over period of SLR
$Q_{s,req}$	[m^3]	Required sediment volume for adaptation
$Q(x,t)$	[m^3]	Discharge at location x at time t
S	[m^3]	Sediment available from redistribution of salt marshes
t	[s]	Time
$TR(x)$	[m]	Along-channel tidal range
V_{eq}	[m^3]	Equilibrium sediment volume in the estuary
$W_{ideal}(x)$	[m]	Ideal width at coordinate x
W_r	[m]	Width at the landward boundary
$W(x)$	[m]	Local width at along-channel coordinate x
$W(x)^+$	[m]	W(x) for Scenario 3 with widened planform
$W_{channel}(x)$	[m]	Along-channel channel width
$W_{shoal}(x)$	[m]	Along-channel shoal width
$W(x,t)$	[m]	Submerged width at location x at time t
x	[m]	Streamwise coordinate measured from the mouth along the centreline
z	[-]	Coefficient in Strahler (1952) (Strahler, 1952) equation
$z(x)$	[-]	Value of z-coefficient at coordinate x
$Z(x,t)$	[m]	Water level at location x at time t
$Z_{max}(x)$	[m]	Maximum water level at location x
$Z_{min}(x)$	[m]	Minimum water level at location x


10

Chapter 10 | Synthesis

In this thesis, I focussed on the dimensions and shapes of, and controls on bar and channel patterns in estuaries. While bars and bends have been studied extensively in rivers, only limited theory and data were available for tidal systems. Therefore, it remained unclear what determines the dimensions and shapes of individual bars and channels and how the planform estuary shape relates to the occurring bar and channel patterns and their dynamics. Below I describe how this thesis advances the knowledge on bar and channel patterns in estuaries.

First, the main conclusions of this thesis are summarised. In this section, I consecutively describe (1) the controls on equilibrium bar and channel patterns, (2) the relations between planform shape, bar and channel pattern and hydrodynamics and (3) temporal dynamics of channels and bars. Thereafter, I compare the morphodynamics of rivers and estuaries, from which culminates to which extent the knowledge available for rivers is applicable to estuaries. Additionally, I give the implications of future sea-level rise and topographic forcing by, for example, inherited geology. In the final section, I make recommendations for future research.

10.1 Main conclusions

10.1.1 Equilibrium bar and channel patterns

Multiple authors have described the shapes of tidal bars in the past (van Veen, 1950; Dalrymple and Choi, 2007). Tidal bars are typically classified as linear, U-shaped or compound bars (Fig. 2.8 in Chapter 2). Although tidal bars were already observed and described in the 1950s (van Veen, 1950), they are still not always recognised as such, for example in the rock record (e.g. Fig. 17 in Longhitano and Steel, 2017). While I reviewed and combined previous classifications (Chapter 2), the underlying mechanism of this classification revealed in what sense different bar classes are similar. All bar types, except for the linear bars, are characterised by so called 'barb channels'. These channels shallow in either the ebb or flood direction, terminating on a shoal. I found that partitioning (i.e. splitting-up) of the bars at the barb channels resulted in a universal relation between bar width and bar length of 1 to 7. This means that more complicated sidebars, U-shaped bars and compound bars can also be described as simple linear bars partly separated by barb channels.

Predictions of tidal bar dimensions were already available based on (linear) stability analyses (Seminara and Tubino, 2001; Schramkowski et al., 2002). These theories predict that bar dimensions predominantly scale with the tidal excursion length, which is the distance a particle of water travels over half a tidal cycle, and a weaker dependency on estuary width. In this thesis, I tested this theory on a large empirical dataset of bar dimensions and found that the correlation with estuary width is much stronger than with tidal excursion length or tidal flow velocity (Chapter 2). More specifically, bar length relates to estuary width to the power of 0.9 and bar width can be approximated by bar length divided by 7. Bar height relates linearly to local water depth, meaning that their height is at approximately mean water level. Another recent dataset with tidal bar dimensions (Saha et al., 2016), numerical model results (Braat et al., 2017) and laboratory scale experiments (Chapter 6) confirm these scaling relations (Fig. 10.1).

Similarly, a scaling relation was found between channel width and fluvial-tidal meander dimensions (Fig. 10.1, see also Chapter 3). This falsified the hypothesis that there is a specific zone in the fluvial tidal transition where extremely sinuous or disproportionally large meanders occur. The implication is that tidal influence cannot be inferred from a single meander dimension, for example measured in a geological outcrop. Measurements in modern systems suggest that a strong along-channel increase in meander or channel dimensions is indicative of tidal influence (Chapter 3).

An important concept for the equilibrium planform pattern of estuaries is that of the ideal estuary (Savenije, 2006; Savenije, 2015; Townend, 2012; Dronkers, 2017) that can be described as an estuary with an exponentially converging planform from the mouth to the upstream river. Estuaries deviate in varying degrees from this ideal shape (Townend, 2012; de Haas et al., 2017) and I found that this is a good indicator for the occurrence of sand bars in estuaries (Chapter 5). The total width of bars in a cross section is also called the summed width of bars. The excess width is defined as the local width minus the 'ideal' width (Eq. 8.3 in Chapter 8). At locations with a large excess width, local flow expansion causes a reduction of the shear stress, which results in the deposition of sediment. Deviation from this trend may occur when insufficient sediment is available for bar formation in the estuary, or the time for adaptation was insufficient.

Surprisingly, a good correlation was found between the channel convergence length and upstream channel width (Chapter 3). While speculative, the cause of the correlation is of interest. According to hydraulic geometry, wider rivers are generally also deeper and smaller rivers are generally shallower (e.g. Lacey, 1930; Leopold and Maddock Jr, 1953; Hey and Thorne, 1986; Savenije, 2003; Kleinhans and van den Berg, 2011). Gisen and Savenije (2015) and Savenije (2015) proposed that the depth of the fluvial-tidal transition zone is set by the upstream river. They also suggested that this depth is rather constant along the estuarine channel, which, on a side note, is in contrast to experimental findings

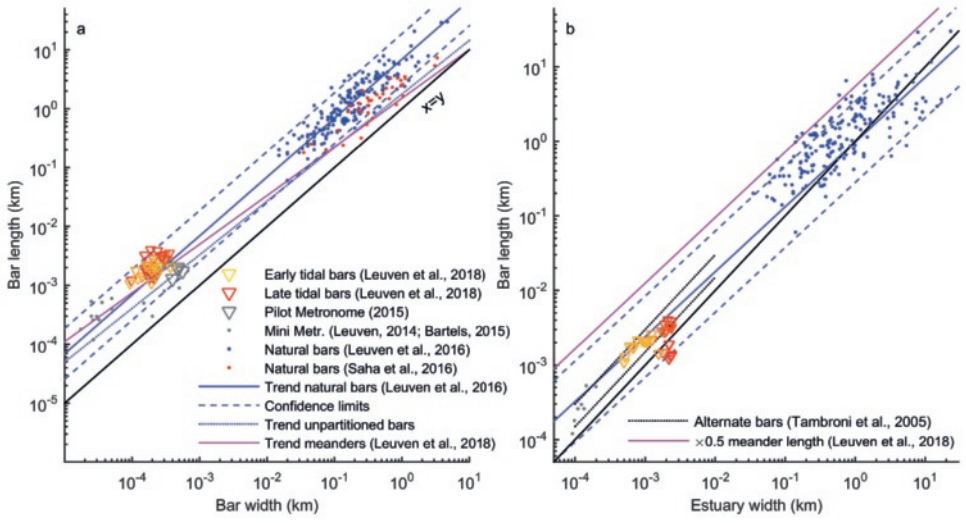

Figure 10.1 (a) Comparison of planform bar dimensions (length versus width) in the experiments and in natural systems. Triangles represent bars in the experiment, with colour indicating the tidal cycle during which the bars were measured: yellow was early in the experiment, red was at the end. (b) The scaling relation between estuary width and bar length that was found for natural systems (Saha et al. (2016) and Chapter 2) holds for the experiments (Tambroni et al. (2005), Leuven (2014), Bartels (2015) and Chapter 6) and fluvial-tidal meander dimensions (Chapter 3).

(Chapters 4 & 6) and numerical modelling (Braat et al., 2017). In an ideal equilibrium estuary (Savenije, 2015), the energy per unit of width is constant: the loss of energy by friction is balanced by the gain of energy by convergence. So, if wider rivers indeed cause deeper estuaries, the friction in these systems is probably less and therefore the required convergence to maintain a constant energy per unit width is lower. For a small river and a shallower fluvial-tidal transition zone, the reasoning is the other way around, thus requiring a stronger convergence. This is in agreement with Fig. 3.4b in Chapter 3, which shows that smaller rivers correlate with a smaller convergence length, which indicates that they are stronger convergent. However, this hypothesis needs further investigation in the future.

10.1.2 Relations between planform shape, bar and channel pattern and hydrodynamics

From the previous section it follows that the individual channel and bar dimensions in estuaries are predictable from the local width and local variations in width (Chapters 2 & 5). However, it still remained unclear how these individual dimensions translate into the bar and channel pattern on the scale of a full estuary. The scaling of bar dimensions with estuary width implies that it is also possible to predict the number of channels and bars in cross-section, i.e. the braiding index (Chapter 5). The number of bars and channels will typically be more abundant at locations where the estuary is relatively wide and vice versa for narrow sections.

Because the location and width of bars was so predictable, it raised the question whether it would also be possible to predict the three-dimensional shape of bars in estuaries. This was indeed the case (Chapter 7), which allowed the description of the along-channel and cross-channel bar pattern with a continuous field of bed elevations rather than discrete elements. A simple hypsometric shape (Strahler, 1952), i.e. a cumulative curve summarising bed elevations, is capable to describe the most dominant along-channel trends in three-dimensional bar patterns. This means that the surface topography of estuaries – the horizontal dimensions – translates in the sub-water morphology – the vertically occurring bed levels (Chapter 7).

All relations derived for bar and channel patterns in this thesis were programmed in an easy-to-use tool (available through GitHub), which only requires the along-channel width profile and tidal amplitude at the mouth as input (Chapter 8). Output consists of spatial maps of bed elevation, flow velocity and salinity, which are the prime abiotic factors for habitat suitability in estuaries (de Jong, 1999; Bouma et al., 2005; Gurnell et al., 2012). Bed elevation is a relevant characteristic for ecology, because it sets the maximum water depth and inundation duration. Based on data for the Western Scheldt, I derived a relation between bed elevation and flow velocity (Chapter 8), which was not yet available. The tool can be used to obtain a first-order estimation of estuarine characteristics when limited data are available (Chapter 8).

The current empirical theory for bar patterns in estuaries (Chapters 7 & 8) oversimplifies morphology on a spatial scale smaller than tidal bars, such as sills in the main channel (van Veen, 1950; Tank, 1996) and shallow channels that cross-cut bars (Jeuken, 2000; Swinkels et al., 2009; de Vet et al., 2017). This means that to improve our predictive capabilities for the morphology of estuaries, empirical or physical theory is needed for the locations where smaller morphological features form and for their typical dimensions.

10.1.3 Temporal dynamics of channels and bars

The temporal dynamics of channels and bars have been studied in natural systems and numerical models with non-erodible boundaries (e.g. Hibma et al., 2003; Hibma et al., 2004; van der Wegen and Roelvink, 2008), which I complemented in this thesis with physical scale experiments (Chapters 4 & 6). Numerical models showed that initially straight channels and bars form, which later connect into a main meandering channel with flood barbs (Hibma et al., 2003; Hibma et al., 2004;

van der Wegen and Roelvink, 2008). Moreover, it is known that bifurcations in tidal systems are surprisingly stable over time with inner bend cutoffs rarely occurring (van Veen, 1950). Novel in this thesis is that estuary banks were freely erodible in our experimental setup. For the process studied, this means that a natural feedback mechanism was included between bar growth and erosion, and estuary widening and narrowing.

In the initial phase of the experiments, alternate bars formed in an initially narrow and straight channel (Chapter 4) (see also Tambroni et al. (2005) and Tambroni et al. (2017) for a case with non-erodible boundaries). After an initial phase with a rhomboid pattern with very short wavelength and high braiding index, straight initial channels formed with alternate bars. The deepest channels occurred sideways of the alternate bars while shallower zones formed in the cross-overs between the alternate bars. This configuration lead to flow divergence on both opposing ends of the channels, causing sediment convergence between alternate bars. Sediment convergence resulted in the build-up of elongated sills parallel to the main flow direction and located between alternate bars. This pattern is superimposed on the alternate bar and channel pattern and is unique to tidal systems. Even under asymmetric flow conditions the sills persisted. Their stable presence triggered the formation of mutually evasive ebb- and flood-dominated channels that bifurcate around the sill. As channel widening progressed, flood barbs formed onto the alternate bars, which in later phases resulted in midchannel bars and a braided pattern. Observations in natural systems may have suggested that mutually evasive ebb- and flood-dominated tidal channels are topographically forced, but Chapter 4 showed that their stable presence is initiated with the onset of tidal bar formation and thus does not necessarily require topographical forcing.

Laboratory scale experiments confirmed the hypotheses for patterns observed in natural systems, i.e. the scaling relations for bars and occurrence of bars (Chapter 6). The experiments showed that the estuary widens rapidly in the initial phase. As widening progressed, former sidebars were cut off from the estuary banks by growing barb channels. This resulted in midchannel bars that diverted the flow to both sides, resulting in a positive feedback mechanism between bank growth and estuary bank erosion (Chapter 6), which is in agreement with earlier observations (Dalrymple and Rhodes, 1995; Hibma et al., 2003). The length and position of incipient tidal bars determine the large-scale quasiperiodic variation in the estuary width. While not continuing indefinitely, the processes of bank erosion and bar formation illustrated that quasiperiodic deviations from the ideal estuary shape can be formed autogenically.

10.2 Implications

10.2.1 Applicability of theory for rivers on estuaries

In this thesis, I repeatedly compared estuaries with rivers, under the assumption that mechanisms of bar formation and scaling of bars in estuaries are similar to bars in rivers (Chapters 2-6). However, this hypothesis had yet to be tested, and after doing so in this thesis, the key similarities and differences between rivers and estuaries were determined. The main similarities are:

1. Recent work on tidal meanders and meanders in the fluvial-tidal transition zone (Finotello et al. (2018) and Chapter 3) revealed that the planform dimensions of tidal channels and the main meandering ebb-tidal channel in estuaries scale similarly with channel width and river discharge as meanders in rivers (e.g. Inglis, 1949; Leopold and Wolman, 1960; Hey and Thorne, 1986). The dimensions largely depend on estuary width, while the braiding index (i.e. the number of bars in cross-section) relates to the width-to-depth ratio or an equivalent thereof (e.g. excess width).
2. Both environments have similar morphological elements. For example, analogies in bar types (rivers vs. estuaries) are: unit bars vs. linear bars and chute bars vs. U-shaped bars. Sidebars,

point bars, and compound bars were identified in both environments. The shape of sills in estuaries is comparable with the morphology of riffles in rivers (Tank, 1996). However, the forming mechanism for riffles is driven by water level gradients, while sills in estuaries are zones of sediment convergence by residual tidal flow. This means that a perfect analogy for sills is still lacking.

3. The mechanisms of bar push and bank pull (Parker et al., 2011; Eke, 2014; van de Lageweg et al., 2014) are applicable in both environments. Flow diversion around midchannel bars can induce bank erosion and therefore local widening, similar as in rivers (e.g. Bridge, 1993). The evolution of alternate bars in a straight tidal channel suggests that initially bar push is the forming mechanism. In later phases, when channel curvature around bars has increased, the mechanism of bank pull takes over. The problem here is that they are co-existing processes that cannot be determined separately, which thus requires further investigation with numerical modelling or experiments.

The key differences between rivers and estuaries are:

1. Bars are slightly more elongated in estuaries with bar length being 6.9 times bar width, compared to a factor of 5.0 for rivers.
2. Estuary planforms and bar patterns show a much stronger along-channel variation. The strong seaward increase in conducting water volume results in a seaward widening planform, which typically results in bar and channel patterns changing from meandering in the landward reach to more braided in the seaward reach.
3. In addition to planform forcing mechanisms, bars are more easily forced in the tidal environment. Sediment transport being in the same order of magnitude in both ebb and flood direction prevents rapid seaward and landward migration. Subsequent diversion of flow around stationary bars makes the planform progressively more irregular.
4. The presence and formation of sills in an estuary is unique to this environment. Imagine a straight tidal channel with alternate bars and perfectly sinuous tidal flow. In this case, divergence of flow in front of and over the bar causes sedimentation on the bar and channel. Subsequent opposing flow shaves off sediment from the same bar and deposits sand on the opposing bar and channel. This results in a net sediment convergence between the alternate bars, forming a straight sill. Their stable presence triggered the formation of mutually evasive ebb- and flood-dominated channels that bifurcate around the sill (see also Fig. 4.4 in Chapter 4).

What are the implications of the similarities and differences between rivers and estuaries?

Because channel and bar dimensions scale similarly with the large-scale planform dimensions in both rivers and estuaries, these relations can be applied and used for estuarine management and geological reconstructions. For example, narrowing of an estuary will most likely lead to the disappearance or shortening of tidal bars as in rivers, which reduces ecologically valuable intertidal area. Similarly, geologists can use the scaling relations between channel dimensions and bar dimensions, where the shape of tidal channel belts or estuaries has been identified, but wherein bar configuration is typically not recognisable and typical flow conditions are unknown. A single measurement or preferably a few measurements of bar or channel dimensions would be enough to reconstruct typical channel width and local tidal prism and therefore also typical flow conditions with the empirical assessment tool presented in this thesis. While the overall bar and channel patterns of an estuary cannot be generalised in a single class (e.g. meandering or braided) as in rivers, the seaward transition from meandering to braided and the strong increase in channel and bar dimensions can be used as an indicator for tidal influence, for example when interpreting the rock record.

However, a more guarded approach should be taken when the dynamic processes of channel migration and bar reworking are involved, because the dynamic behaviour of channels, bars, sills and barb channels in estuaries is unique. This implies that it is not straightforward to apply relations for rivers that consider for example preservation and subsurface architecture (e.g. Storms et al., 1999; Blom and Kleinhans, 2008; van de Lageweg et al., 2015) on estuaries, because the relations depend on the dynamics of channels and bars. Moreover, as a first step forward, the dynamic behaviour should be analysed and described per zone (e.g. meandering zone, braided zone), instead of for the full tidal domain, because the bar pattern affects the dynamic behaviour of the sill and barb channels, and thus also the resulting subsurface architecture.

10.2.2 Effects of sea-level rise

While it was already projected that sea level will rise 1-2 m in the next century and that sediment supply to estuaries is decreasing globally (Walling and Fang, 2003; Yang et al., 2005; Church et al., 2013; Wong et al., 2014; Du et al., 2018), it remained unknown how estuaries will adapt morphologically to their new boundary conditions. Tidal amplitude at the mouth of estuaries will change as a result of reduced friction at the mouth of the estuary by increased channel depth and shifting amphidromic points on the continental shelf (Idier et al., 2017; Pickering et al., 2017). Earlier studies already illustrated that estuary size matters for tidal propagation and amplification in estuaries under sea-level rise (Ensing et al., 2015; Du et al., 2018). However, they did not yet consider morphological adaptation and modifications in tidal amplitude at the mouth of the estuary. Therefore, in this thesis, the effect of an increase in mean sea-level on tidal amplification and the effect of tidal amplitude change on sediment requirement were studied in estuaries worldwide.

Our results show that small (convergence length $< 10^4$, or shallower than 10 m) and large (convergence length $> 10^4$, or deeper than 10 m) estuaries respond in opposing ways to future sea-level rise (Chapter 9). The main threat for large estuaries is sediment starvation and therefore loss of intertidal area, especially if tidal amplitude decreases. If amplitude decreases, the tidal prism decreases. Because channel volume relates to tidal prism, the required sediment for adaptation thus strongly increases. For an increase in tidal prism, the opposite reasoning holds. Drowning estuaries can change from net exporting to net importing (van der Wegen, 2013), but the time for adaption will be too short to restore equilibrium within a millennial timescale. In contrast, small estuaries will face enhanced flood risks, as they are more sensitive to tidal amplification. Here, a small increase in depth results in a large reduction of friction, which favours tidal amplification.

Subsequently, it was tested whether the effect of increased space for estuaries is sufficient to partly mitigate adverse effects of rising sea-level on estuaries (Chapter 9). Managed realignment (i.e. local widening of the estuary) is indeed capable to counteract future amplification in small estuaries. To this end, estuary widening in the landward zone or along the entire estuary are most effective, because increased tidal flat area dampens the tide. In large estuaries with a risk of sediment starvation, the implementation of increased width is most effective when implemented along the entire estuary. Widening in the tide-dominated zone (i.e. before the tidal excursion length) is also effective for the sediment balance, but at the cost of increased water levels. In both cases, tidal prism increases, which increases channel volume and therefore reduces the required sediment.

10.2.3 Effects of topographical forcing

Initial conditions, or, more specifically, inherited geology, can topographically force the bar and channel patterns in estuaries on multiple scales. Geological constraints are thus capable to overrule theory for self-formed estuaries (Pierik et al., 2019). On the bar scale, horizontal constraints force major channel confluences (Chapter 5), while a lack of constraints allows for widening and bar formations (Chapters 5 & 6). On the estuary scale, inherited geology constrains the estuary surface area, which has a feedback on tidal prism and therefore channel depth (Chapter 8). Vertical

constraints, i.e. hard layers in the subsurface, force the formation of midchannel bars, thereby widening the estuary locally (Chapter 6).

For example for the Ems-Dollard Estuary, it was found that channel curvature and number of active channels relate to the degree of alluviation (Pierik et al., 2019). Channels were historically more curved when the channels interfered with a till ridge in the subsurface. The channel shallowed in the 20^{th} century, which caused less exposure of the resistant layers. As a result, the main channel straightened, also affecting the main channel landward of this location. Simultaneously, the secondary channel silted up, making the estuary a one-channel system, decreasing the sinuosity and width-to-depth ratio. This propagation of curvature forced by bars and bends is in line with observations in rivers (van Dijk et al., 2012; Schuurman et al., 2016), where curvature propagates downstream over much more than one meander length because each meander steers the downstream flow momentum, helical flow, and sediment flux.

In the most extreme case of very shallow resistant layers, it is expected that resistant layers can cause severe land loss. For example, in the case of the Sittang Estuary in Myanmar, I hypothesise that channels cannot adapt to their desired volume, resulting in extreme flow velocities (up to 3 m/s) in the outer bends, undercutting banks, which leads to channel displacement of 100-1000 m per year (Steijn et al., 2019). The latter case study illustrates that an analysis of the subsurface should always be included when analysing individual systems and subsequently implemented in morphological models. Although geological constraints can overrule otherwise self-formed patterns, the mechanisms that cause temporal dynamics of channels and bars remain the same or even amplify.

10.2.4 Implication for management of estuaries

Estuaries such as the Western Scheldt are continuously under pressure by human influence. In particular, dike construction and land reclamation (de Vriend et al., 2011) have cut off the ecologically valuable flanking mudflats, salt marshes and freshwater riparian systems from the channels that supply sand and mud during inundation (Kirwan and Megonigal, 2013). The main shipping channels are dredged for access to harbours, enhancing flood risk and reducing intertidal sandbar area that forms valuable ecological habitat (van Dijk et al., 2019). Numerical modelling of the Western Scheldt Estuary also showed that sea-level rise can be an opportunity to restore the multi-channel system and dynamics in estuaries that are dredged (van Dijk et al., 2019), but only under the condition of sufficient sediment supply. Chapter 9 illustrates that the required sediment for adaptation and flood water levels form realistic threats for estuaries. Measurements to reduce adverse effects are thus required right now, before sea-level rise may lead to dike breaching and land loss in densely populated areas.

In this thesis, I showed that narrowing of an estuary leads to a reduction in or disappearance of sand bars and therefore valuable habitat area (Chapters 2 & 5). However, potential measures to counteract this are still not widely employed: increased space for the estuaries would top off high floods and extreme tides, increase important habitats and allow for sedimentation to balance sea-level rise (Chapter 9). Based on the correlation between excess width and bar presence (Chapter 5), it was expected that sections that are locally widened will fill up over time. Pilot numerical models, in which the estuary was locally widened with an empty deep section, showed that these areas are indeed capable to trap sand and mud (Fig. 10.2). Despite political issues with the *Hedwige polder*, longer-term sedimentation would lead to return of land to agriculture following silting up. Also, the *Drowned Land of Saeftinghe* demonstrated that this is feasible.

10.3 Future research

In this thesis, I predominantly focussed on bar filled estuaries, which are a specific type in the range of end-member systems that occur between completely fluvial and completely tidal (Fig. 10.3). Bar filled estuaries are very common: a large part of the world's largest container ports is located along bar filled estuaries and they also abundantly occur in databases with tidal systems (Manning (2007) and Gisen and Savenije (2015) and Chapter 2). While the empirical relations in this thesis were intended for bar filled estuaries, their application to the full range of end-member systems provided reasonable results, even in the most extreme cases of a river and tidal basin (Chapter 8). Nevertheless, it remains largely unknown if and how these end-member systems can transition into each other over time and how the dynamics of channels and bars can steer these transitions.

For each end-member system, I identified the main hydrodynamic forcing and presence of intertidal area (Fig. 10.3). This sorts the systems from a strong fluvial forcing to a more mixed forcing to a strong tidal forcing. The required forcing can be used to construct hypotheses for potential morphological pathways that describe transitions between end-member systems (Fig. 10.3). However, these pathways clearly need further investigation. Therefore, I identified the following three topics for future research that affect the morphological pathways, which are discussed next: (1) testing the effects of sea-level variations, (2) implementing eco-engineering species and (3) improving theory for bar formation and dynamics.

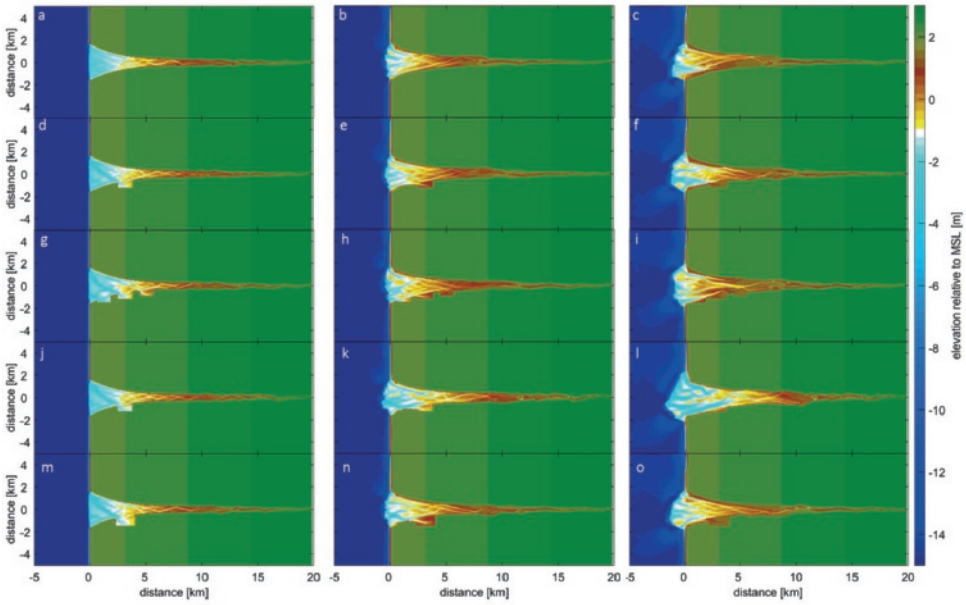

Figure 10.2 The evolution of artificial embayments in numerical models of Braat et al. (2017) over time. Corresponding time steps are from left to right: 50, 340 and 1030 years. In all runs, tidal amplitude was 1.5 m and river discharge was 100 $m^3\ s^{-1}$. All runs included sand and fluvial mud supply, except for row g, which is sand only. The size and number of embayments was varied among runs.

10.3.1 Testing the effects of sea-level rise and potential of managed realignment

An open question concerns the effects of sea-level rise and drop on the large-scale evolution of tidal systems. From geological cases (de Haas et al., 2017), it is known that tidal basins can fill up when sea-level rise decreases and eventually evolve into estuaries or closed coasts. However, it remains unknown how and on which timescale the morphology and planform shape adapt to changing boundary conditions (Fig. 10.3), which could be tested with numerical models and experiments. Because these methodologies reproduce spatial patterns, they can reveal which zones will be most susceptible (i.e. drown first, experience largest floods) for fluctuations in sea-level.

Increased space for estuaries can partly mitigate negative effects of sea-level rise (Chapter 9). However, to study this, only a simplified empirical tool and 1D hydrodynamic model were used so far, which lack predictive capability of the spatial patterns and timescales of morphological evolution. These tools are very useful, because they can provide large scale effects of potential management options in estuaries under pressure within minutes. Nevertheless, it is recommended to investigate the most promising options further with more detailed methods, such as morphological modelling and laboratory scale experiments. Especially after implementation of eco-engineering species, this complementary set of tools can aid in future decision making and estuary management. Room for the River projects (e.g. Rijke et al., 2012) have been widely implemented in the Netherlands to optimise flood safety while maintaining biodiversity. In analogy with these measures, it would be a good idea to systematically analyse the effects of similar measures in the environment of estuaries.

10.3.2 Implementing eco-engineering species

Eco-engineering species are already being used in physical scale experiments (van Dijk et al., 2013a) and numerical models (van Oorschot et al., 2016; Lokhorst et al., 2018; Brückner et al., 2019). From these studies, it is possible to derive generalised rules for colonisation, growth and morphological feedback which together steer further evolution of estuaries, for example increasing shoal elevation and trapping of cohesive sediment (Braat et al., 2017; Braat, 2019). In turn, this will reduce tidal prism and confine the estuary over time (Kleinhans et al., 2018). It remains an open question whether estuaries of varying size and character will respond similarly under the theoretical conditions of unlimited sediment availability along with colonising eco-engineering species (Fig. 10.3). Can colonisation by vegetation, for example, drive the transition from a bar filled estuary to and ideal estuary if enough sediment is available? And which conditions determine whether an ideal estuary or a bar filled estuary forms?

The tool presented in this thesis provides a first step towards answering these questions. However, to be able to use it for long-term evolution, rules for eco-engineering species along with their main morphological feedbacks must be implemented. Only then it is possible to study long-term effects of ecology on planform patterns in estuaries (Fig. 10.3) and study the effect of management options on the potential habitat area. A way to implement this would be to first predict the hypsometric shape in absence of eco-engineering species, subsequently predict the presence of eco-engineering species and then update the hypsometric shape. In case of stabilising species, an increase in bed elevation can be expected, while it is the other way around for destabilising species.

Experiments indicate that systems with unlimited sediment supply and easily erodible boundaries always evolve into bar filled estuaries (Chapters 4 & 6). Therefore, based on these experimental conditions, I hypothesise that bank stability and sediment supply are key for the formation of a bar filled estuary. The addition of crushed walnut shell to simulate the effect of cohesive mud in experiments was found to be insufficient to reduce bank erosion (Braat et al., 2019). Therefore, to test this hypothesis, experiments or models with varying degrees of bank strength and varying degrees of sediment supply are required.

Moreover, pilot experiments showed that decreasing river discharge forces the system to evolve from a bar filled estuary into a tidal basin (Leuven (2014) and supplementary material in Braat et al. (2019)).

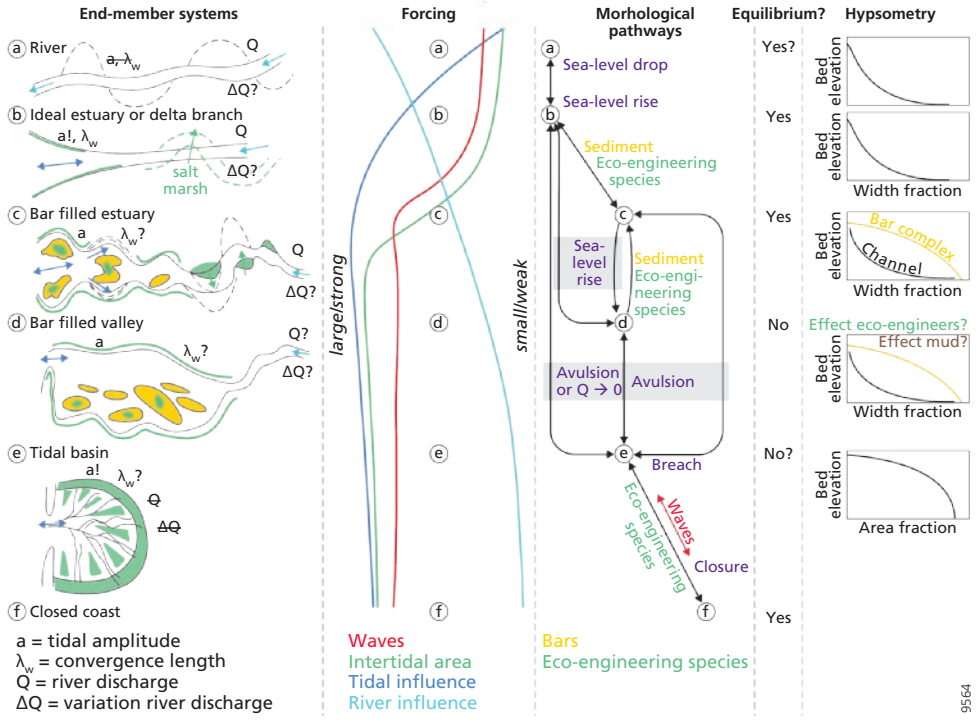

Figure 10.3 [first panel] Morphological end-member systems ranging from fully fluvial dominated (a) to fully tidal dominated (e). [second panel] Relative strength of forcing and presence of intertidal area. [third panel] Hypotheses and mechanisms that explain morphological pathways between end-member systems (partially based on de Haas et al. (2017)). [fourth panel] Indication whether the end-member could be an equilibrium state. [fifth panel] Hypsometric profiles corresponding to the end-member systems.

This implies that processes on the longer term, such as sea-level rise and river avulsions landward of the estuary might have an even stronger effect of the shape and morphology of the system than sediment supply, bank strength and eco-engineering species (Fig. 10.3), which needs further investigation.

10.3.3 Improving predictive theories for bar patterns

There are two essential next steps that should be undertaken to further improve and complete our understanding of bar patterns in tidal systems. First, physics-based theory should be updated such that it adequately predicts tidal bar dimensions, because the required physical relations can illustrate which underlying mechanisms drive bar formation. Second, the causes for the formation and stable presence of mutually evasive ebb- and flood-dominated tidal channels should be studied further.

Previous stability theories (Seminara and Tubino, 2001; Schramkowski et al., 2002) suggested that bar (wave)length partly depends on the transverse bed slope effect, which is the force transporting sediment downslope across the channel (see Baar et al., 2018, for review). However, at very high sediment mobilities, the bed slope effect becomes less important in numerical models, because the proportion of sediment transported in suspension increases and bed slope effects only affect bedload transport (Baar et al., 2018). A recent advance in bar stability theory (Hepkema et al., 2019) suggests that horizontal eddy diffusivity is key to obtaining dependency of bar patterns on estuary dimensions

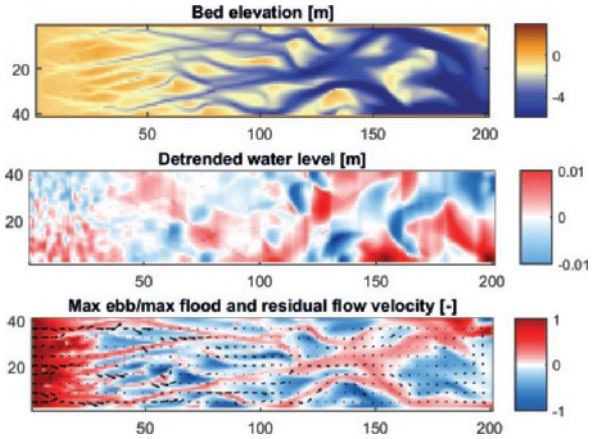

Figure 10.4 [top] Bed levels of a numerical model after 1300 days with a river discharge of 200 m^3/s at the left boundary and a tidal amplitude of 3 m at the right boundary. [middle] Water levels detrended with the along-channel gradient. [bottom] Tidal dominance with ebb dominant being positive and flood dominant being negative.

(width and depth) as was found for natural systems (Dalrymple and Rhodes (1995) and Chapter 2) and in numerical models (Hibma et al., 2003; Hibma et al., 2004; van der Wegen and Roelvink, 2008). The resulting predictions for modern systems with diffusivity are in the appropriate order of magnitude (Hepkema et al., 2019). Because eddy diffusivity only affects suspended sediment transport, this finding also implies that the forming mechanism of tidal bars in natural systems is probably modulated by suspended sediment on top of the bedload transport and bed slope effect that were found to be responsible for bar dimensions in rivers (Struiksma et al., 1985; Seminara, 2006; Crosato and Mosselman, 2009). If this is the case, it has strong implications for the numerical modelling of bar and channel patterns in tidal systems. Nevertheless, diffusivity should be used with caution, because Dam et al. (2016) showed that realistic morphological output can be obtained with only diffusivity and in absence of bed slope effects, which implies that diffusivity strongly affects morphological output in numerical models.

Numerical models (e.g. Delft3D) can be used to further investigate the occurrence of mutually evasive ebb- and flood-dominated channels. Ideally, bar dynamics should be modelled in a straight channel with two open boundaries to simulate a small part of an estuary or strait with along-channel, relatively constant tidal conditions. However, imposing two water level boundaries is problematic, because it would require knowing the phase difference, which evolves over time during the model run. Nevertheless, if this technical difficulty would be solved, thin impermeable walls can subsequently force the formation and position of banks. The latter is convenient, because it allows the investigation of the driving mechanism for the formation of mutually evasive channels. Two opposing hypotheses are that they are either the result of a horizontal perturbation (i.e. cross-channel) or a vertical perturbation (i.e. bed-level gradient). Moreover, in analogy with braided river models (Schuurman and Kleinhans, 2015), the hypothesis that water level gradients drive morphological change can then be tested for tidal bars (Fig. 10.4). It is essential to comprehend the mechanism for the initiation of tidal bifurcations, because it will aid in understanding when tidal bifurcations are stable or instable. In turn, the stability of channels determines whether channels will remain open or close off in the future, which is relevant for management of estuaries.

References

Agisoft (2017). *Agisoft photoscan*. URL: http://www.agisoft.com/.

Ahnert, F. (1960). Estuarine meanders in the Chesapeake Bay Area. *Geographical Review*, 50 (3), pp. 390–401. DOI:10.2307/212282.

Alam, R., Islam, M.S., Hasib, M.R. & Khan, M.Z.H. (2014). Characteristics of hydrodynamic processes in the Meghna Estuary due to dynamic whirl action. *IOSR Journal of Engineering*, 4 (6), pp. 39–50. DOI:10.9790/3021-04633950.

Allen, J.R.L. (1968). *Current ripples, their relation to patterns of water and sediment motion*. North-Holland Publishing Co.: Amsterdam, the Netherlands.

Allen, J.R.L. (1984). *Sedimentary Structures: Their Character and Physical Basis*. Elsevier: Amsterdam, the Netherlands.

Anderson, J.B., Rodriguez, A.B., Milliken, K. & Taviani, M. (2007). Holocene evolution of the galveston bay punctuated by rapid, episodic changes: Implications for future change.

Ashley, G.M. (1980). Channel morphology and sediment movement in a tidal river, Pitt river, British Columbia. *Earth Surface Processes*, 5 (4), pp. 347–368. DOI:10.1002/ESP.3760050406.

Ashmore, P.E. (2001). Gravel-bed river V. In: New Zealand Hydrological Society Inc.: Wellington, New Zealand. Chap. braiding phenomena: Statics and kinetics, pp. 95–114.

Ashmore, P.E. (1982). Laboratory modelling of gravel braided stream morphology. *Earth Surface Processes and Landforms*, 7 (3), pp. 201–225. DOI:10.1002/ESP.3290070301.

Ashmore, P.E. (1991). How do gravel-bed rivers braid? *Canadian Journal of Earth Sciences*, 28 (3), pp. 326–341.

Ashworth, P.J., Best, J.L., Roden, J.E., Bristow, C.S. & Klaassen, G.J. (2000). Morphological evolution and dynamics of a large, sand braid-bar, Jamuna River, Bangladesh. *Sedimentology*, 47 (3), pp. 533–555.

Ashworth, P.J., Best, J.L. & Parsons, D.R. (2015). *Fluvial-Tidal Sedimentology*. Vol. 68. Elsevier: Amsterdam, the Netherlands.

Auerbach, L.W., Goodbred Jr, S.L., Mondal, D.R., Wilson, C.A., Ahmed, K.R., Roy, K., Steckler, M.S., Small, C., Gilligan, J.M. & Ackerly, B.A. (2015). Flood risk of natural and embanked landscapes on the Ganges–Brahmaputra tidal delta plain. *Nature Climate Change*, 5 (2), pp. 153–157. DOI:10.1038/NCLIMATE2472.

Baar, A.W. (2019). *Impact of small-scale transverse bed slope effects on large-scale morphology*. PhD dissertation. Utrecht University, Utrecht, the Netherlands.

Baar, A.W., de Smit, J., Uijttewaal, W.S.J. & Kleinhans, M.G. (2018). Sediment transport of fine sand to fine gravel on transverse bed slopes in rotating annular flume experiments. *Water Resources Research*, 54 (1), pp. 19–45. DOI:10.1002/2017WR020604.

Balke, T., Stock, M., Jensen, K., Bouma, T.J. & Kleyer, M. (2016). A global analysis of the seaward salt marsh extent: The importance of tidal range. *Water Resources Research*, 52 (5), pp. 3775–3786. DOI:10.1002/2015WR018318.

Barnes, T.K., Volety, A.K., Chartier, K., Mazzotti, F.J. & Pearlstine, L. (2007). A habitat suitability index model for the eastern oyster (Crassostrea virginica), a tool for restoration of the Caloosahatchee Estuary, Florida. *Journal of Shellfish Research*, 26 (4), pp. 949–959. DOI:10.2983/0730-8000(2007)26[949:AHSIMF]2.0.CO;2.

Bartels, P.C.J. (2015). *Ups-and-downs of tidal systems: Formation and development of ebb-and flood tidal channels and bars*. MSc thesis. Utrecht University, Utrecht, the Netherlands.

Barua, D. & Koch, F. (1986). Characteristic morphological relationship for the tide dominated channels of the lower Meghna estuary. In: *Proc. Workshop on Erosion and Sediment Transport Processes*. UNESCO, Bangladesh University of Engineering and Technology. Dhaka, Bangladesh, pp. 68–82.

Barwis, J.H. (1977). Sedimentology of some South Carolina tidal-creek point bars, and a comparison with their fluvial counterparts. *Fluvial Sedimentology*, 5, pp. 129–160.

Billy, J., Chaumillon, E., Féniès, H. & Poirier, C. (2012). Tidal and fluvial controls on the morphological evolution of a lobate estuarine tidal bar: The Plassac Tidal Bar in the Gironde Estuary (France). *Geomorphology*, 169, pp. 86–97. DOI:10.1016/J.GEOMORPH.2012.04.015.

Blom, A. & Kleinhans, M.G. (2008). Estimating bed form height from sorting preserved in sedimentary records of river dunes, deltas and bars. In: *River, Coastal and Estuarine Morphodynamics (RCEM 2007)*. Taylor and Francis: Londen, United Kingdom, pp. 641–68.

Blondeaux, P. & Seminara, G. (1985). A unified bar–bend theory of river meanders. *Journal of Fluid Mechanics*, 157, pp. 449–470. DOI:10.1017/S0022112085002440.

Blondeaux, P. & Vittori, G. (2016). A model to predict the migration of sand waves in shallow tidal seas. *Continental Shelf Research*, 112, pp. 31–45. DOI:10.1016/J.CSR.2015.11.011.
Blott, S.J., Pye, K., van der Wal, D. & Neal, A. (2006). Long-term morphological change and its causes in the Mersey Estuary, NW England. *Geomorphology*, 81 (1–2), pp. 185–206. DOI:10.1016/J.GEOMORPH.2006.04.008.
Boelens, T., Schuttelaars, H., Schramkowski, G. & de Mulder, T. (2018). The effect of geometry and tidal forcing on hydrodynamics and net sediment transport in semi-enclosed tidal basins. *Ocean Dynamics*, 68 (10), pp. 1285–1309. DOI:10.1007/S10236-018-1198-9.
Bolla Pittaluga, M., Coco, G. & Kleinhans, M.G. (2015). A unified framework for stability of channel bifurcations in gravel and sand fluvial systems. *Geophysical Research Letters*, 42 (18), pp. 7521–7536. DOI:10.1002/2015GL065175.
Bolle, A., Wang, Z.B., Amos, C. & de Ronde, J. (2010). The influence of changes in tidal asymmetry on residual sediment transport in the Western Scheldt. *Continental Shelf Research*, 30 (8), pp. 871–882. DOI:10.1016/J.CSR.2010.03.001.
Boon, J.D. (1975). Tidal discharge asymmetry in a salt marsh drainage system. *Limnology and Oceanography*, 20 (1), pp. 71–80. DOI:10.4319/LO.1975.20.1.0071.
Boon, J.D. & Byrne, R.J. (1981). On basin hyposmetry and the morphodynamic response of coastal inlet systems. *Marine Geology*, 40 (1-2), pp. 27–48. DOI:10.1016/0025-3227(81)90041-4.
Bouma, H, de Jong, D.J., Twisk, F. & Wolfstein, K. (2005). *A Dutch Ecotope system for coastal waters (ZES. 1), To map the potential occurence of ecological communities in Dutch coastal and transitional waters*. Tech. rep. Rijkswaterstaat, RIKZ/2005.024.
Boyd, R., Dalrymple, R.W. & Zaitlin, B.A. (1992). Classification of clastic coastal depositional environments. *Sedimentary Geology*, 80 (3-4), pp. 139–150. DOI:10.1016/0037-0738(92)90037-R.
Braat, L. (2019). *Morphodynamics and sedimentology of estuaries with sand and mud*. PhD dissertation. Utrecht University, Utrecht, the Netherlands.
Braat, L., van Kessel, T., Leuven, J.R.F.W. & Kleinhans, M.G. (2017). Effects of mud supply on large-scale estuary morphology and development over centuries to millennia. *Earth Surface Dynamics*, 5 (4), pp. 617–652. DOI:10.5194/ESURF-5-617-2017.
Braat, L., Leuven, J.R.F.W., Lokhorst, I.R. & Kleinhans, M.G. (2019). Effects of estuarine mudflat formation on tidal prism and large-scale morphology in experiments. *Earth Surface Processes and Landforms*, 44 (2), pp. 417–432. DOI:10.1002/ESP.4504.
Bridge, J.S. (1993). The interaction between channel geometry, water flow, sediment transport and deposition in braided rivers. *Geological Society, London, Special Publications*, 75 (1), pp. 13–71.
Bridge, J.S. & Best, J. (1997). Preservation of planar laminae due to migration of low-relief bed waves over aggrading upper-stage plane beds: comparison of experimental data with theory. *Sedimentology*, 44 (2), pp. 253–262.
Bridge, J.S. & Tye, R.S. (2000). Interpreting the dimensions of ancient fluvial channel bars, channels, and channel belts from wireline-logs and cores. *AAPG bulletin*, 84 (8), pp. 1205–1228.
Bridge, J. (2003). *Rivers and floodplains*. Blackwell Publishing, Malden, Mass.
Bridges, P.H. & Leeder, M.R. (1976). Sedimentary model for intertidal mudflat channels, with examples from the Solway Firth, Scotland. *Sedimentology*, 23 (4), pp. 533–552. DOI:J.1365-3091.1976.TB00066.X.
Brinkkemper, J.A., Aagaard, T., De Bakker, A.T.M. & Ruessink, B.G. (2018). Shortwave Sand Transport in the Shallow Surf Zone. *Journal of Geophysical Research: Earth Surface*, 123 (5). DOI:10.1029/2017JF004425.
Brivio, L., Ghinassi, M., D'Alpaos, A., Finotello, A., Fontana, A., Roner, M. & Howes, N. (2016). Aggradation and lateral migration shaping geometry of a tidal point bar: An example from salt marshes of the Northern Venice Lagoon (Italy). *Sedimentary Geology*, 343, pp. 141–155. DOI:10.1016/J.SEDGEO.2016.08.005.
Brockway, R., Bowers, D., Hoguane, A., Dove, V. & Vassele, V. (2006). A note on salt intrusion in funnel-shaped estuaries: Application to the Incomati estuary, Mozambique. *Estuarine, Coastal and Shelf Science*, 66 (1), pp. 1–5. DOI:10.1016/J.ECSS.2005.07.014.
Brückner, M.Z.M., Schwartz, C., van Dijk, W., van Oorschot, M., Douma, H. & Kleinhans, M.G. (2019). Salt marsh establishment and eco-engineering effects in dynamic environments determined by species growth and mortality. *[to be submitted]*.
Bruun, P. & Gerritsen, F. (1960). Stability of coastal inlets. *Coastal Engineering Proceedings*, 1 (7), p. 23. DOI:10.9753/ICCE.V7.23.
Byrne, R.J., Gammisch, R.A. & Thomas, G.R. (1980). Tidal prism-inlet area relations for small tidal inlets. *Coastal Engineering Proceedings*, 1 (17), pp. 2517–2533. DOI:10.1061/9780872622647.151.
Camporeale, C., Perona, P., Porporato, A. & Ridolfi, L. (2007). Hierarchy of models for meandering rivers and related morphodynamic processes. *Reviews of Geophysics*, 45 (1), pp. 1–28. DOI:10.1029/2005RG000185.
Canestrelli, A., Lanzoni, S. & Fagherazzi, S. (2014). One-dimensional numerical modeling of the long-term morphodynamic evolution of a tidally-dominated estuary: The Lower Fly River (Papua New Guinea). *Sedimentary Geology*, 301, pp. 107–119. DOI:10.1016/J.SEDGEO.2013.06.009.

Cant, D.J. & Walker, R.G. (1978). Fluvial processes and facies sequences in the sandy braided South Saskatchewan River, Canada. *Sedimentology*, 25 (5), pp. 625–648.
Chandler, J.H., Shiono, K., Rameshwaren, P. & Lane, S.N. (2001). Measuring flume surfaces for hydraulics research using a Kodak DCS460. *The Photogrammetric Record*, 17 (97), pp. 39–61.
Choi, K.S., Dalrymple, R.W., Chun, S.S. & Kim, S.-P. (2004). Sedimentology of modern, inclined heterolithic stratification (IHS) in the macrotidal Han River delta, Korea. *Journal of Sedimentary Research*, 74 (5), pp. 677–689. DOI:10.1306/030804740677.
Choi, K. & Jo, J.H. (2015). Morphodynamics of tidal channels in the open coast macrotidal flat, southern Ganghwa Island in Gyeonggi Bay, west coast of Korea. *Journal of Sedimentary Research*, 85 (6), pp. 582–595. DOI:10.2110/JSR.2015.44.
Church, J.A., Clark, P.U., Cazenave, A., Gregory, J.M., Jevrejeva, S., Levermann, A., Merrifield, M.A., Milne, G.A., Nerem, R.S. & Nunn, P.D. (2013). Climate change 2013: The physical science basis. Contribution of working group I to the fifth assessment report of the intergovernmental panel on climate change. In: Cambridge University Press: Cambridge, United Kingdom. Chap. Sea level change, pp. 1137–1216.
Cleveringa, J. (2013). *Ontwikkeling mesoschaal Westerschelde - instandhouding vaarpassen Schelde Milieuvergunningen terugstorten baggerspecie*. Tech. rep. Zwolle, the Netherlands: Arcadis.
Cleveringa, J. (2007). *Milieueffectrapport Verruiming vaargeul Beneden-Zeeschelde en Westerschelde*. 070622 V. 4.1. Zwolle, the Netherlands: Arcadis.
Coco, G., Zhou, Z., van Maanen, B., Olabarrieta, M., Tinoco, R. & Townend, I. (2013). Morphodynamics of tidal networks: advances and challenges. *Marine Geology*, 346, pp. 1–16. DOI:10.1016/J.MARGEO.2013.08.005.
Colombini, M. (2016). Stability of river bed forms. In: *MARID 2016. Fifth International Conference on Marine and River Dune Dynamics*. Ed. by K.J.J. Van Landeghem, G. T. & J.H. Baas. Bangor University and SHOM. Caernarfon, North Wales, United Kingdom, pp. 41–48.
Costanza, R., d'Arge, R., De Groot, R., Farber, S., Grasso, M., Hannon, B., Limburg, K., Naeem, S., O'Neill, R.V., Paruelo, J., Raskin, R.G., Sutton, P. & van den Belt, M. (1997). The value of the world's ecosystem services and natural capital. *Nature*, 387 (6630), p. 253.
Cozzoli, F., Smolders, S., Eelkema, M., Ysebaert, T., Escaravage, V., Temmerman, S., Meire, P., Herman, P.M.J. & Bouma, T.J. (2017). A modeling approach to assess coastal management effects on benthic habitat quality: A case study on coastal defense and navigability. *Estuarine, Coastal and Shelf Science*, 184, pp. 67–82. DOI:10.1016/J.ECSS.2016.10.043.
Crosato, A. & Mosselman, E. (2009). Simple physics-based predictor for the number of river bars and the transition between meandering and braiding. *Water Resources Research*, 45 (3), W03424.
D'Alpaos, A., Ghinassi, M., Finotello, A., Brivio, L., Bellucci, L.G. & Marani, M. (2017). Tidal meander migration and dynamics: A case study from the Venice Lagoon. *Marine and Petroleum Geology*, 87, pp. 80–90. DOI:10.1016/J.MARPETGEO.2017.04.012.
Dalrymple, R.W. & Choi, K. (2007). Morphologic and facies trends through the fluvial–marine transition in tide-dominated depositional systems: a schematic framework for environmental and sequence-stratigraphic interpretation. *Earth-Science Reviews*, 81 (3), pp. 135–174. DOI:10.1016/J.EARSCIREV.2006.10.002.
Dalrymple, R.W. & Rhodes, R.N. (1995). Estuarine dunes and bars. *Geomorphology and sedimentology of estuaries*, 53, pp. 359–422.
Dalrymple, R.W., Knight, R., Zaitlin, B.A. & Middleton, G.V. (1990). Dynamics and facies model of a macrotidal sand-bar complex, Cobequid Bay–Salmon River Estuary (Bay of Fundy). *Sedimentology*, 37 (4), pp. 577–612.
Dalrymple, R.W., Zaitlin, B.A. & Boyd, R. (1992). Estuarine facies models: conceptual basis and stratigraphic implications: perspective. *Journal of Sedimentary Research*, 62 (6), pp. 1130–1146. DOI:10.1306/D4267A69-2B26-11D7-8648000102C1865D.
Dalrymple, R.W., Mackay, D.A., Ichaso, A.A. & Choi, K.S. (2012). Processes, morphodynamics, and facies of tide-dominated estuaries. In: *Principles of Tidal Sedimentology*. Springer: Dordrecht, the Netherlands, pp. 79–107.
Dam, G., van der Wegen, M., Labeur, R.J. & Roelvink, D. (2016). Modeling centuries of estuarine morphodynamics in the Western Scheldt estuary. *Geophysical Research Letters*, 43 (8), pp. 3839–3847. DOI:10.1002/2015GL066725.
Dam, G., van der Wegen, M., Roelvink, D., Labeur, R. & Bliek, B. (2015). Simulation of long-term morphodynamics of the Western Scheldt. In: *36st IAHR congress, The Hague, Netherlands*.
Dame, R. (2008). Estuaries. In: *Encyclopedia of Ecology*. Ed. by S.E. Jörgensen & B.D. Fath. Academic Press: Oxford, United Kingdom, pp. 1407 –1413. DOI:10.1016/B978-008045405-4.00329-3.
Davidson, N. & Council, N.C. (1991). *Nature Conservation and Estuaries in Great Britain*. Nature Conservancy Council Peterborough.
Davies, G. & Woodroffe, C.D. (2010). Tidal estuary width convergence: Theory and form in North Australian estuaries. *Earth Surface Processes and Landforms*, 35 (7), pp. 737–749. DOI:10.1002/ESP.1864.
Davies, N.S. & Gibling, M.R. (2011). Evolution of fixed-channel alluvial plains in response to Carboniferous vegetation. *Nature Geoscience*, 4 (9), p. 629.

Davies, N.S. & Gibling, M.R. (2013). The sedimentary record of Carboniferous rivers: Continuing influence of land plant evolution on alluvial processes and Palaeozoic ecosystems. *Earth-Science Reviews*, 120, pp. 40–79.
Davis Jr, R.A. & Hayes, M.O. (1984). What is a wave-dominated coast? *Marine Geology*, 60 (1-4), pp. 313–329. DOI:10.1016/0025-3227(84)90155-5.
Davy, A.J., Bishop, G.F. & Costa, C.S.B. (2001). Salicornia L.(Salicornia pusilla J. woods, S. ramosissima J. woods, S. europaea L., S. obscura PW ball & tutin, S. nitens PW ball & tutin, S. fragilis PW ball & tutin and S. dolichostachya moss). *Journal of Ecology*, 89 (4), pp. 681–707.
De Brauwere, A., de Brye, B., Blaise, S. & Deleersnijder, E. (2011). Residence time, exposure time and connectivity in the Scheldt Estuary. *Journal of Marine Systems*, 84 (3-4), pp. 85–95. DOI:10.1016/J.JMARSYS.2010.10.001.
De Haas, T., Pierik, H.J., van der Spek, A.J.F., Cohen, K.M., van Maanen, B. & Kleinhans, M.G. (2017). Holocene evolution of tidal systems in The Netherlands: Effects of rivers, coastal boundary conditions, eco-engineering species, inherited relief and human interference. *Earth-Science Reviews*, 177, pp. 139 –163. DOI:10.1016/J.EARSCIREV.2017.10.006.
De Jong, D.J. (1999). *Ecotopes in the Dutch marine tidal waters: A proposal for a classification of ecotopes and a method to map them*. Tech. rep. RIKZ/99.017. Den Haag, the Netherlands: Rijkswaterstaat.
De Mowbray, T. (1983). The genesis of lateral accretion deposits in recent intertidal mudflat channels, Solway Firth, Scotland. *Sedimentology*, 30 (3), pp. 425–435. DOI:J.1365-3091.1983.TB00681.X.
De Swart, H. & Zimmerman, J. (2009). Morphodynamics of tidal inlet systems. *Annual Review of Fluid Mechanics*, 41, pp. 203–229.
De Vet, P.L.M., van Prooijen, B.C. & Wang, Z.B. (2017). The differences in morphological development between the intertidal flats of the Eastern and Western Scheldt. *Geomorphology*, 281, pp. 31–42.
De Vriend, H.J., Wang, Z.B., Ysebaert, T., Herman, P.M. & Ding, P. (2011). Eco-morphological problems in the Yangtze Estuary and the Western Scheldt. *Wetlands*, 31 (6), pp. 1033–1042. DOI:10.1007/S13157-011-0239-7.
DeConto, R.M. & Pollard, D. (2016). Contribution of Antarctica to past and future sea-level rise. *Nature*, 531 (7596), p. 591. DOI:10.1038/NATURE17145.
Degraer, S., Verfaillie, E., Willems, W., Adriaens, E., Vincx, M. & van Lancker, V. (2008). Habitat suitability modelling as a mapping tool for macrobenthic communities: an example from the Belgian part of the North Sea. *Continental Shelf Research*, 28 (3), pp. 369–379. DOI:10.1016/J.CSR.2007.09.001.
Depreiter, D., Sas, M., Beirinckx, K. & Liek, G.-J. (2012). *Flexible Disposal Strategy: monitoring as a key to understanding and steering environmental responses to dredging and disposal in the Scheldt Estuary*. Tech. rep. Berchem, Belgium: International Marine & Dredging Consultants.
Dieckmann, R., Osterthun, M. & Partenscky, H.W. (1987). Influence of water-level elevation and tidal range on the sedimentation in a German tidal flat area. *Progress in Oceanography*, 18 (1-4), pp. 151–166.
Dieckmann, R., Osterthun, M. & Partenscky, H.W. (1988). A comparison between German and North American tidal inlets. *Coastal Engineering Proceedings*, 1 (21), pp. 2681–2691.
Dissanayake, D.M.P.K., Roelvink, J.A. & van der Wegen, M. (2009). Modelled channel patterns in a schematized tidal inlet. *Coastal Engineering*, 56 (11-12), pp. 1069–1083. DOI:10.1016/J.COASTALENG.2009.08.008.
Dodd, N., Blondeaux, P., Calvete, D., de Swart, H.E., Falqués, A., Hulscher, S.J., Różyński, G. & Vittori, G. (2003). Understanding coastal morphodynamics using stability methods. *Journal of Coastal Research*, 19 (4), pp. 849–865.
Donchyts, G., Schellekens, J., Winsemius, H., Eisemann, E. & van de Giesen, N. (2016). A 30 m resolution surface water mask including estimation of positional and thematic differences using landsat 8, srtm and openstreetmap: a case study in the Murray-Darling Basin, Australia. *Remote Sensing*, 8 (5), p. 386. DOI:10.3390/RS8050386.
Dronkers, J. (2017). Convergence of estuarine channels. *Continental Shelf Research*, 144, pp. 120–133. DOI:10.1016/J.CSR.2017.06.012.
Du, J., Shen, J., Zhang, Y.J., Ye, F., Liu, Z., Wang, Z., Wang, Y.P., Yu, X., Sisson, M. & Wang, H.V. (2018). Tidal Response to Sea-Level Rise in Different Types of Estuaries: The Importance of Length, Bathymetry, and Geometry. *Geophysical Research Letters*, 45 (1), pp. 227–235. DOI:10.1002/2017GL075963.
Durkin, P.R., Boyd, R.L., Hubbard, S.M., Shultz, A.W. & Blum, M.D. (2017). Three-dimensional reconstruction of meander-belt evolution, Cretaceous McMurray formation, Alberta Foreland Basin, Canada. *Journal of Sedimentary Research*, 87 (10), pp. 1075–1099. DOI:10.2110/JSR.2017.59.
Dury, G. (1971). Channel characteristics in a meandering tidal channel: Crooked River, Florida. *Geografiska Annaler: Series A, Physical Geography*, 53 (3-4), pp. 188–197. DOI:10.1080/04353676.1971.11879844.
Dyer, K.R. & Huntley, D.A. (1999). The origin, classification and modelling of sand banks and ridges. *Continental Shelf Research*, 19 (10), pp. 1285–1330.
Eaton, B.C., Church, M. & Davies, T.R.H. (2006). A conceptual model for meander initiation in bedload-dominated streams. *Earth Surface Processes and Landforms*, 31 (7), pp. 875–891. DOI:10.1002/ESP.1297.
Eke, E. (2014). *Numerical modeling of river migration incorporating erosional and depositional bank processes*. PhD dissertation. University of Illinois, Urbana-Champaign, the United States.

Elgar, S. (1987). Relationships involving third moments and bispectra of a harmonic process. *IEEE Transactions on Acoustics Speech and Signal Processing*, 35 (12), pp. 1725–1726. DOI:10.1109/TASSP.1987.1165090.
Elias, E.P.L. & van der Spek, A.J.F. (2006). Long-term morphodynamic evolution of Texel Inlet and its ebb-tidal delta (the Netherlands). *Marine Geology*, 225 (1), pp. 5–21.
Elias, E.P.L., Gelfenbaum, G. & van der Westhuysen, A.J. (2012). Validation of a coupled wave-flow model in a high-energy setting: The mouth of the Columbia River. *Journal of Geophysical Research: Oceans*, 117 (C9), pp. 1–21. DOI:10.1029/2012JC008105.
Elias, E.P.L., van der Spek, A.J.F. & Lazar, M. (2017). The 'Voordelta', the contiguous ebb-tidal deltas in the SW Netherlands: large-scale morphological changes and sediment budget 1965–2013; impacts of large-scale engineering. *Netherlands Journal of Geosciences*, 96 (3), pp. 233–259.
Engelund, F. & Hansen, E. (1967). *A monograph on sediment transport in alluvial streams*. Tech. rep. Copenhagen, Denmark: Technical University of Denmark.
Ensing, E., de Swart, H.E. & Schuttelaars, H.M. (2015). Sensitivity of tidal motion in well-mixed estuaries to cross-sectional shape, deepening, and sea level rise. *Ocean Dynamics*, 65 (7), pp. 933–950. DOI:10.1007/s10236-015-0844-8.
Erkens, G. (2009). *Sediment dynamics in the Rhine catchment: quantification of fluvial response to climate change and human impact*. PhD dissertation. Utrecht University, Utrecht, the Netherlands.
Essink, K. (1999). Ecological effects of dumping of dredged sediments; options for management. *Journal of Coastal Conservation*, 5 (1), pp. 69–80. DOI:10.1007/BF02802741.
Eysink, W.D. (1983). *Basic considerations on the morphology and land accretion potentials in the estuary of the lower Meghna River*. Tech. rep. Dhaka, Bangladesh: Bangladesh Water Development Board.
Eysink, W.D. (1990). Morphologic response of tidal basins to changes. *Coastal Engineering Proceedings*, 1 (22), pp. 1948–1961. DOI:10.1061/9780872627765.149.
Fenies, H. & Faugères, J.-C. (1998). Facies and geometry of tidal channel-fill deposits (Arcachon Lagoon, SW France). *Marine Geology*, 150 (1-4), pp. 131–148. DOI:10.1016/S0025-3227(98)00049-8.
Ferguson, R.I. (1975). Meander irregularity and wavelength estimation. *Journal of Hydrology*, 26 (3-4), pp. 315–333.
Feyrer, F., Newman, K., Nobriga, M. & Sommer, T. (2011). Modeling the effects of future outflow on the abiotic habitat of an imperiled estuarine fish. *Estuaries and Coasts*, 34 (1), pp. 120–128. DOI:10.1007/s12237-010-9343-9.
Finotello, A., Lanzoni, S., Ghinassi, M., Marani, M., Rinaldo, A. & D'Alpaos, A. (2018). Field migration rates of tidal meanders recapitulate fluvial morphodynamics. *Proceedings of the National Academy of Sciences*, 115 (7), pp. 1463–1468. DOI:10.1073/PNAS.1711330115.
Fonstad, M.A., Dietrich, J.T., Courville, B.C., Jensen, J.L. & Carbonneau, P.E. (2013). Topographic structure from motion: A new development in photogrammetric measurement. *Earth Surface Processes and Landforms*, 38 (4), pp. 421–430. DOI:10.1002/ESP.3366.
Fortunato, A.B. & Oliveira, A. (2005). Influence of intertidal flats on tidal asymmetry. *Journal of Coastal Research*, pp. 1062–1067. DOI:10.2112/03-0089.1.
Fortunato, A.B., Oliveira, A. & Baptista, A.M. (1999). On the effect of tidal flats on the hydrodynamics of the Tagus estuary. *Oceanologica Acta*, 22 (1), pp. 31–44. DOI:10.1016/S0399-1784(99)80030-9.
Frascati, A. & Lanzoni, S. (2013). A mathematical model for meandering rivers with varying width. *Journal of Geophysical Research: Earth Surface*, 118 (3), pp. 1641–1657. DOI:10.1002/JGRF.20084.
Friedrichs, C.T. (1995). Stability shear stress and equilibrium cross-sectional geometry of sheltered tidal channels. *Journal of Coastal Research*, 11 (4), pp. 1062–1074.
Friedrichs, C.T. (2010). Contemporary Issues in Estuarine Physics. In: ed. by A. Valle-Levinson. Cambridge University Press. Chap. Barotropic tides in channelized estuaries, pp. 27–61.
Friedrichs, C.T. & Aubrey, D.G. (1988). Non-linear tidal distortion in shallow well-mixed estuaries: a synthesis. *Estuarine, Coastal and Shelf Science*, 27 (5), pp. 521–545.
Friedrichs, C.T. & Aubrey, D.G. (1994). Tidal propagation in strongly convergent channels. *Journal of Geophysical Research*, 99, pp. 3321–3321.
Fujita, Y. & Muramoto, Y. (1985). Studies on the process of development of alternate bars. *Bulletin of the Disaster Prevention Research Institute*, 35 (3), pp. 55–86.
Ganti, V., Straub, K.M., Foufoula-Georgiou, E. & Paola, C. (2011). Space-time dynamics of depositional systems: experimental evidence and theoretical modeling of heavy-tailed statistics. *Journal of Geophysical Research: Earth Surface*, 116 (F2), pp. 1–17. DOI:10.1029/2010JF001893.
Gardiner, S., Nicholls, R. & Tanton, T. (2011). Management Implications of Flood/Ebb tidal dominance: its influence on saltmarsh and intertidal habitat stability in Poole Harbour. In: *Littoral 2010–Adapting to Global Change at the Coast: Leadership, Innovation, and Investment*. EDP Sciences. London, United Kingdom, p. 06004. DOI:10.1051/LITT/201106004.

Garotta, V., Bolla Pittaluga, M. & Seminara, G. (2006). On the migration of tidal free bars. *Physics of Fluids*, 18 (9), pp. 1–14. DOI:10.1063/1.2221346.
Garotta, V., Rummel, A.C. & Seminara, G. (2008). Long-term morphodynamics and hydrodynamics of tidal meandering channels. In: *River, Coastal and Estuarine Morphodynamics conference*. Taylor and Francis/Balkema: Enschede, the Netherlands, pp. 163–168.
Geleynse, N., Storms, J.E.A., Walstra, D.-J.R., Albert Jagers, H.R., Wang, Z.B. & Stive, M.J.F. (2011). Controls on river delta formation; insights from numerical modelling. *Earth and Planetary Science Letters*, 302 (1-2), pp. 217–226. DOI:10.1016/J.EPSL.2010.12.013.
Gerritsen, F. & de Jong, H. (1985). *Stabiliteit van doorstroomprofielen in de Westerschelde*. Tech. rep. WWKZ-83, V016. Vlissingen, the Netherlands: Rijkswaterstaat.
Ghinassi, M., Brivio, L., D'Alpaos, A., Finotello, A., Carniello, L., Marani, M. & Cantelli, A. (2018). Morphodynamic evolution and sedimentology of a microtidal meander bend of the Venice Lagoon (Italy). *Marine and Petroleum Geology*, 65 (4), pp. 1354–1377. DOI:10.1016/J.MARPETGEO.2018.06.011.
Gingras, M.K., MacEachern, J.A., Dashtgard, S.E., Ranger, M.J., Pemberton, S.G. & Hein, F. (2016). The significance of trace fossils in the McMurray Formation, Alberta, Canada. *Bulletin of Canadian Petroleum Geology*, 64 (2), pp. 233–250.
Gisen, J.I.A., Savenije, H.H.G. & Nijzink, R.C. (2015). Revised predictive equations for salt intrusion modelling in estuaries. *Hydrology and Earth System Sciences*, 19 (6), pp. 2791–2803. DOI:10.5194/HESS-19-2791-2015.
Gisen, J.I.A. & Savenije, H.H.G. (2015). Estimating bankfull discharge and depth in ungauged estuaries. *Water Resources Research*, 51 (4), pp. 2298–2316. DOI:10.1002/2014WR016227.
Goodbred Jr, S.L. & Kuehl, S.A. (1999). Holocene and modern sediment budgets for the Ganges-Brahmaputra river system: Evidence for highstand dispersal to flood-plain, shelf, and deep-sea depocenters. *Geology*, 27 (6), pp. 559–562. DOI:10.1130/0091-7613(1999)027<0559:HAMSBF>2.3.CO;2.
Gray, A.J. (1992). *Saltmarshes: morphodynamics, conservation and engineering significance*. Ed. by J.R.L. Allen & K. Pye. Cambridge University Press: Cambridge, United Kingdom. Chap. Saltmarsh plant ecology: zonation and succession revisited, pp. 63–79.
Gurnell, A.M., Bertoldi, W. & Corenblit, D. (2012). Changing river channels: The roles of hydrological processes, plants and pioneer fluvial landforms in humid temperate, mixed load, gravel bed rivers. *Earth-Science Reviews*, 111 (1-2), pp. 129–141. DOI:10.1016/J.EARSCIREV.2011.11.005.
Haasnoot, M. & van de Wolfshaar, K. (2009). Combining a conceptual framework and a spatial analysis tool, HABITAT, to support the implementation of river basin management plans. *International Journal of River Basin Management*, 7 (4), pp. 295–311.
Haasnoot, M., Kwakkel, J.H., Walker, W.E. & ter Maat, J. (2013). Dynamic adaptive policy pathways: A method for crafting robust decisions for a deeply uncertain world. *Global environmental change*, 23 (2), pp. 485–498. DOI:10.1016/J.GLOENVCHA.2012.12.006.
Haring, J. (1967). De verhouding van getijvolume en doorstroomprofiel in de zeegaten Haringvliet, Brouwershavense Gat, Oosterschelde en in de mond van de Rotterdamse Waterweg uit alle beschikbare waarnemingen. *Rijkswaterstaat*, (K 271).
Harris, P.T. (1988). Large-scale bedforms as indicators of mutually evasive sand transport and the sequential infilling of wide-mouthed estuaries. *Sedimentary Geology*, 57 (3-4), pp. 273–298.
Harris, P.T., Hughes, M.G., Baker, E.K., Dalrymple, R.W. & Keene, J.B. (2004). Sediment transport in distributary channels and its export to the pro-deltaic environment in a tidally dominated delta: Fly River, Papua New Guinea. *Continental Shelf Research*, 24 (19), pp. 2431–2454.
Hepkema, T.M., de Swart, H.E. & Schuttelaars, H.M. (2019). The sensitivity of tidal bar wavelength to channel width. *Submitted to Journal of Geophysical Research: Earth Surface*.
Hey, R.D. (1982). Gravel-Bed Rivers. In: ed. by R.D. Hey, J.C. Bathurst & C.R. Thorne. John Wilet and Sons: Chichester, United Kingdom. Chap. Design equations for mobile gravel-bed rivers, pp. 553–574.
Hey, R.D. & Thorne, C.R. (1986). Stable channels with mobile gravel beds. *Journal of Hydraulic Engineering*, 112 (8), pp. 671–689. DOI:10.1061/(ASCE)0733-9429(1986)112:8(671).
Hibma, A, de Vriend, H.J. & Stive, M.J.F. (2003). Numerical modelling of shoal pattern formation in well-mixed elongated estuaries. *Estuarine, Coastal and Shelf Science*, 57 (5), pp. 981–991.
Hibma, A., Schuttelaars, H.M. & de Vriend, H.J. (2004). Initial formation and long-term evolution of channel–shoal patterns. *Continental Shelf Research*, 24 (15), pp. 1637 –1650. DOI:HTTPS://DOI.ORG/10.1016/J.CSR.2004.05.003.
Hijma, M.P. & Cohen, K.M. (2011). Holocene transgression of the Rhine river mouth area, The Netherlands/Southern North Sea: palaeogeography and sequence stratigraphy. *Sedimentology*, 58 (6), pp. 1453–1485.
Hoefel, F. & Elgar, S. (2003). Wave-induced sediment transport and sandbar migration. *Science*, 299 (5614), pp. 1885–1887. DOI:10.1126/SCIENCE.1081448.

Hori, K., Saito, Y., Zhao, Q., Cheng, X., Wang, P., Sato, Y. & Li, C. (2001). Sedimentary facies and Holocene progradation rates of the Changjiang (Yangtze) delta, China. *Geomorphology*, 41 (2-3), pp. 233–248. DOI:10.1016/S0169-555X(01)00119-2.
Howard, A.D. & Hemberger, A.T. (1991). Multivariate characterization of meandering. *Geomorphology*, 4 (3-4), pp. 161–186.
Hu, Z., Belzen, J., Wal, D., Balke, T., Wang, Z.B., Stive, M. & Bouma, T.J. (2015). Windows of opportunity for salt marsh vegetation establishment on bare tidal flats: The importance of temporal and spatial variability in hydrodynamic forcing. *Journal of Geophysical Research: Biogeosciences*, 120 (7), pp. 1450–1469.
Hubbard, S.M., Smith, D.G., Nielsen, H., Leckie, D.A., Fustic, M., Spencer, R.J. & Bloom, L. (2011). Seismic geomorphology and sedimentology of a tidally influenced river deposit, Lower Cretaceous Athabasca oil sands, Alberta, Canada. *AAPG bulletin*, 95 (7), pp. 1123–1145.
Hughes, Z.J. (2012). Tidal channels on tidal flats and marshes. In: *Principles of Tidal Sedimentology*. Springer: Dordrecht, the Netherlands, pp. 269–300. DOI:10.1007/978-94-007-0123-6_11.
Hulscher, S.J., de Swart, H.E. & de Vriend, H.J. (1993). The generation of offshore tidal sand banks and sand waves. *Continental Shelf Research*, 13 (11), pp. 1183–1204.
Hume, T.M. & Herdendorf, C.E. (1990). Morphologic and hydrologic characteristics of tidal inlets on a headland dominated, low littoral drift coast, northeastern New Zealand. *Journal of Coastal Research*, 9, pp. 527–563.
Hume, T.M. & Herdendorf, C.E. (1988). A geomorphic classification of estuaries and its application to coastal resource management–a New Zealand example. *Ocean and Shoreline Management*, 11 (3), pp. 249–274.
Hundey, E.J. & Ashmore, P.E. (2009). Length scale of braided river morphology. *Water Resources Research*, 45 (8), pp. 1–9.
Huthnance, J.M. (1982). On one mechanism forming linear sand banks. *Estuarine, Coastal and Shelf Science*, 14 (1), pp. 79–99.
Idier, D., Paris, F., Le Cozannet, G., Boulahya, F. & Dumas, F. (2017). Sea-level rise impacts on the tides of the European Shelf. *Continental Shelf Research*, 137, pp. 56–71. DOI:10.1016/J.CSR.2017.01.007.
Ikeda, H. (1973). A study on the formation of sand bars in a experimental flume. *Geographical Review of Japan*, 46 (7), pp. 435–451.
Ikeda, S. & Parker, G. (1989). *River Meandering*. American Geophysical Union: Washington DC, the United States.
Ikeda, S., Parker, G. & Sawai, K. (1981). Bend theory of river meanders. Part 1. Linear development. *Journal of Fluid Mechanics*, 112, pp. 363–377. DOI:10.1017/S0022112081000451.
Inglis, C.C. (1949). *The behavior and control of rivers and canals, Central Water-power Irrigation and Navigation Res.* Tech. rep. Research Publication No. 13 Central Water Power.
Israel, C.G. & Dunsbergen, D.W. (1999). Cyclic morphological development of the Ameland Inlet, the Netherlands. In: *Proceedings of Symposium on River, Coastal and Estuarine Morphodynamics (Genova, Italy)*, pp. 705–714.
Jackson, M.D., Yoshida, S., Muggeridge, A.H. & Johnson, H.D. (2005). Three-dimensional reservoir characterization and flow simulation of heterolithic tidal sandstones. *AAPG bulletin*, 89 (4), pp. 507–528. DOI:10.1306/11230404036.
Jang, C.-L. & Shimizu, Y. (2005). Numerical simulations of the behavior of alternate bars with different bank strengths. *Journal of Hydraulic Research*, 43 (6), pp. 596–612. DOI:10.1080/00221680509500380.
Jarrett, J.T. (1976). *Tidal prism-inlet area relationships*. Tech. rep. WES-GITI-3. Vicksburg, the United States: Army engineer water ways experiment station.
Jay, D.A. & Smith, J.D. (1990). Circulation, density distribution and neap-spring transitions in the Columbia River Estuary. *Progress in Oceanography*, 25 (1), pp. 81 –112. DOI:10.1016/0079-6611(90)90004-L.
Jeuken, M.-C.J.L. & Wang, Z.B. (2010). Impact of dredging and dumping on the stability of ebb–flood channel systems. *Coastal Engineering*, 57 (6), pp. 553–566.
Jeuken, M.-C.J.L., Wang, Z.B., Keiller, D., Townend, I. & Liek, G.A. (2003). Morphological response of estuaries to nodal tide variation. In: *International Conference on Estuaries and Coasts*, pp. 166–173.
Jeuken, M.-C.J.L. (2000). *On the morphologic behaviour of tidal channels in the Westerschelde estuary*. PhD dissertation. Utrecht University, Utrecht, the Netherlands.
Johnson, J. (1973). *Bolinas Lagoon Inlet*. Tech. rep. CU Report HEL. Berkeley, the United States: Hydraulic Engineering Laboratory, College of Engineering, pp. 24–15.
Kelly, S. (2006). Braided Rivers: Process, Deposits, Ecology and Management. In: International Association of Sedimentologists. Chap. Scaling and hierarchy in braided rivers and their deposits: examples and implications for reservoir modelling, p. 75. DOI:10.1002/9781444304374.CH4.
Kemp, W.M., Batleson, R., Bergstrom, P., Carter, V., Gallegos, C.L., Hunley, W., Karrh, L., Koch, E.W., Landwehr, J.M., Moore, K.A., Murray, L., Naylor, M., Rybicki, N.B., Stevenson, J.C. & Wilcox, D.J. (2004). Habitat requirements for submerged aquatic vegetation in Chesapeake Bay: Water quality, light regime, and physical-chemical factors. *Estuaries*, 27 (3), pp. 363–377. DOI:10.1007/BF02803529.
Kirby, R. (2000). Practical implications of tidal flat shape. *Continental Shelf Research*, 20 (10), pp. 1061–1077.

Kirwan, M.L. & Guntenspergen, G.R. (2010). Influence of tidal range on the stability of coastal marshland. *Journal of Geophysical Research: Earth Surface*, 115 (F2), pp. 1–11. DOI:10.1029/2009JF001400.
Kirwan, M.L. & Megonigal, J.P. (2013). Tidal wetland stability in the face of human impacts and sea-level rise. *Nature*, 504 (7478), p. 53.
Kirwan, M.L., Walters, D.C., Reay, W.G. & Carr, J.A. (2016). Sea level driven marsh expansion in a coupled model of marsh erosion and migration. *Geophysical Research Letters*, 43 (9), pp. 4366–4373. DOI:10.1002/2016GL068507.
Kleinhans, M.G., Van Rosmalen, T.M., Roosendaal, C. & van der Vegt, M. (2014). Turning the tide: Mutually evasive ebb-and flood-dominant channels and bars in an experimental estuary. *Advances in Geosciences*, 39, pp. 21–26.
Kleinhans, M.G., van der Vegt, M., Leuven, J.R.F.W., Braat, L., Markies, H., Simmelink, A., Roosendaal, C., van Eijk, A., Vrijbergen, P. & van Maarseveen, M. (2017a). Turning the tide: Comparison of tidal flow by periodic sealevel fluctuation and by periodic bed tilting in the Metronome tidal facility. *Earth Surface Dynamics*, 5 (4), pp. 731–756. DOI:10.5194/ESURF-2017-11.
Kleinhans, M.G. (2010). Sorting out river channel patterns. *Progress in Physical Geography*, 34 (3), pp. 287–326. DOI:10.1177/0309133310365300.
Kleinhans, M.G. & van den Berg, J.H. (2011). River channel and bar patterns explained and predicted by an empirical and a physics-based method. *Earth Surface Processes and Landforms*, 36 (6), pp. 721–738. DOI:10.1002/ESP.2090.
Kleinhans, M.G., Schuurman, F., Bakx, W. & Markies, H. (2009). Meandering channel dynamics in highly cohesive sediment on an intertidal mud flat in the Westerschelde estuary, the Netherlands. *Geomorphology*, 105 (3), pp. 261–276. DOI:10.1016/J.GEOMORPH.2008.10.005.
Kleinhans, M.G., Ferguson, R.I., Lane, S.N. & Hardy, R.J. (2013). Splitting rivers at their seams: bifurcations and avulsion. *Earth Surface Processes and Landforms*, 38 (1), pp. 47–61. DOI:10.1002/ESP.3268.
Kleinhans, M.G., Braudrick, C., van Dijk, W.M., van de Lageweg, W.I., Teske, R. & van Oorschot, M. (2015a). Swiftness of biomorphodynamics in Lilliput-to Giant-sized rivers and deltas. *Geomorphology*, 244, pp. 56–73.
Kleinhans, M.G., Scheltinga, R.T., Vegt, M. & Markies, H. (2015b). Turning the tide: Growth and dynamics of a tidal basin and inlet in experiments. *Journal of Geophysical Research: Earth Surface*, 120 (1), pp. 95–119.
Kleinhans, M.G., Leuven, J.R.F.W., Braat, L. & Baar, A.W. (2017b). Scour holes and ripples occur below the hydraulic smooth to rough transition of movable beds. *Sedimentology*, 64 (5), pp. 1381–1401. DOI:10.1111/SED.12358.
Kleinhans, M.G., Braat, L., Brückner, M.Z.M., Weisscher, S.A.H. & Leuven, J.R.F.W. (2018). Estuarine and river channel-bar interaction: vertical bar accretion and topographic forcing stabilise channels. In: *AGU Fall meeting abstract*. Washington DC, the United States.
Kleinjan, I.L. (1938). *Het gebied van de Westerschelde nabij Bath*. Tech. rep. R88a, 88b, 88c. Dordrecht, the Netherlands: Rijkswaterstaat.
Komarova, N.L. & Hulscher, S.J. (2000). Linear instability mechanisms for sand wave formation. *Journal of Fluid Mechanics*, 413, pp. 219–246.
Koster, K., Stafleu, J. & Cohen, K.M. (2017). Generic 3D interpolation of Holocene base-level rise and provision of accommodation space, developed for the Netherlands coastal plain and infilled palaeovalleys. *Basin Research*, 29 (6), pp. 775–797. DOI:10.1111/BRE.12202.
Kraaijenbrink, P.D.A., Shea, J.M., Pellicciotti, F., de Jong, S.M. & Immerzeel, W.W. (2016). Object-based analysis of unmanned aerial vehicle imagery to map and characterise surface features on a debris-covered glacier. *Remote Sensing of Environment*, 186, pp. 581–595. DOI:10.1016/J.RSE.2016.09.013.
Kwadijk, J.C.J., Haasnoot, M., Mulder, J.P.M., Hoogvliet, M.M.C., Jeuken, A.B.M., van der Krogt, R.A.A., van Oostrom, N.G.C., Schelfhout, H.A., van Velzen, E.H., van Waveren, H. & de Wit, M.J.M. (2010). Using adaptation tipping points to prepare for climate change and sea level rise: a case study in the Netherlands. *Wiley Interdisciplinary Reviews: Climate Change*, 1 (5), pp. 729–740. DOI:10.1002/WCC.64.
La Croix, A.D. & Dashtgard, S.E. (2015). A synthesis of depositional trends in intertidal and upper subtidal sediments across the tidal–fluvial transition in the Fraser River, Canada. *Journal of Sedimentary Research*, 85 (6), pp. 683–698. DOI:10.2110/JSR.2015.47.
Lacey, G. (1930). Stable channels in alluvium. In: *Minutes of the Proceedings of the Institution of Civil Engineers*. Vol. 229. Thomas Telford-ICE Virtual Library, pp. 259–292.
Lagasse, P.F., Zevenbergen, L.W., Spitz, W.J. & Thorne, C.R. (2004). Methodology for Predicting Channel Migration. NCHRP Web-Only Document 67 (Project 24-16). National Cooperative Highway Research Program. *Transportation Research Board, Washington, DC*.
Lane, S., Richards, K. & Chandler, J. (1993). Developments in photogrammetry; the geomorphological potential. *Progress in Physical Geography*, 17 (3), pp. 306–328.
Langbein, W. (1963). The hydraulic geometry of a shallow estuary. *Hydrological Sciences Journal*, 8 (3), pp. 84–94. DOI:10.1080/02626666309493340.
Lanzoni, S. & D'Alpaos, A. (2015). On funneling of tidal channels. *Journal of Geophysical Research: Earth Surface*, 120 (3), pp. 433–452. DOI:10.1002/2014JF003203.

Lanzoni, S. & Seminara, G. (1998). On tide propagation in convergent estuaries. *Journal of Geophysical Research*, 103 (C13), pp. 30793–30812. DOI:10.1029/1998JC900015.
Lanzoni, S. & Seminara, G. (2002). Long-term evolution and morphodynamic equilibrium of tidal channels. *Journal of Geophysical Research: Oceans*, 107 (C1), pp. 1–13. DOI:10.1029/2000JC000468.
Lanzoni, S. & Seminara, G. (2006). On the nature of meander instability. *Journal of Geophysical Research: Earth Surface*, 111 (F4), pp. 1–14. DOI:10.1029/2005JF000416.
Lentsch, N., Finotello, A. & Paola, C. (2018). Reduction of deltaic channel mobility by tidal action under rising relative sea level. *Geology*, 46 (7), pp. 599–602. DOI:10.1130/G45087.1.
Lentz, E.E., Thieler, E.R., Plant, N.G., Stippa, S.R., Horton, R.M. & Gesch, D.B. (2016). Evaluation of dynamic coastal response to sea-level rise modifies inundation likelihood. *Nature Climate Change*, 6 (7), p. 696. DOI:10.1038/NCLIMATE2957.
Leopold, L.B., Wolman, M.G. & Miller, J.P. (1964). *Fluvial processes in geomorphology*. Freeman: San Francisco, the United States.
Leopold, L.B. & Wolman, M.G. (1960). River meanders. *Geological Society of America Bulletin*, 71 (6), pp. 769–793.
Leopold, L.B. & Maddock Jr, T. (1953). *The hydraulic geometry of stream channels and some physiographic implications*. Tech. rep. Professional Paper 252. Washington DC, the United States: U.S. Geological Survey.
Leopold, L.B. & Wolman, M.G. (1957). *River channel patterns: braided, meandering, and straight*. Tech. rep. Professional Paper 282- B. Washington DC, the United States: U.S. Geological Survey.
Lesourd, S., Lesueur, P., Brun-Cottan, J.-C., Auffret, J.-P., Poupinet, N. & Laignel, B. (2001). Morphosedimentary evolution of the macrotidal Seine estuary subjected to human impact. *Estuaries and Coasts*, 24 (6), pp. 940–949.
Leuven, J.R.F.W. (2014). *Turning the tide: The effect of river discharge on estuary dynamics and equilibrium*. MSc thesis. Utrecht University, Utrecht, the Netherlands.
Levoy, F., Anthony, E.J., Dronkers, J., Monfort, O., Izabel, G. & Larsonneur, C. (2017). Influence of the 18.6-year lunar nodal tidal cycle on tidal flats: Mont-Saint-Michel Bay, France. *Marine Geology*, 387, pp. 108–113. DOI:10.1016/J.MARGEO.2017.03.009.
Lewin, J. (1976). Initiation of bed forms and meanders in coarse-grained sediment. *Geological Society of America Bulletin*, 87 (2), pp. 281–285.
Lokhorst, I., Braat, L., Leuven, J.R.F.W., Baar, A.W., van Oorschot, M., Selaković, S. & Kleinhans, M.G. (2018). Morphological effects of vegetation on the tidal-fluvial transition in Holocene estuaries. *Earth Surface Dynamics*, 6 (4), pp. 883–901. DOI:10.5194/ESURF-6-883-2018.
Longhitano, S.G. & Steel, R.J. (2017). Deflection of the progradational axis and asymmetry in tidal seaway and strait deltas: insights from two outcrop case studies. *Geological Society, London, Special Publications*, 444 (1), pp. 141–172. DOI:10.1144/SP444.8.
Lotze, H.K., Lenihan, H.S., Bourque, B.J., Bradbury, R.H., Cooke, R.G., Kay, M.C., Kidwell, S.M., Kirby, M.X., Peterson, C.H. & Jackson, J.B. (2006). Depletion, degradation, and recovery potential of estuaries and coastal seas. *Science*, 312 (5781), pp. 1806–1809. DOI:10.1126/SCIENCE.1128035.
Ludwick, J.C. (1975). Tidal currents, sediment transport, and sand banks in Chesapeake Bay entrance, Virginia. In: *Geology and Engineering*. Elsevier, pp. 365–380. DOI:10.1016/B978-0-12-197502-9.50027-7.
Manning, A.J. (2007). *Enhanced UK Estuaries database: explanatory notes and metadata*. Tech. rep. TR167. Wallingford, United Kingdom: HR Wallingford.
Mao, Q., Shi, P., Yin, K., Gan, J. & Qi, Y. (2004). Tides and tidal currents in the Pearl River Estuary. *Continental Shelf Research*, 24 (16), pp. 1797–1808. DOI:10.1016/J.CSR.2004.06.008.
Marani, M., Lanzoni, S., Zandolin, D., Seminara, G. & Rinaldo, A. (2002). Tidal meanders. *Water Resources Research*, 38 (11), pp. 1–14. DOI:10.1029/2001WR000404.
Marciano, R., Wang, Z.B., Hibma, A., de Vriend, H.J. & Defina, A. (2005). Modeling of channel patterns in short tidal basins. *Journal of Geophysical Research: Earth Surface*, 110 (F1), pp. 1–13. DOI:10.1029/2003JF000092.
Martinius, A.W. & van den Berg, J.H. (2011). *Atlas of sedimentary structures in estuarine and tidally-influenced river deposits of the Rhine-Meuse-Scheldt system*. EAGE: Houten, the Netherlands.
Mayor-Mora, R.E. (1977). *Laboratory investigation of tidal inlets on sandy coasts.* Tech. rep. GITI report; 11. Springfield, the United States: U.S. Army, Corps of Engineers.
Mckee, K.L. & Patrick, W. (1988). The relationship of smooth cordgrass (Spartina alterniflora) to tidal datums: a review. *Estuaries*, 11 (3), pp. 143–151.
Meersschaut, Y.M.A., Parker, W.R., Peters, J.J. & Plancke, Y.M.G. (2004). A dredging and disposal strategy for managing the Western Scheldt's morphology and ecology. In: *WODCON Conference*. Hamburg, Germany.
Meininger, P.L., Witte, R.H. & Graveland, J. (2003). *Zeezoogdieren in de Westerschelde: knelpunten en kansen*. Tech. rep. RIKZ/2003.041. Middelburg, the Netherlands: Rijkswaterstaat.
Meyer-Peter, E. & Müller, R (1948). Formulas for bed-load transport. In: *Proceedings of 2nd Meeting: 297 International Association for Hydraulic Structures Research*. IAHR. Stockhold, Sweden, pp. 39–64.

Milliman, J.D. & Syvitski, J.P. (1992). Geomorphic/tectonic control of sediment discharge to the ocean: the importance of small mountainous rivers. *The Journal of Geology*, 100 (5), pp. 525–544. DOI:10.1086/629606.
Misdorp, R., Steyaert, F., Hallie, F. & de Ronde, J. (1990). Climate change, sea level rise and morphological developments in the Dutch Wadden Sea, a marine wetland. In: *Expected effects of climatic change on marine coastal ecosystems*. Springer: Dordrecht, the Netherlands, pp. 123–131.
Monge-Ganuzas, M., Cearreta, A. & Evans, G. (2013). Morphodynamic consequences of dredging and dumping activities along the lower Oka estuary (Urdaibai Biosphere Reserve, southeastern Bay of Biscay, Spain). *Ocean & Coastal Management*, 77, pp. 40–49.
Moore, R.D., Wolf, J., Souza, A.J. & Flint, S.S. (2009). Morphological evolution of the Dee Estuary, Eastern Irish Sea, UK: a tidal asymmetry approach. *Geomorphology*, 103 (4), pp. 588–596.
Morgan, J.A., Brogan, D.J. & Nelson, P.A. (2017). Application of Structure-from-Motion photogrammetry in laboratory flumes. *Geomorphology*, 276, pp. 125–143. DOI:10.1016/J.GEOMORPH.2016.10.021.
Mori, N. & Chang, K.-A. (2003). Experimental study of a horizontal jet in a wavy environment. *Journal of Engineering Mechanics*, 129 (10), pp. 1149–1155.
Mossop, G.D. & Flach, P.D. (1983). Deep channel sedimentation in the Lower Cretaceous McMurray Formation, athabasca oil sands, Alberta. *Sedimentology*, 30 (4), pp. 493–509.
Nguyen, A.D. & Savenije, H.H.G. (2006). Salt intrusion in multi-channel estuaries: a case study in the Mekong Delta, Vietnam. *Hydrology and Earth System Sciences Discussions*, 10 (5), pp. 743–754. DOI:10.5194/HESS-10-743-2006.
Nicholls, R.J. & Cazenave, A. (2010). Sea-level rise and its impact on coastal zones. *Science*, 328 (5985), pp. 1517–1520.
Nnafie, A, van Oyen, T, de Maerschalck, B, van der Vegt, M & van der Wegen, M (2018). Estuarine channel evolution in response to closure of secondary basins: An observational and morphodynamic modeling study of the Western Scheldt Estuary. *Journal of Geophysical Research: Earth Surface*, 123 (1), pp. 167–186. DOI:10.1002/2017JF004364.
Nowacki, D.J., Ogston, A.S., Nittrouer, C.A., Fricke, A.T. & Van, P.D.T. (2015). Sediment dynamics in the lower Mekong River: Transition from tidal river to estuary. *Journal of Geophysical Research: Oceans*, 120 (9), pp. 6363–6383. DOI:10.1002/2015JC010754.
O'Brien, M.P. (1931). Estuary tidal prisms related to entrance areas. *Civil Engineering*, 1 (8), pp. 738–739.
O'Brien, M.P. (1969). Equilibrium flow areas of inlets on sandy coasts. *Journal of the Waterways and Harbors Division*, 95 (1), pp. 43–52. DOI:10.1061/9780872620087.039.
O'Connor, B. (1987). Short and long term changes in estuary capacity. *Journal of the Geological Society*, 144 (1), pp. 187–195.
Off, T. (1963). Rhythmic linear sand bodies caused by tidal currents. *AAPG bulletin*, 47 (2), pp. 324–341.
Olabarrieta, M., Geyer, W.R., Coco, G., Friedrichs, C.T. & Cao, Z. (2018). Effects of Density-Driven Flows on the Long-Term Morphodynamic Evolution of Funnel-Shaped Estuaries. *Journal of Geophysical Research: Earth Surface*, 123 (11), pp. 2901–2924. DOI:10.1029/2017JF004527.
Oost, A.P. (1995). *Dynamics and sedimentary developments of the Dutch Wadden Sea with a special emphasis on the Frisian Inlet: a study of the barrier islands, ebb-tidal deltas, inlets and drainage basins*. PhD dissertation. Utrecht University, Utrecht, the Netherlands.
Paola, C. & Borgman, L. (1991). Reconstructing random topography from preserved stratification. *Sedimentology*, 38 (4), pp. 553–565. DOI:10.1111/J.1365-3091.1991.TB01008.X.
Parker, G. (1976). On the cause and characteristic scales of meandering and braiding in rivers. *Journal of Fluid Mechanics*, 76 (3), pp. 457–480. DOI:10.1017/S0022112076000748.
Parker, G. & Johannesson, H. (1989). Observations on several recent theories of resonance and overdeepening in meandering channels. *River Meandering*, 12, pp. 379–415. DOI:10.1029/WM012P0379.
Parker, G., Shimizu, Y, Wilkerson, G., Eke, E.C., Abad, J.D., Lauer, J., Paola, C., Dietrich, W.E. & Voller, V. (2011). A new framework for modeling the migration of meandering rivers. *Earth Surface Processes and Landforms*, 36 (1), pp. 70–86. DOI:10.1002/ESP.2113.
Pavelsky, T.M. & Smith, L.C. (2008). RivWidth: A software tool for the calculation of river widths from remotely sensed imagery. *IEEE Geoscience and Remote Sensing Letters*, 5 (1), pp. 70–73. DOI:10.1109/LGRS.2007.908305.
Pearson, N.J. & Gingras, M.K. (2006). An ichnological and sedimentological facies model for muddy point-bar deposits. *Journal of Sedimentary Research*, 76 (5), pp. 771–782. DOI:10.2110/JSR.2006.070.
Perillo, G.M. (1995). *Geomorphology and sedimentology of estuaries*. Vol. 53. Elsevier: Amsterdam, the Netherlands.
Pickering, M., Horsburgh, K., Blundell, J., Hirschi, J.-M., Nicholls, R.J., Verlaan, M & Wells, N. (2017). The impact of future sea-level rise on the global tides. *Continental Shelf Research*, 142, pp. 50–68. DOI:10.1016/J.CSR.2017.02.004.
Pierik, H.J., Cohen, K.M. & Stouthamer, E. (2016). A new GIS approach for reconstructing and mapping dynamic late Holocene coastal plain palaeogeography. *Geomorphology*, 270, pp. 55–70. DOI:10.1016/J.GEOMORPH.2016.05.037.

Pierik, H.J., Cohen, K.M., Vos, P.C., van der Spek, A.J.F. & Stouthamer, E. (2017). Late Holocene coastal-plain evolution of the Netherlands: the role of natural preconditions in human-induced sea ingressions. *Proceedings of the Geologists' Association*, 128 (2), pp. 180–197.

Pierik, H.J., Leuven, J.R.F.W., Busschers, F.S., Hijma, M.P. & Kleinhans, M.G. (2019). Depth-limiting resistant layers tune the shape and tidal bar pattern of Holocene alluvial estuaries. *[submitted]*.

Pillsbury, G. (1956). Tidal Hydraulics. Revised Edition, Corps of Engineers. *US Army, May*.

Plancke, Y. & Vos, G.R. (2016). Sediment transport in the Schelde-estuary: a comparison between measurements, transport formula and numerical models. In: *Proceedings of the 4th IAHR Europe Congress 2016: Sustainable Hydraulics in the Era of Global Change*. Liege, Belgium, pp. 498–503.

Powell, M.A., Thieke, R.J. & Mehta, A.J. (2006). Morphodynamic relationships for ebb and flood delta volumes at Florida's tidal entrances. *Ocean Dynamics*, 56 (3-4), pp. 295–307.

Pritchard, D.W. (1967). What is an estuary: physical viewpoint. In: *Estuaries*. Ed. by G.H. Lauff. 83. American Association for the Advancement of Science, pp. 3–5.

Ranasinghe, R., Swinkels, C., Luijendijk, A., Roelvink, D., Bosboom, J., Stive, M. & Walstra, D.J. (2011). Morphodynamic upscaling with the MORFAC approach: Dependencies and sensitivities. *Coastal Engineering*, 58 (8), pp. 806–811. DOI:10.1016/J.COASTALENG.2011.03.010.

Repetto, R. & Tubino, M. (2001). Topographic expressions of bars in channels with variable width. *Physics and Chemistry of the Earth, Part B: Hydrology, Oceans and Atmosphere*, 26 (1), pp. 71–76.

Repetto, R., Tubino, M. & Paola, C. (2002). Planimetric instability of channels with variable width. *Journal of Fluid Mechanics*, 457, pp. 79–109. DOI:10.1017/S0022112001007595.

Reynolds, O. (1887). *On Certain Laws Relating to the Regime of Rivers and on the Possibüity of Experiments at Small Scale*. Tech. rep. London, United Kingdom: Britisch Association.

Reynolds, O. (1889). *On model estuaries in Report of the committee appointed to investigate the action of waves and currents on the beds and fore shores of estuaries by means of working models*. Tech. rep. London, United Kingdom: Britisch Association, pp. 327–343.

Rice, S.P., Church, M., Wooldridge, C.L. & Hickin, E.J. (2009). Morphology and evolution of bars in a wandering gravel-bed river; lower Fraser river, British Columbia, Canada. *Sedimentology*, 56 (3), pp. 709–736.

Rijke, J., van Herk, S., Zevenbergen, C. & Ashley, R. (2012). Room for the River: delivering integrated river basin management in the Netherlands. *International Journal of River Basin Management*, 10 (4), pp. 369–382. DOI:10.1080/15715124.2012.739173.

Robinson, A. (1960). Ebb-flood channel systems in sandy bays and estuaries. *Geography*, 45 (3), pp. 183–199.

Roelvink, J. (2006). Coastal morphodynamic evolution techniques. *Coastal Engineering*, 53 (2-3), pp. 277–287. DOI:10.1016/J.COASTALENG.2005.10.015.

Ruessink, B.G., Michallet, H., Abreu, T., Sancho, F., van der A, D.A., van der Werf, J.J. & Silva, P.A. (2011). Observations of velocities, sand concentrations, and fluxes under velocity-asymmetric oscillatory flows. *Journal of Geophysical Research: Oceans*, 116 (C3), pp. 1–13. DOI:10.1029/2010JC006443.

Ruessink, B.G., Ramaekers, G. & van Rijn, L.C. (2012). On the parameterization of the free-stream non-linear wave orbital motion in nearshore morphodynamic models. *Coastal Engineering*, 65, pp. 56–63. DOI:10.1016/J.COASTALENG.2012.03.006.

Saha, S., Burley, S.D., Banerjee, S., Ghosh, A. & Saraswati, P.K. (2016). The morphology and evolution of tidal sand bodies in the macrotidal Gulf of Khambhat, western India. *Marine and Petroleum Geology*, 77, pp. 714–730. DOI:10.1016/J.MARPETGEO.2016.03.028.

Saito, Y., Yang, Z. & Hori, K. (2001). The Huanghe (Yellow River) and Changjiang (Yangtze River) deltas: a review on their characteristics, evolution and sediment discharge during the Holocene. *Geomorphology*, 41 (2-3), pp. 219–231. DOI:10.1016/S0169-555X(01)00118-0.

Sambrook Smith, G.H., Ashworth, P.J., Best, J.L., Woodward, J. & Simpson, C.J. (2006). The sedimentology and alluvial architecture of the sandy braided South Saskatchewan River, Canada. *Sedimentology*, 53 (2), pp. 413–434.

Sassi, M.G., Hoitink, A.J.F., Brye, B. & Deleersnijder, E. (2012). Downstream hydraulic geometry of a tidally influenced river delta. *Journal of Geophysical Research: Earth Surface*, 117 (F4), pp. 1–13.

Savenije, H.H.G. (1993). Predictive model for salt intrusion in estuaries. *Journal of Hydrology*, 148 (1), pp. 203–218. DOI:10.1016/0022-1694(93)90260-G.

Savenije, H.H.G. (2003). The width of a bankfull channel; Lacey's formula explained. *Journal of Hydrology*, 276 (1), pp. 176–183.

Savenije, H.H.G. (2006). *Salinity and tides in alluvial estuaries*. Elsevier: New York, the United States.

Savenije, H.H.G. (2015). Prediction in ungauged estuaries: an integrated theory. *Water Resources Research*, 51 (4), pp. 2464–2476. DOI:10.1002/2015WR016936.

Schielen, R., Doelman, A. & de Swart, H.E. (1993). On the nonlinear dynamics of free bars in straight channels. *Journal of Fluid Mechanics*, 252, pp. 325–356.

Schramkowski, G.P., Schuttelaars, H.M. & de Swart, H.E. (2002). The effect of geometry and bottom friction on local bed forms in a tidal embayment. *Continental Shelf Research*, 22 (11), pp. 1821–1833. DOI:10.1016/S0278-4343(02)00040-7.

Schramkowski, G.P., Schuttelaars, H.M. & de Swart, H.E. (2004). Non-linear channel–shoal dynamics in long tidal embayments. *Ocean Dynamics*, 54 (3-4), pp. 399–407. DOI:10.1007/s10236-003-0063-6.

Schuerch, M., Spencer, T., Temmerman, S., Kirwan, M.L., Wolff, C., Lincke, D., McOwen, C.J., Pickering, M.D., Reef, R. & Vafeidis, A.T. (2018). Future response of global coastal wetlands to sea-level rise. *Nature*, 561 (7722), p. 231. DOI:10.1038/s41586-018-0476-5.

Schuttelaars, H. & de Swart, H. (2000). Multiple morphodynamic equilibria in tidal embayments. *Journal of Geophysical Research: Oceans*, 105 (C10), pp. 24105–24118. DOI:10.1029/2000JC900110.

Schuurman, F., Shimizu, Y., Iwasaki, T. & Kleinhans, M.G. (2016). Dynamic meandering in response to upstream perturbations and floodplain formation. *Geomorphology*, 253, pp. 94–109. DOI:10.1016/J.GEOMORPH.2015.05.039.

Schuurman, F. & Kleinhans, M.G. (2015). Bar dynamics and bifurcation evolution in a modelled braided sand-bed river. *Earth Surface Processes and Landforms*, 40 (10), pp. 1318–1333.

Schuurman, F., Marra, W.A. & Kleinhans, M.G. (2013). Physics-based modeling of large braided sand-bed rivers: Bar pattern formation, dynamics, and sensitivity. *Journal of Geophysical Research: Earth Surface*, 118 (4), pp. 2509–2527.

Schuurman, F., Ta, W., Post, S., Sokolewicz, M., Busnelli, M. & Kleinhans, M.G. (2018). Response of braiding channel morphodynamics to peak discharge changes in the Upper Yellow River. *Earth Surface Processes and Landforms*, 43 (8), pp. 1648–1662. DOI:10.1002/ESP.4344.

Schwenk, J., Lanzoni, S. & Foufoula-Georgiou, E. (2015). The life of a meander bend: Connecting shape and dynamics via analysis of a numerical model. *Journal of Geophysical Research: Earth Surface*, 120 (4), pp. 690–710.

Seminara, G. (2010). Fluvial sedimentary patterns. *Annual Review of Fluid Mechanics*, 42, pp. 43–66. DOI:10.1146/ANNUREV-FLUID-121108-145612.

Seminara, G. & Tubino, M. (1989). River meandering. In: *River meandering*. Ed. by S. Ikeda & G. Parker. Vol. 12. American Geophysical Union: Washington DC, the United States. Chap. Alternate bars and meandering: free forced and mixed interactions, pp. 267–320.

Seminara, G. & Tubino, M. (2001). Sand bars in tidal channels. Part 1. Free bars. *Journal of Fluid Mechanics*, 440, pp. 49–74. DOI:10.1017/S0022112001004748.

Seminara, G., Lanzoni, S., Bolla Pittaluga, M. & Solari, L. (2001). Estuarine patterns: an introduction to their morphology and mechanics. In: *Geomorphological Fluid Mechanics*. Springer: Berlin, Germany, pp. 455–499.

Seminara, G. (2006). Meanders. *Journal of fluid mechanics*, 554, pp. 271–297. DOI:10.1017/S0022112006008925.

Shigemura, T. (1980). Tidal prism–throat area relationships of the bays of Japan. *Shore and Beach*, 48 (3), pp. 30–35.

Silvestri, S., D'Alpaos, A., Nordio, G. & Carniello, L. (2018). Anthropogenic Modifications Can Significantly Influence the Local Mean Sea Level and Affect the Survival of Salt Marshes in Shallow Tidal Systems. *Journal of Geophysical Research: Earth Surface*, 123 (5), pp. 996–1012. DOI:10.1029/2017JF004503.

Sistermans, P. & Nieuwenhuis, O. (2004). *Western Scheldt Estuary (The Netherlands)*. Tech. rep. Amersfoort, the Netherlands: DHV group.

Solari, L., Seminara, G., Lanzoni, S., Marani, M. & Rinaldo, A. (2002). Sand bars in tidal channels Part 2. Tidal meanders. *Journal of Fluid Mechanics*, 451, pp. 203–238.

Steel, R.J., Plink-Bjorklund, P. & Aschoff, J. (2012). Tidal deposits of the Campanian Western Interior Seaway, Wyoming, Utah and Colorado, USA. In: *Principles of tidal sedimentology*. Springer: Dordrecht, the Netherlands, pp. 437–471. DOI:10.1007/978-94-007-0123-6_17.

Stefanon, L., Carniello, L., D'Alpaos, A. & Lanzoni, S. (2010). Experimental analysis of tidal network growth and development. *Continental Shelf Research*, 30 (8), pp. 950–962.

Steijn, R.C., Cleveringa, J., van der Baan, J., Huizer, T. & Leuven, J.R.F.W. (2019). *Dealing with coastal erosion in the Gulf of Mottama*. Tech. rep. C03141.000064R1r1. Zwolle, the Netherlands: Arcadis Nederland B.V.

Stevens, A., Gelfenbaum, G., MacMahan, J., Reniers, A., Elias, E., Sherwood, C. & Carlson, E. (2017). *Oceanographic measurements and hydrodynamic modeling of the mouth of the Columbia River, Oregon and Washington, 2013*. Tech. rep. U.S. Geological Survey. DOI:10.5066/F7NG4NS1.

Storms, J.E., Dam, R.L.V. & Leclair, S.F. (1999). Preservation of cross-sets due to migration of current ripples over aggrading and non-aggrading beds: comparison of experimental data with theory. *Sedimentology*, 46 (1), pp. 189–200.

Strahler, A.N. (1952). Hypsometric (area-altitude) analysis of erosional topography. *Geological Society of America Bulletin*, 63 (11), pp. 1117–1142. DOI:10.1130/0016-7606(1952)63[1117:HAAOET]2.0.CO;2.

Straub, K.M., Paola, C., Mohrig, D., Wolinsky, M.A. & George, T. (2009). Compensational stacking of channelized sedimentary deposits. *Journal of Sedimentary Research*, 79 (9), pp. 673–688.

Struiksma, N., Olesen, K.W., Flokstra, C. & de Vriend, H.J. (1985). Bed deformation in curved alluvial channels. *Journal of Hydraulic Research*, 23 (1), pp. 57–79.
Swift, D.J. & Field, M.E. (1981). Evolution of a classic sand ridge field: Maryland sector, North American inner shelf. *Sedimentology*, 28 (4), pp. 461–482.
Swinkels, C.M., Jeuken, C.M., Wang, Z.B. & Nicholls, R.J. (2009). Presence of connecting channels in the Western Scheldt Estuary. *Journal of Coastal Research*, 25 (3), pp. 627–640. DOI:10.2112/06-0719.1.
Ta, T.K.O., Nguyen, V.L., Tateishi, M., Kobayashi, I., Tanabe, S. & Saito, Y. (2002). Holocene delta evolution and sediment discharge of the Mekong River, southern Vietnam. *Quaternary Science Reviews*, 21 (16-17), pp. 1807–1819. DOI:10.1016/S0277-3791(02)00007-0.
Tambroni, N., Bolla Pittaluga, M. & Seminara, G. (2005). Laboratory observations of the morphodynamic evolution of tidal channels and tidal inlets. *Journal of Geophysical Research: Earth Surface*, 110 (F4), pp. 1–23. DOI:10.1029/2004JF000243.
Tambroni, N., Luchi, R. & Seminara, G. (2017). Can tide dominance be inferred from the point bar pattern of tidal meandering channels? *Journal of Geophysical Research: Earth Surface*, 122 (2), pp. 492–512. DOI:10.1002/2016JF004139.
Tanabe, S., Nakanishi, T., Ishihara, Y. & Nakashima, R. (2015). Millennial-scale stratigraphy of a tide-dominated incised valley during the last 14 kyr: Spatial and quantitative reconstruction in the Tokyo Lowland, central Japan. *Sedimentology*, 62 (7), pp. 1837–1872. DOI:10.1111/SED.12204.
Tank, F. (1996). *Het gedrag van drempels in de Westerschelde: Literatuurstudie en hypothesen*. IMAU Rapport 96-07. Utrecht, the Netherlands: Universiteit Utrecht.
Temmerman, S. & Kirwan, M.L. (2015). Building land with a rising sea. *Science*, 349 (6248), pp. 588–589. DOI:10.1126/SCIENCE.AAC8312.
Thomson, A.G., Huiskes, A, Cox, R., Wadsworth, R.A. & Boorman, L.A. (2004). Short-term vegetation succession and erosion identified by airborne remote sensing of Westerschelde salt marshes, The Netherlands. *International Journal of Remote Sensing*, 25 (20), pp. 4151–4176. DOI:10.1080/01431160310001647688.
Toffolon, M. & Crosato, A. (2007). Developing macroscale indicators for estuarine morphology: The case of the Scheldt Estuary. *Journal of Coastal Research*, 23 (1), pp. 195–212.
Toffolon, M. & Lanzoni, S. (2010). Morphological equilibrium of short channels dissecting the tidal flats of coastal lagoons. *Journal of Geophysical Research: Earth Surface*, 115 (F4), pp. 1–15. DOI:10.1029/2010JF001673.
Townend, I. (2005). An examination of empirical stability relationships for UK estuaries. *Journal of Coastal Research*, 21 (5), pp. 1042–1053. DOI:10.2112/03-0066R.1.
Townend, I. (2010). An exploration of equilibrium in Venice Lagoon using an idealised form model. *Continental Shelf Research*, 30 (8), pp. 984–999.
Townend, I. (2012). The estimation of estuary dimensions using a simplified form model and the exogenous controls. *Earth Surface Processes and Landforms*, 37 (15), pp. 1573–1583. DOI:10.1002/ESP.3256.
Townend, I., Wright, A. & Price, D. (2000). *An investigation of the gross properties of UK estuaries*. Tech. rep. Southampton, United Kingdom: ABP Research & Consultancy Ltd, p. 73.
Townend, I.H. (2008). Hypsometry of estuaries, creeks and breached sea wall sites. *Proceedings of the Institution of Civil Engineers-Maritime Engineering*, 161 (1), pp. 23–32. DOI:10.1680/MAEN.2008.161.1.23.
Tubino, M., Repetto, R. & Zolezzi, G. (1999). Free bars in rivers. *Journal of Hydraulic Research*, 37 (6), pp. 759–775.
Turner, R.K., Burgess, D., Hadley, D., Coombes, E. & Jackson, N. (2007). A cost–benefit appraisal of coastal managed realignment policy. *Global Environmental Change*, 17 (3-4), pp. 397–407. DOI:10.1016/J.GLOENVCHA.2007.05.006.
Van Braeckel, A., Vandevoorde, B. & van den Bergh, E. (2008). *Schorecotopen van de Schelde. Aanzet tot de ontwikkeling van één schorecotopenstelsel voor Vlaanderen en Nederland*. Tech. rep. Brussel: Instituut voor Natuur- en Bosonderzoek.
Van Dijk, W.M., van de Lageweg, W.I. & Kleinhans, M.G. (2012). Experimental meandering river with chute cutoffs. *Journal of Geophysical Research: Earth Surface*, 117 (F3). F03023, pp. 1–18. DOI:10.1029/2011JF002314.
Van Dijk, W.M., Teske, R., van de Lageweg, W.I. & Kleinhans, M.G. (2013a). Effects of vegetation distribution on experimental river channel dynamics. *Water Resources Research*, 49 (11), pp. 7558–7574. DOI:10.1002/2013WR013574.
Van Dijk, W.M., Leuven, J.R.F.W., Cox, J., Cleveringa, J., Taal, M., Hiatt, M.R., Sonke, W., Verbeek, K., Speckmann, B. & Kleinhans, M.G. (2019). The effect of current dredging and disposal activity on morphodynamics of estuaries. *Submitted*.
Van Dijk, W.M., van der Lageweg, W.I. & Kleinhans, M.G. (2013b). Formation of a cohesive floodplain in a dynamic experimental meandering river. *Earth Surface Processes and Landforms*, 38 (13), pp. 1550–1565.
Van Dijk, W.M., Schuurman, F., van de Lageweg, W.I. & Kleinhans, M.G. (2014). Bifurcation instability and chute cutoff development in meandering gravel-bed rivers. *Geomorphology*, 213, pp. 277–291. DOI:10.1016/J.GEOMORPH.2014.01.018.

Van Eck, G.T.M. & Holzhauer, H. (2007). *Monitoring van de effecten van de verruiming 48'/43': MOVE eindrapport 2006 (Rapport 10)*. Tech. rep. RIKZ/2007.003. Middelburg, the Netherlands: Rijkswaterstaat.
Van Maanen, B., Coco, G. & Bryan, K.R. (2011). A numerical model to simulate the formation and subsequent evolution of tidal channel networks. *Australian Journal of Civil Engineering*, 9 (1), pp. 61–72. DOI:10.1080/14488353.2011.11463969.
Van Maanen, B., Coco, G. & Bryan, K.R. (2013). Modelling the effects of tidal range and initial bathymetry on the morphological evolution of tidal embayments. *Geomorphology*, 191, pp. 23–34. DOI:10.1016/J.GEOMORPH.2013.02.023.
Van Maren, D.S., van Kessel, T., Cronin, K. & Sittoni, L. (2015). The impact of channel deepening and dredging on estuarine sediment concentration. *Continental Shelf Research*, 95, pp. 1–14. DOI:10.1016/J.CSR.2014.12.010.
Van Onselen, E.P. (2017). *Scale effects on waves and sediment mobility in the Metronome tidal facility*. MSc thesis. Utrecht University, Utrecht, the Netherlands.
Van Oorschot, M., Kleinhans, M.G., Geerling, G. & Middelkoop, H. (2016). Distinct patterns of interaction between vegetation and morphodynamics. *Earth Surface Processes and Landforms*, 41 (6), pp. 791–808. DOI:10.1002/ESP.3864.
Van Oorschot, M., Kleinhans, M.G., Buijse, T., Geerling, G. & Middelkoop, H. (2018). Combined effects of climate change and dam construction on riverine ecosystems. *Ecological Engineering*, 120, pp. 329–344. DOI:10.1016/J.ECOLENG.2018.05.037.
Van Rijn, L.C. (1984). Sediment transport, part II: suspended load transport. *Journal of Hydraulic Engineering*, 110 (11), pp. 1613–1641.
Van Rijn, L.C. (1993). *Principles of Sediment Transport in Rivers, Estuaries and Coastal Seas*. Aqua Publications: Amsterdam, the Netherlands.
Van Veen, J. (1944). *Schelderegiem en Schelderegie*. Tech. rep. Reprint 1993. Middelburg, the Netherlands: Rijkswaterstaat.
Van Veen, J. (1950). Eb- en vloedschaarsystemen in de Nederlandse getijwateren. *Tijdschrift Koninklijk Nederlands Aardrijkskundig Genootschap*, 67, pp. 303–325.
Van de Kreeke, J. & Haring, J. (1980). Equilibrium flow areas in the Rhine⊠Meuse delta. *Coastal Engineering*, 3, pp. 97–111.
Van de Lageweg, W.I. & Feldman, H. (2018). Process-based modelling of morphodynamics and bar architecture in confined basins with fluvial and tidal currents. *Marine Geology*, 398, pp. 35–47. DOI:10.1016/J.MARGEO.2018.01.002.
Van de Lageweg, W.I., van Dijk, W.M., Baar, A.W., Rutten, J. & Kleinhans, M.G. (2014). Bank pull or bar push: What drives scroll-bar formation in meandering rivers? *Geology*, 42 (4), pp. 319–322. DOI:10.1130/G35192.1.
Van de Lageweg, W.I., Schuurman, F., Cohen, K.M., Dijk, W.M., Shimizu, Y. & Kleinhans, M.G. (2015). Preservation of meandering river channels in uniformly aggrading channel belts. *Sedimentology*, 63 (3), pp. 586–608. DOI:10.1111/SED.12229.
Van de Lageweg, W.I., Dijk, W.M., Box, D. & Kleinhans, M.G. (2016). Archimetrics: a quantitative tool to predict three-dimensional meander belt sandbody heterogeneity. *The Depositional Record*, 2 (1), pp. 22–46.
Van de Lageweg, W.I., Braat, L., Parsons, D.R. & Kleinhans, M.G. (2018). Controls on mud distribution and architecture along the fluvial-to-marine transition. *Geology*, 46 (11), pp. 971–974. DOI:10.1130/G45504.1.
Van den Berg, J.H., Jeuken, C.J. & Van der Spek, A.J. (1996). Hydraulic processes affecting the morphology and evolution of the Westerschelde estuary. In: *Estuarine Shores: Evolution, Environments and Human Alterations*. Ed. by K.F. Nordstrom & C.T. Roman. John Wiley & Sons Ltd: Chichester, England, pp. 157–184.
Van der Spek, A.J.F. & Beets, D.J. (1992). Mid-Holocene evolution of a tidal basin in the western Netherlands: a model for future changes in the northern Netherlands under conditions of accelerated sea-level rise? *Sedimentary Geology*, 80 (3), pp. 185–197.
Van der Wal, D., Wielemaker-van den Dool, A. & Herman, P.M. (2008). Spatial patterns, rates and mechanisms of saltmarsh cycles (Westerschelde, The Netherlands). *Estuarine, Coastal and Shelf Science*, 76 (2), pp. 357–368. DOI:10.1016/J.ECSS.2007.07.017.
Van der Wegen, M. & Roelvink, J.A. (2008). Long-term morphodynamic evolution of a tidal embayment using a two-dimensional, process-based model. *Journal of Geophysical Research: Oceans*, 113 (C3), pp. 1–23. DOI:10.1029/2006JC003983.
Van der Wegen, M. & Roelvink, J.A. (2012). Reproduction of estuarine bathymetry by means of a process-based model: Western Scheldt case study, the Netherlands. *Geomorphology*, 179, pp. 152–167. DOI:10.1016/J.GEOMORPH.2012.08.007.
Van der Wegen, M. (2013). Numerical modeling of the impact of sea level rise on tidal basin morphodynamics. *Journal of Geophysical Research: Earth Surface*, 118 (2), pp. 447–460.

Verbeek, H, Wang, Z. & Thoolen, P. (1999). Secondary currents in estuarine morphodynamic modelling, a case-study of the Western Scheldt. In: *River, Coastal and Estuarine Morphodynamics*. Springer-Verlag New York: Berlin, Germany, pp. 649–659.
Verbeek, H., van der Male, K. & Jansen, M. (2000). *Het SCALWEST-model*. Tech. rep. RIKZ/OS/2000.814. Middelburg, the Netherlands: Rijkswaterstaat.
Vikolainen, V., Bressers, H. & Lulofs, K. (2014). A shift toward building with nature in the dredging and port development industries: managerial implications for projects in or near natura 2000 areas. *Environmental management*, 54 (1), pp. 3–13. DOI:10.1007/s00267-014-0285-z.
Vinagre, C., Fonseca, V., Cabral, H. & Costa, M.J. (2006). Habitat suitability index models for the juvenile soles, Solea solea and Solea senegalensis, in the Tagus estuary: defining variables for species management. *Fisheries research*, 82 (1-3), pp. 140–149. DOI:10.1016/j.fishres.2006.07.011.
Visconti, F., Camporeale, C. & Ridolfi, L. (2010). Role of discharge variability on pseudomeandering channel morphodynamics: Results from laboratory experiments. *Journal of Geophysical Research: Earth Surface*, 115 (F4).
Vlaswinkel, B.M. & Cantelli, A. (2011). Geometric characteristics and evolution of a tidal channel network in experimental setting. *Earth Surface Processes and Landforms*, 36 (6), pp. 739–752.
Vos, P.C., de Koning, J. & van Eerden, R. (2015). Landscape history of the Oer-IJ tidal system, Noord-Holland (the Netherlands). *Netherlands Journal of Geosciences*, 94 (04), pp. 295–332. DOI:10.1017/njg.2015.27.
Vos, P.C. (2015). *Origin of the Dutch coastal landscape: long-term landscape evolution of the Netherlands during the Holocene, described and visualized in national, regional and local palaeogeographical map series*. PhD dissertation. Utrecht University, Utrecht, the Netherlands.
Vroom, J., de Vet, P.L.M. & van der Werf, J.J. (2015). *Validatie waterbeweging Delft3D-NeVla model Westerscheldemonding*. Tech. rep. 1210301-001-ZKS-0001. Delft, the Netherlands: Deltares.
Walling, D.E. & Fang, D. (2003). Recent trends in the suspended sediment loads of the world's rivers. *Global and Planetary Change*, 39 (1-2), pp. 111–126. DOI:10.1016/S0921-8181(03)00020-1.
Wang, Y., Straub, K.M. & Hajek, E.A. (2011). Scale-dependent compensational stacking: an estimate of autogenic time scales in channelized sedimentary deposits. *Geology*, 39 (9), pp. 811–814. DOI:10.1130/G32068.1.
Wang, Z.B. & Winterwerp, J.C. (2001). Impact of dredging and dumping on the stability of ebb-flood channel systems. In: *Proceedings of the 2nd IAHR symposium on River, Coastal and Estuarine Morphodynamics*, pp. 515–524.
Wang, Z.B., Jeuken, M.-C.J.L. & de Vriend, H.J. (1999). Tidal asymmetry and residual sediment transport in estuaries. *Delft Hydraulics*, (Z2749), Delft, the Netherlands.
Wang, Z.B., Jeuken, M.-C.J.L., Gerritsen, H., de Vriend, H.J. & Kornman, B.A. (2002). Morphology and asymmetry of the vertical tide in the Westerschelde estuary. *Continental Shelf Research*, 22 (17), pp. 2599–2609.
Wang, Z.B., Hoekstra, P., Burchard, H., Ridderinkhof, H., de Swart, H.E. & Stive, M.J.F. (2012). Morphodynamics of the Wadden Sea and its barrier island system. *Ocean & Coastal Management*, 68, pp. 39–57. DOI:10.1016/j.ocecoaman.2011.12.022.
Wang, Z.B., van Maren, D.S., Ding, P.X., Yang, S.L., van Prooijen, B.C., de Vet, P.L.M., Winterwerp, J.C., de Vriend, H.J., Stive, M.J.F. & He, Q. (2015). Human impacts on morphodynamic thresholds in estuarine systems. *Continental Shelf Research*, 111, pp. 174–183. DOI:10.1016/j.csr.2015.08.009.
Wang, Z.B., Elias, E.P., van der Spek, A.J. & Lodder, Q.J. (2018). Sediment budget and morphological development of the Dutch Wadden Sea: impact of accelerated sea-level rise and subsidence until 2100. *Netherlands Journal of Geosciences*, 97 (3), pp. 183–214. DOI:10.1017/njg.2018.8.
Wells, J.T. (1995). Tide-dominated estuaries and tidal rivers. In: *Developments in Sedimentology*. Vol. 53. Elsevier: Amsterdam, the Netherlands, pp. 179–205. DOI:10.1016/S0070-4571(05)80026-3.
Westoby, M.J., Brasington, J., Glasser, N.F., Hambrey, M.J. & Reynolds, J.M. (2012). 'Structure-from-Motion' photogrammetry: A low-cost, effective tool for geoscience applications. *Geomorphology*, 179, pp. 300–314. DOI:10.1016/j.geomorph.2012.08.021.
Whiting, P.J. & Dietrich, W.E. (1993). Experimental constraints on bar migration through bends: Implications for meander wavelength selection. *Water Resources Research*, 29 (4), pp. 1091–1102. DOI:10.1029/92WR02356.
Williams, G.P. (1986). River meanders and channel size. *Journal of Hydrology*, 88 (1-2), pp. 147–164. DOI:10.1016/0022-1694(86)90202-7.
Winterwerp, J.C., Wang, Z.B., Stive, M.J.F., Arends, A., Jeuken, M.-C.J.L., Kuijper, C. & Thoolen, P.M.C. (2001). A new morphological schematization of the Western Scheldt estuary, The Netherlands. In: *Proceedings of the 2nd IAHR symposium on River, Coastal and Estuarine Morphodynamics*, pp. 525–533.
Wolanski, E. (2014). *Estuaries of Australia in 2050 and Beyond*. Springer: Dordrecht, the Netherlands.
Wolanski, E. & Elliott, M. (2015). *Estuarine ecohydrology: An introduction*. Elsevier: Amsterdam, the Netherlands.
Wong, P.P., Losada, I.J., Gattuso, J.-P., Hinkel, J., Khattabi, A., McInnes, K.L., Saito, Y. & Sallenger, A. (2014). Climate Change 2014: Impacts, Adaptation, and Vulnerability. Part A: Global and Sectoral Aspects. Contribution of

Working Group II to the Fifth Assessment Report of the Intergovernmental Panel on Climate Change. In: ed. by C.e.a. Field. Cambridge University Press: Cambridge, United Kingdom. Chap. Coastal systems and low-lying areas, pp. 361–409.
Wood, L.J. (2004). Predicting tidal sand reservoir architecture using data from modern and ancient depositional systems, integration of outcrop and modern analogs in reservoir modeling. *AAPG Memoir*, 80, pp. 45–66.
Wright, L., Coleman, J.M. & Thom, B.G. (1973). Processes of channel development in a high-tide-range environment: Cambridge Gulf-Ord River Delta, Western Australia. *The Journal of Geology*, 81 (1), pp. 15–41.
Wu, F.-C., Shao, Y.-C. & Chen, Y.-C. (2011). Quantifying the forcing effect of channel width variations on free bars: Morphodynamic modeling based on characteristic dissipative Galerkin scheme. *Journal of Geophysical Research: Earth Surface*, 116 (F3). DOI:10.1029/2010JF001941.
Xing, F., Meselhe, E.A., Allison, M.A. & Weathers, H.D. (2017). Analysis and numerical modeling of the flow and sand dynamics in the lower Song Hau channel, Mekong Delta. *Continental Shelf Research*, 147, pp. 62–77. DOI:10.1016/J.CSR.2017.08.003.
Yalin, M. (1971). On the formation of dunes and meanders. In: *Proceedings of the 14th Congress of the International Association for Hydraulic Research*. Vol. 3, pp. 101–108.
Yang, S.L., Zhang, J., Zhu, J., Smith, J.P., Dai, S.B., Gao, A. & Li, P. (2005). Impact of dams on Yangtze River sediment supply to the sea and delta intertidal wetland response. *Journal of Geophysical Research: Earth Surface*, 110 (F3), pp. 1–12. DOI:10.1029/2004JF000271.
Yap, W.Y. & Lam, J.S.L. (2013). 80 million-twenty-foot-equivalent-unit container port? Sustainability issues in port and coastal development. *Ocean & Coastal Management*, 71, pp. 13–25. DOI:10.1016/J.OCECOAMAN.2012.10.011.
Yoshida, S., Johnson, H.D., Pye, K. & Dixon, R.J. (2004). Transgressive changes from tidal estuarine to marine embayment depositional systems: The Lower Cretaceous Woburn Sands of southern England and comparison with Holocene analogs. *AAPG bulletin*, 88 (10), pp. 1433–1460. DOI:10.1306/05140403075.
Yuan, R. & Zhu, J. (2015). The effects of dredging on tidal range and saltwater intrusion in the Pearl River Estuary. *Journal of Coastal Research*, 31 (6), pp. 1357–1362. DOI:10.2112/JCOASTRES-D-14-00224.1.
Zhou, Z., Olabarrieta, M., Stefanon, L., D'Alpaos, A., Carniello, L. & Coco, G. (2014). A comparative study of physical and numerical modeling of tidal network ontogeny. *Journal of Geophysical Research: Earth Surface*, 119 (4), pp. 892–912. DOI:10.1002/2014JF003092.
Zhou, Z., Coco, G., Townend, I., Gong, Z., Wang, Z.B. & Zhang, C. (2018). On the stability relationships between tidal asymmetry and morphologies of tidal basins and estuaries. *Earth Surface Processes and Landforms*, 43 (9), pp. 1943–1959. DOI:10.1002/ESP.4366.
Zolezzi, G., Luchi, R. & Tubino, M. (2012). Modeling morphodynamic processes in meandering rivers with spatial width variations. *Reviews of Geophysics*, 50 (4), pp. 1–24. DOI:10.1029/2012RG000392.

Acknowledgements

De afgelopen vier jaar was als de ontwikkeling van een estuarium: verbreding vanaf een initeel smalle geul, gevolgd door alternerende banken met hier en daar een drempel in de hoofdgeul, quasi-periodisch verbredend, maar geforceerd om de diepte in te gaan waar geologisch begrensd en constant onderhevig aan verandering. Als ik aan mijn PhD denk, dan denk ik regelmatig aan Catullus' *Odi et amo*. Ik heb geleerd om dat laatste de overhand te laten nemen, mede door de fijne groep collega's, vrienden en familie om me heen. Ik kijk terug op een aantal leerzame jaren, waarin ik, naast alle kennis en skills, veel geleerd heb over wat me gelukkig maakt, wat voor mij belangrijk is in werk en hoe ik daarbij het beste uit mezelf haal.

Het getij

Maarten, jij was het getij in mijn estuarium: constant heen en weer aan het stromen en zelden beneden het begin van beweging. Jij herverdeelde het zand, vormde de zandbanken met af en toe een (on)succesvolle bifurcatie. Soms stormde je mijn kamer binnen als een vloedstroom, en ook al ebde het getij daarna langzaam weer weg, je energie, ideeën en kennis lieten altijd een imprint achter op het bankpatroon van mijn estuarium. In de Bachelor Aardwetenschappen was jij degene die me deed realiseren dat ik de juiste studie volgde en ervoor zorgde dat ik een passie ontwikkelde voor water en zand. Gesprekken met jou leidden altijd tot nieuwe inzichten en ideeën, en zijn daarmee erg belangrijk geweest voor de resultaten in dit proefschrift en mijn professionele ontwikkeling.

De zandbanken

Daarnaast hebben de volgende mensen een directe bijdrage geleverd aan het onderzoek in dit proefschrift: **Barend, George, Gerben, Harm Jan, Lisanne, Maarten (van der Vegt), Sanja, Tjalling, Tjeerd** en **Wout**. **Maarten**, je hebt een belangrijke rol gespeeld bij het begrijpen van de natuurkunde: in het begin de stabiliteitstheorie en later met het coderen van het eendimensionale model. **Tjalling**, je hebt me altijd en op alle vlakken geholpen om verder te komen en beter te worden in het onderzoek, telkens met een glimlach en een knipoog. **Lisanne**, vanaf het begin waren we maatjes en hebben we samen zorg gedragen voor de experimenten in de Metronoom. **Tjeerd**, fijn dat je me hebt uitgedaagd om mijn kennis toe te passen op een, zoals je het zelf zegt, 'spannend' vraagstuk. **George Schramkowski**, bedankt voor het beschikbaar maken en uitleggen van je stabiliteitscode. **Wout**, onze samenwerking was altijd efficiënt en effectief en zodoende hebben we samen een hoop bereikt, maar we namen ook altijd de tijd om bij te kletsen of grappen. **Barend**, bedankt voor de prettige samenwerking en samen studenten begeleiden was altijd leuk. **Gerben**, bedankt voor je bijdrage aan de schaling van de golven in de Metronoom. **Harm Jan**, ik ben blij dat we aan het einde van mijn promotie nog een aantal projecten samen hebben kunnen doen en vond het prettig om samen te werken. **Sanja**, lukt het al om deze tekst in het Nederlands te lezen? Инспирисала си ме и постала мој јако добар пријатељ. Увек нам је лепо када идемо на **Муриелине** часове плеса.

I would like to thank my examination committee: **Stefano Lanzoni, Ian Townend, Huib de Swart, Tjeerd Bouma, Zheng Wang** and **Maarten van der Vegt**. Thank you for devoting the time to evaluate my thesis, and acting as opponent during the public defence.

Andy, Bente, Bram, Erik, Jana, Joyce, Kaspar, Lonneke, Marieke, Matthijs, Pauline, Steven, Steye en **Thijs**: bedankt dat jullie met jullie BSc en MSc projecten een bijdrage hebben geleverd aan ons onderzoek. De meeste projecten waren mede door jullie zo succesvol dat het werk uiteindelijk in een publicatie terecht kwam of nog zal komen.

Omdat ons project onderdeel was van het NWO-domein Toegepaste en Technische Wetenschappen (TTW), hadden we halfjaarlijks overleg met de zogenaamde gebruikerscommissie, waarin we de voortgang van het project rapporteerden en vervolgens kansen voor toepassing bespraken. Leden van de gebruikerscommssie: bedankt voor jullie positieve en stimulerende reacties op ons onderzoek, het aandragen van data en suggesties voor verder onderzoek en discussies over de inzetbaarheid van het onderzoek. In het bijzonder wil ik graag nog **Marco** en **Gert-Jan** bedanken voor hulp bij het aanleveren van data voor de Westerschelde en het organiseren van de excursies op de Westerschelde, **Jelmer** voor de leuke en leerzame tijd die ik bij Arcadis heb doorgebracht en **Petra** voor gesprekken die bijdroegen aan mijn loopbaanoriëntatie.

Kim, je kwam in de Zonneveldvleugel regelmatig mijn kamer binnen om even te kletsen, soms gevolgd door (on)gevraagd advies. Als ik het me goed herinner, heb jij me destijds gemotiveerd om financiering aan te vragen om de toolbox verder uit te kunnen werken, wat uiteindelijk ook gelukt is. **Tanya, Jouke** en **Rob**, bedankt voor de goede tijd samen in Myanmar. **Sepehr** en **Maarten**, bedankt voor het leuke veldwerk samen op de Mekong in Vietnam.

Verder wil ik graag al mijn collega's bij het Veldwerk Frankrijk bedanken voor de gezellige tijd. Mede daardoor was het ieder jaar weer een heel leuke onderwijstaak. En wanneer krijg je nou de kans om met collega's in een jaccuzi te zitten? **Philip, Judith, Anne, Lisanne**, ik heb het over jullie. Door al het onderwijs dat ik verzorgd heb, kon ik in 2016 mijn BKO halen. **Martin** en **Maarten** hebben een belangrijke rol gespeeld bij het mogelijk maken hiervan: bedankt daarvoor. Mijn kamer in de Zonneveldvleugel was tevens lange tijd tegenover die van **Martin**, wat leidde tot gezellige werkonderbrekingen, waarbij regelmatig tegeltjeswijsheden van Martin aan bod kwamen.

Onze onderzoeksgroep wil ik bedanken voor alle gezelligheid op werk en daarbuiten. Specifiek de mensen met wie we regelmatig Potluck diners (of varianten daarop) organiseerden of wat gingen drinken na werktijd. Ik kijk ook terug op een gezellige en sucesvolle tijd met de andere PhDs die deel uit maakten van de GEO PhD council. Dank aan iedereen die bij heeft gedragen aan het Latex format voor proefschriften binnen ons departement, onder andere **Eveline, Lisanne, Tjalling** en **Wouter**. **Anne**, fijn dat je deel uit maakte van ons vici-groepje en altijd open stond voor een gesprek of inhoudelijke discussie. **Jana** and **Will**, I am very happy you guys joined our group somewhat later and I particularly enjoyed the drinks and sports together. **Sanja, Muriel** en **Steven**, ik ben blij dat ik jullie beter heb leren kennen en dat we goede vrienden zijn geworden. **Steven**, bedankt voor je hulp bij het controleren van teksten in de laatste fase. **Muriel**, bedankt dat je **Sanja** en mij geïnspireerd hebt om te gaan dansen. **Lisanne**, wat hebben wij veel meegemaakt samen, zowel op werk als daarbuiten. In de karaokebar in Ho Chi Minhstad met **Hung**, op Phu Quoc op de scooter of ernaast (oeps), met de fiets rondom Minneapolis en met het vliegtuigje over de Mississippi. We konden elkaar steunen als we het even niet meer wisten en hebben vaak samen gelachen, om van alles eigenlijk.

De zijtak

Technici, zonder jullie hulp zouden onze experimenten niet gedraaid hebben. **Marcel, Arjan, Chris, Henk, Bas** en **Mark**, bedankt voor al jullie hulp en de gezellige manier waarop dit ging. **Chris**, jij was zo'n warme aanwezigheid in (de kelder van) de Zonneveldvleugel. In ons laatste contact stuurde je me onder andere: "Samen is leuk." Daarna moest je helaas gaan.

De oevers

Inge en **Wiba**, bedankt voor de afgelopen jaren samen. Het maakte niet uit of ik, of een van jullie, nu weer eens aan de andere kant van de wereld zat of niet. Onze cross-sekse relatie was altijd maximaal drie toetsen van me verwijderd. Fijn dat we alles konden delen en elkaar konden adviseren en steunen. **Inge**, wat kunnen we goed praten en bedankt voor de mooie reis langs de Severn. Vanaf de eerste dag Aardwetenschappen zijn we bevriend geraakt en ik ben dankbaar voor alles wat we samen hebben

meegemaakt. **WiBa**, zelfs inhoudelijk vond je het leuk om me te helpen wanneer mogelijk en ik ben blij met je adviezen. Het heeft me geholpen dat jij in dezelfde periode ook bezig was met je PhD en we onze ervaringen konden delen.

Iris en **Daniël**, ik heb me altijd thuis gevoeld bij jullie. Samen wonen met jullie in Utrecht was een feestje en als jullie er bij zijn is het nooit saai. Jullie positieve instelling en nuchtere kijk op zaken werkt aanstekelijk. Een groot deel van dit hoofdstuk heb ik geschreven terwijl ik bij jullie in Londen was, waar jullie me een kant van Londen lieten zien die ik nog niet eerder gezien had. Het was fijn om deel uit te maken van jullie gezellige en warme vriendengroep. **Iris**, nu ben jij aan de beurt. Veel succes en hopelijk plezier met je PhD: ik heb er alle vertrouwen in dat je het tot een goed einde zal brengen.

Anne, ik heb je de afgelopen paar jaar wat minder vaak gezien, maar in de tijd dat we samen hebben gewoond, heb ik erg veel van je geleerd en daar ben ik je erg dankbaar voor. **Laura, Karlijn** en **Carolien**, bedankt voor alle gezellige middagen en avonden.

Armando en **Irene**, bedankt dat jullie me fit hielden op de sportschool. Regelmatig sporten was een belangrijk element voor mijn productiviteit.

Pascalla en **Zefanja**, bedankt voor de leuke uitjes en weekenden die we samen hebben doorgebracht. **Carlos**, met jou kon je bruggen bouwen, of gitaar leren spelen, en volgens mij heb je me ook geïnspireerd en gemotiveerd om te (blijven) schrijven. Ik mis je, maar hoop dat je op een fijne plek bent. **Miranda, Liesbeth** en **Sanne**, ik ben blij dat we elkaar in de afgelopen jaren vaker zijn gaan zien om samen te eten, te kletsen of samen een bordspel te doen.

Opa en **oma**, jullie zijn erg belangrijk voor me geweest in mijn jeugd. Mijn werkdiscipline stamt wellicht voor een belangrijk deel af van wat ik bewust en onbewust van jullie heb meegekregen. Sinds ik naar Utrecht verhuisde, hebben we elkaar minder vaak gezien, maar ik kijk met veel plezier terug op alles wat we samen gedaan hebben. Jammer dat je dit niet meer hebt kunnen meemaken, oma. Je zou erg trots zijn geweest.

Lex, wat hebben we een fijne en leuke tijd gehad samen. Ik ben je erg dankbaar voor alles wat je me geleerd hebt over milieu, klimaat en duurzaamheid en daarnaast was je zorgzaamheid een grote steun tijdens mijn PhD.

De rivier

Stefan en **Rianne**, we waren alle drie bezige bijtjes de afgelopen jaren en het was jammer dat jullie net te ver weg woonden om wat vaker af te spreken of samen te eten. Ondanks dat hebben we samen mooie vakanties meegemaakt, hebben we elkaar geholpen en gesteund wanneer nodig en vonden we het altijd leuk om samen bordspellen te doen.

Papa en **mama**, bedankt dat jullie er altijd voor me waren. Jullie hebben me altijd gemotiveerd en ondersteund in wat ik deed en van plan was te gaan doen. Het was fijn om regelmatig een paar dagen thuis te zijn en jullie zorg maakte thuis ook een hele prettige werkplek. We hebben zelfs nog samen een artikel gepubliceerd over schooltuinieren en ik ben erg trots dat we dat samen voor elkaar kregen. **Papa**, je bent een voorbeeld voor me en hebt altijd je passie en enthousiasme voor onderzoek aan mij overgedragen. **Mama**, het was fijn dat we samen gegroeid zijn in een lastige periode en je onvoorwaardelijke liefde maakte thuis altijd een warme en fijne plek. Ik hoop dat we samen nog veel mooie jaren tegemoet gaan.

List of Publications

Refereed journal articles as first author

Leuven, J.R.F.W., Pierik, H.J., van der Vegt, M., Bouma, T.J. & Kleinhans, M.G. (2019). Sea-level rise induced threats depend on size of tide-influenced estuaries worldwide, [Revision submitted to *Nature Climate Change*]

Leuven, J.R.F.W. & Kleinhans, M.G. (2019). Incipient tidal bars, [Revision submitted to *Journal of Geophysical Research: Earth Surface*]

Leuven, J.R.F.W., van Maanen, B., Lexmond, B., van der Hoek, B., Spruijt, M. & Kleinhans, M.G. (2018). Dimensions of fluvial-tidal meanders: Are they disproportionally large? *Geology*, 46 (10), pp. 923–926. DOI:10.1130/G45144.1

Leuven, J.R.F.W., de Haas, T., Braat, L. & Kleinhans, M.G. (2018). Topographic forcing of tidal sand bar patterns for irregular estuary planforms. *Earth Surface Processes and Landforms*, 43 (1), pp. 172–186. DOI:10.1002/esp.4166

Leuven, J.R.F.W., Selaković, S. & Kleinhans, M.G. (2018). Morphology of bar-built estuaries: Empirical relation between planform shape and depth distribution. *Earth Surface Dynamics*, 6 (3), pp. 763–778. DOI:10.5194/esurf-6-763-2018

Leuven, J.R.F.W., Verhoeve, S.L., van Dijk, W.M., Selaković, S. & Kleinhans, M.G. (2018). Empirical assessment tool for bed levels, flow velocity and salinity in estuaries based on tidal amplitude and space-borne imagery. *Remote Sensing*, 10 (12), pp. 1–32. DOI:10.3390/rs10121915

Leuven, J.R.F.W., Braat, L., van Dijk, W.M., de Haas, T., van Onselen, E., Ruessink, B.G. & Kleinhans, M.G. (2018). Growing forced bars determine nonideal estuary planform. *Journal of Geophysical Research: Earth Surface*, 123 (11), pp. 2971–2992. DOI:10.1029/2018JF004718

Leuven, J.R.F.W., Rutenfrans, A.H.M., Dolfing, A.G. & Leuven, R.S.E.W. (2018). School gardening increases knowledge of primary schoolchildren on edible plants and preference for vegetables. *Food Science and Nutrition*, 6 (7), pp. 1960–1967. DOI:10.1002/fsn3.758

Leuven, J.R.F.W., Kleinhans, M.G., Weisscher, S.A.H. & van der Vegt, M. (2016). Tidal sand bar dimensions and shapes in estuaries. *Earth-Science Reviews* (invited review), 161, pp. 204–223. DOI:10.1016/j.earscirev.2016.08.004

Refereed journal articles as co-author

van Dijk, W.M., **Leuven, J.R.F.W.**, Cox, J., Cleveringa, J., Taal, M., Hiatt, M., Sonke, W., Verbeek, K., Speckmann, B. & Kleinhans, M.G. (2019). The effect of current dredging and disposal activity on morphodynamics of estuaries. [Submitted to *Geophysical Research Letters*]

van Dijk, W.M., **Leuven, J.R.F.W.**, Martens, P.S., Vlaming, J. & Kleinhans, M.G. (2019). Effect of dredging and disposal on tidal bifurcations and flow asymmetry. [To be submitted to *Water Resources Research*]

Pierik, H.J., **Leuven, J.R.F.W.**, Busschers, F.S., Hijma, M.P. & M. G. Kleinhans (2019). Depth-limiting resistant layers tune the shape and tidal bar pattern of Holocene alluvial estuaries. [Submitted to *Nature Geoscience*]

Dolfing, A.G., **Leuven, J.R.F.W.** & Dermody, B.J. (2019). The effects of network topology, climate variability and shocks on the evolution and resilience of a food trade network. *PLoS ONE*, 14 (3), pp. 1–18. DOI:10.1371/journal.pone.0213378

Braat, L., **Leuven, J.R.F.W.**, Lokhorst, I.R., Kleinhans, M.G. (2019). Effects of estuarine mudflat formation on tidal prism and large-scale morphology in experiments. *Earth Surface Processes and Landforms*, 44 (2), pp. 417–432. DOI:10.1002/esp.4504.

Lokhorst, I.R., Braat, L., **Leuven, J.R.F.W.**, Baar, A.W., van Oorschot, M., Selaković, Kleinhans, M.G. (2018). Morphological effects of vegetation on the fluvial-tidal transition in Holocene estuaries. *Earth Surface Dynamics*, 6 (4), pp. 883–901. DOI:10.5194/esurf-6-883-2018.

van Dijk, W.M., Mastbergen, D.R., van den Ham, G.A., **Leuven, J.R.F.W.** & Kleinhans, M.G. (2018), Location and probability of shoal margin collapses in a sandy estuary. *Earth Surface Processes and Landforms*, 43 (11), pp. 2342–2357. DOI:10.1002/esp.4395.

Kleinhans, M.G., van der Vegt, M., **Leuven, J.R.F.W.**, Braat, L., Markies, H., Simmelink, A., Roosendaal, C., van Eijk, A., Vrijbergen, P. & van Maarsenveen, M. (2017) Turning the tide: comparison of tidal flow by periodic sealevel fluctuation and by periodic bed tilting in the Metronome tidal facility. Earth Surface Dynamics, 5 (4), pp. 731–756. DOI:10.5194/esurf-5-731-2017.

Braat, L., van Kessel, T., Leuven, J.R.F.W. & Kleinhans, M.G. (2017). Effects of mud supply on large-scale estuary morphology and development over centuries to millennia. *Earth Surface Dynamics*, 5 (4), pp. 617–652. DOI:10.5194/esurf-5-617-2017.

Kleinhans, M.G., **Leuven, J.R.F.W.**, Braat, L. & Baar, A.W. (2017). Scour holes and ripples occur below the hydraulic smooth to rough transition of movable beds. *Sedimentology*, 64 (5), pp. 1381–1401. DOI:10.1111/sed.12358.

de Haas, T., Braat, L., **Leuven, J.R.F.W.**, Lokhorst, I.R. & Kleinhans, M.G. (2015), Effects of debris flow composition on runout, depositional mechanisms, and deposit morphology in laboratory experiments, *Journal of Geophysical Research: Earth Surface*, 120 (9), pp. 1949–1972. DOI:10.1002/2015JF003525.

Maher, D.T., Santos, I.S., **Leuven, J.R.F.W.**, Oakes, J.M., Erler, D.V., Carvalho, M.C. & Eyre, B.D. (2013). Novel use of cavity ring-down spectroscopy to investigate aquatic carbon cycling from microbial to ecosystem scales. *Environmental Science and Technology*, 47 (22), pp. 12938–12945. DOI:10.1021/es4027776.

Other publications

Steijn, R.C., Cleveringa, J., **Leuven, J.R.F.W.**, van der Baan, J. & van der Zanden, J.J.G. (2019). Extreme coastal dynamics of Sittaung Estuary (Myanmar), Conference paper, *International conference on Asian and Pacific Coasts*, September 2019, Hanoi, Vietnam.

Steijn, R.C., Cleveringa, J., van der Baan, J., Huizer, T. & **Leuven, J.R.F.W.** (2019). Dealing with coastal erosion in the Gulf of Mottama, *Report* C03141.000064R1r1, Arcadis Nederland B.V., Zwolle, the Netherlands.

Kleinhans, M.G., Sonnemans, K., Bolla Pittaluga, M., van der Vegt, M., Braat, L., **Leuven, J.R.F.W.**, Lanzoni, S., Sgarabotto, A., Bogoni, M., Wang Z.B., Tambroni, N., Coco, G. & Todd, D. (2019). Splitting nature at its seams: morphodynamic stability of river and tidal bifurcations, *Proceedings of the HYDRALAB+ Joint User Meeting*, May 2019, Bucharest, Romania.

Leuven, J.R.F.W., Braat, L., & Kleinhans, M.G. (2016). De Metronoom: riviermondingen in schaalexperimenten. *Land + Water: Vakblad voor de praktijk van civiel- en milieutechnici*, 56 (6), pp. 20–21.

Kleinhans, M.G., **Leuven, J.R.F.W.**, Braat, L., van der Vegt, M., van Maarseveen, M., Markies, H., Roosendaal, C. & van Eijk, A. (2016). Reversing tidal flow and estuarine morphodynamics in the Metronome laboratory flume, *Physics of Estuaries and Coastal Seas Conference*, October 2016, Netherlands, PECS proceedings

Selected conference abstracts

Leuven, J.R.F.W., Pierik, H.J., van der Vegt, M., Bouma, T. & Kleinhans, M.G. (2019). A global analysis of the future morphology of estuaries under sea-level rise. *EGU 2019*, Vienna, 7-12 April.

Leuven, J.R.F.W., Pierik, H.J., van der Vegt, M., Bouma, T. & Kleinhans, M.G. (2018). A global analysis of the future morphology of estuaries under sea-level rise. Abstract EP11A-04 presented at *2018 AGU Fall Meeting*, Washington DC., 10-14 December.

Leuven, J.R.F.W., van Maanen, B., Lexmond, B.R., van der Hoek, B.V., Spruijt, M.J. & Kleinhans, M.G. (2017). Dimensions and shapes of tidal-fluvial meanders – are the final meanders of a river unproportionally large? Abstract EP31D-1896 presented at *2017 AGU Fall Meeting*, New Orleans, 11-16 December.

Leuven, J.R.F.W., Verhoeve, S.L., Selaković, S., Bruijns, A.J., van Dijk, W.M. & Kleinhans, M.G. (2017). A tool to estimate bar patterns and flow conditions in estuaries when limited data is available. Abstract EP13E-03 presented at *2017 AGU Fall Meeting*, New Orleans, 11-16 December.

Leuven, J.R.F.W., Braat, L., van Dijk, W.M., de Haas, T. & Kleinhans, M.G. (2017). Bar dynamics and channel junctions in scale-experiments of estuaries. Abstract EP15C-1657 presented at *2017 AGU Fall Meeting*, New Orleans, 11-16 December.

Leuven, J.R.F.W., van Dijk, W.M., Braat, L. & Selaković, S. (2017). Experimental rivers, deltas and estuaries. Presentation at *U.S. Army Corps of Engineers*, Vicksburg, December.

Leuven, J.R.F.W., Braat, L., van Dijk, W.M., Kleinhans, M.G. (2017). Ebb- and flood tidal channels in scale-experiments of estuaries. *RCEM* abstract and poster, Padova, 15-22 September.

Leuven, J.R.F.W., Braat, L., van Dijk, W.M., Kleinhans, M.G. (2017). Ebb- and flood tidal channels in scale-experiments of estuaries. *NCK* abstract and presentation, Den Helder, 15-17 March.

Leuven, J.R.F.W., Braat, L., Weisscher, S.A.H., van der Vegt, M., Kleinhans, M.G. (2016). Tidal bar patterns in estuaries. *SIESD* poster and Summer School Program, Minneapolis.

Leuven, J.R.F.W., Kleinhans, M.G., Weisscher, S.A.H. & van der Vegt, M. (2016). Bar dimensions and bar shapes in estuaries. *EGU 2016*, Vienna, 17-22 April.

Leuven, J.R.F.W., Kleinhans, M.G., Weisscher, S.A.H. & van der Vegt, M. (2016). Bar dimensions and bar shapes in estuaries. *NCK* abstract and presentation, 16-18 March.

Leuven, J.R.F.W., Kleinhans, M.G., Braat, L., van der Vegt, M. (2014). Turning the tide: Experimental estuaries. *NCK* abstract and poster.

About the author

Turn the page to find out more.

Waal

1

Nijmegen

WoesteLand

Conferences

Fieldwork

Travel

Utrecht

3

2

Oude gracht

De Uithof

Utrecht Science Park

DRIFT '66

Universiteit Utrecht

4

Kromme Rijn

Leiden

Delft

Zwolle

According to my parents, my investigations and research started from the moment I was born in the Canisius Wilhelmina Hospital. However, it took about 12 years until my first real involvement with (physical) geography. During my first year at *Stedelijk Gymnasium Nijmegen* I had to organise a summer holiday for my family for Geography. I chose to take my family to Norway.

During my six years on high school I played guitar and was part of multiple bands, music groups and later the school orchestra. In the last two years I switched from guitar to singing. Few people know that I sang Amy Whinehouse's *Valerie* in the The Royal Concertgebouw in Amsterdam. Besides music, I liked to write novels and poetry and was very active as a Harry Potter fan.

I like to play (strategic) board games with friends and family and to go to board game conventions. My collection consists of about 75 games, of which the heaviest is almost 10 kg and the longest takes about a day to play.

In 2009, I moved to Utrecht to study *Earth Sciences* at Utrecht University. Fieldwork in France, Spain and Australia were part of my bachelor program. Patterns of water and sand intrigued me, which explains my continuation with the Master *Earth Surface and Water*. My MSc thesis was about the morphodynamics of estuaries, for which I used a pilot flume in the basement of the Zonneveld Wing. In that period, Maarten Kleinhans obtained funding for his Vici-project on estuaries, in which I enrolled May the 1st, 2015, as a PhD candidate.

I have always been very enthusiastic about teaching. During my studies, I taught 3-day courses in mathematics and geography for high school students at *SSL* (Leiden University). Courses were targeted at passing for their final examinations. Since the start of my PhD, I have been teaching bachelor and master students, and I obtained my university teaching qualification (BKO) in 2016. Teaching tasks included teaching in the yearly fieldwork to France, lecturing in the MSc course on tidal systems and organising multiple work groups.

In 2011-2012 I was the secretary of the student association *Drift '66*. Tim, Inge, WiBa, Rick, Rick and I finalised the merger with the former *U.G.V.* into the *U.A.V.*, which is now the student association for *Earth Sciences*.

As part of my MSc program, I worked at Deltares as an intern on a project of Dirk-Jan Walstra, Joep Storms, Liang Li and Helena van der Vegt. In this project, Fei Chen performed Delft3D model runs of deltas with varying degrees of tidal and fluvial flow and various types of sediment supply. I built analysis tools to study the effect of hydrodynamic and sedimentological forcing on the morphology and stratigraphy of these deltas.

During the last part of my PhD (end of 2018), I collaborated with Jelmer Cleveringa and Rob Steijn in an Arcadis project on bank erosion in the Sittaung Estuary (Myanmar). Here, land is lost by up to 1 km per year, but fortunately we found that the mechanisms and locations where land loss occurs are predictable, allowing for adaptive strategies.

Utrecht University
Faculty of Geosciences
Department of Physical Geography

ISSN 2211-4335